# MODELING NEUROMUSCULAR DISEASES TO DETERMINE MOLECULAR DRIVERS OF PATHOLOGY AND FOR DRUG DISCOVERY

EDITED BY: David Lee Mack, Mark Bothwell, Megan Laura McCain and Alec S. T. Smith

PUBLISHED IN: Frontiers in Cell and Developmental Biology

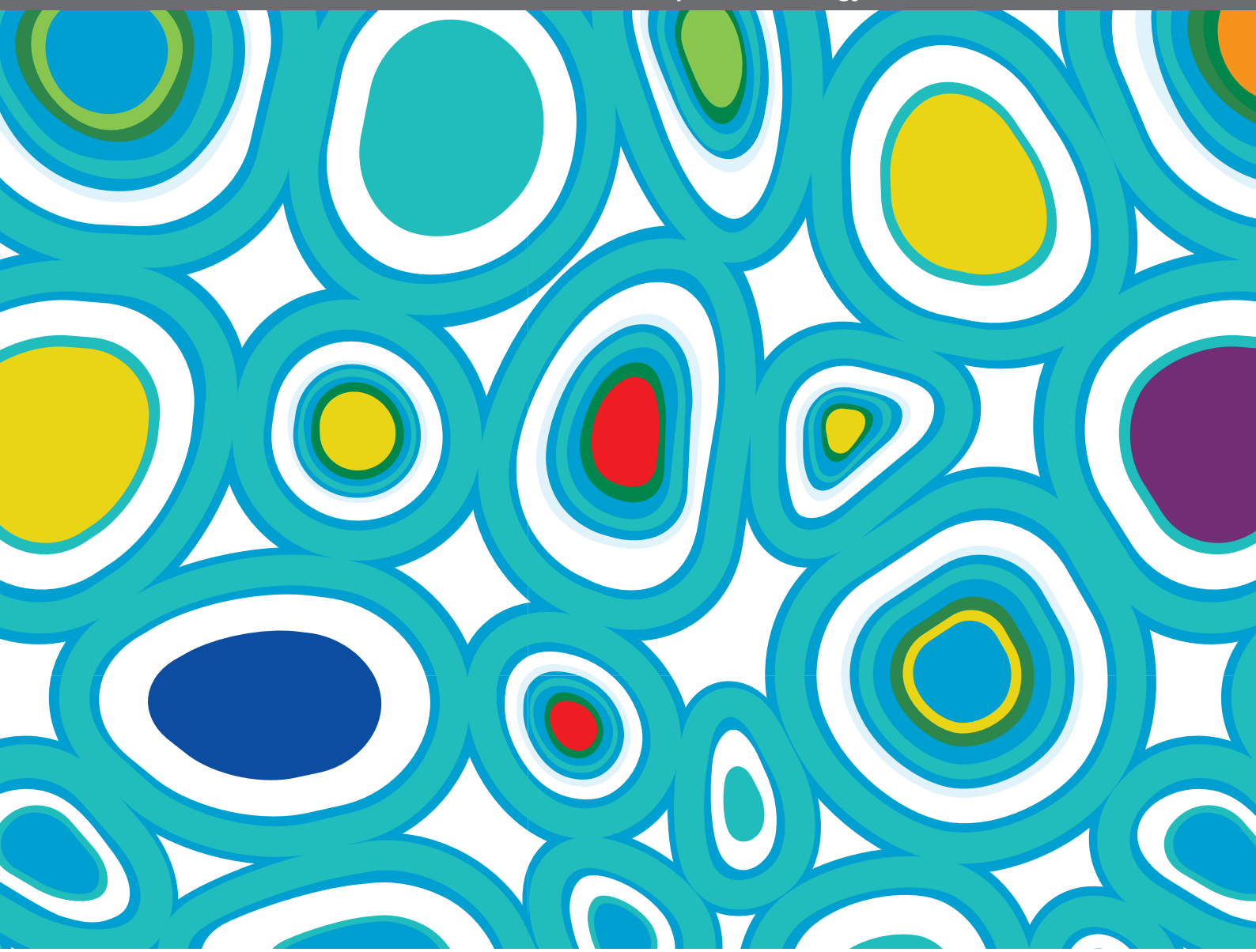

frontiers Research Topics

ISSN 1664-8714
ISBN 978-2-83250-547-2
DOI 10.3389/978-2-83250-547-2

## About Frontiers

Frontiers is more than just an open-access publisher of scholarly articles: it is a pioneering approach to the world of academia, radically improving the way scholarly research is managed. The grand vision of Frontiers is a world where all people have an equal opportunity to seek, share and generate knowledge. Frontiers provides immediate and permanent online open access to all its publications, but this alone is not enough to realize our grand goals.

## Frontiers Journal Series

The Frontiers Journal Series is a multi-tier and interdisciplinary set of open-access, online journals, promising a paradigm shift from the current review, selection and dissemination processes in academic publishing. All Frontiers journals are driven by researchers for researchers; therefore, they constitute a service to the scholarly community. At the same time, the Frontiers Journal Series operates on a revolutionary invention, the tiered publishing system, initially addressing specific communities of scholars, and gradually climbing up to broader public understanding, thus serving the interests of the lay society, too.

## Dedication to Quality

Each Frontiers article is a landmark of the highest quality, thanks to genuinely collaborative interactions between authors and review editors, who include some of the world's best academicians. Research must be certified by peers before entering a stream of knowledge that may eventually reach the public - and shape society; therefore, Frontiers only applies the most rigorous and unbiased reviews.
Frontiers revolutionizes research publishing by freely delivering the most outstanding research, evaluated with no bias from both the academic and social point of view. By applying the most advanced information technologies, Frontiers is catapulting scholarly publishing into a new generation.

## What are Frontiers Research Topics?

Frontiers Research Topics are very popular trademarks of the Frontiers Journals Series: they are collections of at least ten articles, all centered on a particular subject. With their unique mix of varied contributions from Original Research to Review Articles, Frontiers Research Topics unify the most influential researchers, the latest key findings and historical advances in a hot research area! Find out more on how to host your own Frontiers Research Topic or contribute to one as an author by contacting the Frontiers Editorial Office: frontiersin.org/about/contact

# MODELING NEUROMUSCULAR DISEASES TO DETERMINE MOLECULAR DRIVERS OF PATHOLOGY AND FOR DRUG DISCOVERY

Topic Editors:
**David Lee Mack,** University of Washington, United States
**Mark Bothwell,** University of Washington, United States
**Megan Laura McCain,** University of Southern California, United States
**Alec S. T. Smith,** University of Washington, United States

**Citation:** Mack, D. L., Bothwell, M., McCain, M. L., Smith, A. S. T., eds. (2022). Modeling Neuromuscular Diseases to Determine Molecular Drivers of Pathology and for Drug Discovery. Lausanne: Frontiers Media SA.
doi: 10.3389/978-2-83250-547-2

# Table of Contents

frontiers | Frontiers in Cell and Developmental Biology

TYPE Editorial
PUBLISHED 05 October 2022
DOI 10.3389/fcell.2022.1017356



OPEN ACCESS

EDITED AND REVIEWED BY
Atsushi Asakura,
University of Minnesota Twin Cities, United States

*CORRESPONDENCE
Alec S. T. Smith,
astsmith@uw.edu

SPECIALTY SECTION
This article was submitted to Stem Cell Research, a section of the journal Frontiers in Cell and Developmental Biology

RECEIVED 11 August 2022
ACCEPTED 12 September 2022
PUBLISHED 05 October 2022

CITATION
Smith AST, McCain ML, Bothwell M and Mack DL (2022), Editorial: Modeling neuromuscular diseases to determine molecular drivers of pathology and for drug discovery.
*Front. Cell Dev. Biol.* 10:1017356.
doi: 10.3389/fcell.2022.1017356



# Editorial: Modeling neuromuscular diseases to determine molecular drivers of pathology and for drug discovery

Alec S. T. Smith[1,2]*, Megan L. McCain[3,4], Mark Bothwell[1,2] and David L. Mack[1,2,5,6]

[1]Department of Physiology and Biophysics, University of Washington, Seattle, WA, United States, [2]Institute for Stem Cell and Regenerative Medicine, University of Washington, Seattle, WA, United States, [3]Department of Biomedical Engineering, USC Viterbi School of Engineering, University of Southern California, Los Angeles, CA, United States, [4]Department of Stem Cell Biology and Regenerative Medicine, Keck School of Medicine, University of Southern California, Los Angeles, CA, United States, [5]Department of Bioengineering, University of Washington, Seattle, WA, United States, [6]Department of Rehabilitation Medicine, University of Washington, Seattle, WA, United States

KEYWORDS

**neuromuscular disease (NMD), disease modeling, iPSC (induced pluripotent stem cell), cell line (C2C12), therapy screening, *in vitro* versus *in vivo***

Editorial on the Research Topic
Modeling neuromuscular diseases to determine molecular drivers of pathology and for drug discovery

Recent advances in gene editing, organoid technologies, tissue engineering, and neuromuscular differentiation techniques from induced pluripotent stem cells (iPSCs) and other cell sources have produced great strides in modeling neuromuscular diseases. But which models are most appropriate for a given condition? Dogmatic allegiance to specific models that inadequately account for the complexity and/or heterogeneity of a given disease can hamper efforts to predict useful drug targets and screen novel compound efficacy. Perhaps what is needed is a greater willingness to critically appraise new models to understand what they do well, where they fall short, and how they can be leveraged, hand-in-hand, to gain a more holistic understanding of neuromuscular disease processes across spatial scales. This is the goal of our recent Research Topic presented in *Frontiers in Cell and Developmental Biology*. Here, we have collected manuscripts that detail recent advances in modeling neuromuscular tissues and diseases while simultaneously addressing the strengths, weaknesses, and design considerations that should be evaluated when deciding on the suitability of a given model for informing on disease etiology.

Feliciano et al. describe the use of CRISPR gene editing to create an iPSC-based model of Charcot-Marie-Tooth disease (type 2E). Neurons derived from this source recapitulate known pathologic phenotypes observed in patients, including the aberrant accumulation

of neurofilament light chain protein in neuronal cell bodies. Inactivation of the diseased *NEFL* allele *via* gene editing ameliorates the disease phenotype observed in the dish, offering validation of allele-specific editing as a method to treat this peripheral neuropathy. This manuscript offers convincing evidence supporting the use of CRISPR and iPSC-derived neurons as models and screening platforms for inheritable peripheral neuropathic diseases. However, we invite readers to simultaneously consider data presented in Smith et al., which details how CRISPR editing and clonal expansion of iPSCs can lead to the emergence of potentially misleading phenotypes in stem cell-based models of ALS. This manuscript highlights the need to carefully consider data from multiple clones and lines generated using different editing techniques to gain confidence that the phenotype observed is due to the specific mutation in question and not an artifact of the history of a given cell line. By showcasing these papers together, we draw attention both to the potential for novel iPSC-based preclinical models to advance therapeutics as well as the possible difficulties associated with their use in identifying molecular drivers of pathology.

Our Research Topic also presents new culture technologies and discusses their potential for improving cell-based models of neuromuscular disease. Barthelemy et al. detail the use of micromolded hydrogel surfaces to enhance the differentiation and organization of myotubes reprogrammed from skin fibroblasts of muscular dystrophy patients. Such engineered substrates also extend the culture lifetime of patient-derived myotubes, enabling more comprehensive evaluation of patient-specific defects in myogenesis and responses to treatment by antisense oligonucleotides. A complementary approach used to pattern culture surfaces for neurons is presented by Capel et al. who demonstrate that aerosol jet printing can be used to develop intricate neuronal patterns on 2D surfaces. Integration of such complimentary technologies in the future may enable greater control of neuron-muscle interactions *in vitro* to better facilitate the study of neuromuscular function in health and disease. Alternatively, spatial organization of both muscle and neurons can be achieved using compartmentalized chambers, as demonstrated by Smith et al. Here, the authors developed functional neuromuscular junctions (NMJs) in a compartmentalized cell culture device and then examined the role of complement activation in contributing to NMJ functional decline in a cell-based model of Myasthenia Gravis.

The work of Barthelemy, Feliciano, and Smith, along with their co-authors, highlight that obtaining a cell type expressing a specific mutation may be insufficient to accurately model specific disease phenotypes. How the cells are maintained in culture and allowed to interact is of critical importance to ensure the collection of clinically-meaningful data. In support of this idea, we provide a review of design considerations for the development of multi-organ culture models by Malik et al. While not specifically focused on neuromuscular tissues, this review provides valuable discussion of design considerations for complex cell-based models, including organ scaling, vascular dimensions, and appropriate flow rates, all of which can significantly impact the translational potential of the output data.

Despite a great deal of focus on iPSCs in recent years, significant advances in neuromuscular biology continue to be made using immortalized cell lines. In particular, the C2C12 mouse myoblast line has been a driving force of *in vitro* muscle biology for decades. We include work by Shen et al. detailing the use of C2C12s to evaluate *Postn* inhibition as a treatment for myotonic dystrophy (type 1). The presented data demonstrate that *Postn* knockdown enhances myogenesis, potentially *via* modulation of the TGF-β/Smad3 pathway. Similarly, Barrett et al. use C2C12s to investigate the molecular mechanisms underpinning the development of proprioceptive intrafusal fibers in skeletal muscle. These studies illustrate how deeper elucidation of basic muscle biology contributes to identifying molecular drivers of pathologies and underscore that important insights can still be achieved using long-established neuromuscular cell lines that are generally more scalable and uniform than current iPSC derivatives.

The primary research presented in this Research Topic focuses on cell-based models of neuromuscular tissues, which is not intended to detract from the value and importance of *in vivo* models but largely reflects the expertise of the editors. To bring a more balanced perspective, we have invited reviews discussing the relative values and weaknesses of different *in vitro* and *in vivo* models of neuromuscular tissues and diseases. First, Fralish et al. provide a comprehensive overview of available NMJ models in the context of modeling a range of incurable neuromuscular disease states. Second, Hines et al. deliver a perspective on the development of integrative workflows combining human cell-based models with animals to elucidate the complex biology of aminoacyl tRNA synthetase mutant forms of Charcot-Marie-Tooth disease. Third, Hekmatnejad and Rudnicki review transplantation assays as tools for examining muscle stem cell (satellite cell) function *in vivo* as a means to improve transplantation efficiency in cell-based therapies for muscle diseases. Approaches that leverage the respective advantages of *in vitro* and *in vivo* models are likely to become a standard paradigm for neuromuscular disease modeling because they enable rigorous investigations from the molecular level to the complete organism.

The works collected here attempt to highlight recent innovations in neuromuscular disease modeling and re-emphasize that no single model offers the perfect platform to study the entirety of neuromuscular biology and disease. In fact,

we must be critical and honest about the strengths and weaknesses of each model for the field to progress. By combining multiple preclinical models, we can obtain comprehensive and multi-scale phenotypic data that better predict which therapies have the greatest chances of clinical success. Hopefully, the ongoing development and adoption of innovative and integrative preclinical workflows will help increase the number of compounds succeeding during clinical trials and ultimately improve patient outcomes.

## Author contributions

All authors listed have made a substantial, direct, and intellectual contribution to the work and approved it for publication.

## Conflict of interest

The authors declare that the research was conducted in the absence of any commercial or financial relationships that could be construed as a potential conflict of interest.

## Publisher's note

frontiers in Cell and Developmental Biology

ORIGINAL RESEARCH
published: 16 August 2021
doi: 10.3389/fcell.2021.723023

# Allele-Specific Gene Editing Rescues Pathology in a Human Model of Charcot-Marie-Tooth Disease Type 2E

*Carissa M. Feliciano[1,2], Kenneth Wu[2], Hannah L. Watry[2], Chiara B. E. Marley[1,2], Gokul N. Ramadoss[2,3], Hana Y. Ghanim[2], Angela Z. Liu[2,4], Lyandysha V. Zholudeva[2], Todd C. McDevitt[2,5], Mario A. Saporta[6], Bruce R. Conklin[2,4,7,8]* and Luke M. Judge[1,2]**

[1] Department of Pediatrics, University of California, San Francisco, San Francisco, CA, United States, [2] Gladstone Institutes, San Francisco, CA, United States, [3] Biomedical Sciences Ph.D. Program, University of California, San Francisco, San Francisco, CA, United States, [4] Department of Ophthalmology, University of California, San Francisco, San Francisco, CA, United States, [5] Department of Bioengineering and Therapeutic Sciences, University of California, San Francisco, San Francisco, CA, United States, [6] Department of Neurology, Miller School of Medicine, University of Miami, Miami, FL, United States, [7] Department of Medicine, University of California, San Francisco, San Francisco, CA, United States, [8] Innovative Genomics Institute, Berkeley, CA, United States

Many neuromuscular disorders are caused by dominant missense mutations that lead to dominant-negative or gain-of-function pathology. This category of disease is challenging to address via drug treatment or gene augmentation therapy because these strategies may not eliminate the effects of the mutant protein or RNA. Thus, effective treatments are severely lacking for these dominant diseases, which often cause severe disability or death. The targeted inactivation of dominant disease alleles by gene editing is a promising approach with the potential to completely remove the cause of pathology with a single treatment. Here, we demonstrate that allele-specific CRISPR gene editing in a human model of axonal Charcot-Marie-Tooth (CMT) disease rescues pathology caused by a dominant missense mutation in the neurofilament light chain gene (*NEFL*, CMT type 2E). We utilized a rapid and efficient method for generating spinal motor neurons from human induced pluripotent stem cells (iPSCs) derived from a patient with CMT2E. Diseased motor neurons recapitulated known pathologic phenotypes at early time points of differentiation, including aberrant accumulation of neurofilament light chain protein in neuronal cell bodies. We selectively inactivated the disease *NEFL* allele in patient iPSCs using Cas9 enzymes to introduce a frameshift at the pathogenic N98S mutation. Motor neurons carrying this allele-specific frameshift demonstrated an amelioration of the disease phenotype comparable to that seen in an isogenic control with precise correction of the mutation. Our results validate allele-specific gene editing as a therapeutic approach for CMT2E and as a promising strategy to silence dominant mutations in any gene for which heterozygous loss-of-function is well tolerated. This highlights the potential for gene editing as a therapy for currently untreatable dominant neurologic diseases.

**Keywords: induced pluripotent stem cells, Charcot-Marie-Tooth, neuropathy, motor neurons, dominant, CRISPR-Cas9, gene editing**

OPEN ACCESS

***Edited by:***
*Megan Laura McCain, University of Southern California, United States*

***Reviewed by:***
*Anthony Brown, The Ohio State University, United States*
*Vincent Timmerman, University of Antwerp, Belgium*
*Florian Barthelemy, University of California, Los Angeles, United States*

****Correspondence:***
*Bruce R. Conklin*
*bconklin@gladstone.ucsf.edu*
*Luke M. Judge*
*luke.judge@ucsf.edu*

***Specialty section:***
*This article was submitted to Stem Cell Research, a section of the journal Frontiers in Cell and Developmental Biology*

***Received:*** *09 June 2021*
***Accepted:*** *22 July 2021*
***Published:*** *16 August 2021*

***Citation:***
*Feliciano CM, Wu K, Watry HL, Marley CBE, Ramadoss GN, Ghanim HY, Liu AZ, Zholudeva LV, McDevitt TC, Saporta MA, Conklin BR and Judge LM (2021) Allele-Specific Gene Editing Rescues Pathology in a Human Model of Charcot-Marie-Tooth Disease Type 2E. Front. Cell Dev. Biol. 9:723023. doi: 10.3389/fcell.2021.723023*

## INTRODUCTION

Charcot-Marie-Tooth disease (CMT), also known as hereditary motor and sensory neuropathy, is one of the most common inherited neurological disorders, affecting approximately 1 in 2,500 people (Reilly et al., 2011). Patients present with muscle weakness and variable sensory symptoms in the distal limbs, which typically progress in a length-dependent manner, affecting the most distal limbs first. CMT can be further classified by the predominantly affected cell type, by clinical electrophysiological testing, and by underlying genetic cause (Rossor et al., 2015). The demyelinating forms of the disease (CMT1, autosomal dominant and CMT4, autosomal recessive) primarily affect Schwann cells and are characterized by a decrease in nerve conduction velocity (Brennan et al., 2015). The axonal forms of the disease (CMT2, dominant and recessive) are characterized by pathology intrinsic to motor and sensory neurons (Luigetti et al., 2016). The genetic causes of CMT are remarkably diverse, with causative mutations in over 80 genes, and a diverse set of individual mutations reported for many of those genes (DiVincenzo et al., 2014; Timmerman et al., 2014; Pareyson et al., 2017).

Axonal CMT is predominantly caused by autosomal dominant missense mutations, which occur in more than 20 genes with diverse functions (Rossor et al., 2015; Pareyson et al., 2017). A notable example is CMT2E, caused by mutations in the *NEFL* gene, which encodes the neurofilament light chain (NF-L) protein. Neurofilaments are neuron-specific intermediate filaments composed of multiple subunits, including NF-L, that contribute to the radial growth of axons and the maintenance of axonal diameter and function (Szaro and Strong, 2010; Yuan et al., 2017). A multitude of missense mutations throughout the *NEFL* coding sequence cause autosomal dominant CMT2E (Stone et al., 2019). By contrast, loss-of-function mutations in *NEFL* are recessive, and only cause CMT when homozygous—the heterozygous carriers are neurologically normal (Abe et al., 2009; Yum et al., 2009; Fu and Yuan, 2018). These loss-of-function mutations demonstrate that a single functional *NEFL* allele is adequate for normal neurological function and suggest that dominant missense mutations in *NEFL* act via dominant-negative or pathologic gain-of-function mechanisms. The N98S mutation is a prime example of the latter, as a single mutant allele leads to the aberrant accumulation of neurofilaments in neuronal cell bodies and causes a severe and early onset neuropathy in humans and mice (Jordanova et al., 2003; Adebola et al., 2015; Saporta et al., 2015; Zhao et al., 2017; Lancaster et al., 2018).

There is currently no effective treatment for any form of CMT. Viral gene replacement therapy for the motor neuron disease spinal muscular atrophy (SMA) has shown great promise and could represent a viable strategy for the rare recessive forms of CMT2 (Mendell et al., 2017). However, dominant CMT2 likely requires an alternate approach as simply increasing expression of a wild-type gene may not overcome the pathologic effects of the mutant allele, which will continue to be expressed. Advances in gene-editing technologies create an opportunity to develop therapies that interrupt the pathologic processes causing dominant CMT2, and other dominant neurodegenerative disorders, at its genetic source (Porteus, 2019). Since people with a single functional *NEFL* allele have normal neurological function, we reasoned that selective inactivation of dominant missense mutations in *NEFL* via CRISPR-Cas9 gene editing would be therapeutic. We tested this hypothesis using an established human induced pluripotent stem cell (iPSC) model of CMT2E with the N98S mutation in *NEFL* (Saporta et al., 2015).

Here, we report a gene-editing strategy specific for the N98S mutation that efficiently and selectively reduced expression of the mutant allele in CMT2E motor neurons. Edited neurons displayed phenotypes that were similar to unrelated and isogenic controls, indicating that the editing strategy effectively rescued disease-associated pathology. This is the first reported application of gene editing for axonal CMT. It provides proof-of-principle for strategies that could be applied to other dominant-negative inherited neurodegenerative diseases.

## MATERIALS AND METHODS

### iPSC Lines and Culture

The healthy control iPSC line known as wild type C (WTC) used in these studies is an extensively characterized line from a healthy individual (Kreitzer et al., 2013) that is the parental line for the Allen Institute Cell Collection[1]. A CMT2E iPSC line derived from a female individual with the N98S mutation in *NEFL* causing childhood onset CMT has been previously characterized (Saporta et al., 2015; Maciel et al., 2020). The N98S mutation occurs in the Coil1A domain of the neurofilament light chain (NF-L) protein at the 98th amino acid in both human and mouse orthologs. The mutation has also been referred to in the literature as N97S, likely due to variable inclusion of the start codon in the numbering system. iPSCs were cultured in Stemfit Basic02 (Ajinomoto) on plates coated with matrigel (Corning, 356231) at 37°C, 5% $CO_2$, 85% humidity. iPSC cultures were passaged every 3–4 days with Accutase (Stem Cell Technologies, 07920) or ReLeSR (Stem Cell Technologies, 05872) into Stemfit supplemented with 10 μm Y-27632 (SelleckChem, S1049).

### Generating Transgenic iPSC Lines With Inducible Transcription Factors

The iPSCs were engineered to contain a 13-kb vector containing the human transcription factors *NGN2*, *ISL1*, and *LHX3* (hNIL) under the control of doxycycline (Fernandopulle et al., 2018). To knock-in the hNIL construct into safe harbor loci, $1 \times 10^6$ cells were added to 100 μL P3 buffer with 6 μg of the hNIL donor plasmid, and 3 μg of each paired TALEN (Addgene, 59025/59026 or 62196/62197, respectively) targeting either AAVS1 or CLYBL (Cerbini et al., 2015). Cells were transfected using the P3 Primary Cell 4D-Nucleofector X Kit L (Lonza, V4XP-3024) with pulse code DS138. After nucleofection, cells incubated for 5 min at room temperature and were then plated in Stemfit media with 10-μM Y-27632 in a serial dilution into five wells of a six-well plate. Non-transfected cells were plated in the sixth well. After 2–3 days post-nucleofection, cells

[1]http://www.allencell.org/

were fed with Stemfit with Puromycin or G418 (depending on which donor vector was used) and 10-μM Y-27632. Cells were kept on antibiotic selection until all cells in the control wells were dead and only red fluorescent colonies remained in the experimental wells. Fluorescent, antibiotic-resistant colonies were then manually picked and transferred to individual wells of a 48-well plate.

DNA from each clone was extracted using the DNeasy Blood and Tissue Kit (Qiagen, 69506). PCRs were performed with primers spanning the 5′ and 3′ junctions of the integration, with one primer annealing within the construct and the other outside of the corresponding homology arm. A third PCR amplifying the intact safe harbor locus was performed to determine whether the clone harbored a heterozygous or homozygous insertion. PCR primer sequences are listed in **Supplementary Table 1**. For the CMT2E line, we inserted hNIL in the AAVS1 locus (**Supplementary Figure 1**) and obtained a previously published WTC line with hNIL inserted in the AAVS1 locus as a control (Shi et al., 2018). We also independently inserted hNIL in the CLYBL locus of the same parental WTC line (**Supplementary Figure 1**). When performing neuronal differentiation, we found equivalent results with the AAVS1 and CLYBL versions of the WT line. For comparison with the N98S-hNIL-AAVS1 line, we used WTC-hNIL-AAVS1 for all experiments, with the exception of manual image analysis shown in **Figure 2**, in which case we used the WTC-hNIL-CLYBL line.

## CRISPR/Cas9 Gene-Editing Analysis

To prepare the Sp.HiFi Cas9 ribonucleoprotein (RNP) complex, 240 pmol of guide RNA (IDT) was mixed with 120 pmol of Hi-Fi SpCas9 protein (Macrolab) and incubated for 30 min at room temperature. For the Sa.KKH Cas9 RNP complex, 240 pmol of guide RNA (Synthego) was mixed with 120 pmol of Sa.KKH Cas9 protein (Macrolab). The gRNA sequences are listed in **Supplementary Table 2**. After dissociation with Accutase, $3.5 \times 10^5$ cells were resuspended in P3 buffer and mixed with the RNP complex. The iPSCs were transfected using the P3 Primary Cell 4D-Nucleofector X Kit S (Lonza, V4XP-3032) with pulse code DS138. After nucleofection, cells were incubated for 5 min at room temperature and then plated in Stemfit with 10-μM Y-27632 (SelleckChem). Genomic DNA was extracted from edited and unedited cells 3 days post-nucleofection using the DNeasy Blood and Tissue Kit (Qiagen). PCRs were performed with primers spanning the gRNA binding site (**Supplementary Table 1**), and the PCR products were sequenced. The indel frequency at the cut site was determined using Synthego ICE software, which compares the Sanger sequencing traces from the edited and unedited populations (**Supplementary Figure 2**).

## Isolation of Clonal Edited Lines

To generate the N98S-fs line, $3.5 \times 10^5$ cells were transfected with RNP as described above. After nucleofection, $0.1 \times 10^5$ cells were seeded onto a 10-cm plate in Stemfit with 10-μM Y-27632. After 5 days post-nucleofection, colonies were manually picked and transferred to individual wells of a 48-well plate. DNA was extracted from the cells using QuickExtract DNA Extract Solution (Lucigen, QE9050). Clones were genotyped by PCR and Sanger Sequencing (**Supplementary Figure 3B**).

To generate the N98S-corrected line, $3.5 \times 10^5$ cells were nucleofected with RNP and 50 pmol of donor DNA (IDT, **Supplementary Table 1**). To enrich for the homology directed repair (HDR) event and isolate a clone with the desired edit, allele-specific droplet-digital PCR (ddPCR) and sib-selection were performed (Miyaoka et al., 2014; **Supplementary Figure 3C**). After nucleofection, cells were plated at $2.5 \times 10^3$ cells per well in a 96-well plate. DNA was extracted from the cells using QuickExtract and analyzed by allele-specific ddPCR to measure HDR efficiency. The well with the highest HDR efficiency was replated at 10 cells per well in a 96-well plate for an additional round of enrichment. From this round, the well with the highest HDR efficiency (∼11.4%) was replated sparsely into a 10-cm plate for manual clone picking. The clones were genotyped by allele-specific ddPCR and further validated by PCR and Sanger Sequencing (**Supplementary Figure 3D**). The clonal cell line with the desired HDR event underwent an additional round of manual clone picking.

## Integrated, Inducible, and Isogenic Lower Motor Neuron ($i^3$LMN) Differentiation

Induced pluripotent stem cells were differentiated into integrated, inducible, and isogenic lower motor neurons ($i^3$LMNs) as described in Fernandopulle et al. (2018), with the following modifications. On day 3, cells used for immunocytochemistry were seeded at $5–8 \times 10^4$ cells per $cm^2$ onto poly-D-lysine (PDL) (Sigma, P7405) and laminin-coated 12-mm glass coverslips in 24-well plates or PDL and laminin-coated clear bottom imaging 96-well plates. Cells used for RNA and protein assays were seeded at $1–1.5 \times 10^5$ cells per $cm^2$ onto PDL and laminin-coated 6-well plates. On day 4, the media was removed and replaced with fresh Neural Induction Media (NIM) supplemented with B-27 (Gibco, 17504-044), CultureOne (Gibco, A33202-01), 1 μg/mL laminin, 20 ng/mL BDNF (PeproTech, 450-02), 20 ng/mL GDNF (PeproTech, 450-10), and 10 ng/mL NT3 (PeproTech, 450-03). On day 7, a half volume of media was aspirated and replaced with fresh NIM supplemented with B-27, CultureOne, 1 μg/mL laminin, 40 ng/mL BDNF, 40 ng/mL GDNF, and 20 ng/mL NT3. On day 10, a half volume of media was aspirated and replaced with fresh Neural Maintenance Media (NMM) supplemented with B-27, CultureOne, 1 μg/mL laminin, 40 ng/mL BDNF, 40 ng/mL GDNF, and 20 ng/mL NT3.

## Immunofluorescent Staining

Integrated, inducible, and isogenic lower motor neurons used for immunofluorescent staining were seeded onto glass coverslips or clear-bottom imaging 96-well plates on day 3 of the differentiation, which then proceeded as previously described. For fixation, an equivalent volume

of 4% paraformaldehyde (PFA, Alfa Aesar, J61899AK) was added directly to the cell culture media. Cells were incubated in PFA at room temperature for 20 min, then washed with PBS with 0.1% Triton-X (Sigma, X100) (PBS-T) once quickly, followed by two 15-min washes. The cells were blocked and permeabilized for 1 h at room temperature with 5% BSA (Sigma, A4503) in PBS-T. The cells were incubated in primary antibodies at appropriate dilutions (**Supplementary Table 3**) in blocking buffer at 4°C overnight. The following day, the cells were washed with PBS-T at room temperature once quickly, followed by three 10-min washes. The cells were incubated in fluorescent conjugated secondary antibodies diluted at 1:500 in blocking buffer for 1 h at room temperature. The cells were washed with PBS-T once quickly, followed by three 10-min washes. The first 10-min wash contained DAPI dye (Invitrogen, D1306). The coverslips were then mounted onto a slide with VECTASHIELD HardSet Mounting Media (Vector Laboratories, H-1400-10). Images were taken on a Keyence BZ-9000 Fluorescence Microscope or an ImageXpress Micro Confocal system (Molecular Devices).

## RNA Expression Assays

Integrated, inducible, and isogenic lower motor neurons used for RNA-based assays were collected on day 7 of the differentiation. RNA was extracted from iPSCs and i$^3$LMNs using the Quick-RNA Miniprep Kit (Zymo Research, R1055), according to the manufacturer's instructions. RNA concentrations were quantified using the NanoDrop spectrophotometer. Reverse transcription was performed using the iScript cDNA Synthesis Kit (Bio-Rad, 1708891).

To determine mRNA expression for *HB9*, choline acetyltransferase (*CHAT*), and *NEFL*, we used the respective TaqMan gene expression assays (Thermo Fisher Scientific) containing a FAM-labeled probe. All reactions included a GAPDH gene expression assay (Bio-Rad) containing a HEX-labeled probe, which was used as an internal control to normalize levels of mRNA. 5 ng of cDNA were used in the 25-μL reactions measuring *HB9* and *CHAT* expression. 0.25 ng of cDNA were used in the 25-μL reactions measuring *NEFL* expression. The gene expression assay IDs are listed in **Supplementary Table 4**. To determine allele-specific *NEFL* mRNA expression, we used a TaqMan SNP genotyping assay targeting the rs79736124 SNP in the 3′ UTR of *NEFL* (Thermo Fisher Scientific, C_105316276_10). 0.25 ng of cDNA were used in each 25-μL ddPCR reaction.

Each 25-μL ddPCR reaction contained 12.5 μL 2× SuperMix for Probes (no dUTP) (Bio-Rad Laboratories, #186-3024), cDNA, primer and probe mix(es), and water to 25 μL. Droplets were generated using 20 μL of reaction mixture and 70 μL of oil with the QX200 Droplet Generator. Droplets were transferred to a 96-well PCR plate, sealed, and run on a C1000 Thermal Cycler with a deep well block (Bio-Rad Laboratories). All ddPCR reactions were run under the following thermal cycling conditions: (1) 95°C for 10 min; (2) 94°C for 30 s; (3) 58°C for 1 min; (4) steps 2 and 3 repeat 39 times; (5) 98°C for 10 min.

All ddPCR runs were analyzed using the Bio-Rad QuantaSoft Pro Software. The ratio of FAM-positive droplets to HEX positive-droplets was used to calculate the gene expression levels for *HB9*, *CHAT*, and *NEFL*. Fractional abundance of FAM and VIC-positive droplets was used to calculate the percentage of wild-type and mutant *NEFL* mRNA, respectively.

## Western Blots

Integrated, inducible, and isogenic lower motor neurons were harvested on day 10 of the differentiation and lysed in RIPA buffer (Thermo Fisher Scientific, 89901) with Protease Inhibitor (MedChemExpress, HY-K0010). The samples were incubated for 15 min on ice and sonicated for 8 s using a probe sonicator. The samples were then incubated for 10 min on ice and centrifuged at 10,000 rpm for 10 min at 4°C. The supernatant of each sample was transferred to a clean tube. The protein was quantified using the Bio-Rad Protein Assay Dye Reagent Concentrate (Bio-Rad, 5000006).

Samples containing 18 μg of total protein were mixed with NuPAGE Sample Reducing Agent (Thermo Fisher Scientific, NP0009) and NuPAGE LDS Sample Buffer (Thermo Fisher Scientific, NP0008) and incubated at 70°C for 10 min. The reduced samples were electrophoresed in a 4–12% Bis-Tris gel. Protein was transferred onto an iBlot nitrocellulose membrane (Thermo Fisher Scientific, IB301002) using the iBlot system (Thermo Fisher Scientific). The membrane was incubated in Odyssey Blocking Buffer (Li-Cor, 927-4000) and PBS at a 1:1 ratio (blocking buffer) for 1 h at room temperature. Primary antibodies at appropriate dilutions (**Supplementary Table 3**) were prepared in blocking buffer with 0.1% Tween 20 (Sigma, 9005-64-5). The membrane was incubated in the primary antibody solution overnight at 4°C. The following day, the membrane was washed with PBS with 0.1% Tween 20 (PBS-T) once quickly and with TBS (Corning, 46-012-CM) with 0.1% Tween 20 (TBS-T) three times for 10 min each. Fluorescent conjugated secondary antibodies at appropriate dilutions were prepared in blocking buffer. The membrane was incubated in the secondary antibody solution for 1 h at room temperature. The membrane was then washed with TBS-T 3 times for 10 min each and imaged on the Li-Cor Odyssey Fc Imaging System. Protein band intensity was quantified using ImageJ software. NF-L levels were normalized to GAPDH by dividing NF-L signal intensity by GAPDH signal intensity for each biological replicate.

## Image Analysis

To assess the accumulation of NF-L in the cell bodies of i$^3$LMNs, the i$^3$LMNs were fixed and stained with anti-HB9 antibody, anti-NF-L antibody, and DAPI. To maximize consistency and reproducibility of our analysis, all neurons for each experiment were fixed and stained simultaneously using a single aliquot and dilution of each antibody. For the day-7 i$^3$LMNs, ten images were taken per sample on a Keyence BZ-9000 Fluorescence Microscope. For the day-14 i$^3$LMNs, nine images were taken per sample on an ImageXpress Micro Confocal system (Molecular Devices). All images for each experiment were acquired in a single session with constant illumination and exposure parameters. The cell bodies of i$^3$LMNs were then segmented manually, or

automatically using CellProfiler. Before manual segmentation, the images were renamed with alphanumeric codes to allow for blinded analysis. Using ImageJ software, the cell bodies of HB9-positive i$^3$LMNs were manually segmented by a blinded observer. Fluorescence intensity was measured in resulting regions of interest from the green channel to measure NF-L intensity within each cell body. To allow for automatic segmentation in later experiments, we designed a CellProfiler pipeline to define cell bodies with HB9-positive nuclei and measure the average NF-L intensity of each cell body (**Supplementary Figure 5**). For each sample, the average NF-L intensity in the cell bodies was calculated by averaging the intensity values of all the cell bodies across 9–10 images.

## NF-L ELISA Assay

Integrated, inducible, and isogenic lower motor neurons used for the NF-L ELISA Assay were seeded at 30,000 cells per well in a 96-well plate on day 3 of the differentiation. On day 11, a full media change was performed. On day 14, the media from each well was collected and stored at −80°C until the assay was performed. The samples were diluted with water at a 1:25 ratio before quantification. NF-L levels in the media were quantified using the NF-light ELISA kit (Uman Diagnostics, 10-7001).

On day 14, the cells were imaged using the Incucyte S3 Live-Cell Analysis System. Three images per well were analyzed using CellProfiler software to determine the average neurite area (**Supplementary Figure 8**). NF-L levels were normalized to the neurite area by dividing the NF-L concentration by the average neurite area for each well.

## Multi-Electrode Array Analysis

Induced pluripotent stem cells were differentiated into i$^3$LMNs as described in Fernandopulle et al. (2018), with the following modifications. On day 3, cells were seeded at 20,000 cells per well in 10 μL of NIM supplemented with 10-μM Y-27632, 2 μg/mL doxycycline, 40-mM BrdU, and 2-mM Compound E onto polyethylenimine (PEI) (Thermo Fisher Scientific, AC178571000) and laminin-coated 24-well CytoView microelectrode array (MEA) plates (Axion Biosystems, M384-tMEA-24W). After the cells were incubated for 20 min at 37°C, 500 μL of complete media was gently added to each well. On day 4, the media was removed and replaced with fresh NIM supplemented with B-27, CultureOne, 1 μg/mL laminin, 20 ng/mL BDNF, 20 ng/mL GDNF, and 10 ng/mL NT3. On day 7, a half volume of media was aspirated and replaced with fresh NIM supplemented with B-27, CultureOne, 1 μg/mL laminin, 40 ng/mL BDNF, 40 ng/mL GDNF, and 20 ng/mL NT3. Starting on day 10, every 3 days, a half volume of media was aspirated and replaced with BrainPhys media (StemCell, 05791) supplemented with B-27, CultureOne, 1 μg/mL laminin, 40 ng/mL BDNF, 40 ng/mL GDNF, and 20 ng/mL NT3. Spontaneous neural activity was measured for 15 min using the Axion Biosystem Maestro Edge MEA systems. Data was acquired at 12.5 kHz, and spikes were detected in the AxIS Navigator software with an adaptive threshold crossing set to six times the standard deviation of the estimated noise for each electrode. The electrical activity was analyzed using weighted mean firing rate to exclude non-active electrodes for the entire 15-min recording.

# RESULTS

## Rapid Development of CMT2E Phenotypes in iPSC-Derived Motor Neurons

Multiple groups have demonstrated that the *NEFL* N98S mutation leads to a pathologic accumulation of NF-L in the cell bodies of human and mouse neurons *in vitro* and *in vivo* (Adebola et al., 2015; Saporta et al., 2015; Zhao et al., 2017). However, previous methods used to identify phenotypes in motor neurons from CMT2E patient-derived iPSCs were time consuming, often taking ∼6 weeks in total (Saporta et al., 2015). To overcome this challenge, we engineered patient-derived iPSCs with integrated, inducible, and isogenic (i$^3$) transcription factors in order to rapidly and efficiently differentiate them into lower motor neurons (i$^3$LMNs) (Fernandopulle et al., 2018). We inserted a doxycycline-inducible cassette containing *NGN2*, *ISL1*, and *LHX3* into the AAVS1 safe-harbor locus (**Supplementary Figure 1**) of a previously characterized CMT2E iPSC line with the *NEFL* N98S mutation, referred to here as N98S (Saporta et al., 2015; Maciel et al., 2020; Watry et al., 2020). For comparison, we used healthy control (WT) iPSC lines containing the same doxycycline-inducible cassette integrated into AAVS1 or CLYBL, as previously described (Fernandopulle et al., 2018; Shi et al., 2018). Characterization of the complete transcriptome, chromatin accessibility, and chromatin interactions of our WT i$^3$LMNs has been previously published (Song et al., 2019). The publicly available dataset demonstrates that i$^3$LMNs express a combination of both mature (*TUBB3*, *MAP2*, *MAPT*, *SYN1*, *NEFM*, *CHAT*, and *HB9*) and immature (*NES* and *DCX*) neuronal genes. We confirmed that at day 7 of the differentiation, i$^3$LMNs derived from both WT and N98S lines expressed neuronal markers, including neurofilaments, β-III tubulin, and the motor-neuron transcription factor HB9 (*MNX1* gene) (**Figure 1A**). Consistent with these results, gene expression analysis by reverse transcriptase-droplet digital polymerase chain reaction (RT-ddPCR) demonstrated that WT and N98S i$^3$LMNs expressed *MNX1* and the more mature motor neuron marker *CHAT* at day 7 of the differentiation (**Figure 1B**). To further verify the functionality of our patient-derived i$^3$LMNs, we performed electrophysiological analysis using a MEA device. We detected rare spontaneous action potentials on day 7 that progressively increased in frequency for both cell lines without a measurable defect in the firing rate of the N98S i$^3$LMNs (**Figure 1C**).

To confirm that we could detect disease-relevant phenotypes at early time points in our differentiation, we fixed WT and N98S i$^3$LMNs and performed immunofluorescent staining for neurofilament light chain (NF-L) and HB9 using commercially available antibodies (**Figures 2A,B**). We observed dense accumulation of neurofilament staining in N98S i$^3$LMN cell bodies as early as day 7 of differentiation that was not seen in control cells (**Figures 1A**, **2**). For quantification, NF-L

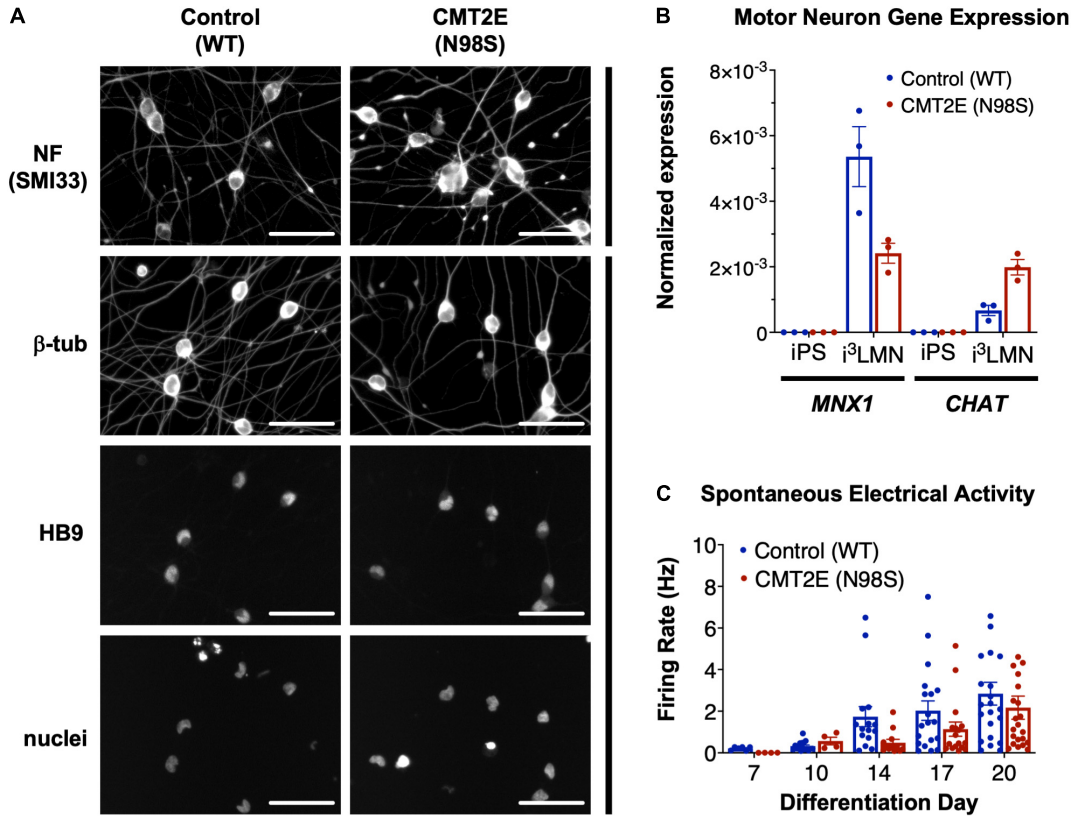


**FIGURE 1 |** Generation of CMT2E (*NEFL*-N98S) motor neurons. **(A)** Expression of neuronal markers by immunofluorescent staining in day-7 $i^3$LMNs derived from healthy control and CMT2E patient iPSC lines. Lower panels are separate RGB channels from the same images, as indicated by a vertical bar. Scale bars = 50 μm. NF = neurofilaments (SMI33 antibody), NF-L = neurofilament light chain, β-tub = βIII-tubulin, DAPI stain for nuclei. **(B)** Total mRNA isolated from undifferentiated iPSCs and day-7 $i^3$LMNs was assayed by RT-ddPCR for expression of motor neuron specific genes *MNX1* and *CHAT*, normalized to *GAPDH*. **(C)** WT and N98S $i^3$LMN were seeded on an MEA plate on day 3 of differentiation and spontaneous electrical activity was recorded starting on day 7 and every few days until day 20. Graph represents serial measurements of the mean firing rate (frequency of action potentials) from replicate wells. MEA data were analyzed using a mixed effects model for repeated measurements (maximum likelihood method). There was a significant effect due to time ($p < 0.005$) but no significant difference between cell lines. For all graphs individual replicate data points are shown with bars representing mean ± S.E.M.

fluorescence intensity in the cell bodies of HB9-positive cell bodies was measured in a blinded fashion. When examining the fluorescence intensity of NF-L staining across all segmented neuronal cell bodies, we observed a marked shift toward high-intensity NF-L staining in N98S $i^3$LMNs, consistent with a misaccumulation phenotype (**Figure 2C**). To further validate this finding, we compared mean NF-L fluorescence intensities in multiple independent $i^3$LMN preparations. We observed a greater than 2-fold increase in mean NF-L fluorescence intensity in the cell bodies of N98S $i^3$LMNs compared to WT $i^3$LMNs (**Figure 2D**). Thus, we were able to replicate the previously described phenotype, but at a significantly earlier time point compared to other iPSC differentiation methods. We anticipated that this finding would facilitate relatively rapid and sensitive measurement of phenotypic rescue in subsequent gene-editing experiments.

## Allele-Specific Editing to Model Therapeutic Strategies in CMT2E iPSCs

To enable allele-specific silencing of the N98S allele, we designed guide RNAs targeting the N98S sequence (**Figure 3A**) for two of the most widely used Cas9 enzymes, derived from *Streptococcus pyogenes* (Sp.) and *Staphylococcus aureus* (Sa.). We selected a high-fidelity engineered Sp. Cas9 variant (Sp.HiFi) that has been shown to have increased selectivity without compromising activity of the naturally occurring enzyme (Vakulskas et al., 2018). We sought to compare the efficiency and allele specificity of

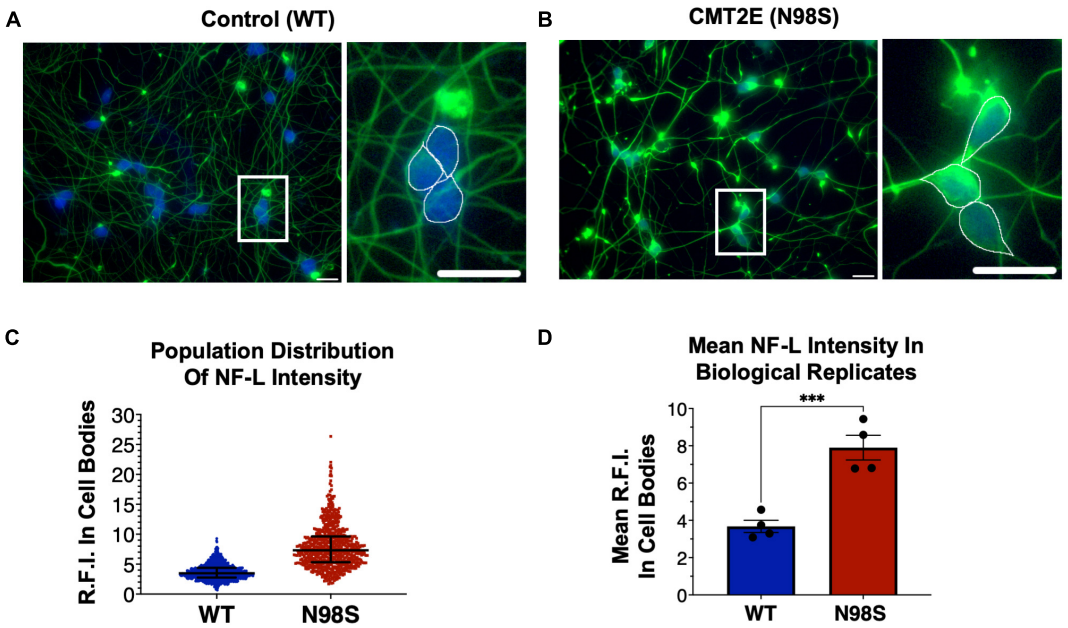


**FIGURE 2 |** Pathologic accumulation of NF-L protein in the cell body of *NEFL*-N98S motor neurons. **(A,B)** Representative images of day-7 WT **(A)** and N98S **(B)** $i^3$LMNs stained with anti-NF-L (green) and anti-HB9 (blue) antibodies. Boxed regions are shown in larger scale to the right of each image with manual cell body segmentation superimposed. Scale bars = 25 μm. **(C)** Distribution of NF-L fluorescence intensity in individual HB9+ cell bodies after manual segmentation. Individual data points are shown with horizontal lines representing median and interquartile range. **(D)** Quantification of mean NF-L fluorescence intensity from four biological replicates per cell line, demonstrating significantly increased intensity in N98S neurons. Points represent mean of >160 neurons quantified in each sample population, bars represent mean of all replicates ± S.E.M., ***$p < 0.001$ by *t*-test.

Sp.HiFi Cas9 with Sa. Cas9 as the latter is significantly smaller (315 fewer amino acids), which is advantageous for delivery, in particular via adeno-associated virus vectors. However, the human *NEFL* sequence lacks a canonical Sa. Cas9 protospacer adjacent motif (PAM) near the N98S mutation so we utilized an engineered variant (Sa.KKH) with an expanded PAM recognition sequence (Kleinstiver et al., 2015). We transfected both N98S and WT iPSCs with the resulting Cas9/gRNA RNP complexes and performed ICE analysis to measure the generation of insertions and deletions (indels) in the target exon. In N98S iPSCs transfected with Sp.HiFi RNP, 45.3% of *NEFL* alleles sequenced had indels at the target site (**Figure 3B**). This is very close to the 50% maximum expected if all N98S alleles in the heterozygous cell population had been edited. In contrast, in WT iPSCs transfected with Sp.HiFi RNP, we measured 1.7% of alleles with indels, demonstrating specificity of this nuclease for the N98S allele. In N98S iPSCs transfected with Sa.KKH RNP, we observed moderate rates of editing with 10.5% of alleles having indels at the target site (**Figure 3B**). In WT iPSCs transfected with Sa.KKH RNP, we observed no detectable indel generation, demonstrating that this nuclease is also specific for the N98S allele. Among the alleles edited by the Sp.HiFi RNP, we detected two categories of indel events: a 1-bp insertion and a 9-bp deletion (**Figure 3C** and **Supplementary Figure 2**). Among the alleles edited by the Sa.KKH RNP, we also detected two categories of indel events, but in this case a 9-bp deletion was predominant, followed by a 15-bp deletion (**Figure 3C** and **Supplementary Figure 2**).

The 9- and 15-bp deletion events are unlikely to disrupt expression of the N98S allele as they do not create a shift in reading frame. On the other hand, the 1-bp insertion, which constituted 87.3% of the total indel events with Sp.HiFi N98S RNP, represents a potential therapeutic edit, as it results in a frameshift mutation. We therefore isolated a clone with a 1-bp insertion at the target site, referred to here as N98S-frameshift (fs). The frameshift mutation leads to a premature stop codon immediately after residue 98 of the N98S allele, which we predicted would effectively interrupt expression from this allele (**Supplementary Figure 3B**). For comparison, we designed a strategy for precise correction of the N98S allele to a wild-type sequence by HDR. To achieve this, we transfected N98S iPSCs with Sp.HiFi RNP and a single-strand DNA oligonucleotide donor (ssODN). The ssODN was designed to precisely repair the N98S mutation and insert a silent mutation to facilitate genotyping. The efficiency of this editing outcome was low (2.5%), so we utilized sib-selection to enrich for cells with the desired HDR event (Miyaoka et al., 2014) (**Supplementary Figure 3C**). We isolated a clone, referred to as N98S-corrected (N98S-cor), with precise repair of the N98S sequence as well as insertion of silent mutation c.297C > T (**Supplementary Figure 3D**).

To evaluate for potential off-target editing events produced by the Sp.Hifi RNP, we used the cutting frequency determination (CFD) score to predict the highest risk off-target sequences present in the genome of our cell lines (Doench et al., 2016). We performed targeted amplification and sequencing of 11 genomic

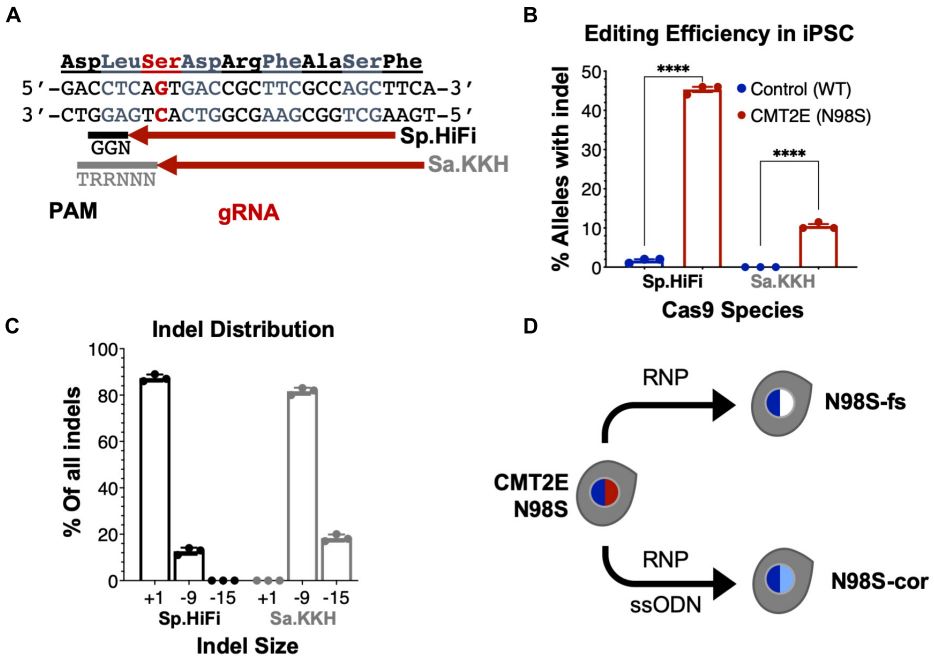


**FIGURE 3 |** Allele-specific editing of *NEFL* N98S mutation in iPSCs. **(A)** *NEFL* target sequence with N98S mutation in red and gRNAs for Sp.HiFi and Sa.KKH Cas9 targeting the antisense strand. The canonical PAM recognition sequences for Sp.HiFi and Sa.KKH are shown in black and gray, respectively. **(B)** Efficiency and specificity of indel generation in control and CMT2E patient lines after transfection with Cas9/gRNA ribonucleoprotein (RNP), measured by ICE analysis, $^{****}p < 0.0001$ by *t*-test. **(C)** Comparison of indel sizes generated in CMT2E patient line by Cas9 enzyme. **(D)** Schematic of the derivation of clonal edited iPSC lines from the CMT2E N98S patient line. Transfection of N98S iPSC with Sp.HiFi RNP produced N98S-fs (frameshift inactivating the mutant allele). Transfection of N98S iPSC with Sp.HiFi RNP plus single-strand oligonucleotide donor (ssODN) produced N98S-cor (precise correction of the mutation). Colored nuclei indicate *NEFL* genotype: dark blue = wild type, red = N98S mutant, white = frameshift (knockout), light blue = correction of N98S to wild type.

loci with CFD score >0.25 (**Supplementary Table 5**) in the parental N98S line and the edited N98S-fs and N98S-cor clones. A heterozygous single-nucleotide deletion (delG) was identified near a predicted target site in an intergenic region of chromosome 13. This deletion was not associated with editing as it was present in all three cell lines and corresponds to a common SNP with allele frequency >0.4 in the global population[2]. We did not find evidence of a mutation induced by gene editing in any of the predicted off-target sites.

## Frameshift Indel Reduces Mutant *NEFL* mRNA and Protein Expression in N98S Motor Neurons

To investigate how allele-specific editing of the N98S allele affects *NEFL* mRNA and protein expression, we differentiated WT, N98S, N98S-fs, and N98S-cor iPSCs into i$^3$LMNs. In addition, we generated i$^3$LMNs from previously characterized iPSC lines with heterozygous (*NEFL*+/−) and homozygous (*NEFL*−/−) excision of the *NEFL* coding exons (Watry et al., 2020). *NEFL*+/− and *NEFL*−/− i$^3$LMNs are isogenic to our WT control and were used as a comparison for *NEFL* mRNA and NF-L protein expression. We measured total *NEFL* mRNA levels in i$^3$LMNs by quantitative RT-ddPCR and found that N98S-fs i$^3$LMNs had 52% less *NEFL* mRNA than their unedited counterparts (**Figure 4A**). This marked reduction in mRNA levels suggested that the early stop codon induced by the heterozygous frameshift mutation may trigger efficient nonsense mediated decay of the mutant transcript. By comparison, *NEFL*+/− i$^3$LMNs had 36% less *NEFL* mRNA than WT i$^3$LMNs (**Figure 4A**). Thus, the frameshift introduced by the 1-bp insertion disrupted expression of the edited allele as effectively as complete excision of the coding sequence. WT, N98S, and N98S-cor i$^3$LMNs all exhibited similar levels of *NEFL* mRNA expression. To compare changes in transcription with protein levels, we measured NF-L protein by western blot in i$^3$LMNs from the same panel of iPSC lines. Like *NEFL* mRNA levels, NF-L protein levels were reduced (by 42%) in N98S-fs i$^3$LMNs compared to N98S i$^3$LMNs (**Figure 4B**). Interestingly, *NEFL*+/− i$^3$LMNs had a non-significant reduction in NF-L protein compared to WT i$^3$LMNs. The reason for the differing degrees of NF-L protein reduction in *NEFL*+/− and N98S-fs i$^3$LMNs is not clear, but may be due to differences in compensatory gene expression, epigenetic effects, or post-transcriptional regulation. WT, N98S, and N98S-cor i$^3$LMNs exhibited similar levels of total NF-L protein. Thus, the accumulation of NF-L protein in the cell bodies of N98S i$^3$LMN is unlikely to be caused by perturbations in protein synthesis or degradation, but is more consistent with a defect in localization and intracellular transport as has been suggested by other *in vitro* studies of NF-L mutations (Perez-Olle et al., 2004; Pérez-Ollé et al., 2005). Neither *NEFL* mRNA nor NF-L

[2]https://www.ncbi.nlm.nih.gov/snp/rs34866221

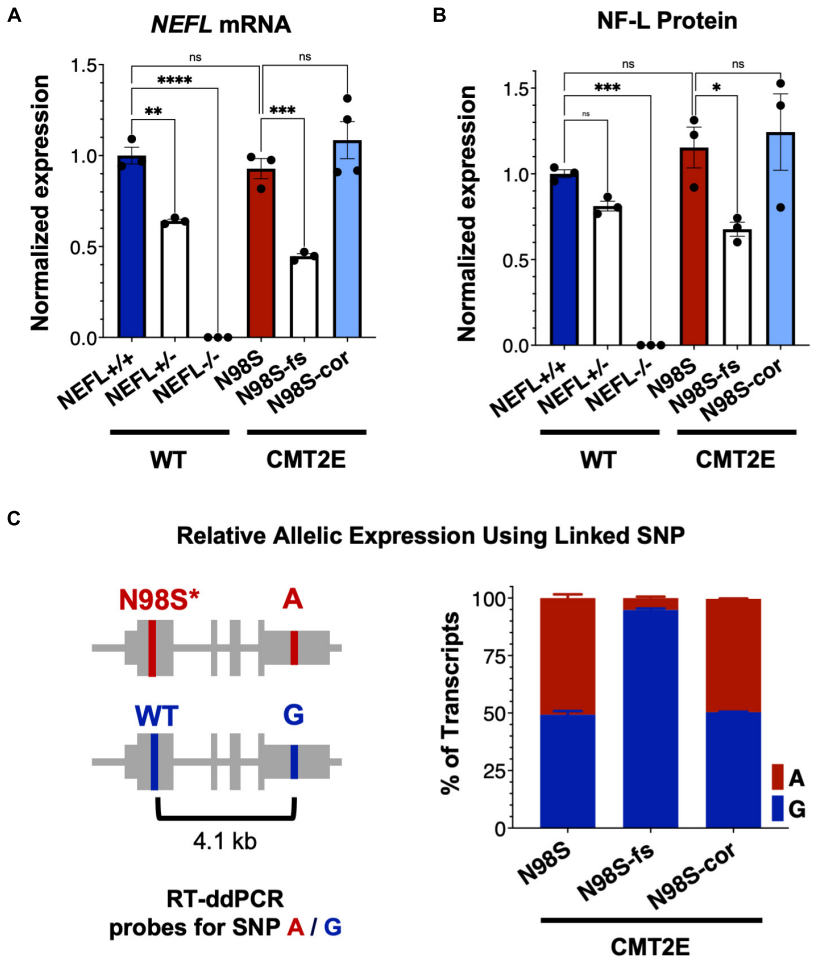


**FIGURE 4 |** *NEFL* expression in allelic series of edited motor neurons. A series of edited iPSCs derived from a healthy control (WT) and CMT2E patient were differentiated into i$^3$LMNs, and RNA was extracted on day 7 or protein on day 10. **(A)** Total *NEFL* transcript expression by quantitative RT-ddPCR, normalized to *GAPDH*. **(B)** Total NF-L protein expression by western blot, normalized to GAPDH. **(C)** Relative expression of *NEFL* alleles in i$^3$LMNs derived from CMT2E patient line and edited subclones. Allele-specific RT-ddPCR targeting a heterozygous SNP in the 3′ UTR was used to genotype transcripts using linkage shown in the schematic. All bar graphs represent mean ± S.E.M. For all graphs ns = not significant, $^*p < 0.05$, $^{**}p < 0.01$, $^{***}p < 0.001$, $^{****}p < 0.0001$ by one-way ANOVA with Šídák's test for multiple comparisons.

protein was detected in the *NEFL*−/− samples, validating the specificity of our assays.

To confirm that the observed decrease in total *NEFL* expression in N98S-fs i$^3$LMNs was specific to the mutant allele, we measured the relative expression of the mutant and wild-type alleles in N98S, N98S-fs, and N98S-cor i$^3$LMNs. Allele specificity was achieved by targeting a RT-ddPCR assay to a heterozygous SNP present in the 3′ untranslated region of the *NEFL* gene in our CMT2E patient line (**Figure 4C**). In N98S and N98S-cor i$^3$LMNs, both alleles were transcribed at equal rates, with each representing 50% of the total transcripts detected. However, in N98S-fs i$^3$LMNs, *NEFL* mutant allele transcripts constituted only 5% of the total *NEFL* transcripts detected, confirming efficient knockdown of the mutant mRNA (**Figure 4C**). Overall, these experiments demonstrate that the frameshift mutation leads to dramatic reduction of mutant *NEFL* mRNA and, presumably, mutant NF-L protein in i$^3$LMNs, while isogenic correction of the N98S mutation with introduction of a silent mutation does not alter *NEFL* expression.

## Selective Inactivation of the N98S Allele Rescues Pathologic Phenotypes in Motor Neurons

To determine if inactivation of the *NEFL* mutant allele prevents the pathologic phenotype, we measured the distribution of NF-L in fixed and stained WT, N98S, N98S-fs, and N98S-cor i$^3$LMNs at day 7 (**Figures 5A–C**). To increase the throughput of this analysis, we developed an automated image analysis pipeline using CellProfiler to identify i$^3$LMN cell bodies and quantify NF-L fluorescence intensity (**Figure 5C** and **Supplementary Figure 5**). Consistent with the manually processed data, N98S i$^3$LMN cell bodies displayed significantly higher NF-L fluorescence intensity values compared to WT. N98S-fs i$^3$LMNs displayed

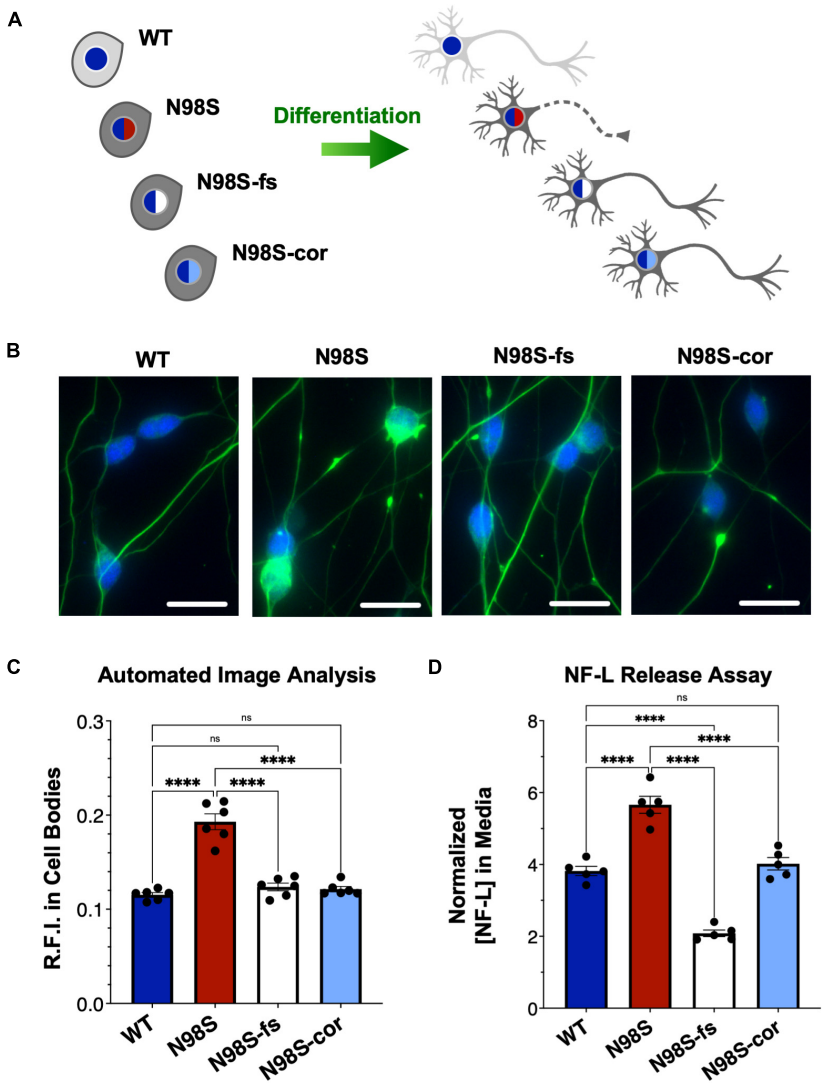


**FIGURE 5 |** Rescue of pathologic phenotypes in edited N98S motor neurons. **(A)** Schematic of allelic series of iPSCs differentiated into healthy (continuous axon) or diseased (dashed axon) i$^3$LMNs. Colored nuclei represent *NEFL* genotypes as described in **Figure 3**. Cytoplasmic shading indicates differential genetic backgrounds, dark gray cells are isogenic. **(B)** Representative images of day-7 i$^3$LMNs stained with anti-NF-L (green) and anti-HB9 (blue) antibodies. Scale bars = 25 μm. **(C)** Quantification of NF-L relative fluorescence intensity (R.F.I.) in HB9+ cell bodies using automated image analysis pipeline. Data points represent mean values from independent differentiations, bars indicate mean of six biological replicates ± S.E.M. **(D)** ELISA for NF-L protein in media from day-14 i$^3$LMNs. NF-L levels were normalized to neurite density measurements to correct for well-to-well variability in cell seeding (**Supplementary Figure 8**). Individual data points shown, bars indicate mean of five biological replicates ± S.E.M. For all graphs ****$p < 0.0001$ by one-way ANOVA with Šídák's test for multiple comparisons.

significantly lower NF-L fluorescence intensity values than N98S i$^3$LMNs, demonstrating that inactivation of the mutant *NEFL* allele prevents the pathologic accumulation of NF-L in the cell bodies of motor neurons. In addition, the NF-L fluorescence intensity values of N98S-fs i$^3$LMNs were indistinguishable from those of WT and N98S-cor i$^3$LMNs, further suggesting that NF-L localization and transport is normalized after inactivation of the N98S mutant allele. To determine whether rescue of this phenotype would persist to later points in differentiation, we repeated the analysis at day 14 (**Supplementary Figure 6**). Again, N98S-fs and N98S-cor i$^3$LMNs had significantly decreased NF-L fluorescence intensity in the cell bodies compared to N98S i$^3$LMNs, to a level indistinguishable from WT i$^3$LMNs. We did observe a smaller magnitude of difference between N98S and the other cell lines at day 14 in this assay, likely because our analysis pipeline was optimized for the earlier time point when neuron cell bodies are less tightly clustered. We also investigated whether gene editing altered the ability of the neurons to generate functional action potentials. MEA analysis demonstrated that the N98S-fs and N98S-cor i$^3$LMNs retained similar spontaneous electrical activity as their unedited N98S counterparts (**Supplementary Figure 7**).

Finally, we assayed NF-L release in the culture media as a means to assess cellular integrity of our i$^3$LMNs. NF-L is

a biomarker of neurodegenerative diseases, as NF-L levels in cerebrospinal fluid and serum reflect the extent of neuroaxonal damage leading to neurofilament release (Lu et al., 2015; Disanto et al., 2017; Hansson et al., 2017). Correspondingly, it has been reported that iPSC-derived motor neuron cultures with the *NEFL*-N98S mutation release more NF-L into the media than healthy controls, consistent with increased axonal degeneration (Maciel et al., 2020). Using a commercially available enzyme-linked immunosorbent assay (ELISA), we measured the levels of NF-L in media from day-14 i$^3$LMN cultures (**Figure 5D**). As expected, media from N98S i$^3$LMNs had significantly higher normalized levels of NF-L than media from WT i$^3$LMNs, suggesting that the N98S mutation results in neuroaxonal damage. N98S-cor and WT i$^3$LMN cultures exhibited equivalent levels of NF-L, confirming that the increase in NF-L levels observed in N98S i$^3$LMNs was due to the N98S mutation rather than inherent cell line variability. In contrast, N98S-fs i$^3$LMNs released significantly less NF-L than all other cell lines, including the WT and N98S-cor controls. This was expected, as overall NF-L expression is reduced in N98S-fs i$^3$LMNs (**Figure 4B**). To determine whether this observation was simply due to changes in intracellular protein expression, we compared cell lines by differences in NF-L released into media (as measured by ELISA, **Figure 5D**) versus differences in intracellular NF-L levels (as measured by western blot, **Figure 4B**). The relative ratios of N98S-fs to N98S-cor were similar: 0.52 for NF-L released in media and 0.55 for intracellular NF-L. This demonstrates that the differences in released NF-L can be completely explained by intracellular protein levels and suggests equivalent degrees of neuronal integrity when comparing the two editing strategies. Conversely, the relative ratios of N98S-fs to parental N98S were 0.37 for NF-L released in media and 0.59 for intracellular NF-L. The larger decrease in NF-L released into the media supports the conclusion that inactivation of the mutant allele leads to both decreased NF-L protein expression, as well as improved neuronal integrity compared to the unedited diseased neurons.

In summary, we conclude that inactivation of the mutant allele by CRISPR-Cas9 gene editing effectively prevents disease phenotypes in i$^3$LMNs derived from a patient with autosomal dominant CMT2E caused by the N98S mutation. Moreover, N98S-fs i$^3$LMNs were phenotypically similar to N98S-cor i$^3$LMNs, suggesting that knockout of the mutant allele is as effective as precise repair of the mutation in this model system.

# DISCUSSION

In this study, we used allele-specific gene editing with engineered Cas9 enzymes to inactivate a missense mutation causing CMT2E, a severe autosomal dominant neuromuscular disease. Cas9-induced inactivation was efficient, selective, and effectively reversed the accompanying pathology in patient iPSC-derived motor neurons without apparent adverse effects. In the process, we incorporated rapid neuronal differentiation and high-throughput automated image analysis to enable measurement of changes in disease phenotypes in a fraction of the time required by previous methodology. Our findings establish the framework for therapeutic development of gene editing for CMT2E and for other motor neuron diseases caused by dominant missense mutations.

## Gene Editing as an Efficient Path to Allele-Specific Gene Inactivation

We selected CRISPR-Cas9-based genome editing because it presents several advantages over other therapeutic strategies, with important clinical implications (Porteus, 2019). First, the therapeutic construct only needs to be active briefly and requires only a single treatment, since the outcome is a permanent change in the cellular genome. In fact, transient expression is desirable as it minimizes the risk of off-target effects and immune response to the vector construct. Second, since it targets the mutation itself, gene editing can achieve complete correction or inactivation of the mutant allele in treated cells, rather than mere attenuation of the mutation's effect. Finally, even single-nucleotide mutations can be targeted by Cas nucleases with a high degree of specificity (Wienert et al., 2019), suggesting the approach could be safely deployed to treat a large number of conditions caused by missense mutations.

We demonstrated that Cas9 enzymes derived from both *S. aureus* and *S. pyogenes* can induce indels specifically at the *NEFL*-N98S mutant allele, and that the latter predominantly leads to a 1-bp insertion that efficiently disrupts mutant allele expression. In contrast, the former preferentially generates 9- and 15-bp deletions that are less useful for disrupting expression of the mutant allele. Interestingly, 9- and 15-bp deletions are predicted by microhomology domains near the cleavage sites for both of our Cas9 nucleases (Bae et al., 2014). Large-scale studies have begun to define the mutational profiles produced by Cas9-induced cleavage and predict outcomes produced by specific gRNA, but our findings highlight how these predictions are not necessarily transferable to alternate enzymes, which differ in the nature of the double-strand breaks produced (Allen et al., 2018; Tycko et al., 2018; Chen et al., 2019). Moreover, these predictions are based on experiments performed in immortalized cell lines and the generalizability to primary and post-mitotic cells is yet to be determined.

We achieved phenotypic rescue using CRISPR gene editing both by generating indels in the *NEFL* allele carrying the N98S mutation and by correcting the N98S mutation to wild type via HDR. In both cases, gene editing starts with the creation of targeted double-strand breaks, but the outcome depends on the endogenous DNA repair machinery that repairs the break—non-homologous end-joining (NHEJ) or HDR (Porteus, 2019). NHEJ is most useful for gene inactivation via frameshift-inducing indels, as in our approach, and is active even in post-mitotic neurons (Bétermier et al., 2014; Shalem et al., 2014; Gaj et al., 2017). Precise correction of a mutant sequence by HDR requires a donor template to facilitate homologous recombination but is typically much less efficient than NHEJ and active only in proliferative cells (Miyaoka et al., 2016). Indeed, in our experiments, editing outcomes from NHEJ were over 10 times more efficient than HDR using the same gRNA and Cas9 enzyme. Both approaches were able to effectively rescue disease

phenotypes in CMT2E i$^3$LMNs, but as HDR is not active in post-mitotic cells like neurons, inactivation of the mutant allele via NHEJ is the more tractable therapeutic strategy. An important caveat is that allele-specific gene inactivation is restricted to genes in which heterozygous loss of function is well tolerated, as is the case for *NEFL*.

## Alternative Strategies and Future Directions

We validated CRISPR reagents that are specific to the human *NEFL*-N98S mutation, but there are a multitude of distinct missense mutations in *NEFL* that cause CMT2E (Stone et al., 2019). The majority occur in the first exon and should be amenable to the same editing strategy that we employed here. However, inducing frameshifts at the site of mutations in distal coding exons may not be therapeutic, as nonsense codons in that context can lead to expression of a pathologic truncated protein rather than nonsense-mediated decay (Lindeboom et al., 2016; Stone et al., 2019). Alternate editing strategies for these mutations include excision of mutant alleles using pairs of guide RNAs, or precise correction using non-nuclease editing technologies such as base editors or PRIME editing (Komor et al., 2016; Anzalone et al., 2019; Watry et al., 2020).

Alternative gene therapy approaches include gene augmentation, more commonly used to treat recessive loss-of-function mutations, and RNA interference; however, both present their own challenges. Gene augmentation in dominant disease can have partial benefits (Mao et al., 2011) yet it requires high levels of exogenous gene expression to overcome effects of the mutant allele, and will be ineffective if the mutant gene product continues to interfere with the function of the wild-type gene product, or causes direct toxicity to the cell (Yu-Wai-Man, 2016; Diakatou et al., 2019). RNA interference, where a vector delivers a small RNA that targets the mutant transcript for degradation, has been used successfully in animal models of dominant disease, including CMT2D (Matsa et al., 2014; Morelli et al., 2019; Zaleta-Rivera et al., 2019). Although promising, this approach needs to overcome significant challenges including efficiency and specificity, particularly for single-nucleotide point mutations. Furthermore, both gene augmentation and RNA interference require long-term persistence of the vector or repeated treatments.

We performed our studies in a human motor neuron model system because motor symptoms are typically the most debilitating in CMT2E and many subtypes of axonal CMT, although sensory neurons are also affected (Adebola et al., 2015; Yang et al., 2016; Zhao et al., 2017; Lancaster et al., 2018). Although we focused on motor neurons, a similar approach could be applied to sensory neurons or glial cells differentiated from patient iPSCs. Limitations of our system include the relatively immature developmental state of the motor neurons, absence of other cell types, and lack of anatomic structures. As a result, we are not able to recapitulate all disease phenotypes, such as axonal atrophy, decreased nerve conduction velocity, and length-dependent axonal degeneration, such as that are present in human patients and animal models. Advances in the development of three-dimensional and heterotypic microtissues derived from iPSC have the potential to overcome some of these limitations in the future.

A limitation of our studies is that we performed editing in stem cells rather than in the neurons directly. Efficient delivery of gene-editing reagents to neurons *in vitro* is challenging, and ongoing work in our group and others is focused on improving methodology to enable routine gene-editing experiments in iPSC-derived neurons. The studies presented here establish a crucial baseline, by identifying candidate therapeutic reagents and validating rapid development of disease-specific phenotypes that can be assayed in high throughput. These tools will be invaluable to answer outstanding questions including whether phenotypic rescue will be variable in patient lines with different genetic backgrounds, applicability to other missense mutations in *NEFL*, allele specificity and repair outcomes in neurons, and the time course for reversing the established disease phenotype. Furthermore, *in vivo* animal experiments will be important to complement the *in vitro* human models. Fortunately, in the case of CMT2E there is an excellent animal model in the N98S knock-in mouse that precisely mimics the human mutation, and is associated with a severe and well characterized phenotype (Adebola et al., 2015; Lancaster et al., 2018). In the case of gene editing, the ultimate therapeutic reagent must be primarily developed and validated in a human system due to species-specific genome sequences, but *in vivo* experiments will be critical to optimize delivery methods, assess functional outcomes, and evaluate systemic side effects.

## DATA AVAILABILITY STATEMENT

The raw data supporting the conclusions of this article will be made available by the authors, without undue reservation.

## ETHICS STATEMENT

The studies involving human participants were reviewed and approved by University of California, San Francisco Human Research Protection Program Institutional Review Board. The patients/participants provided their written informed consent to participate in this study.

## AUTHOR CONTRIBUTIONS

LJ, MS, and BC conceived the project. CF, KW, HW, and LJ designed the experiments. CF performed the majority of experiments and data analysis with assistance from other authors as specified. KW, HG, AL, and HW transfected iPSC and isolated clonal lines. KW optimized neuron differentiation, western blots, and immunofluorescent staining. CM performed selected gene editing and immunofluorescent staining. CM, LZ, and TM conducted multielectrode array analysis. GR helped optimize neuron differentiation and design of the CellProfiler analysis pipeline. CF and LJ wrote the manuscript with assistance from

all authors. All authors contributed to the article and approved the submitted version.

## FUNDING

LJ and BC received funding from the Charcot-Marie-Tooth Association (CMTA). LJ, BC, and TM received support from NIH grant U01-ES032673. GR received support from the NSF Graduate Research Fellowship Program and the UCSF Discovery Fellowship. LZ received support from the Lisa Dean Moseley Foundation. BC received support from the Gladstone Institutes, Innovative Genomics Institute, and NIH grants R01-EY028249, R01-HL130533, R01-HL135358, P01-HL146366, RF1-AG072052 and the Claire Giannini Fund.

## ACKNOWLEDGMENTS

We thank Michael Ward for providing the AAVS1-hNIL iPSC line and AAVS1-hNIL and CLYBL-hNIL plasmids, the Gladstone Stem Cell Core and Cell Line Genetics for their services, and A. Birk, A. Sachdev, P. Dua, Z. Nevin, C. Clelland, and F. Chanut for technical assistance, advice, and critical review of the manuscript.

## SUPPLEMENTARY MATERIAL

The Supplementary Material for this article can be found online at: https://www.frontiersin.org/articles/10.3389/fcell.2021.723023/full#supplementary-material

## REFERENCES

Abe, A., Numakura, C., Saito, K., Koide, H., Oka, N., Honma, A., et al. (2009). Neurofilament light chain polypeptide gene mutations in Charcot-Marie-Tooth disease: nonsense mutation probably causes a recessive phenotype. *J. Hum. Genet.* 54, 94–97. doi: 10.1038/jhg.2008.13

Adebola, A. A., Di Castri, T., He, C.-Z., Salvatierra, L. A., Zhao, J., Brown, K., et al. (2015). Neurofilament light polypeptide gene N98S mutation in mice leads to neurofilament network abnormalities and a Charcot-Marie-Tooth Type 2E phenotype. *Hum. Mol. Genet.* 24, 2163–2174. doi: 10.1093/hmg/ddu736

Allen, F., Crepaldi, L., Alsinet, C., Strong, A. J., Kleshchevnikov, V., De Angeli, P., et al. (2018). Predicting the mutations generated by repair of Cas9-induced double-strand breaks. *Nat. Biotechnol.* 37, 64–72. doi: 10.1038/nbt.4317

Anzalone, A. V., Randolph, P. B., Davis, J. R., Sousa, A. A., Koblan, L. W., Levy, J. M., et al. (2019). Search-and-replace genome editing without double-strand breaks or donor DNA. *Nature* 576, 149–157. doi: 10.1038/s41586-019-1711-4

Bae, S., Kweon, J., Kim, H. S., and Kim, J.-S. (2014). Microhomology-based choice of Cas9 nuclease target sites. *Nat. Methods* 11, 705–706. doi: 10.1038/nmeth.3015

Bétermier, M., Bertrand, P., and Lopez, B. S. (2014). Is non-homologous end-joining really an inherently error-prone process? *PLoS Genet.* 10:e1004086. doi: 10.1371/journal.pgen.1004086

Brennan, K. M., Bai, Y., and Shy, M. E. (2015). Demyelinating CMT–what's known, what's new and what's in store? *Neurosci. Lett.* 596, 14–26. doi: 10.1016/j.neulet.2015.01.059

Cerbini, T., Funahashi, R., Luo, Y., Liu, C., Park, K., Rao, M., et al. (2015). Transcription activator-like effector nuclease (TALEN)-mediated CLYBL targeting enables enhanced transgene expression and one-step generation of dual reporter human induced pluripotent stem cell (iPSC) and neural stem cell (NSC) lines. *PLoS One* 10:e0116032. doi: 10.1371/journal.pone.0116032

Chen, W., McKenna, A., Schreiber, J., Haeussler, M., Yin, Y., Agarwal, V., et al. (2019). Massively parallel profiling and predictive modeling of the outcomes of CRISPR/Cas9-mediated double-strand break repair. *Nucleic Acids Res.* 47, 7989–8003. doi: 10.1093/nar/gkz487

Diakatou, M., Manes, G., Bocquet, B., Meunier, I., and Kalatzis, V. (2019). Genome editing as a treatment for the most prevalent causative genes of autosomal dominant retinitis pigmentosa. *Int. J. Mol. Sci.* 20:2542. doi: 10.3390/ijms20102542

Disanto, G., Barro, C., Benkert, P., Naegelin, Y., Schädelin, S., Giardiello, A., et al. (2017). Serum Neurofilament light: a biomarker of neuronal damage in multiple sclerosis. *Ann. Neurol.* 81, 857–870. doi: 10.1002/ana.24954

DiVincenzo, C., Elzinga, C. D., Medeiros, A. C., Karbassi, I., Jones, J. R., Evans, M. C., et al. (2014). The allelic spectrum of Charcot-Marie-Tooth disease in over 17,000 individuals with neuropathy. *Mol. Genet. Genomic Med.* 2, 522–529. doi: 10.1002/mgg3.106

Doench, J. G., Fusi, N., Sullender, M., Hegde, M., Vaimberg, E. W., Donovan, K. F., et al. (2016). Optimized sgRNA design to maximize activity and minimize off-target effects of CRISPR-Cas9. *Nat. Biotechnol.* 34, 184–191. doi: 10.1038/nbt.3437

Fernandopulle, M. S., Prestil, R., Grunseich, C., Wang, C., Gan, L., and Ward, M. E. (2018). Transcription factor-mediated differentiation of human iPSCs into neurons. *Curr. Protoc. Cell Biol.* 79:e51. doi: 10.1002/cpcb.51

Fu, J., and Yuan, Y. (2018). A novel homozygous nonsense mutation in NEFL causes autosomal recessive Charcot-Marie-Tooth disease. *Neuromuscul. Disord.* 28, 44–47. doi: 10.1016/j.nmd.2017.09.018

Gaj, T., Ojala, D. S., Ekman, F. K., Byrne, L. C., Limsirichai, P., and Schaffer, D. V. (2017). *In vivo* genome editing improves motor function and extends survival in a mouse model of ALS. *Sci. Adv.* 3, eaar3952. doi: 10.1126/sciadv.aar3952

Hansson, O., Janelidze, S., Hall, S., Magdalinou, N., Lees, A. J., Andreasson, U., et al. (2017). Blood-based NfL: a biomarker for differential diagnosis of parkinsonian disorder. *Neurology* 88, 930–937. doi: 10.1212/WNL.0000000000003680

Jordanova, A., De Jonghe, P., Boerkoel, C. F., Takashima, H., De Vriendt, E., Ceuterick, C., et al. (2003). Mutations in the neurofilament light chain gene (NEFL) cause early onset severe Charcot-Marie-Tooth disease. *Brain* 126, 590–597. doi: 10.1093/brain/awg059

Kleinstiver, B. P., Prew, M. S., Tsai, S. Q., Nguyen, N. T., Topkar, V. V., Zheng, Z., et al. (2015). Broadening the targeting range of Staphylococcus aureus CRISPR-Cas9 by modifying PAM recognition. *Nat. Biotechnol.* 33, 1293–1298. doi: 10.1038/nbt.3404

Komor, A. C., Kim, Y. B., Packer, M. S., Zuris, J. A., and Liu, D. R. (2016). Programmable editing of a target base in genomic DNA without double-stranded DNA cleavage. *Nature* 533, 420–424. doi: 10.1038/nature17946

Kreitzer, F. R., Salomonis, N., Sheehan, A., Huang, M., Park, J. S., Spindler, M. J., et al. (2013). A robust method to derive functional neural crest cells from human pluripotent stem cells. *Am. J. Stem Cells* 2, 119–131.

Lancaster, E., Li, J., Hanania, T., Liem, R., Scheideler, M. A., and Scherer, S. S. (2018). Myelinated axons fail to develop properly in a genetically authentic mouse model of Charcot-Marie-Tooth disease type 2E. *Exp. Neurol.* 308, 13–25. doi: 10.1016/j.expneurol.2018.06.010

Lindeboom, R. G. H., Supek, F., and Lehner, B. (2016). The rules and impact of nonsense-mediated mRNA decay in human cancers. *Nat. Genet.* 48, 1112–1118. doi: 10.1038/ng.3664

Lu, C.-H., Macdonald-Wallis, C., Gray, E., Pearce, N., Petzold, A., Norgren, N., et al. (2015). Neurofilament light chain: a prognostic biomarker in amyotrophic lateral sclerosis. *Neurology* 84, 2247–2257. doi: 10.1212/WNL.0000000000001642

Luigetti, M., Fabrizi, G. M., Bisogni, G., Romano, A., Taioli, F., Ferrarini, M., et al. (2016). Charcot-Marie-Tooth type 2 and distal hereditary motor neuropathy: clinical, neurophysiological and genetic findings from a single-centre experience. *Clin. Neurol. Neurosurg.* 144, 67–71. doi: 10.1016/j.clineuro.2016.03.007

Maciel, R., Correa, R., Bosso Taniguchi, J., Prufer Araujo, I., and Saporta, M. A. (2020). Human tridimensional neuronal cultures for phenotypic drug screening in inherited peripheral neuropathies. *Clin. Pharmacol. Ther.* 107, 1231–1239. doi: 10.1002/cpt.1718

Mao, H., James, T., Schwein, A., Shabashvili, A. E., Hauswirth, W. W., Gorbatyuk, M. S., et al. (2011). AAV delivery of wild-type rhodopsin preserves retinal function in a mouse model of autosomal dominant retinitis pigmentosa. *Hum. Gene Ther.* 22, 567–575. doi: 10.1089/hum.2010.140

Matsa, E., Dixon, J. E., Medway, C., Georgiou, O., Patel, M. J., Morgan, K., et al. (2014). Allele-specific RNA interference rescues the long-QT syndrome phenotype in human-induced pluripotency stem cell cardiomyocytes. *Eur. Heart J.* 35, 1078–1087. doi: 10.1093/eurheartj/eht067

Mendell, J. R., Al-Zaidy, S., Shell, R., Arnold, W. D., Rodino-Klapac, L. R., Prior, T. W., et al. (2017). Single-Dose Gene-Replacement Therapy for Spinal Muscular Atrophy. *N. Engl. J. Med.* 377, 1713–1722. doi: 10.1056/NEJMoa1706198

Miyaoka, Y., Berman, J. R., Cooper, S. B., Mayerl, S. J., Chan, A. H., Zhang, B., et al. (2016). Systematic quantification of HDR and NHEJ reveals effects of locus, nuclease, and cell type on genome-editing. *Sci. Rep.* 6:23549. doi: 10.1038/srep23549

Miyaoka, Y., Chan, A. H., Judge, L. M., Yoo, J., Huang, M., Nguyen, T. D., et al. (2014). Isolation of single-base genome-edited human iPS cells without antibiotic selection. *Nat. Methods* 11, 291–293. doi: 10.1038/nmeth.2840

Morelli, K. H., Griffin, L. B., Pyne, N. K., Wallace, L. M., Fowler, A. M., Oprescu, S. N., et al. (2019). Allele-specific RNA interference prevents neuropathy in Charcot-Marie-Tooth disease type 2D mouse models. *J. Clin. Invest.* 129, 5568–5583. doi: 10.1172/JCI130600

Pareyson, D., Saveri, P., and Pisciotta, C. (2017). New developments in Charcot-Marie-Tooth neuropathy and related diseases. *Curr. Opin. Neurol.* 30, 471–480. doi: 10.1097/WCO.0000000000000474

Perez-Olle, R., Jones, S. T., and Liem, R. K. H. (2004). Phenotypic analysis of neurofilament light gene mutations linked to Charcot-Marie-Tooth disease in cell culture models. *Hum. Mol. Genet.* 13, 2207–2220. doi: 10.1093/hmg/ddh236

Pérez-Ollé, R., López-Toledano, M. A., Goryunov, D., Cabrera-Poch, N., Stefanis, L., Brown, K., et al. (2005). Mutations in the neurofilament light gene linked to Charcot-Marie-Tooth disease cause defects in transport. *J. Neurochem.* 93, 861–874. doi: 10.1111/j.1471-4159.2005.03095.x

Porteus, M. H. (2019). A New Class of Medicines through DNA Editing. *N. Engl. J. Med.* 380, 947–959. doi: 10.1056/NEJMra1800729

Reilly, M. M., Murphy, S. M., and Laurá, M. (2011). Charcot-Marie-Tooth disease. *J Peripher. Nerv. Syst.* 16, 1–14. doi: 10.1111/j.1529-8027.2011.00324.x

Rossor, A. M., Evans, M. R. B., and Reilly, M. M. (2015). A practical approach to the genetic neuropathies. *Pract. Neurol.* 15, 187–198. doi: 10.1136/practneurol-2015-001095

Saporta, M. A., Dang, V., Volfson, D., Zou, B., Xie, X. S., Adebola, A., et al. (2015). Axonal Charcot-Marie-Tooth disease patient-derived motor neurons demonstrate disease-specific phenotypes including abnormal electrophysiological properties. *Exp. Neurol.* 263, 190–199. doi: 10.1016/j.expneurol.2014.10.005

Shalem, O., Sanjana, N. E., Hartenian, E., Shi, X., Scott, D. A., Mikkelson, T., et al. (2014). Genome-scale CRISPR-Cas9 knockout screening in human cells. *Science* 343, 84–87. doi: 10.1126/science.1247005

Shi, Y., Lin, S., Staats, K. A., Li, Y., Chang, W.-H., Hung, S.-T., et al. (2018). Haploinsufficiency leads to neurodegeneration in C9ORF72 ALS/FTD human induced motor neurons. *Nat. Med.* 24, 313–325. doi: 10.1038/nm.4490

Song, M., Yang, X., Ren, X., Maliskova, L., Li, B., Jones, I. R., et al. (2019). Mapping cis-regulatory chromatin contacts in neural cells links neuropsychiatric disorder risk variants to target genes. *Nat. Genet.* 51, 1252–1262. doi: 10.1038/s41588-019-0472-1

Stone, E. J., Uchida, A., and Brown, A. (2019). Charcot-Marie-Tooth disease Type 2E/1F mutant neurofilament proteins assemble into neurofilaments. *Cytoskeleton* 76, 423–439. doi: 10.1002/cm.21566

Szaro, B. G., and Strong, M. J. (2010). Post-transcriptional control of neurofilaments: new roles in development, regeneration and neurodegenerative disease. *Trends Neurosci.* 33, 27–37. doi: 10.1016/j.tins.2009.10.002

Timmerman, V., Strickland, A. V., and Züchner, S. (2014). Genetics of Charcot-Marie-Tooth (CMT) Disease within the Frame of the Human Genome Project Success. *Genes* 5, 13–32. doi: 10.3390/genes5010013

Tycko, J., Barrera, L. A., Huston, N. C., Friedland, A. E., Wu, X., Gootenberg, J. S., et al. (2018). Pairwise library screen systematically interrogates Staphylococcus aureus Cas9 specificity in human cells. *Nat. Commun.* 9:2962. doi: 10.1038/s41467-018-05391-2

Vakulskas, C. A., Dever, D. P., Rettig, G. R., Turk, R., Jacobi, A. M., Collingwood, M. A., et al. (2018). A high-fidelity Cas9 mutant delivered as a ribonucleoprotein complex enables efficient gene editing in human hematopoietic stem and progenitor cells. *Nat. Med.* 24, 1216–1224. doi: 10.1038/s41591-018-0137-0

Watry, H. L., Feliciano, C. M., Gjoni, K., Takahashi, G., Miyaoka, Y., Conklin, B. R., et al. (2020). Rapid, precise quantification of large DNA excisions and inversions by ddPCR. *Sci. Rep.* 10:14896. doi: 10.1038/s41598-020-71742-z

Wienert, B., Wyman, S. K., Richardson, C. D., Yeh, C. D., Akcakaya, P., Porritt, M. J., et al. (2019). Unbiased detection of CRISPR off-targets *in vivo* using DISCOVER-Seq. *Science* 364, 286–289. doi: 10.1126/science.aav9023

Yang, Y., Gu, L.-Q., Burnette, W. B., and Li, J. (2016). N98S mutation in NEFL gene is dominantly inherited with a phenotype of polyneuropathy and cerebellar atrophy. *J. Neurol. Sci.* 365, 46–47. doi: 10.1016/j.jns.2016.04.007

Yuan, A., Rao, M. V., Veeranna, and Nixon, R. A. (2017). Neurofilaments and neurofilament proteins in health and disease. *Cold Spring Harb. Perspect. Biol.* 9:a018309. doi: 10.1101/cshperspect.a018309

Yum, S. W., Zhang, J., Mo, K., Li, J., and Scherer, S. S. (2009). A novel recessive Nefl mutation causes a severe, early-onset axonal neuropathy. *Ann. Neurol.* 66, 759–770. doi: 10.1002/ana.21728

Yu-Wai-Man, P. (2016). Genetic manipulation for inherited neurodegenerative diseases: myth or reality? *Br. J. Ophthalmol.* 100, 1322–1331. doi: 10.1136/bjophthalmol-2015-308329

Zaleta-Rivera, K., Dainis, A., Ribeiro, A. J. S., Cordero, P., Rubio, G., Shang, C., et al. (2019). Allele-specific silencing ameliorates restrictive cardiomyopathy attributable to a human myosin regulatory light chain mutation. *Circulation* 140, 765–778. doi: 10.1161/CIRCULATIONAHA.118.036965

Zhao, J., Brown, K., and Liem, R. K. H. (2017). Abnormal neurofilament inclusions and segregations in dorsal root ganglia of a Charcot-Marie-Tooth type 2E mouse model. *PLoS One* 12:e0180038. doi: 10.1371/journal.pone.0180038

**Conflict of Interest:** BC is a founder of Tenaya Therapeutics (https://www.tenayatherapeutics.com/), a company focused on finding treatments for heart failure, including genetic cardiomyopathies. BC holds equity in Tenaya, and Tenaya provides research support for heart failure related research.

The remaining authors declare that the research was conducted in the absence of any commercial or financial relationships that could be construed as a potential conflict of interest.

**Publisher's Note:** All claims expressed in this article are solely those of the authors and do not necessarily represent those of their affiliated organizations, or those of the publisher, the editors and the reviewers. Any product that may be evaluated in this article, or claim that may be made by its manufacturer, is not guaranteed or endorsed by the publisher.

frontiers in Cell and Developmental Biology

ORIGINAL RESEARCH
published: 19 August 2021
doi: 10.3389/fcell.2021.710112

# Inhibition of *Postn* Rescues Myogenesis Defects in Myotonic Dystrophy Type 1 Myoblast Model

*Xiaopeng Shen[1,2,3*†], Zhongxian Liu[1,2,3†], Chunguang Wang[1,2,3†], Feng Xu[1,2,3], Jingyi Zhang[1,2,3], Meng Li[1,2,3], Yang Lei[4], Ao Wang[1,2,3], Chao Bi[1,2,3] and Guoping Zhu[1,2,3*]*

[1] Anhui Provincial Key Laboratory of Molecular Enzymology and Mechanism of Major Diseases, College of Life Sciences, Anhui Normal University, Wuhu, China, [2] Anhui Provincial Key Laboratory of the Conservation and Exploitation of Biological Resources, College of Life Sciences, Anhui Normal University, Wuhu, China, [3] Key Laboratory of Biomedicine in Gene Diseases and Health of Anhui Higher Education Institutes, College of Life Sciences, Anhui Normal University, Wuhu, China, [4] Wuhu Center for Disease Control and Prevention, Wuhu, China

OPEN ACCESS

**Edited by:**
Megan Laura McCain,
University of Southern California,
United States

**Reviewed by:**
Arnaud F. Klein,
Institut National de la Santé et de la Recherche Médicale, France
Hongshuai Li,
University of Pittsburgh, United States

***Correspondence:**
Xiaopeng Shen
shenxiaopeng_cn@ahnu.edu.cn;
xpshen@mail.ustc.edu.cn
Guoping Zhu
gpz2012@ahnu.edu.cn

[†] These authors have contributed equally to this work

**Specialty section:**
This article was submitted to Stem Cell Research, a section of the journal Frontiers in Cell and Developmental Biology

**Received:** 15 May 2021
**Accepted:** 30 July 2021
**Published:** 19 August 2021

**Citation:**
Shen X, Liu Z, Wang C, Xu F, Zhang J, Li M, Lei Y, Wang A, Bi C and Zhu G (2021) Inhibition of Postn Rescues Myogenesis Defects in Myotonic Dystrophy Type 1 Myoblast Model. Front. Cell Dev. Biol. 9:710112. doi: 10.3389/fcell.2021.710112

Myotonic dystrophy type 1 (DM1) is an inherited neuromuscular disease caused by expanded CTG repeats in the 3′ untranslated region (3′UTR) of the *DMPK* gene. The myogenesis process is defective in DM1, which is closely associated with progressive muscle weakness and wasting. Despite many proposed explanations for the myogenesis defects in DM1, the underlying mechanism and the involvement of the extracellular microenvironment remained unknown. Here, we constructed a DM1 myoblast cell model and reproduced the myogenesis defects. By RNA sequencing (RNA-seq), we discovered that periostin (*Postn*) was the most significantly upregulated gene in DM1 myogenesis compared with normal controls. This difference in *Postn* was confirmed by real-time quantitative PCR (RT-qPCR) and western blotting. Moreover, *Postn* was found to be significantly upregulated in skeletal muscle and myoblasts of DM1 patients. Next, we knocked down *Postn* using a short hairpin RNA (shRNA) in DM1 myoblast cells and found that the myogenesis defects in the DM1 group were successfully rescued, as evidenced by increases in the myotube area, the fusion index, and the expression of myogenesis regulatory genes. Similarly, *Postn* knockdown in normal myoblast cells enhanced myogenesis. As POSTN is a secreted protein, we treated the DM1 myoblast cells with a POSTN-neutralizing antibody and found that DM1 myogenesis defects were successfully rescued by POSTN neutralization. We also tested the myogenic ability of myoblasts in the skeletal muscle injury mouse model and found that *Postn* knockdown improved the myogenic ability of DM1 myoblasts. The activity of the TGF-β/Smad3 pathway was upregulated during DM1 myogenesis but repressed when inhibiting *Postn* with a *Postn* shRNA or a POSTN-neutralizing antibody, which suggested that the TGF-β/Smad3 pathway might mediate the function of *Postn* in DM1 myogenesis. These results suggest that *Postn* is a potential therapeutical target for the treatment of myogenesis defects in DM1.

**Keywords: *Postn*, myotonic dystrophy type 1, microenvironment, myoblast, myogenesis**

## INTRODUCTION

Myotonic dystrophy type 1 (DM1) is an autosomal inherited neuromuscular disease caused by aberrant expanded (CTG) trinucleotide repeats in the 3′ untranslated region (3′UTR) of the *DMPK* gene. The copy number of CTG repeats is higher than 50 in DM1 patients but lower than 37 in healthy individuals. The individuals with 38–49 CTG repeats are considered to have premutations. The expanded CTG repeats in DM1 are transcribed, along with the *DMPK* gene, into mRNA containing expanded CUG repeats, referred to as "toxic RNA" (Udd and Krahe, 2012). This toxic RNA forms a hairpin-like secondary structure in cell nuclei, leading to MBNL1 sequestration (Miller et al., 2000) and CELF1 upregulation (Kuyumcu-Martinez et al., 2007; Kalsotra et al., 2010). Both MBNL1 and CELF1 are RNA-binding proteins and regulate alternative splicing of RNA. Thus, the dysregulation of *MBNL1* and *CELF1* leads to isoform switches of several important genes related to skeletal muscle function, including *CLCN1*, *BIN1, TNNT2*, *IR*, and *PKM*, which directly cause DM1 disease phenotypes (Philips et al., 1998; Savkur et al., 2001; Charlet et al., 2002; Mankodi et al., 2002; Ho et al., 2004; Fugier et al., 2011). Among these phenotypes, the myogenesis defect is a particularly serious problem in DM1 as it has been shown to be closely related to progressive muscle weakness and wasting (Kanadia et al., 2003; Ward et al., 2010).

Myogenesis is a complicated and precisely regulated process that produces myotubes of skeletal muscle. Many myogenic regulatory factors (MRFs) have been documented, including *MyoD*, *MyoG*, and *Mrf4* (Hernandez-Hernandez et al., 2017). Myogenesis consists of two stages, cell cycle withdrawal and myoblast fusion (Andre et al., 2018). In the initial stage, myoblast proliferation is required to generate sufficient cells for myoblast fusion. The proliferation process, however, should be terminated to enable the subsequent myogenesis process (Andres and Walsh, 1996). This cell cycle withdrawal is governed by *p21* (Halevy et al., 1995) and *Rb* (Zacksenhaus et al., 1996). Following cell cycle arrest, the myoblasts undergo cell fusion to generate multinucleated myotubes (Schnorrer and Dickson, 2004). Although the detailed mechanism remains elusive, many fusion-related regulators have been discovered, including *Myomaker* (Millay et al., 2013, 2014) and *Myomixer* (Bi et al., 2017). Many studies have proposed possible explanations for the defective myogenesis in DM1. *Celf1* is directly phosphorylated and regulated by *Akt* and *cyclin D3*/*cdk4*, which leads to *CCND1* upregulation and *p21* downregulation and causes impaired myogenesis in DM1 (Timchenko et al., 2001a; Salisbury et al., 2008). Consistently, recent studies have observed suppression of cell cycle withdrawal in DM1 or *Celf1*-overexpressing myoblasts (Furling et al., 2001; Peng et al., 2015), probably due to dysregulation of *cyclin D1* and *p21*. *DMPK*, a rho kinase, may be involved in the regulation of myosin light chain phosphorylation, and its isoform E has been shown to be crucial for normal muscle development (Jansen et al., 1996; Mulders et al., 2011). Although studies have shown that *DMPK* is dispensable for myoblast differentiation (Jansen et al., 1996), the *DMPK* dysregulation that occurs as a result of expanded CUG repeats suggests a potential role of this gene in myoblast differentiation. Moreover, MRFs including *MyoD* and *Six5* are altered in DM1 owing to the expanded CUG repeats and *DMPK* dysregulation, respectively (Inukai et al., 2000; Apponi et al., 2011). Although each of the above findings can partially explain the defective myogenesis in DM1, the underlying mechanism remains unclear.

Periostin (*Postn*) is a matricellular protein that consists of seven domains: a signal peptide, a cysteine-rich domain, a C-terminal region, and four FAS1 domains. *Postn* is well known as an important microenvironment component that favors tumor growth and metastasis. In ovarian cancer, *Postn* is upregulated by the TGF-β pathway and promotes migration and invasion (Yue et al., 2021). *Postn* is also a candidate prognostic marker in colorectal cancers (Oh et al., 2017) and promotes colorectal cancer progression through activating *YAP*/*TAZ* (Ma et al., 2020). In glioma, *Postn* promotes tumor growth, epithelial–mesenchymal transition (EMT), invasion, and resistance to antiangiogenic therapy by recruiting M2 macrophages and activating *STAT3* (Zhou et al., 2015; Park et al., 2016). *Postn* is targeted by *miR-876* and facilitates EMT and fibrosis of hepatocellular carcinoma (Chen et al., 2020). *Postn* also plays an important part in cancer stem cell maintenance by recruiting Wnt ligands to enhance Wnt signaling in cancer stem cells (Malanchi et al., 2011). In addition to its roles in cancer, *Postn* has been reported to regulate skeletal muscle regeneration; it is temporally expressed during skeletal muscle regeneration (Ozdemir et al., 2014), and *Postn* knockout improves muscle recovery and inhibits fibrosis after skeletal muscle injuries. Moreover, POSTN-neutralizing antibody treatment promotes recovery from skeletal muscle injuries in a mouse model (Hara et al., 2018). In a muscular dystrophy mouse model, *Postn* knockout was found to improve myogenesis and inhibit fibrosis by upregulating the TGF-β pathway (Lorts et al., 2012). Nevertheless, the function of *Postn* in regulating DM1 has remained unknown.

In this study, we used a DM1 mouse myoblast cell model to study myogenesis defects in DM1. *Postn* was found to be significantly upregulated both during the DM1 myoblast differentiation process and in skeletal muscles and myoblasts of DM1 patients. By downregulating *Postn* with short hairpin RNA (shRNA) or a neutralizing antibody, the myogenesis defects in DM1 were successfully rescued. Moreover, *Postn* knockdown in DM1 myoblasts improved the efficiencies of myogenesis and regeneration in a skeletal muscle injury mouse model. The TGF-β/Smad3 pathway that was enhanced in the DM1 myogenesis process was suppressed with *Postn* inhibitions, which might mediate the function of *Postn* in the myogenesis process of DM1 myoblasts. These results suggest that *Postn* is a potential therapeutical target for the treatment of DM1.

## MATERIALS AND METHODS

### Cell Culture

C2C12 cells (RRID: CVCL_0188) were provided by the Stem Cell Bank, Chinese Academy of Sciences. C2C12 cells were cultured in high-glucose Dulbecco's Modified Eagle Medium (DMEM, HyClone, Cat #SH30022.01) supplemented with 20% fetal bovine serum (Clark, Cat #FB15015), 50 U/mL

penicillin (Biosharp, Cat #BL505A), and 50 μg/mL streptomycin (Biosharp, Cat #BL505A). *In vitro* myoblast differentiation was induced by switching the above medium to high-glucose DMEM (HyClone) supplemented with 2% horse serum (HyClone, Cat #SH30074.03), 50 U/mL penicillin (Biosharp), 50 μg/mL streptomycin (Biosharp), and 1 μM insulin (Beyotime, Cat#P3376-100IU) when cells were confluent. The *in vitro* myoblast differentiation process typically spanned 6 days. When neutralizing the secreted POSTN during myoblast differentiation, 1.5 μg/ml anti-POSTN antibody (Sino Biological, Cat #50450-RP02, RRID: AB_2891098) was added to the differentiation medium. 1.5 μg/ml IgG control antibody (Santa Cruz Biotechnology, Cat #sc-2025, RRID: AB_737182) was used as control. Both antibodies were added from day 0 to day 6 of *in vitro* myoblast differentiations.

## Construction of Plasmids and Cell Lines

The pcDNA-GFP-$(CUG)_5$ (GFP-CUG5) and pcDNA-GFP-$(CUG)_{200}$ (GFP-CUG200) plasmids were as described previously (Amack and Mahadevan, 2001). The pLL4.0 vector was previously developed by our laboratory (Shen et al., 2020). The pLL4.0 vector was constructed by replacing a CMV-EGFP cassette in the pLL3.7 vector with a PGK-puromycin cassette. Scrambled, shPostn, and shMbnl1 plasmids were generated by ligating the scrambled, *Postn,* and *Mbnl1* shRNA coding sequences into the pLL4.0 vector, respectively. The sequences of the scrambled, *Postn,* and *Mbnl1* shRNAs are listed in **Supplementary Table 1**.

Plasmids were transduced into cells using PolyJet (SignaGen, Cat #SL100688) according to the manufacturer's instructions. Normal (C2C12 GFP-CUG5) and DM1 (C2C12 GFP-CUG200) myoblast cell models were produced by transfecting C2C12 cells with GFP-CUG5 and GFP-CUG200 plasmids, respectively, followed by G418 selection until stable. Control and *Postn* knockdown DM1 myoblast cell lines were produced by transfecting C2C12 GFP-CUG200 cells with the scrambled and shPostn plasmids, respectively, followed by puromycin selection until stable. Control and *Postn* knockdown normal myoblast cell lines were produced by transfecting C2C12-CUG5 cells with the scrambled and shPostn plasmids, respectively, followed by puromycin selection until stable. Control and *Mbnl1* knockdown myoblast cell lines were produced by transfecting C2C12 cells with the scrambled and shMbnl1 plasmids, respectively, followed by puromycin selection until stable.

## Total RNA Extraction and Real-Time Quantitative PCR

Total RNA was extracted using Total RNA Isolation Reagent (Biosharp, Cat #BS259A). Reverse transcription was performed using the FastKing RT Kit (Tiangen, Cat #KR118-02). Quantitative PCR was performed using the Powerup SYBR Master Mix (Applied Biosystems, Cat #A25778). These experiments were conducted according to the corresponding manufacturer's manuals. *Gapdh* was used as a normalized control gene. The primer sequences used in real-time quantitative PCR (RT-qPCR) are listed in **Supplementary Table 1**.

## RNA Sequencing and Data Analysis

The library construction and sequencing steps of RNA sequencing (RNA-seq) were performed by Anhui Microanaly Genetech Co., Ltd. Raw data were subjected to adapter trimming and read filtering using the trim_galore software (Trim Galore, RRID: SCR_011847). The filtered data were aligned to the mouse genome (GRCm38) using Hisat2 (HISAT2, RRID: SCR_015530) and then analyzed with StringTie (RRID: SCR_016323) to generate readcount tables. Differentially expressed genes (DEGs) were determined by DESeq2 (RRID: SCR_015687) (Love et al., 2014) using $|\log2(\text{fold change})| > 1$ and adjusted $P$-value $< 0.05$ as the cutoffs. Gene ontology (GO) and Kyoto Encyclopedia of Genes and Genomes (KEGG) analyses were performed using the clusterProfiler package (clusterProfiler, RRID: SCR_016884) (Yu et al., 2012). RNA-seq data generated during this study are deposited at the Gene Expression Omnibus (GEO) database (GSE174119). The RNA-seq data of tibialis anterior (TA) muscles and myoblasts from healthy, and DM1 individuals were obtained from the GEO database using accession numbers GSE86356 and GSE158216, respectively.

## Protein Extraction and Western Blotting

Intracellular protein samples were extracted using Cell Lysis Buffer (Beyotime, Cat #P0013) supplemented with EASYpack Protease Inhibitors (Roche, Cat #5892970001). Protein concentrations were measured with a BCA protein assay kit (Biosharp, Cat # BL521A) and then adjusted to be the same. Supernatant protein samples were obtained by collecting the culture medium of the corresponding cells. For normalization, the volumes of the cell culture medium were initially the same when culturing cells and the loading volumes of the culture medium were normalized to their corresponding cell numbers when doing gel electrophoresis. Samples were subjected to sodium dodecyl sulfate polyacrylamide gel electrophoresis and the proteins were transferred onto PVDF membranes. The membranes were then blocked and incubated with primary antibodies overnight at 4°C. On the next day, the membranes were incubated with horseradish peroxidase (HRP)-conjugated secondary antibodies and reacted with chemiluminescent substrates (Biosharp, Cat #BL520A). Images were taken with a Tanon 5200 Imaging System. The antibodies and dilutions were as follows: anti-POSTN pAb (1:1,000, Sino Biological, Cat #50450-RP02, RRID: AB_2891098), anti-SMAD3 (1:2,000, Santa Cruz, Cat #sc-101154, RRID: AB_1129525), anti-p-SMAD3 (1:2,000, Santa Cruz, Cat #sc-517575, RRID: AB_2892229), anti-MBNL1 mAb (1:2,000, Novus, Cat #NB110-37256, RRID: AB_792678), anti-GAPDH pAb (1:2,000, Biosharp, Cat #BL006B, RRID: AB_2890028), goat anti-mouse HRP antibody (1:2,000, Biosharp, Cat #BL001A, RRID: AB_2827665), and donkey anti-rabbit HRP antibody (1:2,000, Invitrogen, Cat #31458, RRID: AB_228213). The intensities of the western blot gel bands were measured using ImageJ (RRID: SCR_003070).

## Immunostaining

Samples (cells and slides) were fixed with 4% paraformaldehyde at room temperature. After that, the samples were blocked with

the blocking solution (10% normal goat serum and 0.1% Triton X-100 in PBS). The samples were then incubated with primary antibodies that were diluted in the blocking solution at 4°C overnight. On the next day, the samples were incubated with fluorescence conjugated secondary antibodies and DAPI. The antibodies and dilutions were as follows: anti-myosin heavy chain (MHC) mAb (1:10, DHSB, Catalog No. AB_2147781, and RRID: AB_2147781) and goat anti-mouse Alex Fluor Plus 555-conjugated IgG (1:500, Invitrogen, Catalog No. A32727, and RRID: AB_2633276). All images were obtained with a Leica DMi8 fluorescence microscope and analyzed with ImageJ (RRID: SCR_003070). Fusion index equaled to the ratio of nuclei number in the cells with at least two nuclei vs. total nuclei number. Myotube area equaled to the ratio of the MHC fluorescence positive area vs. the whole area in the immunostaining images.

## Mice and Skeletal Muscle Injury Models

All mouse-related experiments were performed according to the protocols approved by the Institutional Animal Care and Use Committee of Anhui Normal University. Eight-week old male Swiss mice were anesthetized and injected with 25 μl of 10 μM cardiotoxin (CTX, Sigma, Cat #217503) into TA muscles to produce skeletal muscle injury models. On the next day, the CTX injected TA muscles were injected with scramble control and *Postn* knockdown DM1 myoblast cells ($5 \times 10^4$ cells per TA muscle), respectively, to test their myogenic abilities *in vivo*. PBS was used as a sham control. The TA muscles were harvested 14 days after the cell injections and subjected to cryosectioning using OCT (Sakura, Cat #4583). The slices of TA muscles were then stained with hematoxylin & eosin (H&E, Biosharp, Cat #BL700B) and immunostained against MHC to determine muscle regeneration efficiencies after injury.

## Statistical Analysis

All experiments were performed at least three times. Shapiro–Wilk test was used for data normality test. Student's *t*-test was used for two-group comparisons, and one-way analysis of variance (ANOVA) followed by *post hoc* Tukey tests was used for comparisons of three or more groups. An asterisk is used to label significant differences ($P < 0.05$) in the figures. All data are presented as mean ± SD.

# RESULTS

## Myogenesis Was Significantly Impaired in the DM1 Myoblast Cell Model

The myogenesis process is severely impaired in DM1 according to most studies (Amack et al., 2002; Timchenko et al., 2004; Kuyumcu-Martinez et al., 2007; Peng et al., 2015), although several groups have reported no significant change in myogenic abilities in myoblasts derived from some DM1 patients (Jacobs et al., 1990; Loro et al., 2010). Therefore, we first compared the myogenic abilities of DM1 and normal murine myoblast cell models. To construct DM1 and normal myoblast cell models, we stably transfected murine myoblast C2C12 cells with the GFP-CUG5 and GFP-CUG200 plasmids, respectively. Normal and DM1 myoblasts were subjected to *in vitro* myoblast differentiation. At differentiation day 6, the DM1 group displayed markedly less myotube formation compared with the normal control, as visualized by immunostaining against MHC (**Figure 1A**). The myotube area was 51.69% ± 9.51% in the normal group but 14.25% ± 5.24% in the DM1 group; and the fusion index was 43.20% ± 7.34% in the normal group but 15.72% ± 2.77% in the DM1 group (**Figure 1B**). Through RT-qPCR, we found that MRFs (*MyoD*, *MyoG*, *Mef2C*, and *Mrf4*) were significantly inhibited in the DM1 group during *in vitro* myoblast differentiation. Moreover, the essential myoblast fusion markers *Myomaker* and *Myomixer* were also downregulated (**Figure 1C**). These results confirmed that myoblast differentiation and fusion were both impaired in DM1 myoblasts.

## Periostin Might Mediate Aberrant Myogenesis in DM1 Myoblasts

Although many studies have proposed possible explanations for the myogenesis defects in DM1, the underlying mechanism, especially the involvement of the microenvironment, has remained unclear. To investigate this mechanism, we performed RNA-seq on total RNA samples of normal and DM1 myoblasts at differentiation day 4, when myotubes started to form during *in vitro* myoblast differentiation. Principal components analysis (PCA) indicated that the gene expression patterns between normal and DM1 groups were different (**Figure 2A**). Next, we analyzed DEGs of the two groups using DESeq2, with $|\log2(\text{fold change})| > 1$ and adjusted *P*-value $< 0.05$ as the cutoffs for DEG determination. There were 279 upregulated and 158 downregulated genes in the DM1 vs. the normal group (**Figure 2B**). As shown in the heatmap of relative levels of all DEGs in **Figure 2C**, *Postn* was markedly upregulated in the DM1 group. **Table 1** shows the top 20 level-changed genes in the DM1 group. *Pdha2*, *Pcdhga9*, *Lgr5*, *Rarb*, *Trhde*, *Postn*, *Sema5b*, *Tspan8*, and *Sectm1a* were significantly upregulated, while *miR-686*, *Pagr1a*, *Gdf5*, *Myh8*, *Slc25a23*, *Unc13c*, and *Fras1* were significantly downregulated. *Postn* was the most significantly altered gene, with log2(fold change) = 2.86 and adjusted *P*-value = 1.79E−178. We then performed GO and KEGG analyses on all DEGs. The GO results showed that all striated muscle-related biological processes (BP), cellular components (CC), and molecular functions (MF) were inhibited (**Figure 2D**). The KEGG results showed that striated muscle-related pathways (Jak-STAT signaling, insulin signaling, and insulin resistance) were significantly repressed. Surprisingly, some components of the Wnt signaling pathway were upregulated but some other components were downregulated (**Figure 2E**). In summary, *Postn* was the most significantly upregulated gene in the DM1 group, implying that *Postn* might be associated with DM1 pathogenesis.

We then studied the expression levels of *Postn* in various tissues of normal adult mice. *Postn* was highly expressed in spleen, lung, and stomach but showed relatively low expression in skeletal muscle (TA, gastrocnemius, and soleus) (**Figure 3A**). To verify the changes in *Postn* levels observed by RNA-seq, we

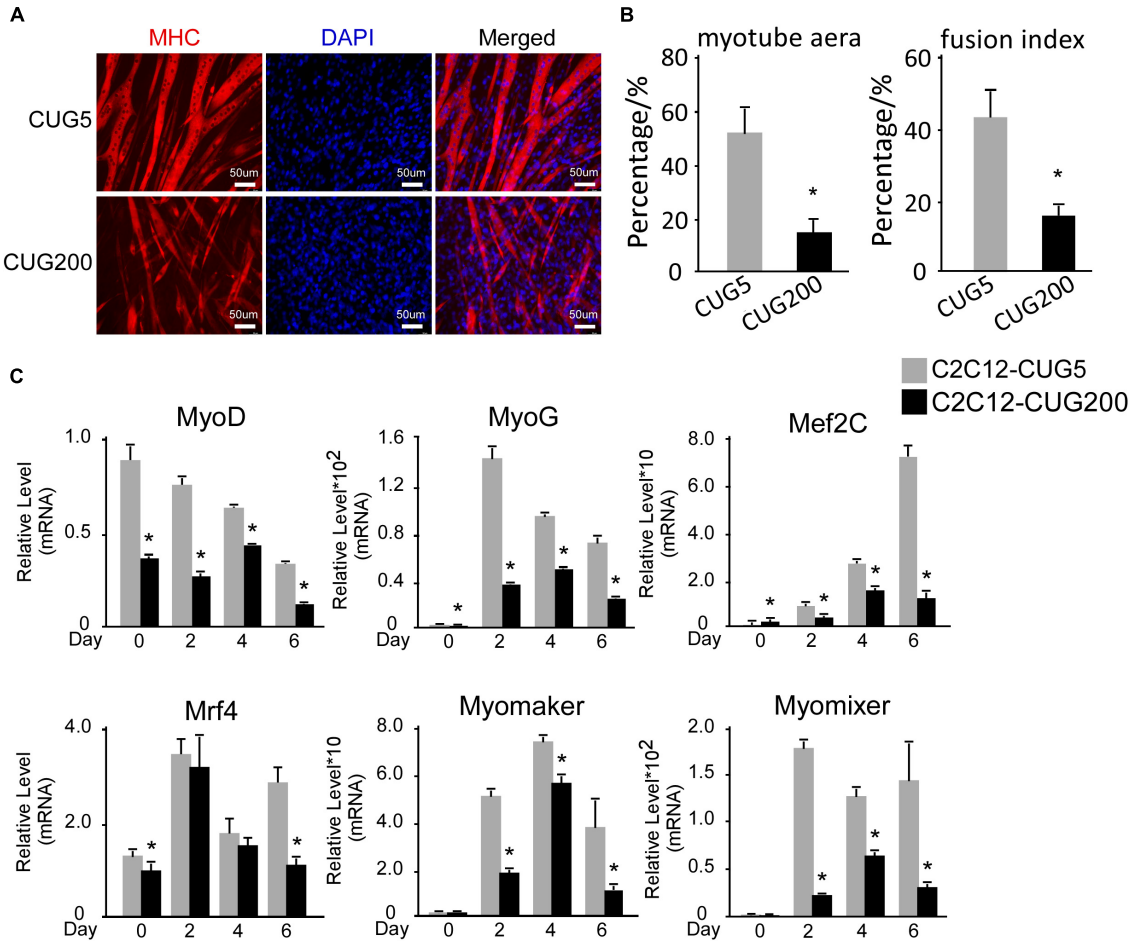


**FIGURE 1 |** Myogenesis was significantly impaired in the myotonic dystrophy type 1 (DM1) myoblast cell model. **(A)** Myotube formation by myoblast cells of both normal control and DM1 groups, detected by immunostaining against myosin heavy chain (MHC) at differentiation day 6. **(B)** Myotube area and fusion index in both the normal control and DM1 groups quantified with ImageJ software. **(C)** Expression levels of myogenic regulatory factors (MRFs; *MyoD*, *MyoG*, *Mef2C*, and *Mrf4*) and fusion markers (*Myomaker* and *Myomixer*) in normal control, and DM1 groups, measured by real-time quantitative PCR (RT-qPCR). All expression levels were normalized to the values of the normal control group at day 0. CUG5, normal control myoblast cells (C2C12 GFP-CUG5); CUG200, DM1 myoblast cells (C2C12 GFP-CUG200); $^*P < 0.05$.

first performed western blotting against POSTN at differentiation day 4 for normal and DM1 myoblasts. As POSTN is a secreted protein, we detected both intracellular and supernatant POSTN levels. Both intracellular and supernatant POSTN were upregulated in DM1 (**Figures 3B,C**). Next, we checked the expression pattern of *Postn* during myoblast differentiation. *Postn* was significantly upregulated from days 4 to 6 of myoblast differentiation in DM1 compared with the normal group (**Figure 3D**). We then investigated whether *POSTN* was also upregulated in the skeletal muscle of DM1 patients. We analyzed an RNA-seq dataset for TA muscle of healthy individuals ($n = 10$) and DM1 patients ($n = 40$) from the DMseq Deep Sequencing Data Repository[1] and found a significant upregulation of *POSTN* in the DM1 group (**Figure 3E**). Moreover, by analyzing the RNA-seq data of myoblasts from healthy and DM1 individuals, we also observed a significant upregulation of *POSTN* in the myoblasts of DM1 patients (**Figure 3F**). Next, we studied if the *Postn* upregulation correlated with the *Mbnl1* downregulation in DM1. By western blotting, we found that the intracellular and secreted POSTN were both significantly upregulated with *Mbnl1* knockdown in C2C12 cells (**Figures 3G,H**). These results suggest a correlation between DM1 pathogenesis and *Postn* upregulation.

## Downregulation of *Postn* Using shRNA Rescued Myogenesis Defects in DM1

As *Postn* was aberrantly upregulated in DM1 myoblast differentiation, we investigated whether downregulation of *Postn* could rescue the myogenesis defect in DM1. We constructed scrambled control and *Postn*-knockdown DM1 myoblast cell lines by stably transfecting C2C12 GFP-CUG200 cells with the scrambled and shPostn plasmids, respectively. Western blots showed that both intracellular and supernatant

[1]http://dmseq.org/

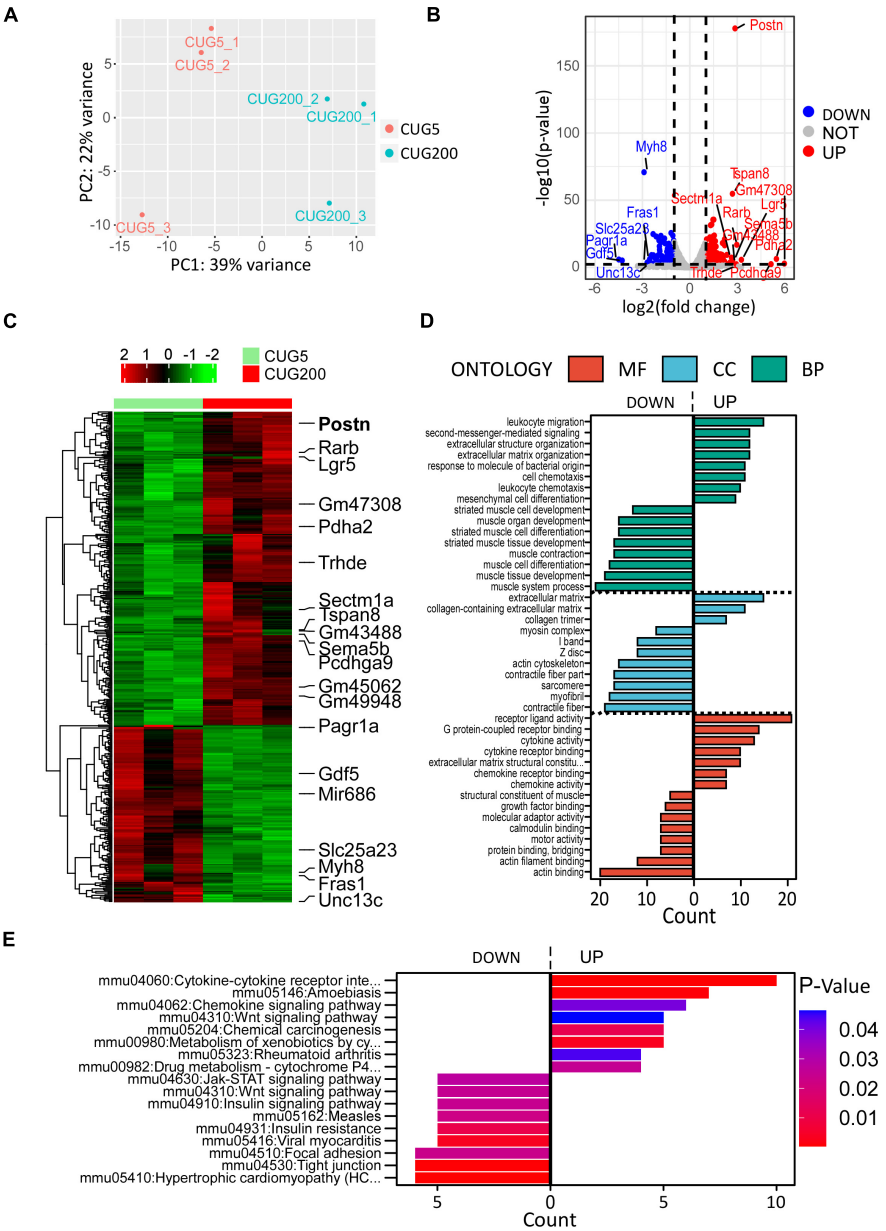


**FIGURE 2 |** Periostin (*Postn*) was the top significantly altered gene in DM1 myoblast differentiation compared with the normal control. **(A)** Principal components analysis (PCA) of RNA sequencing (RNA-seq) data from normal and DM1 groups. Three biological replicates are included for each group. **(B)** Volcano plot showing the differentially expressed genes (DEGs). *Postn* was the top significantly altered gene. **(C)** Heatmap showing relative levels of all DEGs in both groups. **(D)** Gene ontology (GO) analysis of the DEGs. **(E)** Kyoto Encyclopedia of Genes and Genomes (KEGG) analysis of the DEGs. CUG5, normal control myoblast cells (C2C12 GFP-CUG5); CUG200, DM1 myoblast cells (C2C12 GFP-CUG200); MF, molecular function; CC, cellular component; and BP, biological process.

POSTN were significantly downregulated in *Postn*-knockdown DM1 myoblast cells (**Figures 4A,B**). The *Postn* knockdown and control DM1 myoblast cells were subjected to *in vitro* myoblast differentiation. RT-qPCR showed that *Postn* was significantly downregulated throughout the differentiation process (**Figure 4C**). Immunostaining against MHC showed that *Postn* knockdown robustly improved myotube production (**Figure 4D**). The myotube area was 61.32% ± 2.58% in the *Postn* knockdown group but 27.53% ± 4.13% in the scrambled control group; and the fusion index was 41.96% ± 7.38% in the *Postn* knockdown group but 7.64% ± 2.32% in the scrambled control group (**Figure 4E**). Consistently, MRFs (*MyoD*, *MyoG*, *Mef2C*, and *Mrf4*) were all markedly upregulated, and fusion markers (*Myomaker* and *Myomixer*) were also boosted (**Figure 4F**).

We also determined the effect of *Postn* inhibition on normal myoblast differentiation. *Postn*-knockdown and control normal

**TABLE 1 |** Top altered genes in RNA sequencing (RNA-seq).

| Gene | log2(fold change) | Adjusted *P*-value | Direction of change |
|---|---|---|---|
| *Gm45062* | 11.03 | 2.55E−02 | Upregulated |
| *Gm49948* | 8.25 | 1.93E−06 | Upregulated |
| *Gm47308* | 5.98 | 2.02E−03 | Upregulated |
| *Pdha2* | 5.48 | 6.79E−07 | Upregulated |
| *Pcdhga9* | 5.14 | 5.18E−03 | Upregulated |
| *Lgr5* | 3.26 | 2.93E−06 | Upregulated |
| *Rarb* | 2.97 | 1.93E−17 | Upregulated |
| *Trhde* | 2.94 | 6.42E−03 | Upregulated |
| *Postn* | 2.86 | 1.79E−178 | Upregulated |
| *Sema5b* | 2.71 | 4.62E−06 | Upregulated |
| *Tspan8* | 2.70 | 2.18E−55 | Upregulated |
| *Sectm1a* | 2.64 | 7.53E−08 | Upregulated |
| *Gm43488* | 2.62 | 3.34E−04 | Upregulated |
| *miR-686* | −7.41 | 8.74E−08 | Downregulated |
| *Pagr1a* | −4.49 | 1.99E−06 | Downregulated |
| *Gdf5* | −4.29 | 9.99E−06 | Downregulated |
| *Myh8* | −2.90 | 1.97E−71 | Downregulated |
| *Slc25a23* | −2.70 | 3.39E−04 | Downregulated |
| *Unc13c* | −2.58 | 3.32E−02 | Downregulated |
| *Fras1* | −2.54 | 8.09E−07 | Downregulated |

myoblast cell lines were produced by stably transfecting C2C12 GFP-CUG5 cells with the shPostn and scrambled plasmids, respectively. The knockdown efficiency was verified by western blotting (**Figures 5A,B**). Next, we performed *in vitro* myoblast differentiation on these two cell lines. At differentiation day 6, we found that myotube formation in normal myoblast cells was enhanced by *Postn* knockdown, as indicated by immunostaining against MHC (**Figure 5C**). Myotube area and fusion index were both increased with *Postn* knockdown (**Figure 5D**), and the expression levels of MRFs (*MyoD*, *MyoG*, *Mef2C*, and *Mrf4*) were significantly elevated (**Figure 5E**). Taken together, besides rescuing myogenesis defect in DM1 myoblast cells, *Postn* inhibition in normal myoblast promotes the myogenesis process in normal myoblasts.

## Neutralizing Antibody Treatment Against POSTN Also Rescued Myogenesis Defects in DM1

As *Postn* shRNA successfully rescued myogenesis defects in DM1, and POSTN is a secreted protein, we considered whether neutralizing excess extracellular POSTN could also rescue myogenesis defects in DM1. We performed *in vitro* myoblast differentiation on DM1 myoblast cells and treated them with a neutralizing antibody against POSTN and a control IgG, respectively (**Figure 6A**). Immunostaining against MHC at differentiation day 6 showed that myogenesis was improved with POSTN antibody treatment (**Figure 6B**). The myotube area was 56.27% ± 9.08% in the POSTN antibody group but 25.67% ± 7.74% in the control group; and the fusion index was 41.74% ± 12.92% in the POSTN antibody group but 10.22% ± 1.79% in the control group (**Figure 6C**). The RT-qPCR results showed that MRFs and fusion markers were upregulated with POSTN antibody treatment (**Figure 6D**). In conclusion, neutralizing excessive POSTN in the DM1 myoblast extracellular microenvironment could rescue myogenesis defects in DM1.

## Periostin Knockdown Improved the Myogenic Ability of DM1 Myoblasts *in vivo*

To determine whether *Postn* inhibition affected the myogenic ability of DM1 myoblasts *in vivo*, we injected scramble control and *Postn* knockdown DM1 myoblasts into the TA muscles that were treated with CTX to induce skeletal muscle injuries as described previously (Lee et al., 2015). The TA muscles were harvested 2 weeks after the cell injections. By HE staining and immunostaining against MHC, we found that the *Postn* knockdown DM1 myoblasts group displayed a better skeletal muscle morphology than the scramble control group, though the scramble control group also showed slight advantages over the sham control group (**Figures 7A,B**). The distributions of myotube size, on the whole, were the largest in the *Postn* knockdown group, the middle in the scramble control group, and the smallest in the sham group (**Figure 7C**). These results suggested that *Postn* knockdown improved the myogenic ability of DM1 myoblasts, which contributed to skeletal muscle regeneration *in vivo*.

## Periostin Regulated Myogenesis Likely Through the TGF-β/Smad3 Pathway in DM1 Myoblasts

Periostin expression was reported to be controlled by the TGF-β/Smad pathway, which also, in turn, regulated the TGF-β/Smad pathway (Blanchard et al., 2008; Lorts et al., 2012;

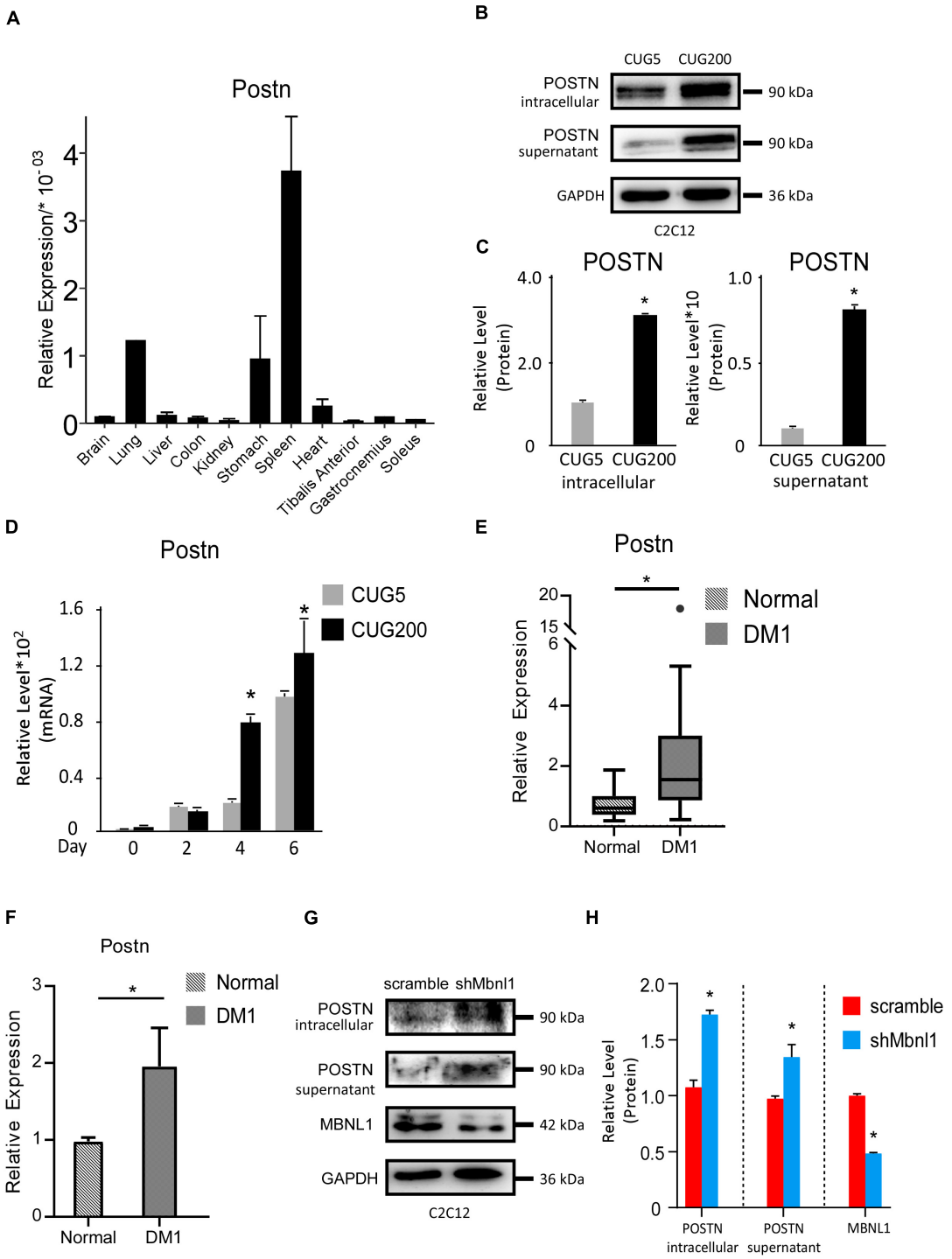


**FIGURE 3 |** Periostin was upregulated in DM1 myogenesis and in skeletal muscle of DM1 patients. **(A)** Expression levels of *Postn* in different tissues of normal adult mice, measured by RT-qPCR. **(B)** Intracellular and supernatant POSTN expression levels in normal and DM1 myoblast cells, detected by western blotting. **(C)** Gel band intensities from panel **(B)** quantified using ImageJ software. Values were normalized to GAPDH. **(D)** Expression levels of *Postn* during *in vitro* myoblast differentiation, measured by RT-qPCR. All expression levels were normalized to the values of the normal control at day 0. **(E)** Expression levels of *Postn* in tibialis anterior (TA) muscle from healthy individuals ($n$ = 10) and DM1 patients ($n$ = 40). **(F)** Expression levels of *Postn* in myoblasts from healthy individuals ($n$ = 3) and DM1 patients ($n$ = 3). **(G)** MBNL1, intracellular and supernatant POSTN expression levels in scramble control and *Mbnl1* knockdown myoblast cells, detected by western blotting. **(H)** Gel band intensities from panel **(G)** quantified using ImageJ software. Values were normalized to GAPDH. CUG5, normal control myoblast cells (C2C12 GFP-CUG5); CUG200, DM1 myoblast cells (C2C12 GFP-CUG200); scramble, scramble control myoblast cells; and shMbnl1, Mbnl1 knockdown myoblast cells; *$P < 0.05$.

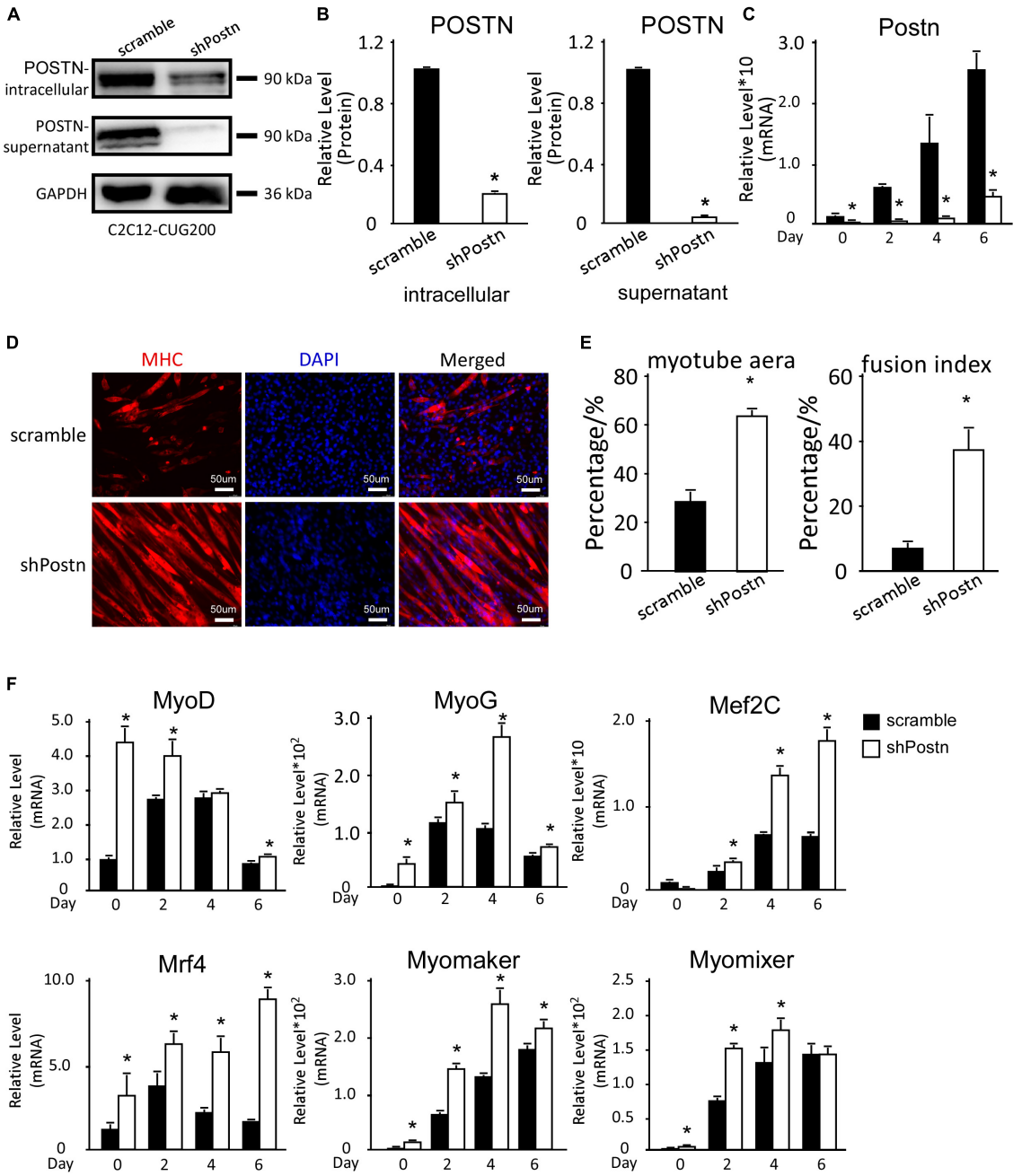


**FIGURE 4 |** Periostin knockdown rescued the myogenesis defects in DM1 myoblast cells. **(A)** *Postn* knockdown in DM1 myoblast cells (C2C12 GFP-CUG200) verified by western blotting. **(B)** Gel band intensities from panel **(A)** quantified using ImageJ software. Values were normalized to GAPDH. **(C)** Expression levels of *Postn* during differentiation in both scrambled control and *Postn*-knockdown groups, measured by RT-qPCR. **(D)** Myotube formation in both scrambled control and *Postn*-knockdown groups, detected by immunostaining against MHC at differentiation day 6. **(E)** Myotube area and fusion index in both groups quantified using ImageJ software. **(F)** Expression levels of MRFs (*MyoD*, *MyoG*, *Mef2C*, and *Mrf4*) and fusion markers (*Myomaker* and *Myomixer*) in both groups, measured by RT-qPCR. All expression levels were normalized to the values of the scrambled control at day 0. Scramble, scrambled control DM1 myoblast cells; shPostn, *Postn*-knockdown DM1 myoblast cells; $^*P < 0.05$.

Noguchi et al., 2016; Mitamura et al., 2018; Yue et al., 2021). TGF-β inhibits the myogenesis process through Smad3 rather than Smad2 (Liu et al., 2001). Thus, we here investigated whether *Postn* regulated myogenesis through the TGF-β/Smad3 pathway in DM1 myoblasts. Compared to normal myoblasts, both p-SMAD3 and SMAD3 were upregulated in DM1 myoblasts at differentiation day 0 and day 4 (**Figures 8A,B**). When inhibiting *Postn* using shRNA, both

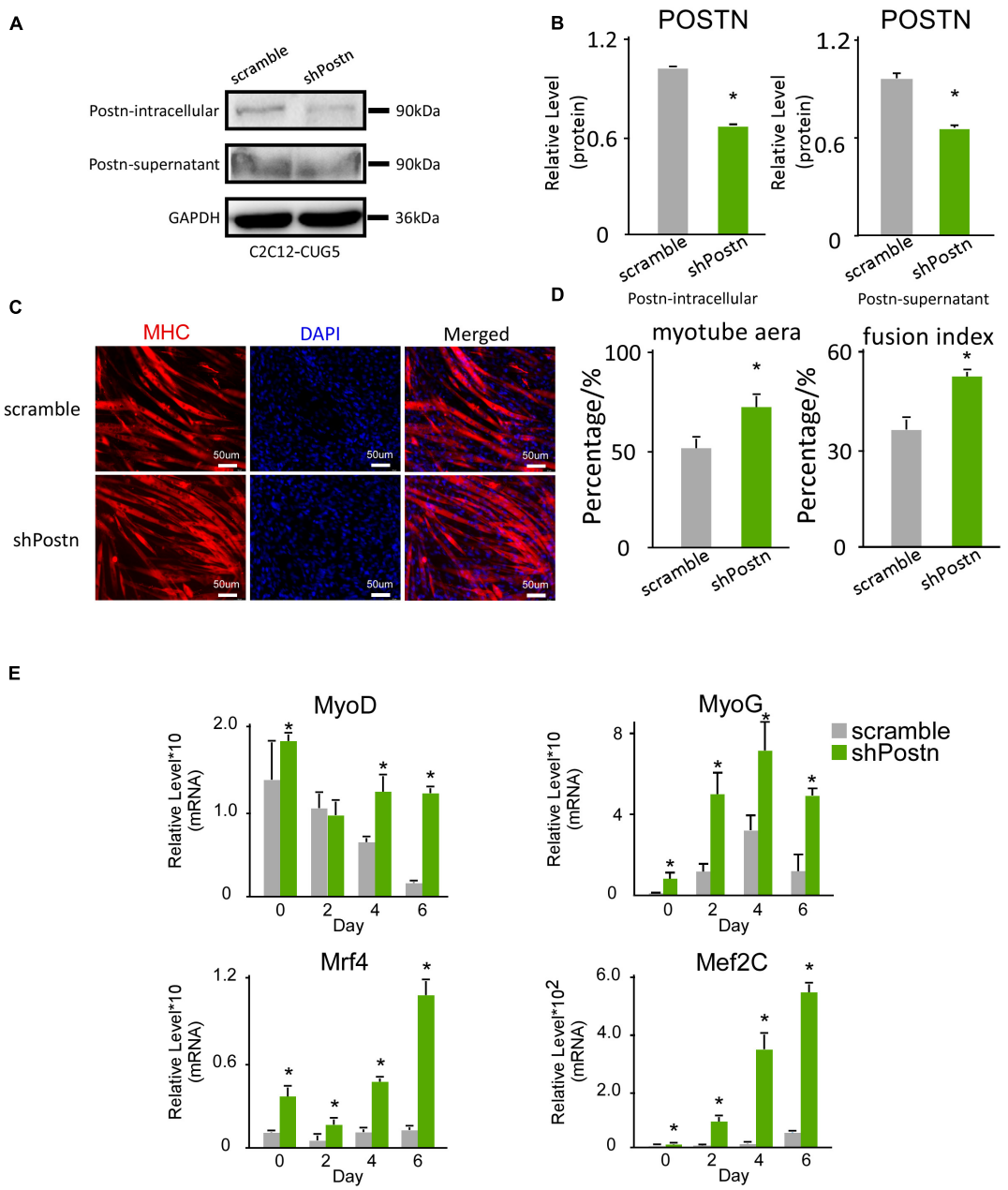


**FIGURE 5 |** Periostin knockdown promoted myogenesis in normal myoblast cells. **(A)** *Postn* knockdown in normal myoblast cells (C2C12 GFP-CUG5), verified by western blots. **(B)** Gel band intensities from panel **(A)** quantified with ImageJ software. Values were normalized to GAPDH. **(C)** Myotube formation in both scrambled control and *Postn*-knockdown groups, detected by immunostaining against MHC at differentiation day 6. **(D)** Myotube area and fusion index in both groups quantified with ImageJ software. **(E)** Expression levels of MRFs (*MyoD*, *MyoG*, *Mef2C*, and *Mrf4*) in both groups, measured by RT-qPCR. All expression levels were normalized to the values of the scramble control at day 0. Scramble, scramble control normal myoblast cells; shPostn, *Postn* knockdown normal myoblast cells; $^*P < 0.05$.

p-SMAD3 and SMAD3 were downregulated in DM1 myoblasts (**Figures 8C,D**). Similarly, both p-SMAD3 and SMAD3 were downregulated when DM1 myoblasts were treated with a POSTN-neutralizing antibody during myoblast differentiation (**Figures 8E,F**). These results suggested that *Postn* might regulate the myogenesis process in DM1 myoblasts through the TGF-β/Smad3 pathway.

## DISCUSSION

In this study, we discovered that *Postn* was aberrantly upregulated during the myogenesis process of DM1 myoblast cells, particularly from *in vitro* differentiation day 4, when myotubes started to form as a result of myoblast fusion. Next, we downregulated *Postn* in DM1 myoblast cells using

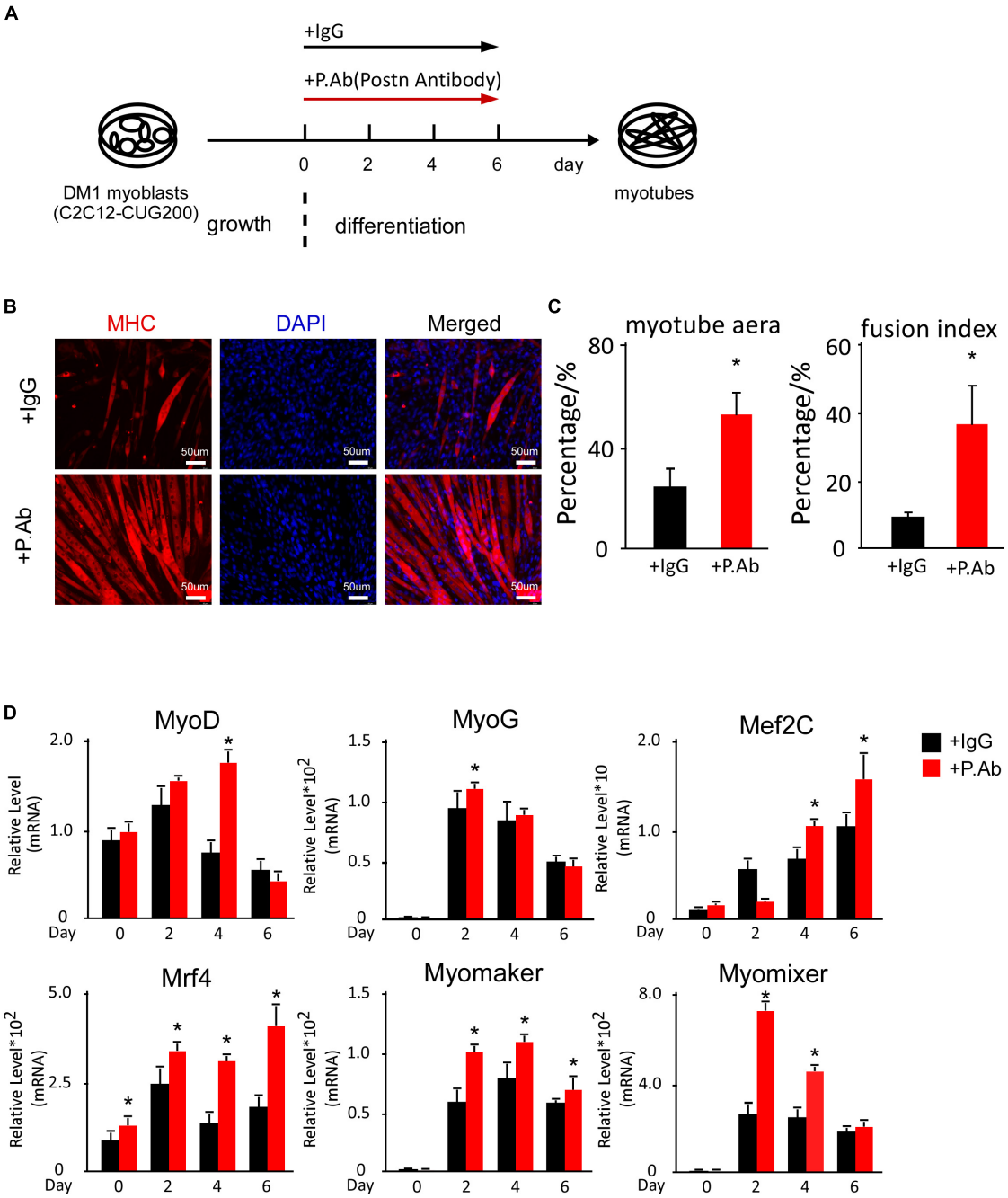


**FIGURE 6 |** POSTN-neutralizing antibody treatment rescued myogenesis defects in DM1 myoblast cells. **(A)** Schematic diagram of the myoblast differentiation processes of DM1 myoblast cells treated with control IgG and POSTN-neutralizing antibody. **(B)** Myotube formation in both control IgG and POSTN-neutralizing antibody groups, detected by immunostaining against MHC at differentiation day 6. **(C)** Myotube area and fusion index in both groups quantified with ImageJ software. **(D)** Expression levels of MRFs (*MyoD*, *MyoG*, *Mef2C*, and *Mrf4*) and fusion markers (*Myomaker* and *Myomixer*) in both groups, measured by RT-qPCR. All expression levels were normalized to the values of the control IgG group at day 0. IgG, control IgG antibody; P.Ab, POSTN neutralizing antibody; $^*P < 0.05$.

both shRNA and a neutralizing antibody and found that the inhibition of *Postn* significantly rescued myogenesis defects in DM1. Consistently, inhibiting *Postn* also improved the myogenic ability of DM1 myoblast cells in the skeletal muscle injury mouse model. The TGF-β/Smad3 pathway might mediate the function of *Postn* in the myogenesis process of DM1 myoblast cells. Moreover, we tested whether *Postn* downregulation also affected the myogenesis process of normal myoblast cells. Knockdown of *Postn* in normal myoblast cells significantly facilitated the myogenesis process. Taken together, these results show that

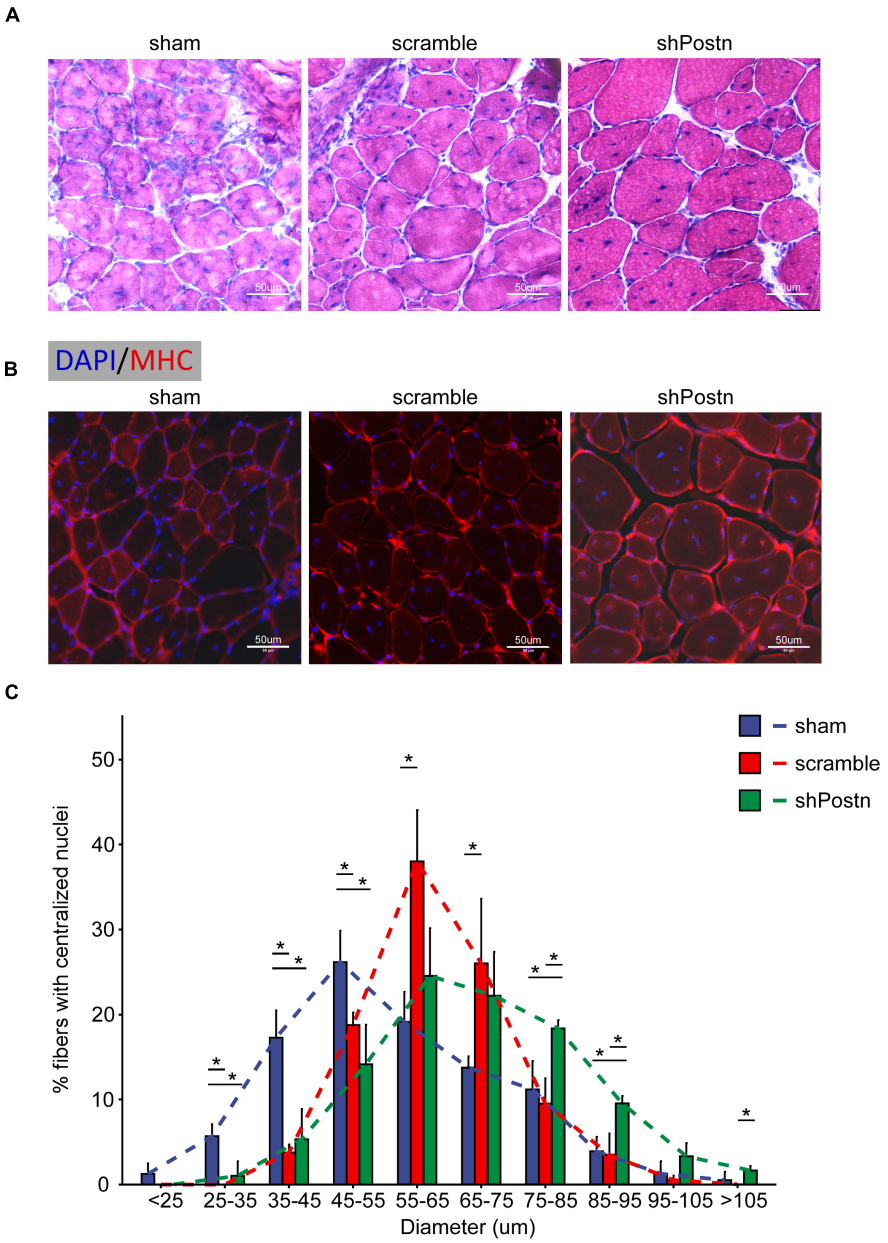


**FIGURE 7 |** Knockdown improved the myogenic ability of DM1 myoblasts *in vivo*. **(A)** H&E staining of cross-sections of the TA muscles from the sham, scramble, and Postn knockdown groups. **(B)** Immunostaining against MHC of cross-sections of the TA muscles from the sham, scramble, and Postn knockdown groups. **(C)** The diameters of myofibers of the TA muscles from the sham, scramble control, and Postn knockdown groups. Sham, PBS; scramble, scramble control DM1 myoblasts; and shPostn, Postn knockdown DM1 myoblasts; $^{*}P < 0.05$.

*Postn*, which encodes an extracellular protein, mediates defective myogenesis in DM1, which contributes to our understanding of the DM1 pathogenic mechanism. Targeting extracellular *Postn* is a potential approach for the therapy of myogenesis defects in DM1, with advantages of delivery convenience compared with classical intracellular therapeutic strategies.

To study myogenesis defects in DM1, we employed a widely used DM1 mouse myoblast cell model, produced by stable transfection with a plasmid containing 200 copies of CTG repeats at the 3′UTR of the *GFP* gene. The control cell model was constructed with a plasmid containing five copies of CTG repeats at the 3′UTR of the *GFP* gene. In previous work, we validated the pathological features of DM1 in this DM1 myoblast model, including ribonuclear foci, aberrant alternative splicing, and defective myogenesis (Shen et al., 2020). Other studies have also suggested using this cell model to investigate myogenesis defects in DM1 (Timchenko et al., 2001b; Peng et al., 2015). Consistently, we observed similar DM1 myogenesis defects to those reported by prior studies.

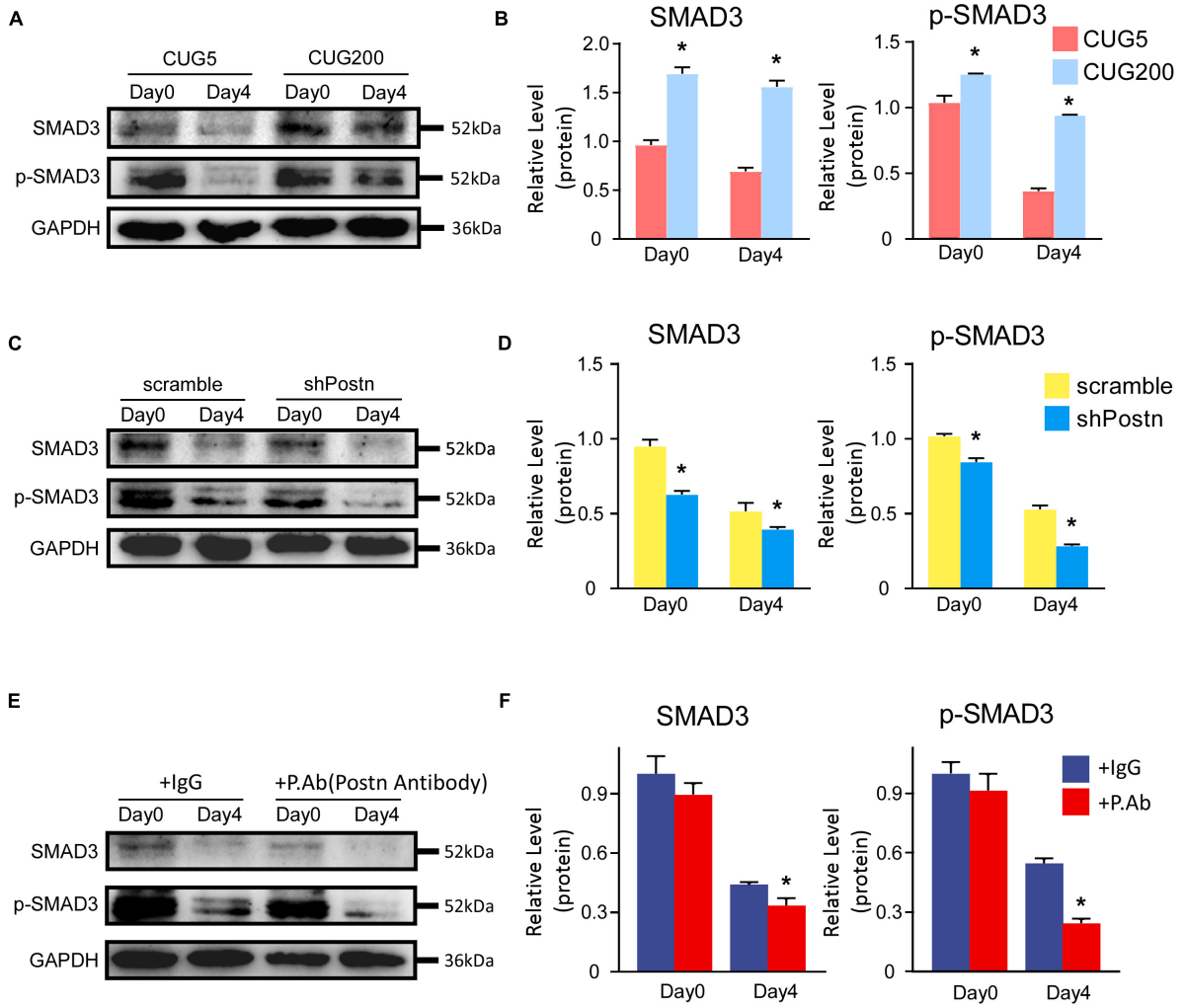


**FIGURE 8 |** *Postn* regulated myogenesis likely through TGF-b/Smad3 pathway in DM1 myoblasts. **(A)** The levels of SMAD3 and p-SMAD3 in normal and DM1 myoblasts at differentiation day 0 and day 4 were determined by western blots. **(B)** Gel band intensities from **(A)** quantified with ImageJ software. GAPDH served as an internal control. All expression levels were normalized to the normal myoblasts at day 0. **(C)** The levels of SMAD3 and p-SMAD3 in scramble control and *Postn* knockdown DM1 myoblasts at differentiation day 0 and day 4 were determined by western blots. **(D)** Gel band intensities from **(C)** quantified with ImageJ software. **(E)** The levels of SMAD3 and p-SMAD3 in the control IgG antibody and POSTN neutralizing antibody treated DM1 myoblasts at differentiation day 0 and day 4 were determined by western blots. **(F)** Gel band intensities from **(E)** quantified with ImageJ software. GAPDH served as an internal control. All expression levels were normalized to the scramble control DM1 myoblasts at day 0. CUG5, normal control myoblast cells (C2C12 GFP-CUG5); CUG200, DM1 myoblast cells (C2C12 GFP-CUG200); scramble, scrambled control DM1 myoblast cells; shPostn, *Postn* knockdown DM1 myoblast cells; IgG, control IgG antibody; P.Ab, POSTN neutralizing antibody; $^*P < 0.05$.

To discover the DEGs during the DM1 myogenesis process, we performed RNA-seq on RNA samples from both the normal and DM1 groups. There were 279 upregulated and 158 downregulated genes in the DM1 group. **Table 1** showed the top 20 level-changed genes in the DM1 group. To our best knowledge, none of these genes were reported to function in DM1 before. Four genes (*Lgr5*, *Gdf5*, *Myh8*, and *Unc13c*) were known to regulate skeletal muscle myogenesis and homeostasis: *Lgr5* is a marker for a group of activated satellite cells for muscle regeneration (Leung et al., 2020); *Gdf5* was found to promote myogenesis process in sciatic denervation mouse model (Traore et al., 2019); *Myh8*, encoding embryonic and neonatal type MHCs, are transient elevated following muscle injury (Schiaffino et al., 2015; Yoshimoto et al., 2020); *Unc13c* facilitates myogenesis process, whose expression is repressed by TNF-α (Meyer et al., 2015). Particularly, there were four genes (*Gm45062*, *Gm49948*, *Gm47308*, and Gm *43488*) upregulated in DM1, whose official gene symbols, however, had not been assigned yet. These top-altered genes deserved further investigations in the future, as their functions were mostly unclear in skeletal muscle and DM1. GO analysis showed that skeletal muscle-related processes and structures were repressed in DM1. These results confirmed the myogenesis defects in DM1 myoblast cells. Moreover, we found that *Postn* was the most significantly altered gene in the DM1 group, with log2(fold change) = 2.86 and adjusted *P*-value = 1.79E−178. The upregulation of DM1 was confirmed

by western blots and RT-qPCR. Through analyzing the datasets from the GEO database, we also discovered that the expression of *Postn* was enhanced in skeletal muscle and myoblasts of DM1 patients. MBNL1 is sequestered by the toxic RNA in DM1, which results in the downregulation of active MBNL1 in cells. We here found that inhibiting *Mbnl1* using shRNA significantly upregulated the intracellular and secreted POSTN, which suggested a correlation between *Mbnl1* and *Postn*. This finding was consistent with the RNA-seq data from a recent study that showed upregulations of *Postn* in DM1 mice models (HSALR20b and Mbnl3/4KO mice) (Tanner et al., 2021). These results imply a potential regulatory role of *Postn* in DM1 pathogenesis. Previous studies have indicated that *Postn* could serve as serum biomarkers for many diseases, including cancer (Dong et al., 2018a,b), rhinosinusitis (Ninomiya et al., 2018), and asthma (Hachim et al., 2020). Based on the upregulations of *Postn* in the DM1 myoblast cell model and the skeletal muscle and myoblasts from DM1 patients, we thought *Postn* might be used as a biomarker for DM1, which, however, needed further verifications of the expressions of *Postn* in the serum of DM1 patients.

We then investigated whether downregulating *Postn* in DM1 myoblasts could rescue myogenesis defects. Knockdown of *Postn* with shRNA significantly increased myogenesis levels in DM1 myoblasts, as characterized by elevated myotube area and fusion index values that were close to those of the normal control group (C2C12 GFP-CUG5), and increased expression levels of MRFs and fusion markers. As POSTN is a secreted protein, we considered whether POSTN in the extracellular microenvironment mediated the myogenesis defects in DM1. We treated DM1 myoblast cells with a POSTN-neutralizing antibody and found that this antibody treatment successfully rescued the myogenesis defects, indicating that POSTN in the microenvironment is at least partially responsible for the defective myogenesis in DM1. In line with our findings here, a previous study demonstrated that a POSTN-neutralizing antibody promoted recovery from muscle injuries (Hara et al., 2018). Combined with the finding that *Postn* was significantly upregulated in skeletal muscle of DM1 patients, these results suggest that targeting extracellular POSTN – for example, using neutralizing antibodies – is a potential approach for treating muscle wasting in DM1. This can be an alternative approach to strengthen myogenesis in addition to previously reported therapeutic strategies against muscular dystrophies, such as stem cell transplantation, the inhibition of myostatin, and IGF-1 supplementation (Shavlakadze et al., 2004; Bo Li et al., 2012; Fakhfakh et al., 2012).

Next, we studied how *Postn* regulated the myogenesis process in DM1. Many studies have revealed that *Postn* had crosstalk with the TGF-β/Smad pathway (Blanchard et al., 2008; Lorts et al., 2012; Noguchi et al., 2016; Mitamura et al., 2018; Yue et al., 2021). TGF-β involved pathway was discovered to inhibit myogenesis and promote myoblast proliferation (Massague et al., 1986; Ge et al., 2011). *Smad3* rather than *Smad2* was responsible for the inhibition of TGF-β on the myogenesis process (Liu et al., 2001). Moreover, TGF-β1 and TGF-β2 were found to be upregulated in DM1 patients and associated with arrhythmia and sudden death (Turillazzi et al., 2013). We here tested the levels of SMAD3 and p-SMAD3 in various myoblast differentiation sets. SMAD3 and p-SMAD3 were significantly upregulated in DM1 myoblast cells. When inhibiting *Postn* using an shRNA or a neutralizing antibody, SMAD3 and p-SMAD3 were significantly downregulated. These results strongly suggested that *Postn* might regulate the myogenesis process in DM1 through the TGF-β/Smad3 pathway. This was in line with a previous study that *Postn* was upregulated in muscular dystrophy and its knockout improved muscle structure and function in the muscular dystrophy mouse model via the TGF-β pathway (Lorts et al., 2012). It was also noticeable that the TGF-β/Smad3 pathway was highly activated in both normal and DM1 myoblasts at differentiation day 0, which was consistent with the previous reports that the activation of TGF-β involved pathway inhibited differentiation but induced quiescence of myoblasts (Rathbone et al., 2011). As to *Postn* knockdown in DM1 myoblasts, both SMAD3 and p-SMAD3 were significantly repressed at differentiation day 0 besides day 4, whereas *Postn* showed a significant upregulation in DM1 myoblasts at differentiation day 4 rather than day 0. This conflicting result implied that there might be complicated underlying mechanisms of *Postn* and the TGF-β/Smad3 pathway in undifferentiated myoblasts.

Moreover, the expression of *Postn* gradually increased during *in vitro* myoblast differentiation in both the normal and DM1 groups; this trend was similar to that of many important myogenesis-facilitating factors (Panda et al., 2014; Lee et al., 2017; Horibata et al., 2020). However, this was contrary to the finding that *Postn* downregulation promoted the myogenesis process in both normal and DM1 myoblasts. Meanwhile, there was no significant difference in *Postn* expression levels between the normal and DM1 groups until day 4. However, when *Postn* was downregulated in myoblast cells of both the normal and DM1 groups using shRNA and a neutralizing antibody, myogenesis and fusion markers (*MyoD*, *MyoG*, *Mef2C*, *Mrf4*, *Myomaker*, and *Myomixer*) displayed significant differences earlier than day 4. According to previous reports, *Postn* is upregulated during the regeneration process following muscle injury and disease, suggesting a possible role of *Postn* in myoblast activation. Based on these conflicting findings, we propose a hypothesis: on the one hand, *Postn* is an important factor for myoblast maintenance and its downregulation promotes myoblast activation and differentiation; on the other hand, *Postn* must be upregulated during myoblast differentiation to maintain undifferentiated myoblasts during and after myogenesis. This hypothesis is consistent with the established role of *POSTN* in maintaining cancer stem cells (Malanchi et al., 2011) and warrants further investigation in the future.

## DATA AVAILABILITY STATEMENT

The datasets presented in this study can be found in online repositories. The names of the repository/repositories and accession number(s) can be found below: https://www.ncbi.nlm.nih.gov/geo/query/acc.cgi?acc=GSE174119, accession: GSE174119.

## AUTHOR CONTRIBUTIONS

XS, ZL, and FX: conceptualization. XS, ZL, and JZ: methodology and software. XS, ZL, CW, FX, JZ, ML, YL, AW, CB, and GZ: investigation. XS and ZL: writing – original draft. XS and GZ: writing – review and editing, and supervision. ZL: visualization. XS: project administration. XS, AW, and CB: funding acquisition.

## FUNDING

This work was supported by the National Natural Science Foundation of China (No. 31701289), the Anhui Provincial Natural Science Foundation (No. 1808085QH234), the Anhui Provincial Funding Scheme to Outstanding Innovative Programs by Returned Scholars (No. 2019LCX003), the Anhui Provincial Key Laboratory of Molecular Enzymology and Mechanism of Major Diseases (No. fzmx202001), the Educational Commission of Anhui Province of China (Nos. KJ2017A319, KJ2019A0498, and KJ2020A0058), and the Foundation for High-level Talents in Higher Education of Anhui Province of China and Funds from the Anhui Normal University (No. 2017XJJ38, start-up funds to XS).

## ACKNOWLEDGMENTS

We thank Hongan Long and Kun Wu from the Ocean University of China for their help with the RNA-seq data analysis.

## SUPPLEMENTARY MATERIAL

The Supplementary Material for this article can be found online at: https://www.frontiersin.org/articles/10.3389/fcell.2021.710112/full#supplementary-material

## REFERENCES

Amack, J. D., and Mahadevan, M. S. (2001). The myotonic dystrophy expanded CUG repeat tract is necessary but not sufficient to disrupt C2C12 myoblast differentiation. *Hum. Mol. Genet.* 10, 1879–1887. doi: 10.1093/hmg/10.18.1879

Amack, J. D., Reagan, S. R., and Mahadevan, M. S. (2002). Mutant DMPK 3′-UTR transcripts disrupt C2C12 myogenic differentiation by compromising MyoD. *J. Cell Biol.* 159, 419–429. doi: 10.1083/jcb.200206020

Andre, L. M., Ausems, C. R. M., Wansink, D. G., and Wieringa, B. (2018). Abnormalities in skeletal muscle myogenesis, growth, and regeneration in myotonic dystrophy. *Front. Neurol.* 9:368. doi: 10.3389/fneur.2018.00368

Andres, V., and Walsh, K. (1996). Myogenin expression, cell cycle withdrawal, and phenotypic differentiation are temporally separable events that precede cell fusion upon myogenesis. *J. Cell Biol.* 132, 657–666. doi: 10.1083/jcb.132.4.657

Apponi, L. H., Corbett, A. H., and Pavlath, G. K. (2011). RNA-binding proteins and gene regulation in myogenesis. *Trends Pharmacol. Sci.* 32, 652–658. doi: 10.1016/j.tips.2011.06.004

Bi, P., Ramirez-Martinez, A., Li, H., Cannavino, J., McAnally, J. R., Shelton, J. M., et al. (2017). Control of muscle formation by the fusogenic micropeptide myomixer. *Science* 356, 323–327. doi: 10.1126/science.aam9361

Blanchard, C., Mingler, M. K., McBride, M., Putnam, P. E., Collins, M. H., Chang, G., et al. (2008). Periostin facilitates eosinophil tissue infiltration in allergic lung and esophageal responses. *Mucosal Immunol.* 1, 289–296. doi: 10.1038/mi.2008.15

Bo Li, Z., Zhang, J., and Wagner, K. R. (2012). Inhibition of myostatin reverses muscle fibrosis through apoptosis. *J. Cell Sci.* 125(Pt 17), 3957–3965. doi: 10.1242/jcs.090365

Charlet, B. N., Savkur, R. S., Singh, G., Philips, A. V., Grice, E. A., and Cooper, T. A. (2002). Loss of the muscle-specific chloride channel in type 1 myotonic dystrophy due to misregulated alternative splicing. *Mol. Cell* 10, 45–53. doi: 10.1016/s1097-2765(02)00572-5

Chen, K., Li, Z., Zhang, M., Wang, B., Peng, T., Shen, Y., et al. (2020). miR-876 inhibits EMT and liver fibrosis via POSTN to suppress metastasis in hepatocellular carcinoma. *Biomed. Res. Int.* 2020:1964219. doi: 10.1155/2020/1964219

Dong, D., Jia, L., Zhang, L., Ma, N., Zhang, A., Zhou, Y., et al. (2018a). Periostin and CA242 as potential diagnostic serum biomarkers complementing CA19.9 in detecting pancreatic cancer. *Cancer Sci.* 109, 2841–2851. doi: 10.1111/cas.13712

Dong, D., Zhang, L., Jia, L., Ji, W., Wang, Z., Ren, L., et al. (2018b). Identification of serum periostin as a potential diagnostic and prognostic marker for colorectal cancer. *Clin. Lab.* 64, 973–981. doi: 10.7754/Clin.Lab.2018.171225

Fakhfakh, R., Lee, S. J., and Tremblay, J. P. (2012). Administration of a soluble activin type IIB receptor promotes the transplantation of human myoblasts in dystrophic mice. *Cell Transplant.* 21, 1419–1430. doi: 10.3727/096368911X627480

Fugier, C., Klein, A. F., Hammer, C., Vassilopoulos, S., Ivarsson, Y., Toussaint, A., et al. (2011). Misregulated alternative splicing of BIN1 is associated with T tubule alterations and muscle weakness in myotonic dystrophy. *Nat. Med.* 17, 720–725. doi: 10.1038/nm.2374

Furling, D., Coiffier, L., Mouly, V., Barbet, J. P., St Guily, J. L., Taneja, K., et al. (2001). Defective satellite cells in congenital myotonic dystrophy. *Hum. Mol. Genet.* 10, 2079–2087. doi: 10.1093/hmg/10.19.2079

Ge, X., McFarlane, C., Vajjala, A., Lokireddy, S., Ng, Z. H., Tan, C. K., et al. (2011). Smad3 signaling is required for satellite cell function and myogenic differentiation of myoblasts. *Cell Res.* 21, 1591–1604. doi: 10.1038/cr.2011.72

Hachim, M. Y., Elemam, N. M., Ramakrishnan, R. K., Hachim, I. Y., Salameh, L., Mahboub, B., et al. (2020). Confounding patient factors affecting the proper interpretation of the periostin level as a biomarker in asthma development. *J. Asthma Allergy* 13, 23–37. doi: 10.2147/JAA.S230892

Halevy, O., Novitch, B. G., Spicer, D. B., Skapek, S. X., Rhee, J., Hannon, G. J., et al. (1995). Correlation of terminal cell cycle arrest of skeletal muscle with induction of p21 by MyoD. *Science* 267, 1018–1021. doi: 10.1126/science.7863327

Hara, M., Yokota, K., Saito, T., Kobayakawa, K., Kijima, K., Yoshizaki, S., et al. (2018). Periostin promotes fibroblast migration and inhibits muscle repair after skeletal muscle injury. *J. Bone Joint Surg. Am.* 100:e108. doi: 10.2106/JBJS.17.01230

Hernandez-Hernandez, J. M., Garcia-Gonzalez, E. G., Brun, C. E., and Rudnicki, M. A. (2017). The myogenic regulatory factors, determinants of muscle development, cell identity and regeneration. *Semin. Cell Dev. Biol.* 72, 10–18. doi: 10.1016/j.semcdb.2017.11.010

Ho, T. H., Charlet, B. N., Poulos, M. G., Singh, G., Swanson, M. S., and Cooper, T. A. (2004). Muscleblind proteins regulate alternative splicing. *EMBO J.* 23, 3103–3112. doi: 10.1038/sj.emboj.7600300

Horibata, Y., Mitsuhashi, S., Shimizu, H., Maejima, S., Sakamoto, H., Aoyama, C., et al. (2020). The phosphatidylcholine transfer protein StarD7 is important for myogenic differentiation in mouse myoblast C2C12 cells and human primary skeletal myoblasts. *Sci. Rep.* 10:2845. doi: 10.1038/s41598-020-59444-y

Inukai, A., Doyu, M., Kato, T., Liang, Y., Kuru, S., Yamamoto, M., et al. (2000). Reduced expression of DMAHP/SIX5 gene in myotonic dystrophy muscle. *Muscle Nerve* 23, 1421–1426. doi: 10.1002/1097-4598(200009)23:9<1421::aid-mus14<3.0.co;2-y

Jacobs, A. E., Benders, A. A., Oosterhof, A., Veerkamp, J. H., van Mier, P., Wevers, R. A., et al. (1990). The calcium homeostasis and the membrane potential of cultured muscle cells from patients with myotonic dystrophy. *Biochim. Biophys. Acta* 1096, 14–19. doi: 10.1016/0925-4439(90)90006-b

Jansen, G., Groenen, P. J., Bachner, D., Jap, P. H., Coerwinkel, M., Oerlemans, F., et al. (1996). Abnormal myotonic dystrophy protein kinase levels produce only mild myopathy in mice. *Nat. Genet.* 13, 316–324. doi: 10.1038/ng0796-316

Kalsotra, A., Wang, K., Li, P. F., and Cooper, T. A. (2010). MicroRNAs coordinate an alternative splicing network during mouse postnatal heart development. *Genes Dev.* 24, 653–658. doi: 10.1101/gad.1894310

Kanadia, R. N., Johnstone, K. A., Mankodi, A., Lungu, C., Thornton, C. A., Esson, D., et al. (2003). A muscleblind knockout model for myotonic dystrophy. *Science* 302, 1978–1980. doi: 10.1126/science.1088583

Kuyumcu-Martinez, N. M., Wang, G. S., and Cooper, T. A. (2007). Increased steady-state levels of CUGBP1 in myotonic dystrophy 1 are due to PKC-mediated hyperphosphorylation. *Mol. Cell* 28, 68–78. doi: 10.1016/j.molcel.2007.07.027

Lee, H. J., Kao, C. Y., Lin, S. C., Xu, M., Xie, X., Tsai, S. Y., et al. (2017). Dysregulation of nuclear receptor COUP-TFII impairs skeletal muscle development. *Sci. Rep.* 7:3136. doi: 10.1038/s41598-017-03475-5

Lee, S. W., Yang, J., Kim, S. Y., Jeong, H. K., Lee, J., Kim, W. J., et al. (2015). MicroRNA-26a induced by hypoxia targets HDAC6 in myogenic differentiation of embryonic stem cells. *Nucleic Acids Res.* 43, 2057–2073. doi: 10.1093/nar/gkv088

Leung, C., Murad, K. B. A., Tan, A. L. T., Yada, S., Sagiraju, S., Bode, P. K., et al. (2020). Lgr5 marks adult progenitor cells contributing to skeletal muscle regeneration and sarcoma formation. *Cell Rep.* 33:108535. doi: 10.1016/j.celrep.2020.108535

Liu, D., Black, B. L., and Derynck, R. (2001). TGF-beta inhibits muscle differentiation through functional repression of myogenic transcription factors by Smad3. *Genes Dev.* 15, 2950–2966. doi: 10.1101/gad.925901

Loro, E., Rinaldi, F., Malena, A., Masiero, E., Novelli, G., Angelini, C., et al. (2010). Normal myogenesis and increased apoptosis in myotonic dystrophy type-1 muscle cells. *Cell Death Differ.* 17, 1315–1324. doi: 10.1038/cdd.2010.33

Lorts, A., Schwanekamp, J. A., Baudino, T. A., McNally, E. M., and Molkentin, J. D. (2012). Deletion of periostin reduces muscular dystrophy and fibrosis in mice by modulating the transforming growth factor-beta pathway. *Proc. Natl. Acad. Sci. U.S.A.* 109, 10978–10983. doi: 10.1073/pnas.1204708109

Love, M. I., Huber, W., and Anders, S. (2014). Moderated estimation of fold change and dispersion for RNA-seq data with DESeq2. *Genome Biol.* 15:550. doi: 10.1186/s13059-014-0550-8

Ma, H., Wang, J., Zhao, X., Wu, T., Huang, Z., Chen, D., et al. (2020). Periostin promotes colorectal tumorigenesis through integrin-FAK-Src pathway-mediated YAP/TAZ activation. *Cell Rep.* 30, 793–806.e796. doi: 10.1016/j.celrep.2019.12.075

Malanchi, I., Santamaria-Martinez, A., Susanto, E., Peng, H., Lehr, H. A., Delaloye, J. F., et al. (2011). Interactions between cancer stem cells and their niche govern metastatic colonization. *Nature* 481, 85–89. doi: 10.1038/nature10694

Mankodi, A., Takahashi, M. P., Jiang, H., Beck, C. L., Bowers, W. J., Moxley, R. T., et al. (2002). Expanded CUG repeats trigger aberrant splicing of ClC-1 chloride channel pre-mRNA and hyperexcitability of skeletal muscle in myotonic dystrophy. *Mol. Cell* 10, 35–44. doi: 10.1016/s1097-2765(02)00563-4

Massague, J., Cheifetz, S., Endo, T., and Nadal-Ginard, B. (1986). Type beta transforming growth factor is an inhibitor of myogenic differentiation. *Proc. Natl. Acad. Sci. U.S.A.* 83, 8206–8210. doi: 10.1073/pnas.83.21.8206

Meyer, S. U., Krebs, S., Thirion, C., Blum, H., Krause, S., and Pfaffl, M. W. (2015). Tumor necrosis factor alpha and insulin-like growth factor 1 induced modifications of the gene expression kinetics of differentiating skeletal muscle cells. *PLoS One* 10:e0139520. doi: 10.1371/journal.pone.0139520

Millay, D. P., O'Rourke, J. R., Sutherland, L. B., Bezprozvannaya, S., Shelton, J. M., Bassel-Duby, R., et al. (2013). Myomaker is a membrane activator of myoblast fusion and muscle formation. *Nature* 499, 301–305. doi: 10.1038/nature12343

Millay, D. P., Sutherland, L. B., Bassel-Duby, R., and Olson, E. N. (2014). Myomaker is essential for muscle regeneration. *Genes Dev.* 28, 1641–1646. doi: 10.1101/gad.247205.114

Miller, J. W., Urbinati, C. R., Teng-Umnuay, P., Stenberg, M. G., Byrne, B. J., Thornton, C. A., et al. (2000). Recruitment of human muscleblind proteins to (CUG)(n) expansions associated with myotonic dystrophy. *EMBO J.* 19, 4439–4448. doi: 10.1093/emboj/19.17.4439

Mitamura, Y., Murai, M., Mitoma, C., and Furue, M. (2018). NRF2 activation inhibits both TGF-beta1- and IL-13-mediated periostin expression in fibroblasts: benefit of cinnamaldehyde for antifibrotic treatment. *Oxid Med. Cell Longev.* 2018:2475047. doi: 10.1155/2018/2475047

Mulders, S. A., van Horssen, R., Gerrits, L., Bennink, M. B., Pluk, H., de Boer-van Huizen, R. T., et al. (2011). Abnormal actomyosin assembly in proliferating and differentiating myoblasts upon expression of a cytosolic DMPK isoform. *Biochim. Biophys. Acta* 1813, 867–877. doi: 10.1016/j.bbamcr.2011.01.024

Ninomiya, T., Noguchi, E., Haruna, T., Hasegawa, M., Yoshida, T., Yamashita, Y., et al. (2018). Periostin as a novel biomarker for postoperative recurrence of chronic rhinosinitis with nasal polyps. *Sci. Rep.* 8:11450. doi: 10.1038/s41598-018-29612-2

Noguchi, T., Nakagome, K., Kobayashi, T., Uchida, Y., Soma, T., Nakamoto, H., et al. (2016). Periostin upregulates the effector functions of eosinophils. *J. Allergy Clin. Immunol.* 138, 1449–1452.e1445. doi: 10.1016/j.jaci.2016.05.020

Oh, H. J., Bae, J. M., Wen, X. Y., Cho, N. Y., Kim, J. H., and Kang, G. H. (2017). Overexpression of POSTN in tumor stroma is a poor prognostic indicator of colorectal cancer. *J. Pathol. Transl. Med.* 51, 306–313. doi: 10.4132/jptm.2017.01.19

Ozdemir, C., Akpulat, U., Sharafi, P., Yildiz, Y., Onbasilar, I., and Kocaefe, C. (2014). Periostin is temporally expressed as an extracellular matrix component in skeletal muscle regeneration and differentiation. *Gene* 553, 130–139. doi: 10.1016/j.gene.2014.10.014

Panda, A. C., Abdelmohsen, K., Yoon, J. H., Martindale, J. L., Yang, X., Curtis, J., et al. (2014). RNA-binding protein AUF1 promotes myogenesis by regulating MEF2C expression levels. *Mol. Cell Biol.* 34, 3106–3119. doi: 10.1128/MCB.00423-14

Park, S. Y., Piao, Y., Jeong, K. J., Dong, J., and de Groot, J. F. (2016). Periostin (POSTN) regulates tumor resistance to antiangiogenic therapy in glioma models. *Mol. Cancer Ther.* 15, 2187–2197. doi: 10.1158/1535-7163.MCT-15-0427

Peng, X., Shen, X., Chen, X., Liang, R., Azares, A. R., and Liu, Y. (2015). Celf1 regulates cell cycle and is partially responsible for defective myoblast differentiation in myotonic dystrophy RNA toxicity. *Biochim. Biophys. Acta* 1852, 1490–1497. doi: 10.1016/j.bbadis.2015.04.010

Philips, A. V., Timchenko, L. T., and Cooper, T. A. (1998). Disruption of splicing regulated by a CUG-binding protein in myotonic dystrophy. *Science* 280, 737–741. doi: 10.1126/science.280.5364.737

Rathbone, C. R., Yamanouchi, K., Chen, X. K., Nevoret-Bell, C. J., Rhoads, R. P., and Allen, R. E. (2011). Effects of transforming growth factor-beta (TGF-beta1) on satellite cell activation and survival during oxidative stress. *J. Muscle Res. Cell Motil.* 32, 99–109. doi: 10.1007/s10974-011-9255-8

Salisbury, E., Sakai, K., Schoser, B., Huichalaf, C., Schneider-Gold, C., Nguyen, H., et al. (2008). Ectopic expression of cyclin D3 corrects differentiation of DM1 myoblasts through activation of RNA CUG-binding protein, CUGBP1. *Exp. Cell Res.* 314, 2266–2278. doi: 10.1016/j.yexcr.2008.04.018

Savkur, R. S., Philips, A. V., and Cooper, T. A. (2001). Aberrant regulation of insulin receptor alternative splicing is associated with insulin resistance in myotonic dystrophy. *Nat. Genet.* 29, 40–47. doi: 10.1038/ng704

Schiaffino, S., Rossi, A. C., Smerdu, V., Leinwand, L. A., and Reggiani, C. (2015). Developmental myosins: expression patterns and functional significance. *Skelet Muscle* 5:22. doi: 10.1186/s13395-015-0046-6

Schnorrer, F., and Dickson, B. J. (2004). Muscle building; mechanisms of myotube guidance and attachment site selection. *Dev. Cell* 7, 9–20. doi: 10.1016/j.devcel.2004.06.010

Shavlakadze, T., White, J., Hoh, J. F., Rosenthal, N., and Grounds, M. D. (2004). Targeted expression of insulin-like growth factor-I reduces early myofiber necrosis in dystrophic mdx mice. *Mol. Ther.* 10, 829–843. doi: 10.1016/j.ymthe.2004.07.026

Shen, X., Xu, F., Li, M., Wu, S., Zhang, J., Wang, A., et al. (2020). miR-322/-503 rescues myoblast defects in myotonic dystrophy type 1 cell model by targeting CUG repeats. *Cell Death Dis.* 11:891. doi: 10.1038/s41419-020-03112-6

Tanner, M. K., Tang, Z., and Thornton, C. A. (2021). Targeted splice sequencing reveals RNA toxicity and therapeutic response in myotonic dystrophy. *Nucleic Acids Res.* 49, 2240–2254. doi: 10.1093/nar/gkab022

Timchenko, N. A., Cai, Z. J., Welm, A. L., Reddy, S., Ashizawa, T., and Timchenko, L. T. (2001a). RNA CUG repeats sequester CUGBP1 and alter protein levels and activity of CUGBP1. *J. Biol. Chem.* 276, 7820–7826. doi: 10.1074/jbc.M005960200

Timchenko, N. A., Iakova, P., Cai, Z. J., Smith, J. R., and Timchenko, L. T. (2001b). Molecular basis for impaired muscle differentiation in myotonic dystrophy. *Mol. Cell Biol.* 21, 6927–6938. doi: 10.1128/MCB.21.20.6927-6938.2001

Timchenko, N. A., Patel, R., Iakova, P., Cai, Z. J., Quan, L., and Timchenko, L. T. (2004). Overexpression of CUG triplet repeat-binding protein, CUGBP1, in

mice inhibits myogenesis. *J. Biol. Chem.* 279, 13129–13139. doi: 10.1074/jbc.M312923200

Traore, M., Gentil, C., Benedetto, C., Hogrel, J. Y., De la Grange, P., Cadot, B., et al. (2019). An embryonic CaVbeta1 isoform promotes muscle mass maintenance via GDF5 signaling in adult mouse. *Sci. Transl. Med.* 11:eaaw1131. doi: 10.1126/scitranslmed.aaw1131

Turillazzi, E., Neri, M., Riezzo, I., Di Paolo, M., Evangelisti, L., and Fineschi, V. (2013). Cardiac fibrosis, arrhythmia and sudden death in myotonic dystrophy type 1: could TGF-ss1 improve the predictive accuracy of patients at risk, opening new therapeutic challenges? *Int. J. Cardiol.* 168, 4976–4978. doi: 10.1016/j.ijcard.2013.07.135

Udd, B., and Krahe, R. (2012). The myotonic dystrophies: molecular, clinical, and therapeutic challenges. *Lancet Neurol.* 11, 891–905. doi: 10.1016/S1474-4422(12)70204-1

Ward, A. J., Rimer, M., Killian, J. M., Dowling, J. J., and Cooper, T. A. (2010). CUGBP1 overexpression in mouse skeletal muscle reproduces features of myotonic dystrophy type 1. *Hum. Mol. Genet.* 19, 3614–3622. doi: 10.1093/hmg/ddq277

Yoshimoto, Y., Ikemoto-Uezumi, M., Hitachi, K., Fukada, S. I., and Uezumi, A. (2020). Methods for accurate assessment of myofiber maturity during skeletal muscle regeneration. *Front. Cell Dev. Biol.* 8:267. doi: 10.3389/fcell.2020.00267

Yu, G., Wang, L. G., Han, Y., and He, Q. Y. (2012). clusterProfiler: an R package for comparing biological themes among gene clusters. *OMICS* 16, 284–287. doi: 10.1089/omi.2011.0118

Yue, H., Li, W., Chen, R., Wang, J., Lu, X., and Li, J. (2021). Stromal POSTN induced by TGF-beta1 facilitates the migration and invasion of ovarian cancer. *Gynecol. Oncol.* 160, 530–538. doi: 10.1016/j.ygyno.2020.11.026

Zacksenhaus, E., Jiang, Z., Chung, D., Marth, J. D., Phillips, R. A., and Gallie, B. L. (1996). pRb controls proliferation, differentiation, and death of skeletal muscle cells and other lineages during embryogenesis. *Genes Dev.* 10, 3051–3064. doi: 10.1101/gad.10.23.3051

Zhou, W., Ke, S. Q., Huang, Z., Flavahan, W., Fang, X., Paul, J., et al. (2015). Periostin secreted by glioblastoma stem cells recruits M2 tumour-associated macrophages and promotes malignant growth. *Nat. Cell Biol.* 17, 170–182. doi: 10.1038/ncb3090

**Conflict of Interest:** The authors declare that the research was conducted in the absence of any commercial or financial relationships that could be construed as a potential conflict of interest.

**Publisher's Note:** All claims expressed in this article are solely those of the authors and do not necessarily represent those of their affiliated organizations, or those of the publisher, the editors and the reviewers. Any product that may be evaluated in this article, or claim that may be made by its manufacturer, is not guaranteed or endorsed by the publisher.

frontiers in Cell and Developmental Biology

ORIGINAL RESEARCH
published: 30 August 2021
doi: 10.3389/fcell.2021.722294

# Digitally Driven Aerosol Jet Printing to Enable Customisable Neuronal Guidance

*Andrew J. Capel[1†], Matthew A. A. Smith[2†], Silvia Taccola[2], Maria Pardo-Figuerez[1], Rowan P. Rimington[1], Mark P. Lewis[1], Steven D. R. Christie[3], Robert W. Kay[2] and Russell A. Harris[2*]*

[1] School of Sport, Exercise and Health Sciences, Loughborough University, Loughborough, United Kingdom, [2] Faculty of Engineering and Physical Sciences, School of Mechanical Engineering, University of Leeds, Leeds, United Kingdom, [3] School of Science, Loughborough University, Loughborough, United Kingdom

OPEN ACCESS

**Edited by:**
*Megan Laura McCain, University of Southern California, United States*

**Reviewed by:**
*Ashutosh Agarwal, University of Miami, United States*
*Johan Lind, Technical University of Denmark, Denmark*
*Rehan Kapadia, University of Southern California, United States*

***Correspondence:**
*Russell A. Harris*
*r.harris@leeds.ac.uk*

*† These authors have contributed equally to this work and share first authorship*

**Specialty section:**
*This article was submitted to Stem Cell Research, a section of the journal Frontiers in Cell and Developmental Biology*

**Received:** *08 June 2021*
**Accepted:** *04 August 2021*
**Published:** *30 August 2021*

**Citation:**
*Capel AJ, Smith MAA, Taccola S, Pardo-Figuerez M, Rimington RP, Lewis MP, Christie SDR, Kay RW and Harris RA (2021) Digitally Driven Aerosol Jet Printing to Enable Customisable Neuronal Guidance. Front. Cell Dev. Biol. 9:722294. doi: 10.3389/fcell.2021.722294*

Digitally driven manufacturing technologies such as aerosol jet printing (AJP) can make a significant contribution to enabling new capabilities in the field of tissue engineering disease modeling and drug screening. AJP is an emerging non-contact and mask-less printing process which has distinct advantages over other patterning technologies as it offers versatile, high-resolution, direct-write deposition of a variety of materials on planar and non-planar surfaces. This research demonstrates the ability of AJP to print digitally controlled patterns that influence neuronal guidance. These consist of patterned poly(3,4-ethylenedioxythiophene)-poly(styrenesulfonate) (PEDOT:PSS) tracks on both glass and poly(potassium 3-sulfopropyl methacrylate) (PKSPMA) coated glass surfaces, promoting selective adhesion of SH-SY5Y neuroblastoma cells. The cell attractive patterns had a maximum height $\geq$0.2 $\mu$m, width and half height $\geq$15 $\mu$m, Ra = 3.5 nm, and RMS = 4.1. The developed biocompatible PEDOT:PSS ink was shown to promote adhesion, growth and differentiation of SH-SY5Y neuronal cells. SH-SY5Y cells cultured directly onto these features exhibited increased nuclei and neuronal alignment on both substrates. In addition, the cell adhesion to the substrate was selective when cultured onto the PKSPMA surfaces resulting in a highly organized neural pattern. This demonstrated the ability to rapidly and flexibly realize intricate and accurate cell patterns by a computer controlled process.

**Keywords: direct write, aerosol jet printing, microfabrication, neuronal alignment, tissue engineering, biomaterials**

## INTRODUCTION

Within the pharmaceutical sector it is estimated <10% of drugs entering phase I clinical trials proceed to market, with the average cost ranging from $0.8b to $1.7b (Takebe et al., 2018). Consequently, there is a requirement for cost effective biological test platforms that accurately recreate human physiology and can rapidly eliminate ineffective or toxic therapeutics, also known as a "fail-fast" approach (Mohs and Greig, 2017). Traditional 2D cell cultures, utilizing homogeneous inert substrates such as glass or tissue culture plastics, are often used to rapidly screen novel treatments but fail to recreate the complex multi-cellular environments seen within the body (Mirbagheri et al., 2019). One strategy to overcome this limitation is the selective deposition of microscale topographical and chemical cues on homogeneous 2D cell culturing

platforms (Bettinger et al., 2009; Mirbagheri et al., 2019; Zhang K. et al., 2019; Shi et al., 2020). These highly structured surfaces composed of various patterns, also known as 2.5 dimensional objects, have been recognized as a promising tool for controlling cells behavior and function, including attachment, migration, proliferation, and differentiation, with cell morphological and functional responses greatly depending on the cell type as well as the pattern type and dimensions (Mirbagheri et al., 2019). As such, these topographical substrates are capable of better mimicking the natural extracellular matrix and have shown great promise as *in vitro* experimental test platforms for applications within both drug discovery and disease modeling in which tissue models should adequately recapitulate the complexity of natural cell organizations (Bettinger et al., 2009; Mirbagheri et al., 2019; Zhang K. et al., 2019; Shi et al., 2020).

A significant challenge in developing these complex micro-environments is the availability of effective and efficient manufacturing processes that allow patterned multi-functional surfaces to be generated (Shick et al., 2019). The specific manufacturing challenges associated with the development of these environments necessitates manufacturing processes that can generate complex micro-topographies, with the capability to rapidly iterate designs, a useful tool when undertaking bioengineered model development (Zhang S. et al., 2019). There is also an increasing requirement for these environments to be biologically active, whereby the cellular environment created is capable of significantly enhancing cellular development (Akhmanova et al., 2015; Janson and Putnam, 2015). This increased functionality can be achieved through both chemical (e.g., polymer brushes) and biological (e.g., growth factors) modifications, supplemented by topographical patterning, multi-material manufacture, and chemical gradients (Liu and Wang, 2014; Koçer and Jonkheijm, 2018). Finally, the manufacture of surfaces from biomimetic molecules such as collagen, fibrin or laminin allows more accurate recreation of *in vivo* biology (Caliari and Burdick, 2016).

Manufacturing processes including photolithography (Karp et al., 2006; Nie and Kumacheva, 2008), soft lithography (Qin et al., 2010; Hardelauf et al., 2014; Filipponi et al., 2016), electrospinning (Denchai et al., 2018), and direct-write techniques (Roth et al., 2004; Lind et al., 2017; Suzuki and Teramoto, 2017; Derakhshanfar et al., 2018; Tse and Smith, 2018; Garma et al., 2019; Yuk et al., 2020) have been used to date for the production of patterned bio-interfaces. However, template driven processes such as photolithography and micro-contact printing do not effectively support mass customization and iterative development of novel material formulations. Alternatively, direct-write techniques such as inkjet and extrusion-based printing, are often limited by material selection and offer limited printing resolution, with a minimum feature size of ∼50 μm (Murphy and Atala, 2014). Having the manufacturing capability to rapidly screen a wider range of biomaterials at a smaller scale with high design flexibility, would facilitate the rapid and iterative development of complex *in vitro* environments.

This research demonstrates the use of Aerosol Jet Printing (AJP) as an enabling manufacturing process which could facilitate the next generation of bespoke *in vitro* environments. Primarily developed for the manufacture of electronic circuitry, AJP is a promising direct write technology that has been applied to a diverse range of applications, including active and passive electronic components, actuators, sensors, as well as a variety of selective chemical and biological responses (Murphy and Atala, 2014; Wilkinson et al., 2019a,b). Within this framework, a comprehensive review on the AJP process and the current state-of-the-art from an applications perspective has been recently published by Wilkinson et al. (2019b). AJP uses a focussed aerosol for the discrete deposition of a wide range of materials with micron scale resolution (∼10 μm) onto a variety of flat and three-dimensional surfaces at nozzle–substrate offsets of 1-5 mm (Grunwald et al., 2010; Cai et al., 2016; Mashayekhi et al., 2016; Secor, 2018). The material is atomized using either focussed ultrasonic energy, or pneumatic shearing of the fluid, depending on the viscosity of the liquid ink, and the required throughput of material for the application. **Figure 1A** illustrates our AJP apparatus, comprising of a high resolution 5-axis stage which moves the substrate below the aerosol stream under Computer Numerical Control (CNC). An overview of the AJP apparatus and process is illustrated in **Figure 1B**. AJP has been applied to print a diverse range of materials including polymers, metal nanoparticles, ceramics, and proteins (De Silva et al., 2006; Holthaus and Rezwan, 2008; Grunwald et al., 2010; Maiwald et al., 2010; Hegge et al., 2011; Tamari et al., 2014; Rahman et al., 2016; Zare Bidoky and Frisbie, 2016; Phuah et al., 2020; Williams et al., 2020).

In the field of bioprinting, the use of AJP as a direct-write technique capable of high-resolution deposition of biological materials for cell patterning have been reported by De Silva et al. (2006), and Grunwald et al. (2010). More recently Phuah et al. (2020) have demonstrated biological function of gelatin from AJP lines printed with a minimum width of 30 μm. These promising outcomes further illustrate the use of AJP in cell patterning, microarray and lab-on-a-chip applications, demonstrating that, compared to some bioprinting techniques, AJP offers the capacity to print a wider range of ink viscosities and at a higher spatial resolution. Although AJP has primarily been used for surface patterning, researchers are beginning to explore its potential for producing 3D microstructures with complex architectures (Saleh et al., 2017). Moreover, multi-material aerosol jet printing has been successfully demonstrated for the printing of multilayer and composite structures (Wang et al., 2016; Wilkinson et al., 2019b). Such capabilities illustrate the possible value of AJP in this field to enable a route for the development of devices with increased performance by harnessing the unique capabilities of the process.

In this work, poly(3,4-ethylenedioxythiophene):poly(styrene sulfonate) (PEDOT:PSS) was selected to investigate AJP for micro-scale deposition to create bespoke neuronal culture environments. Among the materials that promote cell attachment, the polymer PEDOT:PSS has received considerable attention because of its unique set of properties. The excellent biocompatibility, the superior flexibility compared to inorganic conductors, and the mixed ionic-electronic conductivity, which provides enhanced communication between cells and devices, make it an amenable interface with biological tissues (Owens and Malliaras, 2010; Higgins et al., 2012;

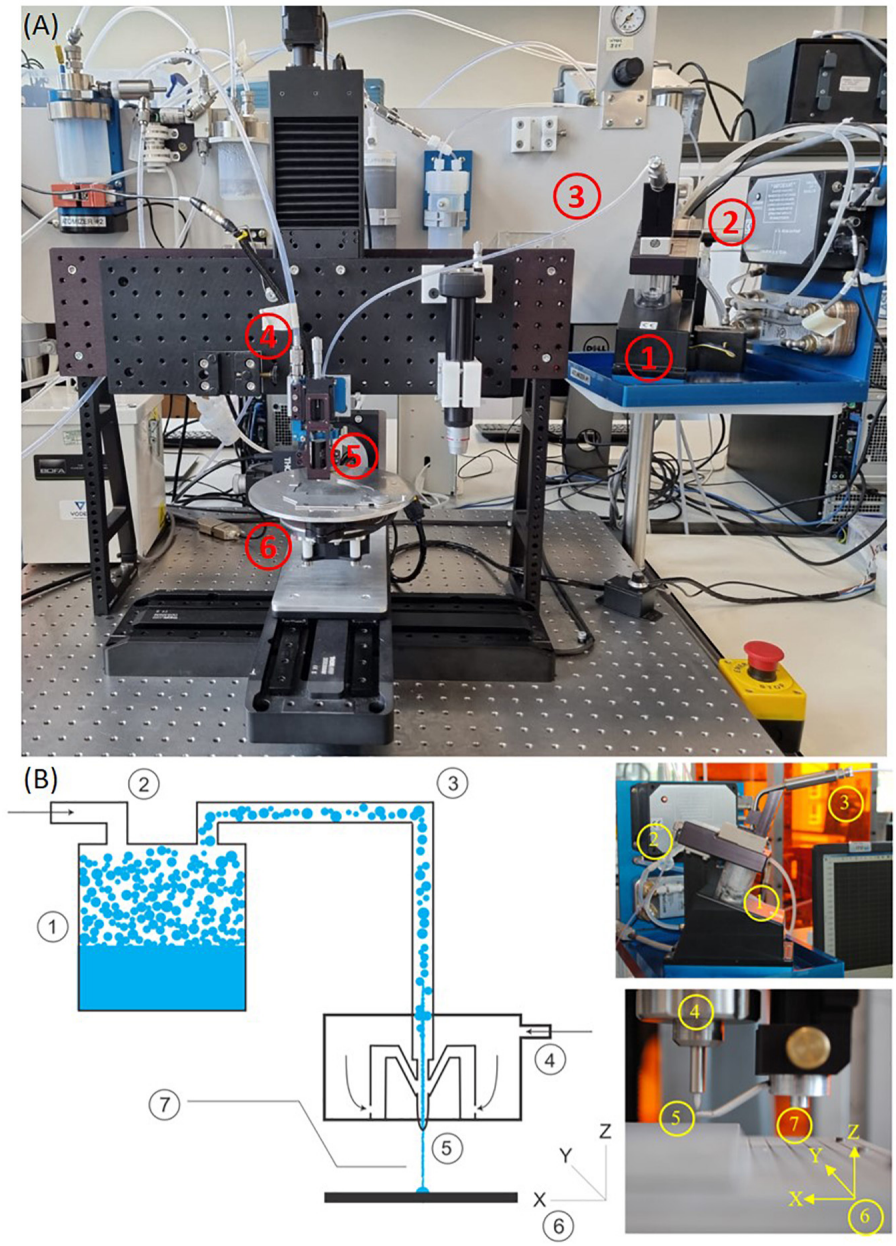


**FIGURE 1 |** A picture of the machine **(A)** and the description **(B)** of AJP technology. (1) A liquid sample is atomized. (2) An inert gas is used to increase the pressure in the atomizer chamber. (3) The aerosol is transported to the deposition head with the gas acting as a sheath around the aerosol. (4) The aerosol is focused and accelerated by a further annular sheath of inert gas. (5) The resulting high velocity jet is deposited onto the substrate. (6) The automated stage is moved to produce a pattern. (7) On/off patterning is achieved by interrupting the jet with a mechanical shutter.

Wang et al., 2016; Ohayon et al., 2017). In addition, PEDOT:PSS-based substrates have been shown to allow the direct electrical stimulation of electrogenic cells (e.g., neurons and muscle cells), regulating or inducing several biological functions (Gomez et al., 2007; Lundin et al., 2011). Such electrical stimulation is not the subject of this current work but its use in this founding research may permit such future extensions on the future. The use of AJP to reliably produce micro-scale printed structures in the region of 20 μm wide from PEDOT:PSS has already been successfully demonstrated by our group (Smith et al., 2018). In this present work, this material was deposited onto both planar glass substrates as well as poly(potassium 3-sulfopropyl methacrylate) (PKSPMA) polymer brush coated glass. PKSPMA polymer brushes have previously been shown to be non-toxic toward the SH-SY5Y neuroblastoma, and due to their hydrophilicity and charged surfaces shown to inhibit cellular adhesion (Pardo-Figuerez et al., 2018). As such when combined with a secondary material that promotes cellular adhesion this

polymer is an ideal selection for creating pre-determined regions of neuronal patterning. This pairing of functional materials to create complex small-scale patterns was investigated to provide a new route to model substrates representing variations of *in vivo* neural environments. During this research, the SH-SY5Y human neuroblastoma cell line was utilized, due to complexities of sourcing primary human motor neurons for experimentation. SH-SY5Y cells are a heterogeneous neuron like cell population, capable of differentiating and propagating neurites following exposure to differentiation media. This cell line also has the ability to display the dopaminergic, adrenergic and cholinergic markers typical of *in vivo* neural biology (Pahlman et al., 1984; Kume et al., 2008; Xie et al., 2010). Without precise control over the features of the culture substrate, *in vitro* neuronal cultures are characterized by chaotic environments with unpredictable neuronal directionality. Recreation of organized network structures, and consequently cellular functionality, is therefore a key step to begin building an *in vitro* model that mimics the neuronal circuits found *in vivo*, increasing the applicability of the models toward investigation of the cellular and molecular mechanisms regulating health and disease of the human nervous system.

# MATERIALS AND METHODS

## Materials

The chemicals (3-aminopropyl)-triethoxysilane (APTES, >98%), triethylamine (TEA, >99.5%), 2-bromoisobutyryl bromide (BIBB, >98%), copper(I) bromide (CuBr, 99.999%), copper(II) bromide ($CuBr_2$, 98%), 2,2′-bipyridyl (Bpy, 99%), 3-sulfopropyl methacrylate potassium salt (KSPMA, 98%), (3-glycidyloxypropyl)trimethoxysilane (GOPS, >98%), tetrahydrofuran (THF, >99%), methanol (MeOH, >99.8%), acetone [$(CH_3)_2C=O$] and ethylene glycol [$(CH_2OH)_2$, >99.8%] were purchased from Sigma-Aldrich (Sigma, United Kingdom). PEDOT:PSS (Clevios PH1000$^{TM}$) was purchased from Heraeus Holding (Germany). Glass slides (1.0–1.2 mm thick in dimensions of 25.4 mm × 76.2 mm) were purchased from Scientific Glass Laboratories Ltd. (United Kingdom). For cell culture experiments, Dulbecco's Modified Eagle Medium (DMEM) GlutaMAX, heat inactivated fetal bovine serum (FBS), Penicillin/Streptomycin (P/S, 10,000 units penicillin and 10 mg streptomycin/mL), alamarBlue® viability assay kit, 4′,6-diamidino-2-phenylindole (DAPI) nuclei counterstain and Alexa Fluor® 488 goat anti-mouse IgG were purchased from Fisher Scientific (United Kingdom). Primary antibody monoclonal anti β tubulin III produced in mouse (∼2.0 mg/mL) was acquired from Sigma. All chemicals and reagents were used as per the manufacturer's instructions.

## Substrate Preparation for Aerosol Jet Printing

### Glass Substrates

Glass slides were washed in acetone, methanol and distilled water ($dH_20$) and exposed to oxygen plasma (Inseto PE-25) at 75W and a 15 $cm^3$ oxygen flow rate for 120 s to remove surface contaminants before the aerosol jet process.

### PKSPMA Polymer Brush Coated Glass Substrates

Glass slides were washed in acetone, methanol and $dH_20$ before being cleaned for 15 min with a $UV/O_3$ cleaner (PR-100, UVP). Cleaned glass slides were placed in a vacuum oven along with 10 drops of APTES on aluminum foil. The vacuum was activated and the glass slides were exposed to the APTES vapor for 30 min at room temperature (RT). Samples were then placed in an oven for 30 min at 110°C. APTES-functionalized samples were placed in dry tubes and purged for 1–2 min with $N_2$. The following reagents were then added by syringe: dry THF (10 mL), dry TEA (0.3 mL, 0.21 g, and 2.1 mmol) and BIBB (0.26 mL, 0.48 g, and 2.10 mmol). The tubes were then $N_2$ purged for an hour with the samples immersed in this solution at 25°C. Samples were taken out and rinsed with THF, methanol and $dH_20$, and then dried under a flow of $N_2$. For the polymer brush attachment, PKSPMA (17.29g and 70.2 mmol) methanol and $dH_20$ (2:1 v/v) were stirred and degassed by bubbling through $N_2$ for 20 min in a 100 mL sealed three-neck round bottom flask. After 10 min the monomer was dissolved and 2, 2′-bipyridyne (0.651 g and 4.17 mmol) and copper(II) bromide (0.0179 g and 0.08 mmol) were added. The mixture was stirred and degassed for an hour at 25°C, followed by the addition of copper(I) bromide (0.230 g and 1.6 mmol). Following this step the monomer solution was transferred into tubes containing the initiator coated samples. A $N_2$ filled balloon was added to maintain an inert atmosphere for 24 h at 25°C. After the polymerization was complete, the samples were washed sequentially with methanol and $dH_20$, and dried under $N_2$.

## Machine Set Up, Material Formulation and Aerosol Processing Parameters

An Optomec Aerosol Jet print engine was engineered into a programmable 5-axis Cartesian stage controlled through a control code (G-Code) input to Mach3 CNC software, which moves the substrate below the aerosol stream with micrometer scale precision. $N_2$ was used as the inert sheath and atomizer gas. This apparatus is illustrated in **Figure 1**. For the initial determination of a suitable print formulation a chemical composition experiment was conducted with: PEDOT:PSS (0.52–1.04%), Ethylene Glycol (0–20%), and $dH_20$ (78.96–99.48%). Full details of the different materials tested are included in the **Supplementary Material** associated with this document (**Supplementary Table 1**). Machine processing parameters were varied with this material to optimize the print quality. A 4-way full factorial matrix style DOE was conducted to investigate the effects of; sheath gas flow rate (30-40 standard cubic centimeters per minute, sccm), atomizer gas flow rate (20-25 sccm), print platform scanning speed (70–90 mm/min) and nozzle height from platform (2.5–3.5 mm). The nozzle size was fixed at 100 μm and the atomizing current was kept constant at 0.65 mA. The surrounding environmental factors were closely controlled to minimize the effect on the final material deposition. The specific material and process combinations are included in the **Supplementary Table 3**.

## Substrate Characterization

Phase contrast microscope images were taken using a LEICA DMIL microscope with a 20× magnification objective. White light interferometry measurements were taken using a 3D Optical Profilometer Zygo NewView 5000. Cross sectional data was analyzed for the maximum height, width at the base of the profile, width at half height and cross-sectional area. Atomic force microscopy measurements were taken using a Veeco Explorer to characterize maximum height, width at the base of the profile, width at half height and surface roughness.

## Substrate Preparation for Biocompatibility Screening

Glass slides were cut into rectangles of an area of 2.5 $cm^2$, washed in acetone, methanol and $dH_20$ and then cleaned with a $UV/O_3$ photo reactor (PR-100, UVP). Samples were each $UV/O_3$ treated for 15 min. Slides were then coated with a 400 μL solution containing varying concentrations of PEDOT:PSS, GOPS, ethylene glycol and $dH_20$ (**Table 1**). These samples were then baked in an oven at 150°C for 15 min to remove any solvent, leaving a film of the PEDOT:PSS material adhered to the surface of the glass.

## Cell Culture Methodology

### Neuronal Culture Procedures

The SH-SY5Y neuroblastoma cell line (ECACC) was cultured in growth media (GM) consisting of DMEM GlutaMAX supplemented with 10% v/v heat inactivated FBS and 1% v/v P/S. Cells were incubated in an humid environment of 5% $CO_2$ atmosphere at 37°C until they reached an 80% confluency. Cells were treated with trypsin enzyme for detachment, counted and plated evenly onto the patterned samples at a density of $1 \times 10^4$ cells/$cm^2$. These samples were cultured in GM for a period of 24 h and thereafter, neuronal differentiation was induced by incubating cells in differentiation media (DM), consisting of DMEM GlutaMAX, 10% heat inactivated FBS, 1% P/S and 10 μM of retinoic acid (RA) differentiating agent for another 72 h. All experimental conditions were compared against untreated glass slides. Patterned samples were then fixed for immunocytochemistry. Prior to experimentation, patterned samples were sterilized by incubation in 70% ethanol, and then left to dry under sterile conditions in a biological safety cabinet, followed by an hour period of UV irradiation.

**TABLE 1 |** Print formulations used to determine biocompatibility.

| Formulation | PEDOT:PSS concentration (v/v%) | Ethylene glycol concentration (v/v%) | $dH_20$ concentration (v/v%) | GOPS concentration (v/v%) |
|---|---|---|---|---|
| 1 | 5 | 30 | 61 | 4 |
| 2 | 5 | 30 | 63 | 2 |
| 3 | 5 | 30 | 64 | 1 |

### PEDOT:PSS Biocompatibility Experimental Treatments

PEDOT:PSS coated glass samples were used to evaluate the direct ($n = 3$) and indirect ($n = 3$) biocompatibility of each polymer per repeat ($n = 2$). To assess direct biocompatibility, $1 \times 10^4$ cells were seeded directly onto the samples. Control wells (CON, non-patterned glass) were also seeded at $1 \times 10^4$ cells per well in 2 mL GM. To assess the in-direct biocompatibility of chemical leachate from each substrate, coated glass samples were placed in acellular wells, containing only medium. Chemically leached medium was then transferred to its corresponding experimental well during each repeat, ensuring that cellular medium was directly representative of either cumulative sample degradation or CON at each specific time-point. Each media only well was pre-incubated with 2 mL GM for 24 h prior to commencing each experiment, to ensure cells were seeded within media that had been exposed to the chemical leachate of each sample. Medium, once transferred to experimental wells, was replenished for further 24 h incubation prior to each subsequent media change. During the last 24 h in which the cells were cultured in GM, DM was added to the media only wells in preparation to induce differentiation in cell cultures.

### Immunocytochemistry

Cells were fixed with 3.7% formaldehyde in phosphate buffered saline solution (PBS) and subsequently blocked and permeablised with 5% goat serum (GS) and 0.2% Triton-X100 in tris-buffered saline (TBS, pH 8.5) for 30 min at RT. Thereafter, a solution with monoclonal mouse anti-β-tubulin III (1:200) antibody and 2% GS in TBS was added and incubated for 2 h. This solution was removed and AlexaFluor488®-conjugated goat anti mouse IgG (1:200) was added along with nuclear counter stain DAPI (1:1000), containing 2% GS and 0.2% Triton-X100 in TBS. The solution was incubated in the dark for an hour and thereafter, samples were rinsed with TBS and mounted onto cover slides using Fluoromount™ Aqueous Mounting Medium.

### Image and Statistical Analysis

Fluorescence microscope images were taken using a LEICA DM2500 fluorescence microscope with a 20× magnification objective. Each experimental condition consisted of a minimum of 2 substrates per technical (biological) repeat, with a minimum of 3 technical repeats per condition. Five random images were taken at the end of the experimental repeat for every sample at every line width, totaling a minimum of 30 images analyzed per condition. Nuclei and neurite alignment were obtained using a customized Fiji macro plugin. The angle of the nuclei/neurite was obtained by using the channels as the reference point. Consequently, vertical lines parallel to the line edges were considered as the point where cells were perfectly aligned (0 degrees). The nuclei/neurite alignment was then cumulatively expressed by interquartile ranges. Statistical analyses and significance of data were determined using IBM© SPSS© Statistics version 23. All the data is presented as mean (±standard deviation), derived from the means of each of the 6 unique substrates (minimum value, 3 technical repeats). Statistical differences between data were measured via a one way

ANOVA followed by a Tukey's *post hoc* test. Differences were considered statistically significant for $p \leq 0.05$.

# RESULTS AND DISCUSSION

## Development of a PEDOT:PSS Material Formulation for Aerosol Jet Printing

Different examples of inks based around commercial formulations of PEDOT:PSS containing a co-solvent regime of $dH_20$ and ethylene glycol can be found in literature for printing with AJP (Ha et al., 2010, 2013; Kim et al., 2013; Aga et al., 2014; Hong et al., 2014a,b; Zare Bidoky and Frisbie, 2016). In this work, Clevios$^{TM}$ PH1000 formulation, a commercially available aqueous dispersion of PEDOT:PSS with a 1.0–1.3% solid content and a viscosity of 15-50 cP (as reported by the supplier H.C. Starck, Leverkusen, Germany) was employed. Using PH1000 as the functional material, a methodology was established for testing the dilution ratios of the two co-solvents (water and ethylene glycol) for AJP to highlight the importance of the initial solvent mixture and define a suitable PEDOT:PSS ink to use during subsequent processing. As a 10% by volume dilution using ethylene glycol is frequently used in the literature (Ha et al., 2010, 2013; Kim et al., 2013; Hong et al., 2014a,b) the upper and lower limits in this experiment were set to 0 and 20% by weight to test around an already proven formulation. The nine material formulations are generated at defined locations between the upper and lower concentration bounds and are reported in **Supplementary Table 1**. The corresponding printed lines were observed by optical microscopy and evaluated in terms of line uniformity, overspray, homogeneity and feature size. Representative images of the printed lines obtained using each formulation are included in the **Supplementary Material** attached to this document (**Supplementary Figure 1**) and the observations of each result are summarized in **Supplementary Table 2**. From this analysis it was evident that formulation P4 (1.04% v/v PEDOT:PSS, 20% v/v ethylene glycol, 78.96% v/v $dH_20$), generated the most uniform line, with minimal overspray and also a narrow line width (**Supplementary Figure 2**). For this reason, it was selected for further investigation.

## Characterization of Machine Processing Parameters to Generate Micro-Features

Producing suitable aerosol-jet printed micro-scale features with the ultrasonic atomizer requires precise control over key processing variables, such as the atomization frequency, the flow rate of the carrier gas that transports the aerosol mist to the substrate (carrier flow), the flow rate of the sheath gas that collimates the aerosol into a narrow beam (sheath flow), nozzle diameter, the speed of the substrate under the beam (stage speed), and the distance between the substrate and the nozzle (working distance). The relationship between adjustable process parameters and the geometry of the aerosol-jet printed lines has been documented previously by Mahajan et al. (2013) in the case of printing silver nanoparticles; within this framework, they evidenced that the critical factors affecting silver track size are the ratio of the sheath and carrier gas flow rates (defined as the focusing ratio) and the stage speed. In particular, they reported that the line width decreases with increasing the focusing ratio and stage speed. Simultaneously, the thickness increases with increasing the focusing ratio but decreases with increasing stage speed. These results were also confirmed in our early studies on the aerosol-jet printing of PEDOT:PSS micro-features (Smith et al., 2018). Moreover, previous results from our group defined the processing conditions to reliably print PEDOT:PSS lines in the region of 20 μm wide (100 μm diameter nozzle, atomizing current 0.65 mA, sheath flow 40 sccm, carrier flow 20 sccm, stage speed 70 mm/min, working distance 3 mm) (Smith et al., 2018). Subtle variations in these key processing parameters can have a significant impact on the rate of material deposition and ultimately the precise geometries deposited onto the substrate.

Starting from the above mentioned previous studies (Mahajan et al., 2013; Smith et al., 2018), the generation of precise micro-features of PEDOT:PSS (formulation P4, 1.04% v/v PEDOT:PSS, 20% v/v ethylene glycol, 78.96% v/v $dH_20$) on glass substrates via AJP was informed by a full factorial design of experimentation (DoE) assessing the relative importance of four variables on PEDOT:PSS track profile: sheath flow, carrier flow, working distance and stage speed (see section "Materials and Methods" and **Supplementary Table 3** for details).

White light interferometry was used to assess the cross sectional area, width at base, width at half height and the step height of the sixteen different PEDOT:PSS tracks deposited via AJP onto glass substrates (see "Materials and Methods" section for details). The results for the full DoE are reported in **Supplementary Table 4**. The PEDOT:PSS tracks printed in these trials showed a width at half height ranging from 20 to 40 μm, a width at base from 30 to 50 μm, and a cross sectional area from 5.5 to 12 $\mu m^2$.

The results of the analysis of the sensitivity of the process to individual variables are displayed in **Supplementary Table 5**. The analysis of two and multi factors interactions are available, respectively, in **Supplementary Tables 6, 7**. These results confirmed that cross sectional area is reduced by increasing sheath gas from 30 to 40 sccm, reducing carrier gas from 25 to 20 sccm, and increasing stage speed from 70 to 90 sccm, and identified the sheath and carrier flow ratio as the primary influence on track profile. The effect of varying the working distance, and the effect of two and multi factor interactions were negligible in comparison. In conclusion, to make large changes to the line geometry, the carrier gas should be changed first. Once a geometry in a suitable region has been achieved, it should be tuned by changes to the sheath gas flow rate and the stage speed.

## Printing Micro-Features for SH-SY5Y Cells Alignment

The analysis of the interactions reported in the previous paragraph informed the settings of processing parameters for the application of PEDOT:PSS aerosol jet printed micro-features to be used to guide neuronal cell culturing. Since previous literature has demonstrated increased SH-SY5Y neurite and

nuclei alignment for cells confined within patterned substrates with a width <100 μm (Nam et al., 2014), we focused on suitable processing parameters to manufacture track sizes of 15, 20, 30, 40, and 50 μm, that would promote significant neuronal alignment. In these experiments, the scanning speed and the working distance were fixed, respectively, at 100 mm/min and 3 mm; for each track size, the corresponding nozzle size, sheath flow and carrier flow are summarized in **Table 2**. Regarding the nozzle size, previous studies have demonstrated that the printed line width and thickness are also a function of this process parameter, evidencing that finer lines are produced from smaller nozzles (Mahajan et al., 2013). However, as focusing ratio increases, the pressure built up in the nozzle represents a limitation for smaller nozzles, as the maximum pressure is reached at lower focusing ratios when compared with larger nozzles. Except for the line widths <20 μm, almost the entire spectrum of line widths achieved using a 100 μm nozzle can be achieved with a 150 μm nozzle at comparatively higher sheath gas flow rates. The use of larger nozzles presents many advantages compared to the smallest ones; larger nozzles yield a wider range of both line width, sustain higher sheath gas flow rates and reduce the risk of clogging (Mahajan et al., 2013). For these reasons, except for 15 and 20 μm lines, the 150 μm nozzle was used for the rest of the target line width.

In order to be employed as a substrate template for neuronal cell culturing, the Aerosol Jet printed PEDOT:PSS patterns must be stable when placed in aqueous physiological conditions for long periods of time without showing delamination or redispersion. Using the above mentioned formulation (formulation P4, 1.04% v/v PEDOT:PSS, 20% v/v ethylene glycol, 78.96% v/v $dH_20$), printed PEDOT:PSS features showed significant degradation when submerged in cell culture media for 72 h, and in some cases complete removal from the glass substrate. To avoid delamination/degradation of the films in aqueous environment, PEDOT:PSS dispersions are typically mixed with other chemical compounds, with notable attention focused toward the silane based cross-linking agent 3-glycidoxypropyltrimethoxysilane (GOPS), that is often adopted to enhance the mechanical stability of PEDOT-based devices on glass and plastic substrates (Zhang et al., 2016; ElMahmoudy et al., 2017). With respect to cell culture applications, while the addition of GOPS promotes PEDOT:PSS adhesion to glass substrates, it must not compromise the biocompatibility of the material. For this reason, the effect of the addition of GOPS adhesion promoter to the previously defined print formulation on the final material biocompatibility was first investigated, and the results are reported as follows.

**TABLE 2 |** Aerosol jet printing (AJP) machine processing parameters used to achieve a range of PEDOT:PSS track widths on a glass substrate.

| Target line width (μm) | Nozzle size (μm) | Sheath gas flow rate (sccm) | Carrier gas flow rate (sccm) |
|---|---|---|---|
| 15 | 100 | 50 | 18 |
| 20 | 100 | 50 | 20 |
| 30 | 150 | 70 | 25 |
| 40 | 150 | 60 | 25 |
| 50 | 150 | 50 | 25 |

*Scanning speed = 100 mm/min, working distance = 3 mm.*

## Development of a Biocompatible PEDOT:PSS Formulation for Neuronal Culture

The effect of the addition of GOPS adhesion promoter to the previously defined PEDOT:PSS formulation on the final material biocompatibility was investigated for the SH-SY5Y neuronal cell line (see **Table 1** and Cell Culture Methodology details in the "Materials and Methods" section). For all the formulations, there was no visible degradation or peeling after incubation in neuronal GM for 72 h. As evidenced in **Figure 2A**, SH-SY5Y cells were shown to demonstrate reduced cellular viability when compared to control after 48 h in growth media (GM) when cultured in the chemical leachate from PEDOT:PSS formulation 1 ($P < 0.05$) and formulation 3 ($P < 0.05$). There was no significant difference when comparing between each of these formulations. However, after 72 h in differentiation media (DM), formulation 2 ($P < 0.0001$) and formulation 3 ($P < 0.05$) displayed increased cellular viability compared to control (**Figure 2B**). When comparing between formulations there was a significant increase in viability shown by formulation 2 ($P < 0.0001$) and formulation 3 ($P < 0.001$), suggesting a cellular preference over formulation 1. This indicates the inclusion of increasing concentrations of the adhesion promotor GOPS to have a negative effect on cellular behavior. This result was confirmed by SH-SY5Y neuronal cells cultured directly onto the materials, which demonstrated a preferential cellular response for formulation 2 ($P < 0.0001$) and formulation 3 ($P < 0.001$) after 48 h in GM (**Figure 2C**). After 72 h in DM, formulation 2 had a preferential cellular response over both formulation 1 ($P < 0.0001$) and also formulation 3 ($P < 0.05$) (**Figure 2D**). The viability data for the 3 formulations suggests that each of these biomaterials is a viable culture material for SH-SY5Y when cultured indirectly in the chemical leachate. However, when cultured directly onto these materials then formulation 2 (2% GOPS) is preferential.

Neurite length was also assessed as a morphological indication of SH-SY5Y differentiation on each of the substrates. **Figures 2E-H** report the morphological staining of SH-SY5Y cells cultured directly on PEDOT:PSS coated glass substrates, respectively, for control (E), formulation 1 (F), formulation 2 (G), and formulation 3 (H). **Figure 2I** shows that the average neurite length increased significantly across each formulation when compared to control (all $P < 0.05$) after 72 h in DM when cultured in the chemical leachate from each material, without any difference when comparing between formulations. However, there was a reduction in neurite length observed in formulation 1 ($P < 0.0001$) and formulation 3 ($P < 0.001$) when compared to control after 72 h in DM when cultured directly onto the

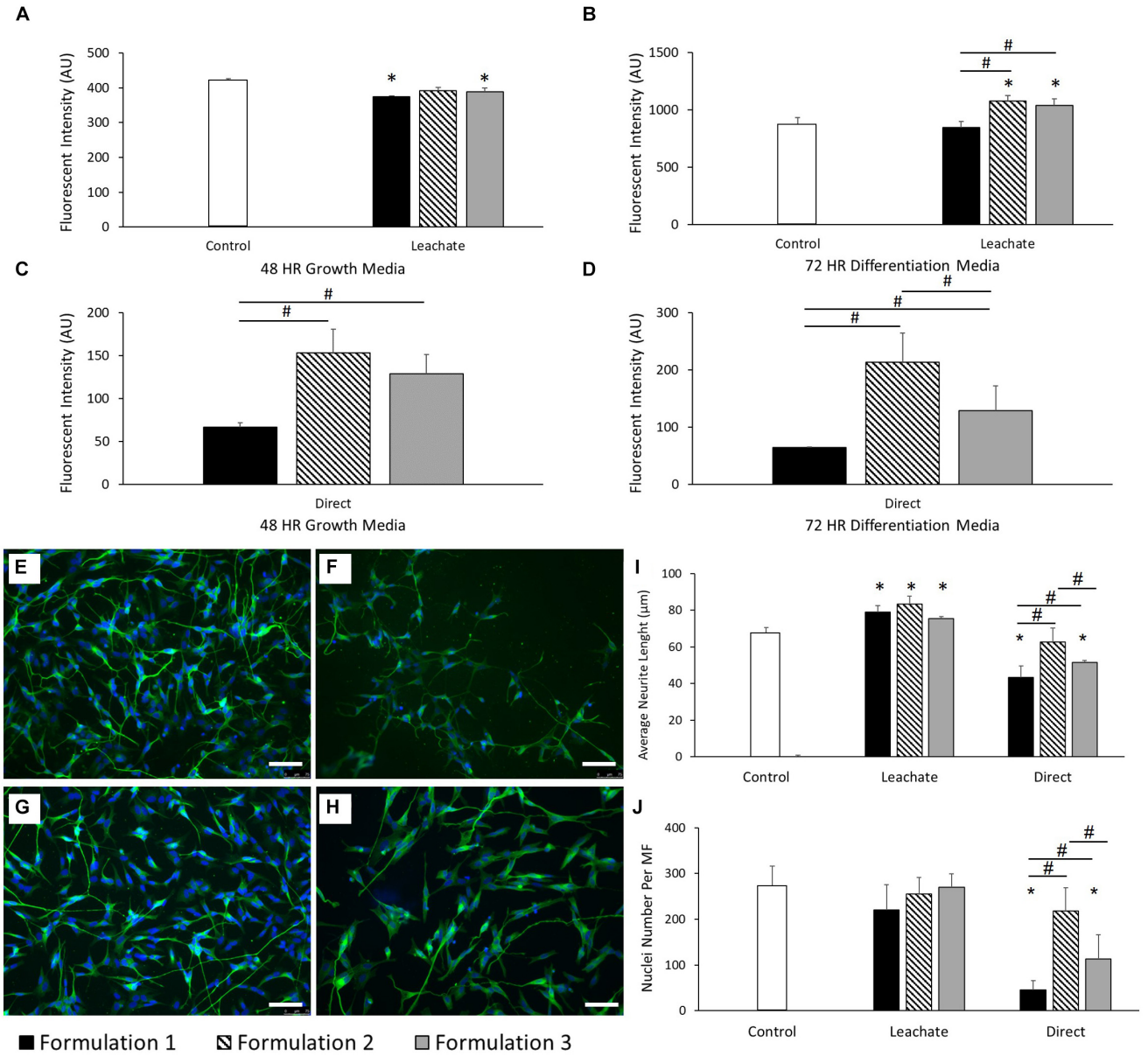


**FIGURE 2 | (A)** Cellular viability of SH-SY5Y neuroblastoma cells cultured in the chemical leachate of PEDOT:PSS coated glass substrates after 48 h in neuronal GM. **(B)** Cellular viability of SH-SY5Y neuroblastoma cells cultured in the chemical leachate of a PEDOT:PSS glass substrates after 72 h in neuronal DM. **(C)** Cellular viability of SH-SY5Y neuroblastoma cells cultured directly onto a PEDOT:PSS glass substrates after 48 h in neuronal GM. **(D)** Cellular viability of SH-SY5Y neuroblastoma cells cultured directly onto a PEDOT:PSS glass substrates after 72 h in neuronal DM. Data presented as mean ± SD from $n = 6$ experimental repeats in each condition. # significantly different within group, * significantly different from control ($P < 0.05$). **(E–H)** Morphological staining of SH-SY5Y neuroblastoma cells cultured directly on PEDOT:PSS coated glass substrates: **(E)** uncoated glass control, **(F)** formulation 1, **(G)** formulation 2, **(H)** Formulation 3. Green = β-tubulin, blue = DAPI. Scale bar = 100 μm. **(I)** Average neurite length of SH-SY5Y neuroblastoma cells after 72 h in DM, cultured in both the chemical leachate of a PEDOT:PSS coated glass substrate and directly onto the material. **(J)** Nuclei number per microscope field (MF, 20× magnification) of SH-SY5Y neuroblastoma cells after 72 h in DM, cultured in both the chemical leachate of a PEDOT:PSS glass substrate and directly onto the material. Data presented as mean ± SD from $n = 6$ experimental repeats in each condition. # significantly different within group, * significantly different from control ($P < 0.05$).

material. There was also a significant increase in neurite length demonstrated by formulation 2 when comparing directly with both formulation 1 ($P < 0.0001$) and formulation 3 ($P < 0.01$). As shown in **Figure 2J**, no significant difference was observed between the nuclei numbers of each condition after 72 h of culture in the chemical leachate of each material. However, formulations 1 ($P < 0.0001$) and 3 ($P < 0.0001$) demonstrated a reduction in nuclei number when compared to both control, and also formulation 2 (all $P < 0.05$), when cultured directly onto the materials. The significant reductions in morphological behavior

demonstrated by formulation 1 discounted the inclusion of this condition in further optimization reported below.

## Topographical Characterization of PEDOT:PSS Micro-Features for SH-SY5Y Cells Alignment on Glass and PKSPMA Coated Glass Substrates

The effect of the addition of the adhesion promoter GOPS on the printability of the PEDOT:PSS formulation P4 was investigated, and the remaining formulations (formulation 2 and 3) were tested for aerosol jet printing deposition. These experiments showed that by using higher concentration of GOPS (>1%) the printing quickly starts to become unstable, resulting in non-uniform patterns, until the complete and permanent clogging of the nozzles. Since the clogging of the nozzle did not occur for lower GOPS concentration, formulation 3 was then selected for the printing of PEDOT:PSS micro-features for SH-SY5Y cells alignment, using the printing parameters reported in **Table 2**. Using this new formulation, there was a noticeable decrease (average 24.2%) in the printed line width at the same process conditions after the addition of the adhesion promotor. This decrease could be accounted for by slightly changing the print parameters so was deemed acceptable. The profile of the printed PEDOT:PSS tracks on glass substrates using this new formulation was analyzed by white light interferometric measurements: a representative example of these measurements is reported in **Figure 3**, which shows the 2D top down graphical representation (A), the 3D graphical representation (B) and the 2D cross sectional graphical representation (C) of a track profile.

The results of white light interferometry measurements of PEDOT:PSS tracks on glass substrate can be analyzed by directly comparing the geometric parameters of the printed tracks (i.e., cross sectional area, width at half height, track width at base). As evidenced in **Figure 3D**, a logarithmic relationship ($R^2$ = 0.906) was observed between track cross sectional area and width at half height, indicating an increase in track width in proportion to the square root of the track area. Equally a linear relationship ($R^2$ = 0.979) between track width at the base and half height (**Figure 3E**) indicates that a comparable track profile was generated throughout the experiments, regardless of alterations in print processing parameters. The linear relationship between width at base and width at half height ($R$ = 0.9426) was confirmed by further analysis via atomic force microscopy (AFM) (**Figure 3F**). Roughness measurements from the AFM suggested a smooth surface (Ra < 3.5 nm, RMS < 4.1). Measurements of the track heights were also taken and are included in the **Supplementary Material** attached to this document (**Supplementary Figure 3**).

The specifics of the line geometry such as the overall shape, maximum height, width at base, width at half height, side wall angle and surface roughness are subject not only to influences from the material formulation and process parameters, but also material/surface interaction and drying characteristics. White light interferometry was also used to assess deposits of PEDOT:PSS onto a PKSPMA coated glass substrate. A logarithmic relationship ($R^2$ = 0.841) was observed between track cross sectional area and width at half height, with the profiles achieved typically being highly comparable to those generated on the non-treated glass substrates (**Figure 3H**). A linear relationship was observed between width at half height and width at the base ($R$ = 0.916), once again suggesting a consistent print profile both across the different track sizes and also when comparing between substrates (**Figure 3I**). The smaller contact angle of water on PKSPMA indicates a more hydrophilic surface than cleaned glass. This resulted in increased spreading of the deposit on the surface resulting in wider lines at the same processing parameters.

The non-linear relationship between cross sectional area and track width, evidenced on both glass ($R^2$ = 0.906) and the PKSPMA ($R^2$ = 0.841), is typical of jetting processes, with track widths typically proportional to the square root of the track area. This trend gives rise to an asymptotic relationship between track width and area. The printed tracks proved to be of a uniform geometry independent of material deposition rates or the overall track width. This was confirmed by a strong linear relationship between track width at the base and track width at half height, on both glass ($R^2$ = 0.979) and the PKSPMA ($R^2$ = 0.916) coated glass substrate.

## Characterization of Neuronal Alignment on PEDOT:PSS Micro-Features Printed Onto a Glass Substrate and a PKSPMA Polymer Brush Coated Glass Substrate

SH-SY5Y cells were cultured onto PEDOT:PSS tracks deposited onto glass substrates via AJP, following the experimental protocol reported in the "Materials and Methods" section. **Figures 4A–F** reports the morphological staining of SH-SY5Y neuroblastoma cells cultured on patterned PEDOT:PSS glass substrates with different track widths. As shown in **Figure 4G**, a significant increase in nuclei alignment (all $P < 0.0001$) was demonstrated across each of the track sizes when compared to control. However, there was no increase in alignment when comparing between tracks of differing widths. The same trend was observed for the neurite alignment with a significant increase (all $P < 0.05$) across track sizes against control, but with no change when comparing between tracks of differing widths (**Figure 4H**). There was however a non-significant reduction in both average nuclei alignment (26.5%) and average neurite alignment (20.3%) when comparing between the 50 and 15 μm tracks. This data indicates a strong cellular response to the topography generated by the AJP printed PEDOT:PSS tracks. There was no statistical significance when comparing average neurite length between all the different substrate conditions indicating no change in cellular differentiation in response to this topography (**Figure 4I**).

These results indicated that the SH-SY5Y cell line responded to the topographical stimulus generated by the AJP deposited tracks, without significant alteration to the morphology of the cell. However, no statistical variation in neurite or nuclei alignment between each of the track sizes was observed. This suggested that whilst the cells responded to the topographical stimulus generated by the jetted bio-substrate, the addition of

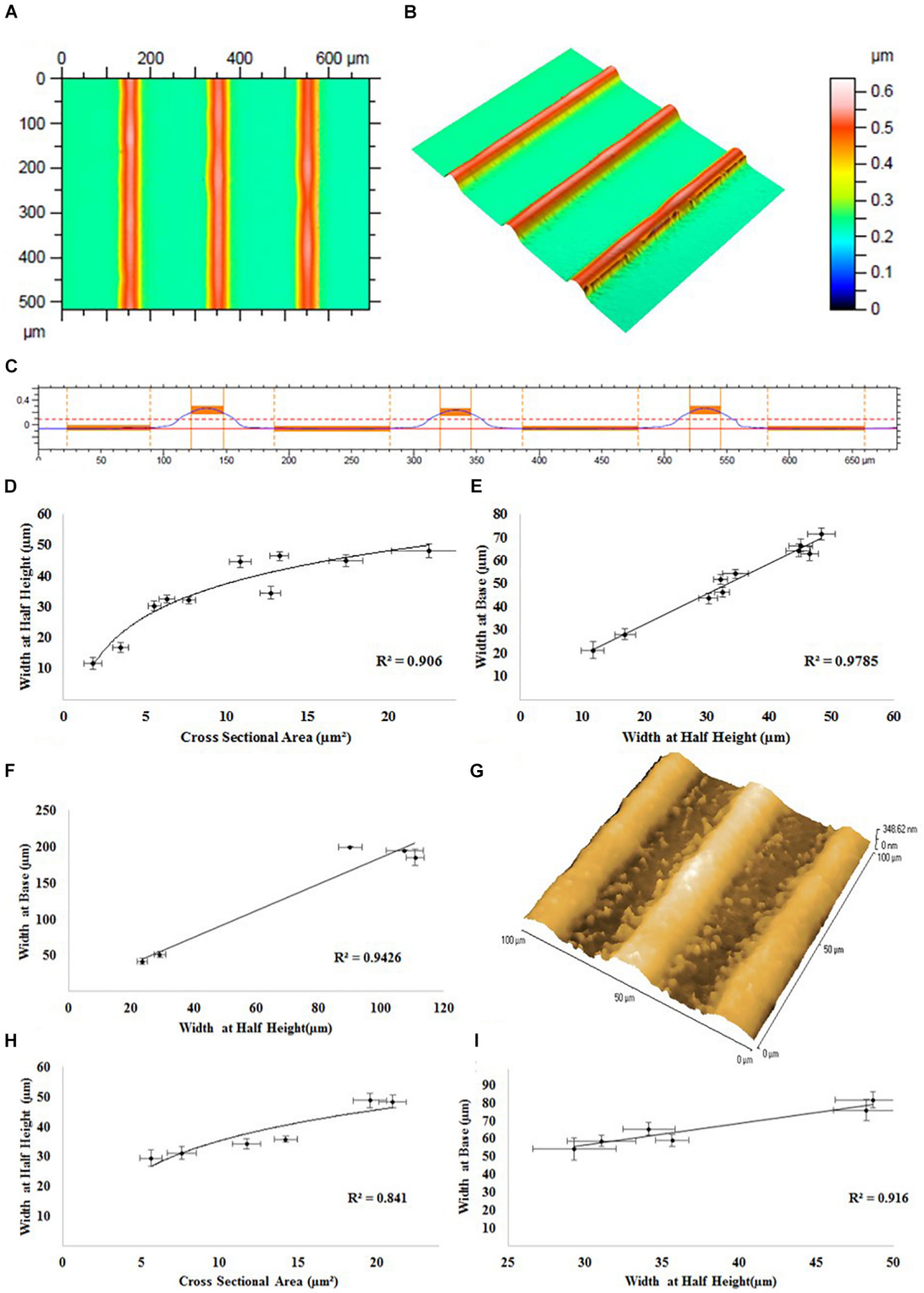


**FIGURE 3 |** Representative white light interferometry measurements of PEDOT:PSS tracks on a glass substrate: **(A)** 2D top down graphical representation, **(B)** 3D graphical representation, and **(C)** 2D cross sectional graphical representation of a track profile. **(D)** Track width at half height vs. track cross sectional area. **(E)** Track width at half height vs. track width at base. **(F)** Atomic force microscopy measurements of PEDOT:PSS tracks on a glass substrate. **(G)** A representative AFM image of the surface of the tracks. White light interferometry measurements of PEDOT:PSS tracks on a PKSPMA coated glass substrate. **(H)** Track width at half height vs. track cross sectional area. **(I)** Track width at half height vs. track width at base.

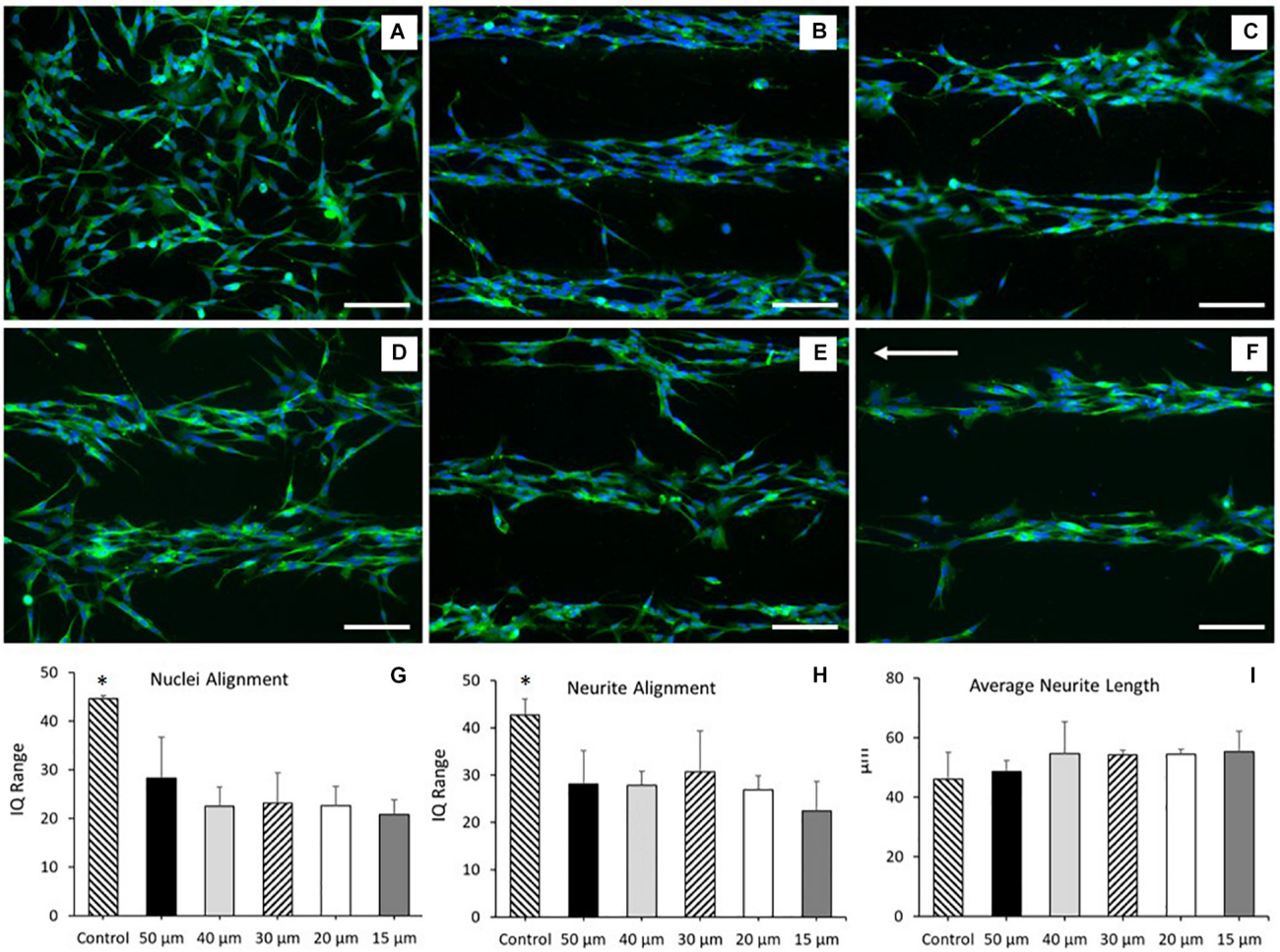


**FIGURE 4 |** Morphological staining of SH-SY5Y neuroblastoma cells cultured on patterned PEDOT:PSS glass substrates. Green = β-tubulin, blue = DAPI. Arrow indicates direction of PEDOT:PSS tracks deposited via aerosol jetting. **(A)** Untreated glass control. **(B)** 50 μm tracks. **(C)** 40 μm tracks. **(D)** 30 μm tracks. **(E)** 20 μm tracks. **(F)** 15 μm tracks. Scale bar = 100 μm. **(G)** Nuclei alignment of SH-SY5Y neuroblastoma cells after 72 h in DM, cultured directly onto a patterned PEDOT:PSS glass substrate. **(H)** Neurite alignment of SH-SY5Y neuroblastoma cells after 72 h in DM, cultured directly onto a patterned PEDOT:PSS glass substrate. **(I)** Average neurite length of SH-SY5Y neuroblastoma cells after 72 h in DM, cultured directly onto a patterned PEDOT:PSS glass substrate. Data presented as mean ± SD from $n = 6$ experimental repeats in each condition. *significantly different from all other conditions ($P < 0.05$).

a secondary chemical stimulus would be required to facilitate greater cellular alignment.

Polymer brush coated glass surfaces have previously been utilized to generate bio-substrates that prevent direct neuronal adhesion, but do not inhibit cellular growth and differentiation elsewhere in the culture (Zhou et al., 2013). PKSPMA polymer brush coated glass substrates have previously been shown to demonstrate these properties, making it an ideal candidate as the "repulsive" chemical coating to complement our "attractive" PEDOT:PSS printed tracks. For this reason, experiments were repeated culturing SH-SY5Y cells onto PEDOT:PSS tracks deposited onto PKSPMA coated glass substrates via AJP. **Figure 5A** report the morphological staining of SH-SY5Y neuroblastoma cells cultured on PEDOT:PSS patterned PKSPMA coated glass substrates with different track widths. **Figure 5B** demonstrates a significant increase in nuclei alignment (all $P < 0.0001$) across each of the track sizes when compared to control. Likewise, tracks >50 μm in width demonstrated reduced nuclei alignment than all the 40 μm ($P < 0.05$), 30 ($P < 0.05$), and 20 μm tracks ($P < 0.001$). No statistical significance was observed when comparing between the 3 smallest track sizes, however, the most aligned nuclei were observed in cells cultured onto the 20 μm tracks (IQ range = 9.3 ± 2.7), indicating a relationship between reduced track width and cellular alignment (**Figure 5C**). All track sizes showed increased neurite alignment when compared with control (all $P < 0.0001$), but with no variation when comparing between tracks of different widths. This indicates that whilst the chemical and topographical cues generated by the substrate resulted in increased neurite alignment, the submicron geometries of SH-SY5Y neurites necessitates a further reduction in track width to facilitate further alignment. There was no statistical significance when comparing

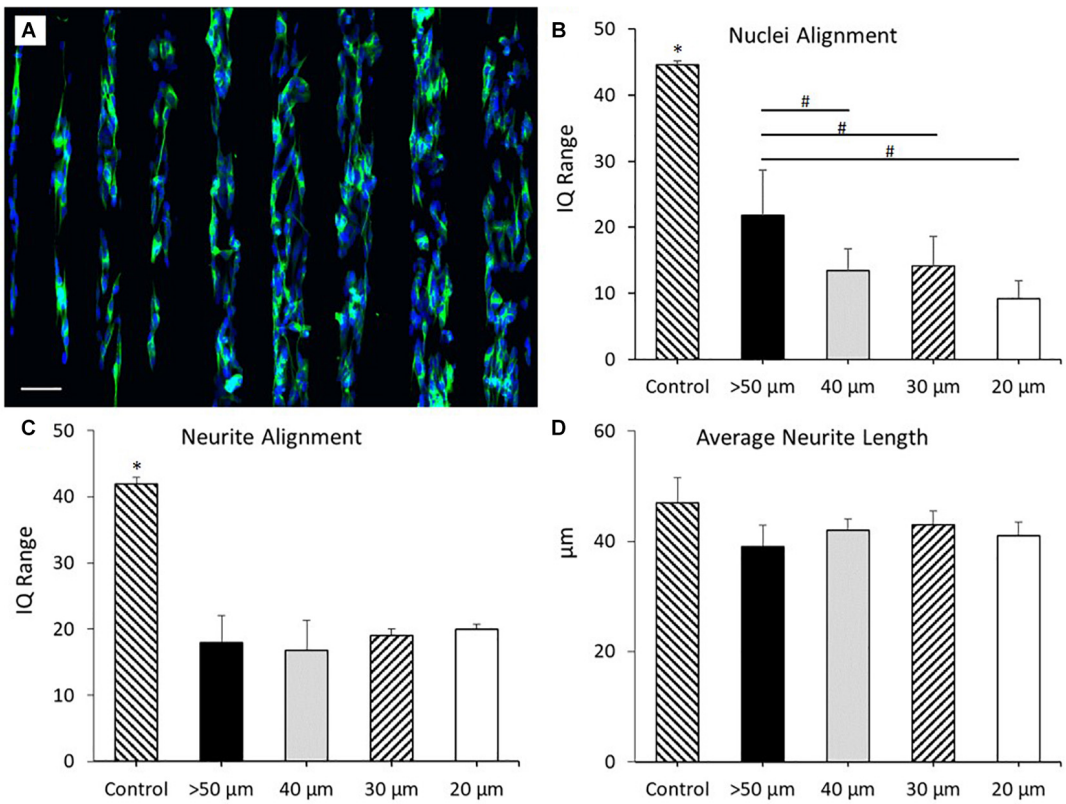


**FIGURE 5 | (A)** Morphological staining of SH-SY5Y neuroblastoma cells cultured on PEDOT:PSS tracks deposited via AJP onto PKSPMA coated glass substrates. Track widths ranging from 20 to 100 μm (left to right). Green = β-tubulin, blue = DAPI. Scale bar = 100 μm. **(B)** Nuclei alignment of SH-SY5Y neuroblastoma cells after 72 h in DM, cultured directly onto a PEDOT:PSS patterned PKSPMA coated glass substrate. **(C)** Neurite alignment of SH-SY5Y neuroblastoma cells after 72 h in DM, cultured directly onto a PEDOT:PSS patterned PKSPMA coated glass substrate. **(D)** Average neurite length of SH-SY5Y neuroblastoma cells after 72 h in DM, cultured directly onto a PEDOT:PSS patterned PKSPMA coated glass substrate. Control condition refers to untreated glass. Data presented as mean ± SD from $n = 6$ experimental repeats in each condition. # significantly different within group, *significantly different from all other conditions ($P < 0.05$).

average neurite length between all the different substrate conditions indicating no change in cellular differentiation in response to this topography (**Figure 5D**).

These results demonstrated that the addition of the "repulsive" PKSPMA coating significantly increased nuclei and neurite alignment across all track sizes. For the smallest of these track sizes (20 μm) nuclei alignment (IQ range) reduced from 22.5 to 9.3 through the addition of the repulsive coating. This trend was consistent when comparing between each of the track sizes, with the highest IQ range for the coated samples (50 μm = 21.8) being lower than all but the 15 μm uncoated substrates.

## Complex PEDOT:PSS Pattern Design Printed Onto PKSPMA Polymer Brush Coated Glass Substrate

To demonstrate some of the potential of this AJP technique, bespoke freeform patterns were generated using the optimized PEDOT:PSS formulation (**Figure 6**) and subsequently used to show designed cell culture formations. The individual patterns in this example were printed within a period of between 6 s (pattern A) and 20 s (pattern D). The print time for the entire set of patterns was <90 s. The designs used were selected to illustrate the ease at which increasing complexity could be achieved and to show the design freedom afforded by this technology. Complementary to the processing speed, is also the efficiency of material usage as the material is only printed where required. This material usage is much lower compared to other manufacturing techniques (Lan et al., 2017).

However, when considering the use of AJP there are some other characteristics that should also be considered. One consideration is the speckling or overspray effect which was observed. This results in a small number of particles outlying the edges of the line track, effecting the edge definition (Reitberger et al., 2016). When printing smaller line widths (<20 μm), high sheath or low atomization gas flow rates can result in areas where the line pinches inwards or discontinues (Tait et al., 2015). The ends of lines are regions of unpredictability, as the deceleration of the stage and the machine shutter lead to additional material build-up. The materials and processing definitions are also not well documented for many new materials. This means that in practical terms, whenever a new material is desired, a significant amount of effort must be put into determining the materials suitable printing parameters, and identifying effects that may be

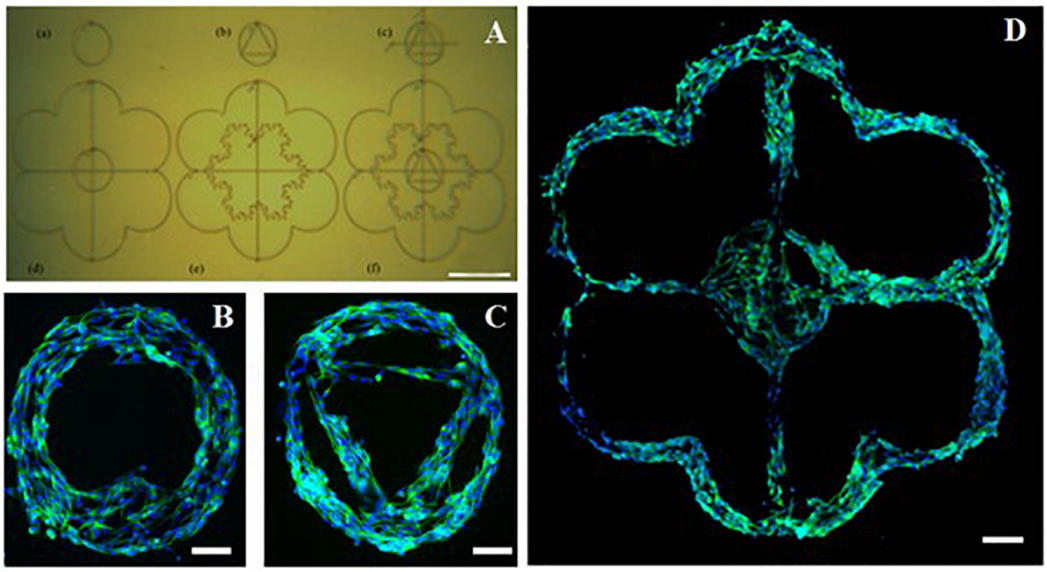


**FIGURE 6 |** Complex poly(3,4-ethylenedioxythiophene)-poly(styrenesulfonate) (PEDOT:PSS) pattern printed onto a poly(potassium 3-sulfopropyl methacrylate) (PKSPMA) coated glass substrate generated via AJP. **(A)** Patterned surface imaged before cell culture. **(B–D)** Morphological staining of SH-SY5Y neuroblastoma cells cultured on patterned substrate. Green = β-tubulin, blue = DAPI. (Scale bar **(A)** = 500 μm, **(B,C)** = 50 μm, **(D)** = 100μm).

specific to the intended application (Agarwala et al., 2017). Most of this definition focusses on line width and surface interactions alone, and currently specifications for height or specific line profiles are not yet commonplace. For this reason, material processing characterization for all new print formulations, such as the data detailed in this research, is important to developing a fuller suite of functional materials for AJP.

## CONCLUSION

In this work a materials formulation (1.04% v/v PEDOT:PSS, 20% v/v ethylene glycol, 78.96% v/v $H_2O$, 1% v/v GOPS) that allowed precise AJP deposition of PEDOT:PSS was developed, capable of producing smooth (Ra $<$ 3.5 nm and RMS $<$ 9 nm) tracks with micro-geometries (widths $<$ 20 μm and depths $<$ 500 nm). The addition of an adhesion promotor (GOPS) allowed these bio-substrates to be exposed to a cell culture environment for a period of 96 h without any feature degradation. These tracks were printed onto both glass and PSKPMA polymer brush coated glass substrates. Subsequently these bio-interfaces were cultured with the SH-SY5Y cell line and shown to induce significant neurite and nuclei alignment within the culture, by generating chemical and topographical cues. We have demonstrated that the process allowed the manufacture of customizable patterns, as well as the use of multiple materials to allow increased substrate functionality. To develop this concept further future work will focus on additional development and characterization of both the bio-substrate, including a comprehensive assessment of bio-substrate electrical properties such as conductivity/impedance within culture mediums, as well as additional characterization of the neuronal population including functional assessment, e.g., live cell calcium imaging, electrical field stimulation, and additional mapping of morphological and genetic development across prolonged experimental time courses. In addition, the application of this technology to biological environments (e.g., ocular, cortical, and/or neuromuscular) whereby controlled cellular development and increased functionality which require complex anisotropic bio-substrates will require additional demonstration.

This manufacturing approach allows the creation of complex 2.5D topographical substrates for *in vitro* cell culture studies while allowing rapid iterative design changes, and so extending the range and diversity of studies that can be explored effectively and economically. The entire design and manufacturing process is digitally driven, thereby providing the capability to rapidly alternate and produce different cell guidance designs, and to do so within time and cost boundaries that would be unachievable by template-based manufacturing approaches. Wider appealing factors of such a digital manufacturing include the ability to remotely receive designs from around the globe to distributed manufacturing locations, thus extending the reach of the research community it may serve. It is suggested that future research could extend capabilities and applications by further developing the range of printable bio-materials, whilst increasing the complexity of design through the generation of multi-material and 3D substrates, opening new possibilities to create realistic *in vitro* cell models. Lastly, but significant to its uptake; this scalable, accurate and reproducible digitally-driven processing technology could enable mass production of these novel substrates, paving the way toward potential industrial translation in a wide variety of practical applications, such as modeling diseases and drug discovery.

## DATA AVAILABILITY STATEMENT

The original contributions generated for this study are included in the article/**Supplementary Material**, further inquiries can be directed to the corresponding author.

## AUTHOR CONTRIBUTIONS

MS, ST, RK, and RH contributed to the manufacturing technology and engineering. AC, MP-F, RR, ML, and SC contributed to the biological and chemical science. All authors contributed to the article and approved the submitted version.

## FUNDING

This work was funded by the United Kingdom Engineering and Physical Sciences Research Council (EPSRC) under grant EP/L02067X/2, EP/P027687/1, and EP/L02067X/1.

## SUPPLEMENTARY MATERIAL

The Supplementary Material for this article can be found online at: https://www.frontiersin.org/articles/10.3389/fcell.2021.722294/full#supplementary-material

**Supplementary Figure 1 |** Print formulations P1–P9 utilized during initial material screen. Nozzle size = 200 μm, sheath and atomizer gas flow rates = 50 sccm, nozzle height = 3 mm, stage speed = 5 mm/s. sccm, standard cubic centimeters per minute.

**Supplementary Figure 2 |** Representative microscopic image of print formulation P4 (Scale bar = 200 μ m).

**Supplementary Figure 3 |** White light interferometry measurements of maximum height vs. cross sectional area for PEDOT:PSS tracks printed onto a glass substrate via AJP.

**Supplementary Table 1 |** Development of an initial PEDOT:PSS material formulation. Nozzle size = 200 μm, sheath and atomizer gas flow rates = 50 sccm, nozzle height = 3 mm, scanning speed = 5 mm/s. sccm, standard cubic centimeters per minute.

**Supplementary Table 2 |** Observations of print formulations P1–P9 utilized during initial material screen.

**Supplementary Table 3 |** Full factorial design of experiment to determine optimized AJP processing parameters for the deposition of PEDOT:PSS onto a glass substrate. Nozzle size = 100 μm. sccm, standard cubic centimeters per minute. The experimental parameters were run three times, on three separate days with a disassembly and clean of the functional end of the machine after each run. The machine was reassembled before each experiment.

**Supplementary Table 4 |** Full details of the matrix style DoE carried out to optimize the machine processing conditions for the AJP of PEDOT:PSS. In each trial, each of the three lines were assessed three times for each geometrical feature ($n$ = 9).

**Supplementary Table 5 |** Analysis of individual variables.

**Supplementary Table 6 |** Analysis of two factor interactions.

**Supplementary Table 7 |** Analysis of three and four factor interactions.

## REFERENCES

Aga, R., Jordan, C., Aga, R. S., Bartsch, C. M., and Heckman, E. M. (2014). "Metal electrode work function modification using aerosol jet printing". *IEEE Electron Device Lett.* 35, 1124–1126. doi: 10.1109/led.2014.2355142

Agarwala, S., Goh, G. L., and Yeong, W. Y. (2017). "Optimizing aerosol jet printing process of silver ink for printed electronics". *IOP Conf. Ser. Mater. Sci. Eng.* 191:12027.

Akhmanova, M., Osidak, E., Domogatsky, S., Rodin, S., and Domogatskaya, A. (2015). Physical, Spatial, and Molecular Aspects of Extracellular Matrix of In Vivo Niches and Artificial Scaffolds Relevant to Stem Cells Research. *Stem Cells Int.* 2015, 167025–167060.

Bettinger, C. J., Langer, R., and Borenstein, J. T. (2009). "Engineering substrate topography at the micro- and nanoscale to control cell function". *Angew. Chem. Int. Ed.* 48, 5406–5415. doi: 10.1002/anie.200805179

Cai, F., Chang, Y. H., Wang, K., Zhang, C., Wang, B., and Papapolymerou, J. (2016). "Low-loss 3-D multilayer transmission lines and interconnects fabricated by additive manufacturing technologies". *IEEE Trans. Microw. Theory Tech.* 64, 3208–3216. doi: 10.1109/tmtt.2016.2601907

Caliari, S., and Burdick, J. (2016). "A practical guide to hydrogels for cell culture". *Nat. Methods* 13, 405–414. doi: 10.1038/nmeth.3839

De Silva, M. N., Paulsen, J., Renn, M. J., and Odde, D. J. (2006). "Two-step cell patterning on planar and complex curved surfaces by precision spraying of polymers". *Biotechnol. Bioeng.* 93, 919–927. doi: 10.1002/bit.20787

Denchai, A., Tartarini, D., and Mele, E. (2018). "Cellular Response to Surface Morphology: Electrospinning and Computational Modeling". *Front. Bioeng. Biotechnol.* 6:155. doi: 10.3389/fbioe.2018.00155

Derakhshanfar, S., Mbeleck, R., Xu, K., Zhang, X., Zhong, W., and Xing, M. (2018). "3D bioprinting for biomedical devices and tissue engineering: A review of recent trends and advances". *Bioactive Mater.* 3, 144–156. doi: 10.1016/j.bioactmat.2017.11.008

ElMahmoudy, M., Inal, S., Charrier, A., Uguz, I., Malliaras, G. G., and Sanaur, S. (2017). "Tailoring the Electrochemical and Mechanical Properties of PEDOT:PSS Films for Bioelectronics". *Macromol. Mater. Eng.* 32:1600497. doi: 10.1002/mame.201600497

Filipponi, L., Livingston, P., Kašpar, O., Tokárová, V., and Nicolau, D. V. (2016). . *Biomed. Microdev.* 18:9.

Garma, L. D., Ferrari, L. M., Scognamiglio, P., Greco, F., and Santoro, F. (2019). "Inkjet-printed PEDOT:PSS multi-electrode arrays for low-cost in vitro electrophysiology". *Lab. Chip* 19, 3776–3786. doi: 10.1039/c9lc00636b

Gomez, N., Lee, J. Y., Nickels, J. D., and Schmidt, C. E. (2007). "Micropatterned Polypyrrole: A Combination of Electrical and Topographical Characteristics for the Stimulation of Cells". *Adv. Funct. Mater.* 17, 1645–1653. doi: 10.1002/adfm.200600669

Grunwald, I., Groth, E., Wirth, I., Schumacher, J., Maiwald, M., Zoellmer, V., et al. (2010). Aerosol jet printing of biological inks by ultrasonic delivery. *Biofabrication* 2:14106.

Ha, M., Seo, J.-W. T., Prabhumirashi, P. L., Zhang, W., Geier, M. L., Renn, M. J., et al. (2013). "Aerosol jet printed, low voltage, electrolyte gated carbon nanotube ring oscillators with sub-5 μs stage delays". *Nano Lett.* 13, 954–960. doi: 10.1021/nl3038773

Ha, M., Xia, Y., Green, A. A., Zhang, W., Renn, M. J., Kim, C. H., et al. (2010). "Printed, sub-3V digital circuits on plastic from aqueous carbon nanotube inks". *ACS Nano* 4, 4388–4395. doi: 10.1021/nn100966s

Hardelauf, H., Waide, S., Sisnaiske, J., Jacob, P., Hausherr, V., Schöbel, N., et al. (2014). "Micropatterning neuronal networks". *Analyst* 139, 3256–3264. doi: 10.1039/c4an00608a

Hegge, W., Bohling, D. A., Chou, J., Mcallister, M., and Schottland, P. (2011). Direct Dielectric Line Printing for Touch Panel Display Jumpers Using Transparent Dielectric Inks and Aerosol Jet Deposition Methods. *Proc. Soc. Informat. Display Int. Sympos.* 42, 837–840. doi: 10.1889/1.3621463

Higgins, M. J., Molino, P. J., Yue, Z., and Wallace, G. G. (2012). "Organic conducting polymer–protein interactions". *Chem. Mater.* 24:828. doi: 10.1021/cm203138j

Holthaus, M. G., and Rezwan, K. (2008). Comparison of Three Microstructure Fabrication Methods for Bone Cell Growth Studies. *Proc. ASME Int. Manufact. Sci. Engine. Confer.* 2008, 483–490.

Hong, K., Kim, S. H., Mahajan, A., and Frisbie, C. D. (2014a). "Aerosol jet printed p-and n-type electrolyte-gated transistors with a variety of electrode materials: exploring practical routes to printed electronics". *ACS Appl. Mater. Interfaces* 6, 18704–18711. doi: 10.1021/am504171u

Hong, K., Kim, Y. H., Kim, S. H., Xie, W., Xu, W. D., Kim, C. H., et al. (2014b). "Aerosol jet printed, sub-2 V complementary circuits constructed from P- and N-type electrolyte gated transistors". *Adv. Mater.* 26, 7032–7037. doi: 10.1002/adma.201401330

Janson, I. A., and Putnam, A. J. (2015). "Extracellular matrix elasticity and topography: Material-based cues that affect cell function via conserved mechanisms". *J. Biomed. Mater. Res. Part A* 103, 1246–1258. doi: 10.1002/jbm.a.35254

Karp, J. M., Yeo, Y., Geng, W., Cannizarro, C., Yan, K., Kohane, D. S., et al. (2006). "A photolithographic method to create cellular micropatterns". *Biomaterials* 27, 4755–4764. doi: 10.1016/j.biomaterials.2006.04.028

Kim, S. H., Hong, K., Lee, K. H., and Frisbie, C. D. (2013). "Performance and stability of aerosol-jet-printed electrolyte-gated transistors based on poly(3-hexylthiophene)". *ACS Appl. Mater. Interfaces* 5, 6580–6585. doi: 10.1021/am401200y

Koçer, G., and Jonkheijm, P. (2018). "About Chemical Strategies to Fabricate Cell-Instructive Biointerfaces with Static and Dynamic Complexity". *Adv. Healthcare Mater.* 7:1701192. doi: 10.1002/adhm.201701192

Kume, T., Kawato, Y., Osakada, F., and Izumi, Y. (2008). "Dibutyryl cyclic AMP induces differentiation of human neuroblastoma SH-SY5Y cells into a noradrenergic phenotype". *Neurosci. Lett.* 443, 199–203. doi: 10.1016/j.neulet.2008.07.079

Lan, X., Lu, X., Chen, M. Y., Scherrer, D., Chung, T., Nguyen, E., et al. (2017). "Direct On-Chip 3-D Aerosol Jet Printing With High Reliability," in *Proceedings of the IEEE Transaction on Components, Packaging and Manufacturing Technology* (New Jersey, NJ: IEEE), 1–8.

Lind, J., Busbee, T., Valentine, A., et al. (2017). "Instrumented cardiac microphysiological devices via multimaterial three-dimensional printing". *Nat. Mater.* 16, 303–308. doi: 10.1038/nmat4782

Liu, X., and Wang, S. (2014). "Three-dimensional nano-biointerface as a new platform for guiding cell fate". *Chem. Soc. Rev.* 43, 2385–2240. doi: 10.1039/c3cs60419e

Lundin, V., Herland, A., Berggren, M., Jager, E. W. H., and Teixeira, A. I. (2011). "Control of Neural Stem Cell Survival by Electroactive Polymer Substrates". *PLoS One* 6:e18624. doi: 10.1371/journal.pone.0018624

Mahajan, A., Frisbie, C. D., and Francis, L. F. (2013). "Optimization of aerosol jet printing for high-resolution, high-aspect ratio silver lines". *ACS Appl. Mater. Interfaces* 5, 4856–4864. doi: 10.1021/am400606y

Maiwald, M., Werner, C., Zöllmer, V., and Busse, M. (2010). "INKtelligent printing for sensorial applications". *Sens. Rev.* 30, 19–23. doi: 10.1108/02602281011010763

Mashayekhi, M., Winchester, L., Evans, L., Pease, T., Laurila, M. M., Mantysalo, M., et al. (2016). "Evaluation of Aerosol, Superfine Inkjet, and Photolithography Printing Techniques for Metallization of Application Specific Printed Electronic Circuits". *IEEE Trans. Electron Devices* 63, 1246–1253. doi: 10.1109/ted.2016.2522388

Mirbagheri, M., Adibnia, V., Hughes, B. R., Waldman, S. D., Banquyc, X., and Hwang, D. K. (2019). Advanced cell culture platforms: a growing quest for emulating natural tissues. *Mater. Horiz.* 6, 45–71. doi: 10.1039/c8mh00803e

Mohs, R. C., and Greig, N. H. (2017). "Drug discovery and development: Role of basic biological research". *Alzheimers Dement.* 11, 651–657. doi: 10.1016/j.trci.2017.10.005

Murphy, S. V., and Atala, A. (2014). "3D bioprinting of tissues and organs". *Nat. Biotechnol.* 32, 773–785. doi: 10.1038/nbt.2958

Nam, K.-H., Jamilpour, N., Mfoumou, E., Wang, F.-Y., Zhang, D. D., and Wong, P. K. (2014). "Probing Mechanoregulation of Neuronal Differentiation by Plasma Lithography Patterned Elastomeric Substrates". *Sci. Rep.* 4:6965.

Nie, Z., and Kumacheva, E. (2008). "Patterning surfaces with functional polymers". *Nat. Mater.* 7, 277–290. doi: 10.1038/nmat2109

Ohayon, D., Pitsalidis, C., Pappa, A.-M., Hama, A., Zhang, Y., Gallais, L., et al. (2017). "Laser Patterning of Self-Assembled Monolayers on PEDOT:PSS Films for Controlled Cell Adhesion". *Adv. Mater. Interfaces* 4:1700191. doi: 10.1002/admi.201700191

Owens, R. M., and Malliaras, G. G. (2010). "Organic Electronics at the Interface with Biology". *MRS Bull.* 35:449. doi: 10.1557/mrs2010.583

Pahlman, S., Ruusala, A.-I., Abrahamsson, L., Mattson, M., and Esccher, T. (1984). "Retinoic acid-induced differentiation of cultured human neuroblastoma cells: a comparison with phorbolester-induced differentiation". *Cell. Differ.* 14, 135–144. doi: 10.1016/0045-6039(84)90038-1

Pardo-Figuerez, M., Martin, N. R. W., Player, D. J., Capel, A. J., Christie, S. D. R., and Lewis, M. P. (2018). "Controlled Arrangement of Neuronal Cells on Surfaces Functionalized with Micropatterned Polymer Brushes". *ACS Biomater. Sci. Eng.* 4, 98–106.

Phuah, E. W. C., Hart, W. L., Sumer, H., and Stoddart, P. R. (2020). "Patterning of Biomaterials by Aerosol Jet Printing: A parametric study". *Bioprinting* 18:e00081. doi: 10.1016/j.bprint.2020.e00081

Qin, D., Xia, Y., and Whitesides, G. M. (2010). "Soft lithography for micro-and nanoscale patterning". *Nat. Protoc.* 5, 491–502. doi: 10.1038/nprot.2009.234

Rahman, M. T., Rahimi, A., Gupta, S., and Panat, R. (2016). "Microscale additive manufacturing and modeling of interdigitated capacitive touch sensors". *Sensors Actuators A Phys.* 248, 94–103. doi: 10.1016/j.sna.2016.07.014

Reitberger, T., Franke, J., Hoffman, G.-A., Overmeyer, L., Lorenz, L., and Wolter, K.-J. (2016). "Integration of polymer optical waveguides by using flexographic and aerosol jet printing," in *Proceedings of 12th International Conference Molded Interconnect Devices*, 2016 (Würzburg: MID).

Roth, E. A., Xu, T., Das, M., Gregory, C., Hickman, J. J., and Boland, T. (2004). "Inkjet printing for high-throughput cell patterning". *Biomaterials* 25, 3707–3715. doi: 10.1016/j.biomaterials.2003.10.052

Saleh, M. S., Hu, C., and Panat, R. (2017). "Three-dimensional microarchitected materials and devices using nanoparticle assembly by pointwise spatial printing". *Sci. Adv.* 3:e1601986. doi: 10.1126/sciadv.1601986

Secor, E. B. (2018). "Principles of aerosol jet printing". *Flex. Print. Electron.* 3:035002. doi: 10.1088/2058-8585/aace28

Shi, Y., Liu, K., Zhang, Z., Tao, X., Chen, H.-Y., Kingshott, P., et al. (2020). "Decoration of Material Surfaces with Complex Physicochemical Signals for Biointerface Applications". *ACS Biomater. Sci. Eng.* 6, 1836–1851. doi: 10.1021/acsbiomaterials.9b01806

Shick, T. M., Kadir, A. Z. A., Ngadiman, N. H. A., and Ma'aram, A. (2019). A review of biomaterials scaffold fabrication in additive manufacturing for tissue engineering. *J. Bioact. Compat. Polym.* 34, 415–435. doi: 10.1177/0883911519877426

Smith, M. A. A., Fry, N. R., Kay, R. W., and Harris, R. A. (2018). "Digitally-Driven Micro Surface Patterning by Hybrid Manufacturing". *SFF Sympos.* 365–375.

Suzuki, S., and Teramoto, Y. (2017). "Simple Inkjet Process To Fabricate Microstructures of Chitinous Nanocrystals for Cell Patterning". *Biomacromolecules* 18, 1993–1999. doi: 10.1021/acs.biomac.7b00527

Tait, J. G., Witkowska, E., Hirade, M., Ke, T.-H., Malinowski, P. E., Steudel, S., et al. (2015). "Uniform Aerosol Jet printed polymer lines with 30 μm width for 140 ppi resolution RGB organic light emitting diodes". *Org. Electron.* 22, 40–43. doi: 10.1016/j.orgel.2015.03.034

Takebe, T., Imai, R., and Ono, S. (2018). "The Current Status of Drug Discovery and Development as Originated in United States Academia: The Influence of Industrial and Academic Collaboration on Drug Discovery and Development". *Clin. Transl. Sci.* 11, 597–606. doi: 10.1111/cts.12577

Tamari, Y., Gautrein, A., Schmiga, C., Binder, S., Glatthaar, M., and Glunz, S. W. (2014). "Synthesis of a Lead-and Particle-free Metal-organic Ink for Front Side Metallization of Crystalline Silicon Solar Cells". *Energy Proc.* 55, 708–714. doi: 10.1016/j.egypro.2014.08.049

Tse, C. C. W., and Smith, P. J. (2018). "Inkjet Printing for Biomedical Applications". *Methods Mol. Biol.* 1771, 107–117.

Wang, K., Chang, Y.-H., Zhang, C., and Wang, B. (2016). "Conductive-on-demand: Tailorable polyimide/carbon nanotube nanocomposite thin film by dual-material aerosol jet printing". *Carbon N Y.* 98, 397–403. doi: 10.1016/j.carbon.2015.11.032

Wilkinson, N. J., Lukic-Mann, M., Shuttleworth, M. P., Kay, R. W., and Harris, R. A. (2019a). Aerosol Jet Printing for the Manufacture of Soft Robotic Devices. *IEEE Int. Confer. Soft Robot.* 2019, 496–501.

Wilkinson, N. J., Smith, M. A. A., Kay, R. W., and Harris, R. A. (2019b). "A review of aerosol jet printing—a non-traditional hybrid process for micro-manufacturing". *Int. J. Adv. Manuf. Technol.* 105, 4599–4619. doi: 10.1007/s00170-019-03438-2

Williams, N. X., Watson, N., Joh, D. Y., Chilkoti, A., and Franklin, A. D. (2020). "Aerosol jet printing of biological inks by ultrasonic delivery". *Biofabrication* 12:025004. doi: 10.1088/1758-5090/ab5cf5

Xie, H., Hu, L., and Li, G. (2010). "SH-SY5Y human neuroblastoma cell line: in vitro cell model of dopaminergic neurons in Parkinson's disease". *Chin. Med. J.* 123, 1086–1092.

Yuk, H., Lu, B., Lin, S., et al. (2020). "3D printing of conducting polymers". *Nat. Commun.* 11:1604.

Zare Bidoky, F., and Frisbie, C. D. (2016). "Parasitic Capacitance Effect on Dynamic Performance of Aerosol-Jet-Printed Sub 2 V Poly(3-hexylthiophene) Electrolyte-Gated Transistors". *ACS Appl. Mater. Interfaces* 8, 27012–27017. doi: 10.1021/acsami.6b08396

Zhang, K., Xiao, X., Wang, X., Fan, Y., and Li, X. (2019). "Topographical patterning: characteristics of current processing techniques, controllable effects on material properties and co-cultured cell fate, updated applications in tissue engineering, and improvement strategies". *J. Mater. Chem. B* 7, 7090–7109. doi: 10.1039/c9tb01682a

Zhang, S., Hubis, E., Girard, C., Kumar, P., DeFranco, J., and Cicoira, F. (2016). "Water stability and orthogonal patterning of flexible micro-electrochemical transistors on plastic". *J. Mater. Chem. C* 4, 1382–1385. doi: 10.1039/c5tc03664j

Zhang, S., Vijayavenkataraman, S., Lu, W. F., and Fuh, J. Y. H. (2019). A review on the use of computational methods to characterize, design, and optimize tissue engineering scaffolds, with a potential in 3D printing fabrication. *J. Biomed. Mater. Res. B Appl. Biomater.* 107, 1329–1351. doi: 10.1002/jbm.b.34226

Zhou, Z., Yu, P., Geller, H. M., and Ober, C. K. (2013). "Biomimetic polymer brushes containing tethered acetylcholine analogs for protein and hippocampal neuronal cell patterning". *Biomacromolecules* 14, 529–537. doi: 10.1021/bm301785b

**Conflict of Interest:** The authors declare that the research was conducted in the absence of any commercial or financial relationships that could be construed as a potential conflict of interest.

**Publisher's Note:** All claims expressed in this article are solely those of the authors and do not necessarily represent those of their affiliated organizations, or those of the publisher, the editors and the reviewers. Any product that may be evaluated in this article, or claim that may be made by its manufacturer, is not guaranteed or endorsed by the publisher.

frontiers in Cell and Developmental Biology

REVIEW
published: 09 September 2021
doi: 10.3389/fcell.2021.721338

# Critical Considerations for the Design of Multi-Organ Microphysiological Systems (MPS)

*Mridu Malik[1,2], Yang Yang[2,3], Parinaz Fathi[4], Gretchen J. Mahler[5] and Mandy B. Esch[2]**

*[1] Department of Bioengineering, University of Maryland, College Park, College Park, MD, United States, [2] Biophysical and Biomedical Measurement Group, Physical Measurement Laboratory, Microsystems and Nanotechnology Division, National Institute of Standards and Technology, Gaithersburg, MD, United States, [3] Department of Chemical Engineering, University of Maryland, College Park, College Park, MD, United States, [4] Department of Bioengineering, Materials Science and Engineering, and Beckman Institute, University of Illinois at Urbana-Champaign, Champaign, IL, United States, [5] Department of Biomedical Engineering, Binghamton University, Binghamton, NY, United States*

Identification and approval of new drugs for use in patients requires extensive preclinical studies and clinical trials. Preclinical studies rely on *in vitro* experiments and animal models of human diseases. The transferability of drug toxicity and efficacy estimates to humans from animal models is being called into question. Subsequent clinical studies often reveal lower than expected efficacy and higher drug toxicity in humans than that seen in animal models. Microphysiological systems (MPS), sometimes called organ or human-on-chip models, present a potential alternative to animal-based models used for drug toxicity screening. This review discusses multi-organ MPS that can be used to model diseases and test the efficacy and safety of drug candidates. The translation of an *in vivo* environment to an *in vitro* system requires physiologically relevant organ scaling, vascular dimensions, and appropriate flow rates. Even small changes in those parameters can alter the outcome of experiments conducted with MPS. With many MPS devices being developed, we have outlined some established standards for designing MPS devices and described techniques to validate the devices. A physiologically realistic mimic of the human body can help determine the dose response and toxicity effects of a new drug candidate with higher predictive power.

**Keywords: MPS, body-on-a-chip, organ-on-a-chip, microfluidics, microphysiological systems**

OPEN ACCESS

***Edited by:***
*Alec S. T. Smith, University of Washington, United States*

***Reviewed by:***
*Hee-Gyeong Yi, Chonnam National University, South Korea*
*Michael Shuler, Cornell University, United States*

****Correspondence:***
*Mandy B. Esch*
*mandy.esch@nist.gov*

***Specialty section:***
*This article was submitted to Stem Cell Research, a section of the journal Frontiers in Cell and Developmental Biology*

***Received:*** *06 June 2021*
***Accepted:*** *05 August 2021*
***Published:*** *09 September 2021*

***Citation:***
*Malik M, Yang Y, Fathi P, Mahler GJ and Esch MB (2021) Critical Considerations for the Design of Multi-Organ Microphysiological Systems (MPS). Front. Cell Dev. Biol. 9:721338. doi: 10.3389/fcell.2021.721338*

## INTRODUCTION

The development of new pharmaceuticals is time-intensive and expensive. A thorough assessment of a drug's efficacy and safety must precede clinical testing in patients. Despite that rigorous evaluation, the success rate of clinical trials is low (Khalid et al., 2017). Preclinical tests conducted with animal models, despite their own benefits, often fail to show the same outcomes in human trials. It has been reported that of the drugs entering human clinical trials, 30% and 58% pass phase II and phase III, respectively (Thomas et al., 2016). The probability of drugs successfully moving from phase I to final approval is only about 9% (Thomas et al., 2016). Upon changing the patient selection process to have "selection biomarkers" as an inclusion or exclusion criteria, the probable success rate of drugs moving from phase I to approval stage increased to about 24% (Thomas et al., 2016). According to reports, out of the approved drugs in the market, 50% of the failures are due to

unanticipated toxicity in patients (Tufts Center for the Study of Drug Development, 2013). Animal studies can falsely label a drug as "safe" or "toxic," pointing to a need for more accurate alternatives to animal testing.

The development of human, cell-based multi-organ microphysiological systems (MPS) as a potential alternative to animal models has been pursued for over 20 years. An MPS is a miniature recapitulation of human organs fabricated *in vitro* to establish the functions of the organs. MPS can replicate the microarchitectures of human organs and mimic the human metabolism. The devices have inter-organ connections that allow drug metabolites generated in one organ or tissue to recirculate to all other organs within the system. In that way, drug metabolites can affect all tissues present in the system, offering the possibility of detecting secondary drug toxicity due to drug metabolites. MPS that are operated with human cells provide a unique opportunity for drugs to be tested in the context of human metabolism rather than that of an animal. The ability of MPS to detect the presence of toxic drug metabolites is an asset in improving the success rate of human clinical trials. The strive to achieve the same structural, functional, and biochemical attributes as a functioning human body makes MPS devices increasingly complex.

In this review, we discuss a variety of recently developed multi-organ MPS. We will also discuss opportunities to establish design criteria for MPS that offer a globally uniform and reproducible approach to experimentation with multi-organ MPS.

## EXAMPLES OF MPS

Single-organ MPS have been constructed to serve as *in vitro* models for several different organs, such as the gastrointestinal (GI) tract (Kim et al., 2012; Lee et al., 2018), heart (Abulaiti et al., 2020), kidney (Wilmer et al., 2016), bladder (Sharma et al., 2021), liver (Deng et al., 2020), brain (Ndyabawe et al., 2021), lung (Huh et al., 2010), skin (Wufuer et al., 2016), skeletal muscle (Grosberg et al., 2012), bone (Bahmaee et al., 2020), vasculature (Wang et al., 2018), immune-system (Mitra et al., 2013), adipose tissue (Liu et al., 2019), and reproductive tract (Park et al., 2020). Here, we briefly discuss liver MPS, due to its significant role in drug metabolism, and a combination of single organ systems to establish more complex multi-organ MPS. We also highlight the development of MPS for three specific modules, namely the microvasculature, neuromuscular junctions, and the immune system, due to the recent interest in those modules, and their role in disease modeling.

### Single and Multi-Organ MPS

Since the liver performs some of the most important processes of human metabolism, much work has been done to develop advanced MPS devices to model the liver (Deng et al., 2019; Moradi et al., 2020). The use of 3D human cell cultures, as opposed to 2D cultures, provides an advantage to the MPS. Further, using non-parenchymal cells in co-culture with hepatocytes enhances (Kostadinova et al., 2013) and regulates drug metabolism. Prodanov et al. (2016) used a unique approach to build a complex, multi-cellular 3D liver-on-chip model. Stacking 2D monolayers of hepatocytes, endothelial cells and Kupffer cells with 3D dispersal of stellate cells in collagen yielded an organotypic *in vitro* model of the liver (Prodanov et al., 2016).

Adding recirculating fluidic flow to multi-cellular 3D liver cultures provides an opportunity for fast-paced nutrient and gas exchange that further enhances *in vitro* liver metabolism (Esch et al., 2015). Lasli et al. (2019) co-cultured HepG2 and human umbilical vein endothelial cells (HUVECs) to form spheroids, which were then moved onto a chip system to establish a steatosis disease-on-a-chip model. They used a network of interconnected hexagonal microwells to help assess the hepatic function in the model for the purpose of its applicability in drug toxicity testing at a later stage.

To mimic the oxygen gradient present in the *in vivo* liver, Kang et al. (2020) created an *in vitro* liver model with a microfluidic platform capable of generating gradients of varying oxygen concentrations. This hypoxia-on-a-chip platform was used to demonstrate the metabolic and genetic responses of hepatocytes to oxygen gradients (Kang et al., 2020). In-depth reviews of liver-on-a-chip models have recently been published by Deng et al. (2019) and Moradi et al. (2020).

Interconnections between two or more organs are built to analyze drug-drug, and drug-organ interactions, and secondary drug toxicity. Both the drug candidate and the information researchers need to gather with the MPS determine the number of organ chambers that are incorporated into an MPS. For example, the question of how much drug is available in the bloodstream after oral administration can be answered with a two-organ system that contains physiologically relevant amounts of blood surrogate. Several systems that mimic the first-pass metabolism and the subsequent bioavailability of drugs or toxicants in the systemic circulation have been developed since 2009. Mahler et al. (2009) presented a proof-of-concept gut-liver MPS that replicates *in vitro* the dose-dependent toxicity of acetaminophen on liver cells after metabolism by intestinal epithelium and liver. Another two-tissue system with GI-tract, liver, and "other organ" compartment designed by Esch et al. (2014) was used to investigate the effects of orally ingested polystyrene nanoparticles on the liver. The "gut-liver-other tissue" design used fluorescently labeled nanoparticles to track their travel across the gut barrier into the liver, and the eventual liver toxicity. Lee and Sung integrated a 3D gut model with a HepG2 cell layer, representing the liver, into a microfluidic device to determine the absorption and metabolism of digested lipids (Lee and Sung, 2018).

The integral role of the microbiome in gut function and homeostasis is represented in a gut-on-a-chip model using bacteria such as *Escherichia coli* (Tovaglieri et al., 2019), *Faecalibacterium prausnitzii* (Zhang J. et al., 2021), and *Lactobacillus rhamnosus* and *Bacteroides caccae* (Shah et al., 2016). The co-culture of epithelial cells with microbes to model microbe-host cell relationships provides a better understanding of their involvement in diseased and healthy intestinal conditions. Jalili-Firoozinezhad et al. (2019) successfully incorporated aerobic and anaerobic human gut microbiota on an intestinal chip with a hypoxia gradient. Compared to aerobic conditions, the inclusion of a hypoxia gradient improved

the intestinal barrier function, and a more physiologically relevant level of microbial diversity was observed, allowing for microbiome-related therapeutic discovery and development in the future.

The true strength of MPS lies in their capacity to not only reveal primary drug action on human organs, but also secondary drug effects stemming from drug metabolites. Some of the first experiments aimed at testing this capability were conducted with three- and four-tissue devices. For example, a three-chamber MPS with cell lines representing liver, bone marrow, and tumor tissue was used to demonstrate the anticancer properties of 5-fluorouracil (5-FU) metabolites (Sung et al., 2010). The dynamics of the MPS were modeled using the same principles as physiologically based pharmacokinetic (PBPK) models to predict the effects of 5-FU itself and its metabolites on each organ cultured within the system (Sung et al., 2010).

Similarly, a four-organ device developed by Oleaga et al. (2016) showed that four tissues can survive and continue to function well for 14 days when cultured with a common cell culture medium. The recirculating flow of fluid in the device allowed the tested drugs to reach each tissue within the MPS and display multi-organ toxicity (Oleaga et al., 2016).

Miller and Schuler (2016) extended the concept of a multi-organ MPS to include up to 14 tissue chambers. The 14-chamber design was tested with tissues of five organs. Barrier tissues (skin, GI tract, and lung) and non-barrier tissues (fat, kidney, heart, adrenal glands, liver, spleen, pancreas, bone marrow, brain, muscle) were connected via fluidic channels that enable inter-organ interactions. This work demonstrated the feasibility of establishing a multi-organ MPS with more than four organ tissues and using it to measure basic cellular functions such as CYP450 enzyme activity, urea, and albumin synthesis, as well as tight junction maintenance.

While many MPS devices are closed microfluidic systems, an open multi-organ MPS was designed by Tsamandouras et al. (2017). As opposed to a closed system, an open system lacks one or more of the walls of the device, generating a liquid-air interface. The design by Tsamandouras et al. (2017) consists of a pump-based liver-gut MPS integrated on a polysulfone plastic plate, with recirculating flow of fluid. The system is based on the multi-well plate concept with a transwell-style gut MPS and 3D perfused liver MPS in combination with a mixing chamber. The initial design was later extended by Edington et al. (2018) to four, seven, and 10-organ MPS with internal recirculation and a pneumatic pump. A functional phenotypic co-culture was maintained for 2 weeks in the four-way MPS; this system was further extended to a seven-way and a 10-way MPS that sustained cell co-cultures for 3 weeks and 4 weeks, respectively.

## MPS for Modeling the Microvasculature

In the body, nutrients, oxygen, drugs, and other solutes must first cross the endothelial barrier before they can act on tissues. Because the endothelium is of broad interest—*in vitro* models have been used to model angiogenesis, thrombosis, and circulating cancer cell attachment—there are many microfluidic *in vitro* models of the vasculature available. Moses et al. (2020) discuss the advantages and disadvantages of some of the most recent vasculature-on-chip models.

The vasculature is particularly important for densely populated 3D tissues. Such tissues can develop a necrotic core due to the lack of nutrient and oxygen supply to the center. To construct tissues for use in MPS, the addition of blood vessels to 3D tissues helps better mimic the physiological rate at which drugs enter those tissues.

Miller et al. (2012) designed a biocompatible vasculature network where they first 3D printed mechanically stiff carbohydrate filaments (called carbohydrate glass) to form free-standing 3D fiber networks. The voids of those networks were filled with extracellular matrix (ECM) and cells and then cell culture medium was introduced. The medium dissolved the fibers, resulting in a channel network that was perfusable and that was surrounded by ECM and cells. When perfused with medium, cell function in the core of the tissue was healthier than in the non-perfused version.

Morgan et al. (2013) developed user-defined geometries of vascular networks using hydrogels to satisfy the needs of a variety of tissue models. Bischel et al. (2013) created 3D lumens through ECM hydrogels with different microchannel geometries and lined them with endothelial cells. A similar model with perfused functional vascular channels and multiple cell types was earlier developed by Lee et al. (2014) using 3D bioprinting technology. That work revealed the ability of vascular channels to present a functional physical barrier *in vitro*.

Vascular networks made from sacrificial material embedded in ECM or hydrogels hold a distinctive advantage over vascularized, microfluidic channels made of plastic, polydimethyl siloxane (PDMS), or other polymers because they allow cells to grow and remodel in the space between endothelial cells and ECM. A proper perfusion system clears secreted products and allows cell-cell interaction. Cochrane et al. (2019) present a detailed review of recent experimental vascular models and their importance in drug development.

While angiogenesis, the formation of new blood vessels from pre-existing vasculature, is important to normal growth and development *in vivo*, it is also necessary for tumor growth. In the absence of adequate vasculature, tumor cells become oxygen and nutrient-starved, which limits their survival and proliferation. This situation impacts the efficacy of radiation therapy (Gray et al., 1953), requiring 2.5–3-fold higher radiation doses (Joiner and Kogel van der, 2009). This knowledge has brought about the development of cancer therapeutics by inhibiting angiogenesis. Stroock and Fischbach (2010) discuss the development of microfluidic tumor models by combining vasculature and tumor tissue engineering with microfluidic technology to study antiangiogenic therapy. Patient-specific tumor microenvironments were also created by Truong et al. (2019) to analyze the tumor-stromal fibroblast crosstalk on a 3D microfluidic device. The use of patient-derived fibroblasts enabled a better understanding of their molecular and cellular influence on the tumor compared to generic, non-patient fibroblasts. Marturano-Kruik et al. (2018) developed a bone perivascular niche-on-a-chip model with stable vasculature within a 3D native bone matrix-on-a-chip. With this model, they

achieved long-lasting, self-assembled vascular networks without the need for angiogenic factors to model the colonization of cancer cells in the bone.

The role of the immune system in tumor environment development is crucial and better understood (discussed in section "MPS for Modeling the Immune System"), however, the interaction of platelets with cancer cells remains to be better explored. Tumors can remodel vascular networks, leading to platelet extravasation (Schulte et al., 2011), which is difficult to model in animal models (Boussommier-Calleja et al., 2016). Saha et al. (2020) constructed an ovarian tumor-blood vessel-integrated organ-on-a-chip (OvCa-Chip) to study the time-dependent activity of endothelial cells in ovarian cancer and the eventual leakage of platelets through blood vessels. Using that model, they also tested a therapeutic strategy to prevent platelet extravasation in a cancer environment and validated their results with human ovarian cancer biopsy samples. With the rapid advancement in tumor-on-chip models, there have been numerous studies to incorporate the tumor microenvironment, discussed elsewhere in a comprehensive review on the topic (Wan et al., 2020).

Achieving a fully perfusable *in vitro* system within a 3D tissue is still challenging. Recent advances in pre-vascularizing tissues to achieve perfusion and engineering functional capillary beds to support the exchange between internal and external vessels (Zhang S. et al., 2021) can broaden the biomedical application of MPS even further.

## MPS for Modeling Neuromuscular Junctions

Neuromuscular junctions (NMJ) are modeled *in vitro* to explore clinical applications such as muscle and motor neuron-related diseases and spinal cord injuries. To successfully generate a functional NMJ, a combination of human motor neurons and skeletal muscle is established, which has been difficult to achieve perfectly *in vitro*. Although initial models involved simple culturing of dissociated motor neurons on a 2D layer of myotubes on a culture surface (Guo et al., 2011; Umbach et al., 2012), image analysis of such systems showed poor clustering of acetylcholine receptors and irregular co-localization of synaptic markers (Umbach et al., 2012). The MPS devices are aimed to model neurodegenerative disorders such as Alzheimer's disease, amyotrophic lateral sclerosis (ALS), and tumors of the central nervous system like glioblastoma. To overcome the shortcomings of simple co-cultures, more sophisticated neuromuscular tissues are engineered *in vitro* using microfabricated devices with human stem cell-derived cell sources.

Compartmentalized MPS culture motor neurons and engineered muscle bundles in individual compartments connected by axon-permissive channels. Using this approach, Mills et al. (2018) modeled NMJ formation and endocrine signaling in a microfluidic device, shown in **Figure 1**, using primary mouse myoblast-derived and embryonic stem cell-derived motor neurons. Santhanam et al. (2018) used the same approach to develop a functional NMJ system targeted to evaluate drug response and toxicity for ALS and other neurodegenerative diseases. The use of serum-free medium and stem cell-derived human myotubes and motor neurons in the device showed the possibility of developing patient-specific dose-response studies by incorporating patient-derived induced pluripotent stem cells (iPSCs). Osaki et al. (2018) used this model with iPSC-derived muscle cells and motor neurons to demonstrate reduced muscle atrophy and dysfunction in response to two ALS drugs, bosutinib, and rapamycin. The physiologically relevant layout of the compartmentalized MPS with human cells helps elucidate the pathogenesis of neuromuscular diseases and generate dose-response curves to potential drugs.

Smith et al. (2013) first proposed an *in vitro* system in 2013 to assess NMJ functionality and apply it to drug discovery research. They used the system to measure real-time responses of the cultured cells to chemical challenges, suggesting the possibilities of its application in preclinical drug screening. Guo et al. (2020) were able to use a compartmentalized NMJ model to reproduce clinical assays for assessing ALS deficits, but *in vitro*. This technology has set the path to use functional cell-based approaches, instead of preclinical models, for faster screening of novel therapies for ALS.

## MPS for Modeling the Immune System

One area that is gaining increasing interest in tissue-chip research is modeling components of the immune system. Many of these systems have been reviewed in detail elsewhere recently (Shanti et al., 2018; Kim et al., 2019; Sun et al., 2019; Greenlee and King, 2020; Maharjan et al., 2020), including discussions of microfluidic models of bone marrow, lymph nodes, the thymus gland, lymphatic cancer metastases, and inflammation. Human immune response in diseased conditions or during drug consumption is difficult to predict from an animal model. We will provide a brief overview of the latest developments in immune-on-chip models in the gut, liver, and tumor environment here.

Immune cell activation and the subsequent presentation of information to other cells plays a major role in generating an immune response to antigens. Dendritic cells typically capture antigens and subsequently migrate to lymph nodes to present antigens to T cells. Several on-chip immune studies have aimed to model immune cell migration in response to stimuli. Mitra et al. (2013) developed an *in vitro* model to study human cell line-derived dendritic cell migration with T cell activation. They demonstrated that mature dendritic cells migrate toward T cells in response to a CCL19 gradient, leading to T cell activation by the dendritic cells. Gopalakrishnan et al. (2015) developed a microfluidic device that incorporated an activator chamber to provide stimuli to cells in a migratory chamber. They demonstrated that immature dendritic cells from the migratory chamber moved toward the activator chamber when it contained a co-culture of dendritic cells and stimulated macrophages or mature dendritic cells (generated from C57Bl/6 bone marrow cells) stimulated with bacteria.

Although immune components such as macrophages have been included in a variety of single organ systems (Huh et al., 2010; Jones et al., 2012; Hamza and Irimia, 2015), their integration in a recirculating multiorgan MPS device is not advancing as rapidly. A recent article by Sasserath et al. (2020)

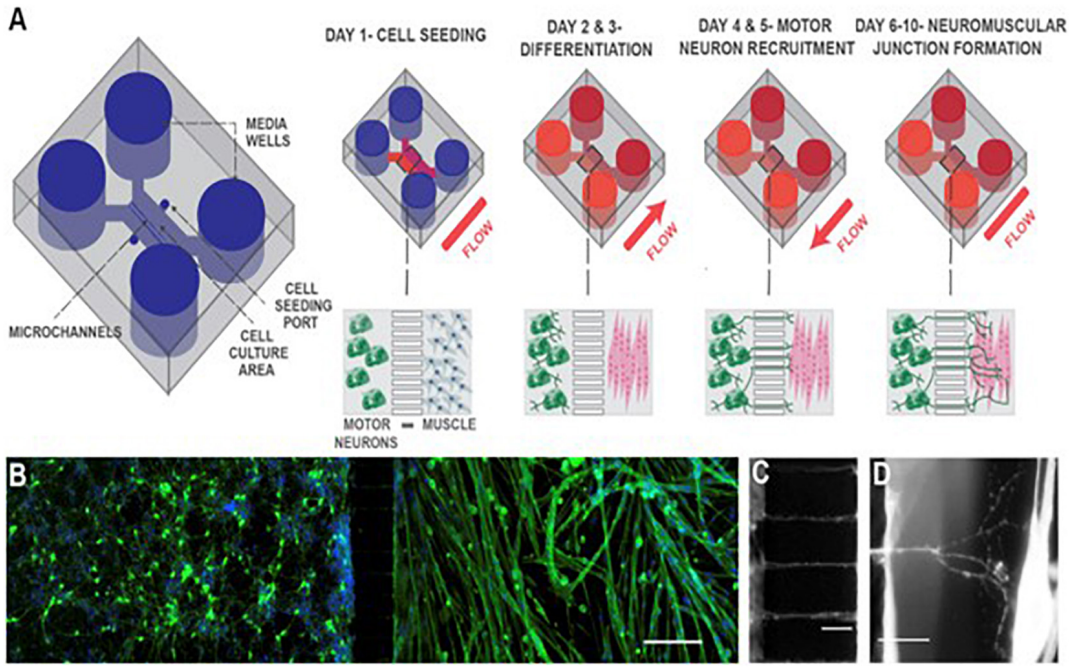


**FIGURE 1 |** Schematic of neuromuscular junction microfluidic device. **(A)** Primary myoblasts and mouse embryonic stem cell-derived motor neurons were seeded in separate cell culture compartments in a microfluidic device via the cell seeding ports. Myoblasts were then differentiated (over 2 days), forming multinucleated myofibers. During this period, motor neurons were kept fluidically isolated. Motor neuron processes were then recruited across the microchannel, via a chemotactic gradient of gradient of glial cell-derived neurotrophic factor (GDNF) and brain-derived neurotrophic factor (BDNF) (days 4 and 5) generated by small but sustained fluid flow from the muscle to the motor neuron compartment. NMJs were allowed to mature until day 10, under static conditions. **(B)** Fluorescent image of microfluidic device showing motor neurons in the left-hand side compartment and muscle fibers in the right-hand side after 6 days of culture. Muscle fibers were stained for actin (green) and motor neurons were visualized by the Hb9:GFP reporter (green). Nuclei were stained with DAPI (blue). Scale bar represents 200 μm. **(C)** A close-up fluorescent image of neurite processes crossing the central microchannels. Scale bar represents 50 μm. **(D)** A close-up fluorescent image showing a neurite process extending, branching, and contacting a muscle fiber. Scale bar represents 50 μm. Reprinted from Mills et al. (2018) with permission from Elsevier.

presented the integration of a monocyte-derived cell line, THP-1, as a recirculating immune component in a multiorgan human model. The monocytes were added as part of the recirculating medium (blood surrogate) and allowed to flow through the three-organ system. The model showed activation of THP-1 cells in response to recirculation of amiodarone, a cardiotoxin tested in the study.

One aspect of the immune system that is of significance in microfluidic device development and has a potential of clinical importance is that of cancer-immune interactions (Parlato et al., 2021). Cancer cells exhibit immune-evasive behaviors that can limit the ability of the immune system to recognize and eliminate cancer cells. Microfluidic models have been employed to better understand these interactions. Aung et al. (2020) used a fluidic system incorporating a bilayer hydrogel to coculture human cell line derived breast cancer cells or spheroids, monocytes, and endothelial cells (HUVEC). They determined that T cell extravasation into the cancer-containing constructs occurred for both MCF7 and MDA-MB-231 breast cancer cell lines, and that extravasation was promoted by the presence of monocytes. This study demonstrated that various chemokines, such as those associated with hypoxia and loss of endothelial cell tight junction proteins, may play a role in T cell infiltration into tumors. Other studies have examined the interactions of cancer cells with lymphatic endothelial cells during metastasis formation. For example, Ayuso et al. (2020) developed a microfluidic model of tumor-lymphatic interactions and used it to demonstrate that cancer cells condition lymphatic endothelial cells to increase vessel permeability. Pisano et al. (2015) combined transwells with fluidic flow to evaluate the separate and combined effects of transmural and luminal flow on cancer cell invasion across an endothelial cell layer.

Microfluidic models have also been used to model inflammation (Irimia and Wang, 2018). Trapecar et al. (2020) modeled the gut-liver axis to develop a better understanding of the link between gut and liver diseases. They incorporated circulating Treg and Th17 cells within their system and found that during acute T cell-mediated inflammation, microbiome-derived short-chain fatty acids increased CD4+ T effector cell activation and liver injury. Shin and Kim (2018) developed a gut inflammation-on-a-chip model using a human intestinal epithelial cell line (Caco-2BBE) to understand the intercellular host-microbiome cross-talk that occurs in chemically-induced inflammation. Their studies identified barrier dysfunction as a critical trigger of intestinal inflammation and found that the efficacy of probiotics was altered when intestinal barrier function was disrupted.

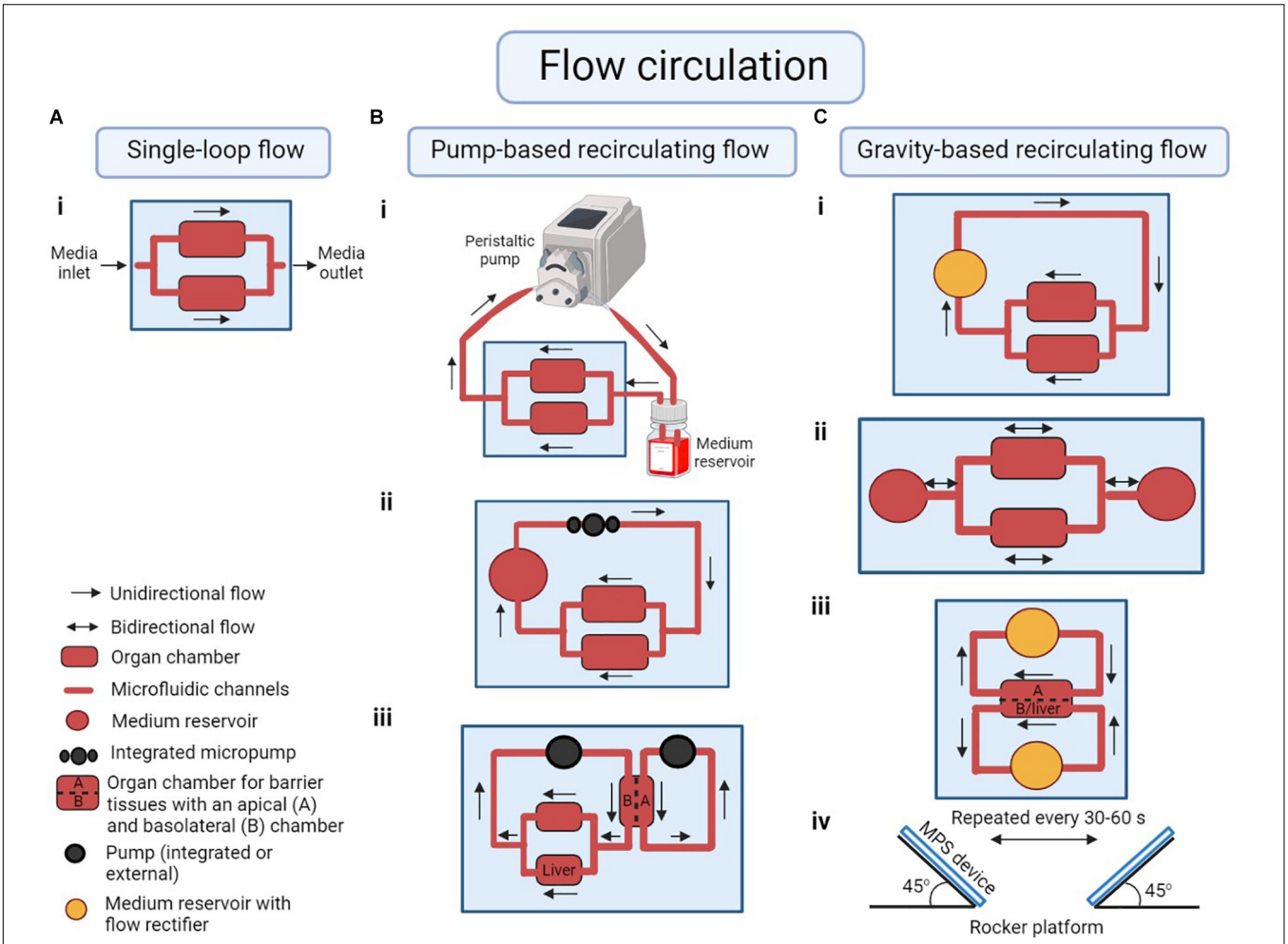


**FIGURE 2 |** Examples of modes of flow circulation in a microphysiological system (MPS). **(A)** (i) Single-loop flow: unidirectional flow of medium across the organ chambers without recirculation. **(B)** Pump-based recirculating flow of medium using (i) an external peristaltic pump and medium reservoir to represent organs not cultured in any of the cell culture chambers in the system, (ii) an integrated on-chip pump, (iii) multiple integrated or external pumps to circulate medium through the apical side of a barrier tissue as well as the basolateral side of the tissue plus any other organ chambers (for example a liver-gastrointestinal tract MPS). **(C)** Gravity-based recirculating flow of medium following (i) unidirectional or (ii) bidirectional flow patterns with on-chip medium reservoirs. (iii) Medium reservoirs with flow rectifiers (or a valve) can be used in a liver-gastrointestinal tract model to regulate unidirectional flow in both apical and basolateral/liver chambers. (iv) The flow in pumpless systems is created by placing the device on a rocker platform at an angle, alternating the rocking motion every 30–60 s. Illustration is created using BioRender.com[‡].

Overall, recent attempts at microfluidic modeling of immune interactions have enabled not only the recapitulation of tissue structure and function but also the development of new hypotheses and understandings of biological phenomena that would not have been possible without the use of these microphysiological models.

## MPS TECHNOLOGIES

### Fluid Recirculation Methods

The transport system for the movement of nutrients, gases, and metabolites in an MPS is based on the techniques of microfluidics. As opposed to single perfusion systems, recirculation of fluid in the MPS allows transport of metabolites from one organ into other organ units, producing valuable pharmacokinetic information. Circulation of cell culture medium across tissues mimics the flow of blood in the human body. The cell culture medium is therefore sometimes referred to as blood surrogate.

Two or more organ chambers are connected via microchannels to establish communication between them in the MPS. Microchannel geometry and fluid circulation method are based on the specific nature of the tissue and organ-organ relationship of interest. For example, to mimic hemodynamic stimulation of cardiomyocytes, a peristaltic pump can be used with a cardiovascular chip to replicate the pressure-volume changes in the ventricle (Giridharan et al., 2010). Microchannel geometry is manipulated to increase nutrient and oxygen delivery. Ideally, the flow across tissues is

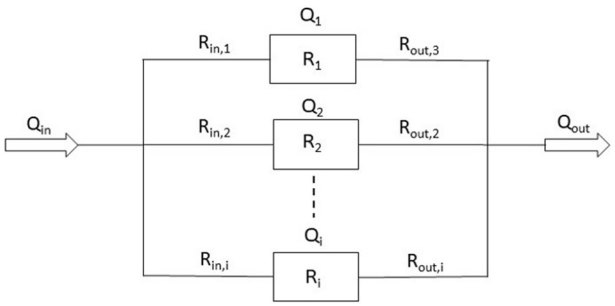


**FIGURE 3 |** Schematic of the fluidic resistances of an MPS in which organ chambers are arranged in parallel ($Q_i$ = flow rate through chamber i. $\Delta p$ = pressure drop across the channel/chamber segments. $R_{in,i}$ = hydraulic resistances of inlet channel i. $R_i$ = hydraulic resistance of organ chamber i. $R_{out,i}$ = hydraulic resistance of outlet channel i.).

maintained at near-physiological rates that replicate *in vivo* rates of exposure of tissues to nutrients and drugs. However, due to the micro-scale of the channels and chambers, many physical and chemical factors influence the flow of fluid. Capillary forces and flow rates are affected by the area and smoothness of the substrate. Lack of precision during the fabrication process can alter the working of the device to a great extent. Esch and Mahler discuss fabrication techniques suitable for building body-on-chip devices and how to experiment with them (Esch and Mahler, 2019).

Barrier tissue cells, such as gut cells, are generally seeded on a porous substrate where the top and the bottom portions have independent hollow fluidic channels to allow nutrient and drug transport across the barrier tissue. To further mimic the *in vivo* environment, specific organ-like forms, such as the villous shape of the intestine, can be designed using micro-molding techniques (Esch et al., 2012). Esch et al. (2012) used SU-8 layers to fabricate a microfluidic chamber and a porous membrane across the chamber. The structure could be made flat or into a 3D form by fabricating pillars of different sizes on the silicon surface (Esch et al., 2012).

A factor that distinguishes different MPSs from each other is the method of fluid recirculation. Fluid recirculation in MPS is generally created by an active pumping mechanism, or by gravity-driven flow (**Figure 2**). External pumps such as peristaltic pumps or syringe pumps were the first to be used in MPS (Huh et al., 2010). Those pumps provide an easy way to create fluidic flow, but when used with multi-organ MPS, they require the flow to be split into multiple streams. Those streams must be regulated to create near-physiological flow rates for each organ chamber. Sin et al. (2004) developed a pump-driven three-compartment model on a 2.5 cm × 2.5 cm silicon chip with etched microchannels and chambers. They also included micropillar arrays to control the flow distribution in organ chambers (Sin et al., 2004). Zhang et al. (2009) combined micropillar arrays with hydrogel encapsulation to protect the cells from direct exposure to shear stress due to perfusion.

One way to achieve customized flow rates is to arrange all organ chambers in parallel so that the pressure drop across all chambers is the same (**Figure 3**). Then, by adjusting each organ chamber's hydraulic resistance (including the inlet channel, organ chamber, and outlet channel), the flow in each chamber can be restricted to near-physiological values suitable for the tissue cultured within (Eq. 1 Bruus, 2008).

$$Q_{\mathrm{i}} = \frac{\triangle p}{R_{\mathrm{in,i}} + R_{\mathrm{i}} + R_{\mathrm{out,i}}} \tag{1}$$

Here, $Q_i$ is the flow rate through chamber i in $m^3/s$, $\Delta p$ is the pressure drop across the channel/chamber segments in pascal (Pa), and $R_{in,i}$, $R_i$, $R_{out,i}$ are the hydraulic resistance of inlet channel i, hydraulic resistance of organ chamber i, and hydraulic resistance of outlet channel i in $Pa{\cdot}s/m^3$, respectively. When designed with a particular length and depth, the widths of inlet and outlet channels lend themselves to adjusting the hydraulic resistances of each channel/chamber segment (Eq. 2; Bruus, 2008).

$$R = \frac{12\eta L}{wh^3} * \left[1 - \frac{192h}{\pi^5 w}\tanh\left(\frac{\pi w}{2h}\right)\right]^{-1} \tag{2}$$

Here, $R$ is the resistance across the device in $Pa{\cdot}s/m^3$, $\eta$ is the dynamic viscosity of the cell culture medium in Pa·s, $L$ is the length of the channel in meters, $h$ is the height of the channel in meters, and $w$ is the width of the channel in meters. This equation is valid for channel dimensions that are such that $w > h$.

With more traditional devices being closed systems, Frey et al. (2014) developed a unique, open channel based MPS using an array of hanging drops as multiple parallel multi-organ microsystems. They used a peristaltic pump and open channels to form a microfluidic network between neighboring hanging drops (Frey et al., 2014).

However, because external pumps connect to MPS via tubing, the use of such pumps requires the presence of fluid volumes that create higher fluid-to-tissue ratios than would be physiological, often surpassing *in vivo* ranges.

Microfabricated on-board pumps, on the other hand, are integrated into the MPS itself and can help with reducing the volume of fluid needed to operate it. For example, Bowen and Scott incorporated a PDMS-based peristaltic pump and additional PDMS-based valves that recovered samples from the device (Bowen and Martin, 2010). Different placements and dimensions of the pump and valves were used to optimize flow rates. Schimek et al. (2013) used an on-board peristaltic micropump to operate a two-organ MPS. The pump produced pulsatile flow at a wide, adjustable range, creating physiological conditions for the growth of endothelial cells.

However, active pumping mechanisms can sometimes suffer from complications such as the formation of air bubbles, and possible leaking of medium.

To improve the reliability of fluidic flow, Sung et al. (2010) developed an MPS with gravity-driven flow, eliminating the need for a pump. The design consisted of multiple layers of PDMS with fluidic channels and organ chambers in the middle layers. To induce fluidic flow, the device was placed on a rocking platform that changed its angle periodically. In absence of a pump, all the fluidic components, i.e., microchambers, microchannels, and

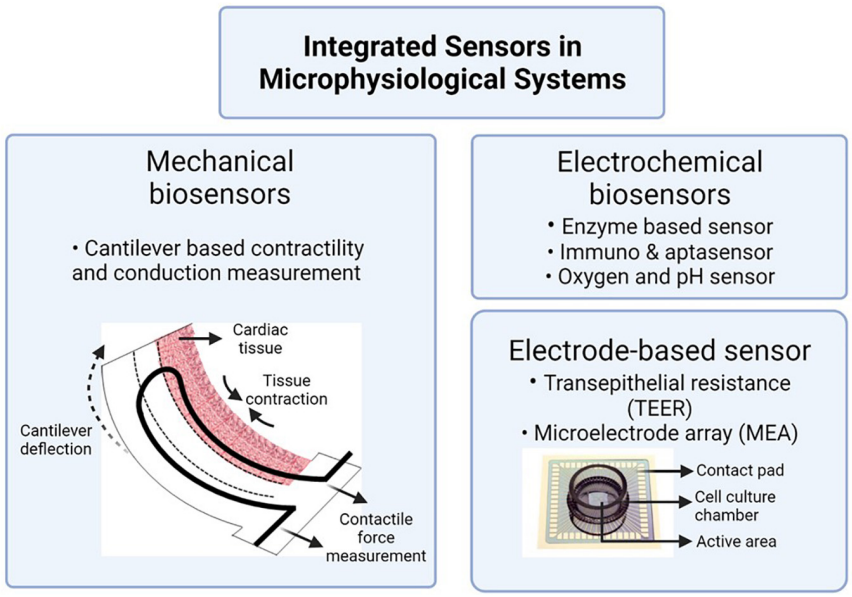


**FIGURE 4 |** Integrated sensors to assess tissue health in MPS. Image is created using BioRender.com[‡].

reservoirs were constructed on the chip without any external fluid or gas loops. Similarly, Oleaga et al. (2016) employed a range of platform tilt angles and oscillation times to achieve flow rates in the physiological range, and a human MPS company designed a variety of toxicology models that use gravity-based flow systems (Oleaga et al., 2016, 2018; McAleer et al., 2019a).

The flow Sung et al. (2010) and Oleaga et al. (2016) created in their systems is bidirectional, reversing direction periodically, albeit staying below a threshold shear rate. A tilt angle of 8° with two oscillations per minute resulted in maximum shear stress of 0.025 Pa (0.25 dynes/cm$^2$) (Oleaga et al., 2016). Tissues that typically only experience low mechanical shear due to interstitial fluidic flow *in vivo,* are not disturbed by such low-grade, bidirectional shear (Esch et al., 2015).

Another advantage of gravity-driven flow is that MPS designs can be compact, eliminating long interconnecting channels from the designs as shown with the recently developed body cube (Chen et al., 2020), and thereby lowering the overall liquid volume needed to operate the systems to near-physiological blood surrogate levels (Chen et al., 2020). As opposed to a higher fluid volume that does not entirely represent the physiological scenario, such low liquid volume systems provide the ability to produce secondary metabolites at near-physiological concentrations.

However, when operated with small amounts of cell culture medium, gravity-driven, bidirectional flow can result in a small volume of cell culture medium that remains inside the cell culture chambers, not entering the liquid reservoirs on either side of the device, and not experiencing mixing with the remainder of the cell culture medium. That phenomenon can lead to poor oxygenation and a poor supply of nutrients in the middle of the cell culture chambers. When designing such bidirectional flow systems, care must be taken to operate the MPS with enough cell culture medium to achieve full recirculation of all cell culture medium.

Gravity-driven systems can also include passive, flow-rectifying elements that create unidirectional flow (Esch et al., 2016; Wang and Shuler, 2018; Yang et al., 2019; Fathi et al., 2020). Unidirectional flow is needed when tissues that experience high mechanical shear due to fluid flow *in vivo* are to be cultured within the system (most notably the endothelium). Yang et al. (2019) has found that such tissues thrive under unidirectional flow and display higher levels of inflammation under bidirectional flow, validating the use of unidirectional flow for producing functional endothelial cells.

Gravity-driven MPS often do not contain flow-regulating valves, thus the fluidic flow inside those systems is regulated by balancing the pressure drops and adjusting the hydraulic resistances as discussed for externally pumped systems that do not contain valves (Eq. 1 and 2).

## Integrated Sensors

Many MPS contain tissues and fluid volumes that represent between 1/10,000 and 1/250,000 of the organ and fluid volumes present in the human body. That scaling makes it possible to use reasonable numbers of cells to construct each tissue (˜50,000–750,000 cells per tissue). But a drawback of the relatively small size is a limitation on the types of analysis that can be performed. Due to the small volumes of cell culture medium, often 1,000 μL or less, retrieval of fluid samples from the system for external analysis, without disturbing its dynamics, is a challenge. Nevertheless, analysis of tissue health is often accomplished by measuring concentrations of soluble proteins such as albumin, urea, and inflammation markers in the cell culture medium taken from the MPS at various times. Microfabricated, system-integrated sensors that measure the physiological response of

tissues to chemicals or drugs can provide for such analysis without distorting metabolite and marker concentrations.

Owing to the significant role in drug metabolism, several types of sensors were developed to evaluate the status of liver tissue. For example, aptamer-based electrochemical sensors have been used to detect liver-generated proteins through protein binding to the electrode and the subsequent change in electrode redox properties. Son et al. (2017) added a sensing channel adjacent to the liver chamber, separated by a polyethylene glycol (PEG) hydrogel barrier. Detection occurs in the sensing channel via a standard fluorescence-based antibody sandwich assay (i.e., primary antibody-coated, non-fluorescent capture beads and secondary antibody-coated, fluorescent detection beads). Upon diffusion of proteins of interest into the sensing channel and binding to the capture beads, the fluorescent beads bind and aggregate on the surface of the capture bead; the resulting fluorescence intensity is detected through imaging.

Bavli et al. (2016) included luminescence and enzyme-based sensors to measure oxygen and glucose/lactose concentrations in the system. Monitoring those small molecules provides vital information about the status of metabolism inside the system. Similarly, Sin et al. (2004) developed a dissolved oxygen sensor as a proof-of-concept model to measure gas exchange in an MPS. Instead of the widely used Clark electrodes, which consume oxygen in order to detect it, Sin et al. (2004) integrated a non-invasive, fluorescence-based oxygen-sensing system and confirmed that oxygen exchange is adequate inside the device. The oxygen sensing was based on phase-sensitive detection using a ruthenium complex as a fluorescent probe. A calibration curve of observed phase angles and known partial oxygen concentrations ($pO_2$) was used to find the oxygen exchange in the system with respect to the changes measured in phase angle.

Cardiac models are typically combined with added equipment to monitor heart cell function. Contractile forces of heart muscle cells can be assessed using a cantilever deflection system. Cantilever deflection is used to record changes in cardiac and skeletal muscle contractile forces in response to drug exposure (Smith et al., 2014; Oleaga et al., 2016; Sasserath et al., 2020). Cantilevers are microfabricated from silicon-on-insulator wafers on the device layer and with a window underneath that allows access to laser light. Contraction of cardiomyocytes or skeletal cells seeded on top of the cantilevers is measured from laser deflection in response to the cantilever bending during muscle movement. **Figure 4** depicts the working of a cantilever along with other commonly integrated sensors in MPS.

Electrical activity and beat frequency of cardiomyocytes and electrical activity of skeletal muscle cells can be measured by growing the cells on microelectrode arrays (MEAs). In 1980, Pine (1980) used the MEAs to record action potentials of dissociated neuron culture from neonatal rats. MEAs remain the gold standard for electrophysiological assessment of cardiomyocytes *in vitro*. While a standard MEA has about 60 electrodes, Sasserath et al. (2020) used a customized MEA with 10 recording/stimulating electrodes, each with a diameter of 200 μm, and one grounding electrode of diameter 2,000 μm. The electrodes are linked to a stimulus generator to induce electrical stimulation to the cells.

Kanagasabapathi et al. (2013) adhered PDMS-based microchannels on commercially available MEAs to investigate the effects of tetrodotoxin on a model of the central nervous system. Over the years, electrode-cell conformity has improved to achieve a better signal-to-noise ratio. One such example is the tower design of a 3D hippocampal network by Rowe et al. (2007), which was later used by Musick et al. (2009) to record cortical neural electrical activity.

When using barrier tissues in MPS, assessment of the tissue's barrier integrity holds immense significance. Integration of electrodes to measure transendothelial and transepithelial electrical resistance (TEER) helps evaluate that barrier function. For example, the endothelial lining of blood vessels in the brain (blood brain barrier, BBB) plays a crucial role in regulating and protecting the central nervous system. Douville et al. (2010) first reported the use of TEER electrodes to assess the integrity of the BBB in real-time. A combination of different electrode-based sensing techniques, both MEA and TEER electrodes, was used by Maoz et al. (2017) to validate cardiomyocyte beat-rates and endothelial barrier function in response to inflammatory cytokine and isoproterenol.

In addition to models of the blood brain barrier, TEER is also used in vascular, gut (Esch et al., 2016), lung (Walter et al., 2016), skin (Sriram et al., 2018), and kidney (Douville et al., 2010) models. In most cases, Ag/AgCl electrodes are integrated into the cell culture platform to read TEER values. TEER measurements are heavily dependent on electrode placement, cell layers, and membrane geometry. In the case of MPS, the placement of organ chambers (e.g., tower or adjacent), temperature, and cell culture conditions can also change the TEER measurement (Srinivasan et al., 2015). While TEER values are widely studied and standardized for transwell cultures, more work needs to be done to have comparable data across different microphysiological systems.

## MPS for Acute and Long-Term Toxicity Measurements

The length of operation of MPS is based on the purpose of the study to be conducted. Experiments designed to test acute toxicity can be accomplished with a short drug exposure time of under 48–72 h. An example of an acute response study is that published by Oleaga et al. (2016) who challenged their four-organ, pumpless MPS with five different test compounds for 48 h. Toxicity of each drug on liver, muscle, brain, and heart was observed during that exposure time. Chen et al. (2020) reported the development of a simple yet reliable MPS device for short-term operation (up to 72 h) with near-physiological amounts of fluid volume in the system. The cell viability and liver function assays showed a successful short-term operation of the MPS with a near-physiological amount of blood surrogate (Chen et al., 2020).

Identifying the effects of chronic drug exposure, however, requires MPS operation for longer than 72 h. Longer operation of the device can be challenging because it requires continued tissue function when tissues are cultured with a common cell culture medium that addresses the needs of all tissues, but

may no longer be specialized for any tissue in particular. The increased experimental time also means functional and morphological assessment of the cells in the model for a longer duration. The maintenance of tissue integrity with continued assessment can present a challenge of its own. Nutrients are consumed, and cellular waste products accumulate over time. In addition, the dynamic nature of MPS results in an even higher rate of metabolite synthesis and secretion compared to static cultures and even more so in co-cultures (Guzzardi et al., 2009). A relatively simple way to solve this problem is to replace part of the consumed cell culture medium with fresh medium every day. Using this technique, MPS have been operated for 7 days (Oleaga et al., 2018), 14 days (Oleaga et al., 2016), and for up to 28 days (Maschmeyer et al., 2015; Xiao et al., 2017; Oleaga et al., 2019). A period of 28 days is the minimum duration to evaluate repeat dose toxicity in animal models, leading to the use of this long-term *in vitro* time frame. Similar to removing cell culture medium for the purpose of tissue-health assessment, a drawback of a daily medium exchange is that concentration profiles of both drug and drug metabolites may no longer entirely reflect their natural, physiological profiles.

While several models have been developed that can maintain the cultures for a long period, exposure to the drug over the entire duration has not been entirely achieved. Wagner et al. (2013) exposed a liver-skin MPS to troglitazone drug repeatedly at 12 h intervals for 7 days to test the system for repeated dose substance exposure. The group observed an increase in cytochrome P450 3A4 enzyme level at day 7 of exposure compared to the controls. A detailed review by Zhao et al. (2019) documents the advancements in multi-organs MPS development for long-term exposure investigations. While current long-term exposure analysis is still primarily performed in animals, the steady development of MPS is moving toward substituting animal-based chronic exposure testing as well.

## DESIGN PRINCIPLES FOR MPS

To date, many single-organ and multi-organ MPS that focus on different aspects of device performance and drug testing have been published. Despite a considerable variety in designs, certain features of MPS have proven useful over time. Such features ensure the feasibility, reproducibility, and physiological relevance of the devices. Knowing the design criteria of an MPS can provide insight into its possible applicability to another group's work. Here we discuss some design components that are often utilized in MPS development. Of those components, we discuss three essential design elements (**Table 1**) that we think researchers can use to compare their MPS with those of others.

### Functional Organ Volumes

Multi-organ MPS are designed to replicate key aspects of human physiology. Indeed, the power of MPS lies in the devices' potential to recreate human drug metabolism with drug and metabolite concentration profiles that can closely mimic those occurring *in vivo*. Achieving that outcome requires MPS to be designed with a few yet important design criteria in mind.

**TABLE 1 |** Factors considered for the design of MPS.

| Design criteria | Suggested range | Considerations |
|---|---|---|
| Scaling factor | 50,000–100,000 | Impacts the size of the system.<br>A higher scaling factor will generate a larger system, increasing the fluid volume, and the number of cells needed to reach functional organ volume ratios, thus making the device more expensive.<br>A lower scaling factor will generate a smaller system, with small volume of blood surrogate but also possibly cause difficulty in system operation. |
| Liquid volume | 1/10,000–1/250,000 of the *in vivo* organ and fluid volume | Higher fluid volume can dilute the metabolites produced in the device, making measurements of metabolite toxicity less relevant to what occurs *in vivo*. |
| Fluid-to-cell ratio in tissues | $10^3$–$10^6$ cells based on scaffold area | Value is based on the physiological cell density, functional organ volume (eliminate the volume occupied by the scaffold material) and seeding area. |

First, as suggested by Wikswo (2014) in their seminal paper, an ideal MPS reproduces the relationships of functional *in vivo* organ volumes. The underlying assumption is that the amount of drug that is absorbed, consumed, and/or metabolized *in vivo* depends on the activity of available enzymes, which, in an MPS, depends on both, the quality of tissues and tissue volumes (Eqs. 3-1, 3-2 Bruus, 2008). The drug metabolism rate is directly proportional to the organ volume where metabolism takes place. When considering the volumes of tissues, particular attention must be given to the function of different tissues within an organ. To correctly relate functional organ volumes *in vitro*, each organ of the human body must be considered in terms of its function with regards to drug absorption, metabolism, and elimination, and each tissue should be scaled to keep the physiological volume ratios intact (Wikswo, 2014).

$$V_o \frac{dC_o}{dt} = Q_O C_b - \frac{Q_o C_o}{P_o} - CL_{int} f C_o \tag{3-1}$$

$$V_o \frac{dC_o}{dt} = Q_O C_b - \frac{Q_o C_o}{P_o} - V_o \sum \frac{V_m f C_o}{K_m + f C_o} \tag{3-2}$$

In Equation 3-1, $V_o$ is the volume of an organ in milliliters, $t$ is time in minutes, $C_b$ is the concentration of drug in blood in mmol/mL, $C_o$ is the concentration of drug in the organ in mmol/mL, $Q_o$ is the blood flow rate going through the organ in mL/min, $P_o$ is the partition coefficient of drug in the organ, $CL_{int}$ is the intrinsic clearance of the drug in the organ in mL/min and $f$ is the unbound fraction of drug. For the metabolism of drugs in the organ that follow Michaelis-Menten kinetics, the equation could be written as Eq. 3-2. Here, $V_m$ is the maximum reaction rate of the enzyme in mmol/(mL·min), and $K_m$ is the Michaelis constant of the enzyme mmol/mL.

When replicating functional units of an organ, it is also important to consider the source of cells used to create the tissue mimic and the level of enzyme activity within those cells. The goal is to achieve drug conversion rates that are close to those *in vivo*

(Eqs. 3-1 and 3-2). One of the most important considerations, for example, is the design of the liver tissue. The closer the metabolic activity of liver cells inside the MPS matches that of liver cells *in vivo*, the better the liver will replicate *in vivo* concentrations of drug metabolites. However, *in vitro* enzyme activities rarely match *in vivo* activities, and an extra volume of cells may be needed to reach a certain *in vivo* functional organ volume.

Due to the difference in *in vitro* and *in vivo* metabolic activity, an analysis of the enzymatic activity involved in the metabolic pathway is a critical first step to ascertain the proper functioning of an MPS.

## Blood Surrogate Volume and Formulation

Culture conditions for multi-organ MPS differ considerably from single-organ MPS due to the many cell growth requirements of the different tissues. The local *in vivo* environments of human organs provide certain biochemical characteristics such as growth factors and cytokines. Those features have been shown to have a significant influence on the development and function of organs, thus making it good practice to include them in MPS as well (Wang et al., 2020).

In *in vitro* conditions, blood surrogate is a substitute for blood, which is why it must recapitulate human physiological oxygen transport characteristics. In addition, the common cell culture medium that recirculates among all organ chambers must be able to support the phenotypic and functional requirements of all those tissues. Even though there is currently no universal serum-free medium, trying different formulations of a minimal medium can help determine the right medium. To start, a base medium can be created using an already existing cell-type specific medium or choosing a medium suitable for a high demanding cell line, followed by the addition of supplements or growth factors. For example, because of the liver's high metabolic demand and its integral role in drug metabolism, the formulation of a common MPS cell culture medium is often based on liver cell culture medium (Sung et al., 2019). Additional growth factors that support other cell types can be added to that base medium. Zhang et al. (2009) were able to create a blood surrogate that supported four cell types.

Alternately, to ensure optimum culture conditions for all cell types present in the MPS, it is good practice to perform a growth assessment in the intended medium and adjust the formulation based on the cells' responses.

Fluid content in the MPS device is divided into the circulating volume of blood surrogate in the system (all liquid or cell culture medium that resides in fluidic channels, reservoirs, sensor cavities, or that simply flows across a tissue on its surface) and the interstitial liquid volume (liquid or cell culture medium that is present within the organ chamber volume that is occupied by the tissue volume, i.e., the scaffold or matrix and the actual cells). The volume of cell culture medium that functions as blood surrogate within an MPS must be carefully considered. Both the amount of interstitial liquid and the volume of blood surrogate should ideally be close to physiological levels. To achieve a reasonable number of 50,000–750,000 cells per tissue, the *in vitro* tissue and fluid volume is kept between 1/10,000 and 1/250,000 of the *in vivo* organ and fluid volume. Reporting the liquid volumes used with an MPS can help when comparing data obtained with different designs, thus becoming a vital evaluation factor in our opinion.

The blood surrogate volume for an MPS can be calculated by dividing the typical volume of blood in a human body by the scaling factor used to calculate the functional organ volumes for all other organs. Since the blood surrogate collects within the medium reservoirs and gets redistributed from there, it pools all metabolites from the different organ chambers. An increase in blood surrogate volume larger than normal physiological volumes will dilute drug metabolites, leading to difficulty in assessing the drug efficacy or potential toxicity. To support this statement, we ran a PBPK simulation for clinical data of lidocaine artery plasma concentration change over time after an intravenous administration of 3 mg/kg body weight (Tucker and Boas, 1971; **Figure 5**). Upon increasing the blood volume by 10 times, the concentration of monoethylglycinexylidide (MEGX, a metabolite of lidocaine) in plasma was seen to be lowered. This reiterates the importance of following physiological values of blood volume *in vitro* to accurately determine the concentration of toxicant in the system.

The need to regulate the blood surrogate volume so it remains close to physiological levels is solved by using a scaling factor. It determines the physical size of the system and how much blood surrogate volume it should be operated with. Designing an MPS system with a physiological equivalent of *in vivo* blood volume often translates to a small volume of culture medium 60–300 μL, which makes it difficult to operate the MPS. Scaling factor is one of the most important characteristics of an MPS thus qualifying as second of the three important criteria for MPS evaluation.

Currently, MPS scaling factors range between 50,000 and 400,000. Scaling factors between 50,000 and 100,000 are likely the most useful because smaller systems will require very small volumes of blood surrogate, making it difficult to operate the system and successfully sample medium for drug concentration analyses. If the system is large, all organ mimics will require many cells to replicate functional organ volume ratios. This type of device may become expensive when working with tissues constructed from primary cells or stem cell sources.

The body-in-a-cube design by Chen et al. (2020) uses 80 μL of blood surrogate, 1/73,000 of the blood volume (with a scaling factor of 73,000), to achieve near-physiological volumes. The group was able to demonstrate successful functioning of the four-organ MPS with this small circulating volume of fluid for 72 h.

## Fluid-to-Cell-Ratios in Tissues and Cell Culture

As mentioned in section "Blood Surrogate Volume and Formulation," the amount of fluid within an MPS is an important determinant of how well the sensors in the devices can detect the presence of toxic metabolites. Too much liquid will dilute metabolites and make their effects on tissues less pronounced. The amount of fluid within each tissue, i.e., the amount of liquid

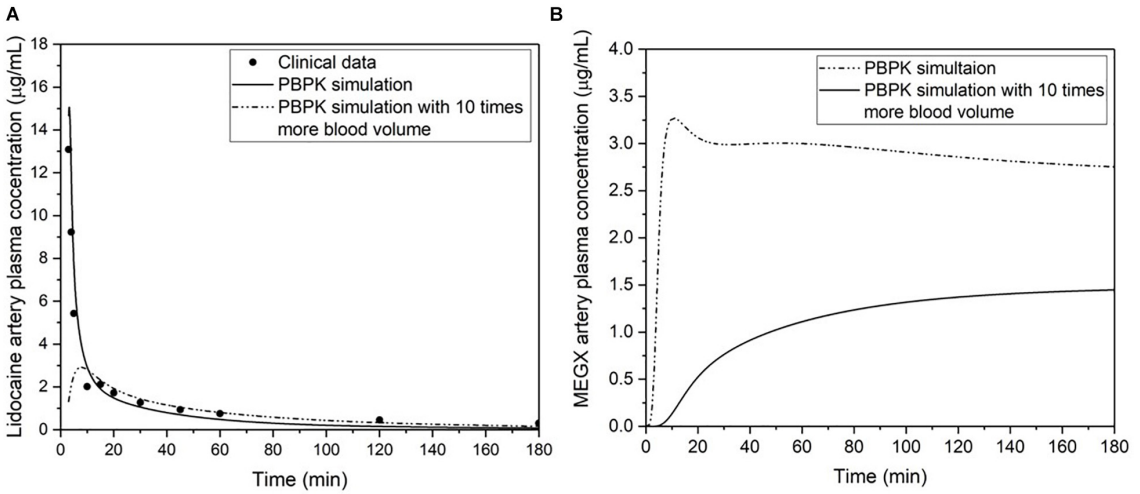


**FIGURE 5 | (A)** The PBPK simulation and clinical data of lidocaine artery plasma concentration change over time after an intravenous administration of 3 mg/kg body weight (Tucker and Boas, 1971). **(B)** Comparison of two simulations for the artery plasma concentration change of monoethylglycinexylidide (MEGX, a metabolite of lidocaine) after an intravenous administration of 3 mg/kg body weight, and using published parameters for MEGX unbound fraction (Feely and Grimm, 1991), partition coefficient (Dillane and Finucane, 2010), and *in vitro* liver kinetics (Bargetzi et al., 1989). One simulation is modeled with physiological parameters, and the other is modeled with 10 times more blood volume while keeping all the other parameters equal and at physiological values.

that represents the interstitial liquid plays a similar role as the blood surrogate.

To construct tissues for MPS, cells are typically seeded onto scaffolds or into hydrogels and allowed to mature before exposing the MPS to drugs or chemicals. Natural biomaterials such as collagen and fibrin (protein-based), hyaluronic acid and cellulose (polysaccharide-based), and decellularized ECM can support cell adhesion and growth because they are compositionally consistent from batch to batch.

Since the response of a drug or chemical in the human body is highly dependent on the local environment of the body, it is imperative to replicate the *in vivo* environment as closely as possible. The cell density for individual organs and the seeding ratio of cells making up a particular tissue are based on the physiological density of cells in the human body. A typical organ in the human body is about 100–500 mL in size with about $10^9$ cells per organ, with some organs having more and some having slightly less (McClelland et al., 2012). However, to make a physiologically relevant model, the average cell number in an *in vitro* system is based on the dimensions of the scaffold and ranges from $10^3$ to $10^6$ cells. A higher cell density than this can result in overcrowding of the attachment surface, potentially leading to cell mortality and irregular metabolite buildup. This difference between the *in vivo* and *in vitro* cell densities needs to be considered when calculating functional organ volumes. To obtain more accurate *in vitro* values, the volume that is occupied by cell culture scaffolding material could be subtracted from the overall chamber volume (Chen et al., 2020).

Currently, most 3D cell cultures do not yet replicate *in vivo* cell densities, and therefore contain larger amounts of interstitial liquid than would be physiological. Maintaining an optimum cell count and continuous fluid flow facilitates molecular crosstalk among tissues in a multiorgan device (Guzzardi et al., 2009). Reporting the cell density for an MPS in combination with the scaling factor and liquid volume will help assess its performance as a predictor of clinical outcomes.

For the purposes of proof-of-concept, *in vitro* organs are often made with cells from immortalized cell lines. Cell lines have the advantage of being highly reproducible and easy to access; however, compared to native cells, the cell signaling pathways and their metabolism may differ considerably due to cell line transformation (Zeilinger et al., 2016). The use of primary cells in early passages, i.e., with minimum number of subcultures done from the primary culture, helps limit this problem and create more realistic organ models.

The development of tissues using stem cells also provides a suitable alternative to using cell lines. Stem cell-derived tissues can be obtained from human adult, embryonic, or induced pluripotent stem cells (iPSCs). The cells can be seeded on a 3D matrix and allowed to undergo division and differentiation. The complexity and intricacy of a 3D model can limit the diffusion characteristics in the engineered tissue. Some of these limitations can be overcome by localizing the metabolically active cells to the periphery of the 3D model. McMurtrey (2016) outlines analytical models to determine the oxygen and nutrient diffusion in 3D constructs computationally.

A well-designed MPS must also be able to maintain cell viability during the entire length of an experiment. During the operation, the cellular functions of the involved tissues should be observed based on the study objectives. These may involve continued monitoring of enzymatic activity, and metabolite synthesis in liver cells, electrical activity in cardiac or neuronal cells, and barrier integrity in endothelial cells. A detailed record of "what" and "how" of each aspect of experimental design helps in understanding and reproducing any study.

## Fluid Flow Rates

When trying to replicate *in vivo* drug metabolism rates in an MPS, it is important to also consider flow rates and fluid residence times within each organ compartment. It has previously been proposed that the rate of drug absorption and conversion in the liver and in any other tissue is determined by the amount of time the blood surrogate spends inside the organ chamber (Eqs. 4-1, 4-2; Bruus, 2008). Therefore, *in vivo* perfusion rates per organ volume should be replicated in an MPS as well.

$$t_{res} = \frac{V_o}{Q_o} \tag{4-1}$$

$$\frac{dC_o}{dt} = \frac{C_b}{t_{res}} - \frac{C_o}{t_r P_o} - \frac{CL_{int} f C_o}{V_o} \tag{4-2}$$

Here, $t_{res}$ is the residence time of blood flow in the organ in minutes, $V_o$ is the volume of an organ in milliliters, $t$ is the time in minutes, $C_b$ is the concentration of drug in blood in mmol/mL $C_o$ is the concentration of drug in the organ in mmol/mL, $Q_o$ is the blood flow rate going through the organ in mL/min, $CL_{int}$ is the intrinsic clearance of the drug in the organ in mL/s and $f$ is the unbound fraction of drug.

When optimizing flow rates, the adequacy of oxygen supply to each tissue must also be carefully considered. Since cell culture medium has a limited capacity to carry oxygen throughout the system, a limited oxygen supply may also limit metabolic conversion rates. Faster flow rates can potentially alleviate this limitation. The cell culture medium should also be able to take up new oxygen and release carbon dioxide while recirculating, potentially through an open reservoir, or through breathable MPS construction materials. On the other hand, as discussed in section "MPS for Modeling the Immune System," the shear generated by fluidic flow must not exceed the threshold at which it will cause damage to the cells cultured in the MPS. *In vivo*, most cells (other than endothelia or epithelia) are only subject to small shear stress derived from the interstitial flow of liquid. Hence, unless the cells of a tissue are protected by an epithelial cell layer or an endothelial cell layer, the shear resulting from the flow of cell culture medium inside an organ chamber is typically kept below 0.025 Pa (0.25 dynes/cm$^2$) (Oleaga et al., 2016).

## Organ Chamber Arrangement and PBPK-Guided Designs

To create a multi-organ MPS, individual organ mimics are coupled together in a physiologically relevant manner. For example, an MPS that mimics the first-pass metabolism of orally taken drugs combines the GI-tract epithelium with liver tissue so that the drug must first pass through the epithelium before reaching the liver and the fluidic system that represents the body's systemic circulation (Esch et al., 2014).

For more complex systems with more organ mimics, PBPK models are used as a guide to construct MPS (Sung et al., 2014, 2019). Using this method, organ chambers are connected to each other in a row or in parallel, depending on how they are connected in the body. As a basic principle, a PBPK model assumes the MPS to be a collection of interconnected compartments. Organ chamber connected via vascular channels provide pharmacodynamic information that individual organ-on-chip devices are unable to achieve. A semi-permeable membrane between vascular and endothelial cells facilitates drug transport and metabolism studies. A fluidically connected vascular network of organ chips enables the study of drug distribution in the organ. Studies show that linking multiple organ on chip systems by using scaling techniques can help advance pharmacokinetic and pharmacodynamic studies (Chang et al., 2017; Cyr et al., 2017).

An advantage of using PBPK models to design MPS is that such a model can also be created for the MPS itself. All design considerations, like organ chamber sizes and flow rates, are computationally entered into the model, and upon solving the model's mass balance equations, the expected time-dependent drug concentration is obtained. Comparing computationally obtained drug and drug metabolite concentrations with concentrations obtained experimentally with the corresponding MPS can help verify any assumptions that were used to design the system, and gain confidence in the tissue responses that were observed. Adiwidjaja et al. (2020) implemented a PBPK model to determine optimal dosage and potential drug interactions with imatinib, a chronic myeloid leukemia drug, using *in vitro* drug metabolism and *in vivo* pharmacokinetic data. The model was then extrapolated to children by factoring in the change in organ size, volume and drug metabolism.

Due to the simplified representation of the human body when using *in vitro* MPS, extrapolation of information from *in vitro to in vivo* (IVIVE) system requires the use of mathematical models. One such example is the study conducted by Herland et al. (2020). These authors show adaptation of a computational model of the *in vitro* linked multi-organ chip to the pharmacokinetic/pharmacodynamic (PKPD) profiles of orally taken and injectable drugs observed in humans *in vivo* (Herland et al., 2020).

## Device Material

Certain considerations in selecting an MPS material include its cost, reusability, sterility, opacity, hydrophilicity, and breathability. There are a variety of biocompatible materials that have been used to make MPS. An integral part of designing a functioning tissue is the proper selection of biocompatible, non-toxic device materials. Since silicon is a material for which many microfabrication processes are available (especially deep reactive ion etching processes), some of the first devices were made from silicon and used with a glass or plastic cover (Sin et al., 2004; Tatosian and Shuler, 2009).

Silicon can also be used to create templates for casting silicone materials such as PDMS. PDMS has become one of the most used materials for MPS fabrication because it is inexpensive, and a single silicon template can be used to cast hundreds of PDMS devices. PDMS also has the advantage of being stretchable, a property that has been used successfully to re-create the mechanical stretching the lung epithelium experiences during the breathing process (Huh et al., 2010). However, when using PDMS, some drug loss can occur due to its affinity to hydrophobic compounds (Vernetti et al., 2017).

More recently, MPS have been made from 3D-printed polymers (Esch et al., 2016; Chen et al., 2020). Like PDMS devices, 3D-printed systems must be checked for drug and drug metabolite losses due to adsorption to device surfaces. Pre-coating of the material to reduce its drug binding properties can act as a potential solution. Parylene, a biocompatible polymer, coated on a 3D printed device does not absorb or react to drugs or metabolites. Esch et al. (2016) used parylene C to coat the 3D printed polymer of their device platform and two-organ chips. This system is primarily advantageous in cases where the drugs to be tested are hydrophobic and cannot be tested with PDMS systems due to adsorption issues.

Since cell culture is highly dependent on the physical and chemical properties of the environment, recreating the *in vivo* environment in an *in vitro* setup takes precedence. A recent development, 3D bioprinting of cell types and other materials provides increased control over the structural and cellular environment in a one-step process. Yi et al. (2019) designed a glioblastoma (GBM)-on-chip model using 3D bioprinting process to mimic the *in vivo* environmental cues of the disease. They used patient derived cancer cell-laden bioink along with silicon ink to print the cells onto a sterilized surface modified slide glass, creating a GBM-on-chip model. This approach helped Yi et al. (2019) achieve an anatomically similar spatial tissue organization of GBM *in vitro*. Combining the strengths of bioprinting with those of microfluidics can give rise to a physiologically realistic alternate to animal models. Fetah et al. (2019) provide a detailed review on the recent advancements in the use of bioprinting in organ-on-chip systems.

## DRUG TOXICITY TESTING WITH MPS

To enable widespread adoption of MPS for drug toxicity screening, the devices need to be reliable, affordable and validated. Device validation often involves the use of a model drug whose toxic effects on the human body are known. While both single and multi-organ MPS can be used to detect any drug's direct effects on tissues, it is a particular strength of multi-organ MPS to also uncover secondary toxicity from drug metabolites.

This was demonstrated by a study conducted by Sung et al. (2010) using the anticancer drug 5-fluorouracil (5-FU) in their experiments. *In vitro* testing of breast cancer drug, tamoxifen, with verapamil showed off-target effect on contractility, beat frequency and conduction velocity of cardiac cells by the metabolites of tamoxifen (McAleer et al., 2019a). Terfenedine, currently withdrawn antihistamine drug, is a commonly used cardiotoxin for proof-of-concept studies. A 28-day co-culture of hepatocytes and cardiomyocytes in MPS by Oleaga et al. (2018) was used to show that non-cardiotoxic drugs, terfenadine and cyclophosphamide, generate cardiotoxic metabolites upon liver transformation. *In vitro* experiments in another liver-heart MPS revealed that the toxic effects of terfenadine were dependent on the concentration of drug within the cardiomyocytes rather than the concentration in the media (McAleer et al., 2019b). Using the experimental drug response data, McAleer et al. (2019b) created a PKPD model that correctly predicted the pharmacokinetics of terfenadine and its metabolites in the MPS. Other model toxicants could be drugs that passed trials with animal models but showed toxicity in clinical trials with humans.

The interconnected organs in an MPS device provide an understanding of the fate of the drug in the body, and the collective response of the organs to the drug, thus creating an efficient model for toxicity studies. *In vitro* studies also help determine the potential experimental dose range of a drug or a combination of multiple drugs which can then be tested in a clinical setting.

MPS devices can also be used for drug testing in both the pre-clinical phase and post-release market phase. After the approval of a drug, complications such as failed phase 4 clinical trials, post-market failure, and black-box warnings can arise (Mol et al., 2013). Many commercially available drugs cause hepatotoxicity or cardiotoxicity, calling for the need to conduct comprehensive drug safety assessment even post-approval (Minotti, 2010). Drugs that passed clinical trials and then show failures post-approval are good candidates for proof-of-concept MPS studies that aim to uncover rare or longer-term effects. Database (AdisInsight; ClinicalTrials.gov, 2000) on safety analysis of developed drugs or drugs under development, drug toxicity profiles, and mechanisms of drug action can aid in designing experiments for MPS validation.

## CONCLUSION

The lengthy and expensive process of drug development often results in failed clinical trials with humans due to low efficacy or higher than expected toxicity, putting into question the reliability of animal testing as a method for drug evaluation.

The development of *in vitro* human body mimics is a challenging, but exciting goal with abundant research prospects. Multi-organ MPS present a promising route to improve outcome predictions of clinical trials. The devices are designed to be as physiologically realistic as possible by factoring in functional organ volumes, fluid flow rates, and fluid-to-cell ratios. In addition, regulating the blood surrogate volume to physiological levels is of utmost importance to obtain precise concentrations of drug metabolites in the blood surrogate volume. With the development of MPS, the scope of drug development is vast. Easy, reliable, and standardized models for drug testing can aid in development of personalized medicines as well. The use of patient-derived stem cells in MPS can provide patient-specific reactions to the drug or a combination of drugs.

The novelty of MPS also brings variability in functionality. Reporting of MPS design criteria such as scaling factor, fluid volumes, and cellular components used in the research can help standardize the process and make the use of MPS accurate and reproducible.

## AUTHOR CONTRIBUTIONS

ME: conceptualization. MM and ME: writing – original draft. PF: writing – MPS for the immune system (section "MPS for

Modeling the Immune System"). MM, GM, and ME: writing – review and editing. YY: mathematical equations and PBPK models (**Figure 5**). All authors contributed to the article and approved the submitted version.

## FUNDING

This article was supported in part by the National Institutes of Health (1R01 ES028788).

## REFERENCES


Abulaiti, M., Yalikun, Y., Murata, K., Sato, A., Sami, M. M., Sasaki, Y., et al. (2020). Establishment of a heart-on-a-chip microdevice based on human iPS cells for the evaluation of human heart tissue function. *Sci. Rep.* 10:19201.

AdisInsight. *Home - AdisInsight*. Available online at: https://adisinsight.springer.com/.

Adiwidjaja, J., Boddy, A. V., and McLachlan, A. J. (2020). Implementation of a Physiologically Based Pharmacokinetic Modeling Approach to Guide Optimal Dosing Regimens for Imatinib and Potential Drug Interactions in Paediatrics. *Front. Pharmacol.* 10:1672. doi: 10.3389/fphar.2019.01672

Aung, A., Kumar, V., Theprungsirikul, J., Davey, S. K., and Varghese, S. (2020). An Engineered Tumor-on-a-Chip Device with Breast Cancer–Immune Cell Interactions for Assessing T-cell Recruitment. *Cancer Res.* 80, 263–275. doi: 10.1158/0008-5472.can-19-0342

Ayuso, J. M., Gong, M. M., Skala, M. C., Harari, P. M., and Beebe, D. J. (2020). Human Tumor-Lymphatic Microfluidic Model Reveals Differential Conditioning of Lymphatic Vessels by Breast Cancer Cells. *Adv. Healthc. Mater.* 9, 5–12.

Bahmaee, H., Owen, R., Boyle, L., Perrault, C. M., Garcia-Granada, A. A., Reilly, G. C., et al. (2020). Design and Evaluation of an Osteogenesis-on-a-Chip Microfluidic Device Incorporating 3D Cell Culture. *Front. Bioeng. Biotechnol.* 8:557111. doi: 10.3389/fbioe.2020.557111

Bargetzi, M. J., Aoyama, T., Gonzalez, F. J., and Meyer, U. A. (1989). Lidocaine metabolism in human liver microsomes by cytochrome P450IIIA4. *Clin. Pharmacol. Ther.* 46, 521–527. doi: 10.1038/clpt.1989.180

Bavli, D., Prill, S., Ezra, E., Levy, G., Cohen, M., Vinken, M., et al. (2016). Real-time monitoring of metabolic function in liver-on-chip microdevices tracks the dynamics of mitochondrial dysfunction. *Proc. Natl. Acad. Sci. U. S. A.* 113, E2231–E2240.

Bischel, L. L., Young, E. W. K., Mader, B. R., and Beebe, D. J. (2013). Tubeless microfluidic angiogenesis assay with three-dimensional endothelial-lined microvessels. *Biomaterials* 34, 1471–1477. doi: 10.1016/j.biomaterials.2012.11.005

Boussommier-Calleja, A., Li, R., Chen, M. B., Wong, S. C., and Kamm, R. D. (2016). Microfluidics: a new tool for modeling cancer-immune interactions. *Trends Cancer* 2, 6–19. doi: 10.1016/j.trecan.2015.12.003

Bowen, A. L., and Martin, R. S. (2010). Integration of On-Chip Peristaltic Pumps and Injection Valves with Microchip Electrophoresis and Electrochemical Detection. *Electrophoresis* 31, 2534–2540. doi: 10.1002/elps.201000029

Bruus, H. (2008). *Theoretical Microfluidics*. Oxford: Oxford University Press.

Chang, S.-Y., Weber, E. J., Sidorenko, V. S., Chapron, A., Yeung, C. K., Gao, C., et al. (2017). Human liver-kidney model elucidates the mechanisms of aristolochic acid nephrotoxicity. *JCI Insight* 2:e95978. doi: 10.1172/jci.insight.95978

Chen, L., Yang, Y., Ueno, H., and Esch, M. B. (2020). Body-in-a-cube: a microphysiological system for multi-tissue co-culture with near-physiological amounts of blood surrogate. *Microphysiol Syst.* 4:10.21037/ms–19–8.

ClinicalTrials.gov. (2000). *Home - ClinicalTrials.gov*. Available online at: https://clinicaltrials.gov/.

Cochrane, A., Albers, H. J., Passier, R., Mummery, C. L., Berg, A. V. D., Orlova, V. V., et al. (2019). Advanced in vitro models of vascular biology: human induced pluripotent stem cells and organ-on-chip technology. *Adv. Drug Deliv. Rev.* 140, 68–77. doi: 10.1016/j.addr.2018.06.007

Cyr, K. J., Avaldi, O. M., and Wikswo, J. P. (2017). Circadian hormone control in a human-on-a-chip: in vitro biology's ignored component? *Exp. Biol. Med.* 242, 1714–1731. doi: 10.1177/1535370217732766

Deng, J., Cong, Y., Han, X., Wei, W., Lu, Y., Liu, T., et al. (2020). A liver-on-a-chip for hepatoprotective activity assessment. *Biomicrofluidics* 14:064107. doi: 10.1063/5.0024767

Deng, J., Wei, W., Chen, Z., Lin, B., Zhao, W., Luo, Y., et al. (2019). Engineered Liver-On-A-Chip Platform to Mimic Liver Functions and Its Biomedical Applications: a Review. *Micromachines* 10:676. doi: 10.3390/mi10100676

Dillane, D., and Finucane, B. T. (2010). Local anesthetic systemic toxicity. *Can. J. Anesth. Can. Anesth.* 57, 368–380.

Douville, N. J., Tung, Y.-C., Li, R., Wang, J. D., El-Sayed, M. E. H., and Takayama, S. (2010). Fabrication of Two-Layered Channel System with Embedded Electrodes to Measure Resistance Across Epithelial and Endothelial Barriers. *Anal. Chem.* 82, 2505–2511. doi: 10.1021/ac9029345

Edington, C. D., Chen, W. L. K., Geishecker, E., Kassis, T., Soenksen, L. R., Bhushan, B. M., et al. (2018). Interconnected Microphysiological Systems for Quantitative Biology and Pharmacology Studies. *Sci. Rep.* 8:4530.

Esch, M. B., and Mahler, G. J. (2019). "Chapter 11 - Body-on-a-chip systems: design, fabrication, and applications," in *Microfluidic Cell Culture Systems (Second Edition)*, eds J. T. Borenstein, V. Tandon, S. L. Tao, and J. L. Charest (Amsterdam: Elsevier), 323–350. doi: 10.1016/B978-0-12-813671-3.00011-6

Esch, M. B., Mahler, G. J., Stokol, T., and Shuler, M. L. (2014). Body-on-a-Chip Simulation with Gastrointestinal Tract and Liver Tissues Suggests that Ingested Nanoparticles Have the Potential to Cause Liver Injury. *Lab. Chip* 14, 3081–3092. doi: 10.1039/c4lc00371c

Esch, M. B., Prot, J.-M., Wang, Y. I., Miller, P., Llamas-Vidales, J. R., Naughton, B. A., et al. (2015). Multi-cellular 3D human primary liver cell culture elevates metabolic activity under fluidic flow. *Lab. Chip* 15, 2269–2277. doi: 10.1039/c5lc00237k

Esch, M. B., Sung, J. H., Yang, J., Yu, C., Yu, J., March, J. C., et al. (2012). On chip porous polymer membranes for integration of gastrointestinal tract epithelium with microfluidic 'body-on-a-chip' devices. *Biomed. Microdevices* 14, 895–906. doi: 10.1007/s10544-012-9669-0

Esch, M. B., Ueno, H., Applegate, D. R., and Shuler, M. L. (2016). Modular, pumpless body-on-a-chip platform for the co-culture of GI tract epithelium and 3D primary liver tissue. *Lab. Chip* 16, 2719–2729. doi: 10.1039/c6lc00461j

Fathi, P., Holland, G., Pan, D., and Esch, M. B. (2020). Lymphatic Vessel on a Chip with Capability for Exposure to Cyclic Fluidic Flow. *ACS Appl. Bio Mater.* 3, 6697–6707. doi: 10.1021/acsabm.0c00609

Feely, J., and Grimm, T. A. (1991). comparison of drug protein binding and alpha 1-acid glycoprotein concentration in Chinese and Caucasians. *Br. J. Clin. Pharmacol.* 31, 551–552. doi: 10.1111/j.1365-2125.1991.tb05579.x

Fetah, K., Tebon, P., Goudie, M. J., and Eichenbaum, J. (2019). The emergence of 3D bioprinting in organ-on-chip systems. *Prog. Biomed. Eng.* 1:012001. doi: 10.1088/2516-1091/ab23df

Frey, O., Misun, P. M., Fluri, D. A., Hengstler, J. G., and Hierlemann, A. (2014). Reconfigurable microfluidic hanging drop network for multi-tissue interaction and analysis. *Nat. Commun.* 5:4250.

Giridharan, G. A., Nguyen, M.-D., Estrada, R., Parichehreh, V., Hamid, T., Ismahil, M. A., et al. (2010). Microfluidic Cardiac Cell Culture Model (μCCCM). *Anal. Chem.* 82, 7581–7587.

Gopalakrishnan, N., Hannam, R., Casoni, G. P., Barriet, D., Ribe, J. M., Haug, M., et al. (2015). Infection and immunity on a chip: a compartmentalised microfluidic platform to monitor immune cell behaviour in real time. *Lab. Chip* 15, 1481–1487. doi: 10.1039/c4lc01438c

Gray, L. H., Conger, A. D., Ebert, M., Hornsey, S., and Scott, O. C. A. (1953). The Concentration of Oxygen Dissolved in Tissues at the Time of Irradiation as a Factor in Radiotherapy. *Br. J. Radiol.* 26, 638–648. doi: 10.1259/0007-1285-26-312-638

Greenlee, J. D., and King, M. R. (2020). Engineered fluidic systems to understand lymphatic cancer metastasis. *Biomicrofluidics* 14:011502. doi: 10.1063/1.5133970

Grosberg, A., Nesmith, A. P., Goss, J. A., Brigham, M. D., McCain, M. L., and Parker, K. K. (2012). Muscle on a Chip: in Vitro Contractility Assays for Smooth

and Striated Muscle. *J. Pharmacol. Toxicol. Methods* 65, 126–35. doi: 10.1016/j.vascn.2012.04.001

Guo, X., Gonzalez, M., Stancescu, M., Vandenburgh, H. H., and Hickman, J. J. (2011). Neuromuscular junction formation between human stem cell-derived motoneurons and human skeletal muscle in a defined system. *Biomaterials* 32, 9602–9611. doi: 10.1016/j.biomaterials.2011.09.014

Guo, X., Smith, V., Jackson, M., Tran, M., Thomas, M., Patel, A., et al. (2020). A Human-Based Functional NMJ System for Personalized ALS Modeling and Drug Testing. *Adv. Ther.* 3:2000133. doi: 10.1002/adtp.202000133

Guzzardi, M. A., Vozzi, F., and Ahluwalia, A. D. (2009). Study of the crosstalk between hepatocytes and endothelial cells using a novel multicompartmental bioreactor: a comparison between connected cultures and cocultures. *Tissue Eng. Part A* 15, 3635–3644. doi: 10.1089/ten.tea.2008.0695

Hamza, B., and Irimia, D. (2015). Whole blood human neutrophil trafficking in a microfluidic model of infection and inflammation. *Lab. Chip* 15, 2625–2633. doi: 10.1039/c5lc00245a

Herland, A., Maoz, B. M., Das, D., Somayaji, M. R., Prantil-Baun, R., Novak, R., et al. (2020). Quantitative prediction of human drug pharmacokinetic responses using multiple vascularized organ chips coupled by fluid transfer. *Nat. Biomed. Eng.* 4, 421–436. doi: 10.1038/s41551-019-0498-9

Huh, D., Matthews, B. D., Mammoto, A., Montoya-Zavala, M., Hsin, H. Y., and Ingber, D. E. (2010). Reconstituting Organ-Level Lung Functions on a Chip. *Science* 328, 1662–1668. doi: 10.1126/science.1188302

Irimia, D., and Wang, X. (2018). Inflammation-on-a-Chip: probing the Immune System Ex Vivo. *Trends Biotechnol.* 36, 923–937. doi: 10.1016/j.tibtech.2018.03.011

Jalili-Firoozinezhad, S., Gazzaniga, F. S., Calamari, E. L., Camacho, D. M., Fadel, C. W., Bein, A., et al. (2019). A complex human gut microbiome cultured in an anaerobic intestine-on-a-chip. *Nat. Biomed. Eng.* 3, 520–531. doi: 10.1038/s41551-019-0397-0

Joiner, M. C., and Kogel van der, A. (2009). *Basic Clinical Radiobiology Fourth Edition*. Florida: CRC Press.

Jones, C. N., Dalli, J., Dimisko, L., Wong, E., Serhan, C. N., and Irimia, D. (2012). Microfluidic chambers for monitoring leukocyte trafficking and humanized nano-proresolving medicines interactions. *Proc. Natl. Acad. Sci. U. S. A.* 109, 20560–20565. doi: 10.1073/pnas.1210269109

Kanagasabapathi, T. T., Franco, M., Barone, R. A., Martinoia, S., Wadman, W. J., and Decré, M. M. J. (2013). Selective pharmacological manipulation of cortical–thalamic co-cultures in a dual-compartment device. *J. Neurosci. Methods* 214, 1–8. doi: 10.1016/j.jneumeth.2012.12.019

Kang, Y. B., Eo, J., Bulutoglu, B., Yarmush, M. L., and Usta, O. B. (2020). Progressive hypoxia-on-a-chip: an in vitro oxygen gradient model for capturing the effects of hypoxia on primary hepatocytes in health and disease. *Biotechnol. Bioeng.* 117, 763–775. doi: 10.1002/bit.27225

Khalid, N., Kobayashi, I., and Nakajima, M. (2017). Recent lab-on-chip developments for novel drug discovery. *WIREs Syst. Biol. Med.* 9:e1381. doi: 10.1002/wsbm.1381

Kim, H. J., Huh, D., Hamilton, G., and Ingber, D. E. (2012). Human gut-on-a-chip inhabited by microbial flora that experiences intestinal peristalsis-like motions and flow. *Lab. Chip* 12, 2165–2174. doi: 10.1039/c2lc40074j

Kim, S., Shah, S. B., Graney, P. L., and Singh, A. (2019). Multiscale engineering of immune cells and lymphoid organs. *Nat. Rev. Mater.* 4, 355–378. doi: 10.1038/s41578-019-0100-9

Kostadinova, R., Boess, F., Applegate, D., Suter, L., Weiser, T., Singer, T., et al. (2013). long-term three-dimensional liver co-culture system for improved prediction of clinically relevant drug-induced hepatotoxicity. *Toxicol. Appl. Pharmacol.* 268, 1–16. doi: 10.1016/j.taap.2013.01.012

Lasli, S., Kim, H.-J., Lee, K., Suurmond, C.-A. E., Goudie, M., Bandaru, P., et al. (2019). A Human Liver-on-a-Chip Platform for Modeling Nonalcoholic Fatty Liver Disease. *Adv. Biosyst.* 3:1900104.

Lee, K. K., McCauley, H. A., Broda, T. R., Kofron, M. J., Wells, J. M., and Hong, C. I. (2018). Human stomach-on-a-chip with luminal flow and peristaltic-like motility. *Lab. Chip* 18, 3079–3085. doi: 10.1039/c8lc00910d

Lee, S. Y., and Sung, J. H. (2018). Gut–liver on a chip toward an in vitro model of hepatic steatosis. *Biotechnol. Bioeng.* 115, 2817–2827. doi: 10.1002/bit.26793

Lee, V. K., Kim, D. Y., Ngo, H., Lee, Y., Seo, L., Yoo, S.-S., et al. (2014). Creating Perfused Functional Vascular Channels Using 3D Bio-Printing Technology. *Biomaterials* 35, 8092–8102. doi: 10.1016/j.biomaterials.2014.05.083

Liu, Y., Kongsuphol, P., Chiam, S. Y., Zhang, Q. X., Gourikutty, S. B. N., Saha, S., et al. (2019). Adipose-on-a-chip: a dynamic microphysiological in vitro model of the human adipose for immune-metabolic analysis in type II diabetes. *Lab. Chip* 19, 241–253. doi: 10.1039/c8lc00481a

Maharjan, S., Cecen, B., and Zhang, Y. S. (2020). 3D Immunocompetent Organ-on-a-Chip Models. *Small Methods* 4, 1–21.

Mahler, G. J., Esch, M. B., Glahn, R. P., and Shuler, M. L. (2009). Characterization of a gastrointestinal tract microscale cell culture analog used to predict drug toxicity. *Biotechnol. Bioeng.* 104, 193–205. doi: 10.1002/bit.22366

Maoz, B. M., Herland, A., Henry, O. Y. F., Leineweber, W. D., Yadid, M., Doyle, J., et al. (2017). Organs-on-Chips with combined multi-electrode array and transepithelial electrical resistance measurement capabilities. *Lab. Chip* 17, 2294–2302. doi: 10.1039/c7lc00412e

Marturano-Kruik, A., Nava, M. M., Yeager, K., Chramiec, A., Hao, L., Robinson, S., et al. (2018). Human bone perivascular niche-on-a-chip for studying metastatic colonization. *Proc. Natl. Acad. Sci. U. S. A.* 115, 1256–1261. doi: 10.1073/pnas.1714282115

Maschmeyer, I., Lorenz, A. K., Schimek, K., Hasenberg, T., Ramme, A. P., Hübner, J., et al. (2015). A four-organ-chip for interconnected long-term co-culture of human intestine, liver, skin and kidney equivalents. *Lab. Chip* 15, 2688–2699. doi: 10.1039/c5lc00392j

McAleer, C. W., Long, C. J., Elbrecht, D., Sasserath, T., Bridges, L. R., Rumsey, J. W., et al. (2019a). Multi-organ system for the evaluation of efficacy and off-target toxicity of anticancer therapeutics. *Sci. Transl. Med.* 11:eaav1386. doi: 10.1126/scitranslmed.aav1386

McAleer, C. W., Pointon, A., Long, C. J., Brighton, R. L., Wilkin, B. D., Bridges, L. R., et al. (2019b). On the potential of in vitro organ-chip models to define temporal pharmacokinetic-pharmacodynamic relationships. *Sci. Rep.* 9:9619.

McClelland, R. E., Dennis, R., Reid, L. M., Stegemann, J. P., Palsson, B., and Macdonald, J. M. (2012). "Chapter 6 - Tissue Engineering," in *Introduction to Biomedical Engineering (Third Edition)*, eds J. D. Enderle and J. D. Bronzino (Cambridge: Academic Press), 273–357.

McMurtrey, R. J. (2016). Analytic Models of Oxygen and Nutrient Diffusion, Metabolism Dynamics, and Architecture Optimization in Three-Dimensional Tissue Constructs with Applications and Insights in Cerebral Organoids. *Tissue Eng. Part C Methods* 22, 221–249. doi: 10.1089/ten.tec.2015.0375

Miller, J. S., Stevens, K. R., Yang, M. T., Baker, B. M., Nguyen, D.-H. T., Cohen, D. M., et al. (2012). Rapid casting of patterned vascular networks for perfusable engineered 3D tissues. *Nat. Mater.* 11, 768–774. doi: 10.1038/nmat3357

Miller, P., and Schuler, M. L. (2016). Design and demonstration of a pumpless 14 compartment microphysiological system - Dimensions. *Biotechnol. Bioeng.* 113, 2213–2227. doi: 10.1002/bit.25989

Mills, R., Taylor-Weiner, H., Correia, J. C., Agudelo, L. Z., Allodi, I., Kolonelou, C., et al. (2018). Neurturin is a PGC-1α1-controlled myokine that promotes motor neuron recruitment and neuromuscular junction formation. *Mol. Metab.* 7, 12–22. doi: 10.1016/j.molmet.2017.11.001

Minotti, G. (2010). *Cardiotoxicity of Non-Cardiovascular Drugs*. Hoboken: John Wiley & Sons.

Mitra, B., Jindal, R., Lee, S., Dong, D. X., Li, L., Sharma, N., et al. (2013). Microdevice integrating innate and adaptive immune responses associated with antigen presentation by dendritic cells. *RSC Adv.* 3, 16002–16010. doi: 10.1039/c3ra41308j

Mol, P. G. M., Arnardottir, A. H., Motola, D., Vrijlandth, P. J., Duijnhoven, R. G., and Haaijer-Ruskamp, F. (2013). Post-Approval Safety Issues with Innovative Drugs: a European Cohort Study. *Drug Saf.* 36, 1105–1115. doi: 10.1007/s40264-013-0094-y

Moradi, E., Jalili-Firoozinezhad, S., and Solati-Hashjin, M. (2020). Microfluidic organ-on-a-chip models of human liver tissue. *Acta Biomater.* 116, 67–83. doi: 10.1016/j.actbio.2020.08.041

Morgan, J. P., Delnero, P. F., Zheng, Y., Verbridge, S. S., Chen, J., Craven, M., et al. (2013). Formation of microvascular networks in vitro. *Nat. Protoc.* 8, 1820–1836.

Moses, S. R., Adorno, J. J., Palmer, A. F., and Song, J. W. (2020). Vessel-on-a-chip models for studying microvascular physiology, transport, and function in vitro. *Am. J. Physiol. Cell Physiol.* 320, C92–C105.

Musick, K., Khatami, D., and Wheeler, B. C. (2009). Three-dimensional micro-electrode array for recording dissociated neuronal cultures. *Lab. Chip* 9, 2036–2042. doi: 10.1039/b820596e

Ndyabawe, K., Cipriano, M., Zhao, W., Haidekker, M., Yao, K., Leidong, M., et al. (2021). Brain-on-a-Chip Device for Modeling Multiregional Networks. ACS Biomater. *Sci. Eng.* 7, 350–359. doi: 10.1021/acsbiomaterials.0c00895

Oleaga, C., Bernabini, C., Smith, A. S. T., Srinivasan, B., Jackson, M., McLamb, W., et al. (2016). Multi-Organ toxicity demonstration in a functional human in vitro system composed of four organs. *Sci. Rep.* 6:20030. doi: 10.1038/srep20030

Oleaga, C., Lavado, A., Riu, A., Rothemund, S., Carmona-Moran, C. A., Persaud, K., et al. (2019). Long-Term Electrical and Mechanical Function Monitoring of a Human-on-a-Chip System. *Adv. Funct. Mater.* 29:1805792. doi: 10.1002/adfm.201805792

Oleaga, C., Riu, A., Rothemund, S., Lavado, A., McAleer, C. W., Long, C. J., et al. (2018). Investigation of the effect of hepatic metabolism on off-target cardiotoxicity in a multi-organ human-on-a-chip system. *Biomaterials* 182, 176–190. doi: 10.1016/j.biomaterials.2018.07.062

Osaki, T., Uzel, S. G. M., and Kamm, R. D. (2018). Microphysiological 3D model of amyotrophic lateral sclerosis (ALS) from human iPS-derived muscle cells and optogenetic motor neurons. *Sci. Adv.* 4, eaat5847. doi: 10.1126/sciadv.aat5847

Park, S.-R., Kim, S.-R., Lee, J. W., Park, C. H., Yu, W.-J., Lee, S.-J., et al. (2020). Development of a novel dual reproductive organ on a chip: recapitulating bidirectional endocrine crosstalk between the uterine endometrium and the ovary. *Biofabrication* 13:015001. doi: 10.1088/1758-5090/abbd29

Parlato, S., Grisanti, G., Sinibaldi, G., Peruzzi, G., Casciola, C. M., and Gabriele, L. (2021). Tumor-on-a-chip platforms to study cancer-immune system crosstalk in the era of immunotherapy. *Lab. Chip* 21, 234–253. doi: 10.1039/d0lc00799d

Pine, J. (1980). Recording action potentials from cultured neurons with extracellular microcircuit electrodes. *J. Neurosci. Methods* 2, 19–31. doi: 10.1016/0165-0270(80)90042-4

Pisano, M., Triacca, V., Barbee, K. A., and Swartz, M. A. (2015). An in vitro model of the tumor-lymphatic microenvironment with simultaneous transendothelial and luminal flows reveals mechanisms of flow enhanced invasion. *Integr. Biol.* 7, 525–533. doi: 10.1039/c5ib00085h

Prodanov, L., Jindal, R., Bale, S. S., Hegde, M., McCarty, W. J., Goldberg, I., et al. (2016). Long-term maintenance of a microfluidic 3D human liver sinusoid. *Biotechnol. Bioeng.* 113, 241–246. doi: 10.1002/bit.25700

Rowe, L., Almasri, M., Lee, K., Fogleman, N., Brewer, G. J., Nam, Y., et al. (2007). Active 3-D microscaffold system with fluid perfusion for culturing in vitro neuronal networks. *Lab. Chip* 7, 475–482. doi: 10.1039/b700795g

Saha, B., Mathur, T., Handley, K. F., Hu, W., Afshar-Kharghan, V., Sood, A. K., et al. (2020). OvCa-Chip microsystem recreates vascular endothelium–mediated platelet extravasation in ovarian cancer. *Blood Adv.* 4, 3329–3342. doi: 10.1182/bloodadvances.2020001632

Santhanam, N., Lee, K., Guo, X., Sommerhage, F., Cai, Y., Jackson, M., et al. (2018). Stem cell derived phenotypic human neuromuscular junction model for dose response evaluation of therapeutics. *Biomaterials* 166, 64–78. doi: 10.1016/j.biomaterials.2018.02.047

Sasserath, T., Rumsey, J. W., McAleer, C. W., Bridges, L. R., Long, C. J., Elbrecht, D., et al. (2020). Differential Monocyte Actuation in a Three-Organ Functional Innate Immune System-on-a-Chip. *Adv. Sci.* 7:2000323. doi: 10.1002/advs.202000323

Schimek, K., Busek, M., Brincker, S., Groth, B., Hoffmann, S., Lauster, R., et al. (2013). Integrating biological vasculature into a multi-organ-chip microsystem. *Lab. Chip* 13, 3588–3598. doi: 10.1039/c3lc50217a

Schulte, D., Küppers, V., Dartsch, N., Broermann, A., Li, H., Zarbock, A., et al. (2011). Stabilizing the VE-cadherin-catenin complex blocks leukocyte extravasation and vascular permeability. *EMBO J.* 30, 4157–4170. doi: 10.1038/emboj.2011.304

Shah, P., Fritz, J. V., Glaab, E., Desai, M. S., Greenhalgh, K., Frachet, A., et al. (2016). A microfluidics-based in vitro model of the gastrointestinal human-microbe interface. *Nat. Commun.* 7:11535.

Shanti, A., Teo, J., and Stefanini, C. (2018). In vitro immune organs-on-chip for drug development: a review. *Pharmaceutics* 10:278. doi: 10.3390/pharmaceutics10040278

Sharma, K., Dhar, N., Thacker, V. V., Simonet, T. M., Signorino-Gelo, F., Knott, G., et al. (2021). Dynamic persistence of intracellular bacterial communities of uropathogenic *Escherichia coli* in a human bladder-chip model of urinary tract infections. *bioRxiv* [Preprint]. doi: 10.1101/2021.01.03.424836

Shin, W., and Kim, H. J. (2018). Intestinal barrier dysfunction orchestrates the onset of inflammatory host-microbiome cross-talk in a human gut inflammation-on-a-chip. *Proc. Natl. Acad. Sci. U. S. A.* 115, E10539–E10547.

Sin, A., Chin, K. C., Jamil, M. F., Kostov, Y., Rao, G., and Schuler, M. L. (2004). The Design and Fabrication of Three-Chamber Microscale Cell Culture Analog Devices with Integrated Dissolved Oxygen Sensors. *Biotechnol. Prog.* 20, 338–345. doi: 10.1021/bp034077d

Smith, A. S. T., Long, C. J., Pirozzi, K., and Hickman, J. J. A. (2013). functional system for high-content screening of neuromuscular junctions in vitro. *Technology* 1, 37–48. doi: 10.1142/s2339547813500015

Smith, A. S. T., Long, C. J., Pirozzi, K., Najjar, S., McAleer, C., Vandenburgh, H. H., et al. (2014). A multiplexed chip-based assay system for investigating the functional development of human skeletal myotubes in vitro. *J. Biotechnol.* 0, 15–18. doi: 10.1016/j.jbiotec.2014.05.029

Son, K. J., Gheibi, P., Stybayeva, G., Rahimian, A., and Revzin, A. (2017). Detecting cell-secreted growth factors in microfluidic devices using bead-based biosensors. *Microsyst. Nanoeng.* 3:17025.

Srinivasan, B., Kolli, A. R., Esch, M. B., Abaci, H. E., Schuler, M. L., and Hickman, J. J. T. E. E. R. (2015). measurement techniques for in vitro barrier model systems. *J. Lab. Autom.* 20, 107–126. doi: 10.1177/2211068214561025

Sriram, G., Alberti, M., Dancik, Y., Wu, B., Wu, R., Feng, Z., et al. (2018). Full-thickness human skin-on-chip with enhanced epidermal morphogenesis and barrier function. *Mater. Today* 21, 326–340. doi: 10.1016/j.mattod.2017.11.002

Stroock, A. D., and Fischbach, C. (2010). Microfluidic Culture Models of Tumor Angiogenesis. *Tissue Eng. Part A* 16, 2143–2146. doi: 10.1089/ten.tea.2009.0689

Sun, W., Luo, Z., Lee, J., Kim, H.-J., Lee, K., Tebon, P., et al. (2019). Organ-on-a-Chip for Cancer and Immune Organs Modeling. *Adv. Healthc. Mater.* 8, 1–12.

Sung, J. H., Kam, C., and Shuler, M. L. A. (2010). microfluidic device for a pharmacokinetic–pharmacodynamic (PK–PD) model on a chip. *Lab. Chip* 10, 446–455. doi: 10.1039/b917763a

Sung, J. H., Srinivasan, B., Esch, M. B., McLamb, W. T., Bernabini, C., Schuler, M. L., et al. (2014). Using physiologically-based pharmacokinetic-guided 'body-on-a-chip' systems to predict mammalian response to drug and chemical exposure. *Exp. Biol. Med.* 239, 1225–1239. doi: 10.1177/1535370214529397

Sung, J. H., Wang, Y., and Shuler, M. L. (2019). Strategies for using mathematical modeling approaches to design and interpret multi-organ microphysiological systems (MPS). *APL Bioeng.* 3:021501. doi: 10.1063/1.5097675

Tatosian, D. A., and Shuler, M. L. A. (2009). novel system for evaluation of drug mixtures for potential efficacy in treating multidrug resistant cancers. *Biotechnol. Bioeng.* 103, 187–198. doi: 10.1002/bit.22219

Thomas, D., Burns, J., Audette, J., Carrol, A., Dow-Hygelund, C., and Hay, M. J. (2016). *Clinical Development Success Rates 2006-2015*. San Diego: Biomedtracker.

Tovaglieri, A., Sontheimer-Phelps, A., Geirnaert, A., Prantil-Baun, R., Camacho, D. M., Chou, D. B., et al. (2019). Species-specific enhancement of enterohemorrhagic E. coli pathogenesis mediated by microbiome metabolites. *Microbiome* 7:43.

Trapecar, M., Communal, C., Velazquez, J., Maass, C. A., Huang, Y.-J., Schneider, K., et al. (2020). Gut-Liver Physiomimetics Reveal Paradoxical Modulation of IBD-Related Inflammation by Short-Chain Fatty Acids. *Cell Syst.* 10, 223–239.e9.

Truong, D. D., Kratz, A., Park, J. G., Barrientos, E. S., Saini, H., Nguyen, T., et al. (2019). A Human Organotypic Microfluidic Tumor Model Permits Investigation of the Interplay between Patient-Derived Fibroblasts and Breast Cancer Cells. *Cancer Res.* 79, 3139–3151. doi: 10.1158/0008-5472.can-18-2293

Tsamandouras, N., Chen, W. L. K., Edington, C. D., Stokes, C. L., Griffith, L. G., and Cirit, M. (2017). Integrated gut and liver microphysiological systems for quantitative in vitro pharmacokinetic studies. *AAPS J.* 19, 1499–1512. doi: 10.1208/s12248-017-0122-4

Tucker, G. T., and Boas, R. A. (1971). Pharmacokinetic Aspects of Intravenous Regional Anesthesia. *Anesthesiology* 34, 538–549. doi: 10.1097/00000542-197106000-00014

Tufts Center for the Study of Drug Development. (2013). Causes of clinical failures vary widely by therapeutic class, phase of study. *Tufts CSDD Impact Rep.* 15, 1–4.

Umbach, J. A., Adams, K. L., Gundersen, C. B., and Novitch, B. G. (2012). Functional neuromuscular junctions formed by embryonic stem cell-derived motor neurons. *PloS One* 7:e36049. doi: 10.1371/journal.pone.0036049

Vernetti, L., Gough, A., Baetz, N., Blutt, S., Broughman, J. R., Brown, J. A., et al. (2017). Functional Coupling of Human Microphysiology Systems: intestine, Liver, Kidney Proximal Tubule, Blood-Brain Barrier and Skeletal Muscle. *Sci. Rep.* 7:44517.

Wagner, I., Materne, E.-M., Brincker, S., Süssbier, U., Frädrich, C., Busek, M., et al. (2013). A dynamic multi-organ-chip for long-term cultivation and substance testing proven by 3D human liver and skin tissue co-culture. *Lab. Chip* 13, 3538–3547. doi: 10.1039/c3lc50234a

Walter, F. R., Valkai, S., Kincses, A., Petneházi, A., Czeller, T., and Veszelka, S. (2016). A versatile lab-on-a-chip tool for modeling biological barriers. *Sens. Actuators B Chem.* 222, 1209–1219. doi: 10.1016/j.snb.2015.07.110

Wan, L., Neumann, C. A., and LeDuc, P. R. (2020). Tumor-on-a-chip for integrating a 3D tumor microenvironment: chemical and mechanical factors. *Lab. Chip* 20, 873–888. doi: 10.1039/c9lc00550a

Wang, H.-F., Ran, R., Liu, Y., Hui, Y., Zeng, B., Chen, D., et al. (2018). Tumor-Vasculature-on-a-Chip for Investigating Nanoparticle Extravasation and Tumor Accumulation. *ACS Nano* 12, 11600–11609. doi: 10.1021/acsnano.8b06846

Wang, K., Man, K., Liu, J., Liu, Y., Chen, Q., Zhou, Y., et al. (2020). Microphysiological Systems: design, Fabrication, and Applications. *ACS Biomater. Sci. Eng.* 6, 3231–3257. doi: 10.1021/acsbiomaterials.9b01667

Wang, Y. I., and Shuler, M. L. (2018). UniChip enables long-term recirculating unidirectional perfusion with gravity-driven flow for microphysiological systems. *Lab. Chip* 18, 2563–2574. doi: 10.1039/c8lc00394g

Wikswo, J. P. (2014). The relevance and potential roles of microphysiological systems in biology and medicine. *Exp. Biol. Med. Maywood NJ* 239, 1061–1072. doi: 10.1177/1535370214542068

Wilmer, M. J., Ng, C. P., Lanz, H. L., Vulto, P., Suter-Dick, L., and Masereeuw, R. (2016). Kidney-on-a-Chip Technology for Drug-Induced Nephrotoxicity Screening. *Trends Biotechnol.* 34, 156–170. doi: 10.1016/j.tibtech.2015.11.001

Wufuer, M., Lee, G., Hur, W., Jeon, B., Kim, B. J., Choi, T. H., et al. (2016). Skin-on-a-chip model simulating inflammation, edema and drug-based treatment. *Sci. Rep.* 6:37471.

Xiao, S., Coppeta, J. R., Rogers, H. B., Isenberg, B. C., Zhu, J., Olalekan, S. A., et al. (2017). A microfluidic culture model of the human reproductive tract and 28-day menstrual cycle. *Nat. Commun.* 8:14584.

Yang, Y., Fathi, P., Holland, G., Pan, D., Wang, N. S., and Esch, M. B. (2019). Pumpless microfluidic devices for generating healthy and diseased endothelia. *Lab. Chip* 19, 3212–3219. doi: 10.1039/c9lc00446g

Yi, H.-G., Jeong, Y. H., Kim, Y., Choi, Y.-J., Moon, H. E., Park, S. H., et al. (2019). A bioprinted human-glioblastoma-on-a-chip for the identification of patient-specific responses to chemoradiotherapy. *Nat. Biomed. Eng.* 3, 509–519. doi: 10.1038/s41551-019-0363-x

Zeilinger, K., Freyer, N., Damm, G., Seehofer, D., and Knöspel, F. (2016). Cell sources for in vitro human liver cell culture models. *Exp. Biol. Med.* 241, 1684–1698. doi: 10.1177/1535370216657448

Zhang, C., Zhao, Z., Rahim, N. A. A., Noort, D., and Yu, H. (2009). Towards a human-on-chip: culturing multiple cell types on a chip with compartmentalized microenvironments. *Lab. Chip* 9, 3185–3192. doi: 10.1039/b915147h

Zhang, J., Huang, Y.-J., Yoon, J. Y., Kemmitt, J., Wright, C., Schneider, K., et al. (2021). Primary Human Colonic Mucosal Barrier Crosstalk with Super Oxygen-Sensitive Faecalibacterium prausnitzii in Continuous Culture. *Med* 2, 74–98.e9.

Zhang, S., Wan, Z., and Kamm, R. D. (2021). Vascularized organoids on a chip: strategies for engineering organoids with functional vasculature. *Lab. Chip* 21, 473–488. doi: 10.1039/d0lc01186j

Zhao, Y., Kankala, R. K., Wang, S.-B., and Chen, A.-Z. (2019). Multi-Organs-on-Chips: towards Long-Term Biomedical Investigations. *Molecules* 24:675. doi: 10.3390/molecules24040675

**Author Disclaimer:** ‡Certain commercial entities, equipment or materials may be identified in this document to describe an experimental procedure or concept adequately. Such identification is not intended to imply recommendation or endorsement by the National Institute of Standards and Technology, nor is it intended to imply that the entities, materials, or equipment are necessarily the best available for the purpose.

**Conflict of Interest:** The authors declare that the research was conducted in the absence of any commercial or financial relationships that could be construed as a potential conflict of interest.

**Publisher's Note:** All claims expressed in this article are solely those of the authors and do not necessarily represent those of their affiliated organizations, or those of the publisher, the editors and the reviewers. Any product that may be evaluated in this article, or claim that may be made by its manufacturer, is not guaranteed or endorsed by the publisher.

frontiers in Cell and Developmental Biology

ORIGINAL RESEARCH
published: 29 September 2021
doi: 10.3389/fcell.2021.728707

# Human Induced Pluripotent Stem Cell-Derived TDP-43 Mutant Neurons Exhibit Consistent Functional Phenotypes Across Multiple Gene Edited Lines Despite Transcriptomic and Splicing Discrepancies

*Alec S. T. Smith[1,2], Changho Chun[3], Jennifer Hesson[2,4], Julie Mathieu[2,4], Paul N. Valdmanis[5], David L. Mack[1,2,3,6], Byung-Ok Choi[7,8,9], Deok-Ho Kim[3,10,11,12]* and Mark Bothwell[1,2]**

[1] Department of Physiology and Biophysics, University of Washington, Seattle, WA, United States, [2] Institute for Stem Cell and Regenerative Medicine, University of Washington, Seattle, WA, United States, [3] Department of Bioengineering, University of Washington, Seattle, WA, United States, [4] Department of Comparative Medicine, University of Washington, Seattle, WA, United States, [5] Division of Medical Genetics, University of Washington, Seattle, WA, United States, [6] Department of Rehabilitation Medicine, University of Washington, Seattle, WA, United States, [7] Department of Neurology, Samsung Medical Center, Sungkyunkwan University School of Medicine, Seoul, South Korea, [8] Stem Cell and Regenerative Medicine Institute, Samsung Medical Center, Seoul, South Korea, [9] Department of Health Sciences and Technology, The Samsung Advanced Institute for Health Sciences & Technology (SAIHST), Sungkyunkwan University, Seoul, South Korea, [10] Department of Biomedical Engineering, Johns Hopkins University, Baltimore, MD, United States, [11] Department of Medicine, Johns Hopkins University School of Medicine, Baltimore, MD, United States, [12] Department of Neurology, Johns Hopkins University School of Medicine, Baltimore, MD, United States

Gene editing technologies hold great potential to enhance our ability to model inheritable neurodegenerative diseases. Specifically, engineering multiple amyotrophic lateral sclerosis (ALS) mutations into isogenic cell populations facilitates determination of whether different causal mutations cause pathology *via* shared mechanisms, and provides the capacity to separate these mechanisms from genotype-specific effects. As gene-edited, cell-based models of human disease become more commonplace, there is an urgent need to verify that these models constitute consistent and accurate representations of native biology. Here, commercially sourced, induced pluripotent stem cell-derived motor neurons from Cellular Dynamics International, edited to express the ALS-relevant mutations TDP-43$^{M337V}$ and TDP-43$^{Q331K}$ were compared with in-house derived lines engineered to express the TDP-43$^{Q331K}$ mutation within the WTC11 background. Our results highlight electrophysiological and mitochondrial deficits in these edited cells that correlate with patient-derived cells, suggesting a consistent cellular phenotype arising from TDP-43 mutation. However, significant differences in the transcriptomic profiles and splicing behavior of the edited cells underscores the need for careful comparison of multiple lines when attempting to use these cells as a means to better understand the onset and progression of ALS in humans.

**Keywords: ALS (amyotrophic lateral sclerosis), iPSC (induced pluripotent stem cell), transcriptomics, electrophysiologic analysis, disease model**

OPEN ACCESS

***Edited by:***
*Ian Ellis,*
*University of Dundee, United Kingdom*

***Reviewed by:***
*Basant K. Patel,*
*Indian Institute of Technology Hyderabad, India*
*Simon David Topp,*
*King's College London, United Kingdom*

***Correspondence:**
*Deok-Ho Kim*
*dhkim@jhu.edu*
*Mark Bothwell*
*mab@uw.edu*

***Specialty section:***
*This article was submitted to Stem Cell Research, a section of the journal Frontiers in Cell and Developmental Biology*

***Received:*** *21 June 2021*
***Accepted:*** *06 September 2021*
***Published:*** *29 September 2021*

***Citation:***
*Smith AST, Chun C, Hesson J, Mathieu J, Valdmanis PN, Mack DL, Choi B-O, Kim D-H and Bothwell M (2021) Human Induced Pluripotent Stem Cell-Derived TDP-43 Mutant Neurons Exhibit Consistent Functional Phenotypes Across Multiple Gene Edited Lines Despite Transcriptomic and Splicing Discrepancies. Front. Cell Dev. Biol. 9:728707. doi: 10.3389/fcell.2021.728707*

## INTRODUCTION

Amyotrophic lateral sclerosis (ALS) is a clinically and genetically heterogeneous neurodegenerative disease with an incidence rate of roughly 1 in 50,000 people (Chiò et al., 2013). It manifests as degenerative changes (and eventual loss) of upper and lower motor neurons, leading to progressive muscular atrophy and weakness, increased fatigue, and problems with swallowing that typically result in respiratory failure and death. The condition is currently incurable and carries significant personal, societal, and economic burden (Lopez-Bastida et al., 2009; Schepelmann et al., 2010). Riluzole and Edaravone are the only drugs in the United States or Europe currently licensed for use in ALS patients but they are typically only capable of prolonging life by a few months (Bensimon et al., 1994; Petrov et al., 2017; Jackson et al., 2019; Shefner et al., 2019).

There is an urgent need to develop novel therapeutic options capable of ameliorating ALS symptoms or slowing disease progression to improve patient care and quality of life. It is envisioned that greater mechanistic understanding of ALS etiology will enable the identification of suitable biomarkers and therapeutic targets, which will in turn lead to the development of novel treatments. However, the clinical and genetic heterogeneity inherent to ALS pathophysiology makes accurate modeling of the disease difficult and reduces the predictive power of current preclinical animal and cell-based models (Benatar, 2007; Scott et al., 2008; Marangi and Traynor, 2015; Grad et al., 2017).

Induced pluripotent stem cell (iPSC)-based motor neuron models have significantly increased our capacity to model ALS, as well as other neurodegenerative diseases, in human cells (Liu and Deng, 2016; Pasteuning-Vuhman et al., 2020). Recent advances in gene editing techniques hold the potential to further expand these capabilities by enabling the study of phenotypic changes caused by multiple ALS-relevant mutations expressed against consistent background genotypes and in reference to isogenic controls (Heman-Ackah et al., 2016). Such models are now enabling detailed analysis of disease progression *in vitro*, as well as comparison of phenotypic differences across multiple causal mutations to isolate common ALS etiological features from mutation specific effects.

As promising as these technologies are, there remains a need to ensure that the gene editing strategies utilized to create ALS-relevant lines produce cells that are not only accurate representations of the human disease but also exhibit consistent phenotypes regardless of the editing strategy employed (Berry et al., 2018). This is particularly important for commercially sourced cells, that are likely to be more widely adopted than those created in academic labs, and certainly a favored option for drug companies due to ease of scaling and consistency considerations. To address these concerns, this manuscript aims to characterize the phenotype of commercially sourced motor neurons bearing two ALS-relevant mutations in the TDP-43 gene, *TARDBP*. Both the Q331K and the M337V variants were provided by Cellular Dynamics International (CDI) and were created using nuclease-mediated engineering that employed the same nuclease but was based on separate donor templates. Each mutant line was engineered from the same iPSC source used to produce their wild type iCell motor neuron line. The phenotypes of these cells were directly compared to that of an in house engineered line expressing the TDP-43$^{Q331K}$ mutation in the WTC11 genotype. Analysis revealed consistent deficits in electrophysiological metrics, mitochondrial structure, and metabolic function in these engineered lines that correlated with results from patient-derived sources and previous studies. However, RNA-seq analysis revealed significant differences in gene expression profiles and splicing behavior between the commercial and in house developed mutant lines. Most notably, differences in stathmin-2 splice activity and *CHCHD2* expression patterns highlight the phenotypic inconsistency exhibited by these gene edited iPSC-derived motor neurons. The presence of significant transcriptomic differences between iPSC-derived motor neurons edited to express the same mutation in TDP-43 highlights the need for caution when attempting to define any observed phenotypes as representative of ALS cellular pathology.

## RESULTS

### Establishment of TDP-43 Mutant Induced Pluripotent Stem Cell Lines and Confirmation of a Motor Neuron Phenotype in Differentiated Cells

Cellular Dynamics International markets human iPSC-derived motor neurons bearing two distinct gene edited point mutations in the *TARDBP* locus, producing heterozygous TDP-43$^{M337V}$ and TDP$^{Q331K}$ genotypes (**Supplementary Figure 1**). In order to compare the phenotype of these cells to those subjected to a different CRISPR-based engineering strategy, a TDP-43$^{Q331K+/-}$ mutation was engineered into the widely used WTC11 iPSC line (Kreitzer et al., 2013; Miyaoka et al., 2014). The Q331K variant was chosen in this instance as it generated a stronger phenotype in a transgenic mouse line than a similar transgenic line expressing the M337V variant (Arnold et al., 2013). A schematic diagram of the genome editing strategy used to introduce the Q331K point mutation into the *TARDBP* locus of human WTC11 iPSCs is provided in **Figure 1A**. Using this strategy, a cytosine base was replaced with an adenine, resulting in a precision point mutation of Glutamine to Lysine at position 331 (CAG- > AAG) in the translated amino acid sequence. This was confirmed by Sanger sequencing of the target site (**Figure 1B**). TDP-43$^{Q331K+/-}$ heterozygous clones were selected for subsequent expansion to facilitate direct comparisons with the commercial lines and to increase the clinical relevance of any phenotypic observations as familial ALS patients typically harbor heterozygous disease-causing mutations in their genomes. All selected clones were karyotyped prior to further expansion and were found to bear normal XY karyotypes (**Figure 1C**).

Human iPSC cultures were differentiated into regionally unspecified neural progenitor cells using a monolayer differentiation method adapted from Shi et al. (2012). These cells were subsequently exposed to culture conditions promoting differentiation toward a ventral, spinal phenotype, essentially as described by Amoroso et al. (2013). This protocol led to the

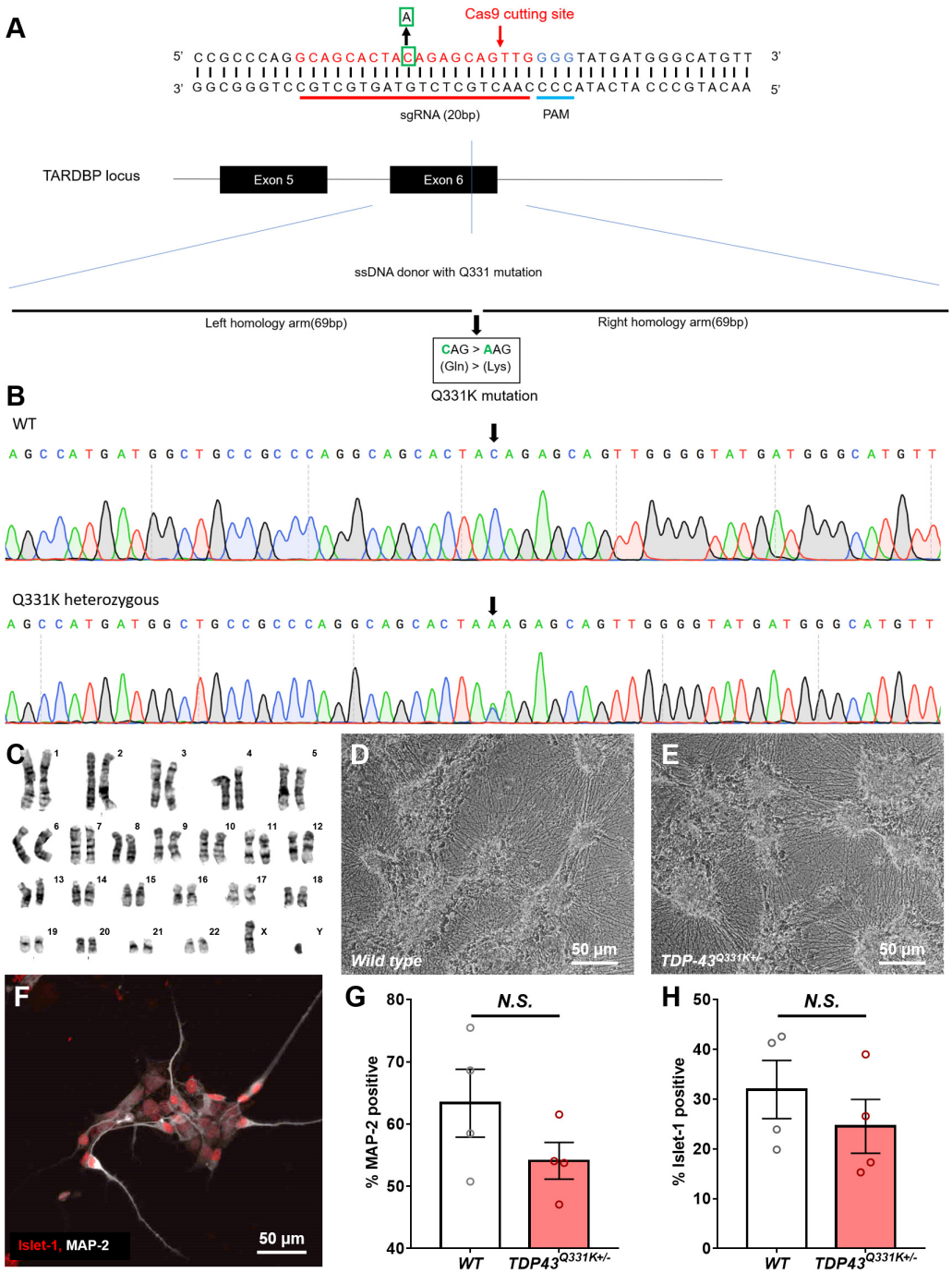


**FIGURE 1 |** Production of a CRISPR-edited TDP-43$^{Q331K+/-}$ mutant WTC11 iPSC line and its subsequent differentiation into motor neurons. **(A)** Schematic diagram of the genome editing strategy used to introduce a Q331K point mutation into the *TARDBP* locus of human WTC11 iPSCs. The sgRNA is marked in red, and the PAM sequence is presented in blue. The Cas9 cutting site in exon 6 of human *TARDBP* is indicated by a red arrow. The base C in the green square is replaced with an A, thus resulting in Gln331Lyss (CAG- > AAG), producing a single precision point mutation. The long sequence below is a single stranded DNA (ssDNA) donor with the desired mutation and homologous arms (left 69 bp and right 69 bp). **(B)** Sequencing data confirming the presence of a heterozygous point mutation (C- > A) in the examined WTC11 line, facilitating the Gln331Lys mutation in the translated amino acid sequence. **(C)** Karyotype analysis of our CRISPR-edited *TDP-43*$^{Q331K+/-}$ WTC11 line, illustrating a normal male karyotype following gene editing. **(D,E)** Bright field images of wild type and *TDP-43*$^{Q331K+/-}$ mutant motor neurons differentiated from WTC11 iPSCs. Images were collected at day 45 post-induction. **(F)** Immunocytochemical stain, illustrating positive staining for the motor neuron-specific marker Islet-1 in our human motor neurons differentiated in house from WTC11 iPSCs. **(G,H)** Percentage of MAP-2 and Islet-1 positive cells present in wild type and *TDP-43*$^{Q331K+/-}$ mutant WTC11 populations subjected to our motor neuron differentiation protocol. Observed differences were not statistically significant between groups (N.S.). Analysis was performed at 26 days post-induction.

development of cells bearing a distinct neuronal morphology, characterized as multipolar cell bodies supporting extensive neuritic outgrowth (**Figures 1D,E**). These cells stained positive for the motor neuron-specific transcription factor Islet 1 (**Figure 1F**), indicating successful commitment to the motor neuron lineage. Immunocytochemical analysis of these cultures found that 63 ± 5.5% of the wild type population were positive for the pan neuronal marker microtubule associated protein 2 (MAP-2), whereas 32 ± 5.9% were positive for Islet-1. Similarly, populations derived from the TDP-$43^{Q331K+/-}$ line were found to be 54 ± 3.0% positive for MAP-2 and 25 ± 5.4% positive for Islet-1. All Islet-1 positive cells examined also stained positive for MAP-2 in populations derived from both lines and observed differences in Islet-1 expression levels between mutant and control populations were not found to be statistically significant (**Figures 1G,H**).

Previous studies have shown that iPSC-derived motor neurons bearing ALS relevant *TARDBP* mutations exhibit significant levels of translocation of the TDP-43 protein from the normal nuclear location to the cytoplasm, associated with disruption of nuclear RNA splicing functions and with the formation of potentially toxic cytoplasmic aggregates (Winton et al., 2008; Zhang et al., 2009). This phenomenon resembles the TDP-43 proteinopathy reported in the vast majority of ALS patients and serves as an important indicator of correct disease recapitulation in cell-based models of the disease. In order to test whether the described CRISPR-edited WTC11 TDP-$43^{Q331K+/-}$ line exhibited similar features, cells were stained and examined for TDP-43 subcellular localization. While all TDP-43 staining was restricted to the nucleus in wild type controls, mutant neurons displayed substantial levels of cytoplasmic staining and the emergence of distinct puncta indicative of protein aggregate formation (**Figures 2A,B**). Quantification of cytoplasmic intensity using ImageJ highlighted significant increases in TDP-43 positivity levels outside of the nucleus in TDP-43 mutant cells compared with wild type controls (**Figure 2C**).

Association of TDP-43 with cytoplasmic stress granules may contribute to seeding of cytoplasmic TDP-43 aggregation (Khalfallah et al., 2018) and oxidative stress likewise promotes cytoplasmic redistribution of TDP-43 (Zuo et al., 2021), suggesting that cellular stress may be an important determinant of TDP-43 redistribution. Our motor neuron differentiation protocol involves the replating of cells at multiple stages and relies on mechanical trituration to break up cell clusters during passage, leading us to ask whether the mechanical stress of our culture methods might influence cytoplasmic accumulation of TDP-43. To address this question, parallel differentiations were conducted using enzymatic dissociation with TrypLE instead of mechanical dissociation and the resulting levels of cytoplasmic TDP-43 were then quantified (**Figure 2D**). Results indicate that mechanical trituration during differentiation of iPSCs expressing mutant TDP-43 led to significant increases in TDP-43 aggregation. A small increase in cytoplasmic TDP-43 aggregation in mechanically triturated wild type controls was not found to bear statistical significance. Enzymatically dissociated mutant cells still exhibited a small but significant increase in cytoplasmic TDP-43 expression compared to wild type but this difference was substantially smaller than that observed in mechanically dissociated cells.

## Comparison of Splice Activity and Transcriptomes in Commercially Sourced and In-House Generated CRISPR-Edited Amyotrophic Lateral Sclerosis Lines

Bulk RNA-seq was performed on differentiated CDI and WTC11 populations. While presence of the Q331K mutation was confirmed for the WTC11 mutant line by Sanger Sequencing during its derivation, no similar confirmation had been performed for the commercial cells. We therefore began by confirming the presence of the M337V and Q331K mutations in the respective CDI lines prior to any downstream analysis using the raw RNA-seq reads (**Supplementary Table 1**).

Once presence of the mutations was confirmed in all lines, RNA-seq datasets were then used to compare and contrast the transcriptomes of TDP-43 wild type and mutant neurons derived from these sources (**Supplementary Table 2**). As expected, preliminary analysis of normalized expression values indicated that both CDI and WTC11 cultures exhibited strong expression of typical motor neuron markers such as Islet1 and choline acetyltransferase (ChAT). Conversely, expression of stem cell markers was notably absent, confirming the efficiency of the differentiation protocols employed for each cell type. Unsurprisingly, substantial expression of markers of V1, V2, and V3 ventral spinal cord interneurons were present in both CDI and WTC11 cultures, although the proportion of different interneuron classes differed. Both cultures were devoid of markers of astrocytes, but expressed substantial levels of an oligodendrocyte marker.

Gene ontology (GO) biological process enrichment analysis was used to compare TDP-43 mutant cell lines for changes in cell signaling (relative to their control cell lines) (**Figures 3A–F**). WTC11 wild type and mutant lines exhibited significant differences in processes related to cell cycle, likely indicating differing levels of contaminating proliferating cells in the examined cultures. CDI cells showed no such contamination, thereby confirming the presence of a purer population. Despite this difference, consistent changes were observed, including down regulation of processes governing nervous system development in both CDI and WTC11 *TDP-43*$^{Q331K+/-}$ mutants and upregulation of angiogenic and hypoxic processes across all mutant cell types examined. This consistency, despite differing levels of contaminating proliferating cells likely indicate these altered processes as significant in contributing to ALS cellular pathology in *TDP-43*$^{Q331K+/-}$ mutant neurons. In the CDI lines, more biological processes were affected in the Q331K variant compared with M337V mutant cells; a result that likely reflects the stronger phenotype observed in Q331K mutant mice (Arnold et al., 2013).

Previous studies have indicated that ALS-associated TDP-43 mutations or TDP-43 proteinopathy associated with non-familial ALS cause mis-splicing of *STMN2* gene transcripts, splicing

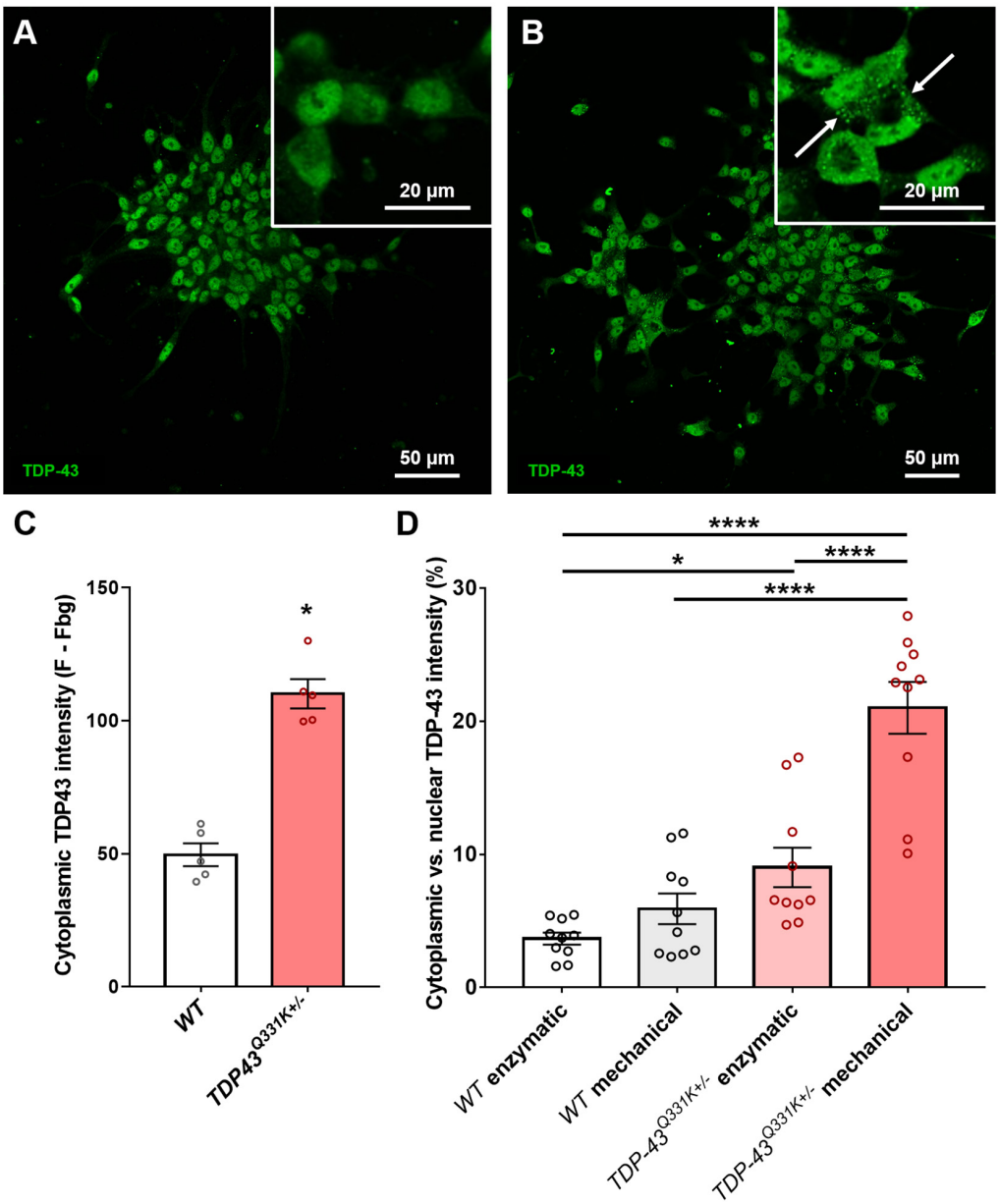


**FIGURE 2 |** Quantification of TDP-43 cytosolic translocation in WTC11 wild type and *TDP-43*$^{Q331K+/-}$ iPSC-derived motor neuron populations. **(A,B)** Immunocytochemical stains for TDP-43 in motor neuron populations differentiated in house from both wild type and *TDP-43*$^{Q331K+/-}$ mutant WTC11 iPSCs. Mutant cells exhibited significant levels of cytoplasmic staining, indicating translocation of the protein from its normal nuclear location (white arrows). **(C)** Quantification of the comparative levels of cytoplasmic TDP-43 staining observed in mutant cells and wild type (*WT*) controls. **(D)** Levels of cytoplasmic TDP-43 (expressed as a percentage of signal intensity measured in nuclei) observed in wild type and mutant neurons exposed to either mechanical or enzymatic dissociation during differentiation. Analysis was performed at 25 days post-induction, with passaging performed at day 20. *$p < 0.05$, ****$p < 0.0001$.

in a cryptic exon that results in greatly diminished steady-state levels of stathmin-2 mRNA and protein (Melamed et al., 2019). Consequently, we examined RNA-seq data for evidence of expression of the *STMN2* cryptic exon (**Figure 3G**). WTC11 *TDP-43*$^{Q331K+/-}$ motor neurons expressed small amounts of the *STMN2* cryptic exon while wild type cells did not. Conversely, *STMN2* cryptic exon expression was absent in both *TDP-43*$^{M337V+/-}$ and *TDP-43*$^{Q331K+/-}$ motor neurons from CDI (**Supplementary Figure 2**), highlighting a significant deviation in phenotype from both the WTC11 lines examined in this study and those discussed in previous work. These results were confirmed by RT-qPCR, which showed significant upregulation of transcripts bearing the cryptic exon in WTC11 mutant neurons compared with controls. Although these mutant neurons exhibited greater expression of transcripts bearing the cryptic exon, the proportion of such transcripts was not

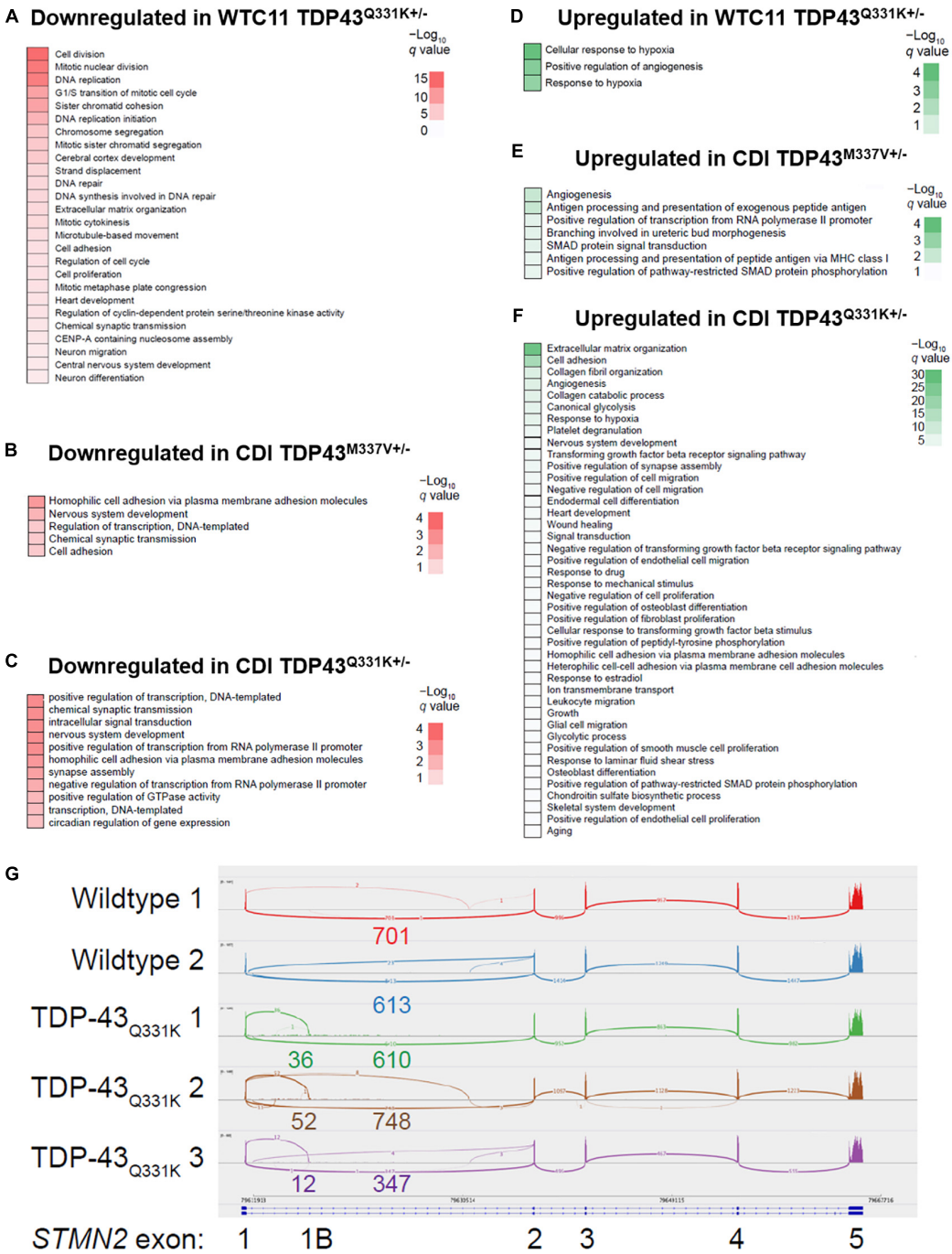


**FIGURE 3 |** Effects of TDP-43 mutation on gene expression profiles and *STMN2* splicing behavior in CDI versus WTC11 motor neuron populations. **(A)** Gene ontology (GO) enrichment for genes downregulated in WTC11 TDP-43$^{Q331K+/-}$ mutant samples compared with wild type controls. **(B)** GO enrichment for genes downregulated in CDI TDP-43$^{M337V+/-}$ mutant samples compared with wild type controls. **(C)** GO enrichment for genes downregulated in CDI TDP-43$^{Q331K+/-}$ mutant samples compared with wild type controls. **(D)** GO enrichment for genes upregulated in WTC11 TDP-43$^{Q331K+/-}$ mutant samples compared with wild type controls. **(E)** GO enrichment for genes upregulated in CDI TDP-43$^{M337V+/-}$ mutant samples compared with wild type controls. **(F)** GO enrichment for genes upregulated in CDI TDP-43$^{Q331K+/-}$ mutant samples compared with wild type controls. **(G)** Integrated Genome Viewer Sashimi plot of splicing at STMN2. Three replicates of the TDP-43$^{Q331K+/-}$ line demonstrate skipping to an intronic sequence.

sufficient to diminish the total quantity of STMN2 mRNA expressed. As mis-splicing of the STMN2 cryptic exon is believed to result from redistribution of TDP-43 from the nucleus to cytoplasm (Prudencio et al., 2020), the lack of mis-splicing in the CDI neurons is consistent with lack of cytoplasmic TDP-43 observed in these cells.

## Comparison of Electrophysiological Phenotypes Between Commercially Sourced and In-House Generated CRISPR-Edited Amyotrophic Lateral Sclerosis Lines

Given the differences in transcriptome and *STMN2* splicing behavior between CDI and WTC11 motor neuron populations, electrophysiological characterization was sought as a means to compare functional development in these lines. Whole cell patch clamp was used to assess CDI cell action potential firing properties at 21 days post-thaw. This timepoint was selected as preliminary analysis indicated that a 3-week culture was necessary to promote the adoption of a mature electrophysiological phenotype in wild type controls (**Supplementary Figure 3**). In-house differentiated cells were examined at days 45–50 (and day 90) post-induction as initial studies indicated that length of culture was required for wild type controls to reach comparable functionality to that of their CDI counterparts.

Cells were binned based on their capacity to elicit repetitive action potential trains in response to 500 ms depolarizing current injections as previously described (Devlin et al., 2015; **Figure 4A**). TDP-43$^{Q331K+/-}$ WTC11 motor neurons showed comparable levels of function to wild type controls at day 50, with roughly 50% of patched cells exhibiting repetitive firing behavior (**Figure 4B**). Cells at day 90 showed a substantial decrease in repetitive activity in mutant cells compared with controls, indicating a progressive loss of function that mirrors previously reported results (Devlin et al., 2015; **Figure 4C**). In CDI cells, the TDP-43$^{M337V+/-}$ line exhibited no significant change in firing patterns at day 21, whereas the TDP-43$^{rmQ331K+/-}$ line displayed levels of function comparable to WTC11 mutant cells at day 90 (**Figure 4D**). In addition, both the M337V and the Q331K variants exhibited significantly more depolarized resting membrane potentials (RMPs) compared with wild type controls (**Figure 4E**); a hallmark indicator of poorer functional development and stability in cultured neurons. Specifically, average RMP in wild type cells was $-54.8 \pm 2.0$ mV, compared with $-45.6 \pm 2.6$ and $-43.7 \pm 2.6$ mV in M337V and Q331K variants, respectively. No change in RMP was observed in WTC11 mutant cells at either day 50 or day 90 post-induction (**Supplementary Figure 4**).

Further characterization of TDP-43 mutant motor neuron electrophysiology was performed using multielectrode arrays (MEAs) in order to probe how altered action potential firing properties manifest at the population level. Following 21 days culture on MEAs (**Supplementary Figure 5**), CDI cells bearing M337V and Q331K mutations exhibited significant differences in population level function, with a notable decrease in burst fire behavior but an increase in burst duration and weighted mean firing rates (**Figures 4F–H**). Specifically, burst fire behavior was measured at $24.2 \pm 3.3$ bursts per minute (bpm) in wild type cells, $12.6 \pm 2.5$ bpm in M337V mutants, and $13.9 \pm 1.5$ bpm in Q331K populations. Burst durations were measured at $0.27 \pm 0.01$ s for wild type cells, $0.45 \pm 0.05$ s for M337V cells, and $0.59 \pm 0.03$ s for Q331K mutants. Overall weighted mean firing was recorded at $0.93 \pm 0.15$ Hz for wild type, $1.19 \pm 0.23$ Hz for M337V, and $1.63 \pm 0.15$ Hz for Q331K. A burst of neuronal activity is defined as a recording period where the time between detected depolarizing spikes is less than 100 ms for a minimum of 10 consecutive spikes (Chiappalone et al., 2005; Kapucu et al., 2012). Increased burst behavior is associated with maturing neuronal networks (Chiappalone et al., 2005) and a strong indicator of functional competency in cultured neurons. The observation that fewer bursts occurred in examined cultures, but that these events were longer once initiated, was noteworthy as it suggests an overall drop in spontaneous neuronal activation in mutant cells, but an increase in repetitive firing once activated, potentially mirroring hyperexcitability of ALS central and peripheral neurons in patients (Wainger et al., 2014; Noto et al., 2016; Do-Ha et al., 2018). WTC11-derived motor neuron populations exhibited a similar reduction in burst firing behavior in mutant cells ($104.2 \pm 21.9$ bpm for wild type versus $25.5 \pm 4.2$ bpm for Q331K mutants) as well as a trend toward increased burst duration in the Q331K variants ($0.22$ s $\pm 0.008$ for wild type and $0.25 \pm 0.011$ s for Q331K mutants; **Figures 4I–K**). Interestingly, weighted mean firing rate was reduced in WTC11 mutant cells but increased in CDI mutant lines compared with controls. This difference may reflect the significant difference in baseline firing rates between WTC11 and CDI control cells. Since the burst incidence rate was substantially higher in the WTC11 line, the significant reduction in burst activity observed in both mutant populations may have had a more drastic impact on the overall mean firing rate for the WTC11 cells than it did for the CDI neurons.

*In vivo*, spinal cord motor neurons synapse directly with skeletal muscle fibers and therefore should not form functional networks in culture. As such, the presented burst fire data likely indicate the presence of an interneuron population in the WTC11 cultures, which would facilitate network development and lead to the observed bursting behavior. Initial characterization of differentiated motor neurons revealed that the proportion of cells expressing the pan-neuronal marker MAP-2 was greater than the proportion of cells expressing the motor neuron marker, Islet-1, supporting this conclusion. Analysis of bulk RNA-seq data (discussed above) confirmed significant expression (relative to motor neuron-specific Islet1 expression) of V2a/V2b interneuron markers as well as lower expression of V3 markers in these cell populations.

## Analysis of Mitochondrial Structure and Metabolic Function in Commercially Sourced and In-House Generated CRISPR-Edited Amyotrophic Lateral Sclerosis Lines

To further compare and contrast the cellular phenotypes exhibited by CRISPR-edited TDP-43 mutant motor neurons from CDI and WTC11 sources, the structure and function of resident mitochondria were examined. Given the importance of metabolic dysfunction in contributing to ALS disease onset and progression (Tefera and Borges, 2017), the capacity for CRISPR-edited cell-based models of the disease to recapitulate this

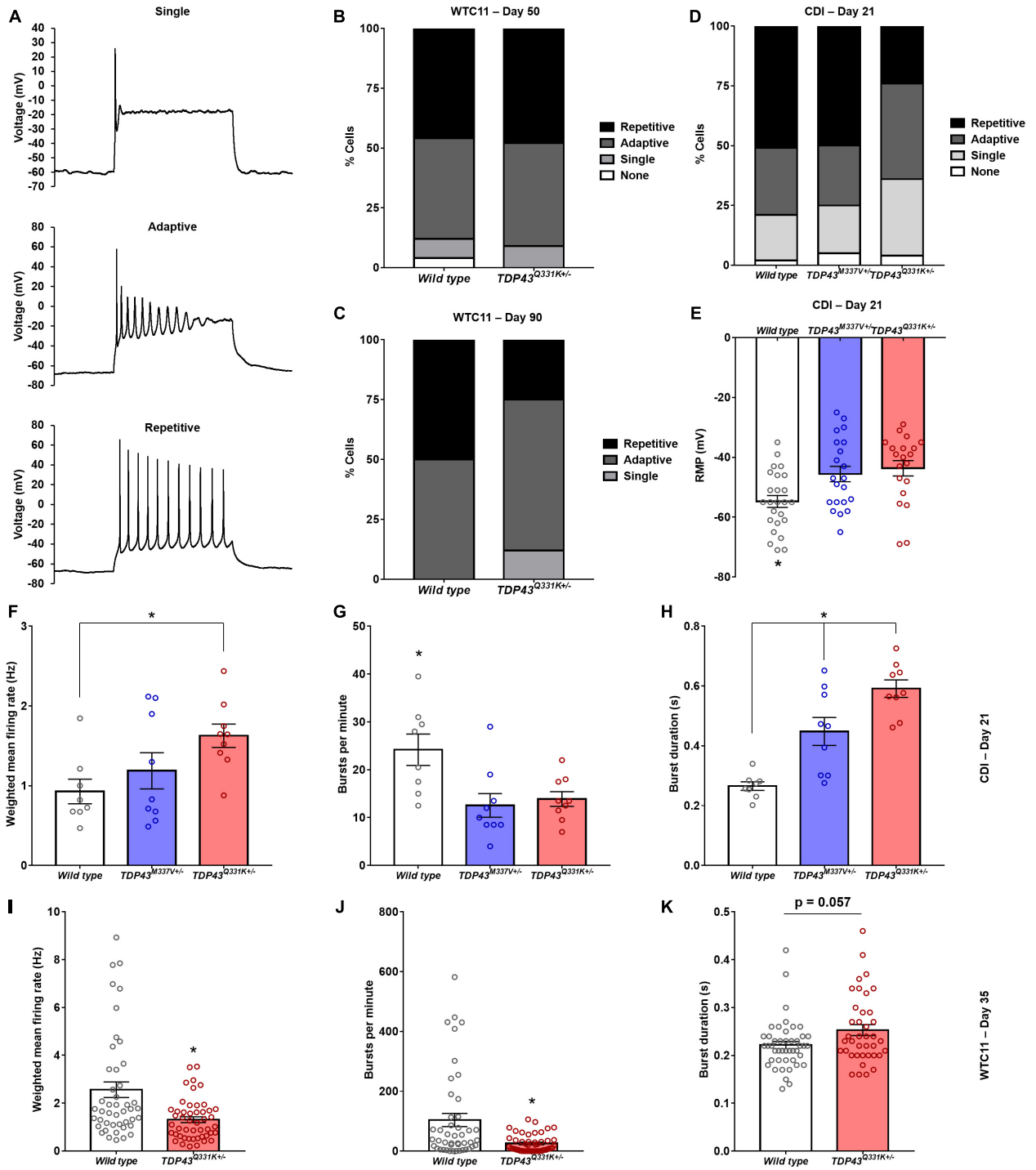


**FIGURE 4 |** Electrophysiological assessment of WTC11 and CDI iPSC-derived motor neuron function. **(A)** Representative action potential firing properties recorded from CDI iPSC-derived motor neurons illustrating increasing functional maturation. **(B)** Percentage of WTC11 cells from wild type ($n$ = 25) and TDP-43$^{Q331K+/-}$ ($n$ = 20) motor neuron populations exhibiting different action potential firing behaviors during whole cell patch clamp analysis at day 50 post-induction. A contingency table comparing cell type against firing behavior found that the two factors were not significantly related ($p$ = 0.25), suggesting that frequency of firing type occurrence within each population is not dependent on the cell type examined at this timepoint. **(C)** Analysis of WTC11 motor neuron firing types at day 90 post-induction. At this time point, a contingency table comparing cell type against firing behavior found that the two factors were significantly related ($p < 0.0001$), suggesting that frequency of firing type occurrence within each population is dependent on the cell type examined. **(D)** Percentage of CDI cells from wild type ($n$ = 43), TDP-43$^{M337V+/-}$ ($n$ = 20), and TDP-43$^{Q331K+/-}$ ($n$ = 25) motor neuron populations exhibiting different action potential firing behaviors during whole cell patch clamp analysis at 21 days post-thaw. A contingency table comparing cell type against firing behavior found that the two factors were significantly

*(Continued)*

**FIGURE 4 |** (Continued)
related ($p$ = 0.0018), suggesting that frequency of firing type occurrence within each population is dependent on the cell type examined. **(E)** Resting membrane potentials measured from CDI wild type and mutant TDP-43 mutant motor neurons by whole cell patch clamp at 21 days post-thaw. *$p \leq 0.017$. **(F)** Spontaneous rate of fire recorded from CDI motor neuron populations maintained on microelectrode arrays (MEAs). *$p$ = 0.034. **(G)** Spontaneous burst fire behavior recorded from CDI motor neuron populations maintained on MEAs. *$p \leq 0.021$. **(H)** Duration of spontaneous burst activity recorded from CDI motor neuron populations maintained on MEAs. *$p \leq 0.015$. For panels **(F–H)**, the timepoint examined is 21 days post-thaw and $n$ = 8 (wild type) or 9 (TDP-43$^{M337V+/-}$ and TDP-43$^{Q331K+/-}$). **(I)** Spontaneous rate of fire recorded from WTC11 motor neuron populations maintained on MEAs. *$p$ = 0.0004. **(J)** Spontaneous burst fire behavior recorded from WTC11 motor neuron populations maintained on MEAs. *$p$ = 0.0005. **(K)** Duration of spontaneous burst activity recorded from WTC11 motor neuron populations maintained on MEAs. *$p$ = 0.057. For panels **(I–K)**, the timepoint examined is 35 days post-induction and $n$ = 45 (wild type) or 48 (TDP-43$^{Q331K+/-}$).

pathological feature is an important point to verify. Furthermore, GO biological process analysis of the collected RNA-seq data highlighted consistent alterations to pathways regulating hypoxia in both CDI and WTC11 neurons, underscoring the need to characterize mitochondrial phenotype in these cells.

Transmission electron microscope (TEM) images were collected from wild type and TDP-43 mutant samples to characterize morphological differences in mitochondria resident within these cells (**Figures 5A–C**). In the CDI lines, a significant increase in cross-sectional area, along with a decrease in circularity, was observed in the mitochondria of mutant cells (**Figures 5D,E**). Specifically, average cross-sectional area in wild type CDI neurons was measured as $0.14 \pm 0.009$ versus $0.18 \pm 0.012$ and $0.19 \pm 0.010$ $\mu m^2$ in M337V and Q331K variants, respectively. Circularity in wild type cells was measured as $0.62 \pm 0.02$ versus $0.50 \pm 0.02$ and $0.56 \pm 0.02$ in M337V and Q331K variants, respectively.

In addition to these readouts, mitochondria were binned as possessing "normal" or "altered" cristae structure based on the presence or absence of regularly spaced transverse protrusions throughout the entirety of the mitochondrial matrix (**Figure 5F**). Under these conditions, both M337V and Q331K variants exhibited a statistically significant increase in the number of observed "altered" cristae morphologies from examined cells. Together, these data suggest that TDP-43 mutations in iPSC-derived motor neurons lead to gross alterations in the size, elongation and cristae structure of resident mitochondria.

Similar results were observed in WTC11 motor neuron populations (**Figures 5G–I**), with wild type cells exhibiting an average cross-sectional area of $0.07 \pm 0.004$ $\mu m^2$ compared with $0.09 \pm 0.006$ $\mu m^2$ in the TDP-43$^{Q331K}$ mutants. Circularity also decreased in WTC11 cell lines, going from $0.80 \pm 0.01$ $\mu m^2$ in wild type cells to $0.78 \pm 0.01$ $\mu m^2$ in the mutant line, although this difference was not statistically significant. These results highlight a consistency in mitochondrial phenotype between the two cell sources, albeit less pronounced in the in-house produced cells. Comparison of the WTC11 CRISPR-engineered neuron populations with cells derived from an ALS patient line bearing a *TDP-43*$^{G298S+/-}$ genotype further supported the notion that this alteration in mitochondrial structure was representative of TDP-43 mutant ALS. Specifically, the patient-derived cells showed a high degree of "altered" cristae morphologies, coupled with larger (cross-sectional area of $0.09 \pm 0.005$ $\mu m^2$), less rounded mitochondria (circularity of $0.77 \pm 0.01$), largely recapitulating the phenotype observed in the CRISPR-edited WTC11 lines.

Mitochondrial dysfunction is often associated with increased production of reactive oxygen species (ROS). In view of the altered mitochondrial morphology associated with TDP-43 mutations, we performed analysis of ROS production in these lines using fluorescent dye probes. These results indicated that TDP-43 mutant cells exhibit higher relative expression levels of markers of oxidative stress, as well as superoxide and nitric oxide, than their wild type counterparts (**Figures 6A–G**). This increase was consistent between CDI and WTC11 cell sources and mirrors results reported previously for *C9orf72* mutant neuron lines (Lopez-Gonzalez et al., 2016). Based on the observed deficits in mitochondrial structure and function, Seahorse analysis was used to quantify oxygen consumption rates (OCRs) in these mutant motor neuron lines. Unfortunately, CDI cells were not able to survive the Seahorse assay protocol, possibly due to the purified nature of the cultures in question. WTC11 neuronal populations did survive and exhibited a significant drop in the basal OCR of *TDP-43*$^{Q331K+/-}$ mutant cells, compared with wild type controls, as well as an additional reduction in OCR in response to FCCP exposure (**Figures 6H–J**). Specifically, measured basal OCR in wild type cells was $143.5 \pm 3.5$ and $87.6 \pm 10.7$ pMol/min in *TDP-43*$^{Q331K+/-}$ mutant cells. OCR in response to FCCP exposure was $27.4 \pm 1.7$ pMol/min in wild type cells and $6.2 \pm 1.8$ pMol/min in *TDP-43*$^{Q331K+/-}$ mutant neurons.

Taken together, these data highlight a significant reduction in oxidative metabolism in *TDP-43*$^{Q331K+/-}$ mutant cells, coupled with an increase in ROS production, that correlates with altered cristae regularity and mitochondrial structure. Given the potential importance of these observations in adding to our understanding of cellular phenotypes in ALS, the RNA-seq data was interrogated for specific gene expression changes that may contribute to the highlighted mitochondrial phenotype. In data for the CDI motor neurons, the most heavily down-regulated gene for both M337V and Q331K variants was *CHCHD2*, a gene encoding the protein Coiled-Coil-Helix-Coiled-Coil-Helix Domain Containing 2. The downregulation of *CHCHD2* was confirmed in CDI cells *via* immunocytochemistry and RT-qPCR (**Supplementary Figure 6**). Remarkably, however, *CHCHD2* expression in the WTC11 motor neuron populations was found to be significantly upregulated in *TDP-43*$^{Q331K+/-}$ mutant cells; the exact opposite result from that observed in CDI cells. A recent study found that a small chromosomal abnormality that frequently arises during expansion of human embryonic stem cells (20q11.21 amplification) causes loss of *CHCHD2* expression (Markouli et al., 2019). Such a culture artifact could potentially account for the diminished *CHCHD2* gene expression

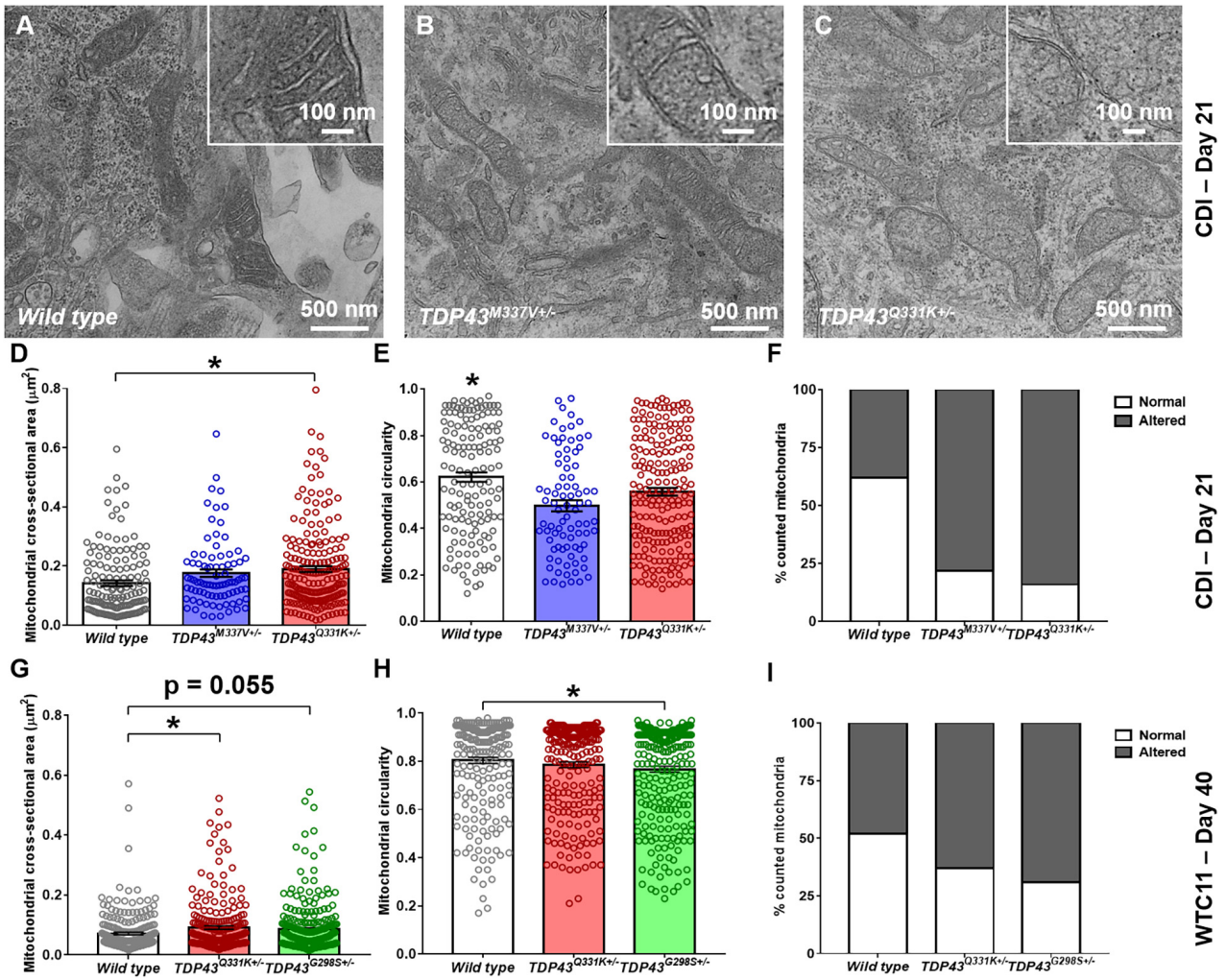


**FIGURE 5 |** Analysis of mitochondrial structure in CDI and WTC11 wild type and TDP-43 mutant motor neurons. **(A–C)** Representative transmission electron micrographs (TEM) of mitochondria within CDI motor neurons. Insets illustrate details of cristae structure from mitochondria within each image. **(D)** Cross-sectional area measured from TEM images of mitochondria in CDI wild type ($n$ = 144), TDP-43$^{M337V+/-}$ ($n$ = 85), and TDP-43$^{Q331K+/-}$ ($n$ = 202) motor neurons. Data from wild type and TDP-43$^{Q331K+/-}$ samples were significantly different from each other (*$p$ = 0.0016). **(E)** Circularity measured from TEM images of mitochondria in CDI wild type, TDP-43$^{M337V+/-}$, and TDP-43$^{Q331K+/-}$ motor neurons. Data from wild type neurons was significantly different from both TDP-43$^{M337V+/-}$ and TDP-43$^{Q331K+/-}$ samples (*$p \leq 0.037$). **(F)** Percentage of mitochondria in CDI wild type ($n$ = 43), TDP-43$^{M337V+/-}$ ($n$ = 20), and TDP-43$^{Q331K+/-}$ motor neuron populations exhibiting normal and altered cristae structure, with normal being defined as regular, well defined cristae throughout the entire observable mitochondrial structure. A contingency table comparing cell type against cristae structure found that the two factors are significantly related ($p$ = 0.0018), suggesting that frequency of normal cristae occurrence within each population is dependent on the cell type examined. **(G)** Cross-sectional area measured from TEM images of mitochondria in WTC11 wild type ($n$ = 229) and TDP-43$^{Q331K+/-}$ ($n$ = 238) motor neurons and compared to results obtained from an ALS patient-derived iPSC line bearing a TDP-43$^{G298S+/-}$ mutation ($n$ = 361). Data from wild type and TDP-43$^{Q331K+/-}$ samples were significantly different from each other (*$p$ = 0.025), whereas data from wild type and TDP-43$^{G298S+/-}$ patient samples were approaching significance ($p$ = 0.055). **(H)** Circularity measured from TEM images of mitochondria in WTC11 wild type and TDP-43$^{Q331K+/-}$ motor neurons and compared to results obtained from an ALS patient-derived iPSC line bearing a TDP-43$^{G298S+/-}$ mutation. Data from wild type and TDP-43$^{Q331K+/-}$ samples were not significantly different from each other ($p$ = 0.0817), whereas data from wild type and TDP-43$^{G298S+/-}$ mutant samples were (*$p$ = 0.0035). **(I)** Percentage of mitochondria in WTC11 wild type and TDP-43$^{Q331K+/-}$, as well as TDP-43$^{G298S+/-}$ patient iPSC-derived, motor neuron populations exhibiting normal and altered cristae structure. A contingency table comparing cell type against cristae structure found that the two factors are significantly related ($p$ = 0.0018), suggesting that frequency of normal cristae occurrence within each population is dependent on the cell type examined.

in the CDI TDP-43 mutant lines. This chromosomal abnormality is too small to be apparent in karyotypic analysis. However, 20q11.21 amplification is known to cause increased expression of *BCL2L1*, *ID1*, and *HM13*; three genes encoded at this locus. RNA-seq data revealed a modest increase in expression of *BCL2L1*, *ID1*, and *HM13* in the CDI TDP-43 mutant lines (data not shown) indicating that this 20q11.21 amplification may be present in these cells.

Loss of CHCHD2 activity has been reported to disrupt mitochondrial cristae structure (Zhou et al., 2018; Liu et al., 2020). However, as similarly abnormal mitochondrial structures were observed in two different *TDP-43*$^{Q331K+/-}$ lines with

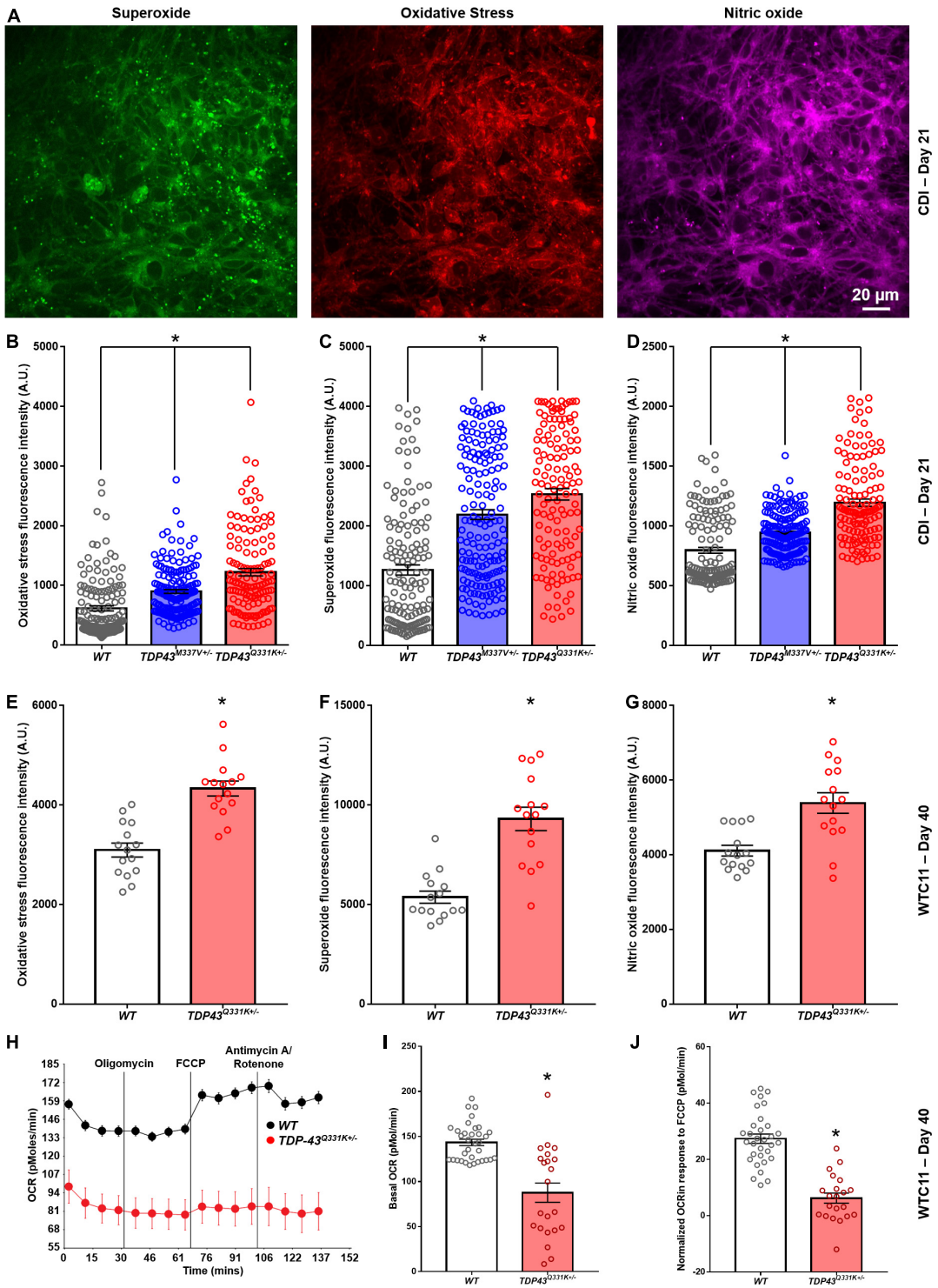


**FIGURE 6 |** Analysis of reactive oxygen species production in CDI and WTC11 wild type and TDP-43 mutant motor neurons. **(A)** Representative staining from TDP-43$^{Q331K+/-}$ mutant motor neurons illustrating expression of superoxide, nitric oxide, and markers of oxidative stress collected from CDI cells. **(B)** Levels of oxidative stress measured from CDI wild type ($n$ = 276), TDP-43$^{M337V+/-}$ ($n$ = 304), and TDP-43$^{Q331K+/-}$ ($n$ = 262) motor neurons. All experimental groups were significantly different from each other (*$p < 0.0001$). **(C)** Levels of superoxide measured from CDI wild type, TDP-43$^{M337V+/-}$, and TDP-43$^{Q331K+/-}$ motor neurons. All experimental groups were significantly different from each other (*$p \leq 0.02$). **(D)** Levels of nitric oxide measured from CDI wild type, TDP-43$^{M337V+/-}$, and TDP-43$^{Q331K+/-}$ motor neurons. All experimental groups were significantly different from each other (*$p < 0.0001$). **(E)** Levels of oxidative stress measured from

*(Continued)*

**FIGURE 6 |** (Continued)
WTC11 wild type ($n$ = 15) and TDP-43$^{Q331K+/-}$ ($n$ = 15) motor neurons. *$p < 0.0001$. **(F)** Levels of superoxide measured from WTC11 wild type ($n$ = 15) and TDP-43$^{Q331K+/-}$ ($n$ = 15) motor neurons. *$p < 0.0001$. **(G)** Levels of nitric oxide measured from WTC11 wild type ($n$ = 15) and TDP-43$^{Q331K+/-}$ ($n$ = 15) motor neurons. *$p = 0.0003$. **(H)** Seahorse metabolic profiles measured from culture wells housing WTC11 wild type ($n$ = 34) or TDP-43$^{Q331K+/-}$ ($n$ = 22) motor neurons. Measurements were taken at baseline and then following exposure to oligomycin, FCCP, and rotenone/antimycin A. **(I)** Basal oxygen consumption rate measured from WTC11 wild type ($n$ = 34) or TDP-43$^{Q331K+/-}$ ($n$ = 22) motor neuron populations. *$p < 0.0001$. **(J)** Normalized oxygen consumption rate measured from WTC11 wild type or TDP-43$^{Q331K+/-}$ motor neuron populations exposed to FCCP *$p < 0.0001$.

oppositely altered levels of *CHCHD2* expression, the line-specific loss of *CHCHD2* expression does not appear to be responsible for the observed mitochondrial effects.

## DISCUSSION

CRISPR-mediated gene editing, combined with cutting edge iPSC technology, holds significant potential for modeling human disease. Critical factors to consider when seeking to implement such methodologies for the study of disease etiology and progression is whether CRISPR-engineered phenotypes represent accurate depictions of the *in vivo* condition and whether these phenotypes are consistent regardless of the editing strategy employed. This study therefore sought to characterize the cellular phenotype of iPSC-derived motor neurons bearing CRISPR-engineered, ALS-relevant TDP-43 mutations. In addition, this work compared and contrasted the structural and functional differences that arose between TDP-43 mutant cells derived by different teams using distinct gene editing strategies. Critically, this comparison involved assessment of commercially sourced iPSC-derived neurons since such cells are typically used by drug companies for large-scale preclinical drug screens to reduce variability and enable normalization of results across sites (Scott et al., 2013).

Transcriptomic assessment of in-house derived and commercially sourced lines highlighted the relative purity and consistency of the commercial cells. While both CDI and WTC11 populations exhibited strong expression of motor neuron-specific transcripts, all these differentiated lines expressed significant levels of V1, V2 and V3 interneuron markers, and an oligodendrocyte marker, indicating the presence of a mixed population of ventral spinal neurons and supporting cells. Furthermore, although consistent levels of the motor neuron marker Islet1, substantial variance was observed in levels of ChAT expression, indicating a potential difference in the maturation state of motor neurons derived from these two sources. Variance in the number of contaminating proliferating cells between WTC11 wild type and *TDP-43*$^{Q331K+/-}$ mutant populations also underscored the heterogeneity of the in-house differentiated lines. While methods for purifying iPSC-derived neurons from mixed differentiation runs have been described previously (Yuan et al., 2011), such techniques were not employed here as many of the assays employed in this study (Seahorse, MEA, etc.) required large numbers of cells and the attrition rates associated with antibody-based purification methods would have made such assays untenable. Despite differences in the base rate of fire and the associated rate of decline between CDI and WTC11 mutant populations, the consistent trends mirror results reported previously for patient-derived lines (Devlin et al., 2015), suggesting that the observed electrophysiological phenotype in these gene edited neuronal populations is representative of the human disease. Furthermore, the consistency of the observed electrophysiological dysfunction engenders confidence that this phenotypic aspect was not an artifact of the specific editing strategy used to create the mutant lines.

One of the hallmarks of ALS is mitochondrial dysfunction and some effort has been made to characterize the functional deficits of these organelles within iPSC-based models of *C9orf72*-mediated ALS (Lopez-Gonzalez et al., 2016). While mitochondrial defects in TDP-43 mutant neurons have been reported in rodent cells (Wang et al., 2013), to the best of our knowledge none have been reported previously in human neurons. RNA-seq results for both CDI and WTC11 mutant lines highlighted alterations in biological processes associated with regulating hypoxia, further underscoring the importance of characterizing metabolic behavior in these lines. TEM analysis revealed significant alterations in mitochondrial area and circularity, with mutant cells producing larger, more elongated organelles (suggesting increased fusion) with a significant reduction in the presence and regularity of cristae structures. This was coupled with increases in expression of oxidative stress markers and a substantial reduction in OCRs in TDP-43 mutant WTC11 neurons. Although similar increases in ROS production have been previously reported for *C9orf72* mutant cells (Lopez-Gonzalez et al., 2016), to the best of our knowledge, this study is the first to characterize the extent of mitochondrial dysfunction in human TDP-43 mutant neurons. Again, the consistency of phenotype observed between CDI and WTC11 populations, as well as the correlation of the collected data with results from patient-derived *TDP-43*$^{G298S+/-}$ cells, provides confidence in the relevance of the phenotype in terms of modeling ALS. However, results from the analysis of *CHCHD2* expression caution against over interpretation of the data. *CHCHD2* forms a heterodimer with closely related *CHCHD10*. This dimer is responsible for regulating cytochrome c oxidase activity within the inner mitochondrial membrane and regulating cristae structure. *CHCHD2* mutations are already associated with several neurodegenerative diseases, including frontotemporal dementia (Che et al., 2018) and Parkinson's disease (Funayama et al., 2015; Meng et al., 2017), while *CHCHD10* mutations have also been found to cause ALS (Dols-Icardo et al., 2015; Zhang et al., 2015). As such, dysregulation of CHCHD2 in TDP-43 mutant cells could be a major contributor to ALS pathology in these patients. The CDI RNA-seq data seem to suggest that *CHCHD2* downregulation is one of the most profound impacts of TDP-43 mutation. However, previous

work has indicated that *CHCHD2* is a gene that exhibits variable expression behavior across otherwise consistent iPSC lines (Zhu et al., 2016). Secondly, a number of studies based on iPSC models of neurodegenerative disease have reported *CHCHD2* mis-regulation and suggested this as a factor contributing to disease pathology (Shimojima et al., 2015; Xu et al., 2017; De Angelis et al., 2019). The emergence of altered *CHCHD2* expression in a variety of gene mutations responsible for dissimilar genetic diseases raises the red flag that such changes in gene expression may represent some stochastic and disease-unrelated epigenetic event associated with reprogramming and/or subcloning. Taking into account the available literature, it must be noted that the results reported here may likewise constitute an artifact of the subcloning associated with the generation of the gene edited CDI lines and not an actual effect of the mutation in the *TARDBP* gene. Such a hypothesis would seem to be supported by the WTC11 results, which conversely showed a significant upregulation of *CHCHD2* expression in the TDP-43 mutant line compared with isogenic controls.

The critical role of *CHCHD2* in regulating normal mitochondrial structure and function underscores the importance of comparing phenotypes across multiple lines when attempting to identify mechanisms contributing to ALS cellular characteristics. While the CDI results in isolation seem to highlight mis-regulation of *CHCHD2* as a potential contributor to cellular pathology in ALS, results from the WTC11 line indicate that such pathological features are present even without *CHCHD2* downregulation. As such, one can be relatively confident that the mitochondrial phenotype observed in this study represents a consistent feature of TDP-43 mutation in iPSC-derived neurons and may therefore be representative of ALS. This assumption is further supported by results from the patient-derived TDP-$43^{G298S+/-}$ line, which confirm the presence of structural aberrations in the mitochondria of unedited mutant neurons. However, the role of *CHCHD2* mis-regulation in contributing to this defect requires further examination.

Extensive evidence points to expression of a cryptic exon in *STMN2* transcripts that may account for some features of the phenotype observed in cell-based models of ALS, such as diminished axonal regenerative capacity (Klim et al., 2019; Melamed et al., 2019). In the present study, alternative splicing of *STMN2* gene transcripts was observed in WTC11 *TDP-43*$^{Q331K+/-}$ motor neurons but was notably absent in the comparable line from CDI. Furthermore, where present, the extent of STMN2 mis-splicing was not sufficient to reduce the overall level of STMN2 mRNA expression. Thus, stathmin-2 dysfunction is not responsible for the electrophysiological or mitochondrial abnormalities that were observed in both lines. All other aspects of phenotype characterized in this study showed consistency with in-house edited lines (that did show *STMN2* cryptic exon expression), indicating that at least some aspects of ALS cellular pathology can develop in cultured neurons in the absence of *STMN2* mis-splicing. These results serve to highlight the need for caution when interpreting the phenotypes of individual iPSC-lines as accurate models of disease and variations observed in *STMN2* splicing further underscore this point.

In this study, WTC11 mutant neurons exhibited significant TDP-43 translocation from the nucleus, in line with previous work (Winton et al., 2008; Zhang et al., 2009). Replacement of mechanical trituration with enzymatic dissociation led to significant reductions in the level of cytoplasmic TDP-43 expression observed. Since the level of cytoplasmic TDP-43 translocation would likely affect transcriptomic and splicing changes in the resulting cells, the provision of more gentle differentiation methods may reduce the phenotypic impact of the mutation by limiting stress granule formation. This observation raises the interesting possibility that aggregation of TDP-43 in ALS is stress dependent (Wolozin and Ivanov, 2019; Zuo et al., 2021), which might explain why ALS manifests as a late onset disease since it takes time for stresses to accumulate throughout life. This could also help explain why the clinical manifestations are so variable as they are dependent on the levels of environmental stress the patient is subjected to, which could vary significantly throughout an individual's lifetime. Regardless, these data highlight that culture history can contribute to phenotype in iPSC-derived neuronal models of ALS, further underscoring the need to carefully dissect mutation-dependent effects from environmental cues when investigating disease mechanisms using such model systems.

In summary, commercial and in-house iPSC-derived motor neurons exhibited consistent electrophysiological phenotypes in TDP-43 mutant cultures. These results correlate with previously reported data from patient-derived cells, suggesting an accurate portrayal of functional decline in response to CRISPR-engineered mutations in *TARDBP*. Consistent dysregulation of mitochondrial structure and function was also observed across these mutant lines, indicating that degradation of cristae structure and increased ROS production occurs in response to TDP-43 mutation. While electrophysiological and mitochondrial abnormalities were consistently observed across all iPSC lines bearing *TARDBP* gene mutations, occurrence of *CHCHD2* mis-regulation and mis-splicing leading to *STMN2* cryptic exon expression showed line-specific variability, potentially due to differences in culture history and levels of mechanical stress during differentiation. These results indicate that TDP-43 mutant ALS possesses a complex cellular pathology that likely arises from multiple mechanisms, which reinforces the importance of confirming results in multiple lines to ensure accuracy when using CRISPR-based iPSC models to make predictions related to ALS disease mechanisms and/or drug responses.

## MATERIALS AND METHODS

Unless otherwise stated, all incubation steps were carried out at 37°C/5% $CO_2$.

### CRISPR-Mediated Introduction of *TARDBP* Mutation Into WTC11 Induced Pluripotent Stem Cells

Working with the University of Washington's Institute for Stem Cell and Regenerative Medicine Ellison Stem Cell Core, heterozygous TDP-$43^{Q331K}$ mutations were introduced into the

WTC11 iPSC line, using methods described previously (Miyaoka et al., 2014). Cas9 guide RNAs (gRNA) targeting the *TARDBP* coding region were designed using a combination of web-based tools (CRISPoR and CRISPR-Scan websites). Particular attention was paid to the gRNA placement within the gene, off-target predictions, and SNP locations. To limit the exposure of the DNA to the genome editing enzyme and reduce off-target events, Cas9 protein and gRNA were introduced as ribonucleoprotein complexes. One million WTC-11 iPSC were electroporated with Cas9 (0.6 μM, Sigma) and gRNA (3 μM, Synthego) along with a ssDNA donor (2 μM, IDT) using Amaxa nucleofector (Human Stem Cell kit 2) in presence of ROCK inhibitor. Individual clones were handpicked and plated into 96 well plates. DNA was extracted using Quick Extract DNA extraction solution (Epicentre #QE09050) and nested PCR was performed using Forward (GCTTATTTTTCCTCTGGCTTTAGA) and Reverse (GATCCCCAACCAATTGCTGC) primers. The PCR product was purified using EXO-SAP enzyme (ThermoFisher) and sent for Sanger sequencing analysis (through Genewiz). Topo-cloning of PCR amplicons was performed for picked lines to validate their genotype. Clones harboring the Q331K mutation were amplified and sent for G-band karyotyping (outsourced to Diagnostic Cytogenetics Inc., Seattle, WA, United States).

gRNA sequence: GCAGCACTACAGAGCAGTTG

ssDNA sequence: GGTGGTGGGATGAACTTTGGTGCGTT CAGCATTAATCCAGCCATGATGGCTGCCGCCCAGGCAGC ACTAAAGAGCAGTTGGGGTATGATGGGCATGTTAGCCAG CCAGCAGAACCAGTCAGGCCCATCGGGTAATAACC.

## Cell Culture

Commercially sourced (iCell) human iPSC-derived motor neurons were purchased from CDI and were stored, thawed, and maintained according to the manufacturer's protocol. Two different TDP-43 mutant lines were used in this study; M337V (CDI: CUS-MNC-1 × 01279.418) and Q331K (CDI: CUS-MNC-1 × 01279.435). In all experiments, the described mutant neurons were compared to an isogenic control iPSC-derived motor neuron line (CDI: R1049).

Culture surfaces were first treated with a 0.07% polyethylenimine solution (Sigma-Aldrich) and incubated overnight. Treated surfaces were then washed three times with sterile distilled water and allowed to dry for 1 h. Dried surfaces were treated with 5 μg/mL laminin (Sigma-Aldrich) and again incubated overnight. After incubation, the laminin solution was aspirated and cells plated immediately at 55,000 cells per $cm^2$ using the medium provided by the manufacturer. Cultured motor neurons were fed every 2–3 days (50% medium replacement) and analyzed between days 20 and 22 of culture in all experiments described below.

WTC11 iPSCs (Kreitzer et al., 2013; Miyaoka et al., 2014) were passaged onto Matrigel-coated six-well plates and incubated at 37°C/5% $CO_2$ in mTeSR until they reached ∼80% confluency. At this point, cultures were differentiated into regionally unspecified neural progenitor cells using a monolayer differentiation method adapted from Shi et al. (2012). These cells were then passaged onto 0.01% poly-L-ornithine (Sigma-Aldrich, St. Louis, MO, United States)/5 μg/mL laminin (Sigma-Aldrich)-coated surfaces and exposed to culture conditions promoting motor neuron differentiation, essentially as described by Amoroso et al. (2013). At days 20–25 post-induction, neurons were again passaged and replated onto final substrates (coated with poly-L-ornithine and laminin) for downstream experiments. In all experiments, cells were maintained in culture until they reached 40–50 days post-induction (or 90 days for certain patch clamp experiments) before being used in terminal analyses. All cells used in the described experiments were differentiated from WTC11 colonies between passage 45 and 55.

## RNA-Seq Analysis

Bulk RNA samples from WTC11 cells were isolated using the Trizol reagent and according to the manufacturers' protocol. Quality of the isolated RNA was confirmed using TapeStation; only samples with an RIN value of 8.5 or greater were used for library preparation. Once RNA samples were isolated, library preparation was outsourced to the Fred Hutch Genomics Core (Seattle, WA, United States). Collection of raw RNA-seq data sets for the CDI lines was outsourced to Verge Genomics on behalf of the cell manufacturer and provided to the authors upon completion.

For both data sets, reads were aligned to the hg38 genome using TopHat (v.2.0.14) (Trapnell et al., 2010, 2012) to generate BAM files. Sequences were aligned to human mRNAs to generate FPKM values using Cufflinks v.2.2.1 (Trapnell et al., 2010, 2012) with the following parameters: "–library-norm-method quartile" and removing ribosomal, snoRNA and mitochondrial sequences. Differentially expressed transcripts (Jensen–Shannon divergence false discovery rate $< 0.05$) were obtained *via* Cuffdiff as part of the Cufflinks package. The overlap of differentially expressed genes between the two sets of samples was evaluated by the DAVID v6.7 GO program using a Benjamini *P*-value of $<0.05$ for significance (Huang Da et al., 2009a,b). WTC11 samples had between 120 and 130 million 50 bp paired-end reads. For TDP43 wild type versus Q331K, there were 753 downregulated and 782 significantly upregulated ($q < 0.05$ and log2fc $> 1.5$) genes, mapped to the hg38 refGene dataset. CDI samples had between 16.6 and 21.7 million 75 bp single-end reads. For CDI M337V versus control, 220 down-regulated and 254 upregulated genes were identified ($q < 0.05$ and log2fc $> 0.5$). For CDI Q331K versus control, 453 downregulated and 1062 upregulated genes were identified ($q < 0.05$ and log2fc $> 0.5$).

## Quantitative RT-PCR

RNA isolation from neuronal cultures was carried out using the Trizol reagent and according to the manufacturers' protocol. cDNA synthesis was achieved using the iScript Reverse Transcription Supermix for RT-qPCR (Bio-Rad) and according to the manufacturer's protocol. Quantitative RT-PCR (qRT-PCR) was carried out using the PrimePCR system provided by Bio-Rad. Ninety-six-well plates were ordered preloaded with primer pairs developed and validated by the manufacturer. The exception to this was the *STMN2* and truncated *STMN2* primers, which were derived from previously published work (Melamed et al., 2019). In this case, PCR products were run on a polyacrylamide

gel, excised, and sent for sequencing to ensure the specificity of the primers used.

PCR reaction mixtures were prepared using the SsoAdvanced Universal SYBR Green Supermix with 500 ng of cDNA used per reaction. Plates were then run on a CFX96 real-time polymerase chain reaction (RT-PCR) detection system (Bio-Rad) and associated software using the thermal cycling protocol provided with the SsoAdvanced Universal SYBR Green Supermix kit. Detection thresholds for data analysis were set at the base of the linear phase and the resulting Ct values were analyzed by relative quantification, using the $2^{\wedge-\Delta\Delta Ct}$ method (Livak and Schmittgen, 2001). Gene expression in both M337V and Q331K mutant neurons were normalized to expression levels of glyceraldehyde 3-phosphate dehydrogenase (GAPDH) and expressed relative to levels recorded in normal isogenic control cells.

## Immunocytochemistry

Cells were fixed in 4% paraformaldehyde for 15 min and blocked with 5% goat serum in PBS for 1 h at room temperature. Cells were then incubated with primary antibodies diluted in 1% goat serum in PBS overnight at 4°C. The next day, cells were washed three times with PBS. They were then incubated in a secondary antibody solution containing secondary antibodies diluted in 1% goat serum in PBS. Counterstaining was performed with VECTASHIELD containing DAPI (Vector Labs). Images were taken at the Garvey Imaging Core at the University of Washington's Institute for Stem Cell and Regenerative Medicine using a Nikon A1 Confocal System on a Ti-E inverted microscope platform. Twelve-bit 1024 × 1024 pixel images were acquired with Nikon NIS Elements 3.1 software. Antibodies used in this study were as follows: mouse anti-neurofilament (1 in 500, Millipore), mouse anti-microtubule associated protein-2 (1 in 1000, Millipore), mouse anti-Islet-1 (1 in 10, DSHB), rabbit anti-microtubule associated protein-2 (1 in 1000, Millipore), rabbit anti-CHCHD2 (1 in 300, Proteintech), Alexafluor-594 conjugated goat-anti-mouse secondary antibody (1:200, Invitrogen), and Alexafluor-488 conjugated goat-anti-rabbit secondary antibody (1:200, Invitrogen). In addition to the described methods above, the flurometric cellular ROS detection assay (Abcam) was carried out using the stains provided in the kit and according to the manufacturer's protocol.

## Transmission Electron Microscopy

Cells were fixed in 4% Glutaraldehyde in a sodium cacodylate buffer and stored at 4°C overnight. Fixed cells were washed 5 × 5 min in 0.1 M cacodylate buffer, then post-fixed in osmium ferrocyanide for 1 h on ice. Cells were next washed 5 × 5 min in $ddH_2O$ and then incubated in a 1% thiocarbohydrazide solution for 20 min at room temperature. Cells were then washed again 5 × 5 min in $ddH_2O$ before being placed in 2% osmium tetroxide for 30 min at room temperature. Finally, cells were again washed 5 × 5 min in $ddH_2O$ before being en bloc stained in 1% uranyl acetate (aqueous) overnight at 4°C.

The next day, cells were washed 5 × 5 min in $ddH_2O$, then en bloc stained in Walton's lead aspartate for 30 min at 60°C. Following five more 5-min washes in $ddH_2O$, cells were dehydrated in ice cold 30, 50, 70, and 95% EtOH, then allowed to come to room temperature. This was then followed by two changes of 100% EtOH and two changes of propylene oxide. Then, cells were infiltrated in a 1:1 mixture of propylene oxide: Durcupan resin for 2 h, followed by overnight infiltration in fresh Durcupan. The next day, cells were given a fresh change of Durcupan for 2 h and then placed in flat embedding molds and polymerized in a 60°C oven for 2 days. Eighty nanometers sections were then cut using a Leica EM UC7 ultra microtome and imaged on a JEOL 1230 TEM, at 80 kV.

## Image Analysis

Assessment of CHCHD2 and ROS staining intensity from confocal images of normal and TDP-43 mutant cells was performed using ImageJ. Similarly, measurement of mitochondrial size and circularity from TEM images was carried out in ImageJ. Assessment of gross mitochondrial structure was performed manually as previously described (Costa et al., 2018). Briefly, 30 micrographs were randomly taken for each cell type, and at least 100 mitochondria were counted and labeled either "normal" or "altered." Normal mitochondria were defined as exhibiting organized and parallel cristae that ran perpendicular to each mitochondrion's primary axis. Only cells observed with cristae spaced throughout the entire mitochondrial matrix were counted as normal to ensure consistency of analysis. Mitochondria that could not match these criteria exactly were placed in the "altered" group. All image analysis was blinded to remove bias.

## Electrophysiology

Whole-cell patch clamp recordings were performed on the 37°C heated stage of an inverted DIC microscope (Nikon) connected to an EPC10 patch clamp amplifier and computer running Patchmaster software (HEKA). Coverslips supporting cultured motor neurons were loaded onto the stage and bathed in a Tyrode's solution containing 140 mM NaCl, 5.4 mM KCl, 1.8 mM $CaCl_2$, 1 mM $MgCl_2$, 10 mM glucose, and 10 mM HEPES. An intracellular recording solution containing 120 mM L-aspartic acid, 20 mM KCl, 5 mM NaCl, 1 mM $MgCl_2$, 3 mM $Mg^{2+}$-ATP, 5 mM EGTA, and 10 mM HEPES was employed and borosilicate glass patch pipettes (World Precision Instruments) with a resistance in the range of 3–6 MΩ were used for all recordings. Offset potentials were nulled before formation of a gigaΩ seal and fast and slow capacitance was compensated for in all recordings. Membrane potentials were corrected by subtraction of a 15 mV tip potential, calculated using the HEKA software. Cells that required more than 100 pA of current to achieve a −70 mV resting membrane potential were excluded as excessive application of current is indicative of poor patch quality and/or membrane integrity.

To generate a single action potential, a 5 ms depolarizing current pulse of sufficient intensity (1–2 nA) was applied. Depolarization-evoked repetitive firing was achieved *via*

application of a series of 500 ms current injections starting at −30 pA and increasing in 10 pA increments. Both single action potentials and repetitive firing behavior were recorded in current-clamp mode. Inward and outward currents were evoked in voltage-clamp mode *via* a series of 500 ms depolarizing steps from –120 to +30 mV in 10 mV increments. Gap-free recordings of spontaneous activity in patched neurons were performed in current-clamp mode for 30 s with 0 pA current injection to provide a measure of the maximum diastolic potential held by the cell without current input. All recordings and analyses of action potential waveforms and currents were performed using the Patchmaster software suite.

Population level function in motor neuron cultures was assessed in 48-well MEA plates using the Maestro MEA system (Axion Biosystems). During data acquisition, standard recording settings for spontaneous neuronal spikes were used (Axis software, version 2.5), and cells were maintained at 37°C/5% $CO_2$ throughout the 2-min recording period. The standard settings have 130× gain, and record from 1 to 25,000 Hz, with a low-pass digital filter of 2 kHz for noise reduction. In all experiments, spike detection was set at 5× the standard deviation of the noise and network burst detection was recorded if at least 25% of the electrodes in a given well showed synchronous activity. Reported results were calculated by averaging all of the electrodes in each well, then averaging data from duplicate wells.

### Oxygen Consumption Measurement Using the Seahorse Cellular Flux Assay

Seahorse assays were performed essentially as previously reported (Hussein et al., 2020). WTC11 neurons were seeded onto 96-well Seahorse plates at 100,000 cells/well at day 25 post-induction and maintained until day 45. Culture medium was then exchanged for base medium [unbuffered DMEM (Sigma D5030)] supplemented with sodium pyruvate (Gibco, 1 mM) and 25-mM glucose for 1 h prior to the assay. Substrates and selective inhibitors were injected during the measurements to achieve final concentrations of glucose (2.5 mM), 4-(trifluoromethoxy) phenylhydrazone (FCCP, 300–500 nM), oligomycin (2.5 mM), antimycin (2.5 mM), rotenone (2.5 mM), palmitate (50 mM in BSA), BSA, and ETO (50 mM). The OCR values were normalized to the number of cells present in each well, quantified by hoechst staining (HO33342; Sigma-Aldrich). Changes in OCR in response to substrates and inhibitors addition were defined as the maximal change after the chemical injection compared to the last OCR value recorded before the injection.

### Statistical Analysis

All experiments were performed at least in triplicate, and repeated using 2–3 independent vials of cells for CDI cultures or independent differentiation runs for WTC11 neurons. Significant differences between groups were evaluated using unpaired *t*-tests for two conditions, or one-way ANOVA, with *post hoc* tests for multiple comparisons, for experiments with three or more groups. Mann–Whitney *U* tests and ANOVA on ranks were used to analyze the statistical significance of differences arising between sets of non-normally distributed data. For repetitive firing analysis and normal versus altered mitochondrial structure comparisons, contingency tables were constructed and used to run Chi-squared tests to determine whether the distribution of data was dependent on cell type. In all experiments, a *p*-value of less than 0.05 was considered significant. All statistical tests were performed using the GraphPad Prism statistics software.

## DATA AVAILABILITY STATEMENT

The datasets presented in this study can be found in online repositories. The names of the repository/repositories and accession number(s) can be found below: ArrayExpress, accession no. E-MTAB-10666.

## AUTHOR CONTRIBUTIONS

AS conducted the majority of the experiments and wrote the manuscript. CC assisted with motor neuron differentiation and performed analysis of TDP-43 cytoplasmic inclusions. JH and JM were responsible for engineering the Q331K mutation into the *TARDBP* locus using CRISPR-Cas9 gene editing. PV conducted the RNA-seq analysis. DM, B-OC, D-HK, and MB oversaw the project, provided feedback on collected data, and provided edits to the manuscript. All authors contributed to the article and approved the submitted version.

## FUNDING

This work was supported by the National Institutes of Health (NIH) KL2 TR002317 (to AS), R01 NS094388 (to D-HK and MB), and a grant from the Korea Health Technology R&D Project through the Korea Health Industry Development Institute (KHIDI), funded by the Ministry of Health and Welfare, South Korea (grant number HI19C0642; to D-HK).

## ACKNOWLEDGMENTS

Our thanks to Edward Parker for his assistance with the sample preparation for TEM and subsequent imaging. We would also like to thank Abdiasis Hussein for his assistance with the Seahorse experiments. Our thanks to CDI for providing cells used in this study as well as providing the examined RNA-seq data for these lines.

## SUPPLEMENTARY MATERIAL

The Supplementary Material for this article can be found online at: https://www.frontiersin.org/articles/10.3389/fcell.2021.728707/full#supplementary-material

## REFERENCES


Amoroso, M. W., Croft, G. F., Williams, D. J., O'keeffe, S., Carrasco, M. A., Davis, A. R., et al. (2013). Accelerated high-yield generation of limb-innervating motor neurons from human stem cells. *J. Neurosci.* 33, 574–586. doi: 10.1523/jneurosci.0906-12.2013

Arnold, E. S., Ling, S.-C., Huelga, S. C., Lagier-Tourenne, C., Polymenidou, M., Ditsworth, D., et al. (2013). ALS-linked TDP-43 mutations produce aberrant RNA splicing and adult-onset motor neuron disease without aggregation or loss of nuclear TDP-43. *Proc. Natl. Acad. Sci. U.S.A.* 110, E736–E745.

Benatar, M. (2007). Lost in translation: treatment trials in the SOD1 mouse and in human ALS. *Neurobiol. Dis.* 26, 1–13. doi: 10.1016/j.nbd.2006.12.015

Bensimon, G., Lacomblez, L., Meininger, V. F., and Group, A. R. S. (1994). A controlled trial of riluzole in amyotrophic lateral sclerosis. *N. Engl. J. Med.* 330, 585–591. doi: 10.1056/nejm199403033300901

Berry, B. J., Smith, A. S. T., Young, J. E., and Mack, D. L. (2018). Advances and current challenges associated with the use of human induced pluripotent stem cells in modeling neurodegenerative disease. *Cells Tissues Organs* 205, 331–349. doi: 10.1159/000493018

Che, X. Q., Zhao, Q. H., Huang, Y., Li, X., Ren, R. J., Chen, S. D., et al. (2018). Mutation screening of the CHCHD2 gene for Alzheimer's disease and frontotemporal dementia in chinese mainland population. *J. Alzheimers Dis.* 61, 1283–1288. doi: 10.3233/jad-170692

Chiappalone, M., Novellino, A., Vajda, I., Vato, A., Martinoia, S., and Van Pelt, J. (2005). Burst detection algorithms for the analysis of spatio-temporal patterns in cortical networks of neurons. *Neurocomputing* 65, 653–662. doi: 10.1016/j.neucom.2004.10.094

Chiò, A., Logroscino, G., Traynor, B. J., Collins, J., Simeone, J. C., Goldstein, L. A., et al. (2013). Global epidemiology of amyotrophic lateral sclerosis: a systematic review of the published literature. *Neuroepidemiology* 41, 118–130. doi: 10.1159/000351153

Costa, R. M. D., Karmirian, K., and Rehen, S. K. (2018). Deformation of mitochondrial cristae in human neural progenitor cells exposed to valproic acid. *An. Acad. Bras. Cienc.* 90, 2223–2232. doi: 10.1590/0001-3765201820170762

De Angelis, M. T., Santamaria, G., Parrotta, E. I., Scalise, S., Lo Conte, M., Gasparini, S., et al. (2019). Establishment and characterization of induced pluripotent stem cells (iPSCs) from central nervous system lupus erythematosus. *J. Cell. Mol. Med.* 23, 7382–7394. doi: 10.1111/jcmm.14598

Devlin, A. C., Burr, K., Borooah, S., Foster, J. D., Cleary, E. M., Geti, I., et al. (2015). Human iPSC-derived motoneurons harbouring TARDBP or C9ORF72 ALS mutations are dysfunctional despite maintaining viability. *Nat. Commun.* 6:5999.

Do-Ha, D., Buskila, Y., and Ooi, L. (2018). Impairments in motor neurons, interneurons and astrocytes contribute to hyperexcitability in ALS: underlying mechanisms and paths to therapy. *Mol. Neurobiol.* 55, 1410–1418. doi: 10.1007/s12035-017-0392-y

Dols-Icardo, O., Nebot, I., Gorostidi, A., Ortega-Cubero, S., Hernández, I., Rojas-García, R., et al. (2015). Analysis of the CHCHD10 gene in patients with frontotemporal dementia and amyotrophic lateral sclerosis from Spain. *Brain* 138, e400–e400.

Funayama, M., Ohe, K., Amo, T., Furuya, N., Yamaguchi, J., Saiki, S., et al. (2015). CHCHD2 mutations in autosomal dominant late-onset Parkinson's disease: a genome-wide linkage and sequencing study. *Lancet Neurol.* 14, 274–282. doi: 10.1016/s1474-4422(14)70266-2

Grad, L. I., Rouleau, G. A., Ravits, J., and Cashman, N. R. (2017). Clinical spectrum of amyotrophic lateral sclerosis (ALS). *Cold Spring Harb. Perspect. Med.* 7:a024117.

Heman-Ackah, S. M., Bassett, A. R., and Wood, M. J. A. (2016). Precision modulation of neurodegenerative disease-related gene expression in human iPSC-Derived neurons. *Sci. Rep.* 6:28420.

Huang Da, W., Sherman, B. T., and Lempicki, R. A. (2009a). Bioinformatics enrichment tools: paths toward the comprehensive functional analysis of large gene lists. *Nucleic Acids Res.* 37, 1–13. doi: 10.1093/nar/gkn923

Huang Da, W., Sherman, B. T., and Lempicki, R. A. (2009b). Systematic and integrative analysis of large gene lists using DAVID bioinformatics resources. *Nat. Protoc.* 4, 44–57.

Hussein, A. M., Wang, Y., Mathieu, J., Margaretha, L., Song, C., Jones, D. C., et al. (2020). Metabolic control over mTOR-dependent diapause-like state. *Dev. Cell* 52, 236–250.e237.

Jackson, C., Heiman-Patterson, T., Kittrell, P., Baranovsky, T., Mcananama, G., Bower, L., et al. (2019). Radicava (edaravone) for amyotrophic lateral sclerosis: US experience at 1 year after launch. *Amyotroph. Lateral Scler Frontotemporal Degener.* 20, 605–610. doi: 10.1080/21678421.2019.1645858

Kapucu, F. E., Tanskanen, J. M. A., Mikkonen, J. E., Ylä-Outinen, L., Narkilahti, S., and Hyttinen, J.a.K. (2012). Burst analysis tool for developing neuronal networks exhibiting highly varying action potential dynamics. *Front. Comput. Neurosci.* 6:38. doi: 10.3389/fncom.2012.00038

Khalfallah, Y., Kuta, R., Grasmuck, C., Prat, A., Durham, H. D., and Vande Velde, C. (2018). TDP-43 regulation of stress granule dynamics in neurodegenerative disease-relevant cell types. *Sci. Rep.* 8:7551.

Klim, J. R., Williams, L. A., Limone, F., Guerra San Juan, I., Davis-Dusenbery, B. N., et al. (2019). ALS-implicated protein TDP-43 sustains levels of STMN2, a mediator of motor neuron growth and repair. *Nat. Neurosci.* 22, 167–179. doi: 10.1038/s41593-018-0300-4

Kreitzer, F. R., Salomonis, N., Sheehan, A., Huang, M., Park, J. S., Spindler, M. J., et al. (2013). A robust method to derive functional neural crest cells from human pluripotent stem cells. *Am. J. Stem Cells* 2:119.

Liu, Y., and Deng, W. (2016). Reverse engineering human neurodegenerative disease using pluripotent stem cell technology. *Brain Res.* 1638, 30–41. doi: 10.1016/j.brainres.2015.09.023

Liu, Y.-T., Huang, X., Nguyen, D., Shammas, M. K., Wu, B. P., Dombi, E., et al. (2020). Loss of CHCHD2 and CHCHD10 activates OMA1 peptidase to disrupt mitochondrial cristae phenocopying patient mutations. *Hum. Mol. Genet.* 29, 1547–1567. doi: 10.1093/hmg/ddaa077

Livak, K. J., and Schmittgen, T. D. (2001). Analysis of relative gene expression data using real-time quantitative PCR and the 2(-Delta Delta C(T)) Method. *Methods* 25, 402–408. doi: 10.1006/meth.2001.1262

Lopez-Bastida, J., Perestelo-Perez, L., Monton-Alvarez, F., Serrano-Aguilar, P., and Alfonso-Sanchez, J. L. (2009). Social economic costs and health-related quality of life in patients with amyotrophic lateral sclerosis in Spain. *Amyotroph. Lateral Scler.* 10, 237–243. doi: 10.1080/17482960802430781

Lopez-Gonzalez, R., Lu, Y., Gendron, T. F., Karydas, A., Tran, H., Yang, D., et al. (2016). Poly(GR) in C9ORF72-Related ALS/FTD compromises mitochondrial function and increases oxidative stress and DNA damage in iPSC-derived motor neurons. *Neuron* 92, 383–391. doi: 10.1016/j.neuron.2016.09.015

Marangi, G., and Traynor, B. J. (2015). Genetic causes of amyotrophic lateral sclerosis: new genetic analysis methodologies entailing new opportunities and challenges. *Brain Res.* 1607, 75–93. doi: 10.1016/j.brainres.2014.10.009

Markouli, C., Couvreu De Deckersberg, E., Regin, M., Nguyen, H. T., Zambelli, F., Keller, A., et al. (2019). Gain of 20q11.21 in human pluripotent stem cells impairs TGF-β-dependent neuroectodermal commitment. *Stem Cell Rep.* 13, 163–176. doi: 10.1016/j.stemcr.2019.05.005

Melamed, Z. E., López-Erauskin, J., Baughn, M. W., Zhang, O., Drenner, K., Sun, Y., et al. (2019). Premature polyadenylation-mediated loss of stathmin-2 is a hallmark of TDP-43-dependent neurodegeneration. *Nat. Neurosci.* 22, 180–190. doi: 10.1038/s41593-018-0293-z

Meng, H., Yamashita, C., Shiba-Fukushima, K., Inoshita, T., Funayama, M., Sato, S., et al. (2017). Loss of Parkinson's disease-associated protein CHCHD2 affects mitochondrial crista structure and destabilizes cytochrome c. *Nat. Commun.* 8:15500.

Miyaoka, Y., Chan, A. H., Judge, L. M., Yoo, J., Huang, M., Nguyen, T. D., et al. (2014). Isolation of single-base genome-edited human iPS cells without antibiotic selection. *Nat. Methods* 11, 291–293. doi: 10.1038/nmeth.2840

Noto, Y., Shibuya, K., Vucic, S., and Kiernan, M. C. (2016). Novel therapies in development that inhibit motor neuron hyperexcitability in amyotrophic lateral sclerosis. *Expert Rev. Neurother.* 16, 1147–1154. doi: 10.1080/14737175.2016.1197774

Pasteuning-Vuhman, S., De Jongh, R., Timmers, A., and Pasterkamp, R. J. (2020). Towards advanced iPSC-based drug development for neurodegenerative disease. *Trends Mol. Med.* 27, 263–279. doi: 10.1016/j.molmed.2020.09.013

Petrov, D., Mansfield, C., Moussy, A., and Hermine, O. (2017). ALS clinical trials review: 20 years of failure. are we any closer to registering a new treatment? *Front. Aging Neurosci.* 9:68. doi: 10.3389/fnagi.2017.00068

Prudencio, M., Humphrey, J., Pickles, S., Brown, A.-L., Hill, S. E., Kachergus, J. M., et al. (2020). Truncated stathmin-2 is a marker of TDP-43 pathology in frontotemporal dementia. *J. Clin. Invest.* 130, 6080–6092.

Schepelmann, K., Winter, Y., Spottke, A. E., Claus, D., Grothe, C., Schroder, R., et al. (2010). Socioeconomic burden of amyotrophic lateral sclerosis, myasthenia gravis and facioscapulohumeral muscular dystrophy. *J. Neurol.* 257, 15–23. doi: 10.1007/s00415-009-5256-6

Scott, C. W., Peters, M. F., and Dragan, Y. P. (2013). Human induced pluripotent stem cells and their use in drug discovery for toxicity testing. *Toxicol. Lett.* 219, 49–58. doi: 10.1016/j.toxlet.2013.02.020

Scott, S., Kranz, J. E., Cole, J., Lincecum, J. M., Thompson, K., Kelly, N., et al. (2008). Design, power, and interpretation of studies in the standard murine model of ALS. *Amyotroph. Lateral Scler.* 9, 4–15. doi: 10.1080/17482960701856300

Shefner, J., Heiman-Patterson, T., Pioro, E. P., Wiedau-Pazos, M., Apple, S., Liu, S., et al. (2019). Long-term edaravone efficacy in ALS: post-hoc analyses of study 19 (MCI186-19). *Muscle Nerve* 61, 218–221. doi: 10.1002/mus.26740

Shi, Y., Kirwan, P., and Livesey, F. J. (2012). Directed differentiation of human pluripotent stem cells to cerebral cortex neurons and neural networks. *Nat. Protoc.* 7:1836. doi: 10.1038/nprot.2012.116

Shimojima, K., Okumura, A., Hayashi, M., Kondo, T., Inoue, H., and Yamamoto, T. (2015). CHCHD2 is down-regulated in neuronal cells differentiated from iPS cells derived from patients with lissencephaly. *Genomics* 106, 196–203.

Tefera, T. W., and Borges, K. (2017). Metabolic dysfunctions in amyotrophic lateral sclerosis pathogenesis and potential metabolic treatments. *Front. Neurosci.* 10:611. doi: 10.3389/fnins.2016.00611

Trapnell, C., Roberts, A., Goff, L., Pertea, G., Kim, D., Kelley, D. R., et al. (2012). Differential gene and transcript expression analysis of RNA-seq experiments with TopHat and Cufflinks. *Nat. Protoc.* 7, 562–578. doi: 10.1038/nprot.2012.016

Trapnell, C., Williams, B. A., Pertea, G., Mortazavi, A., Kwan, G., Van Baren, M. J., et al. (2010). Transcript assembly and quantification by RNA-Seq reveals unannotated transcripts and isoform switching during cell differentiation. *Nat. Biotechnol.* 28, 511–515. doi: 10.1038/nbt.1621

Wainger, B. J., Kiskinis, E., Mellin, C., Wiskow, O., Han, S. S., Sandoe, J., et al. (2014). Intrinsic membrane hyperexcitability of amyotrophic lateral sclerosis patient-derived motor neurons. *Cell Rep.* 7, 1–11. doi: 10.1016/j.celrep.2014.03.019

Wang, W., Li, L., Lin, W.-L., Dickson, D. W., Petrucelli, L., Zhang, T., et al. (2013). The ALS disease-associated mutant TDP-43 impairs mitochondrial dynamics and function in motor neurons. *Hum. Mol. Genet.* 22, 4706–4719. doi: 10.1093/hmg/ddt319

Winton, M. J., Igaz, L. M., Wong, M. M., Kwong, L. K., Trojanowski, J. Q., and Lee, V. M.-Y. (2008). Disturbance of nuclear and cytoplasmic TAR DNA-binding protein (TDP-43) induces disease-like redistribution, sequestration, and aggregate formation. *J. Biol. Chem.* 283, 13302–13309.

Wolozin, B., and Ivanov, P. (2019). Stress granules and neurodegeneration. *Nat. Rev. Neurosci.* 20, 649–666.

Xu, X., Tay, Y., Sim, B., Yoon, S.-I., Huang, Y., Ooi, J., et al. (2017). Reversal of phenotypic abnormalities by CRISPR/Cas9-mediated gene correction in huntington disease patient-derived induced pluripotent stem cells. *Stem Cell Rep.* 8, 619–633. doi: 10.1016/j.stemcr.2017.01.022

Yuan, S. H., Martin, J., Elia, J., Flippin, J., Paramban, R. I., Hefferan, M. P., et al. (2011). Cell-surface marker signatures for the isolation of neural stem cells, glia and neurons derived from human pluripotent stem cells. *PLoS One* 6:e17540. doi: 10.1371/journal.pone.0017540

Zhang, M., Xi, Z., Zinman, L., Bruni, A. C., Maletta, R. G., Curcio, S. A., et al. (2015). Mutation analysis of CHCHD10 in different neurodegenerative diseases. *Brain* 138, e380–e380.

Zhang, Y.-J., Xu, Y.-F., Cook, C., Gendron, T. F., Roettges, P., Link, C. D., et al. (2009). Aberrant cleavage of TDP-43 enhances aggregation and cellular toxicity. *Proc. Natl. Acad. Sci. U.S.A.* 106, 7607–7612. doi: 10.1073/pnas.0900688106

Zhou, W., Ma, D., Sun, A. X., Tran, H.-D., Ma, D.-L., Singh, B. K., et al. (2018). PD-linked CHCHD2 mutations impair CHCHD10 and MICOS complex leading to mitochondria dysfunction. *Hum. Mol. Genet.* 28, 1100–1116.

Zhu, L., Gomez-Duran, A., Saretzki, G., Jin, S., Tilgner, K., Melguizo-Sanchis, D., et al. (2016). The mitochondrial protein CHCHD2 primes the differentiation potential of human induced pluripotent stem cells to neuroectodermal lineages. *J. Cell Biol.* 215, 187–202. doi: 10.1083/jcb.201601061

Zuo, X., Zhou, J., Li, Y., Wu, K., Chen, Z., Luo, Z., et al. (2021). TDP-43 aggregation induced by oxidative stress causes global mitochondrial imbalance in ALS. *Nat. Struct. Mol. Biol.* 28, 132–142. doi: 10.1038/s41594-020-00537-7

**Conflict of Interest:** The authors declare that the research was conducted in the absence of any commercial or financial relationships that could be construed as a potential conflict of interest.

**Publisher's Note:** All claims expressed in this article are solely those of the authors and do not necessarily represent those of their affiliated organizations, or those of the publisher, the editors and the reviewers. Any product that may be evaluated in this article, or claim that may be made by its manufacturer, is not guaranteed or endorsed by the publisher.

frontiers in Cell and Developmental Biology

REVIEW
published: 27 October 2021
doi: 10.3389/fcell.2021.764732

# Neuromuscular Development and Disease: Learning From *in vitro* and *in vivo* Models

*Zachary Fralish, Ethan M. Lotz, Taylor Chavez, Alastair Khodabukus and Nenad Bursac**

*Department of Biomedical Engineering, Pratt School of Engineering, Duke University, Durham, NC, United States*

The neuromuscular junction (NMJ) is a specialized cholinergic synaptic interface between a motor neuron and a skeletal muscle fiber that translates presynaptic electrical impulses into motor function. NMJ formation and maintenance require tightly regulated signaling and cellular communication among motor neurons, myogenic cells, and Schwann cells. Neuromuscular diseases (NMDs) can result in loss of NMJ function and motor input leading to paralysis or even death. Although small animal models have been instrumental in advancing our understanding of the NMJ structure and function, the complexities of studying this multi-tissue system *in vivo* and poor clinical outcomes of candidate therapies developed in small animal models has driven the need for *in vitro* models of functional human NMJ to complement animal studies. In this review, we discuss prevailing models of NMDs and highlight the current progress and ongoing challenges in developing human iPSC-derived (hiPSC) 3D cell culture models of functional NMJs. We first review *in vivo* development of motor neurons, skeletal muscle, Schwann cells, and the NMJ alongside current methods for directing the differentiation of relevant cell types from hiPSCs. We further compare the efficacy of modeling NMDs in animals and human cell culture systems in the context of five NMDs: amyotrophic lateral sclerosis, myasthenia gravis, Duchenne muscular dystrophy, myotonic dystrophy, and Pompe disease. Finally, we discuss further work necessary for hiPSC-derived NMJ models to function as effective personalized NMD platforms.

**Keywords: tissue engineering, induced pluripotent stem cells, disease modeling, neuromuscular junction, human skeletal muscle, muscular dystrophy, drug development, organ on a chip**

OPEN ACCESS

***Edited by:***
*Alec S. T. Smith,*
*University of Washington,*
*United States*

***Reviewed by:***
*Gabsang Lee,*
*Johns Hopkins University,*
*United States*
*Darren Player,*
*University College London,*
*United Kingdom*

****Correspondence:***
*Nenad Bursac*
*nenad.bursac@duke.edu*

***Specialty section:***
*This article was submitted to Stem Cell Research, a section of the journal Frontiers in Cell and Developmental Biology*

***Received:*** *25 August 2021*
***Accepted:*** *06 October 2021*
***Published:*** *27 October 2021*

***Citation:***
*Fralish Z, Lotz EM, Chavez T, Khodabukus A and Bursac N (2021) Neuromuscular Development and Disease: Learning From in vitro and in vivo Models. Front. Cell Dev. Biol. 9:764732. doi: 10.3389/fcell.2021.764732*

## INTRODUCTION

Neuromuscular diseases (NMDs) are a broadly defined group of disorders that lead to progressive impairment of motor function. The NMDs primarily involve dysfunction of motor neurons (MNs), skeletal muscle (SkM), or their synaptic connection, the neuromuscular junction (NMJ). Different NMDs have distinct tissue origins such as MNs [e.g., amyotrophic lateral sclerosis (ALS) either from direct loss or retrograde degeneration of MNs], muscle [e.g., Duchenne muscular dystrophy (DMD) or myotonic dystrophy (DM)], NMJs [e.g., myasthenia gravis (MG) or congenital myasthenic syndromes (CMS)], or a combination thereof (e.g., Pompe disease). Regardless of the origin, the structural and/or functional deficit in a targeted tissue will resonate throughout the entire motor unit, leading to multiple shared symptoms among different NMDs. NMDs are estimated to affect 160 per 100,000 people worldwide (Deenen et al., 2015); however, despite this high prevalence, outcomes are often fatal as few curative treatments are available.

Therefore, comprehensive biomimetic and clinically predictive *in vitro* and *in vivo* NMD models are essential for accelerating our understanding of the underlying disease mechanisms and development of effective therapeutics (Babin et al., 2014; Aartsma-Rus and van Putten, 2019). Animal models have been invaluable to our current understanding of NMDs as they capture important clinical features of the disease. Still, currently available animal models do not fully recapitulate the diverse range of disease phenotypes nor disease severity due to the complex genetic and non-genetic nature of human NMDs.

In recent years, high clinical and genetic heterogeneity of NMDs has prompted the considerations of personalized approaches to study and treat these devastating diseases. Historically, investigations of human NMDs have been hindered due to difficulty imaging NMJs *in vivo,* limited capability to isolate neural stem cells, and the postmitotic nature of adult MNs complicating *in vitro* studies. Over the past decade, advances in human induced pluripotent stem cell (hiPSC) technology, have provided a novel source of human somatic cells for pre-clinical research. hiPSCs can be generated from ethical and accessible sources, such as the skin and blood, and function as a potentially unlimited, patient-specific source of traditionally inaccessible cells such as MNs and cardiomyocytes. Additionally, hiPSC-derived cells can be integrated into two- (2D) and three-dimensional (3D) culture systems to enable novel studies of human development, disease, and pharmacology. hiPSC-based derivations of MNs and SkM, in particular, provide easily accessible, highly expandable sources of patient-specific NMD-relevant tissues. Notably, these platforms complement animal models creating an efficient and predictive system for patient specific NMD modeling and drug development. Incorporation of hiPSC-derived MNs and SkM into 3D cultures and organ-on-a-chip systems adds necessary structural complexity and genetic and environmental control over the cell-specific behavior. These tissue-engineered motor units recapitulate the nature of functional NMJs offering potential for improved mechanistic understanding of complex NMDs (Osaki et al., 2018; Bakooshli et al., 2019; Vila et al., 2019; Faustino Martins et al., 2020; Rimington et al., 2021).

In this review, we first explore the individual components of the NMJ including how they interact and contribute to NMJ functionality. We then compare current animal and *in vitro* hiPSC models of NMDs, focusing on ALS, MG, DMD, DM, and Pompe disease. We end by discussing the future of NMD modeling and strategies to address limitations in creating *in vitro* functional motor units that would allow predictive, patient-specific studies and treatment of NMDs.

# DEVELOPMENT

Understanding embryonic development of NMJs and their physiological roles is important to critically analyze methods to derive relevant cell types from hiPSCs and to compare biomimetic nature and effectiveness of the current and future tissue-engineered NMD models. Therefore, we provide an overview of MN, SkM, and Schwann cell (SC) development and draw parallels to current methods to differentiate these cells from hiPSCs. We finalize this section by describing NMJ development and function.

## Motor Neuron Development

Over the past decade, methods to differentiate hiPSCs into neuronal cells has rapidly progressed due to increased understanding of early neural development and commitment of neuroprogenitor cells to highly specialized neural subtypes, including MNs (Deenen et al., 2015). MNs are found throughout the CNS and can be divided into upper MNs (UMNs) or lower MNs (LMNs), which, despite their shared nomenclature, are developmentally and genetically distinct. Different NMDs, such as primary lateral sclerosis, progressive muscular atrophy, or ALS, can target either or both of UMNs and LMNs (Liewluck and Saperstein, 2015) making their distinction an important consideration when modeling NMDs. UMNs originate from the pre-motor and primary motor regions of the cerebral cortex. Their axons form glutamatergic connections with LMNs located in the brainstem and ventral horn of the spinal cord. Axons of LMNs project beyond the CNS forming cholinergic synapses with multiple tissue types to control a wide variety of physiological processes. As a result of these regional differences, the genetic and molecular events leading to MN development diverge early. Therefore, it is important to consider the development of the CNS in its entirety and understand the molecular mechanisms underlying MN diversity to develop physiologically relevant models for NMDs.

Cells of the developing vertebrate nervous system are derived from the ectoderm which forms during gastrulation (**Figures 1A–C**). Inhibition of TGFβ and FGF initiates neurulation causing the ectoderm to fold inward generating three new regions: (1) neural tube, (2) neural crest, and (3) external ectoderm (Ozair et al., 2013). Each region contains cell progenies restricted to a limited number of distinct fates, and those found in the neural tube are destined to form the brain and spinal cord. Signaling molecules from the mesodermal notochord coordinate the formation of the neural tube in the proper spatial orientation along the rostral–caudal and dorsal–ventral axes (Muhr et al., 1999). After neurulation, morphogen production and its subsequent spatio-temporal organization along the two axes causes axial patterning of the neural tube responsible for regional specification of neural subtypes (Wichterle et al., 2002; Li et al., 2005).

Regionalization is first specified in the brain with cells assuming a rostral forebrain identity in the absence of morphogens. These cells continue to develop into the neurons comprising the telencephalic region of the brain, which houses the cerebral cortex where mature UMNs reside (Watanabe et al., 2005). The remaining cells are driven caudally in response to a WNT gradient established by dorsal roof plate cells. This gradient dictates caudal forebrain, midbrain, and hindbrain identities (Nordstrom et al., 2002). LMNs with a distinct spinal character require further caudalization. A major contributing factor to this LMN caudalization is retinoic acid (RA) signaling that leads to rostral identities of the cervical and upper thoracic spinal segments. Presomitic cells of the surrounding paraxial mesoderm

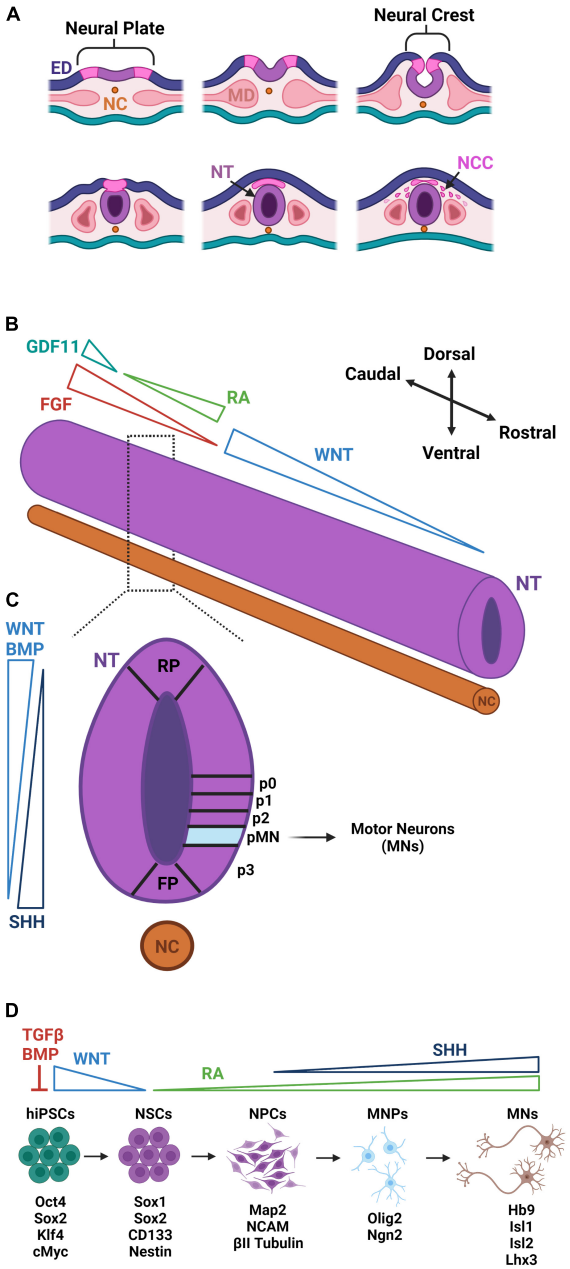


**FIGURE 1 |** Early development and hiPSC-based differentiation of motor neurons. **(A)** After the notochord (NC) signals inward folding of the ectoderm at the neural plate, the neural crest is brought together forming the neural tube (NT). The neural crest then forms neural crest cells (NCCs) which differentiate in the peripheral nervous system. The cells of mesoderm (MD) differentiate into somites and, eventually, the musculoskeletal system. **(B)** Along the rostral–caudal axis of the NT, WNT gradients dictate regionalization of the brain and RA/FGF/GDF11 gradients dictate segmentation of the spinal cord. **(C)** Along the dorsal–ventral axis of the NT, antithetical WNT/BMP [derived from the roof plate (RP)] and SHH gradients [derived from the floor plate (FP)] dictate patterning and the formation of the five ventral progenitor cell domains (p0, p1, p2, pMN, and p3). The pMN domain is the source of subsequent MN specification. **(D)** hiPSC-derivations of MNs begin with dual SMAD inhibition of TGFβ and BMP pathways to trigger neural stem cell (NSC) differentiation. WNT and RA signaling direct NSC differentiation into neural progenitor cells

*(Continued)*

**FIGURE 1 |** (Continued)
(NPCs) of the spinal cord region. With the addition of SHH signaling, NPCs further differentiate to Olig2-expressing MN progenitors (MNPs). Suppression of Olig2 and upregulation of Ngn2 commit MNPs to a post-mitotic MN lineage that express Hb9, Isl1, Isl2, and Lhx3. Distinct colors are used to denote approximate correspondence between stages of hiPSC differentiation in panel **(D)** and embryonic development in panel **(C)**.

convert retinaldehyde to RA via their expression of aldehyde dehydrogenase 1 A2 (ALDH1A2) (Liu et al., 2001). Decreased ALDH1A2 expression is found caudally and corresponds to decreased RA signaling (Liu et al., 2001) and increased FGF signaling, which govern the caudalization of neural precursors to identities of thoracic and lumbar spinal segments (Irioka et al., 2005). High expression of FGF alongside an increasing gradient of GDF11 dictate pattern a sacral spinal identity associated with the most caudal region of the developing spinal cord (Diez del Corral and Storey, 2004). Differential expression of HOX-family genes corresponds to cervical (HOX4 – HOX6), thoracic (HOX8 and HOX9), and lumbar (HOX10 and HOX11) positional identities along the spinal cord (Dasen and Jessell, 2009).

Neural precursors are also subject to dorsal–ventral patterning concurrent to rostral–caudal patterning. WNTs and BMPs derived from roof plate cells mediate dorsal patterning (Son et al., 2011). In contrast, exposure to increasing concentrations of sonic hedgehog (SHH) secreted by floor plate cells drives ventral patterning (Ericson et al., 1996). Dorsal–ventral patterning for the development of UMNs remains poorly understood. On the other hand, ventral positioning of LMN progenitors is known to require a coordinated balance between the antagonizing effects of BMPs/WNTs and SHH (Jessell, 2000). The ventral spinal cord consists of five domains that further restrict neural progenitors to a specific lineage. Interestingly, the MN progenitor (pMN) domain required for LMN specification is also required for oligodendrocyte specification (Ravanelli and Appel, 2015). OLIG2 expression is the earliest marker used to identify progenitors committed to the pMN domain (Ravanelli and Appel, 2015). Over time, oligodendrocyte progenitors will continue to express OLIG2 while committed MN progenitors will begin to express NGN2 which represses OLIG2 expression (Ravanelli and Appel, 2015). Continued expression of NGN2 induces HB9, signifying the formation of a post-mitotic MN (Lee et al., 2009).

Lower motor neurons at this stage are referred to as having a general character until organized into distinct motor columns that correspond to targeted regions of innervation. These regions include the median motor column (MMC), which innervates axial SkM, spinal accessory column (SAC), which innervates the branchial SkM of the face and neck, phrenic motor column (PMC), which innervates the SkM of the diaphragm, lateral motor column (LMC), which innervates appendage muscle, hypaxial motor column (HMC), which innervates intercostal and abdominal SkM, and preganglionic motor column (PGC), which synapse onto ganglionic neurons of the autonomic nervous system (ANS) (Nicolopoulos-Stournaras and Iles, 1983). Each motor column is organized along the

rostro-caudal axis and is identified by a unique gene signature (Francius and Clotman, 2014).

## Generation of Motor Neurons From Pluripotent Stem Cells

Over the past decade, a variety of protocols have been used to derive MNs from hiPSCs. These methods vary in length and efficiency; however, they are designed on the genetic and molecular principles of embryonic development (**Figure 1D**). Historically, neural induction was performed in suspended aggregates of hiPSCs, called embryoid bodies (EBs), in serum-free media without exogenous morphogens. Under these conditions, differentiating hiPSCs undergo spontaneous FGF and BMP inhibition, which naturally guides their differentiation to a neural fate (LaVaute et al., 2009). These early protocols were long and inefficient, often producing high experimental variability. Dramatic improvements came with the discovery that early inhibition of BMP and TGFβ signaling through SMAD inhibition selectively blocks the formation of mesodermal and endodermal cell fates leading to higher percentages of PAX6 and SOX2 expressing neural progenitors at earlier time points (Chambers et al., 2009). Based upon this discovery, dual-SMAD inhibition is now standard practice for the neuralization of hiPSCs in both monolayer cultures as well as EBs. The small molecule, SB431542, is the most utilized TGFβ inhibitor, and is commonly paired with a small molecule inhibitor of BMP (LDN193189, DMH1, or dorsomorphin) or recombinant Noggin, a naturally occurring BMP inhibitor.

After neuralization, neural precursors are committed to MN progenitors by following common patterning principles of caudalization and ventralization. MN differentiation efficiency and culture length have been improved by optimizing the concentrations and timing of patterning morphogens like WNTs, BMPs, RA, FGFs, and SHH (Nordstrom et al., 2002). Although experimental reproducibility has been improved, the variability and length of derivation protocols has remained a challenge. Specifically, the general application of RA and SHH for MN differentiation has been inefficient with yields ranging between 30 and 60% over a culture duration of 21–40 days (Hu and Zhang, 2009; Hester et al., 2011). Early activation of WNTs with CHIR99021 (CHIR) was shown to significantly improve MN differentiation efficiency and speed resulting in an 80% yield in 14 days (Maury et al., 2015). Moreover, when CHIR was continuously added throughout the differentiation, 90% of cells became mature MNs within 12 days (Du et al., 2015). This continued activation of WNTs stabilized excessive ventralization, maintaining a higher population of cells in the pMN domain and reducing the population of NKX2.2 expressing interneuron progenitors of the p3 domain (Du et al., 2015). While expedited protocols for MN generation may benefit cell manufacturing and screening, how accurately "fast-tracked" methods recapitulate adult MN cell physiology and maturation remains unclear.

## Skeletal Muscle Development

Development of skeletal muscle (SkM) begins with the paraxial mesoderm (Wachtler, 1992). The paraxial mesoderm (PM) forms in the primitive streak/blastopore during gastrulation and is comprised of two bilateral strips of presomitic mesoderm (PSM) flanking the neural tube and notochord (White et al., 2005; **Figure 2A**). Cells acquiring the PM fate require suppression of BMP signaling *in vivo* (Winnier et al., 1995). In the posterior compartments of the PM, there is an unsegmented progenitor zone comprised of neuromesodermal progenitors (NMP) (Tzouanacou et al., 2009) and other progenitor cells which give rise to the paraxial mesoderm, neural tube derivatives, lateral plate derivatives, and notochord (Takemoto et al., 2011; Garriock et al., 2015). Cells within the progenitor zone develop into skeletal muscle progenitor cells as a result of WNT and FGF signaling gradients which target transcription factors essential for PSM specification and patterning such as brachyury (T), Tbx6, and Msgn1 (Ciruna and Rossant, 2001; Nowotschin et al., 2012). Differentiated cells acquire the identity of mesoderm progenitor cells (MPCs) within the most posterior region of the PSM (Chalamalasetty et al., 2014).

In the next stage of development, MPCs attain the posterior PSM (pPSM) fate characterized by the downregulation of *T* and expression of *Msgn1* and *Tbx6* (Chalamalasetty et al., 2014). In the posterior two-thirds of the PSM, MPCs and pPSMs experience oscillations of the segmentation clock (pulses of Notch, FGF, and WNT signaling) to control the production of somites (Dubrulle et al., 2001; Aulehla et al., 2003). As skeletal muscle cells continue to develop, reach the determination front then enter the anterior third of the PSM (Dubrulle et al., 2001). At the determination front, the oscillations of the segmentation clock cease, *Msgn1* is downregulated, and *Pax3, Mesp2, Foxc1/2,* and *Meox1/2* genes are upregulated (Kume et al., 2001; Mankoo et al., 2003). Within the anterior PSM, retinoic acid (RA) counteracts the WNT and FGF signaling (Sakai et al., 2001). Furthermore, a posterior fissure forms at the junction between $Mesp2^{+}$ and $Mesp2^{-}$ cells to create new somites (Dubrulle et al., 2001; Aulehla et al., 2003). Shortly after somites are formed, they become subdivided into ventral mesenchymal sclerotome and dorsal epithelial dermomyotome, the latter of which contains SkM (alongside dermis and brown fat) progenitors and maintains *Pax3* expression (Lepper and Fan, 2010; Sanchez-Gurmaches and Guertin, 2014). Soon after its formation, primary myogenesis begins when dorsally located dermomyotomal cells lose Pax3 expression and upregulate myogenic factor *Myf5* (Ott et al., 1991). These early myogenic cells delaminate from the dermomyotome and contribute to the formation of the first embryonic muscles—myotomes (Denetclaw et al., 1997). Myogenesis then officially commences with primary myogenesis and the generation of primary myofibers that serve as the foundation for adult muscle formation.

During secondary myogenesis, myogenic progenitors expressing transcription factor *Pax7* sustain muscle growth by fusing among themselves or to existing primary myofibers generating β-enolase expressing secondary or fetal myofibers (Fougerousse et al., 2001). A subset of these Pax7+ progenitors localize under the basal lamina where the eventually become satellite cells which contribute to the repair and regeneration of damaged muscle fibers in adults (Dumont et al., 2015a). During

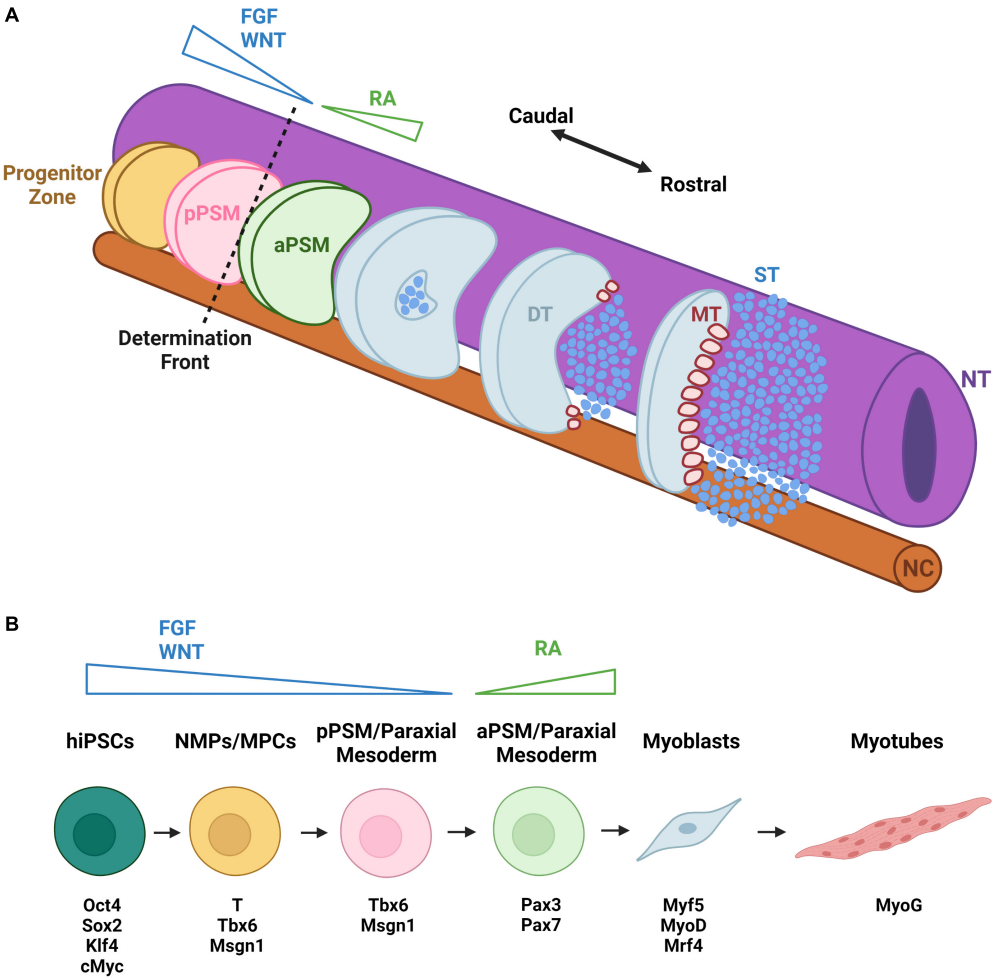


**FIGURE 2 |** Early development and hiPSC-based differentiation of skeletal muscle. **(A)** Caudal-rostral development of SkM occurs bilaterally along the neural tube (NT) and notochord (NC). From the progenitor zone, cells migrate to the posterior presomitic mesoderm (pPSM) with a decreasing gradient of FGF and WNT signals. They then cross the determination front to enter the anterior presomitic mesoderm (aPSM). With increasing retinoic acid (RA) gradient, somite formation begins. As cells continue to travel rostrally, the dermomyotome (DT), sclerotome (ST), and myotome (MT) form, initiating primary myogenesis. **(B)** hiPSC differentiation to skeletal muscle begins with WNT and FGF activation, inducing a shift into neuromesodermal progenitors (NMPs) and then muscle progenitor cells (MPCs) expressing the transcription factors T, Tbx6, and Msgn1. Subsequent loss of T expression leads to formation of paraxial mesoderm cells resembling skeletal muscle progenitors of pPSM. Through RA activation, these muscle progenitors begin to express the muscle stem cell markers Pax3 and Pax7 and eventually differentiate into myoblasts expressing early myogenic markers Myf5, MyoD, and Mrf4. The myoblasts can fuse into myotubes that express the late muscle differentiation marker MyoG. Distinct colors are used to denote approximate correspondence between stages of hiPSC differentiation in panel **(B)** and embryonic development in panel **(A)**.

muscle fiber maturation, expression of embryonic myosin heavy chain changes to adult myosin heavy chain isoforms with oxidative, slow twitch or glycolytic, fast twitch fiber phenotypes (Khodabukus, 2021). Additionally, actin and myosin assemble into sarcomeres, sarcomeres assemble into myofibrils, NMJs are formed at the sarcolemma, and triads are established from a network of tubules for facilitated neural excitation (Pourquié et al., 2018). Secondary and later stages of myogenesis are controlled by TGFβ (Gu et al., 2016), hepatocyte growth factor (HGF) (Bladt et al., 1995), WNT (van der Velden et al., 2006), and insulin-like growth factor (IGF) (Chargé and Rudnicki, 2004) signaling. The final phases of myogenesis are controlled by transcription factors including *Myf5*, *MyoD*, *Myomaker,* and *MyoG* to facilitate the fusion of muscle progenitor cells, hypertrophy of myofibers, and innervation by MNs to generate fully functional SkM (Zhang et al., 2020).

## Generation of Skeletal Muscle From Pluripotent Stem Cells

The derivations of SkM from hiPSCs typically fall under one of two major approaches (Kodaka et al., 2017; Jiwlawat et al., 2018). The first approach involves transgene-based approaches whereby hiPSCs are directly reprogrammed into myogenic progenitor cells through overexpression of muscle specific transcription factors (Kodaka et al., 2017). The second approach involves transgene-free methods whereby developmental myogenesis in hiPSCs is recapitulated through the administration of

small molecules, such as FGF2 and GSK3β inhibitor, which activate or inhibit myogenic signaling pathways (Jiwlawat et al., 2018; **Figure 2B**).

The transgene-based approaches generate myogenic progenitors from hiPSCs or their mesodermal derivatives by transient or constitutive overexpression of master regulators of myogenesis, such as PAX7 (Darabi et al., 2012; Rao et al., 2018) or MYOD1 (Abujarour et al., 2014; Albini and Puri, 2014; Maffioletti et al., 2015). Overexpression of exogenous myogenic genes has been accomplished through mRNA transfection (Warren et al., 2010), as well as transduction with adenoviral (Goudenege et al., 2012) or lentiviral (Albini and Puri, 2014; Maffioletti et al., 2015; Rao et al., 2018) vectors. Through these transdifferentiation methods, as many as 90% of cells commit to a myogenic identity and can differentiate into SkM progenitor cells (Tanaka et al., 2013; Abujarour et al., 2014; Rao et al., 2018). Use of fluorescence reporter genes co-expressed with transcription factors can allow further cell purification by fluorescence-activated cell sorting (FACS) (Darabi et al., 2012; Rao et al., 2018). Alternatively, activation of endogenous transcription factors (e.g., Pax7) using CRISPR/Cas9 methodology can lead to stable epigenetic reprogramming of hiPSCs and generation of myogenic progenitor cells (Kwon et al., 2020). The resulting SkM progenitors derived using transgene-based approaches survive and function when implanted in immunocompromised mice (Darabi et al., 2012; Kwon et al., 2020), while 3D engineered tissues generated from these cells can become functional muscle with the ability to survive and function *in vivo* (Rao et al., 2018). Nevertheless, these differentiation methods do not reflect normal development and despite the ability to obtain large numbers of human myogenic progenitors, regulatory concerns regarding genetic modification of cells may limit their potential therapeutic use (Jiwlawat et al., 2018).

A second approach, known as directed differentiation, mimics myogenic development through sequential addition of small molecules to activate or suppress specific signaling pathways. For example, CHIR-99021 activates WNT signaling through GSK3β inhibition, LDN-193189 inhibits BMP signaling, and HGF and IGF1 activate their respective signaling pathways (Chal et al., 2016). Despite no genetic modification and reliance on natural developmental ques, directed differentiation protocols require significantly longer culture time and exhibit considerably lower yields and higher heterogeneity of myogenic cells compared to transgene-based methods (Kodaka et al., 2017; Jiwlawat et al., 2018). Purity of myogenic progenitors can be increased by sorting for cell surface markers such as CDH13 (Nalbandian et al., 2021), FGFR4 (Nalbandian et al., 2021), ERBB3 (Hicks et al., 2018), and NGFR (Hicks et al., 2018), however, use of FACS further decreases cell yield. Recent protocols for expansion and cryopreservation of FACS-sorted hiPSC-derived myogenic progenitors may offer means to obtain clinically relevant cell quantities (van der Wal et al., 2018).

Recent transcriptomic analyses have shown that hiPSC-derived myogenic progenitors are developmentally immature and arrested between embryonic and fetal muscle stem cell stages (Xi et al., 2020; Nayak et al., 2021). Nevertheless, they can successfully fuse into myotubes that exhibit key functional behaviors of SkM, including generation of calcium transients and contractile force and robust response to acetylcholine (Skoglund et al., 2014; Rao et al., 2018), albeit at lower levels compared to primary human myotubes (Rao et al., 2018). Further advances in maturity of hiPSC-derived SkM cells will lead to improved modeling of human NMDs *in vitro*.

## Schwann Cell Development

Schwann cells are varied group of glial cells that produce protective myelin sheaths and support NMJ function, remodeling, and regeneration (Son et al., 1996). SCs undergo three main transitions during development: (1) from migrating neural crest cells (NCCs) to SC precursors (SCPs), (2) SCPs to immature SCs, and (3) immature SCs to a mature myelinating or non-myelinating SCs (Jessen and Mirsky, 2005). These transitions and SC survival are dependent upon morphogens secreted from axons with which SCPs and SCs continuously associate (Jessen and Mirsky, 1999). However, the molecular mechanisms that regulate neural crest cell differentiation into SCs have not been fully elucidated.

Early in the process of neurulation, dorsally located NCCs segregate from the neural tube and migrate in ventrally (Jessen and Mirsky, 2005). The basic helix-loop-helix (bHLH) transcription factor Sox10 is expressed early by all NCCs (Kuhlbrodt et al., 1998; Woodhoo and Sommer, 2008). While high expression of Sox10 persists in glial and melanocyte NCC derivatives of the peripheral nervous system (PNS), its expression is downregulated in other NCC derivatives (Kuhlbrodt et al., 1998; Woodhoo and Sommer, 2008). The continued high expression of Sox10 is dependent on the expression of Pax3 (Kioussi et al., 1995; Blanchard et al., 1996; Doddrell et al., 2012), which is regulated in part by histone deacetylases 1 and 2 (HDAC1/2) (Jacob et al., 2011). Together, Sox10 and Pax3 induce the expression of key SC lineage genes including fatty acid binding protein 7 (Fabp7) and myelin protein zero (MP0) (Kioussi et al., 1995; Blanchard et al., 1996; Doddrell et al., 2012).

While Sox10 is necessary for SC specification, it is not sufficient. In the developing PNS, SCPs migrate alongside MN axons extending to targeted regions of innervation (Jessen and Mirsky, 1999). Moreover, migrating SCPs are dependent upon signals from these axons, such as Neuregulin-1 (NRG1), for appropriate development and survival (Jessen and Mirsky, 1999). In NCC cultures, NRG1 suppresses neuronal differentiation and promotes glial specification (Shah et al., 1994). NRG1 binds ErbB2/3, an obligate heteromeric receptor tyrosine kinase pair, on SCPs to activate key downstream signal transduction cascades that are essential for both proliferation and directed migration (Newbern and Birchmeier, 2010).

Immature SCs develop after SCPs cease migration and populate axons that are still projecting to their targeted region of innervation, while acquiring a set of properties that clearly distinguish them from SCPs. Specifically, they cease migration, become dependent on autocrine signaling for survival, and deposit an organized basal lamina (Jessen and Mirsky, 2005). Additionally, increased notch signaling is a critical mediator of the SCP transition to immature SCs, with a loss of notch signaling preventing immature SC formation (Woodhoo et al., 2009).

## Generation of Schwann Cells From Pluripotent Stem Cells

Methods to differentiate hiPSCs into SCs have mimicked developmental process by first generating neural crest-derived SC precursors from hiPSCs. Neural crest stem cells have been derived from hiPSCs via FACS selection of p75+ cells derived from EBs cultured in stromal-cell-conditioned media, FGF2, and B-27 supplement (Liu et al., 2012). These cells were subsequently differentiated into a nearly pure population of SCs expressing glial fibrillary acidic protein, S100, and p75 through culture in mesenchymal stem cell medium supplemented with Neuregulin-1 for 40 days. A similar method using EB formation and FGF2 treatment was later developed that shortened the time of induction to 6 days (Huang et al., 2017).

To overcome the challenges with low reproducibility and throughput in EB cultures, methods for directed differentiation of hiPSCs to SCs have been developed. Specifically, sequential treatment of naïve hiPSCs with TGF-β and GSK-3β inhibitors followed by NRG1 produced SC precursors in 18 days (Kim et al., 2017). These precursors were further differentiated through treatment with NRG1, retinoic acid, platelet-derived growth factor-BB (PDGF-BB), and forskolin into SCs. This method shortened the total differentiation time from approximately 41 days (Huang et al., 2017) to approximately 32 days (Kim et al., 2017). However, a more recent protocol has been developed for the derivation of direct Schwann-cell precursors (SCPs) from SOX10-reporting hiPSCs that only required a total differentiation time of 21 days and allowed for *in vitro* culture up to 80 days with maintained expression of the SC proteins S100b, glial fibrillary acidic protein (GFAP), and galactosylceramidase (Mukherjee-Clavin et al., 2019). With all these methods, differentiated SCs show increased expression of SC-specific markers such as GFAP and S100β.

In addition to protein expression, hiPSC-derived SCs have been studied for their secretion rates of neurotrophic factors (Huang et al., 2017; Kim et al., 2017), ability to myelinate primary neurons (Liu et al., 2012; Kim et al., 2017), and ability to accelerate nerve healing within rodent sciatic nerve injury models (Huang et al., 2017; Kim et al., 2017). hiPSC-derived SCs have additionally been used in coculture with hiPSC-derived neurons to allow for stronger neuronal outgrowth within a 3D tissue-engineered skin model (Muller et al., 2018). Recent studies have further confirmed critical physiological roles of SCs in the stabilization and maintenance of NMJs *in vitro* (Singh and Vazquez, 2019; Martins et al., 2020), forming a foundation for the future development of novel biomimetic NMD models.

## Neuromuscular Junction Development

The NMJ is a chemical synapse formed between MNs and SkM that allows the transmission of motor commands from the CNS (**Figure 3**). MNs communicate with SkM through the release of acetylcholine (ACh) into the synaptic cleft of the NMJ. ACh receptors (AChRs) located on muscle fibers are activated and depolarize the muscle cell which triggers calcium release from the sarcoplasmic reticulum initiating a contraction (Fambrough, 1979). Reciprocal signaling between MNs and SkM is important for the formation and maintenance of NMJs as highlighted by the coordination required for complex movements and sensory-motor feedback.

During development, immature SCs migrate with MNs toward the periphery (Sugiura and Lin, 2011) and differentiate into either axonal SCs that myelinate axon extensions or terminal SCs that support the NMJ formation. Terminal SCs proliferate extensively around the NMJ (Hirata et al., 1997) and then cover or "cap" the nerve terminal with their processes (Court et al., 2008). Muscular innervation is preceded by the localization of small aneural AChR clusters to the central region of muscle fibers in a process called prepatterning. During this process, the MN terminal releases agrin which binds to the muscle-specific kinase (MuSK) co-receptor, low-density lipoprotein receptor related protein 4 (LRP4), promoting activation and transphosphorylation of MuSK. SC processes contact pre-patterned AChR clusters prior to the nerve and cover more of the postsynaptic membrane than axonal terminals during early synapse formation (Flanagan-Steet et al., 2005). Additionally, SCs express active agrin and encourage aggregation of AChRs on muscle fibers (Yang et al., 2001). In mice, SC loss results in MN defasciculation, but MNs still project toward muscle targets implying that SCs are not required for initial nerve–muscle contacts (Woldeyesus et al., 1999; Lin et al., 2000). However, further growth and maintenance of this early synapses is halted in SC absence (Riethmacher et al., 1997), suggesting that SCs are critical for NMJ homeostasis.

Eventually, innervation of muscle fibers induces the formation of larger, neural AChR clusters forming stable NMJs in the middle region of muscle fibers. Mice with a mutated agrin gene ($agrin^{-/-}$) are unable to form NMJs; however, these mice can form aneural AChR clusters on muscle fibers prior to innervation (Lin et al., 2001). Conversely, aneural clusters are not formed in $MuSK^{-/-}$ mice, and their muscle fibers demonstrate a uniform distribution of AChRs with a broader region of innervation containing highly branched MN terminals. Neuronal agrin does not induce AChR clusters in $MuSK^{-/-}$ muscle cells (Glass et al., 1996); however, agrin sensitivity can be restored through expression of wild-type MuSK (Zhou et al., 1999). Interestingly, synapse formation can be rescued in $agrin^{-/-}$ mice with ectopic MuSK expression (Kim and Burden, 2008). Together, this suggests the importance of MuSK for aneural AChR clustering and prepatterning prior to innervation while agrin is also needed for neural AChR clustering and NMJ formation. Additionally, SC processes influence nerve terminal growth and are required for both the formation and maintenance of developing NMJs (Reddy et al., 2003).

Neuromuscular junction formation is also influenced by several extracellular components. For example, MuSK has a cysteine-rich domain (CRD) that shares homology with the WNT receptor, Frizzled. As a result, WNT proteins bind and activate MuSK prior to innervation, when neural agrin is absent (Barik et al., 2016). This signaling can regulate axon guidance as well as induce aneural cluster formation (Li et al., 2018). Moreover, both canonical and non-canonical WNT pathways are affected in transgenic mice with MuSK CRD deletions (Messeant et al., 2017). Many components of the extracellular

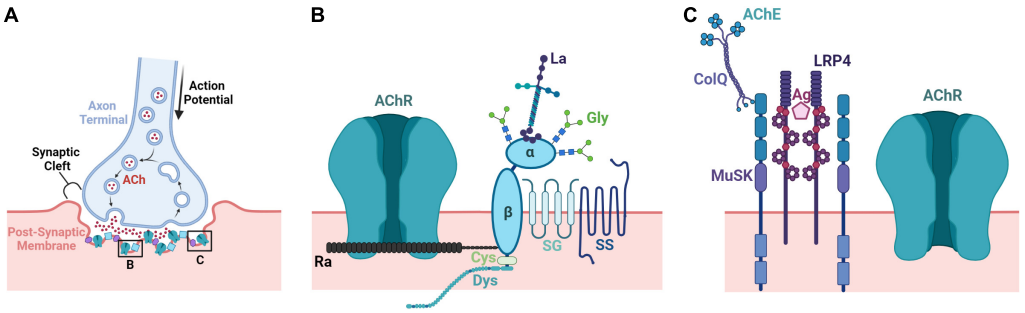


**FIGURE 3 |** Structural and molecular architecture of the neuromuscular junction. **(A)** The NMJ is comprised of three components: (1) the axonal terminal of an MN (pre-synapse), (2) the basal lamina of the synapse (synaptic cleft), and (3) the sarcolemma (membrane) of a muscle fiber (post-synapse). Following the conduction of an action potential to the axon terminal, $Ca^{2+}$ influx occurs at the presynaptic terminal releasing ACh-containing vesicles into the synaptic cleft. Released ACh can then bind to AChRs on the sarcolemma creating an endplate potential and eventually muscle contraction. **(B)** AChE secreted by the muscle binds to ColQ and inactivates residual ACh within the synapse. ColQ binds to MuSK to help stabilize the synapse. The synaptogenic proteoglycan agrin secreted by MNs binds to LRP4 to facilitate formation of the NMJ. **(C)** AChRs are stabilized by dystrophin-associated glycan (DAG) complexes. The AChR-clustering protein rapsyn connects AChRs to the DAG complex and dystrophin anchors the complex to the SkM cytoskeleton. Lamins and glycans additionally connect the complex to the ECM while the sarcoglycan and sarcospan stabilize the DAG complex within the membrane. ACh, acetylcholine; AChE, acetylcholine esterase; ColQ, collagen Q; MuSK, muscle-specific tyrosine kinase receptor; Ag, agrin; LRP4, low density lipoprotein receptor 4; AChR, acetylcholine receptor; AChR, acetylcholine receptor; La, laminin; α/β, α/β dystroglycan; Gly, glycans; SG, sarcoglycan; SS, sarcospan; Ra, rapsyn; Cys, cysteine; Dys, dystrophin.

matrix (ECM) have important regulatory roles in myogenesis and synaptogenesis. Within the synaptic basal lamina, ECM molecules help guide the process of innervation and are crucial to formation of post-synaptic density as well as organization and maintenance of functional appositions of the pre- and post-synaptic elements. The dystrophin-associated glycoprotein complex (DGC), through its α-dystroglycan subunit, organizes a functional scaffold in the basal lamina including perlecan, acetylcholinesterase/ColQ, and laminin that stabilizes AChR clusters (Jacobson et al., 2001). The DGC additionally connects networks of laminins and collagens to one another by nidogen and anchors them to the sarcolemma through the sarcoglycan-sarcospan subcomplex and intracellular cytoskeleton through dystrophin (Fox et al., 1991; Jacobson et al., 2001). The laminin β2 chain plays a role in synapse maturation by binding and clustering voltage-dependent calcium channels (VDCC) in the active zone of the NMJ. A reduced number of active zones and pre-synaptic release of ACh is observed in mice lacking laminin β2 (Rogers and Nishimune, 2017). Mice lacking ColQ, collagen XIII, collagen IV, or collagen VI also exhibit immature nerve terminals and/or NMJs (Sigoillot et al., 2016; Cescon et al., 2018; Zainul et al., 2018).

After forming functional NMJs with their target, MNs impinge on muscle fiber structural and functional diversity. A single muscle is composed of several fiber types that are innervated by specific classes of MNs. MNs are subdivided into three groups based on the type of muscle fiber they innervate: (1) alpha MNs, which innervate force generating extrafusal fibers, (2) gamma MNs, which innervate the proprioceptive intrafusal fibers, and (3) beta MNs, which innervate both extrafusal and intrafusal fibers. Alpha MNs are the most abundant of these classes and are categorized as SFR (slow-twitch, fatigue-resistant), FFR (fast-twitch, fatigue-resistant), and FF (fast-twitch, fatigable) reflecting the type of extrafusal muscle fiber they innervate (Totosy de Zepetnek et al., 1992). MNs are intrinsically competent to recognize and connect to either fast or slow muscle fibers (Landmesser, 2001). Slow MNs start to specifically express the synaptic vesicle glycoprotein 2a (SV2A) (Chakkalakal et al., 2010) as well as the estrogen-related receptor beta (ESRRB) (Enjin et al., 2010) soon after birth. Conversely, fast MNs specifically express the calcitonin-related polypeptide alpha (CALCA) and the chondrolectin (CHODL) (Enjin et al., 2010). The Notch ligand delta-like homolog1 (DLK1) has also been identified as a necessary regulator of fast MNs (Muller et al., 2014). Understanding of the influence of innervation by specific MN types upon SkM phenotype could provide important insight into certain NMDs that preferentially target specific muscle fiber types.

## CURRENT MODELS FOR STUDIES OF NEUROMUSCULAR JUNCTION FUNCTION AND DISEASE

### Animal Models

Various animal models have been broadly utilized to advance our understanding of the formation, function, and malfunction of NMJs during the development and progression of NMDs. Moreover, they have been used to study the pathophysiology and develop pharmacotherapies for NMDs. Specifically, *Caenorhabditis elegans* (Sleigh and Sattelle, 2010), zebrafish (Babin et al., 2014), *Drosophila* (Shields et al., 2017), and mice (Hsieh-Li et al., 2000) have been extensively employed to investigate the precise anatomy and function of NMJs. Their ease of genetic manipulation, tractable anatomy, relatively rapid growth, and low cost have contributed to their extensive use (Dawson et al., 2018). The mouse NMJ has been particularly useful due to its large size and accessibility, facilitating microscopic studies by immunofluorescence histology and

functional analyses by electrophysiology (Webster, 2018). The imaging studies, in particular, have enabled enhanced understanding of how localization and density of pre-synaptic, post-synaptic, and synaptic proteins are rearranged or lost in disease states.

However, experimental results in animal models may have limited translational value due to distinct anatomical differences between animal and human NMJs. For example, the murine NMJ and human NMJ exhibit substantially different proteomes and the larger, more pretzeled murine NMJ readily remodels with age whereas the smaller, more fragmented human NMJ is mostly conserved (Jones et al., 2017). Interestingly, the density of the active portion of the human NMJ is greater compared to its mouse counterpart (Jones et al., 2017). Additionally, disease phenotypes in animals can vary widely from those in humans in terms of progression, severity, and etiology (Vainzof et al., 2008). High levels of inbreeding limit genetic diversity within common animal models and controlled environments prevent genetic drift, while removing common viral and microbial agents that can influence human NMD pathogenesis (Dawson et al., 2018). The inability of animals to fully capture the genotypic heterogeneity and allelic variations observed across human individuals has hindered the clinical success of NMD drugs validated through animal models (Vainzof et al., 2008). Only a small fraction of drugs that enter clinical trials are approved as many result in unanticipated drug responses and toxicities (Vainzof et al., 2008). This situation has prompted development of *in vitro* human models of NMJ and NMDs that could allow studies of disease and pharmacological effects in a personalized and clinically more relevant fashion.

## Two-Dimensional *in vitro* Models

When developing *in vitro* models of NMJ, it is important to both consider its anatomical structure and enable relevant biological and functional studies. Initial rodent models of NMJ entailed mixed 2D co-cultures of myotubes with dissociated MNs (Kengaku et al., 1991) or spinal cord explants (Askanas et al., 1987), either plated simultaneously or sequentially (**Figure 4A**). Axonal projections in these co-cultures extended from the MNs to form NMJs with the myotubes that in turn exhibited functional post-synaptic potentials. Development of *in vitro* human models of the NMJ (Guo et al., 2011; Demestre et al., 2015; Yoshida et al., 2015) have additionally opened doors to personalized modeling of NMDs. For example, hiPSCs from spinal muscular atrophy (SMA) patients exhibited impaired AChR clustering which was ameliorated with valproic acid and antisense oligonucleotide treatment (Yoshida et al., 2015). The main advantages of these 2D culture models were relative simplicity and use of a flat substrate allowing for efficient and direct analysis of cell morphology and pathological features.

However, AChR clustering in mixed 2D co-cultures exhibits poor co-localization of pre- and post-synaptic structures compared to native NMJs, hindering the ability to recapitulate the intricacies of specific NMDs (Das et al., 2010; Umbach et al., 2012). Specifically, without proper spatial cues, myoblasts in mixed 2D cultures fuse into randomly oriented and branched myotubes limiting formation of elongated myofibrils and mature sarcomeres (Bettadapur et al., 2016). These myotubes will often delaminate after few days of culture as they start to generate more mechanical stress against the underlying substrate, thus not providing sufficient time for proper NMJ maturation (Wang et al., 2012; Sun et al., 2013). Anatomical considerations also hinder physiological relevance of these models. *In situ*, the soma of the MNs reside in the spinal cord with only the axons projecting and physically interacting with the myofibers. Plating MNs on top of myotubes in mixed 2D co-cultures is therefore anatomically incorrect and may alter the physiology of one or both cell types. Additionally, measuring SkM force generation is not possible on most conventional culture substrates and individual analysis of each cell type, both functional and molecular, is often impractical.

To overcome these technical challenges, researchers have developed several types of tunable culture surfaces and microfabricated devices to engineer more biomimetic NMJs with improved anatomical organization. Use of topographical cues, such as polylactic acid (PLA) or polycaprolactone (PCL) nanofibers, served to align murine myoblasts and improve NMJ formation with co-cultured rat embryonic spinal MNs (Luo et al., 2018; Das et al., 2020). Micropatterning of alternating soft and stiff extracellular matrix strips increased expression of the NMJ markers MuSK and LRP4, improved myoblast fusion, and augmented AChR cluster size when rat primary MNs were co-cultured with both human and mouse SkM cells (Happe et al., 2017). Micropatterning techniques have also been shown to promote hiPSC-derived MN survival (Burbulla et al., 2016) and align human myoblasts (Ebrahimi et al., 2018).

Furthermore, incorporation of SCs has improved viability and survival of MNs in long-term 2D cultures *in vitro* while supporting longer, myelin ensheathed axonal projections in rodent models *in vivo* (Haastert et al., 2005; Honkanen et al., 2007; Paivalainen et al., 2008; Viader et al., 2011; Hyung et al., 2015). Within human cell lines, increased myotube number, length, and viability were observed in both SC/SkM cocultures and SC/SkM/MN tricultures highlighting the synergistic relationships among these cell types (Singh and Vazquez, 2019). Additionally, self-organization of hiPSC-derived NMJs has been accomplished following simultaneous generation of MNs, SkM, and SCs from a bipotent NMP population (Lin et al., 2019) fated to form both spinal neuroectodermal and associated musculoskeletal mesodermal cell derivatives (Gouti et al., 2017). Within this system, contractile and electrophysiological activity driven by functional NMJs was supported by the presence of terminal SCs and myelinated axons.

Additionally, development of compartmentalized 2D NMJ models has allowed for MN somas and myotubes to be spatially separated increasing the biomimetic nature of these co-cultures (**Figure 4B**). In the first example of a compartmentalized NMJ model, neurons derived from murine embryonic stem cells and fused C2C12 myoblasts were cultured separately in a microfluidic device and connected only through axon extensions (Park et al., 2013). Similar compartmentalized 2D models have been used to study rodent synaptic formation (Tong et al., 2014), AChR clustering (Southam et al., 2013), and MN-induced calcium transients in myotubes (Ionescu et al., 2016).

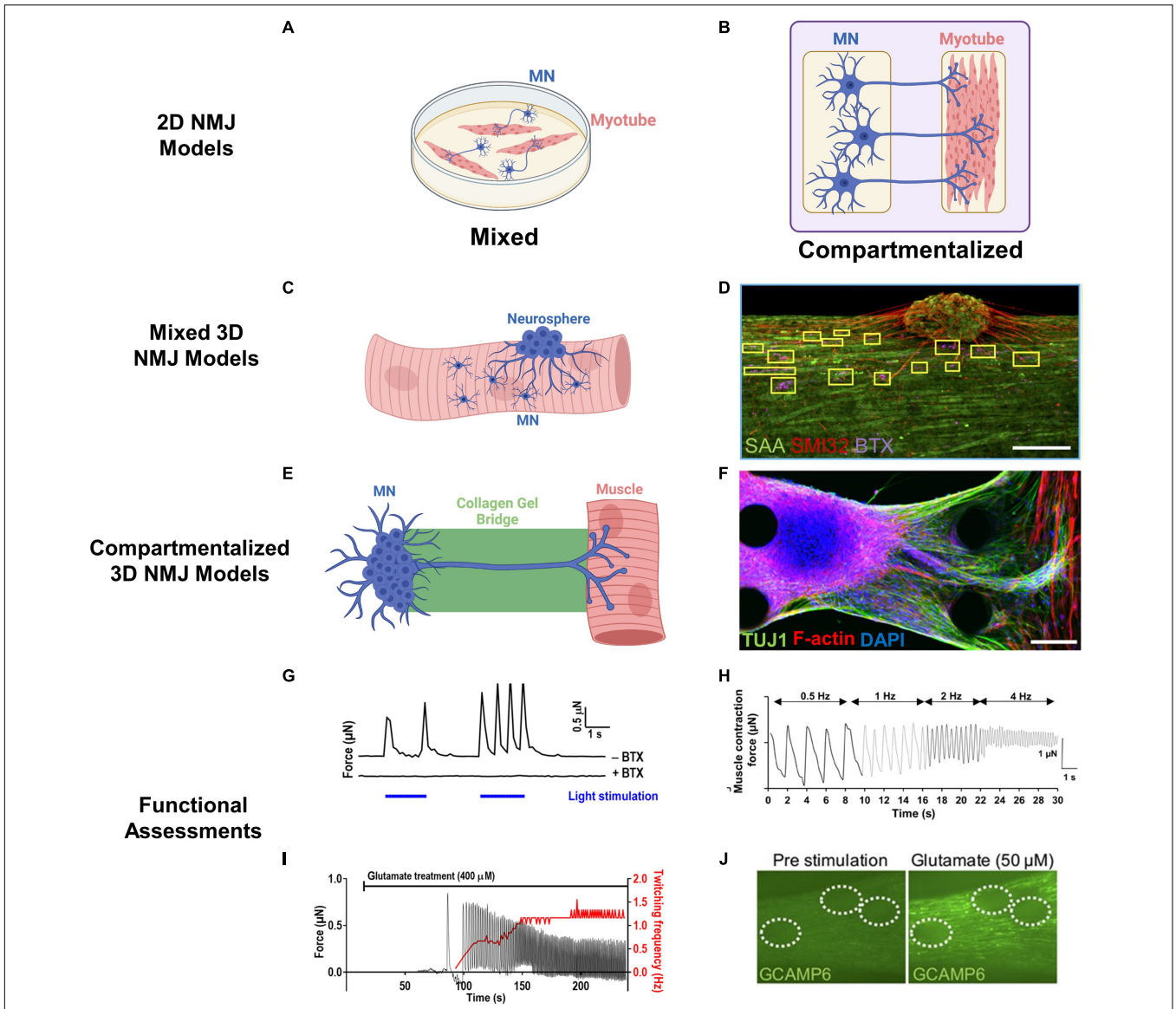


**FIGURE 4 |** Engineered NMJ models. **(A,B)** Schematics of 2D NMJ co-culture models in mixed **(A)** and compartmentalized **(B)** configuration. **(C)** Mixed 3D NMJ co-culture systems incorporate MNs or neurospheres into SkM during 3D tissue formation. **(D)** Representative mixed 3D NMJ model with immunofluorescent staining of muscle sarcomeres (SAA), neurite extensions (SMI32), and acetylcholine receptors (BTX). Scale bar, 200 μm (Bakooshli et al., 2019; Copyright 2019, *eLIFE*). **(E)** Compartmentalized 3D NMJ co-culture systems culture MNs and SkM in separate compartments bridged by an extracellular matrix gel to facilitate axonal outreach and SkM innervation. **(F)** Representative compartmentalized NMJ model with immunofluorescent staining of neurite extensions (TUJ1) and myotubes [filamentous (F)-actin]. Scale bars, 100 μm (Osaki et al., 2018; Copyright 2018, *Science Advances*). **(G)** Example of optogenetic control of 3D NMJ models through blue light illumination (blue bars) of $ChR2^{H134R}$-HBG3-MN neurospheres inducing contraction in muscle (*y*-axis) as measured by pillar displacement within a microfluidic system. Administration of α-bungarotoxin (BTX) prevented MN-induced contractions (Uzel et al., 2016; Copyright 2016, *Science Advances*). **(H)** Example of muscle contraction induced by electrical stimulation of MNs at varying frequencies (0.5–4 Hz) (Osaki et al., 2018; Copyright 2018, *Science Advances*). **(I)** Representative recording of contractile force (*y*-axis) in 3D SkM-MN co-culture induced by glutamate stimulation of neurospheres (Uzel et al., 2016; Copyright 2016, *Science Advances*). **(J)** Representative recording of glutamate-induced $Ca^{2+}$ transients in 3D SkM-MN co-culture with muscle-specific expression of GCaMP6 reporter. MN neurospheres are encircled by dashed lines (Bakooshli et al., 2019; Copyright 2019, *eLIFE*).

A compartmentalized 2D NMJ model between primary embryonic rat MNs and myotubes inside an automated device allowed measurements of MN-initiated muscle contractile force through cantilever displacement (Smith et al., 2013). Similar studies testing effects of bungarotoxin, BOTOX®, and curare were performed in a human co-culture platform where video recording analysis was used to measure amplitude and frequency of MN-induced myotube contractions (Santhanam et al., 2018). Additionally, lentiviral transduction of human MNs with channelrhodopsins has enabled a more precise, light-mediated control over MN activity in NMJ co-cultures (Steinbeck et al., 2016). Use of single-donor hiPSC-derived

SkM cells and MNs has further enabled patient-specific disease modeling (Guo et al., 2020a) with capability to assess NMJ function in response to electrical stimulation of MNs. While these 2D compartmentalized platforms partly recapitulate *in vivo* organization through physical separation of MNs and SkM cells, they lack the structural 3D complexity of the native innervated muscle.

## Three-Dimensional *in vitro* Models

The lack of the 3D cell–cell and cell–ECM interactions in 2D NMJ models has prompted the development of 3D *in vitro* models of innervated SkM (**Figures 4C–F**), which despite being more expensive, time-consuming, and lower throughput than 2D cultures, are expected to provide a more physiologically relevant platform for NMD studies. The first example of a mixed 3D NMJ model incorporated fetal rodent nerve explants within 3D SkM constructs resulting in the formation of functional NMJs and expression of more mature myosin heavy chain (MHC) isoforms (Larkin et al., 2006). A similar mixing technique using neonatal rat myoblasts and embryonic ventral horn neurons improved myotube cytoskeletal organization and augmented force production of engineered SkM (Martin et al., 2015). Direct co-culture of mouse-derived MN spheroids and SkM allowed for contraction following glutamic acid activation of MNs that could be inhibited by curare treatment, a NMJ antagonist (Morimoto et al., 2013). However, compared to native NMJs, AChRs clustering remained relatively diffuse in these systems (Morimoto et al., 2013). These first-generation 3D NMJ models demonstrated the utility of 3D platforms to generate functional NMJs but their non-compartmentalize nature and use of embryonic rodent cells limit their utility for studies of human NMDs.

Consequently, recent efforts have focused on the development of human 3D NMJ co-cultures. For example, addition of hiPSC-MN clusters into 3D SkM/hydrogel suspensions or to pre-formed SkM tissues allowed generation of mixed 3D NMJ models (**Figures 4C,D**) where consequences of functional connectivity between MNs and muscle fibers were studied by recording calcium transients or contractile force generation (Osaki et al., 2018; Bakooshli et al., 2019; Rimington et al., 2021). Compared to 2D monolayers, 3D MN spheroid co-culture with SkM increased axon length and expression of SMI32, a marker of MN maturity (Rimington et al., 2021), while the presence of MNs improved the overall structure and function of myotubes (Bakooshli et al., 2019; Rimington et al., 2021), revealing the mutually beneficial effects of MNs and SkM within 3D co-culture systems. Interestingly, functional innervation was achieved following 2 weeks of culture within 3D, but not in comparable 2D NMJ co-cultures, and expression of the mature AChR ε-subunit was observed only in 3D NMJ co-cultures (Bakooshli et al., 2019). Beyond mixed 3D NMJ models, compartmentalized microdevices (**Figures 4E,F**) have been developed to spatially separate MN spheroids and engineered SkM and connect them via axon-permissive channels to more appropriately mimic *in vivo* muscle innervation (Uzel et al., 2016; Osaki et al., 2018; Vila et al., 2021). Through this compartmentalization, visualization of 3D neurite outgrowth and engineered SkM innervation is greatly simplified, similar to studies in 2D compartmentalized co-cultures.

Incorporation of SCs can further improve longevity and biomimetic organization of 3D NMJ models as shown in rodent co-cultures, where MN–SC interactions led to extended, myelinated axonal projections of MNs with improved viability (Gingras et al., 2008; Hyung et al., 2021), while optical stimulation of murine MNs acted reciprocally on SCs to enhance the myelination process, leading to the formation of thicker myelin sheaths (Hyung et al., 2019). Similarly, in human organoids, NMJs identified by accumulation of αBTX clusters in muscle fibers encompassed both myelinated axons and capping terminal SCs and were shown to be functional by curare-induced block of muscle activity (Faustino Martins et al., 2020).

Motor neuron activation within 3D NMJ models has been achieved through addition of the neurotransmitter glutamate (Osaki et al., 2018; Bakooshli et al., 2019) or its mimic *N*-Methyl-D-aspartate (NMDA), optogenetic control (Osaki et al., 2018; Vila et al., 2019, 2021), or direct electrical stimulation (Osaki et al., 2018; Rimington et al., 2021). Glutamate stimulates MNs (**Figure 4I**) through binding to α-amino-3-hydroxy-5-methyl-4-isoxazolepropionic (AMPA), kainic acid (KA), and NMDA receptors while NMDA specifically targets NMDA receptors (Newcomer et al., 2000). High doses of glutamate or NMDA can be used to study excitotoxicity (over-activation of glutamate receptors) while lower doses can access NMJ model sensitivity (Liu et al., 2007). Optogenetic control in NMJ models (**Figure 4G**) relies on genetic modification of MNs to express light-sensitive channels, such as channelrhodopsin, that induce an action potential and subsequent muscle contraction in response to blue light. This method, though utilizing genetically altered MNs, allows for spatiotemporal and noninvasive control over motor units. Direct electrical stimulation, while impractical in mixed co-culture systems as it would excite both MNs and SkM cells, can be implemented in compartmentalized systems to stimulate MNs (**Figure 4H**).

To assess NMJ functionality, recordings of calcium transients have been used as an indicator of MN-induced muscle excitation and gCaMP6 (Bakooshli et al., 2019), a genetically encoded calcium indicator, has been used to visualize calcium flow through muscles (**Figure 4J**). Furthermore, MN-innervated engineered SkM tissues can be cultured on microfabricated pillars, displacement of which can be imaged to assess muscle contractions induced via glutamate or light-stimulated MN activity (Uzel et al., 2016; Vila et al., 2019, 2021; Afshar et al., 2020). In addition to indirect functional measurements by video recordings, contractile force generation in mixed 3D NMJ co-cultures can be directly measured by a force transducer (Martin et al., 2015; Rizzuto et al., 2017; Rimington et al., 2021), which allows for assessment of the muscle force-length relationship and could be used for detailed functional studies in compartmentalized 3D NMJ models, similar to those performed in native nerve-muscle preparations (Martin et al., 2015; Rizzuto et al., 2017). Finally, transfer of MN activity to SkM can be blocked through a variety of AChR inhibitors including α-bungarotoxin (Osaki et al., 2018; Vila et al., 2019) and

tubocurarine (Bakooshli et al., 2019; Rimington et al., 2021) to further validate NMJ functionality.

## NEUROMUSCULAR DISEASES

Neuromuscular diseases originate from various pathophysiological mechanisms, exhibit diverse symptoms, and differentially affect the NMJ (**Figure 5**). As such, they have historically been divided into subcategories and viewed through either a neurogenic or myogenic lens. However, increasing evidence for the important roles of cellular crosstalk in NMD pathogenesis suggest that modeling of the entire motor unit is necessary for proper studies of NMDs. In the following section, we present five NMD examples with diverse causes and manifestations highlighting the pathogenic roles of both MNs and SkM. First, we discuss ALS, a genetic disorder viewed to primarily affect MNs. Second, we consider MG, an autoimmune disorder focused upon the NMJ. Third, we examine DMD, a muscular dystrophy resulting from loss or truncation of the sarcolemmal protein dystrophin. Fourth, we review DM, a muscular dystrophy arising from toxic RNA repeats. Fifth, we discuss Pompe disease, a glycogen storage disorder affecting multiple cell types. For each NMD, we highlight most representative *in vitro* (**Table 1**) and *in vivo* models and offer perspective on future progress needed to advance NMD modeling toward translational applications.

### Amyotrophic Lateral Sclerosis

Amyotrophic lateral sclerosis is late-onset, progressive NMD caused by SkM and MN wasting resulting in paralysis, respiratory failure, and death (Brown and Al-Chalabi, 2017). It is characterized by muscle stiffness and spasticity, but many patients also exhibit cognitive and behavioral changes (Oskarsson et al., 2018). Unfortunately, no ALS-specific biomarkers are currently known resulting in lengthy diagnosis periods and delayed treatments (Oskarsson et al., 2018). While no curative therapy is currently available, approved drugs, such as Edaravone and Riluzole, limit disease progression and may lengthen patient survival up to several months (Jaiswal, 2019). Approximately 90–95% of patients have sporadic ALS and 5–10% have familial disease, with no clear clinical or pathological differences between the groups (Loeffler et al., 2016). Over 100 genes have been attributed to familial ALS with the most commonly affected genes being *C9ORF72*, *SOD1*, *TARDBP*, and *FUS*, typically in combination (Wroe et al., 2008). The precise molecular mechanisms of ALS are unknown; however, many contributing factors have been proposed including protein aggregation (Ross and Poirier, 2004), excitotoxicity (Rothstein, 1995), aberrant nucleocytoplasmic or endosomal transport (Zhang et al., 2015), dysfunctional RNA metabolism (Strong, 2010), oxidative stress (Barber and Shaw, 2010), and axonal deformations (Bilsland et al., 2010). Although MN degradation is characteristic of ALS, denervation of the NMJ occurs first (Tremblay et al., 2017). Interestingly, ALS exhibits a preferential degradation of MNs with early loss of fast-fatigable MNs followed by fast fatigue-resistant, and then slow MNs (Tremblay et al., 2017). NMJs in ALS patients exhibit endplate fragmentation (Bjornskov et al., 1975), smaller endplates and nerve terminals (Tsujihata et al., 1984), flattened synaptic clefts (Yoshihara et al., 1998), and reduced mitochondrial presence within the nerve terminal (Tsujihata et al., 1984). Some small nerve terminals have been observed over distorted endplates, suggesting the possibility for NMJ regeneration (Yoshihara et al., 1998).

While ALS research has primarily focused upon MN pathology, studies with animal models have underlined the importance of pre-symptomatic SkM changes including atrophy and denervation (Loeffler et al., 2016). Prior to disease onset in *SOD1* mice, there is an upregulation in muscle developmental genes (De Oliveira et al., 2014), a decrease in CDK5 (myogenic marker) (Park and Vincent, 2008), sarcoplasmic accumulation of neuronal NOS (Suzuki et al., 2010), and a loss in muscle volume (Kraft et al., 2007). Muscle-specific overexpression of *SOD1* in mice has caused oxidative stress and muscular wasting without motor defects (Dobrowolny et al., 2008), while neuron-specific expression of *SOD1* did not result in neuron abnormalities (Lino et al., 2002). Satellite cells from pre-symptomatic mice exhibit upregulated Pax7 expression (Manzano et al., 2011) and reduced proliferative capacity (Manzano et al., 2013). ALS patients exhibit a similar dysfunction in satellite cell proliferation (Scaramozza et al., 2014), indicating intrinsic muscle pathology in ALS as satellite cells are not directly innervated. Additionally, electrophysiological postsynaptic alterations presented in *SOD1* mice prior to 6 weeks of age (Rocha et al., 2013) and decreased expression of choline acetyltransferase (ChAT) and vesicular acetylcholine transporter resulted in cholinergic dysfunction prior to MN degradation (Casas et al., 2016). In these mice, early NMJ dysfunction is accompanied by $Ca^{2+}$ and reactive oxygen species accumulation, mitochondrial failure, and impaired transport within axons (Fischer-Hayes et al., 2013; Pollari et al., 2014). Clinically, pathophysiological axonal excitability is more pronounced within distal axonal branches (Nakata et al., 2006) and muscle denervation occurs before spinal cord MN degradation (Pollari et al., 2014). Based upon these observations, the "dying back" hypothesis of ALS suggests that this disease progresses through a retrograde degeneration of MNs from the periphery (Moloney et al., 2014) contrasting with the "dying forward" hypothesis that suggests glutamate excitotoxicity from cortical MNs advances forward to the periphery (Eisen et al., 1992). Additionally, astrocytes express most ALS related genes, and their dysregulation leads to neuroinflammation, oxidative stress, excitotoxicity, and protein aggregation further supporting the non-cell autonomous nature of ALS (Halpern et al., 2019).

Several animal models of ALS have been developed with a variety of mutations. Transgenic mice expressing mutant human *SOD1* have been heavily studied and particularly useful in understanding pathophysiology of ALS. These mice progressively accumulate *SOD1* within their muscles causing endoplasmic reticulum stress (Chen et al., 2015), recapitulate characteristic degradation of MNs and paralysis, and importantly demonstrate the non-cell autonomous nature of ALS (Nagai et al., 2007). Additionally, these mice exhibit altered gene expression related to muscle repair (De Oliveira et al., 2014), reduction in muscle volume (Marcuzzo et al., 2011), decreased proliferative capacity

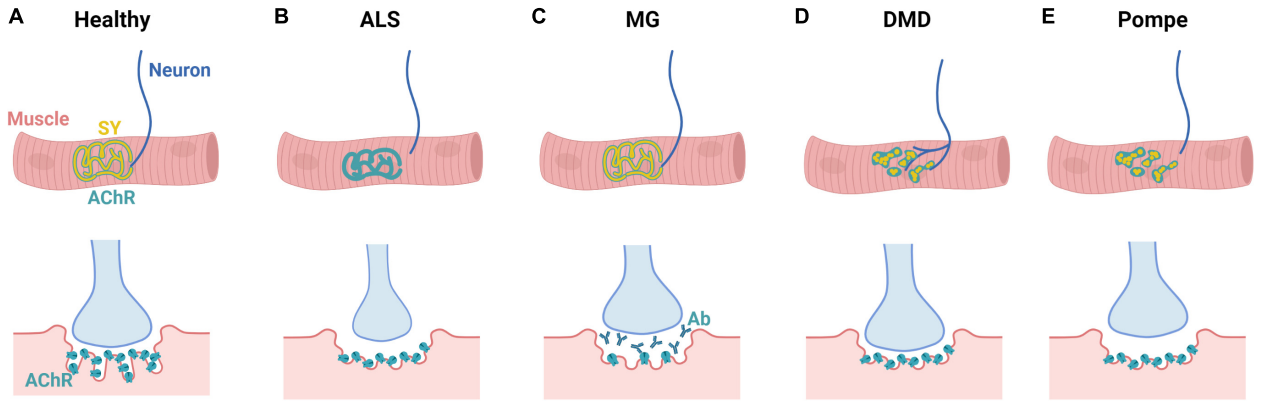


**FIGURE 5 |** NMD-specific changes in NMJ morphology. **(A)** Mature human NMJs present with a characteristic "pretzel" shape and contain both synaptophysin (SY) and acetylcholine receptors (AChRs). NMJ endplates exhibit distinct membrane folds that extend into the muscle cell cytoplasm. **(B)** In ALS, marked decrease in synaptophysin and NMJ size occurs alongside denervation. Additionally, ALS patients present with smaller nerve terminals and flattened synaptic clefts. **(C)** In MG, NMJ morphology is generally maintained; however, there is synaptic accumulation of autoantibodies (Ab), decrease in AChRs, and shortening of synaptic clefts. **(D)** In DMD, there is marked axonal branching and NMJ fragmentation alongside shortening of the synaptic cleft. **(E)** In Pompe disease, there is denervation alongside NMJ fragmentation and increased rates of MN apoptosis.

of satellite cells (Manzano et al., 2013), and a slow fiber-type shift (Hegedus et al., 2007). Studies with *SOD1* mice have been useful to identify potential treatments with glial cell line-derived neurotrophic factor (GDNF) to rescue MN function through overexpression within the SkM (Li et al., 2007), stem cell-based delivery (Suzuki et al., 2007), and intramuscular injection of GDNF (Suzuki et al., 2008). Unfortunately, overexpression of healthy human *SOD1* in these mice results in axonopathy undermining mutational importance within this disease model (Joyce et al., 2011) and spontaneous copy number deletions limit disease severity increasing variability within *SOD1* mouse studies (Zwiegers et al., 2014). Additionally, rodent astrocytes exhibit significantly varied expression of many ALS-related genes, are less structurally and functionally diverse, and express a 10-fold decrease in glial fibrillary acidic protein-positive processes than human astrocytes, further limiting translational relevance of this model when studying the role of astrocytes in ALS (Oberheim et al., 2009).

To specifically study the effect of ALS on MN populations, hiPSC-based platforms have been widely employed. The first example of drug screening in ALS hiPSC-derived MNs used cells from patients with *TARDBP* mutations that exhibited decreased neurite length, which allowed identification of anacardic acid (a histone acetyltransferase inhibitor) as a potential ALS therapeutic agent (Egawa et al., 2012). These platforms have been expanded to the other ALS-associated mutations and have included assessments of membrane hyperexcitability (Wainger et al., 2014), vesicle trafficking (Shi et al., 2018), ER perturbation (Kiskinis et al., 2014), lysosomal biogenesis (Shi et al., 2018), and oxidative stress (Kiskinis et al., 2014). To model sporadic ALS in hiPSC-MNs, several models were combined to recapitulate heterogeneous neuronal degeneration, protein aggregation, and cell death and identify ropinirole as a potential therapeutic candidate (Fujimori et al., 2018). However, these models utilize rather immature neurons to model a disease that presents in mid to late life and only consider cell-autonomous effects of ALS. Accelerated aging through molecular manipulation, such as progerin overexpression (Miller et al., 2013), may improve the clinical relevance of these models.

To investigate non-cell autonomous contributions to ALS in a cell-specific manner, hiPSC-derived SkM and astrocyte models of ALS have been developed. Initial hiPSC-derived ALS SkM cells induced through both MyoD overexpression (Lenzi et al., 2016) and small molecule differentiation (Swartz et al., 2016) exhibited typical maturation patterns with limited pathologic alterations. Recently, however, a SkM model derived from *SOD1*-mutant ALS patient hiPSCs exhibited delayed and lower rates of fusion, smaller myotube size, limited AChR expression, metabolic dysfunction, and significantly reduced force production compared to healthy cells (Badu-Mensah et al., 2020). Additionally, a model using hiPSC-derived myotubes from *C9ORF72* mutant patients exhibited pathological RNA foci, dipeptide repeat proteins, oxidative stress, and TDP-43 aggregation (Lynch et al., 2019). Beyond cultured hiPSC-SkM cells, hiPSC-derived astrocytes from ALS patients exhibit decreased expression of LC3-II causing p62 accumulation and modulated autophagy in HEK293T cells treated with astrocyte conditioned media (Madill et al., 2017). Additionally, *C9ORF72* mutant hiPSC-derived astrocytes exhibited pathological RNA foci and dipeptide repeat proteins while causing MNs to undergo progressive action potential loss upon co-culture (Zhao et al., 2020). Through CRISPR-based removal of the *C9ORF72* repeat, these phenotypes were reverted indicating both cell-autonomous astrocyte pathology and non-cell autonomous MN pathophysiology attributed to astrocytes (Zhao et al., 2020). Metabolically, *C9ORF72*-mutated astrocytes exhibit increased oxidative stress and senescence while secreting paracrine factors to induce oxidative stress in healthy MNs (Birger et al., 2019).

**TABLE 1 |** Selected *in vitro* human models of NMD.

| NMD | 2D/3D | Cell types | Observed disease characteristics | References | Future directions |
|---|---|---|---|---|---|
| ALS | 2D | MN | Membrane hyperexcitability, aberrant vesicle trafficking, ER perturbation, reduced lysosomal biogenesis, oxidative stress | Kiskinis et al. (2014); Wainger et al. (2014); Shi et al. (2018) | • Generation of hiPSC-derived MN subtypes<br>• Incorporation of different MN subtypes into NMJ models<br>• Comparison to patient NMJ morphology<br>• Investigations into origin of NMJ abnormalities<br>• Addition of SCs |
| | | SkM | Limited fusion, smaller myotubes, limited AChR expression, metabolic dysfunction, reduced force, pathological RNA foci, oxidative stress, TDP-43 aggregation | Lynch et al. (2019); Badu-Mensah et al. (2020) | |
| | 3D | MN/SkM | Higher MN degradation rates, fewer contractions, increased SkM apoptosis, axonal varicosities, limited axonal growth, increased excitability | Osaki et al. (2018); Guo et al. (2020b) | |
| MG | 2D | MN/SkM | Reduced contractility, increased NMJ complement deposition | Steinbeck et al. (2016) | • Use of MG donor cells for MNs and SkM<br>• Comparison to patient NMJ morphology<br>• Addition of autoreactive T-cells, macrophages, and SCs |
| | 3D | MN/SkM | Decreased number of MN-activated myofibers, localized deposition of complement C3c protein on AChRs, phenotypic and functional responses that match donor disease severity | Bakooshli et al. (2019); Vila et al. (2019) | |
| DMD | 2D | MN | Increased $Ca^{2+}$ overload, cytoskeletal disorganization | Patel et al. (2019) | • Modeling fibrosis<br>• Comparison to patient NMJ morphology<br>• Investigations into origin of NMJ abnormalities<br>• Addition of immune cells, SCs, and FAPs |
| | | SkM | Satellite cell dysfunction, impaired myotube formation, altered $Ca^{2+}$ handling, decreased AChR clustering | Blau et al. (1983); Imbert et al. (1995); Kong and Anderson (1999); Wang Y.X. et al. (2019) | |
| | 3D | SkM | Decreased fusion, lowered contractile force, atrophic myotubes, decreased nuclear anisotropy | Nesmith et al. (2016); Al Tanoury et al. (2021); Ebrahimi et al. (2021) | |
| | | MN/SkM | Loss of AChR and NMJ volumes, impaired contractility, downregulation of NMJ genes | Paredes-Redondo et al. (2021) | |
| DM | 2D | MN | Ribonucleic foci, splicing abnormalities | Xia et al. (2015) | • Improved stability of toxic repeats<br>• 3D NMJ model development<br>• Analysis with fast muscle fiber subtypes<br>• Addition of immune cells and SCs |
| | | SkM | RNA splicing abnormalities, formation of ribonucleic foci | Gao et al. (2016); Ueki et al. (2017); Martineau et al. (2018) | |
| | | MN/SkM | Diminished synaptogenesis and increased neurite outgrowth | Marteyn et al. (2011) | |
| | 3D | SkM | Ribonucleic foci, lowered MBNL expression, reduced myotube diameter | Fernández-Garibay et al. (2021) | |
| Pompe | 2D | MN | Glycogen and secondary lipid accumulation, increased apoptosis, enlarged lysosomes | Huang et al. (2019); Cheng et al. (2021) | • Increased maturation and longer culture for baseline functional weakness<br>• NMJ model development<br>• Analysis with fast muscle fiber subtypes<br>• Addition of microglia and SCs |
| | | SkM | Limited GAA activity, glycogen accumulation | Sato et al. (2016); van der Wal et al. (2017) | |
| | 3D | SkM | Lack of GAA activity, increased glycogen levels, lysosomal enlargement, expected transcriptomic changes | Wang et al. (2021) | |

To combine these cell types *in vitro*, a compartmentalized ALS-on-a-chip model was developed to co-culture engineered 3D SkM tissues with heterogeneous (MNs and astrocytes) hiPSC-derived neural spheroids within a microfluidic device (Osaki et al., 2018). Functional NMJs were formed by axonal outgrowth from spheroids into SkM and light was used to stimulate the channelrhodopsin-2–expressing MNs to induce muscle contraction (Osaki et al., 2018). Engineered ALS motor units within this system exhibited higher degradation rates, induced fewer muscle contractions, and increased SkM apoptosis. These features were reversed through treatments with rapamycin and/or bosutinib as potential therapeutic agents (Osaki et al., 2018). A microfluidic compartmentalized 2D co-culture system made of hiPSC-MNs derived from three ALS mutant lines and primary wild-type myotubes exhibited axonal varicosities, limited axonal growth, and increased excitability (Guo et al., 2020b). Functional NMJs with ALS MNs were decreased in number and fidelity and showed increased fatigue index, while the Deanna protocol nutritional supplementation was found to correct these deficits in all lines (Guo et al., 2020b).

To improve upon our understanding of the underlying mechanisms of ALS pathology and to develop curative therapies, it will be critical to complement studies in both animal models and *in vitro* systems. ALS animal models with a wide variety of mutations have allowed for significant advancement in our understanding of the disease. However, limited disease severity and phenotypes, especially within supporting cells such as astrocytes (Oberheim et al., 2009), are likely to undermine clinical success of ALS therapeutics validated in animal models. Increasing disease severity in mice by additional knockdown of SOD1 in astrocytes, assessing the impact of different genetic backgrounds, and increased physical activity via treadmill running or swimming may yield more translationally relevant *in vivo* ALS models. For *in vitro* studies, current ALS-on-a-chip models (Osaki et al., 2018; Guo et al., 2020b) hold great potential for clinically relevant disease modeling and predictive drug screening as they exhibit therapeutically reversible ALS phenotypes and utilize platforms that support high-throughput studies. However, these models have yet to be analyzed to assess if they appropriately recapitulate pathological decrease in synaptophysin concentration, marked denervation, shrunken nerve terminals, and flattened synaptic clefts observed in ALS patients (Bjornskov et al., 1975; Tsujihata et al., 1984; Yoshihara et al., 1998). Further developments to *in vitro* ALS human models will be required to better recapitulate ALS pathology and disease progression. First, modular ALS platforms combined with non-invasive longitudinal and functional assessments can be utilized to help answer the fundamental question if ALS disease progression is due to direct loss of cortical MNs or their retrograde degeneration originating from muscle. Second, improved methodologies to generate hiPSC-derived MN subtypes will allow for further investigations into the preferential subtype-specific MN degradation observed in ALS (Tremblay et al., 2017). Third, incorporation of supportive cell types such as SCs will create a more realistic model of disease as SCs from ALS patients exhibit abnormal morphology with disorganized processes that extend into synaptic clefts (Bruneteau et al., 2015). In *SOD1* mouse studies, similar disorganized processes were seen within SCs alongside upregulated galectin-3, a marker of phagocytosis (Martineau et al., 2020). These extensions may block the synaptic cleft, disrupting MN-SkM communication and contributing to ALS pathology, offering an interesting area for investigations within *in vitro* models.

## Myasthenia Gravis

Myasthenia gravis is a rare autoimmune disorder characterized by accelerated fatigue within voluntary muscles, primarily in extraocular and facial muscles, proximal limbs, and neck extensors (Jayam Trouth et al., 2012). Weakness is highly variable and worsened by a variety of factors including heat, stress, and exercise (Jayam Trouth et al., 2012). MG is associated with accumulation of autoantibodies against NMJ proteins including muscle specific tyrosine kinase (MuSK), low-density lipoprotein receptor-related protein 4 (LRP4), and, most significantly, the nicotinic acetylcholine receptor (nAChR) (Nacu et al., 2015). The accumulation results from T cell-directed attack upon these postsynaptic membrane proteins (Ha and Richman, 2015). MG is often initially identified by ptosis and can be further classified into several subgroups based on autoantibody type and clinical features (Nacu et al., 2015). There are a wide range of treatments approved for MG including immunosuppression, anticholinesterase drugs, immunomodulation, and thymectomy (Farmakidis et al., 2018), but none provide curative outcomes.

Although the primary investigations of MG have focused on NMJ morphology and function, there have been reports of pathophysiological alterations in SkM. Human muscle atrophy was shown to present early in MG progression (Zouvelou et al., 2012) and accelerated atrophy was seen in type II fibers as compared to type I fibers (Wang et al., 2018). Additionally, accumulated anti-nAChR antibodies have been shown to modulate muscular IL-6 production altering mTOR signaling which may be responsible for MG-associated muscle fatigue (Maurer et al., 2015). Muscle biopsies from MG patients showed increased $Pax7^{+}$ satellite cell pool, while isolated MG myoblasts exhibited increased proliferation and differentiation potential (Attia et al., 2017). A similar increase in satellite cell number, proliferation, and differentiation was observed in anti-nAChR mouse models of MG (Attia et al., 2017). Additionally, these mice exhibited delayed SkM maturation following development indicated by lower MyoG expression, reduced fiber size, and increased embryonic myosin heavy chain expression (Attia et al., 2017).

The role of autoantibodies in MG have been confirmed in multiple animal studies. Rabbits treated with anti-nAChR antibodies showed characteristic MG symptoms, confirming the autoimmune nature of MG (Patrick and Lindstrom, 1973). Similarly, administration of autoantibodies against LRP4 and MuSK in mouse models have reproduced MG symptoms indicating important roles of these receptors in disease (Wang et al., 2018). While useful in understanding NMJ dysfunction, acute induction of symptoms through autoantibody administration does not appropriately mimic the chronic progression of MG (Wang et al., 2018). Furthermore, immunized mice inconsistently exhibit clinically observable weakness, rarely present with extraocular muscle fatigue, and fail to recapitulate the dynamic nature of MG disease severity (Wang et al., 2018). Finally, there are additional auto-antibodies implicated in MG against proteins such as titin (Aarli, 2001), agrin (Gasperi et al., 2014), and cortactin (Gallardo et al., 2014) that are not considered in these models.

As MG is an autoimmune disorder, *in vitro* models of MG can be developed by adding patient serum to an existing NMJ platform. The first example of this utilized a 2D co-culture of optogenetically active hESC-derived MNs with primary myotubes to induce a reversible reduction in muscle contraction amplitude by treatment with IgG or active complement protein from MG patients (Steinbeck et al., 2016). In a 3D co-culture model of hiPSC-derived MNs and engineered SkM tissue,

localized deposition of complement C3c protein was shown in AChRs of NMJs and treatment with MG IgG decreased number of MN-activated myofibers (Bakooshli et al., 2019). Additionally, automated optogenetic control was incorporated into a 3D MN-SkM culture system and differential responses to sera from donors were measured according to phenotype severity (Vila et al., 2019). Recently, hPSC-derived axial stem cells have been used to generate human neuromuscular organoids containing MNs, SCs, and SkM and study MG (Martins et al., 2020). This model showed reduced NMJ volumes alongside decreased rate and amplitude of contraction in response to MG sera. Although these models have recapitulated some aspects of MG through addition of patient sera, they are limited as they do not utilize MG patient-derived cells.

Overall, understanding the multi-organ nature of MG will require investigations in both animals and *in vitro* human model systems. While animal models are suitable for investigating the involvement of NMJs and immune system, they do not capture MG disease severity, resulting in failure of multiple MG treatments in clinical trials despite prior validation in animals (Mantegazza et al., 2016). Furthermore, direct analyses of heterocellular interactions important for MG pathology in animal models are hindered by the complexity of *in vivo* environments. On the other hand, *in vitro* models exhibit phenotypic and functional responses to patient sera that match disease severity in human donors (Vila et al., 2019) and can enable unique studies to elucidate the roles of cellular crosstalk in disease progression; however, they do not model systemic pathogenesis. Therefore, the next generation of *in vitro* MG models should incorporate immune cells to better recapitulate the autoimmune inflammatory environment. Specifically, incorporation of autoreactive T-cells would allow for investigations of the pathological development of autoantibodies beyond studying the effect of MG serum addition within existing platforms. In animal models of MG, macrophages can act as antigen-presenting cells and help produce self-AChR antibodies (Kinoshita et al., 1988) and as such, their incorporation into human *in vitro* systems (Juhas et al., 2018) would allow systematic studies of their roles in MG autoimmunity. Finally, further studies of SCs within *in vitro* models of MG should be performed to analyze their localization to the presynaptic membranes and potential neuroinflammatory roles (Ydens et al., 2013), including involvement in clinically observed pathological features such as disorganized axonal microorganelles, accumulation of Reich granules, and lipopigments (Kimura and Nezu, 1989).

## Duchenne Muscular Dystrophy

Duchenne muscular dystrophy, a genetic myopathy with the highest prevalence of 7.1 in 100,000 male births (Crisafulli et al., 2020), is a fatal X-linked disorder caused by mutations in the dystrophin gene (Yiu and Kornberg, 2015). Dystrophin is an integral member of the dystrophin glycoprotein complex (DGC) that transmits contractile forces from the sarcomere to the ECM and functions as a molecular shock absorber (Le et al., 2018). In mature myofibers, dystrophin deficiency leads to sarcolemmal instability (Weller et al., 1990), abnormal calcium homeostasis (Tutdibi et al., 1999), and muscle degeneration (Torres and Duchen, 1987). In SCs, dystrophin regulates muscle stem cell commitment via epigenetic modifications (Chang et al., 2018) and regulation of cell polarity (Dumont et al., 2015b; Wang Y.X. et al., 2019). Loss of dystrophin results in increased levels of myogenic progenitors with an impaired ability to commit to differentiation resulting in diminished regenerative ability (Dumont et al., 2015b; Wang Y.X. et al., 2019). Together, this impaired satellite cell function, impeded muscle regeneration, and constant cycles of muscle degeneration result in progressive muscle weakness, loss of ambulation, and ultimately death due to respiratory failure (Yiu and Kornberg, 2015).

In addition to roles within SkM, dystrophin regulates neuronal function and is vital for healthy NMJ maintenance (Tintignac et al., 2015). Dystrophin and other members of the DGC are enriched at post-synaptic folds of the NMJ (Waite et al., 2009) and stabilize nAChRs (Zaccaria et al., 1998). Dystrophic myofibers are associated with increased rates of NMJ branching, fracturing, and transmission failure (Pratt et al., 2013, 2015a), suggesting a role of dystrophin in NMJ remodeling and/or maintenance. The role of dystrophin at the pre-synaptic level of NMJ structure and function is less clear. Increased pre-synaptic nerve terminal branching, axon sprouting, and denervation have been observed in mdx mice (Pratt et al., 2015b; van der Pijl et al., 2016) and humans (Nagao et al., 2003). These structural changes seen in dystrophic NMJs result in functional deficits including altered EMG characteristics and decreased safety factor of neuromuscular transmission in both patients (Priez et al., 1992) and mice (van der Pijl et al., 2016). Clinically, NMJ dysfunction results in increased sensitivity and slowed recovery from neuromuscular blocking drugs such as rocuronium and mivacurium (Ihmsen et al., 2009), contraindicating their use as anesthetics in DMD patients (Breucking et al., 2000). Lastly, dystrophin also regulates neuronal development and function in the brain which most likely contributes to the increased incidence of neurological abnormalities including autism, attention deficit disorder, and learning disabilities in DMD patients (Ricotti et al., 2016).

The majority of our understanding of DMD has been derived from a range of preclinical animal models (Wells, 2018) with the most common model being the *mdx* mouse which has a naturally occurring nonsense point mutation in exon 23 preventing dystrophin protein expression (Manning and O'Malley, 2015). The *mdx* mice exhibit several expected disease features including fibrosis (Gregorevic et al., 2008), respiratory dysfunction (Burns et al., 2018), cardiomyopathy (Mareedu et al., 2021), metabolic dysfunction (Moore et al., 2020), and muscle weakness (Barton et al., 2005). However, the mdx phenotype is milder and has a slower progression compared to clinical symptoms in DMD patients (Dangain and Vrbova, 1984). Disease severity of the *mdx* mouse model can be increased by the knockout of utrophin, which undergoes compensatory upregulation in *mdx* mice to protect against membrane instability (Deconinck et al., 1997). Alternatively, disease severity can be increased by knockout of the telomerase gene (*mdx*/*mTR*) which shortens telomere length and induces a more severe SkM (Sacco et al., 2010) and cardiac

(Mourkioti et al., 2013) pathology. Larger preclinical animal models including rats (Larcher et al., 2014), rabbits (Sui et al., 2018), dogs (Nghiem and Kornegay, 2019), and pigs (Selsby et al., 2015) show greater disease severity and lethality than the traditional *mdx* mouse model. However, ethical concerns (Yokota et al., 2012) and secondary complications such as inability to feed (Gaschen et al., 1999) have limited their use to date. From larger animals, the golden retriever muscular dystrophy model (GRMD) (Nghiem and Kornegay, 2019) has been studied the most, but financial, ethical, and animal number concerns limit its use (Wells, 2018). Nevertheless, these preclinical models played important roles in validating current standard of care glucocorticoid therapy (Hudecki et al., 1993) and eteplirsen, a novel antisense oligonucleotide treatment approved by the FDA in 2016 (Khan et al., 2019).

Despite some success, numerous candidate therapeutics identified in animal studies have failed to be effective in humans driving the development of improved model systems (Rybalka et al., 2020). A primary limitation of current animal models is their low genetic and epigenetic diversity. DMD in humans is caused by over 4700 different mutations, and disease severity and response to pharmacological agents is heavily influenced by a range of disease modifiers such as expression levels of latent TGFB binding protein 4 (LTBP4) (Flanigan et al., 2013) and osteopontin-1 (Kyriakides et al., 2011). Disease severity of the *mdx* mouse model has been improved by crossing the *mdx* mutation onto the DBA/2J background, which contains a pro-fibrotic polymorphism in LTBP4 (Heydemann et al., 2009), resulting in greater fibrosis and functional impairment (van Putten et al., 2019). In the past decade, the development of genome editing tools such as TALEN and CRISPR-Cas9 has enabled the generation of humanized *mdx* mouse models (Aartsma-Rus and van Putten, 2019). These mice specifically model human dystrophin mutations to enable preclinical validation of gene editing therapies using CRISPR-Cas9 (Min et al., 2019) or antisense oligonucleotide (Veltrop et al., 2018) technologies.

While animal models can be genetically modified to include aspects of patients' genetic diversity, true personalized disease platforms require use of patients' tissues or cells. *In vitro* 2D studies of mouse or human DMD myoblasts have been utilized to model satellite cell dysfunction (Wang Y.X. et al., 2019), impaired myotube formation (Blau et al., 1983), and altered $Ca^{2+}$ handling (Imbert et al., 1995). Myotubes lacking dystrophin or other members of the DGC display decreased AChR clustering (Kong and Anderson, 1999), indicating that post-synaptic NMJ abnormalities can occur in the absence of neural cells. When engineered into 3D tissues, DMD primary and immortalized patient cells display decreased fusion and force of contraction, atrophic myotubes, and decreased nuclear anisotropy (Nesmith et al., 2016; Al Tanoury et al., 2021; Ebrahimi et al., 2021). Large scale personalized platforms amenable to pharmacological screens will require the use of patient hiPSCs due to ethical and proliferative limitations of muscle biopsy-derived primary cells and a need for non-muscle cells such as MNs (Wang J. et al., 2019). Encouragingly, two chemicals (ginsenoside and fenofibrate) identified to improve fusion rate in hiPSC-derived DMD myoblasts were both found to improve muscle structure and function in *mdx* mice (Sun et al., 2020). Similarly, prednisolone, the current standard of care for DMD patients, rescued fusion, force of contraction, and branching defects in hiPSC-derived DMD myotubes (Al Tanoury et al., 2021), further implying a potentially predictive nature of these *in vitro* assays. In addition to drug development, hiPSC-derived DMD cells from patients with a wide-range of mutations can be utilized for optimization and validation of gene therapies such as guide RNA design for CRISPR-Cas9 mediated genome editing (Min et al., 2019).

Furthermore, hiPSC-based disease models allow building complex tissues to enable studies of the multi-cellular crosstalk in DMD pathogenesis. For example, astrocytes (Patel et al., 2019) and glutamatergic sensory neurons (Ruggieri et al., 2019) generated from DMD hiPSCs displayed increased $Ca^{2+}$ overload and cytoskeletal disorganization indicating that neuronal involvement can be also studied using DMD hiPSC derivatives. Multicellular 3D cultures comprised of hiPSC-derived myoblasts, neurons, endothelial cells, and fibroblasts were successfully generated from both healthy and DMD cells (Maffioletti et al., 2018; Mazaleyrat et al., 2020), but the roles of cellular crosstalk in NMJ function and dysfunction in these cultures remain to be studied. Interestingly, in a primary and immortalized cell line based human 3D co-culture system, endothelial cells were required for DMD fibroblasts to undergo fibrinogenesis, suggesting that complex multicellular 3D platforms may be required to study mechanisms of DMD with high fidelity (Bersini et al., 2018). Recently, a compartmentalized optogenetic neuromuscular DMD model was developed by culturing hiPSC-derived DMD and isogenic control myoblasts with MN spheroids derived from wild-type channelrhodopsin-expressing murine or human ESCs (Paredes-Redondo et al., 2021). In this model, pharmacological inhibition of TGFβ signaling induced partial restoration of AChR and NMJ volumes along with significant up-regulation of MuSK expression (Paredes-Redondo et al., 2021). Besides SkM DMD platforms, hiPSC-derived DMD cardiomyocytes exhibit impaired contractile function (Chemello et al., 2021), altered calcium-handling (Chemello et al., 2021), and mitochondrial dysfunction (Sun et al., 2020), and have been utilized for *in vitro* studies of drug (Lin et al., 2015) and gene (Kyrychenko et al., 2017; Long et al., 2018; Chemello et al., 2021) therapies for DMD.

Since DMD arises from a range of mutations and its progression strongly depends on a variety of disease modifiers, complementary studies in animal and *in vitro* models will be required for improved understanding of disease mechanisms and development of effective therapeutic approaches. While translational relevance of current animal models is limited by low genetic and epigenetic diversity, genome editing technologies such as CRISPR can now enable improved phenotypic and mutational representation in animals (Pickar-Oliver et al., 2021). Regardless of these improvements, use of patient-derived cells will be necessary for truly personalized disease modeling. Recent 3D NMJ DMD models have provided a useful platform for studying NMJ dysfunction *in vitro* (Paredes-Redondo et al., 2021), but fully patient-specific DMD NMJ models remain

to be developed. In these models, it will be important to perform careful morphological analysis of axonal branching and NMJ fragmentation to evaluate how well patient phenotypes are recapitulated (Pratt et al., 2013, 2015a). Similar to ALS models, the DMD platforms can be utilized in modular fashion to determine roles of distinct cellular and environmental components in NMJ pathology. For example, SCs within the *mdx* model exhibit disorganized processes directed away from endplates which may block innervation, indicating a potential role of SCs in DMD pathology (Personius and Sawyer, 2005) which remains to be studied *in vitro*. DMD patient and mouse muscles are also characterized by pro-inflammatory immune cell infiltration, which results in increased levels of neutrophils, T cells, and macrophages. Replicating this pro-inflammatory milieu *in vitro* could shed novel mechanistic insights into the effects of inflammation on NMJ structure and function in DMD. While the altered inflammatory milieu is thought to stimulate FAP proliferation and fibrosis (Juban et al., 2018), current DMD models do not exhibit fibrotic changes, thus the incorporation of both inflammatory and FAP cells will likely be essential to fully replicate the advanced stages of disease.

## Myotonic Dystrophy

Myotonic dystrophy is the most prevalent form of muscular dystrophy in adults and is classified into Type I (DM1) and II (DM2). DM1 results from a series of CTG repeats in the DM protein kinase (DMPK) gene, while DM2 results from a series of CCTG repeats in the Zinc Finger 9 (ZNF9) gene (Thornton, 2014). The major pathogenic consequence of these DNA tandem repeats is gain-of-function of the resulting mutant RNA that form hairpin-like structures which bind and sequester RNA-binding proteins (Brouwer et al., 2009). This results in the sequestering and dysregulation of splice factors such as musclebind-like (MBNL) and CUG-binding proteins (CUGBP) (Fernandez-Costa et al., 2011). Ultimately, this leads to alternative splicing of multiple mRNAs including members of the DGC (Nakamori et al., 2007) and t-tubule proteins (Fugier et al., 2011) which contributes to the characteristic progressive myopathy and myotonia in DM. DM1 and 2 have a greater impact on fast muscle fibers and are associated with variable muscle fiber diameter, fiber splitting, and fibrofatty replacement (Vihola et al., 2003). Histologically, DM2 can be distinguished by pyknotic nuclear clumps that occur before the onset of muscle weakness (Meola and Cardani, 2015).

Aberrant splicing is not limited to SkM but occurs in multiple organs including the cardiac and neurological systems (Lee and Cooper, 2009). In DM1, splicing factors in the MBNL family accumulate within ribonuclear foci within both pre-synaptic MNs and post-synaptic nuclei leading to NMJ instability (Wheeler et al., 2007). DM1 patients exhibit thinned axon and myelin sheets without denervation (Fardeau and Tome, 1980). Additionally, repetitive nerve stimulation and single fiber electromyography in DM1 patients show abnormal nerve conduction and pathological jitter suggesting NMJ instability (Bombelli et al., 2016). DM1 mouse models exhibiting pathophysiological levels of CTG repeats in the DM1 region show distal denervation of diaphragm NMJs, reduced AChRs on the post synaptic membrane, and loss of unmyelinated fibers (Panaite et al., 2008). Furthermore, variable levels of axonal neuropathy (17–46%), axonal loss, and myelin sheath thinning have been reported in both DM1 patients (Peric et al., 2013) and mice (Panaite et al., 2011). Functionally, these structural alterations lead to abnormal nerve conduction and pathological jitter in DM1 patients (Bombelli et al., 2016). Currently there are no curative therapeutics for either DM1 or DM2 (Pascual-Gilabert et al., 2021). However, nearly two dozen preclinical and clinical drug development programs are currently active encompassing repurposed drugs, gene therapy, oligonucleotide therapeutics, and novel chemical treatments (Pascual-Gilabert et al., 2021).

Several animal models have been developed to study DM1 disease mechanisms and investigate potential therapies. DM1 was first modeled in DMPK knockout mice which only developed mild myopathy (Jansen et al., 1996), mild cardiac conduction dysfunction (Berul et al., 1999), and failed to replicate the multisystemic patient phenotype (Jansen et al., 1996). Through the overexpression of DMPK with toxic CTG repeats, a stronger disease phenotype was developed with ribonuclear foci changes, SkM atrophy, slowed growth, weakness, and myotonia (Vignaud et al., 2010). Neurologically, these mice exhibit RNA toxicity within Bergmann glia and Purkinje cell hyperexcitability, and reduced motor coordination representative of DM1 patients (Sicot et al., 2017). However, they still exhibit mild splicing defects and disease phenotype compared to patients (Huguet et al., 2012). Alternatively, myotonia and alternative splicing defects can be induced by combined MBNL1 inactivation and expression of untranslated CUG ($HSA_{LR}$ model), but this does not lead to muscle wasting or denervation (Wheeler et al., 2007). Overexpression of CUGBP1 causes more severe myopathy and cardiomyopathy but is limited by high mortality and breeding issues. Through no individual mouse models capture all disease features or fully recapitulate severity seen in patients, they have provided significant mechanistic insights into the genetic causes of specific disease phenotypes.

Due to the multisystemic nature of DM, multiple muscle and non-muscle cell lines have been utilized to study DM pathology (Matloka et al., 2018). HEK, HeLa, and C2 cells with CTG repeats inserted in the 3′UTR of a truncated *DMPK* gene have replicated splicing misregulations and ribonuclear foci phenotypes (Philips et al., 1998; Warf and Berglund, 2007). *In vitro* drug screens to ameliorate these phenotypes have been utilized to identify novel therapeutics for DM (Warf and Berglund, 2007; Konieczny et al., 2017). DM patient-derived primary myoblast cultures exhibit metabolic alterations (Renna et al., 2017), splicing abnormalities (Laustriat et al., 2015), and ribonucleic foci formation (Fardaei et al., 2002). Myotube cultures have also been generated from MyoD overexpression in DM fibroblasts (Kuyumcu-Martinez and Cooper, 2006; Ravel-Chapuis et al., 2012) and hiPSCs (Gao et al., 2016; Ueki et al., 2017; Martineau et al., 2018) from DM patients. Similar to primary myoblasts, these cells exhibited RNA splicing abnormalities and formation of ribonucleic foci. Recently, the first 3D *in vitro* human muscle model of DM1 was developed by encapsulating patient-derived fibroblasts overexpressing MyoD in micromolded gelatin methacryloyl-carboxymethyl cellulose methacrylate hydrogels (Fernández-Garibay et al., 2021). Furthermore, for studies of neuromuscular

abnormalities, DM patient ESCs were differentiated into MNs and co-cultured together with healthy SkM (Marteyn et al., 2011) and found to exhibit diminished synaptogenesis and increased neurite outgrowth associated with low expression of genes in the *SLITRK* family.

Additionally, hiPSC lines derived from DM patients have been used to study pathological alterations in distinct cell types (Gao et al., 2016; Ueki et al., 2017; Martineau et al., 2018). The neurological component of DM1 has been studied in hiPSC-derived neurons and astroglia which display expected ribonucleic foci and splicing abnormalities. These models have been used to demonstrate proof-of-principle phenotypic reversal through genome editing (Xia et al., 2015). While all models demonstrate histological alterations, no *in vitro* studies have shown myogenic or neuronal functional deficits. Additionally, CTG repeats have been shown to be unstable in pluripotent cells (Du et al., 2013) and CTG repeats do not expand when naive hiPSCs are differentiated into cardiomyocytes, muscle, or neurons as seen *in vivo*. Recently, DM1 hiPSC-derived cardiomyocytes from DM1 patients with varied CTG repeat lengths exhibited toxic RNA foci and mis-spliced *MBNL1/2* transcripts and showed two distinct ions channel ($Na^+$ and $Ca^{2+}$) perturbations (Poulin et al., 2021). This platform revealed the underlying mechanism of electrical cardiac alterations in DM1 and can be used in the future to validate potential therapeutics in a high throughput fashion by monitoring action potential propagation and ionic currents in the human DM1 cardiomyocytes.

Overall, translationally relevant DM modeling is complicated by the multifaceted influences of DM throughout the entire body, most notably within neurological and muscular tissues. Although mouse models have greatly expanded our understanding of this pathogenic RNA disease, no single mouse model has exhibited severity comparable to patients or encompassed the myriad of DM phenotypes present *in vivo*. For example, DM1 patients exhibit toxic RNA accumulation whereas $HSA_{LR}$ mice do not, which may contribute to the lack of denervation-like features in these mice (Wheeler et al., 2007). Intercrossing mouse lines may improve recapitulation of DM pathology and even show pathological synergy between symptoms. However, further development of patient-derived *in vitro* NMJ models will be critical for the ability to directly analyze the human DM NMJ. First, further optimization of hiPSC culture and differentiation protocols to produce myogenic and neuronal cells with stable CTG repeats that exhibit functional deficits will be critical. Second, novel methods for differentiating specific muscle subtypes from hiPSCs will augment our ability to accurately model and study DM as it preferentially affects fast muscle fibers (Vihola et al., 2003). Third, in DM1 patients, SCs exhibit abnormal glycogen accumulation and crystalline structures within their processes (Borenstein et al., 1977) and may contribute to disease progression through unknown mechanisms which remain to be studied in NMJ-SC co-cultures. Fourth, DM1 patients and mice show increased pro-inflammatory gene signatures and upregulation of the IL-6 pathway (Nakamori et al., 2017) and tumor necrosis factor superfamily member 12 (TNFSF12) signaling (Yadava et al., 2015). Incorporation of immune cells in DM NMJ models would allow important studies of how inflammation may contribute DM progression.

## Pompe Disease

Pompe disease, also known as glycogen storage disease type II (GSDII), is a rare metabolic autosomal recessive disorder that results from deficiency of acid α-glucosidase (GAA) (Reuser et al., 1995). Pompe disease is categorized into two major types based upon disease onset and GAA enzyme activity, although a continuous spectrum of phenotypes exists. Infantile-onset Pompe disease (IOPD) is caused by very low GAA enzyme activity and results in fatal cardiac, neurologic, hepatic, and muscular dysfunction between ages 1 and 2 (Lim et al., 2014). In contrast, late-onset Pompe disease (LOPD) involves higher GAA activity which results in slower disease progression (Chan et al., 2017). GAA breaks down lysosomal glycogen, and its dysfunction leads to intralysosomal glycogen accumulation in various tissues but most abundantly within skeletal and cardiac muscle (Reuser et al., 1995). The build-up of glycogen in striated muscle leads to lysosomal enlargement, vacuolation (Prater et al., 2013), autophagosome proliferation (Nascimbeni et al., 2015), and lipofuscin aggregation (Feeney et al., 2014). These alterations are hypothesized to disrupt cellular and sarcomere architecture resulting in progressive muscle weakening and ultimately respiratory or cardiac failure (Reuser et al., 1995). However, neuromuscular abnormalities such as increased neuromuscular jitter and variance in response latency are seen within Pompe patient muscle prior to muscle weakness (Stålberg and Trontelj, 1997). This suggests that neurological dysfunction could be a key driver of muscle weakness and myopathy in Pompe disease.

In Pompe patients and mice, glycogen accumulation occurs in the brain (Mancall et al., 1965; Lee et al., 2011), central nervous system (CNS) (Mancall et al., 1965; Martini et al., 2001; DeRuisseau et al., 2009), and MNs (Gambetti et al., 1971; DeRuisseau et al., 2009). Furthermore, Pompe MNs have three-fold higher soma size (Mancall et al., 1965) and are more apoptotic (Turner et al., 2016), resulting in decreased motor output and neuronal loss (DeRuisseau et al., 2009). Pompe mice also exhibit significant NMJ alterations due to both presynaptic changes, such as reduced myelin thickness and neurofilament proteins, and postsynaptic changes, such as NMJ fragmentation (Falk et al., 2015). These structural alterations result in impaired neural output including increased numbers of denervated NMJs (Falk et al., 2015), decreased burst amplitude (DeRuisseau et al., 2009), and increased spontaneous EMG activity (Hobson-Webb et al., 2011). In addition to MNs, structural alterations and glycogen accumulation are found in neuronal support cells including astroglia and SCs (Martin et al., 1973). These alterations can lead to secondary disease traits including cognitive declines (Spiridigliozzi et al., 2017), speech disorders (Muller et al., 2009), and sensorineural and/or conductive hearing loss (Prater et al., 2012) demonstrating the wide ranging impacts of GAA deficiency.

Pompe disease has been predominantly modeled in the GAA knockout mice (Raben et al., 2001) that recapitulate key disease features such as striated muscle and nervous tissue glycogen

accumulation (DeRuisseau et al., 2009), lysosomal abnormalities (Doyle et al., 2019), neuropathology (DeRuisseau et al., 2009), cardiac defects (Han et al., 2016), and muscle weakness (Lee et al., 2018). However, despite a complete lack of GAA, these mice exhibit a LOPD phenotype with late onset, slow disease progression, and normal breathing in normoxic conditions (Han et al., 2016; Gatto et al., 2017). Recently, crossing the GAA KO mice to the DBA2/J background resulted in a much more severe disease phenotype including early lethality, respiratory defects during normoxia, and more severe cardiomyopathy (Colella et al., 2020). While the pro-fibrotic polymorphism in LTBP4 found in the DBA2/J background has not been implicated in Pompe disease, polymorphisms in angiotensin-converting enzyme (ACE) and alpha-actinin 3 (ACTN3) (De Filippi et al., 2014) impact disease onset within LOPD. The classical GAA KO mouse model has been essential for identifying and validating potential therapeutics (Doyle et al., 2019) and has allowed for deeper understanding of the roles of the mTOR pathway, lysosomal dysregulation, and autophagocytosis in Pompe disease progression (Han et al., 2016; Gatto et al., 2017). In addition to mouse models, a novel zebrafish model, in which GAA activity is significantly reduced but not totally absent, displays significant motor behavior and NMJ abnormalities (Bragato et al., 2020). When this model was used as a drug screening platform, 3-bromopyruvic acid (Bragato et al., 2020) and 3,4-diaminopyridine phosphate (Cinzia et al., 2021) were found to increase AChR abundance, improve NMJ structure, and recover typical movement patterns. A baboon model of Pompe disease is currently used as a large animal preclinical model which has shown utility for therapeutic evaluation (Rastall et al., 2016). However, considering nearly 600 reported mutations within Pompe patients and the impact of disease gene modifiers (De Filippi et al., 2014), these models are unable to fully recapitulate human genetic complexity of the disease (Fukuda et al., 2007).

Current clinical therapy for Pompe disease is enzyme replacement therapy (ERT) which systemically delivers the recombinant human GAA (rhGAA) to break-down accumulated glycogen. While ERT significantly prolongs patient lifespan and augments quality of life (Kishnani et al., 2009), it is limited by inefficient delivery to SkM tissues (van der Ploeg et al., 2010), neutralization by host antibodies (De Vries et al., 2017), high dose requirements (Chien and Hwu, 2007), variable patient response (Kishnani et al., 2010), and high cost ($300,000 per year) (Güngör et al., 2013). Importantly, rhGAA does not appear to impact disease phenotypes in neurons nor does it cross the blood-brain barrier to help treat other neurological disease symptoms. Furthermore, restoration of SkM GAA activity does not restore nerve-invoked contractile function in GAA KO mice suggesting therapies should target neuronal tissues (Falk et al., 2015). In support, neuron-specific gene therapy in Pompe mice improved motor coordination, decreased astrogliosis, and increased myelination (Lee et al., 2018). However, early administration of AAV9-hGAA (age 1 month) led to the greatest restoration of GAA activity and overall function, while late administration (age 15 months) was not effective, reflecting how this treatment was unable to reverse a deficit in NMJ function and force production despite removing muscular glycogen accumulation (Todd et al., 2015).

In addition to studies in animal models and patients, *in vitro* human cell culture systems play important roles in modeling genetic diversity and neuromuscular dysfunction in Pompe disease. Specifically, human myotube cultures accurately model clinical differences between IOPD and LOPD patients (Raben et al., 2010), with IOPD myotubes displaying lysosomal enlargement (Spampanato et al., 2013) and LOPD myotubes exhibiting autophagosome accumulation (Nascimbeni et al., 2012). Glycogen accumulation and lysosomal enlargement in primary and hiPSC-derived IOPD myotubes could be prevented by overexpression of transcription factor EB (TFEB), a regulator of autophagy and lysosomal biogenesis (Spampanato et al., 2013; Sato et al., 2016). These findings were translated to GAA KO mice, where AAV delivery of TFEB ameliorated muscle pathology and restored contractile function (Gatto et al., 2017). Recently, the first *in vitro* 3D model of human Pompe disease SkM was reported using primary muscle cells (Wang et al., 2021). This model exhibited the expected lack of GAA activity, increased glycogen levels, lysosomal enlargement, and transcriptomic changes characteristic of Pompe disease but displayed no innate functional weakness (Wang et al., 2021). However, functional deficits could be induced by causing lysosomal stress with chloroquine, enforcing glycogen utilization by glucose starvation, or glycogen phosphorylase inhibition (Wang et al., 2021). Compared to 2D models, this biomimetic platform better recapitulates the *in vivo* Pompe phenotype for studies of glycogen accumulation and responses to candidate pharmacological and gene therapies.

Like other myopathies, large-scale and patient-specific studies of Pompe disease will require the utilization of hiPSCs. Encouragingly, hiPSC-derived myotubes generated through MyoD overexpression (Sato et al., 2016) or directed differentiation exhibit expected reductions in GAA activity and glycogen accumulation (van der Wal et al., 2017). Their utility as drug screening platforms has been shown by the ability of recombinant GAA (Yoshida et al., 2017), lentivirus encoding GAA (Sato et al., 2016), and antisense oligonucleotide (van der Wal et al., 2017) treatments to recover GAA enzyme activity and normalize cellular glycogen levels. The CNS involvement in Pompe disease has been modeled *in vitro* with hiPSC-derived neural stem cells which exhibited glycogen and secondary lipid accumulation, increased apoptosis, and enlarged lysosomes (Huang et al., 2019; Cheng et al., 2021). Lysosome size and glycogen accumulation could be decreased with rhGAA, hydroxypropyl-β-cyclodextrin, antioxidants (δ-tocopherol and ebselen), or PI3-K inhibitors (wortmannin and PX-866) (Huang et al., 2019; Cheng et al., 2021). Importantly, ebselen was able to increase GAA activity in the brain of GAA KO mice suggesting that these *in vitro* platforms could identify compounds that target neuronal tissues in Pompe patients (Huang et al., 2019). However, modeling of Pompe NMJ structure and function in hiPSC platforms has not been reported to date.

Overall, Pompe disease causes systemic accumulation of glycogen leading to a myriad of symptoms including cognitive decline, muscular wasting, and NMJ dysfunction. While

animal models have been critical for therapeutic developments and understanding Pompe pathology, they do not recreate human genetic complexity. Further complications arise from variations in clinical features between IOPD and LOPD patients underlining the importance of complementing animal studies with *in vitro* disease modeling platforms. Promisingly, hiPSC-derived Pompe disease myotubes exhibit expected reductions in GAA activity and glycogen accumulation and can be utilized for personalized drug screening (Sato et al., 2016; van der Wal et al., 2017; Yoshida et al., 2017). However, current *in vitro* models of 3D Pompe muscle do not model functional weakness in the absence of exogenous stressors such as those inducing lysosomal deficiency or glucose starvation (Wang et al., 2021). Functional weakness could potentially be gained by increasing experimental duration or muscle maturation as done in 2D micropatterned cultures that increased pathological LAMP1-positive lysosome accumulation in hiPSC-derived Pompe myotubes (Jiwlawat et al., 2019). Alternatively, the lack of baseline functional deficit in engineered Pompe muscles could point to the requisite NMJ involvement, warranting the development of hiPSC-derived NMJ models of Pompe disease. Additional incorporation of SCs and microglia would be of particular interest as these cells also show glycogen accumulation and cytoplasmic ballooning (Martin et al., 1973) and can contribute to Pompe pathogenesis. Since reduced myelin is seen in Pompe mice (Falk et al., 2015), effects of SC myelination should be also assessed in human *in vitro* models. Finally, ERT is more effective in fast than slow muscle fibers (Hawes et al., 2007), thus the ability to differentiate specific muscle fiber subtypes from Pompe hiPSCs would further augment translational relevance of these *in vitro* models.

## DISCUSSION

Decades of work using both *in vitro* and *in vivo* models of NMDs have led to important mechanistic insights and notable therapeutic advances. Here, we have compared the utility of these models for studying the NMJ structure and function and discussed the current state of disease modeling in the context of five specific NMDs. Animal models have been essential for our understanding of the clinical features of NMDs, but their limited genetic diversity and non-human physiology hinder their ability to fully recapitulate human NMD phenotypes, severity, and progression. Advances in genome editing technologies have facilitated generation of animal models with human mutations, providing a means to generate improved preclinical models for testing pharmacological and gene therapies for NMDs. Nevertheless, truly personalized disease modeling that accurately represents patient genetic and epigenetic diversity will require development of high-fidelity *in vitro* human NMJ platforms.

Recent advances in tissue-engineering methodologies have increased our *in vitro* modeling capabilities and furthered our understanding of human NMDs. hiPSC-derived models, in particular, hold promise for use in large-scale pharmaceutical testing, systematic analysis of disease mechanisms, and development of patient-specific treatments. However, additional progress will be needed to fully recapitulate NMD progression and complexity *in vitro* to allow for meaningful studies of underlying pathological mechanisms and drug responses (**Figure 6**). Specifically, hiPSC-derived NMJ models remain immature compared to primary NMJ models even after lengthy differentiation protocols. Therefore, improved differentiation methods will be necessary to not only replicate but accelerate developmental processes to obtain hiPSC-derived MNs and SkM cells and generate NMJs with mature structure and functionality akin to those of native motor units. Modifications of existing differentiation protocols to derive specific MN subtypes and SkM fiber types and stimulate NMJ maturation (Zhang et al., 2016) will allow development of *in vitro* models that can investigate why specific types of NMJs are distinctly affected by different NMDs and will enable targeted pharmacological testing of most affected tissues, such as type II muscle fibers in MG (Wang et al., 2018).

Replicating native, mature functional properties of NMJs will be crucial for accurate *in vitro* modeling of NMDs that often occur in adulthood. The immature state of hiPSC-derived cells remains a significant hurdle to generating predictive *in vitro* disease models or developing safe and effective regenerative therapies. Development of high-fidelity human NMJ models of NMDs is further complicated by the lack of detailed histological and functional descriptions of NMJs in NMD patients. Therefore, evaluation of *in vitro* human NMJ function and dysfunction as well as early formation relies largely on comparisons with murine models of development and disease. On the other hand, duration of human MN neurogenesis and maturation *in vivo* (Gogliotti et al., 2012; Stein et al., 2014) and *in vitro* (Johnson et al., 2007; Wainger et al., 2014) is substantially longer compared to murine counterparts, requiring longer-lasting and costly *in vitro* protocols to achieve mature MN states. Accelerating human MN maturation is commonly performed via small molecule inhibition of Notch. Disruption of Notch signaling accelerates neuronal differentiation by delaying the cell cycle transition from G1 to S phase increasing the commitment of progenitors toward neurogenesis (Crawford and Roelink, 2007; Borghese et al., 2010) and pre-MNs toward a post-mitotic, mature MN fate (Maury et al., 2015). While the small molecules that stimulate cell cycle exit have proven successful in accelerating MN maturation, their effects on the acquisition of distinct MN fates (e.g., MMC, SAC, PMC, LMC, HMC, PGC, ANS) are unexplored. As different MN subtypes emerge at distinct developmental stages *in vivo*, premature cell cycle exit could obstruct the ability to activate later MN subtype programs, which will require future investigations.

Similar to MNs, the immature state of current engineered SkM tissues lessens their physiological relevance and utility in disease modeling. A number of methods have been employed to enhance *in vitro* SkM maturation including dynamic culture (Juhas and Bursac, 2014), mechanical stretch (Powell et al., 2002), electrical stimulation (Khodabukus et al., 2019), growth factors (Ebrahimi et al., 2018), hormones (Butler-Browne et al., 1984), and small molecules (Selvaraj et al., 2019). Interestingly, some of these same interventions are also beneficial to both MN and NMJ formation, maturation, and regeneration. For example, electrical stimulation increases axon regeneration and recovery of motor function in sciatic nerve injury in Sprague-Dawley rats

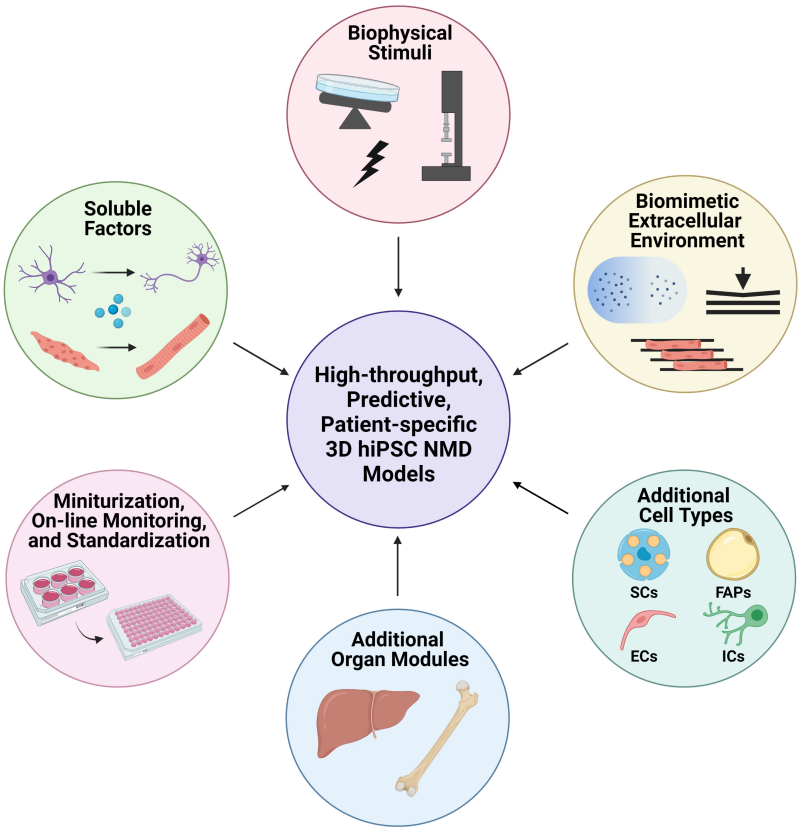


**FIGURE 6 |** Future developments of hiPSC-derived NMD models. Optimization of soluble factor treatments will be needed to improve maturity of MNs, SkM, and NMJs toward their respective *in vivo*-mimetic phenotypes. Incorporation of biophysical stimulation during cell culture such as electrical stimulation, mechanical stretch, and media agitation are expected to further improve functional maturity of NMJs. Biomaterial design and microfabrication/microfluidics techniques can be applied to generate biomimetic microenvironments for cell growth via controlled presentation of developmentally relevant gradients in growth factors, topography, and stiffness. As the function of native NMJs relies on complex multi-cellular interactions, the ability to incorporate Schwann cells (SCs), endothelial cells (ECs), fibro-adipogenic progenitors (FAPs), and immune system cells (ICs) would improve modeling of *in vivo* states and our understanding of NMJ physiology and pathology. Incorporation of additional organ compartments sharing culture media with NMJs, such as intestine, gut, and liver will better emulate human drug responses, while adding bone, ligament, cartilage, and fat compartments will allow studies of the organ-organ crosstalk in NMDs. Finally, further miniaturization and standardization of culture systems along with development of non-invasive metabolic and functional readouts will enable establishment of versatile NMD platforms for high-throughput drug discovery research.

(Fu et al., 2020) and improves alignment and maturation of human myotubes in culture (Ahadian et al., 2012; Khodabukus et al., 2019). As functional innervation is required for muscle maturation and mature muscle contributes to maintaining functional NMJs, it will be important to develop methods that will improve overall maturation state in NMJ co-cultures. Additionally, myonuclei are typically localized at the periphery of muscle fibers, but specialized myonuclei are anchored below the mature postsynaptic membrane *in vivo* (Grady et al., 2005). Advances in single-nucleus RNA sequencing have revealed hundreds of novel genes expressed within postsynaptic myonuclei (Petrany et al., 2020). Genetic knockdown of a small subset of these genes revealed Gramd1b as a positive and Ufsp1 as a negative modulator of AchR clustering suggesting that novel insights into NMJ maturation and maintenance can be obtained from sequencing datasets. Similar studies of transcriptional specialization within modular neuromuscular cultures (consisting of multiple compartments and cell types) would improve our understanding of NMJ development leading to effective methods to increase NMJ maturation.

Ultimately, besides accelerated maturation of MNs and SkM cells, the incorporation of additional non-myogenic muscle-resident cell types, such as SCs, fibro-adipogenic progenitors (FAPs), and endothelial cells will be required to recreate native NMJ complexity. Here, heterocellular interactions can stimulate formation and advanced maturation of biomimetic NMJs to model both normal physiology and disease. For example, SCs are essential in the formation and maintenance of the adult NMJ (Ko and Robitaille, 2015) and their incorporation into NMJ models has supported MN and SkM viability, myelinated axons, and extended culture times (Singh and Vazquez, 2019; Hyung et al., 2021). Unfortunately, they have been underrepresented within NMD models despite their suggested disease-modifying roles in ALS (Bruneteau et al., 2015), MG (Kimura and Nezu, 1989), DMD (Personius and Sawyer, 2005), DM (Borenstein et al., 1977), and Pompe disease (Martin et al., 1973). Similarly,

FAPs reside adjacent to NMJs, neighboring SCs and MNs, where they actively influence SCs and maintain NMJ integrity (Hogarth et al., 2019; Uezumi et al., 2021). Subpopulations of FAPs are dysregulated in many NMDs and accumulate within atrophied ALS mouse muscles (Gonzalez et al., 2017), exhibit varied gene signatures in response to denervation and cardiotoxin injury (Madaro et al., 2018), and activate IL-6-STAT3 signaling in response to denervation that may lead to fibrosis related to NMDs (Madaro et al., 2018). Vascular cells have critical roles in NMJ development, maintenance, and regeneration *in vivo* (Sawada et al., 2014) as well as secrete neurotrophic factors that support axonal growth *in vitro* (Grasman and Kaplan, 2017). Their roles in NMJ formation and function also remain to be explored and further elucidate their potential roles in NMDs.

Generation of advanced *in vitro* NMD models and platforms for predictive drug screening will also require the incorporation of cell of the immune system and cells involved in drug metabolism, respectively. The immune system is a critical regulator of both neurological (Prinz and Priller, 2017) and muscular (Farup et al., 2015) homeostasis, injury response, and pathology. The chronic injury cycles characteristic of multiple NMDs result in persistent and increased infiltration of monocytes/macrophages (Acharyya et al., 2007), T lymphocytes (Uzawa et al., 2021), and mast cells (Trias et al., 2017) at NMJs. These cells secrete multiple factors that induce a chronic pro-inflammatory environment and contribute to disease progression through several mechanisms that increase oxidative stress and alter stem cell function. Similarly, accurate modeling of autoimmune diseases such as MG will require incorporation of T and B lymphocytes to model chronic inflammation and autoantibody production (Uzawa et al., 2021). Realistic *in vitro* modeling of pharmacodynamics and expected drug concentrations in the bloodstream will necessitate incorporation of additional organ-on-chip (OOC) modules containing extramuscular tissues such as intestine, gut, liver, and fat. These multiplexed culture systems will be able to identify unexpected drug toxicities due to organ-organ crosstalk, such as that seen for bleomycin cardiomyocyte toxicity only in the presence of lung tissue (Skardal et al., 2017). Multiplexed OOC platforms will also enable studies of the more intimate tissue-tissue relationships between skeletal muscle and bone, ligament, or cartilage, which can be perturbed in NMDs as well as in various musculoskeletal degenerative diseases. In support of the feasibility of these complex systems, up to 10 unique OOC modules have been successfully interconnected to form a body-on-a-chip (BOC) platform (Novak et al., 2020). While additional tissue maturation within each OOC module is required, BOC platforms would have the unique potential to permit modular crosstalk studies allowing understanding of the NMD progression on a systemic level.

Beyond incorporation of additional cell types, further advancements in biomaterial design and microfabrication technologies will be critical for successful engineering of microphysiological systems that replicate *in vivo* 3D microenvironments of developing or diseased NMJs. For example, 3D hydrogels that incorporate the basement membrane proteins laminin and collagen IV have been shown to support increased contractile force generation in muscle-only (Hinds et al., 2011) and muscle-neuron (Vilmont et al., 2016) culture platforms and uniquely enable tau aggregation in organoid models of Alzheimer's disease (Choi et al., 2014). Recent advancements in the design of smart biomaterials that allow spatiotemporal control of growth factor, topographical, and stiffness gradients (Darnell and Mooney, 2017; Kowalski et al., 2018), combined with use of microfluidic devices to establish tissue compartmentalization and gradients of soluble factors (Sun et al., 2019), offer opportunities to precisely influence the migration, proliferation, differentiation, and maturation of hiPSC derivatives through mimicry of the native ECM architecture and biophysical and biochemical cues. For example, 3D bioprinting (Kang et al., 2016; Zhang et al., 2018) of bioactive biomaterials to enable compartmentalized growth and differentiation of MNs and SkM (Osaki et al., 2018; Narayanan et al., 2021), along with microfluidic approaches to establish a local microenvironment supportive of NMJ formation and maturation via spatially defined delivery of auxiliary cells and agrin (Tourovskaia et al., 2008), could provide means to generate highly functional NMJs amenable to rigorous studies of NMD pathology.

Current *in vitro* NMJ models are mainly utilized for small-scale, stand-alone studies, or to supplement whole-organ and organism-level *in vivo* investigations with human cell- and tissue-specific data. Combining animal studies from a single genetic background with *in vitro* validations in hiPSC-based models from genetically diverse patients are likely to improve the predictive value of preclinical therapeutic tests. Eventually, however, advances in hiPSC technology along with miniaturization and standardization of microphysiological systems are expected to enable self-sufficient, high-throughput *in vitro* pharmacological screens with directly translational outcomes. Altogether, we anticipate that future advances in patient-specific hiPSC-based *in vitro* modeling of NMDs will be instrumental for gaining deeper understanding of human NMD pathophysiology and will lead to streamlined developments of pharmacotherapies for these devastating disorders.

## AUTHOR CONTRIBUTIONS

ZF, EL, and TC wrote the manuscript. TC and ZF generated figures for the manuscript. AK and NB edited the manuscript. All authors contributed to the article and approved the submitted version.

## FUNDING

This work was supported by NIH grants AR055226 and AR070543 from National Institute of Arthritis and Musculoskeletal and Skin Disease, grant UG3TR002142 from the NIH Common Fund for the Microphysiological Systems Initiative, grant U01EB028901 from National Institute of Biomedical Imaging and Bioengineering, and the Jain foundation. The content of the manuscript is solely the responsibility of the authors and does not necessarily represent the official views of the National Institutes of Health.

## REFERENCES


Aarli, J. A. (2001). Titin, thymoma, and myasthenia gravis. *Arch. Neurol.* 58, 869–870. doi: 10.1001/archneur.58.6.869

Aartsma-Rus, A., and van Putten, M. (2019). The use of genetically humanized animal models for personalized medicine approaches. *Dis. Models Mech.* 13:dmm041673. doi: 10.1242/dmm.041673

Abujarour, R., Bennett, M., Valamehr, B., Lee, T. T., Robinson, M., Robbins, D., et al. (2014). Myogenic differentiation of muscular dystrophy-specific induced pluripotent stem cells for use in drug discovery. *Stem Cells Transl. Med.* 3, 149–160. doi: 10.5966/sctm.2013-0095

Acharyya, S., Villalta, S. A., Bakkar, N., Bupha-Intr, T., Janssen, P. M., Carathers, M., et al. (2007). Interplay of IKK/NF-κB signaling in macrophages and myofibers promotes muscle degeneration in Duchenne muscular dystrophy. *J. Clin. Invest.* 117, 889–901. doi: 10.1172/JCI30556

Afshar, M. E., Abraha, H. Y., Bakooshli, M. A., Davoudi, S., Thavandiran, N., Tung, K., et al. (2020). A 96-well culture platform enables longitudinal analyses of engineered human skeletal muscle microtissue strength. *Sci. Rep.* 10:6918. doi: 10.1038/s41598-020-62837-8

Ahadian, S., Ramon-Azcon, J., Ostrovidov, S., Camci-Unal, G., Hosseini, V., Kaji, H., et al. (2012). Interdigitated array of Pt electrodes for electrical stimulation and engineering of aligned muscle tissue. *Lab Chip* 12, 3491–3503. doi: 10.1039/c2lc40479f

Al Tanoury, Z., Zimmerman, J. F., Rao, J., Sieiro, D., Mcnamara, H. M., Cherrier, T., et al. (2021). Prednisolone rescues Duchenne muscular dystrophy phenotypes in human pluripotent stem cell–derived skeletal muscle in vitro. *Proc. Natl. Acad. Sci. U.S.A.* 118:e2022960118. doi: 10.1073/pnas.2022960118

Albini, S., and Puri, P. L. (2014). Generation of myospheres from hESCs by epigenetic reprogramming. *J. Vis. Exp. JoVE* 88:51243. doi: 10.3791/51243

Askanas, V., Kwan, H., Alvarez, R. B., Engel, W. K., Kobayashi, T., Martinuzzi, A., et al. (1987). De novo neuromuscular junction formation on human muscle fibres cultured in monolayer and innervated by foetal rat spinal cord: ultrastructural and ultrastructural–cytochemical studies. *J. Neurocytol.* 16, 523–537. doi: 10.1007/BF01668506

Attia, M., Maurer, M., Robinet, M., Le Grand, F., Fadel, E., Le Panse, R., et al. (2017). Muscle satellite cells are functionally impaired in myasthenia gravis: consequences on muscle regeneration. *Acta Neuropathol.* 134, 869–888. doi: 10.1007/s00401-017-1754-2

Aulehla, A., Wehrle, C., Brand-Saberi, B., Kemler, R., Gossler, A., Kanzler, B., et al. (2003). Wnt3a plays a major role in the segmentation clock controlling somitogenesis. *Dev. Cell* 4, 395–406. doi: 10.1016/S1534-5807(03)00055-8

Babin, P. J., Goizet, C., and Raldua, D. (2014). Zebrafish models of human motor neuron diseases: advantages and limitations. *Prog. Neurobiol.* 118, 36–58. doi: 10.1016/j.pneurobio.2014.03.001

Badu-Mensah, A., Guo, X., Mcaleer, C. W., Rumsey, J. W., and Hickman, J. J. (2020). Functional skeletal muscle model derived from SOD1-mutant ALS patient iPSCs recapitulates hallmarks of disease progression. *Sci. Rep.* 10:14302. doi: 10.1038/s41598-020-70510-3

Bakooshli, M. A., Lippmann, E. S., Mulcahy, B., Iyer, N., Nguyen, C. T., Tung, K., et al. (2019). A 3D culture model of innervated human skeletal muscle enables studies of the adult neuromuscular junction. *Elife* 8:e44530. doi: 10.7554/eLife.44530.033

Barber, S. C., and Shaw, P. J. (2010). Oxidative stress in ALS: key role in motor neuron injury and therapeutic target. *Free Radic. Biol. Med.* 48, 629–641. doi: 10.1016/j.freeradbiomed.2009.11.018

Barik, A., Li, L., Sathyamurthy, A., Xiong, W. C., and Mei, L. (2016). Schwann cells in neuromuscular junction formation and maintenance. *J. Neurosci.* 36, 9770–9781. doi: 10.1523/JNEUROSCI.0174-16.2016

Barton, E. R., Morris, L., Kawana, M., Bish, L. T., and Toursel, T. (2005). Systemic administration of L-arginine benefits mdx skeletal muscle function. *Muscle Nerve* 32, 751–760. doi: 10.1002/mus.20425

Bersini, S., Gilardi, M., Ugolini, G. S., Sansoni, V., Talo, G., Perego, S., et al. (2018). Engineering an environment for the study of fibrosis: a 3D human muscle model with endothelium specificity and endomysium. *Cell Rep.* 25, 3858–3868.e3854. doi: 10.1016/j.celrep.2018.11.092

Berul, C. I., Maguire, C. T., Aronovitz, M. J., Greenwood, J., Miller, C., Gehrmann, J., et al. (1999). DMPK dosage alterations result in atrioventricular conduction abnormalities in a mouse myotonic dystrophy model. *J. Clin. Invest.* 103, R1–R7. doi: 10.1172/JCI5346

Bettadapur, A., Suh, G. C., Geisse, N. A., Wang, E. R., Hua, C., Huber, H. A., et al. (2016). Prolonged culture of aligned skeletal myotubes on micromolded gelatin hydrogels. *Sci. Rep.* 6:28855. doi: 10.1038/srep28855

Bilsland, L. G., Sahai, E., Kelly, G., Golding, M., Greensmith, L., and Schiavo, G. (2010). Deficits in axonal transport precede ALS symptoms in vivo. *Proc. Natl. Acad. Sci. U.S.A.* 107, 20523–20528. doi: 10.1073/pnas.1006869107

Birger, A., Ben-Dor, I., Ottolenghi, M., Turetsky, T., Gil, Y., Sweetat, S., et al. (2019). Human iPSC-derived astrocytes from ALS patients with mutated C9ORF72 show increased oxidative stress and neurotoxicity. *EBioMedicine* 50, 274–289. doi: 10.1016/j.ebiom.2019.11.026

Bjornskov, E. K., Dekker, N. P., Norris, F. H., and Stuart, M. E. (1975). End-plate morphology in amyotrophic lateral sclerosis. *Arch. Neurol.* 32, 711–712. doi: 10.1001/archneur.1975.00490520081016

Bladt, F., Riethmacher, D., Isenmann, S., Aguzzi, A., and Birchmeier, C. (1995). Essential role for the c-met receptor in the migration of myogenic precursor cells into the limb bud. *Nature* 376, 768–771. doi: 10.1038/376768a0

Blanchard, A. D., Sinanan, A., Parmantier, E., Zwart, R., Broos, L., Meijer, D., et al. (1996). Oct-6 (SCIP/Tst-1) is expressed in Schwann cell precursors, embryonic Schwann cells, and postnatal myelinating Schwann cells: comparison with Oct-1, Krox-20, and Pax-3. *J. Neurosci. Res.* 46, 630–640. doi: 10.1002/(SICI)1097-4547(19961201)46:5<630::AID-JNR11>3.0.CO;2-0

Blau, H. M., Webster, C., and Pavlath, G. K. (1983). Defective myoblasts identified in Duchenne muscular dystrophy. *Proc. Natl. Acad. Sci. U.S.A.* 80, 4856–4860. doi: 10.1073/pnas.80.15.4856

Bombelli, F., Lispi, L., Porrini, S. C., Giacanelli, M., Terracciano, C., Massa, R., et al. (2016). Neuromuscular transmission abnormalities in myotonic dystrophy type 1: a neurophysiological study. *Clin. Neurol. Neurosurg.* 150, 84–88. doi: 10.1016/j.clineuro.2016.08.020

Borenstein, S., Noël, P., Jacquy, J., and Flamentdurand, J. (1977). Myotonic dystrophy with nerve hypertrophy: report of a case with electrophysiological and ultrastructural study of the sural nerve. *J. Neurol. Sci.* 34, 87–99. doi: 10.1016/0022-510X(77)90094-6

Borghese, L., Dolezalova, D., Opitz, T., Haupt, S., Leinhaas, A., Steinfarz, B., et al. (2010). Inhibition of notch signaling in human embryonic stem cell-derived neural stem cells delays G1/S phase transition and accelerates neuronal differentiation in vitro and in vivo. *Stem Cells* 28, 955–964. doi: 10.1002/stem.408

Bragato, C., Carra, S., Blasevich, F., Salerno, F., Brix, A., Bassi, A., et al. (2020). Glycogen storage in a zebrafish Pompe disease model is reduced by 3-BrPA treatment. *Biochim. Biophys. Acta (BBA) Mol. Basis Dis.* 1866:165662. doi: 10.1016/j.bbadis.2020.165662

Breucking, E., Reimnitz, P., Schara, U., and Mortier, W. (2000). [Anesthetic complications. The incidence of severe anesthetic complications in patients and families with progressive muscular dystrophy of the Duchenne and Becker types]. *Anaesthesist* 49, 187–195. doi: 10.1007/s001010050813

Brouwer, J. R., Willemsen, R., and Oostra, B. A. (2009). Microsatellite repeat instability and neurological disease. *Bioessays* 31, 71–83. doi: 10.1002/bies.080122

Brown, R. H., and Al-Chalabi, A. (2017). Amyotrophic lateral sclerosis. *N. Engl. J. Med.* 377, 162–172. doi: 10.1056/NEJMra1603471

Bruneteau, G., Bauché, S., Gonzalez De Aguilar, J. L., Brochier, G., Mandjee, N., Tanguy, M. L., et al. (2015). Endplate denervation correlates with Nogo-A muscle expression in amyotrophic lateral sclerosis patients. *Ann. Clin. Transl. Neurol.* 2, 362–372. doi: 10.1002/acn3.179

Burbulla, L. F., Beaumont, K. G., Mrksich, M., and Krainc, D. (2016). Micropatterning facilitates the long-term growth and analysis of iPSC-derived individual human neurons and neuronal networks. *Adv. Healthc. Mater.* 5, 1894–1903. doi: 10.1002/adhm.201500900

Burns, D. P., Canavan, L., Rowland, J., O'flaherty, R., Brannock, M., Drummond, S. E., et al. (2018). Recovery of respiratory function in mdx mice co-treated with neutralizing interleukin-6 receptor antibodies and urocortin-2. *J. Physiol.* 596, 5175–5197. doi: 10.1113/JP276954

Butler-Browne, G. S., Herlicoviez, D., and Whalen, R. G. (1984). Effects of hypothyroidism on myosin isozyme transitions in developing rat muscle. *FEBS Lett.* 166, 71–75. doi: 10.1016/0014-5793(84)80047-2

Casas, C., Manzano, R., Vaz, R., Osta, R., and Brites, D. (2016). Synaptic failure: focus in an integrative view of ALS. *Brain Plast.* 1, 159–175. doi: 10.3233/BPL-140001

Cescon, M., Gregorio, I., Eiber, N., Borgia, D., Fusto, A., Sabatelli, P., et al. (2018). Collagen VI is required for the structural and functional integrity of the neuromuscular junction. *Acta Neuropathol.* 136, 483–499. doi: 10.1007/s00401-018-1860-9

Chakkalakal, J. V., Nishimune, H., Ruas, J. L., Spiegelman, B. M., and Sanes, J. R. (2010). Retrograde influence of muscle fibers on their innervation revealed by a novel marker for slow motoneurons. *Development* 137, 3489–3499. doi: 10.1242/dev.053348

Chal, J., Al Tanoury, Z., Hestin, M., Gobert, B., Aivio, S., Hick, A., et al. (2016). Generation of human muscle fibers and satellite-like cells from human pluripotent stem cells in vitro. *Nat. Protoc.* 11, 1833–1850. doi: 10.1038/nprot.2016.110

Chalamalasetty, R. B., Garriock, R. J., Dunty, W. C., Kennedy, M. W., Jailwala, P., Si, H., et al. (2014). Mesogenin 1 is a master regulator of paraxial presomitic mesoderm differentiation. *Development* 141, 4285–4297. doi: 10.1242/dev.110908

Chambers, S. M., Fasano, C. A., Papapetrou, E. P., Tomishima, M., Sadelain, M., and Studer, L. (2009). Highly efficient neural conversion of human ES and iPS cells by dual inhibition of SMAD signaling. *Nat. Biotechnol.* 27, 275–280. doi: 10.1038/nbt.1529

Chan, J., Desai, A. K., Kazi, Z. B., Corey, K., Austin, S., Hobson-Webb, L. D., et al. (2017). The emerging phenotype of late-onset Pompe disease: a systematic literature review. *Mol. Genet. Metab.* 120, 163–172. doi: 10.1016/j.ymgme.2016.12.004

Chang, N. C., Sincennes, M. C., Chevalier, F. P., Brun, C. E., Lacaria, M., Segales, J., et al. (2018). The dystrophin glycoprotein complex regulates the epigenetic activation of muscle stem cell commitment. *Cell Stem Cell* 22, 755–768 e756. doi: 10.1016/j.stem.2018.03.022

Chargé, S. B., and Rudnicki, M. A. (2004). Cellular and molecular regulation of muscle regeneration. *Physiol. Rev.* 84, 209–238. doi: 10.1152/physrev.00019.2003

Chemello, F., Chai, A. C., Li, H., Rodriguez-Caycedo, C., Sanchez-Ortiz, E., Atmanli, A., et al. (2021). Precise correction of Duchenne muscular dystrophy exon deletion mutations by base and prime editing. *Sci. Adv.* 7:eabg4910. doi: 10.1126/sciadv.abg4910

Chen, D., Wang, Y., and Chin, E. R. (2015). Activation of the endoplasmic reticulum stress response in skeletal muscle of G93A* SOD1 amyotrophic lateral sclerosis mice. *Front. Cell. Neurosci.* 9:170. doi: 10.3389/fncel.2015.00170

Cheng, Y.-S., Yang, S., Hong, J., Li, R., Beers, J., Zou, J., et al. (2021). Modeling CNS involvement in pompe disease using neural stem cells generated from patient-derived induced pluripotent stem cells. *Cells* 10:8. doi: 10.3390/cells10010008

Chien, Y.-H., and Hwu, W.-L. (2007). A review of treatment of Pompe disease in infants. *Biol. Targets Ther.* 1, 195.

Choi, S. H., Kim, Y. H., Hebisch, M., Sliwinski, C., Lee, S., D'avanzo, C., et al. (2014). A three-dimensional human neural cell culture model of Alzheimer's disease. *Nature* 515, 274–278. doi: 10.1038/nature13800

Cinzia, B., Flavia, B., Gary, I., Renato, M., and Lorenzo, M. (2021). Therapeutic efficacy of 3, 4-Diaminopyridine phosphate on neuromuscular junction in Pompe disease. *Biomed. Pharmacother.* 137:111357. doi: 10.1016/j.biopha.2021.111357

Ciruna, B., and Rossant, J. (2001). FGF signaling regulates mesoderm cell fate specification and morphogenetic movement at the primitive streak. *Dev. Cell* 1, 37–49. doi: 10.1016/S1534-5807(01)00017-X

Colella, P., Sellier, P., Gomez, M. J., Biferi, M. G., Tanniou, G., Guerchet, N., et al. (2020). Gene therapy with secreted acid alpha-glucosidase rescues Pompe disease in a novel mouse model with early-onset spinal cord and respiratory defects. *EBioMedicine* 61:103052. doi: 10.1016/j.ebiom.2020.103052

Court, F. A., Gillingwater, T. H., Melrose, S., Sherman, D. L., Greenshields, K. N., Morton, A. J., et al. (2008). Identity, developmental restriction and reactivity of extralaminar cells capping mammalian neuromuscular junctions. *J. Cell Sci.* 121, 3901–3911. doi: 10.1242/jcs.031047

Crawford, T. Q., and Roelink, H. (2007). The notch response inhibitor DAPT enhances neuronal differentiation in embryonic stem cell-derived embryoid bodies independently of sonic hedgehog signaling. *Dev. Dyn.* 236, 886–892. doi: 10.1002/dvdy.21083

Crisafulli, S., Sultana, J., Fontana, A., Salvo, F., Messina, S., and Trifirò, G. (2020). Global epidemiology of Duchenne muscular dystrophy: an updated systematic review and meta-analysis. *Orphanet J. Rare Dis.* 15, 1–20. doi: 10.1186/s13023-020-01430-8

Dangain, J., and Vrbova, G. (1984). Muscle development in mdx mutant mice. *Muscle Nerve* 7, 700–704. doi: 10.1002/mus.880070903

Darabi, R., Arpke, R. W., Irion, S., Dimos, J. T., Grskovic, M., Kyba, M., et al. (2012). Human ES-and iPS-derived myogenic progenitors restore DYSTROPHIN and improve contractility upon transplantation in dystrophic mice. *Cell Stem Cell* 10, 610–619. doi: 10.1016/j.stem.2012.02.015

Darnell, M., and Mooney, D. J. (2017). Leveraging advances in biology to design biomaterials. *Nat. Mater.* 16, 1178–1185. doi: 10.1038/nmat4991

Das, M., Rumsey, J. W., Bhargava, N., Stancescu, M., and Hickman, J. J. (2010). A defined long-term in vitro tissue engineered model of neuromuscular junctions. *Biomaterials* 31, 4880–4888. doi: 10.1016/j.biomaterials.2010.02.055

Das, S., Browne, K. D., Laimo, F. A., Maggiore, J. C., Hilman, M. C., Kaisaier, H., et al. (2020). Pre-innervated tissue-engineered muscle promotes a pro-regenerative microenvironment following volumetric muscle loss. *Commun. Biol.* 3:330. doi: 10.1038/s42003-020-1056-4

Dasen, J. S., and Jessell, T. M. (2009). Hox networks and the origins of motor neuron diversity. *Curr. Top. Dev. Biol.* 88, 169–200. doi: 10.1016/S0070-2153(09)88006-X

Dawson, T. M., Golde, T. E., and Lagier-Tourenne, C. (2018). Animal models of neurodegenerative diseases. *Nat. Neurosci.* 21, 1370–1379. doi: 10.1038/s41593-018-0236-8

De Filippi, P., Saeidi, K., Ravaglia, S., Dardis, A., Angelini, C., Mongini, T., et al. (2014). Genotype-phenotype correlation in Pompe disease, a step forward. *Orphanet J. Rare Dis.* 9:102. doi: 10.1186/s13023-014-0102-z

De Oliveira, G. P., Maximino, J. R., Maschietto, M., Zanoteli, E., Puga, R. D., Lima, L., et al. (2014). Early gene expression changes in skeletal muscle from SOD1 g93a amyotrophic lateral sclerosis animal model. *Cell. Mol. Neurobiol.* 34, 451–462. doi: 10.1007/s10571-014-0029-x

De Vries, J. M., Kuperus, E., Hoogeveen-Westerveld, M., Kroos, M. A., Wens, S. C., Stok, M., et al. (2017). Pompe disease in adulthood: effects of antibody formation on enzyme replacement therapy. *Genet. Med.* 19, 90–97. doi: 10.1038/gim.2016.70

Deconinck, A. E., Rafael, J. A., Skinner, J. A., Brown, S. C., Potter, A. C., Metzinger, L., et al. (1997). Utrophin-dystrophin-deficient mice as a model for Duchenne muscular dystrophy. *Cell* 90, 717–727. doi: 10.1016/S0092-8674(00)80532-2

Deenen, J. C., Horlings, C. G., Verschuuren, J. J., Verbeek, A. L., and Van Engelen, B. G. (2015). The Epidemiology of neuromuscular disorders: a comprehensive overview of the literature. *J. Neuromuscul. Dis.* 2, 73–85. doi: 10.3233/JND-140045

Demestre, M., Orth, M., Föhr, K., Achberger, K., Ludolph, A. C., Liebau, S., et al. (2015). Formation and characterisation of neuromuscular junctions between hiPSC derived motoneurons and myotubes. *Stem Cell Res.* 15, 328–336. doi: 10.1016/j.scr.2015.07.005

Denetclaw, W., Christ, B., and Ordahl, C. P. (1997). Location and growth of epaxial myotome precursor cells. *Development* 124, 1601–1610. doi: 10.1242/dev.124.8.1601

DeRuisseau, L. R., Fuller, D. D., Qiu, K., Deruisseau, K. C., Donnelly, W. H., Mah, C., et al. (2009). Neural deficits contribute to respiratory insufficiency in Pompe disease. *Proc. Natl. Acad. Sci. U.S.A.* 106, 9419–9424. doi: 10.1073/pnas.0902534106

Diez del Corral, R., and Storey, K. G. (2004). Opposing FGF and retinoid pathways: a signalling switch that controls differentiation and patterning onset in the extending vertebrate body axis. *Bioessays* 26, 857–869. doi: 10.1002/bies.20080

Dobrowolny, G., Aucello, M., Rizzuto, E., Beccafico, S., Mammucari, C., Bonconpagni, S., et al. (2008). Skeletal muscle is a primary target of SOD1G93A-mediated toxicity. *Cell Metab.* 8, 425–436. doi: 10.1016/j.cmet.2008.09.002

Doddrell, R. D., Dun, X. P., Moate, R. M., Jessen, K. R., Mirsky, R., and Parkinson, D. B. (2012). Regulation of Schwann cell differentiation and proliferation by the Pax-3 transcription factor. *Glia* 60, 1269–1278. doi: 10.1002/glia.22346

Doyle, B. M., Turner, S. M., Sunshine, M. D., Doerfler, P. A., Poirier, A. E., Vaught, L. A., et al. (2019). Aav gene therapy utilizing glycosylation-independent lysosomal targeting tagged gaa in the hypoglossal motor system of pompe mice. *Mol. Ther. Methods Clin. Dev.* 15, 194–203. doi: 10.1016/j.omtm.2019.08.009

Du, J., Campau, E., Soragni, E., Jespersen, C., and Gottesfeld, J. M. (2013). Length-dependent CTG CAG triplet-repeat expansion in myotonic dystrophy patient-derived induced pluripotent stem cells. *Hum. Mol. Genet.* 22, 5276–5287. doi: 10.1093/hmg/ddt386

Du, Z. W., Chen, H., Liu, H., Lu, J., Qian, K., Huang, C. L., et al. (2015). Generation and expansion of highly pure motor neuron progenitors from human pluripotent stem cells. *Nat. Commun.* 6:6626. doi: 10.1038/ncomms7626

Dubrulle, J., Mcgrew, M. J., and Pourquié, O. (2001). FGF signaling controls somite boundary position and regulates segmentation clock control of spatiotemporal Hox gene activation. *Cell* 106, 219–232. doi: 10.1016/S0092-8674(01)00437-8

Dumont, N. A., Wang, Y. X., and Rudnicki, M. A. (2015a). Intrinsic and extrinsic mechanisms regulating satellite cell function. *Development* 142, 1572–1581. doi: 10.1242/dev.114223

Dumont, N. A., Wang, Y. X., Von Maltzahn, J., Pasut, A., Bentzinger, C. F., Brun, C. E., et al. (2015b). Dystrophin expression in muscle stem cells regulates their polarity and asymmetric division. *Nat. Med.* 21, 1455–1463. doi: 10.1038/nm.3990

Ebrahimi, M., Lad, H., Fusto, A., Tiper, Y., Datye, A., Nguyen, C. T., et al. (2021). De novo revertant fiber formation and therapy testing in a 3D culture model of Duchenne muscular dystrophy skeletal muscle(). *Acta Biomater.* 132, 227–244. doi: 10.1016/j.actbio.2021.05.020

Ebrahimi, M., Ostrovidov, S., Salehi, S., Kim, S. B., Bae, H., and Khademhosseini, A. (2018). Enhanced skeletal muscle formation on microfluidic spun gelatin methacryloyl (GelMA) fibres using surface patterning and agrin treatment. *J. Tissue Eng. Regen. Med.* 12, 2151–2163. doi: 10.1002/term.2738

Egawa, N., Kitaoka, S., Tsukita, K., Naitoh, M., Takahashi, K., Yamamoto, T., et al. (2012). Drug screening for ALS using patient-specific induced pluripotent stem cells. *Sci. Transl. Med.* 4:145ra104. doi: 10.1126/scitranslmed.3004052

Eisen, A., Kim, S., and Pant, B. (1992). Amyotrophic lateral sclerosis (ALS): a phylogenetic disease of the corticomotoneuron? *Muscle Nerve* 15, 219–224. doi: 10.1002/mus.880150215

Enjin, A., Rabe, N., Nakanishi, S. T., Vallstedt, A., Gezelius, H., Memic, F., et al. (2010). Identification of novel spinal cholinergic genetic subtypes disclose Chodl and Pitx2 as markers for fast motor neurons and partition cells. *J. Comp. Neurol.* 518, 2284–2304. doi: 10.1002/cne.22332

Ericson, J., Morton, S., Kawakami, A., Roelink, H., and Jessell, T. M. (1996). Two critical periods of Sonic Hedgehog signaling required for the specification of motor neuron identity. *Cell* 87, 661–673. doi: 10.1016/S0092-8674(00)81386-0

Falk, D. J., Todd, A. G., Lee, S., Soustek, M. S., Elmallah, M. K., Fuller, D. D., et al. (2015). Peripheral nerve and neuromuscular junction pathology in Pompe disease. *Hum. Mol. Genet.* 24, 625–636. doi: 10.1093/hmg/ddu476

Fambrough, D. M. (1979). Control of acetylcholine receptors in skeletal muscle. *Physiol. Rev.* 59, 165–227. doi: 10.1152/physrev.1979.59.1.165

Fardaei, M., Rogers, M. T., Thorpe, H. M., Larkin, K., Hamshere, M. G., Harper, P. S., et al. (2002). Three proteins, MBNL, MBLL and MBXL, co-localize in vivo with nuclear foci of expanded-repeat transcripts in DM1 and DM2 cells. *Hum. Mol. Genet.* 11, 805–814. doi: 10.1093/hmg/11.7.805

Fardeau, M., and Tome, F. (1980). "Light and electron microscopic study of motor endplates in the adult and neo-natal forms of dystrophia myotonica," in *Proceedings of the INSEREM Symposium on Ontogenesis and Functional Mechanisms of Peripheral Synapses: Ontogenesis and Functional Mechanisms of Peripheral Synapses*, (Amsterdam: Elsevier), 287–298.

Farmakidis, C., Pasnoor, M., Dimachkie, M. M., and Barohn, R. J. (2018). Treatment of myasthenia gravis. *Neurol. Clin.* 36, 311–337. doi: 10.1016/j.ncl.2018.01.011

Farup, J., Madaro, L., Puri, P., and Mikkelsen, U. (2015). Interactions between muscle stem cells, mesenchymal-derived cells and immune cells in muscle homeostasis, regeneration and disease. *Cell Death Dis.* 6:e1830. doi: 10.1038/cddis.2015.198

Faustino Martins, J. M., Fischer, C., Urzi, A., Vidal, R., Kunz, S., Ruffault, P. L., et al. (2020). Self-Organizing 3D human trunk neuromuscular organoids. *Cell Stem Cell* 27:498. doi: 10.1016/j.stem.2020.08.011

Feeney, E. J., Austin, S., Chien, Y.-H., Mandel, H., Schoser, B., Prater, S., et al. (2014). The value of muscle biopsies in Pompe disease: identifying lipofuscin inclusions in juvenile-and adult-onset patients. *Acta Neuropathol. Commun.* 2:2. doi: 10.1186/2051-5960-2-2

Fernández-Garibay, X., Ortega, M. A., Cerro-Herreros, E., Comelles, J., Martínez, E., Artero, R., et al. (2021). Bioengineered in vitro 3D model of myotonic dystrophy type 1 human skeletal muscle. *Biofabrication* 13:035035. doi: 10.1088/1758-5090/abf6ae

Fernandez-Costa, J. M., Llamusi, M. B., Garcia-Lopez, A., and Artero, R. (2011). Alternative splicing regulation by Muscleblind proteins: from development to disease. *Biol. Rev.* 86, 947–958. doi: 10.1111/j.1469-185X.2011.00180.x

Fischer-Hayes, L. R., Brotherton, T., and Glass, J. D. (2013). Axonal degeneration in the peripheral nervous system: implications for the pathogenesis of amyotrophic lateral sclerosis. *Exp. Neurol.* 246, 6–13. doi: 10.1016/j.expneurol.2013.05.001

Flanagan-Steet, H., Fox, M. A., Meyer, D., and Sanes, J. R. (2005). Neuromuscular synapses can form in vivo by incorporation of initially aneural postsynaptic specializations. *Development* 132, 4471–4481. doi: 10.1242/dev.02044

Flanigan, K. M., Ceco, E., Lamar, K. M., Kaminoh, Y., Dunn, D. M., Mendell, J. R., et al. (2013). LTBP4 genotype predicts age of ambulatory loss in Duchenne muscular dystrophy. *Ann. Neurol.* 73, 481–488. doi: 10.1002/ana.23819

Fougerousse, F., Edom-Vovard, F., Merkulova, T., Ott, M. O., Durand, M., Butler-Browne, G., et al. (2001). The muscle-specific enolase is an early marker of human myogenesis. *J. Muscle Res. Cell Motil.* 22, 535–544. doi: 10.1023/A:1015008208007

Fox, J. W., Mayer, U., Nischt, R., Aumailley, M., Reinhardt, D., Wiedemann, H., et al. (1991). Recombinant nidogen consists of three globular domains and mediates binding of laminin to collagen type IV. *EMBO J.* 10, 3137–3146. doi: 10.1002/j.1460-2075.1991.tb04875.x

Francius, C., and Clotman, F. (2014). Generating spinal motor neuron diversity: a long quest for neuronal identity. *Cell. Mol. Life Sci.* 71, 813–829. doi: 10.1007/s00018-013-1398-x

Fu, T., Jiang, L., Peng, Y., Li, Z., Liu, S., Lu, J., et al. (2020). Electrical muscle stimulation accelerates functional recovery after nerve injury. *Neuroscience* 426, 179–188. doi: 10.1016/j.neuroscience.2019.10.052

Fugier, C., Klein, A. F., Hammer, C., Vassilopoulos, S., Ivarsson, Y., Toussaint, A., et al. (2011). Misregulated alternative splicing of BIN1 is associated with T tubule alterations and muscle weakness in myotonic dystrophy. *Nat. Med.* 17, 720–725. doi: 10.1038/nm.2374

Fujimori, K., Ishikawa, M., Otomo, A., Atsuta, N., Nakamura, R., Akiyama, T., et al. (2018). Modeling sporadic ALS in iPSC-derived motor neurons identifies a potential therapeutic agent. *Nat. Med.* 24, 1579–1589. doi: 10.1038/s41591-018-0140-5

Fukuda, T., Roberts, A., Plotz, P. H., and Raben, N. (2007). Acid alpha-glucosidase deficiency (Pompe disease). *Curr. Neurol. Neurosci. Rep.* 7, 71–77. doi: 10.1007/s11910-007-0024-4

Gallardo, E., Martínez-Hernández, E., Titulaer, M. J., Huijbers, M. G., Martínez, M. A., Ramos, A., et al. (2014). Cortactin autoantibodies in myasthenia gravis. *Autoimmun. Rev.* 13, 1003–1007. doi: 10.1016/j.autrev.2014.08.039

Gambetti, P., Dimauro, S., and Baker, L. (1971). Nervous system in Pompe's disease: ultrastructure and biochemistry. *J. Neuropathol. Exp. Neurol.* 30, 412–430. doi: 10.1097/00005072-197107000-00008

Gao, Y., Guo, X., Santostefano, K., Wang, Y., Reid, T., Zeng, D., et al. (2016). Genome therapy of myotonic dystrophy type 1 iPS cells for development of autologous stem cell therapy. *Mol. Ther.* 24, 1378–1387. doi: 10.1038/mt.2016.97

Garriock, R. J., Chalamalasetty, R. B., Kennedy, M. W., Canizales, L. C., Lewandoski, M., and Yamaguchi, T. P. (2015). Lineage tracing of neuromesodermal progenitors reveals novel Wnt-dependent roles in trunk progenitor cell maintenance and differentiation. *Development* 142, 1628–1638. doi: 10.1242/dev.111922

Gaschen, L., Lang, J., Lin, S., Adé-Damilano, M., Busato, A., Lombard, C. W., et al. (1999). Cardiomyopathy in dystrophin-deficient hypertrophic feline muscular dystrophy. *J. Vet. Intern. Med.* 13, 346–356. doi: 10.1111/j.1939-1676.1999.tb02193.x

Gasperi, C., Melms, A., Schoser, B., Zhang, Y., Meltoranta, J., Risson, V., et al. (2014). Anti-agrin autoantibodies in myasthenia gravis. *Neurology* 82, 1976–1983. doi: 10.1212/WNL.0000000000000478

Gatto, F., Rossi, B., Tarallo, A., Polishchuk, E., Polishchuk, R., Carrella, A., et al. (2017). AAV-mediated transcription factor EB (TFEB) gene delivery ameliorates muscle pathology and function in the murine model of Pompe Disease. *Sci. Rep.* 7:15089. doi: 10.1038/s41598-017-15352-2

Gingras, M., Beaulieu, M. M., Gagnon, V., Durham, H. D., and Berthod, F. (2008). In vitro study of axonal migration and myelination of motor neurons in a

three-dimensional tissue-engineered model. *Glia* 56, 354–364. doi: 10.1002/glia.20617

Glass, D. J., Bowen, D. C., Stitt, T. N., Radziejewski, C., Bruno, J., Ryan, T. E., et al. (1996). Agrin acts via a MuSK receptor complex. *Cell* 85, 513–523. doi: 10.1016/S0092-8674(00)81252-0

Gogliotti, R. G., Quinlan, K. A., Barlow, C. B., Heier, C. R., Heckman, C. J., and Didonato, C. J. (2012). Motor neuron rescue in spinal muscular atrophy mice demonstrates that sensory-motor defects are a consequence, not a cause, of motor neuron dysfunction. *J. Neurosci.* 32, 3818–3829. doi: 10.1523/JNEUROSCI.5775-11.2012

Gonzalez, D., Contreras, O., Rebolledo, D. L., Espinoza, J. P., Van Zundert, B., and Brandan, E. (2017). ALS skeletal muscle shows enhanced TGF-β signaling, fibrosis and induction of fibro/adipogenic progenitor markers. *PLoS One* 12:e0177649. doi: 10.1371/journal.pone.0177649

Goudenege, S., Lebel, C., Huot, N. B., Dufour, C., Fujii, I., Gekas, J., et al. (2012). Myoblasts derived from normal hESCs and dystrophic hiPSCs efficiently fuse with existing muscle fibers following transplantation. *Mol. Ther.* 20, 2153–2167. doi: 10.1038/mt.2012.188

Gouti, M., Delile, J., Stamataki, D., Wymeersch, F. J., Huang, Y., Kleinjung, J., et al. (2017). A gene regulatory network balances neural and mesoderm specification during vertebrate trunk development. *Dev. Cell* 41, 243–261.e247. doi: 10.1016/j.devcel.2017.04.002

Grady, R. M., Starr, D. A., Ackerman, G. L., Sanes, J. R., and Han, M. (2005). Syne proteins anchor muscle nuclei at the neuromuscular junction. *Proc. Natl. Acad. Sci. U.S.A.* 102, 4359–4364. doi: 10.1073/pnas.0500711102

Grasman, J. M., and Kaplan, D. L. (2017). Human endothelial cells secrete neurotropic factors to direct axonal growth of peripheral nerves. *Sci. Rep.* 7:4092. doi: 10.1038/s41598-017-04460-8

Gregorevic, P., Blankinship, M. J., Allen, J. M., and Chamberlain, J. S. (2008). Systemic microdystrophin gene delivery improves skeletal muscle structure and function in old dystrophic mdx mice. *Mol. Ther.* 16, 657–664. doi: 10.1038/mt.2008.28

Gu, J.-M., Wang, D. J., Peterson, J. M., Shintaku, J., Liyanarachchi, S., Coppola, V., et al. (2016). An NF-κB-EphrinA5-dependent communication between NG2+ interstitial cells and myoblasts promotes muscle growth in neonates. *Dev. Cell* 36, 215–224. doi: 10.1016/j.devcel.2015.12.018

Güngör, D., Kruijshaar, M. E., Plug, I., D'agostino, R. B., Hagemans, M. L., Van Doorn, P. A., et al. (2013). Impact of enzyme replacement therapy on survival in adults with Pompe disease: results from a prospective international observational study. *Orphanet J. Rare Dis.* 8:49. doi: 10.1186/1750-1172-8-49

Guo, X., Badu-Mensah, A., Thomas, M. C., Mcaleer, C. W., and Hickman, J. J. (2020a). Characterization of functional human skeletal myotubes and neuromuscular junction derived—from the same induced pluripotent stem cell source. *Bioengineering* 7:133. doi: 10.3390/bioengineering7040133

Guo, X., Gonzalez, M., Stancescu, M., Vandenburgh, H. H., and Hickman, J. J. (2011). Neuromuscular junction formation between human stem cell-derived motoneurons and human skeletal muscle in a defined system. *Biomaterials* 32, 9602–9611. doi: 10.1016/j.biomaterials.2011.09.014

Guo, X., Smith, V., Jackson, M., Tran, M., Thomas, M., Patel, A., et al. (2020b). A human-based functional NMJ system for personalized ALS modeling and drug testing. *Adv. Therap.* 3:2000133. doi: 10.1002/adtp.202000133

Ha, J. C., and Richman, D. P. (2015). Myasthenia gravis and related disorders: pathology and molecular pathogenesis. *Biochim. Biophys. Acta (BBA) Mol. Basis Dis.* 1852, 651–657. doi: 10.1016/j.bbadis.2014.11.022

Haastert, K., Grosskreutz, J., Jaeckel, M., Laderer, C., Bufler, J., Grothe, C., et al. (2005). Rat embryonic motoneurons in long-term co-culture with Schwann cells–a system to investigate motoneuron diseases on a cellular level in vitro. *J. Neurosci. Methods* 142, 275–284. doi: 10.1016/j.jneumeth.2004.09.003

Halpern, M., Brennand, K. J., and Gregory, J. (2019). Examining the relationship between astrocyte dysfunction and neurodegeneration in ALS using hiPSCs. *Neurobiol. Dis.* 132:104562. doi: 10.1016/j.nbd.2019.104562

Han, S.-O., Li, S., and Koeberl, D. D. (2016). Salmeterol enhances the cardiac response to gene therapy in Pompe disease. *Mol. Genet. Metab.* 118, 35–40. doi: 10.1016/j.ymgme.2016.03.006

Happe, C. L., Tenerelli, K. P., Gromova, A. K., Kolb, F., and Engler, A. J. (2017). Mechanically patterned neuromuscular junctions-in-a-dish have improved functional maturation. *Mol. Biol. Cell* 28, 1950–1958. doi: 10.1091/mbc.e17-01-0046

Hawes, M. L., Kennedy, W., O'callaghan, M. W., and Thurberg, B. L. (2007). Differential muscular glycogen clearance after enzyme replacement therapy in a mouse model of Pompe disease. *Mol. Genet. Metab.* 91, 343–351. doi: 10.1016/j.ymgme.2007.04.018

Hegedus, J., Putman, C., and Gordon, T. (2007). Time course of preferential motor unit loss in the SOD1G93A mouse model of amyotrophic lateral sclerosis. *Neurobiol. Dis.* 28, 154–164. doi: 10.1016/j.nbd.2007.07.003

Hester, M. E., Murtha, M. J., Song, S., Rao, M., Miranda, C. J., Meyer, K., et al. (2011). Rapid and efficient generation of functional motor neurons from human pluripotent stem cells using gene delivered transcription factor codes. *Mol. Ther.* 19, 1905–1912. doi: 10.1038/mt.2011.135

Heydemann, A., Ceco, E., Lim, J. E., Hadhazy, M., Ryder, P., Moran, J. L., et al. (2009). Latent TGF-beta-binding protein 4 modifies muscular dystrophy in mice. *J. Clin. Invest.* 119, 3703–3712. doi: 10.1172/JCI39845

Hicks, M. R., Hiserodt, J., Paras, K., Fujiwara, W., Eskin, A., Jan, M., et al. (2018). ERBB3 and NGFR mark a distinct skeletal muscle progenitor cell in human development and hPSCs. *Nat. Cell Biol.* 20, 46–57. doi: 10.1038/s41556-017-0010-2

Hinds, S., Bian, W., Dennis, R. G., and Bursac, N. (2011). The role of extracellular matrix composition in structure and function of bioengineered skeletal muscle. *Biomaterials* 32, 3575–3583. doi: 10.1016/j.biomaterials.2011.01.062

Hirata, K., Zhou, C., Nakamura, K., and Kawabuchi, M. (1997). Postnatal development of Schwann cells at neuromuscular junctions, with special reference to synapse elimination. *J. Neurocytol.* 26, 799–809. doi: 10.1023/A:1018570500052

Hobson-Webb, L. D., Dearmey, S., and Kishnani, P. S. (2011). The clinical and electrodiagnostic characteristics of Pompe disease with post-enzyme replacement therapy findings. *Clin. Neurophysiol.* 122, 2312–2317. doi: 10.1016/j.clinph.2011.04.016

Hogarth, M. W., Defour, A., Lazarski, C., Gallardo, E., Manera, J. D., Partridge, T. A., et al. (2019). Fibroadipogenic progenitors are responsible for muscle loss in limb girdle muscular dystrophy 2B. *Nat. Commun.* 10:2430. doi: 10.1038/s41467-019-10438-z

Honkanen, H., Lahti, O., Nissinen, M., Myllyla, R. M., Kangas, S., Paivalainen, S., et al. (2007). Isolation, purification and expansion of myelination-competent, neonatal mouse Schwann cells. *Eur. J. Neurosci.* 26, 953–964. doi: 10.1111/j.1460-9568.2007.05726.x

Hsieh-Li, H. M., Chang, J. G., Jong, Y. J., Wu, M. H., Wang, N. M., Tsai, C. H., et al. (2000). A mouse model for spinal muscular atrophy. *Nat. Genet.* 24, 66–70. doi: 10.1038/71709

Hu, B. Y., and Zhang, S. C. (2009). Differentiation of spinal motor neurons from pluripotent human stem cells. *Nat. Protoc.* 4, 1295–1304. doi: 10.1038/nprot.2009.127

Huang, C.-W., Huang, W.-C., Qiu, X., Da Silva, F. F. F., Wang, A., Patel, S., et al. (2017). The differentiation stage of transplanted stem cells modulates nerve regeneration. *Sci. Rep.* 7:17401. doi: 10.1038/s41598-017-17043-4

Huang, H.-P., Chiang, W., Stone, L., Kang, C.-K., Chuang, C.-Y., and Kuo, H.-C. (2019). Using human Pompe disease-induced pluripotent stem cell-derived neural cells to identify compounds with therapeutic potential. *Hum. Mol. Genet.* 28, 3880–3894. doi: 10.1093/hmg/ddz218

Hudecki, M. S., Pollina, C. M., Granchelli, J. A., Daly, M. K., Byrnes, T., Wang, J. C., et al. (1993). Strength and endurance in the therapeutic evaluation of prednisolone-treated MDX mice. *Res. Commun. Chem. Pathol. Pharmacol.* 79, 45–60.

Huguet, A., Medja, F., Nicole, A., Vignaud, A., Guiraud-Dogan, C., Ferry, A., et al. (2012). Molecular, physiological, and motor performance defects in DMSXL mice carrying> 1,000 CTG repeats from the human DM1 locus. *PLoS Genet.* 8:e1003043. doi: 10.1371/journal.pgen.1003043

Hyung, S., Lee, S. R., Kim, J., Kim, Y., Kim, S., Kim, H. N., et al. (2021). A 3D disease and regeneration model of peripheral nervous system-on-a-chip. *Sci. Adv.* 7:eabd9749. doi: 10.1126/sciadv.abd9749

Hyung, S., Lee, S. R., Kim, Y. J., Bang, S., Tahk, D., Park, J. C., et al. (2019). Optogenetic neuronal stimulation promotes axon outgrowth and myelination of motor neurons in a three-dimensional motor neuron-Schwann cell coculture model on a microfluidic biochip. *Biotechnol. Bioeng* 116, 2425–2438. doi: 10.1002/bit.27083

Hyung, S., Yoon Lee, B., Park, J. C., Kim, J., Hur, E. M., and Francis Suh, J. K. (2015). Coculture of primary motor neurons and schwann cells as a model for in vitro myelination. *Sci. Rep.* 5:15122.

Ihmsen, H., Schmidt, J., Schwilden, H., Schmitt, H. J., and Muenster, T. (2009). Influence of disease progression on the neuromuscular blocking effect of mivacurium in children and adolescents with Duchenne muscular dystrophy. *Anesthesiology* 110, 1016–1019. doi: 10.1097/ALN.0b013e31819daf31

Imbert, N., Cognard, C., Duport, G., Guillou, C., and Raymond, G. (1995). Abnormal calcium homeostasis in Duchenne muscular dystrophy myotubes contracting in vitro. *Cell Calcium* 18, 177–186. doi: 10.1016/0143-4160(95)90062-4

Ionescu, A., Zahavi, E. E., Gradus, T., Ben-Yaakov, K., and Perlson, E. (2016). Compartmental microfluidic system for studying muscle–neuron communication and neuromuscular junction maintenance. *Eur. J. Cell Biol.* 95, 69–88. doi: 10.1016/j.ejcb.2015.11.004

Irioka, T., Watanabe, K., Mizusawa, H., Mizuseki, K., and Sasai, Y. (2005). Distinct effects of caudalizing factors on regional specification of embryonic stem cell-derived neural precursors. *Dev. Brain Res.* 154, 63–70. doi: 10.1016/j.devbrainres.2004.10.004

Jacob, C., Christen, C. N., Pereira, J. A., Somandin, C., Baggiolini, A., Lotscher, P., et al. (2011). HDAC1 and HDAC2 control the transcriptional program of myelination and the survival of Schwann cells. *Nat. Neurosci.* 14, 429–436. doi: 10.1038/nn.2762

Jacobson, C., Cote, P. D., Rossi, S. G., Rotundo, R. L., and Carbonetto, S. (2001). The dystroglycan complex is necessary for stabilization of acetylcholine receptor clusters at neuromuscular junctions and formation of the synaptic basement membrane. *J. Cell Biol.* 152, 435–450. doi: 10.1083/jcb.152.3.435

Jaiswal, M. K. (2019). Riluzole and edaravone: a tale of two amyotrophic lateral sclerosis drugs. *Med. Res. Rev.* 39, 733–748. doi: 10.1002/med.21528

Jansen, G., Groenen, P. J., Bächner, D., Jap, P. H., Coerwinkel, M., Oerlemans, F., et al. (1996). Abnormal myotonic dystrophy protein kinase levels produce only mild myopathy in mice. *Nat. Genet.* 13, 316–324. doi: 10.1038/ng0796-316

Jayam Trouth, A., Dabi, A., Solieman, N., Kurukumbi, M., and Kalyanam, J. (2012). Myasthenia gravis: a review. *Autoimmune Dis.* 2012:874680. doi: 10.1155/2012/874680

Jessell, T. M. (2000). Neuronal specification in the spinal cord: inductive signals and transcriptional codes. *Nat. Rev. Genet.* 1, 20–29. doi: 10.1038/35049541

Jessen, K. R., and Mirsky, R. (1999). Schwann cells and their precursors emerge as major regulators of nerve development. *Trends Neurosci.* 22, 402–410. doi: 10.1016/S0166-2236(98)01391-5

Jessen, K. R., and Mirsky, R. (2005). The origin and development of glial cells in peripheral nerves. *Nat. Rev. Neurosci.* 6, 671–682. doi: 10.1038/nrn1746

Jiwlawat, N., Lynch, E., Jeffrey, J., Van Dyke, J. M., and Suzuki, M. (2018). Current progress and challenges for skeletal muscle differentiation from human pluripotent stem cells using transgene-free approaches. *Stem Cells Int.* 2018:6241681. doi: 10.1155/2018/6241681

Jiwlawat, N., Lynch, E. M., Napiwocki, B. N., Stempien, A., Ashton, R. S., Kamp, T. J., et al. (2019). Micropatterned substrates with physiological stiffness promote cell maturation and Pompe disease phenotype in human induced pluripotent stem cell-derived skeletal myocytes. *Biotechnol. Bioeng.* 116, 2377–2392. doi: 10.1002/bit.27075

Johnson, M. A., Weick, J. P., Pearce, R. A., and Zhang, S. C. (2007). Functional neural development from human embryonic stem cells: accelerated synaptic activity via astrocyte coculture. *J. Neurosci.* 27, 3069–3077. doi: 10.1523/JNEUROSCI.4562-06.2007

Jones, R. A., Harrison, C., Eaton, S. L., Hurtado, M. L., Graham, L. C., Alkhammash, L., et al. (2017). Cellular and molecular anatomy of the human neuromuscular junction. *Cell Rep.* 21, 2348–2356. doi: 10.1016/j.celrep.2017.11.008

Joyce, P. I., Fratta, P., Fisher, E. M., and Acevedo-Arozena, A. (2011). SOD1 and TDP-43 animal models of amyotrophic lateral sclerosis: recent advances in understanding disease toward the development of clinical treatments. *Mamm. Genome* 22, 420–448. doi: 10.1007/s00335-011-9339-1

Juban, G., Saclier, M., Yacoub-Youssef, H., Kernou, A., Arnold, L., Boisson, C., et al. (2018). AMPK activation regulates LTBP4-dependent TGF-β1 secretion by pro-inflammatory macrophages and controls fibrosis in Duchenne muscular dystrophy. *Cell Rep.* 25, 2163–2176.e2166. doi: 10.1016/j.celrep.2018.10.077

Juhas, M., Abutaleb, N., Wang, J. T., Ye, J., Shaikh, Z., Sriworarat, C., et al. (2018). Incorporation of macrophages into engineered skeletal muscle enables enhanced muscle regeneration. *Nat. Biomed. Eng.* 2, 942–954. doi: 10.1038/s41551-018-0290-2

Juhas, M., and Bursac, N. (2014). Roles of adherent myogenic cells and dynamic culture in engineered muscle function and maintenance of satellite cells. *Biomaterials* 35, 9438–9446. doi: 10.1016/j.biomaterials.2014.07.035

Kang, H.-W., Lee, S. J., Ko, I. K., Kengla, C., Yoo, J. J., and Atala, A. (2016). A 3D bioprinting system to produce human-scale tissue constructs with structural integrity. *Nat. Biotechnol.* 34, 312–319. doi: 10.1038/nbt.3413

Kengaku, M., Kawata, A., Kawashima, S., and Nakane, M. (1991). Role of fibronectin in the inhibitory effect of TGF-beta on choline acetyltransferase activity in co-cultures of spinal cord neurons and myotubes. *Brain Res. Dev. Brain Res.* 61, 281–284. doi: 10.1016/0165-3806(91)90144-8

Khan, N., Eliopoulos, H., Han, L., Kinane, T. B., Lowes, L. P., Mendell, J. R., et al. (2019). Eteplirsen treatment attenuates respiratory decline in ambulatory and non-ambulatory patients with duchenne muscular dystrophy. *J. Neuromuscul. Dis.* 6, 213–225. doi: 10.3233/JND-180351

Khodabukus, A. (2021). Tissue-Engineered skeletal muscle models to study muscle function, plasticity, and disease. *Front. Physiol.* 12:619710. doi: 10.3389/fphys.2021.619710

Khodabukus, A., Madden, L., Prabhu, N. K., Koves, T. R., Jackman, C. P., Muoio, D. M., et al. (2019). Electrical stimulation increases hypertrophy and metabolic flux in tissue-engineered human skeletal muscle. *Biomaterials* 198, 259–269. doi: 10.1016/j.biomaterials.2018.08.058

Kim, H.-S., Lee, J., Lee, D. Y., Kim, Y.-D., Kim, J. Y., Lim, H. J., et al. (2017). Schwann cell precursors from human pluripotent stem cells as a potential therapeutic target for myelin repair. *Stem Cell Rep.* 8, 1714–1726. doi: 10.1016/j.stemcr.2017.04.011

Kim, N., and Burden, S. J. (2008). MuSK controls where motor axons grow and form synapses. *Nat. Neurosci.* 11, 19–27. doi: 10.1038/nn2026

Kimura, S., and Nezu, A. (1989). Peripheral nerve involvement in myasthenia gravis. *Brain Dev.* 11, 429–432. doi: 10.1016/S0387-7604(89)80030-0

Kinoshita, I., Nakamura, T., Satoh, A., Matsuo, H., Seto, M., Tomita, I., et al. (1988). Role of the macrophage in the pathogenesis of experimental autoimmune myasthenia gravis. *J. Neurol. Sci.* 87, 49–59. doi: 10.1016/0022-510X(88)90053-6

Kioussi, C., Gross, M. K., and Gruss, P. (1995). Pax3: a paired domain gene as a regulator in PNS myelination. *Neuron* 15, 553–562. doi: 10.1016/0896-6273(95)90144-2

Kishnani, P. S., Corzo, D., Leslie, N. D., Gruskin, D., Van Der Ploeg, A., Clancy, J. P., et al. (2009). Early treatment with alglucosidase alfa prolongs long-term survival of infants with Pompe disease. *Pediatr. Res.* 66, 329–335. doi: 10.1203/PDR.0b013e3181b24e94

Kishnani, P. S., Goldenberg, P. C., Dearmey, S. L., Heller, J., Benjamin, D., Young, S., et al. (2010). Cross-reactive immunologic material status affects treatment outcomes in Pompe disease infants. *Mol. Genet. Metab.* 99, 26–33. doi: 10.1016/j.ymgme.2009.08.003

Kiskinis, E., Sandoe, J., Williams, L. A., Boulting, G. L., Moccia, R., Wainger, B. J., et al. (2014). Pathways disrupted in human ALS motor neurons identified through genetic correction of mutant SOD1. *Cell Stem Cell* 14, 781–795. doi: 10.1016/j.stem.2014.03.004

Ko, C. P., and Robitaille, R. (2015). Perisynaptic schwann cells at the neuromuscular synapse: adaptable, multitasking glial cells. *Cold Spring Harb. Perspect. Biol.* 7:a020503. doi: 10.1101/cshperspect.a020503

Kodaka, Y., Rabu, G., and Asakura, A. (2017). Skeletal muscle cell induction from pluripotent stem cells. *Stem Cells Int.* 2017:1376151. doi: 10.1155/2017/1376151

Kong, J., and Anderson, J. E. (1999). Dystrophin is required for organizing large acetylcholine receptor aggregates. *Brain Res.* 839, 298–304. doi: 10.1016/S0006-8993(99)01737-0

Konieczny, P., Selma-Soriano, E., Rapisarda, A. S., Fernandez-Costa, J. M., Perez-Alonso, M., and Artero, R. (2017). Myotonic dystrophy: candidate small molecule therapeutics. *Drug Discov. Today* 22, 1740–1748. doi: 10.1016/j.drudis.2017.07.011

Kowalski, P. S., Bhattacharya, C., Afewerki, S., and Langer, R. (2018). Smart biomaterials: recent advances and future directions. *ACS Biomater. Sci. Eng.* 4, 3809–3817. doi: 10.1021/acsbiomaterials.8b00889

Kraft, A. D., Resch, J. M., Johnson, D. A., and Johnson, J. A. (2007). Activation of the Nrf2–ARE pathway in muscle and spinal cord during ALS-like pathology in mice expressing mutant SOD1. *Exp. Neurol.* 207, 107–117. doi: 10.1016/j.expneurol.2007.05.026

Kuhlbrodt, K., Herbarth, B., Sock, E., Hermans-Borgmeyer, I., and Wegner, M. (1998). Sox10, a novel transcriptional modulator in glial cells. *J. Neurosci.* 18, 237–250. doi: 10.1523/JNEUROSCI.18-01-00237.1998

Kume, T., Jiang, H., Topczewska, J. M., and Hogan, B. L. (2001). The murine winged helix transcription factors, Foxc1 and Foxc2, are both required for cardiovascular development and somitogenesis. *Genes Dev.* 15, 2470–2482. doi: 10.1101/gad.907301

Kuyumcu-Martinez, N. M., and Cooper, T. A. (2006). Misregulation of alternative splicing causes pathogenesis in myotonic dystrophy. *Altern. Splicing Dis.* 44, 133–159. doi: 10.1007/978-3-540-34449-0_7

Kwon, J. B., Vankara, A., Ettyreddy, A. R., Bohning, J. D., and Gersbach, C. A. (2020). Myogenic progenitor cell lineage specification by CRISPR/Cas9-based transcriptional activators. *Stem Cell Rep.* 14, 755–769. doi: 10.1016/j.stemcr.2020.03.026

Kyriakides, T., Pegoraro, E., Hoffman, E. P., Piva, L., Cagnin, S., Lanfranchi, G., et al. (2011). SPP1 genotype is a determinant of disease severity in Duchenne muscular dystrophy: predicting the severity of Duchenne muscular dystrophy: implications for treatment. *Neurology* 77:1858. author reply 1858-1859 doi: 10.1212/WNL.0b013e318239b9ae

Kyrychenko, V., Kyrychenko, S., Tiburcy, M., Shelton, J. M., Long, C., Schneider, J. W., et al. (2017). Functional correction of dystrophin actin binding domain mutations by genome editing. *JCI Insight* 2:e95918. doi: 10.1172/jci.insight.95918

Landmesser, L. T. (2001). The acquisition of motoneuron subtype identity and motor circuit formation. *Int. J. Dev. Neurosci.* 19, 175–182. doi: 10.1016/S0736-5748(00)00090-3

Larcher, T., Lafoux, A., Tesson, L., Remy, S., Thepenier, V., Francois, V., et al. (2014). Characterization of dystrophin deficient rats: a new model for Duchenne muscular dystrophy. *PLoS One* 9:e110371. doi: 10.1371/journal.pone.0110371

Larkin, L. M., Van Der Meulen, J. H., Dennis, R. G., and Kennedy, J. B. (2006). Functional evaluation of nerve-skeletal muscle constructs engineered in vitro. *In Vitro Cell. Dev. Biol. Anim.* 42, 75–82. doi: 10.1290/0509064.1

Laustriat, D., Gide, J., Barrault, L., Chautard, E., Benoit, C., Auboeuf, D., et al. (2015). In vitro and in vivo modulation of alternative splicing by the biguanide metformin. *Mol. Ther. Nucleic Acids* 4:e262. doi: 10.1038/mtna.2015.35

LaVaute, T. M., Yoo, Y. D., Pankratz, M. T., Weick, J. P., Gerstner, J. R., and Zhang, S. C. (2009). Regulation of neural specification from human embryonic stem cells by BMP and FGF. *Stem Cells* 27, 1741–1749. doi: 10.1002/stem.99

Le, S., Yu, M., Hovan, L., Zhao, Z., Ervasti, J., and Yan, J. (2018). Dystrophin as a molecular shock absorber. *ACS Nano* 12, 12140–12148. doi: 10.1021/acsnano.8b05721

Lee, J. E., and Cooper, T. A. (2009). Pathogenic mechanisms of myotonic dystrophy. *Biochem. Soc. Trans.* 37, 1281–1286. doi: 10.1042/BST0371281

Lee, K.-Z., Qiu, K., Sandhu, M. S., Elmallah, M. K., Falk, D. J., Lane, M. A., et al. (2011). Hypoglossal neuropathology and respiratory activity in pompe mice. *Front. Physiol.* 2:31. doi: 10.3389/fphys.2011.00031

Lee, N.-C., Hwu, W.-L., Muramatsu, S.-I., Falk, D. J., Byrne, B. J., Cheng, C.-H., et al. (2018). A neuron-specific gene therapy relieves motor deficits in Pompe disease mice. *Mol. Neurobiol.* 55, 5299–5309. doi: 10.1007/s12035-017-0763-4

Lee, S., Lee, B., Lee, J. W., and Lee, S. K. (2009). Retinoid signaling and neurogenin2 function are coupled for the specification of spinal motor neurons through a chromatin modifier CBP. *Neuron* 62, 641–654. doi: 10.1016/j.neuron.2009.04.025

Lenzi, J., Pagani, F., De Santis, R., Limatola, C., Bozzoni, I., Di Angelantonio, S., et al. (2016). Differentiation of control and ALS mutant human iPSCs into functional skeletal muscle cells, a tool for the study of neuromuscolar diseases. *Stem Cell Res.* 17, 140–147. doi: 10.1016/j.scr.2016.06.003

Lepper, C., and Fan, C. M. (2010). Inducible lineage tracing of Pax7-descendant cells reveals embryonic origin of adult satellite cells. *Genesis* 48, 424–436. doi: 10.1002/dvg.20630

Li, L., Xiong, W. C., and Mei, L. (2018). Neuromuscular junction formation, aging, and disorders. *Annu. Rev. Physiol.* 80, 159–188. doi: 10.1146/annurev-physiol-022516-034255

Li, W., Brakefield, D., Pan, Y., Hunter, D., Myckatyn, T. M., and Parsadanian, A. (2007). Muscle-derived but not centrally derived transgene GDNF is neuroprotective in G93A-SOD1 mouse model of ALS. *Exp. Neurol.* 203, 457–471. doi: 10.1016/j.expneurol.2006.08.028

Li, X. J., Du, Z. W., Zarnowska, E. D., Pankratz, M., Hansen, L. O., Pearce, R. A., et al. (2005). Specification of motoneurons from human embryonic stem cells. *Nat. Biotechnol.* 23, 215–221. doi: 10.1038/nbt1063

Liewluck, T., and Saperstein, D. S. (2015). Progressive muscular atrophy. *Neurol. Clin.* 33, 761–773. doi: 10.1016/j.ncl.2015.07.005

Lim, J.-A., Li, L., and Raben, N. (2014). Pompe disease: from pathophysiology to therapy and back again. *Front. Aging Neurosci.* 6:177. doi: 10.3389/fnagi.2014.00177

Lin, B., Li, Y., Han, L., Kaplan, A. D., Ao, Y., Kalra, S., et al. (2015). Modeling and study of the mechanism of dilated cardiomyopathy using induced pluripotent stem cells derived from individuals with Duchenne muscular dystrophy. *Dis. Model. Mech.* 8, 457–466. doi: 10.1242/dmm.019505

Lin, C. Y., Yoshida, M., Li, L. T., Ikenaka, A., Oshima, S., Nakagawa, K., et al. (2019). iPSC-derived functional human neuromuscular junctions model the pathophysiology of neuromuscular diseases. *JCI Insight* 4:e124299. doi: 10.1172/jci.insight.124299

Lin, W., Burgess, R. W., Dominguez, B., Pfaff, S. L., Sanes, J. R., and Lee, K. F. (2001). Distinct roles of nerve and muscle in postsynaptic differentiation of the neuromuscular synapse. *Nature* 410, 1057–1064. doi: 10.1038/35074025

Lin, W., Sanchez, H. B., Deerinck, T., Morris, J. K., Ellisman, M., and Lee, K.-F. (2000). Aberrant development of motor axons and neuromuscular synapses in erbB2-deficient mice. *Proc. Natl. Acad. Sci. U.S.A.* 97, 1299–1304. doi: 10.1073/pnas.97.3.1299

Lino, M. M., Schneider, C., and Caroni, P. (2002). Accumulation of SOD1 mutants in postnatal motoneurons does not cause motoneuron pathology or motoneuron disease. *J. Neurosci.* 22, 4825–4832. doi: 10.1523/JNEUROSCI.22-12-04825.2002

Liu, J. P., Laufer, E., and Jessell, T. M. (2001). Assigning the positional identity of spinal motor neurons: rostrocaudal patterning of Hox-c expression by FGFs, Gdf11, and retinoids. *Neuron* 32, 997–1012. doi: 10.1016/S0896-6273(01)00544-X

Liu, Q., Spusta, S. C., Mi, R., Lassiter, R. N., Stark, M. R., Höke, A., et al. (2012). Human neural crest stem cells derived from human ESCs and induced pluripotent stem cells: induction, maintenance, and differentiation into functional schwann cells. *Stem Cells Transl. Med.* 1, 266–278. doi: 10.5966/sctm.2011-0042

Liu, Y., Wong, T. P., Aarts, M., Rooyakkers, A., Liu, L., Lai, T. W., et al. (2007). NMDA receptor subunits have differential roles in mediating excitotoxic neuronal death both in vitro and in vivo. *J. Neurosci.* 27, 2846–2857. doi: 10.1523/JNEUROSCI.0116-07.2007

Loeffler, J. P., Picchiarelli, G., Dupuis, L., and Gonzalez De Aguilar, J. L. (2016). The role of skeletal muscle in amyotrophic lateral sclerosis. *Brain Pathol.* 26, 227–236. doi: 10.1111/bpa.12350

Long, C., Li, H., Tiburcy, M., Rodriguez-Caycedo, C., Kyrychenko, V., Zhou, H., et al. (2018). Correction of diverse muscular dystrophy mutations in human engineered heart muscle by single-site genome editing. *Sci. Adv.* 4:eaa9004. doi: 10.1126/sciadv.aap9004

Luo, B., Tian, L., Chen, N., Ramakrishna, S., Thakor, N., and Yang, I. H. (2018). Electrospun nanofibers facilitate better alignment, differentiation, and long-term culture in an in vitro model of the neuromuscular junction (NMJ). *Biomater. Sci.* 6, 3262–3272. doi: 10.1039/C8BM00720A

Lynch, E., Semrad, T., Belsito, V. S., Fitzgibbons, C., Reilly, M., Hayakawa, K., et al. (2019). C9ORF72-related cellular pathology in skeletal myocytes derived from ALS-patient induced pluripotent stem cells. *Dis. Model. Mech.* 12:dmm039552. doi: 10.1242/dmm.039552

Madaro, L., Passafaro, M., Sala, D., Etxaniz, U., Lugarini, F., Proietti, D., et al. (2018). Denervation-activated STAT3–IL-6 signalling in fibro-adipogenic progenitors promotes myofibres atrophy and fibrosis. *Nat. Cell Biol.* 20, 917–927. doi: 10.1038/s41556-018-0151-y

Madill, M., Mcdonagh, K., Ma, J., Vajda, A., Mcloughlin, P., O'brien, T., et al. (2017). Amyotrophic lateral sclerosis patient iPSC-derived astrocytes impair autophagy via non-cell autonomous mechanisms. *Mol. Brain* 10:22. doi: 10.1186/s13041-017-0300-4

Maffioletti, S. M., Gerli, M. F., Ragazzi, M., Dastidar, S., Benedetti, S., Loperfido, M., et al. (2015). Efficient derivation and inducible differentiation of expandable skeletal myogenic cells from human ES and patient-specific iPS cells. *Nat. Protoc.* 10, 941–958. doi: 10.1038/nprot.2015.057

Maffioletti, S. M., Sarcar, S., Henderson, A. B. H., Mannhardt, I., Pinton, L., Moyle, L. A., et al. (2018). Three-Dimensional human iPSC-Derived artificial skeletal muscles model muscular dystrophies and enable multilineage tissue engineering. *Cell Rep.* 23, 899–908. doi: 10.1016/j.celrep.2018.03.091

Mancall, E. L., Aponte, G. E., and Berry, R. G. (1965). Pompe's disease (diffuse glycogenosis) with neuronal storage. *J. Neuropathol. Exp. Neurol.* 24, 85–96. doi: 10.1097/00005072-196501000-00008

Mankoo, B. S., Skuntz, S., Harrigan, I., Grigorieva, E., Candia, A., Wright, C. V., et al. (2003). The concerted action of Meox homeobox genes is required upstream of genetic pathways essential for the formation, patterning and differentiation of somites. *Development* 130, 4655–4664. doi: 10.1242/dev.00687

Manning, J., and O'Malley, D. (2015). What has the mdx mouse model of Duchenne muscular dystrophy contributed to our understanding of this disease? *J. Muscle Res. Cell Motil.* 36, 155–167. doi: 10.1007/s10974-015-9406-4

Mantegazza, R., Cordiglieri, C., Consonni, A., and Baggi, F. (2016). Animal models of myasthenia gravis: utility and limitations. *Int, J. Gen. Med.* 9:53. doi: 10.2147/IJGM.S88552

Manzano, R., Toivonen, J. M., Calvo, A. C., Oliván, S., Zaragoza, P., Rodellar, C., et al. (2013). Altered in vitro proliferation of mouse SOD1-G93A skeletal muscle satellite cells. *Neurodegener. Dis.* 11, 153–164. doi: 10.1159/000338061

Manzano, R., Toivonen, J. M., Oliván, S., Calvo, A. C., Moreno-Igoa, M., Muñoz, M. J., et al. (2011). Altered expression of myogenic regulatory factors in the mouse model of amyotrophic lateral sclerosis. *Neurodegener. Dis.* 8, 386–396. doi: 10.1159/000324159

Marcuzzo, S., Zucca, I., Mastropietro, A., De Rosbo, N. K., Cavalcante, P., Tartari, S., et al. (2011). Hind limb muscle atrophy precedes cerebral neuronal degeneration in G93A-SOD1 mouse model of amyotrophic lateral sclerosis: a longitudinal MRI study. *Exp. Neurol.* 231, 30–37. doi: 10.1016/j.expneurol.2011.05.007

Mareedu, S., Pachon, R., Thilagavathi, J., Fefelova, N., Balakrishnan, R., Niranjan, N., et al. (2021). Sarcolipin haploinsufficiency prevents dystrophic cardiomyopathy in mdx mice. *Am. J. Physiol. Heart Circ. Physiol.* 320, H200–H210. doi: 10.1152/ajpheart.00601.2020

Marteyn, A., Maury, Y., Gauthier, M. M., Lecuyer, C., Vernet, R., Denis, J. A., et al. (2011). Mutant human embryonic stem cells reveal neurite and synapse formation defects in type 1 myotonic dystrophy. *Cell Stem Cell* 8, 434–444. doi: 10.1016/j.stem.2011.02.004

Martin, J., De Barsy, T., Van Hoof, F., and Palladini, G. (1973). Pompe's disease: an inborn lysosomal disorder with storage of glycogen. *Acta Neuropathol.* 23, 229–244. doi: 10.1007/BF00687878

Martin, N. R., Passey, S. L., Player, D. J., Mudera, V., Baar, K., Greensmith, L., et al. (2015). Neuromuscular junction formation in tissue-engineered skeletal muscle augments contractile function and improves cytoskeletal organization. *Tissue Eng. Part A* 21, 2595–2604. doi: 10.1089/ten.tea.2015.0146

Martineau, É, Arbour, D., Vallée, J., and Robitaille, R. (2020). Properties of Glial Cell at the Neuromuscular Junction are Incompatible with synaptic repair in the SOD1G37R ALS mouse model. *J. Neurosci.* 40, 7759–7777. doi: 10.1523/JNEUROSCI.1748-18.2020

Martineau, L., Racine, V., Benichou, S. A., and Puymirat, J. (2018). Lymphoblastoids cell lines–Derived iPSC line from a 26-year-old myotonic dystrophy type 1 patient carrying (CTG) 200 expansion in the DMPK gene: CHUQi001-A. *Stem Cell Res.* 26, 103–106. doi: 10.1016/j.scr.2017.12.010

Martini, C., Ciana, G., Benettoni, A., Katouzian, F., Severini, G., Bussani, R., et al. (2001). Intractable fever and cortical neuronal glycogen storage in glycogenosis type 2. *Neurology* 57, 906–908. doi: 10.1212/WNL.57.5.906

Martins, J.-M. F., Fischer, C., Urzi, A., Vidal, R., Kunz, S., Ruffault, P.-L., et al. (2020). Self-organizing 3D human trunk neuromuscular organoids. *Cell Stem Cell* 26, 172–186.e176. doi: 10.1016/j.stem.2019.12.007

Matloka, M., Klein, A. F., Rau, F., and Furling, D. (2018). Cells of matter—in vitro models for myotonic dystrophy. *Front. Neurol.* 9:361. doi: 10.3389/fneur.2018.00361

Maurer, M., Bougoin, S., Feferman, T., Frenkian, M., Bismuth, J., Mouly, V., et al. (2015). IL-6 and Akt are involved in muscular pathogenesis in myasthenia gravis. *Acta Neuropathol. Commun.* 3, 1–14. doi: 10.1186/s40478-014-0179-6

Maury, Y., Come, J., Piskorowski, R. A., Salah-Mohellibi, N., Chevaleyre, V., Peschanski, M., et al. (2015). Combinatorial analysis of developmental cues efficiently converts human pluripotent stem cells into multiple neuronal subtypes. *Nat. Biotechnol.* 33, 89–96. doi: 10.1038/nbt.3049

Mazaleyrat, K., Badja, C., Broucqsault, N., Chevalier, R., Laberthonniere, C., Dion, C., et al. (2020). Multilineage differentiation for formation of innervated skeletal muscle fibers from healthy and diseased human pluripotent stem cells. *Cells* 9:1531. doi: 10.3390/cells9061531

Meola, G., and Cardani, R. (2015). Myotonic dystrophy type 2: an update on clinical aspects, genetic and pathomolecular mechanism. *J. Neuromuscul. Dis.* 2, S59–S71. doi: 10.3233/JND-150088

Messeant, J., Ezan, J., Delers, P., Glebov, K., Marchiol, C., Lager, F., et al. (2017). Wnt proteins contribute to neuromuscular junction formation through distinct signaling pathways. *Development* 144, 1712–1724. doi: 10.1242/dev.146167

Miller, J. D., Ganat, Y. M., Kishinevsky, S., Bowman, R. L., Liu, B., Tu, E. Y., et al. (2013). Human iPSC-based modeling of late-onset disease via progerin-induced aging. *Cell Stem Cell* 13, 691–705. doi: 10.1016/j.stem.2013.11.006

Min, Y. L., Li, H., Rodriguez-Caycedo, C., Mireault, A. A., Huang, J., Shelton, J. M., et al. (2019). CRISPR-Cas9 corrects Duchenne muscular dystrophy exon 44 deletion mutations in mice and human cells. *Sci. Adv.* 5:eaav4324. doi: 10.1126/sciadv.aav4324

Moloney, E. B., De Winter, F., and Verhaagen, J. (2014). ALS as a distal axonopathy: molecular mechanisms affecting neuromuscular junction stability in the presymptomatic stages of the disease. *Front. Neurosci.* 8:252. doi: 10.3389/fnins.2014.00252

Moore, T. M., Lin, A. J., Strumwasser, A. R., Cory, K., Whitney, K., Ho, T., et al. (2020). Mitochondrial dysfunction is an early consequence of partial or complete dystrophin loss in mdx mice. *Front. Physiol.* 11:690. doi: 10.21203/rs.2.23961/v1

Morimoto, Y., Kato-Negishi, M., Onoe, H., and Takeuchi, S. (2013). Three-dimensional neuron-muscle constructs with neuromuscular junctions. *Biomaterials* 34, 9413–9419. doi: 10.1016/j.biomaterials.2013.08.062

Mourkioti, F., Kustan, J., Kraft, P., Day, J. W., Zhao, M. M., Kost-Alimova, M., et al. (2013). Role of telomere dysfunction in cardiac failure in Duchenne muscular dystrophy. *Nat. Cell Biol.* 15, 895–904. doi: 10.1038/ncb2790

Muhr, J., Graziano, E., Wilson, S., Jessell, T. M., and Edlund, T. (1999). Convergent inductive signals specify midbrain, hindbrain, and spinal cord identity in gastrula stage chick embryos. *Neuron* 23, 689–702. doi: 10.1016/S0896-6273(01)80028-3

Mukherjee-Clavin, B., Mi, R., Kern, B., Choi, I. Y., Lim, H., Oh, Y., et al. (2019). Comparison of three congruent patient-specific cell types for the modelling of a human genetic Schwann-cell disorder. *Nat. Biomed. Eng.* 3, 571–582. doi: 10.1038/s41551-019-0381-8

Muller, C. W., Jones, H. N., O'grady, G., Suarez, A., Heller, J. H., and Kishnani, P. S. (2009). Language and speech function in children with infantile Pompe disease. *J. Pediatr. Neurol.* 7, 147–156.

Muller, D., Cherukuri, P., Henningfeld, K., Poh, C. H., Wittler, L., Grote, P., et al. (2014). Dlk1 promotes a fast motor neuron biophysical signature required for peak force execution. *Science* 343, 1264–1266. doi: 10.1126/science.1246448

Muller, Q., Beaudet, M.-J., De Serres-Bérard, T., Bellenfant, S., Flacher, V., and Berthod, F. (2018). Development of an innervated tissue-engineered skin with human sensory neurons and Schwann cells differentiated from iPS cells. *Acta Biomater.* 82, 93–101. doi: 10.1016/j.actbio.2018.10.011

Nacu, A., Andersen, J. B., Lisnic, V., Owe, J. F., and Gilhus, N. E. (2015). Complicating autoimmune diseases in myasthenia gravis: a review. *Autoimmunity* 48, 362–368. doi: 10.3109/08916934.2015.1030614

Nagai, M., Re, D. B., Nagata, T., Chalazonitis, A., Jessell, T. M., Wichterle, H., et al. (2007). Astrocytes expressing ALS-linked mutated SOD1 release factors selectively toxic to motor neurons. *Nat. Neurosci.* 10, 615–622. doi: 10.1038/nn1876

Nagao, M., Kato, S., Hayashi, H., and Misawa, H. (2003). Hyperproliferation of synapses on spinal motor neurons of Duchenne muscular dystrophy and myotonic dystrophy patients. *Acta Neuropathol.* 106, 557–560. doi: 10.1007/s00401-003-0759-1

Nakamori, M., Hamanaka, K., Thomas, J. D., Wang, E. T., Hayashi, Y. K., Takahashi, M. P., et al. (2017). Aberrant myokine signaling in congenital myotonic dystrophy. *Cell Rep.* 21, 1240–1252. doi: 10.1016/j.celrep.2017.10.018

Nakamori, M., Kimura, T., Fujimura, H., Takahashi, M. P., and Sakoda, S. (2007). Altered mRNA splicing of dystrophin in type 1 myotonic dystrophy. *Muscle Nerve* 36, 251–257. doi: 10.1002/mus.20809

Nakata, M., Kuwabara, S., Kanai, K., Misawa, S., Tamura, N., Sawai, S., et al. (2006). Distal excitability changes in motor axons in amyotrophic lateral sclerosis. *Clin. Neurophysiol.* 117, 1444–1448. doi: 10.1016/j.clinph.2006.04.005

Nalbandian, M., Zhao, M., Sasaki-Honda, M., Jonouchi, T., Lucena-Cacace, A., Mizusawa, T., et al. (2021). Characterization of hiPSC-derived muscle progenitors reveals distinctive markers for myogenic cell purification toward cell therapy. *Stem Cell Rep.* 16, 883–898. doi: 10.1016/j.stemcr.2021.03.004

Narayanan, N., Lengemann, P., Kim, K. H., Kuang, L., Sobreira, T., Hedrick, V., et al. (2021). Harnessing nerve–muscle cell interactions for biomaterials-based skeletal muscle regeneration. *J. Biomed. Mater. Res. Part A* 109, 289–299. doi: 10.1002/jbm.a.37022

Nascimbeni, A. C., Fanin, M., Masiero, E., Angelini, C., and Sandri, M. (2012). The role of autophagy in the pathogenesis of glycogen storage disease type II (GSDII). *Cell Death Differ.* 19, 1698–1708. doi: 10.1038/cdd.2012.52

Nascimbeni, A. C., Fanin, M., Tasca, E., Angelini, C., and Sandri, M. (2015). Impaired autophagy affects acid α−glucosidase processing and enzyme replacement therapy efficacy in late-onset glycogen storage disease type II. *Neuropathol. Appl. Neurobiol.* 41, 672–675. doi: 10.1111/nan.12214

Nayak, P., Colas, A., Mercola, M., Varghese, S., and Subramaniam, S. (2021). Temporal mechanisms of myogenic specification in human induced pluripotent stem cells. *Sci. Adv.* 7:eabf7412. doi: 10.1126/sciadv.abf7412

Nesmith, A. P., Wagner, M. A., Pasqualini, F. S., O'connor, B. B., Pincus, M. J., August, P. R., et al. (2016). A human in vitro model of Duchenne muscular dystrophy muscle formation and contractility. *J. Cell Biol.* 215, 47–56. doi: 10.1083/jcb.201603111

Newbern, J., and Birchmeier, C. (2010). Nrg1/ErbB signaling networks in Schwann cell development and myelination. *Semin. Cell Dev. Biol.* 21, 922–928. doi: 10.1016/j.semcdb.2010.08.008

Newcomer, J. W., Farber, N. B., and Olney, J. W. (2000). NMDA receptor function, memory, and brain aging. *Dialogues Clin. Neurosci.* 2:219. doi: 10.31887/DCNS.2000.2.3/jnewcomer

Nghiem, P. P., and Kornegay, J. N. (2019). Gene therapies in canine models for Duchenne muscular dystrophy. *Hum. Genet.* 138, 483–489. doi: 10.1007/s00439-019-01976-z

Nicolopoulos-Stournaras, S., and Iles, J. F. (1983). Motor neuron columns in the lumbar spinal cord of the rat. *J. Comp. Neurol.* 217, 75–85. doi: 10.1002/cne.902170107

Nordstrom, U., Jessell, T. M., and Edlund, T. (2002). Progressive induction of caudal neural character by graded Wnt signaling. *Nat. Neurosci.* 5, 525–532. doi: 10.1038/nn0602-854

Novak, R., Ingram, M., Marquez, S., Das, D., Delahanty, A., Herland, A., et al. (2020). Robotic fluidic coupling and interrogation of multiple vascularized organ chips. *Nat. Biomed. Eng.* 4, 407–420.

Nowotschin, S., Ferrer-Vaquer, A., Concepcion, D., Papaioannou, V. E., and Hadjantonakis, A.-K. (2012). Interaction of Wnt3a, Msgn1 and Tbx6 in neural versus paraxial mesoderm lineage commitment and paraxial mesoderm differentiation in the mouse embryo. *Dev. Biol.* 367, 1–14. doi: 10.1016/j.ydbio.2012.04.012

Oberheim, N. A., Takano, T., Han, X., He, W., Lin, J. H., Wang, F., et al. (2009). Uniquely hominid features of adult human astrocytes. *J. Neurosci.* 29, 3276–3287. doi: 10.1523/JNEUROSCI.4707-08.2009

Osaki, T., Uzel, S. G., and Kamm, R. D. (2018). Microphysiological 3D model of amyotrophic lateral sclerosis (ALS) from human iPS-derived muscle cells and optogenetic motor neurons. *Sci. Adv.* 4:eaat5847. doi: 10.1126/sciadv.aat5847

Oskarsson, B., Gendron, T. F., and Staff, N. P. (2018). Amyotrophic lateral sclerosis: an update for 2018. *Mayo Clin. Proc.* 93, 1617–1628. doi: 10.1016/j.mayocp.2018.04.007

Ott, M.-O., Bober, E., Lyons, G., Arnold, H., and Buckingham, M. (1991). Early expression of the myogenic regulatory gene, myf-5, in precursor cells of skeletal muscle in the mouse embryo. *Development* 111, 1097–1107. doi: 10.1242/dev.111.4.1097

Ozair, M. Z., Kintner, C., and Brivanlou, A. H. (2013). Neural induction and early patterning in vertebrates. *Wiley Interdiscip. Rev. Dev. Biol.* 2, 479–498. doi: 10.1002/wdev.90

Paivalainen, S., Nissinen, M., Honkanen, H., Lahti, O., Kangas, S. M., Peltonen, J., et al. (2008). Myelination in mouse dorsal root ganglion/Schwann cell cocultures. *Mol. Cell. Neurosci.* 37, 568–578. doi: 10.1016/j.mcn.2007.12.005

Panaite, P.-A., Gantelet, E., Kraftsik, R., Gourdon, G., Kuntzer, T., and Barakat-Walter, I. (2008). Myotonic dystrophy transgenic mice exhibit pathologic abnormalities in diaphragm neuromuscular junctions and phrenic nerves. *J. Neuropathol. Exp. Neurol.* 67, 763–772. doi: 10.1097/NEN.0b013e318180ec64

Panaite, P.-A., Kielar, M., Kraftsik, R., Gourdon, G., Kuntzer, T., and Barakat-Walter, I. (2011). Peripheral neuropathy is linked to a severe form of myotonic dystrophy in transgenic mice. *J. Neuropathol. Exp. Neurol.* 70, 678–685. doi: 10.1097/NEN.0b013e3182260939

Paredes-Redondo, A., Harley, P., Maniati, E., Ryan, D., Louzada, S., Meng, J., et al. (2021). Optogenetic modeling of human neuromuscular circuits in Duchenne muscular dystrophy with CRISPR and pharmacological corrections. *Sci. Adv.* 7:eabi8787. doi: 10.1126/sciadv.abi8787

Park, H. S., Liu, S., Mcdonald, J., Thakor, N., and Yang, I. H. (2013). "Neuromuscular junction in a microfluidic device," in *Proceedings of the 2013 35th Annual International Conference of the IEEE Engineering in Medicine and Biology Society (EMBC)*, (Piscataway, NJ: IEEE), 2833–2835.

Park, K. H., and Vincent, I. (2008). Presymptomatic biochemical changes in hindlimb muscle of G93A human Cu/Zn superoxide dismutase 1 transgenic mouse model of amyotrophic lateral sclerosis. *Biochim. Biophys. Acta (BBA) Mol. Basis Dis.* 1782, 462–468. doi: 10.1016/j.bbadis.2008.04.001

Pascual-Gilabert, M., López-Castel, A., and Artero, R. (2021). Myotonic dystrophy type 1 drug development: a pipeline toward the market. *Drug Discov. Today* 26, 1765–1772. doi: 10.1016/j.drudis.2021.03.024

Patel, A. M., Wierda, K., Thorrez, L., Van Putten, M., De Smedt, J., Ribeiro, L., et al. (2019). Dystrophin deficiency leads to dysfunctional glutamate clearance in iPSC derived astrocytes. *Transl. Psychiatry* 9:200. doi: 10.1038/s41398-019-0535-1

Patrick, J., and Lindstrom, J. (1973). Autoimmune response to acetylcholine receptor. *Science* 180, 871–872. doi: 10.1126/science.180.4088.871

Peric, S., Stojanovic, V. R., Nikolic, A., Kacar, A., Basta, I., Pavlovic, S., et al. (2013). Peripheral neuropathy in patients with myotonic dystrophy type 1. *Neurol. Res.* 35, 331–335. doi: 10.1179/1743132812Y.0000000144

Personius, K. E., and Sawyer, R. P. (2005). Terminal Schwann cell structure is altered in diaphragm of mdx mice. *Muscle Nerve* 32, 656–663. doi: 10.1002/mus.20405

Petrany, M. J., Swoboda, C. O., Sun, C., Chetal, K., Chen, X., Weirauch, M. T., et al. (2020). Single-nucleus RNA-seq identifies transcriptional heterogeneity in multinucleated skeletal myofibers. *Nat. Commun.* 11:6374. doi: 10.1038/s41467-020-20063-w

Philips, A. V., Timchenko, L. T., and Cooper, T. A. (1998). Disruption of splicing regulated by a CUG-binding protein in myotonic dystrophy. *Science* 280, 737–741. doi: 10.1126/science.280.5364.737

Pickar-Oliver, A., Gough, V., Bohning, J. D., Liu, S., Robinson-Hamm, J. N., Daniels, H., et al. (2021). Full-length dystrophin restoration via targeted genomic integration by aav-crispr in a humanized mouse model of duchenne muscular dystrophy. *Mol. Ther.* (in press). doi: 10.1016/j.ymthe.2021.09.003

Pollari, E., Goldsteins, G., Bart, G., Koistinaho, J., and Giniatullin, R. (2014). The role of oxidative stress in degeneration of the neuromuscular junction in amyotrophic lateral sclerosis. *Front. Cell. Neurosci.* 8:131. doi: 10.3389/fncel.2014.00131

Poulin, H., Mercier, A., Djemai, M., Pouliot, V., Deschenes, I., Boutjdir, M., et al. (2021). iPSC-derived cardiomyocytes from patients with myotonic dystrophy type 1 have abnormal ion channel functions and slower conduction velocities. *Sci. Rep.* 11:2500. doi: 10.1038/s41598-021-82007-8

Pourquié, O., Al Tanoury, Z., and Chal, J. (2018). "Chapter Five – the long road to making muscle in vitro," in *Current Topics in Developmental Biology*, ed. A. H. Brivanlou (Cambridge, MA: Academic Press), 123–142. doi: 10.1016/bs.ctdb.2018.03.003

Powell, C. A., Smiley, B. L., Mills, J., and Vandenburgh, H. H. (2002). Mechanical stimulation improves tissue-engineered human skeletal muscle. *Am. J. Physiol. Cell Physiol.* 283, C1557–C1565. doi: 10.1152/ajpcell.00595.2001

Prater, S. N., Banugaria, S. G., Dearmey, S. M., Botha, E. G., Stege, E. M., Case, L. E., et al. (2012). The emerging phenotype of long-term survivors with infantile Pompe disease. *Genet. Med.* 14, 800–810. doi: 10.1038/gim.2012.44

Prater, S. N., Patel, T. T., Buckley, A. F., Mandel, H., Vlodavski, E., Banugaria, S. G., et al. (2013). Skeletal muscle pathology of infantile Pompe disease during long-term enzyme replacement therapy. *Orphanet J. Rare Dis.* 8:90. doi: 10.1186/1750-1172-8-90

Pratt, S. J., Shah, S. B., Ward, C. W., Inacio, M. P., Stains, J. P., and Lovering, R. M. (2013). Effects of in vivo injury on the neuromuscular junction in healthy and dystrophic muscles. *J. Physiol.* 591, 559–570. doi: 10.1113/jphysiol.2012.241679

Pratt, S. J., Shah, S. B., Ward, C. W., Kerr, J. P., Stains, J. P., and Lovering, R. M. (2015a). Recovery of altered neuromuscular junction morphology and muscle function in mdx mice after injury. *Cell. Mol. Life Sci.* 72, 153–164. doi: 10.1007/s00018-014-1663-7

Pratt, S. J., Valencia, A. P., Le, G. K., Shah, S. B., and Lovering, R. M. (2015b). Pre- and postsynaptic changes in the neuromuscular junction in dystrophic mice. *Front. Physiol.* 6:252. doi: 10.3389/fphys.2015.00252

Priez, A., Duchene, J., and Goubel, F. (1992). Duchenne muscular dystrophy quantification: a multivariate analysis of surface EMG. *Med. Biol. Eng. Comput.* 30, 283–291. doi: 10.1007/BF02446966

Prinz, M., and Priller, J. (2017). The role of peripheral immune cells in the CNS in steady state and disease. *Nat. Neurosci.* 20, 136–144. doi: 10.1038/nn.4475

Raben, N., Lu, N., Nagaraju, K., Rivera, Y., Lee, A., Yan, B., et al. (2001). Conditional tissue-specific expression of the acid α-glucosidase (GAA) gene in the GAA knockout mice: implications for therapy. *Hum. Mol. Genet.* 10, 2039–2047. doi: 10.1093/hmg/10.19.2039

Raben, N., Ralston, E., Chien, Y.-H., Baum, R., Schreiner, C., Hwu, W.-L., et al. (2010). Differences in the predominance of lysosomal and autophagic pathologies between infants and adults with Pompe disease: implications for therapy. *Mol. Genet. Metab.* 101, 324–331. doi: 10.1016/j.ymgme.2010.08.001

Rao, L., Qian, Y., Khodabukus, A., Ribar, T., and Bursac, N. (2018). Engineering human pluripotent stem cells into a functional skeletal muscle tissue. *Nat. Commun.* 9:126. doi: 10.1038/s41467-017-02636-4

Rastall, D., Seregin, S., Aldhamen, Y., Kaiser, L., Mullins, C., Liou, A., et al. (2016). Long-term, high-level hepatic secretion of acid α-glucosidase for Pompe disease achieved in non-human primates using helper-dependent adenovirus. *Gene Ther.* 23, 743–752. doi: 10.1038/gt.2016.53

Ravanelli, A. M., and Appel, B. (2015). Motor neurons and oligodendrocytes arise from distinct cell lineages by progenitor recruitment. *Genes Dev.* 29, 2504–2515. doi: 10.1101/gad.271312.115

Ravel-Chapuis, A., Bélanger, G., Yadava, R. S., Mahadevan, M. S., Desgroseillers, L., Côté, J., et al. (2012). The RNA-binding protein Staufen1 is increased in DM1 skeletal muscle and promotes alternative pre-mRNA splicing. *J. Cell Biol.* 196, 699–712. doi: 10.1083/jcb.201108113

Reddy, L. V., Koirala, S., Sugiura, Y., Herrera, A. A., and Ko, C.-P. (2003). Glial cells maintain synaptic structure and function and promote development of the neuromuscular junction in vivo. *Neuron* 40, 563–580. doi: 10.1016/S0896-6273(03)00682-2

Renna, L. V., Bosè, F., Iachettini, S., Fossati, B., Saraceno, L., Milani, V., et al. (2017). Receptor and post-receptor abnormalities contribute to insulin resistance in myotonic dystrophy type 1 and type 2 skeletal muscle. *PLoS One* 12:e0184987. doi: 10.1371/journal.pone.0184987

Reuser, A. J., Kroos, M. A., Hermans, M. M., Bijvoet, A. G., Verbeet, M., Van Diggelen, O. A., et al. (1995). Glycogenosis type II (acid maltase deficiency). *Muscle Nerve* 18, S61–S69. doi: 10.1002/mus.880181414

Ricotti, V., Mandy, W. P., Scoto, M., Pane, M., Deconinck, N., Messina, S., et al. (2016). Neurodevelopmental, emotional, and behavioural problems in Duchenne muscular dystrophy in relation to underlying dystrophin gene mutations. *Dev. Med. Child Neurol.* 58, 77–84. doi: 10.1111/dmcn.12922

Riethmacher, D., Sonnenberg-Riethmacher, E., Brinkmann, V., Yamaai, T., Lewin, G. R., and Birchmeier, C. (1997). Severe neuropathies in mice with targeted mutations in the ErbB3 receptor. *Nature* 389, 725–730. doi: 10.1038/39593

Rimington, R. P., Fleming, J. W., Capel, A. J., Wheeler, P. C., and Lewis, M. P. (2021). Bioengineered model of the human motor unit with physiologically functional neuromuscular junctions. *Sci. Rep.* 11:11695. doi: 10.1038/s41598-021-91203-5

Rizzuto, E., Pisu, S., Nicoletti, C., Del Prete, Z., and Musarò, A. (2017). Measuring neuromuscular junction functionality. *JoVE J. Vis. Exp.* 2017:e55227. doi: 10.3791/55227

Rocha, M. C., Pousinha, P. A., Correia, A. M., Sebastião, A. M., and Ribeiro, J. A. (2013). Early changes of neuromuscular transmission in the SOD1 (G93A) mice model of ALS start long before motor symptoms onset. *PLoS One* 8:e73846. doi: 10.1371/journal.pone.0073846

Rogers, R. S., and Nishimune, H. (2017). The role of laminins in the organization and function of neuromuscular junctions. *Matrix Biol.* 57-58, 86–105. doi: 10.1016/j.matbio.2016.08.008

Ross, C. A., and Poirier, M. A. (2004). Protein aggregation and neurodegenerative disease. *Nat. Med.* 10, S10–S17. doi: 10.1038/nm1066

Rothstein, J. D. (1995). Excitotoxicity and neurodegeneration in amyotrophic lateral sclerosis. *Clin. Neurosci. (New York, NY)* 3, 348–359.

Ruggieri, S., Viggiano, L., Annese, T., Rubolino, C., Gerbino, A., De Zio, R., et al. (2019). DP71 and SERCA2 alteration in human neurons of a Duchenne muscular dystrophy patient. *Stem Cell Res. Ther.* 10:29. doi: 10.1186/s13287-018-1125-5

Rybalka, E., Timpani, C. A., Debruin, D. A., Bagaric, R. M., Campelj, D. G., and Hayes, A. (2020). The failed clinical story of myostatin inhibitors against Duchenne Muscular Dystrophy: Exploring the biology behind the battle. *Cells* 9:2657. doi: 10.3390/cells9122657

Sacco, A., Mourkioti, F., Tran, R., Choi, J., Llewellyn, M., Kraft, P., et al. (2010). Short telomeres and stem cell exhaustion model Duchenne muscular dystrophy in mdx/mTR mice. *Cell* 143, 1059–1071. doi: 10.1016/j.cell.2010.11.039

Sakai, Y., Meno, C., Fujii, H., Nishino, J., Shiratori, H., Saijoh, Y., et al. (2001). The retinoic acid-inactivating enzyme CYP26 is essential for establishing an uneven distribution of retinoic acid along the anterio-posterior axis within the mouse embryo. *Genes Dev.* 15, 213–225. doi: 10.1101/gad.851501

Sanchez-Gurmaches, J., and Guertin, D. A. (2014). Adipocytes arise from multiple lineages that are heterogeneously and dynamically distributed. *Nat. Commun.* 5:4099. doi: 10.1038/ncomms5099

Santhanam, N., Kumanchik, L., Guo, X., Sommerhage, F., Cai, Y., Jackson, M., et al. (2018). Stem cell derived phenotypic human neuromuscular junction model for dose response evaluation of therapeutics. *Biomaterials* 166, 64–78. doi: 10.1016/j.biomaterials.2018.02.047

Sato, Y., Kobayashi, H., Higuchi, T., Shimada, Y., Ida, H., and Ohashi, T. (2016). TFEB overexpression promotes glycogen clearance of Pompe disease iPSC-derived skeletal muscle. *Mol. Ther. Methods Clin. Dev.* 3:16054. doi: 10.1038/mtm.2016.54

Sawada, M., Matsumoto, M., and Sawamoto, K. (2014). Vascular regulation of adult neurogenesis under physiological and pathological conditions. *Front. Neurosci.* 8:53. doi: 10.3389/fnins.2014.00053

Scaramozza, A., Marchese, V., Papa, V., Salaroli, R., Soraru, G., Angelini, C., et al. (2014). Skeletal muscle satellite cells in amyotrophic lateral sclerosis. *Ultrastruct. Pathol.* 38, 295–302. doi: 10.3109/01913123.2014.937842

Selsby, J. T., Ross, J. W., Nonneman, D., and Hollinger, K. (2015). Porcine models of muscular dystrophy. *ILAR J.* 56, 116–126. doi: 10.1093/ilar/ilv015

Selvaraj, S., Mondragon-Gonzalez, R., Xu, B., Magli, A., Kim, H., Laine, J., et al. (2019). Screening identifies small molecules that enhance the maturation of human pluripotent stem cell-derived myotubes. *Elife* 8:e47970. doi: 10.7554/eLife.47970.030

Shah, N. M., Marchionni, M. A., Isaacs, I., Stroobant, P., and Anderson, D. J. (1994). Glial growth factor restricts mammalian neural crest stem cells to a glial fate. *Cell* 77, 349–360. doi: 10.1016/0092-8674(94)90150-3

Shi, Y., Lin, S., Staats, K. A., Li, Y., Chang, W.-H., Hung, S.-T., et al. (2018). Haploinsufficiency leads to neurodegeneration in C9ORF72 ALS/FTD human induced motor neurons. *Nat. Med.* 24:313. doi: 10.1038/nm.4490

Shields, M. C., Bowers, M. R., Fulcer, M. M., Bollig, M. K., Rock, P. J., Sutton, B. R., et al. (2017). *Drosophila* studies support a role for a presynaptic synaptotagmin mutation in a human congenital myasthenic syndrome. *PLoS One* 12:e0184817. doi: 10.1371/journal.pone.0184817

Sicot, G., Servais, L., Dinca, D. M., Leroy, A., Prigogine, C., Medja, F., et al. (2017). Downregulation of the glial GLT1 glutamate transporter and Purkinje cell dysfunction in a mouse model of myotonic dystrophy. *Cell Rep.* 19, 2718–2729. doi: 10.1016/j.celrep.2017.06.006

Sigoillot, S. M., Bourgeois, F., Karmouch, J., Molgo, J., Dobbertin, A., Chevalier, C., et al. (2016). Neuromuscular junction immaturity and muscle atrophy are

hallmarks of the ColQ-deficient mouse, a model of congenital myasthenic syndrome with acetylcholinesterase deficiency. *FASEB J.* 30, 2382–2399. doi: 10.1096/fj.201500162

Singh, T., and Vazquez, M. (2019). Time-dependent addition of neuronal and Schwann cells increase myotube viability and length in an in vitro tri-culture model of the neuromuscular junction. *Regener. Eng. Transl. Med.* 5, 402–413. doi: 10.1007/s40883-019-00095-5

Skardal, A., Murphy, S. V., Devarasetty, M., Mead, I., Kang, H.-W., Seol, Y.-J., et al. (2017). Multi-tissue interactions in an integrated three-tissue organ-on-a-chip platform. *Sci. Rep.* 7:8837. doi: 10.1038/s41598-017-08879-x

Skoglund, G., Laine, J., Darabi, R., Fournier, E., Perlingeiro, R., and Tabti, N. (2014). Physiological and ultrastructural features of human induced pluripotent and embryonic stem cell-derived skeletal myocytes in vitro. *Proc. Natl. Acad. Sci. U.S.A.* 111, 8275–8280. doi: 10.1073/pnas.1322258111

Sleigh, J., and Sattelle, D. (2010). C. elegans models of neuromuscular diseases expedite translational research. *Transl. Neurosci.* 1, 214–227. doi: 10.2478/v10134-010-0032-9

Smith, A., Long, C., Pirozzi, K., and Hickman, J. (2013). A functional system for high-content screening of neuromuscular junctions in vitro. *Technology* 1, 37–48. doi: 10.1142/S2339547813500015

Son, E. Y., Ichida, J. K., Wainger, B. J., Toma, J. S., Rafuse, V. F., Woolf, C. J., et al. (2011). Conversion of mouse and human fibroblasts into functional spinal motor neurons. *Cell Stem Cell* 9, 205–218. doi: 10.1016/j.stem.2011.07.014

Son, Y.-J., Trachtenberg, J. T., and Thompson, W. J. (1996). Schwann cells induce and guide sprouting and reinnervation of neuromuscular junctions. *Trends Neurosci.* 19, 280–285. doi: 10.1016/S0166-2236(96)10032-1

Southam, K. A., King, A. E., Blizzard, C. A., Mccormack, G. H., and Dickson, T. C. (2013). Microfluidic primary culture model of the lower motor neuron–neuromuscular junction circuit. *J. Neurosci. Methods* 218, 164–169. doi: 10.1016/j.jneumeth.2013.06.002

Spampanato, C., Feeney, E., Li, L., Cardone, M., Lim, J. A., Annunziata, F., et al. (2013). Transcription factor EB (TFEB) is a new therapeutic target for Pompe disease. *EMBO Mol. Med.* 5, 691–706. doi: 10.1002/emmm.201202176

Spiridigliozzi, G. A., Keeling, L. A., Stefanescu, M., Li, C., Austin, S., and Kishnani, P. S. (2017). Cognitive and academic outcomes in long-term survivors of infantile-onset Pompe disease: a longitudinal follow-up. *Mol. Genet. Metab.* 121, 127–137. doi: 10.1016/j.ymgme.2017.04.014

Stålberg, E., and Trontelj, J. V. (1997). The study of normal and abnormal neuromuscular transmission with single fibre electromyography. *J. Neurosci. Methods* 74, 145–154. doi: 10.1016/S0165-0270(97)02245-0

Stein, J. L., De La Torre-Ubieta, L., Tian, Y., Parikshak, N. N., Hernandez, I. A., Marchetto, M. C., et al. (2014). A quantitative framework to evaluate modeling of cortical development by neural stem cells. *Neuron* 83, 69–86. doi: 10.1016/j.neuron.2014.05.035

Steinbeck, J. A., Jaiswal, M. K., Calder, E. L., Kishinevsky, S., Weishaupt, A., Toyka, K. V., et al. (2016). Functional connectivity under optogenetic control allows modeling of human neuromuscular disease. *Cell Stem Cell* 18, 134–143. doi: 10.1016/j.stem.2015.10.002

Strong, M. J. (2010). The evidence for altered RNA metabolism in amyotrophic lateral sclerosis (ALS). *J. Neurol. Sci.* 288, 1–12. doi: 10.1016/j.jns.2009.09.029

Sugiura, Y., and Lin, W. (2011). Neuron–glia interactions: the roles of Schwann cells in neuromuscular synapse formation and function. *Biosci. Rep.* 31, 295–302. doi: 10.1042/BSR20100107

Sui, T., Lau, Y. S., Liu, D., Liu, T., Xu, L., Gao, Y., et al. (2018). A novel rabbit model of Duchenne muscular dystrophy generated by CRISPR/Cas9. *Dis. Model. Mech.* 11:dmm032201. doi: 10.1242/dmm.032201

Sun, C., Choi, I. Y., Gonzalez, Y. I. R., Andersen, P., Talbot, C. C. Jr., Iyer, S. R., et al. (2020). Duchenne muscular dystrophy hiPSC-derived myoblast drug screen identifies compounds that ameliorate disease in mdx mice. *JCI Insight* 5:e134287. doi: 10.1172/jci.insight.134287

Sun, J., Ma, X., Chu, H. T., Feng, B., Tuan, R. S., and Jiang, Y. (2019). Biomaterials and advanced biofabrication techniques in hiPSCs based neuromyopathic disease modeling. *Front. Bioeng. Biotechnol.* 7:373. doi: 10.3389/fbioe.2019.00373

Sun, Y., Duffy, R., Lee, A., and Feinberg, A. W. (2013). Optimizing the structure and contractility of engineered skeletal muscle thin films. *Acta Biomater.* 9, 7885–7894. doi: 10.1016/j.actbio.2013.04.036

Suzuki, M., Mchugh, J., Tork, C., Shelley, B., Hayes, A., Bellantuono, I., et al. (2008). Direct muscle delivery of GDNF with human mesenchymal stem cells improves motor neuron survival and function in a rat model of familial ALS. *Mol. Ther.* 16, 2002–2010. doi: 10.1038/mt.2008.197

Suzuki, M., Mchugh, J., Tork, C., Shelley, B., Klein, S. M., Aebischer, P., et al. (2007). GDNF secreting human neural progenitor cells protect dying motor neurons, but not their projection to muscle, in a rat model of familial ALS. *PLoS One* 2:e689. doi: 10.1371/journal.pone.0000689

Suzuki, N., Mizuno, H., Warita, H., Takeda, S. I., Itoyama, Y., and Aoki, M. (2010). Neuronal NOS is dislocated during muscle atrophy in amyotrophic lateral sclerosis. *J. Neurol. Sci.* 294, 95–101. doi: 10.1016/j.jns.2010.03.022

Swartz, E. W., Baek, J., Pribadi, M., Wojta, K. J., Almeida, S., Karydas, A., et al. (2016). A novel protocol for directed differentiation of C9orf72-associated human induced pluripotent stem cells into contractile skeletal myotubes. *Stem Cells Transl. Med.* 5, 1461–1472. doi: 10.5966/sctm.2015-0340

Takemoto, T., Uchikawa, M., Yoshida, M., Bell, D. M., Lovell-Badge, R., Papaioannou, V. E., et al. (2011). Tbx6-dependent Sox2 regulation determines neural or mesodermal fate in axial stem cells. *Nature* 470, 394–398. doi: 10.1038/nature09729

Tanaka, A., Woltjen, K., Miyake, K., Hotta, A., Ikeya, M., Yamamoto, T., et al. (2013). Efficient and reproducible myogenic differentiation from human iPS cells: prospects for modeling Miyoshi Myopathy in vitro. *PLoS One* 8:e61540. doi: 10.1371/journal.pone.0061540

Thornton, C. A. (2014). Myotonic dystrophy. *Neurol. Clin.* 32, 705–719. doi: 10.1016/j.ncl.2014.04.011

Tintignac, L. A., Brenner, H.-R., and Rüegg, M. A. (2015). Mechanisms regulating neuromuscular junction development and function and causes of muscle wasting. *Physiol. Rev.* 95, 809–852. doi: 10.1152/physrev.00033.2014

Todd, A. G., Mcelroy, J. A., Grange, R. W., Fuller, D. D., Walter, G. A., Byrne, B. J., et al. (2015). Correcting neuromuscular deficits with gene therapy in pompe disease. *Ann. Neurol.* 78:222. doi: 10.1002/ana.24433

Tong, Z., Seira, O., Casas, C., Reginensi, D., Homs-Corbera, A., Samitier, J., et al. (2014). Engineering a functional neuro-muscular junction model in a chip. *RSC Adv.* 4, 54788–54797. doi: 10.1039/C4RA10219C

Torres, L., and Duchen, L. (1987). The mutant mdx: inherited myopathy in the mouse: morphological studies of nerves, muscles and end-plates. *Brain* 110, 269–299. doi: 10.1093/brain/110.2.269

Totosy de Zepetnek, J., Zung, H., Erdebil, S., and Gordon, T. (1992). Motor-unit categorization based on contractile and histochemical properties: a glycogen depletion analysis of normal and reinnervated rat tibialis anterior muscle. *J. Neurophysiol.* 67, 1404–1415. doi: 10.1152/jn.1992.67.5.1404

Tourovskaia, A., Li, N., and Folch, A. (2008). Localized acetylcholine receptor clustering dynamics in response to microfluidic focal stimulation with agrin. *Biophys. J.* 95, 3009–3016. doi: 10.1529/biophysj.107.128173

Tremblay, E., Martineau, É, and Robitaille, R. (2017). Opposite synaptic alterations at the neuromuscular junction in an ALS mouse model: when motor units matter. *J. Neurosci.* 37, 8901–8918. doi: 10.1523/JNEUROSCI.3090-16.2017

Trias, E., Ibarburu, S., Barreto-Núñez, R., Varela, V., Moura, I. C., Dubreuil, P., et al. (2017). Evidence for mast cells contributing to neuromuscular pathology in an inherited model of ALS. *JCI Insight* 2:e95934. doi: 10.1172/jci.insight.95934

Tsujihata, M., Hazama, R., Yoshimura, T., Satoh, A., Mori, M., and Nagataki, S. (1984). The motor end-plate fine structure and ultrastructural localization of acetylcholine receptors in amyotrophic lateral sclerosis. *Muscle Nerve* 7, 243–249. doi: 10.1002/mus.880070310

Turner, S. M., Hoyt, A. K., Elmallah, M. K., Falk, D. J., Byrne, B. J., and Fuller, D. D. (2016). Neuropathology in respiratory-related motoneurons in young Pompe (Gaa−/−) mice. *Respir. Physiol. Neurobiol.* 227, 48–55. doi: 10.1016/j.resp.2016.02.007

Tutdibi, O., Brinkmeier, H., Rüdel, R., and Föhr, K. (1999). Increased calcium entry into dystrophin-deficient muscle fibres of MDX and ADR-MDX mice is reduced by ion channel blockers. *J. Physiol.* 515, 859–868. doi: 10.1111/j.1469-7793.1999.859ab.x

Tzouanacou, E., Wegener, A., Wymeersch, F. J., Wilson, V., and Nicolas, J.-F. (2009). Redefining the progression of lineage segregations during mammalian embryogenesis by clonal analysis. *Dev. Cell* 17, 365–376. doi: 10.1016/j.devcel.2009.08.002

Ueki, J., Nakamori, M., Nakamura, M., Nishikawa, M., Yoshida, Y., Tanaka, A., et al. (2017). Myotonic dystrophy type 1 patient-derived iPSCs for the investigation of CTG repeat instability. *Sci. Rep.* 7:42522. doi: 10.1038/srep42522

Uezumi, A., Ikemoto-Uezumi, M., Zhou, H., Kurosawa, T., Yoshimoto, Y., Nakatani, M., et al. (2021). Mesenchymal Bmp3b expression maintains skeletal muscle integrity and decreases in age-related sarcopenia. *J. Clin. Invest.* 131:e139617. doi: 10.1172/JCI139617

Umbach, J. A., Adams, K. L., Gundersen, C. B., and Novitch, B. G. (2012). Functional neuromuscular junctions formed by embryonic stem cell-derived motor neurons. *PLoS One* 7:e36049. doi: 10.1371/journal.pone.0036049

Uzawa, A., Kuwabara, S., Suzuki, S., Imai, T., Murai, H., Ozawa, Y., et al. (2021). Roles of cytokines and T cells in the pathogenesis of myasthenia gravis. *Clin. Exp. Immunol.* 203, 366–374. doi: 10.1111/cei.13546

Uzel, S. G., Platt, R. J., Subramanian, V., Pearl, T. M., Rowlands, C. J., Chan, V., et al. (2016). Microfluidic device for the formation of optically excitable, three-dimensional, compartmentalized motor units. *Sci. Adv.* 2:e1501429. doi: 10.1126/sciadv.1501429

Vainzof, M., Ayub-Guerrieri, D., Onofre, P. C., Martins, P. C., Lopes, V. F., Zilberztajn, D., et al. (2008). Animal models for genetic neuromuscular diseases. *J. Mol. Neurosci.* 34, 241–248. doi: 10.1007/s12031-007-9023-9

van der Pijl, E. M., Van Putten, M., Niks, E. H., Verschuuren, J. J., Aartsma-Rus, A., and Plomp, J. J. (2016). Characterization of neuromuscular synapse function abnormalities in multiple Duchenne muscular dystrophy mouse models. *Eur. J. Neurosci.* 43, 1623–1635. doi: 10.1111/ejn.13249

van der Ploeg, A. T., Clemens, P. R., Corzo, D., Escolar, D. M., Florence, J., Groeneveld, G. J., et al. (2010). A randomized study of alglucosidase alfa in late-onset Pompe's disease. *N. Engl. J. Med.* 362, 1396–1406. doi: 10.1056/NEJMoa0909859

van der Velden, J. L., Langen, R. C., Kelders, M. C., Wouters, E. F., Janssen-Heininger, Y. M., and Schols, A. M. (2006). Inhibition of glycogen synthase kinase-3β activity is sufficient to stimulate myogenic differentiation. *Am. J. Physiol. Cell Physiol.* 290, C453–C462. doi: 10.1152/ajpcell.00068.2005

van der Wal, E., Bergsma, A. J., Van Gestel, T. J., Lm, S., Zaehres, H., Araúzo-Bravo, M. J., et al. (2017). GAA deficiency in Pompe disease is alleviated by exon inclusion in iPSC-derived skeletal muscle cells. *Mol. Ther. Nucleic Acids* 7, 101–115. doi: 10.1016/j.omtn.2017.03.002

van der Wal, E., Herrero-Hernandez, P., Wan, R., Broeders, M., In 'T Groen, S. L. M., Van Gestel, T. J. M., et al. (2018). Large-Scale expansion of human iPSC-derived skeletal muscle cells for disease modeling and cell-based therapeutic strategies. *Stem Cell Rep.* 10, 1975–1990. doi: 10.1016/j.stemcr.2018.04.002

van Putten, M., Putker, K., Overzier, M., Adamzek, W. A., Pasteuning-Vuhman, S., Plomp, J. J., et al. (2019). Natural disease history of the D2-mdx mouse model for Duchenne muscular dystrophy. *FASEB J.* 33, 8110–8124. doi: 10.1096/fj.201802488R

Veltrop, M., Van Vliet, L., Hulsker, M., Claassens, J., Brouwers, C., Breukel, C., et al. (2018). A dystrophic Duchenne mouse model for testing human antisense oligonucleotides. *PLoS One* 13:e0193289. doi: 10.1371/journal.pone.0193289

Viader, A., Golden, J. P., Baloh, R. H., Schmidt, R. E., Hunter, D. A., and Milbrandt, J. (2011). Schwann cell mitochondrial metabolism supports long-term axonal survival and peripheral nerve function. *J. Neurosci.* 31, 10128–10140. doi: 10.1523/JNEUROSCI.0884-11.2011

Vignaud, A., Ferry, A., Huguet, A., Baraibar, M., Trollet, C., Hyzewicz, J., et al. (2010). Progressive skeletal muscle weakness in transgenic mice expressing CTG expansions is associated with the activation of the ubiquitin–proteasome pathway. *Neuromuscul. Disord.* 20, 319–325. doi: 10.1016/j.nmd.2010.03.006

Vihola, A., Bassez, G., Meola, G., Zhang, S., Haapasalo, H., Paetau, A., et al. (2003). Histopathological differences of myotonic dystrophy type 1 (DM1) and PROMM/DM2. *Neurology* 60, 1854–1857. doi: 10.1212/01.WNL.0000065898.61358.09

Vila, O., Chavez, M., Ma, S. P., Yeager, K., Zholudeva, L. V., Colón-Mercado, J. M., et al. (2021). Bioengineered optogenetic model of human neuromuscular junction. *Biomaterials* 276:121033. doi: 10.1016/j.biomaterials.2021.121033

Vila, O. F., Uzel, S. G., Ma, S. P., Williams, D., Pak, J., Kamm, R. D., et al. (2019). Quantification of human neuromuscular function through optogenetics. *Theranostics* 9:1232. doi: 10.7150/thno.25735

Vilmont, V., Cadot, B., Ouanounou, G., and Gomes, E. R. (2016). A system for studying mechanisms of neuromuscular junction development and maintenance. *Development* 143, 2464–2477. doi: 10.1242/dev.130278

Wachtler, F. (1992). The basic embryology of skeletal muscle formation in vertebrates: the avian model. *Semin. Dev. Biol.* 3, 217–227.

Wainger, B. J., Kiskinis, E., Mellin, C., Wiskow, O., Han, S. S., Sandoe, J., et al. (2014). Intrinsic membrane hyperexcitability of amyotrophic lateral sclerosis patient-derived motor neurons. *Cell Rep.* 7, 1–11. doi: 10.1016/j.celrep.2014.03.019

Waite, A., Tinsley, C. L., Locke, M., and Blake, D. J. (2009). The neurobiology of the dystrophin-associated glycoprotein complex. *Ann. Med.* 41, 344–359. doi: 10.1080/07853890802668522

Wang, J., Khodabukus, A., Rao, L., Vandusen, K., Abutaleb, N., and Bursac, N. (2019). Engineered skeletal muscles for disease modeling and drug discovery. *Biomaterials* 221:119416. doi: 10.1016/j.biomaterials.2019.119416

Wang, J., Xiao, Y., Zhang, K., Luo, B., and Shen, C. (2018). Introducing autoimmunity at the synapse by a novel animal model of experimental autoimmune myasthenia gravis. *Neuroscience* 374, 264–270. doi: 10.1016/j.neuroscience.2018.01.042

Wang, J., Zhou, C. J., Khodabukus, A., Tran, S., Han, S.-O., Carlson, A. L., et al. (2021). Three-dimensional tissue-engineered human skeletal muscle model of Pompe disease. *Commun. Biol.* 4:524. doi: 10.1038/s42003-021-02059-4

Wang, P. Y., Thissen, H., and Tsai, W. B. (2012). The roles of RGD and grooved topography in the adhesion, morphology, and differentiation of C2C12 skeletal myoblasts. *Biotechnol. Bioeng.* 109, 2104–2115. doi: 10.1002/bit.24452

Wang, Y. X., Feige, P., Brun, C. E., Hekmatnejad, B., Dumont, N. A., Renaud, J. M., et al. (2019). EGFR-Aurka signaling rescues polarity and regeneration defects in dystrophin-deficient muscle stem cells by increasing asymmetric divisions. *Cell Stem Cell* 24, 419–432.e416. doi: 10.1016/j.stem.2019.01.002

Warf, M. B., and Berglund, J. A. (2007). MBNL binds similar RNA structures in the CUG repeats of myotonic dystrophy and its pre-mRNA substrate cardiac troponin T. *RNA* 13, 2238–2251. doi: 10.1261/rna.610607

Warren, L., Manos, P. D., Ahfeldt, T., Loh, Y.-H., Li, H., Lau, F., et al. (2010). Highly efficient reprogramming to pluripotency and directed differentiation of human cells with synthetic modified mRNA. *Cell Stem Cell* 7, 618–630. doi: 10.1016/j.stem.2010.08.012

Watanabe, K., Kamiya, D., Nishiyama, A., Katayama, T., Nozaki, S., Kawasaki, H., et al. (2005). Directed differentiation of telencephalic precursors from embryonic stem cells. *Nat. Neurosci.* 8, 288–296. doi: 10.1038/nn1402

Webster, R. G. (2018). Animal models of the neuromuscular junction, vitally informative for understanding function and the molecular mechanisms of congenital myasthenic syndromes. *Int. J. Mol. Sci.* 19:1326. doi: 10.3390/ijms19051326

Weller, B., Karpati, G., and Carpenter, S. (1990). Dystrophin-deficient mdx muscle fibers are preferentially vulnerable to necrosis induced by experimental lengthening contractions. *J. Neurol. Sci.* 100, 9–13. doi: 10.1016/0022-510X(90)90005-8

Wells, D. J. (2018). *Tracking Progress: An Update on Animal Models for Duchenne Muscular Dystrophy*. Cambridge: The Company of Biologists Ltd. doi: 10.1242/dmm.035774

Wheeler, T., Krym, M., and Thornton, C. (2007). Ribonuclear foci at the neuromuscular junction in myotonic dystrophy type 1. *Neuromuscul. Disord.* 17, 242–247. doi: 10.1016/j.nmd.2006.12.015

White, P. H., Farkas, D. R., and Chapman, D. L. (2005). Regulation of Tbx6 expression by Notch signaling. *Genesis* 42, 61–70. doi: 10.1002/gene.20124

Wichterle, H., Lieberam, I., Porter, J. A., and Jessell, T. M. (2002). Directed differentiation of embryonic stem cells into motor neurons. *Cell* 110, 385–397. doi: 10.1016/S0092-8674(02)00835-8

Winnier, G., Blessing, M., Labosky, P. A., and Hogan, B. (1995). Bone morphogenetic protein-4 is required for mesoderm formation and patterning in the mouse. *Genes Dev.* 9, 2105–2116. doi: 10.1101/gad.9.17.2105

Woldeyesus, M. T., Britsch, S., Riethmacher, D., Xu, L., Sonnenberg-Riethmacher, E., Abou-Rebyeh, F., et al. (1999). Peripheral nervous system defects in erbB2 mutants following genetic rescue of heart development. *Genes Dev.* 13, 2538–2548. doi: 10.1101/gad.13.19.2538

Woodhoo, A., Alonso, M. B., Droggiti, A., Turmaine, M., D'antonio, M., Parkinson, D. B., et al. (2009). Notch controls embryonic Schwann cell differentiation,

postnatal myelination and adult plasticity. *Nat. Neurosci.* 12, 839–847. doi: 10.1038/nn.2323

Woodhoo, A., and Sommer, L. (2008). Development of the Schwann cell lineage: from the neural crest to the myelinated nerve. *Glia* 56, 1481–1490. doi: 10.1002/glia.20723

Wroe, R., Wai-Ling Butler, A., Andersen, P. M., Powell, J. F., and Al-Chalabi, A. (2008). ALSOD: the amyotrophic lateral sclerosis online database. *Amyotroph. Lateral Scler.* 9, 249–250. doi: 10.1080/17482960802146106

Xi, H., Langerman, J., Sabri, S., Chien, P., Young, C. S., Younesi, S., et al. (2020). A human skeletal muscle atlas identifies the trajectories of stem and progenitor cells across development and from human pluripotent stem cells. *Cell Stem Cell* 27, 158–176.e110. doi: 10.1016/j.stem.2020.04.017

Xia, G., Gao, Y., Jin, S., Subramony, S., Terada, N., Ranum, L. P., et al. (2015). Genome modification leads to phenotype reversal in human myotonic dystrophy type 1 induced pluripotent stem cell-derived neural stem cells. *Stem Cells* 33, 1829–1838. doi: 10.1002/stem.1970

Yadava, R. S., Foff, E. P., Yu, Q., Gladman, J. T., Kim, Y. K., Bhatt, K. S., et al. (2015). TWEAK/Fn14, a pathway and novel therapeutic target in myotonic dystrophy. *Hum. Mol. Genet.* 24, 2035–2048. doi: 10.1093/hmg/ddu617

Yang, J.-F., Cao, G., Koirala, S., Reddy, L. V., and Ko, C.-P. (2001). Schwann cells express active agrin and enhance aggregation of acetylcholine receptors on muscle fibers. *J. Neurosci.* 21, 9572–9584. doi: 10.1523/JNEUROSCI.21-24-09572.2001

Ydens, E., Lornet, G., Smits, V., Goethals, S., Timmerman, V., and Janssens, S. (2013). The neuroinflammatory role of Schwann cells in disease. *Neurobiol. Dis.* 55, 95–103. doi: 10.1016/j.nbd.2013.03.005

Yiu, E. M., and Kornberg, A. J. (2015). Duchenne muscular dystrophy. *J. Paediatr. Child Health* 51, 759–764. doi: 10.1111/jpc.12868

Yokota, T., Duddy, W., Echigoya, Y., and Kolski, H. (2012). Exon skipping for nonsense mutations in Duchenne muscular dystrophy: too many mutations, too few patients? *Expert Opin. Biol. Ther.* 12, 1141–1152. doi: 10.1517/14712598.2012.693469

Yoshida, M., Kitaoka, S., Egawa, N., Yamane, M., Ikeda, R., Tsukita, K., et al. (2015). Modeling the early phenotype at the neuromuscular junction of spinal muscular atrophy using patient-derived iPSCs. *Stem Cell Rep.* 4, 561–568. doi: 10.1016/j.stemcr.2015.02.010

Yoshida, T., Awaya, T., Jonouchi, T., Kimura, R., Kimura, S., Era, T., et al. (2017). A skeletal muscle model of infantile-onset Pompe disease with patient-specific iPS cells. *Sci. Rep.* 7:13473. doi: 10.1038/s41598-017-14063-y

Yoshihara, T., Ishii, T., Iwata, M., and Nomoto, M. (1998). Ultrastructural and histochemical study of the motor end plates of the intrinsic laryngeal muscles in amyotrophic lateral sclerosis. *Ultrastruct. Pathol.* 22, 121–126. doi: 10.3109/01913129809032266

Zaccaria, M. L., Egle De Stefano, M., Properzi, F., Gotti, C., Petrucci, T. C., and Paggi, P. (1998). Disassembly of the cholinergic postsynaptic apparatus induced by axotomy in mouse sympathetic neurons: the loss of dystrophin and β-dystroglycan immunoreactivity precedes that of the acetylcholine receptor. *J. Neuropathol. Exp. Neurol.* 57, 768–779. doi: 10.1097/00005072-199808000-00006

Zainul, Z., Heikkinen, A., Koivisto, H., Rautalahti, I., Kallio, M., Lin, S., et al. (2018). Collagen XIII is required for neuromuscular synapse regeneration and functional recovery after peripheral nerve injury. *J. Neurosci.* 38, 4243–4258. doi: 10.1523/JNEUROSCI.3119-17.2018

Zhang, B. G., Quigley, A. F., Bourke, J. L., Nowell, C. J., Myers, D. E., Choong, P. F., et al. (2016). Combination of agrin and laminin increase acetylcholine receptor clustering and enhance functional neuromuscular junction formation in vitro. *Dev. Neurobiol.* 76, 551–565. doi: 10.1002/dneu.22331

Zhang, H., Wen, J., Bigot, A., Chen, J., Shang, R., Mouly, V., et al. (2020). Human myotube formation is determined by MyoD–Myomixer/Myomaker axis. *Sci. Adv.* 6:eabc4062. doi: 10.1126/sciadv.abc4062

Zhang, K., Donnelly, C. J., Haeusler, A. R., Grima, J. C., Machamer, J. B., Steinwald, P., et al. (2015). The C9orf72 repeat expansion disrupts nucleocytoplasmic transport. *Nature* 525, 56–61. doi: 10.1038/nature14973

Zhang, Q., Nguyen, P. D., Shi, S., Burrell, J. C., Cullen, D. K., and Le, A. D. (2018). 3D bio-printed scaffold-free nerve constructs with human gingiva-derived mesenchymal stem cells promote rat facial nerve regeneration. *Sci. Rep.* 8:6634. doi: 10.1038/s41598-018-24888-w

Zhao, C., Devlin, A. C., Chouhan, A. K., Selvaraj, B. T., Stavrou, M., Burr, K., et al. (2020). Mutant C9orf72 human iPSC-derived astrocytes cause non-cell autonomous motor neuron pathophysiology. *Glia* 68, 1046–1064. doi: 10.1002/glia.23761

Zhou, H., Glass, D. J., Yancopoulos, G. D., and Sanes, J. R. (1999). Distinct domains of MuSK mediate its abilities to induce and to associate with postsynaptic specializations. *J. Cell Biol.* 146, 1133–1146. doi: 10.1083/jcb.146.5.1133

Zouvelou, V., Rentzos, M., Toulas, P., and Evdokimidis, I. (2012). AchR-positive myasthenia gravis with MRI evidence of early muscle atrophy. *J. Clin. Neurosci.* 19, 918–919. doi: 10.1016/j.jocn.2011.09.022

Zwiegers, P., Lee, G., and Shaw, C. A. (2014). Reduction in hSOD1 copy number significantly impacts ALS phenotype presentation in G37R (line 29) mice: implications for the assessment of putative therapeutic agents. *J. Negat. Results Biomed.* 13, 1–9. doi: 10.1186/1477-5751-13-14

**Conflict of Interest:** The authors declare that the research was conducted in the absence of any commercial or financial relationships that could be construed as a potential conflict of interest.

**Publisher's Note:** All claims expressed in this article are solely those of the authors and do not necessarily represent those of their affiliated organizations, or those of the publisher, the editors and the reviewers. Any product that may be evaluated in this article, or claim that may be made by its manufacturer, is not guaranteed or endorsed by the publisher.

frontiers in Cell and Developmental Biology

ORIGINAL RESEARCH
published: 22 November 2021
doi: 10.3389/fcell.2021.745897

# A Functional Human-on-a-Chip Autoimmune Disease Model of Myasthenia Gravis for Development of Therapeutics

*Virginia M. Smith[1,2], Huan Nguyen[1], John W. Rumsey[2], Christopher J. Long[2], Michael L. Shuler[2] and James J. Hickman[1,2]**

[1] Hybrid Systems Lab, NanoScience Technology Center, University of Central Florida, Orlando, FL, United States,
[2] Hesperos, Inc., Orlando, FL, United States

OPEN ACCESS

**Edited by:**
Alec S. T. Smith,
University of Washington,
United States

**Reviewed by:**
Masatoshi Suzuki,
University of Wisconsin-Madison,
United States
Chiara Cordiglieri,
National Institute of Molecular Genetics (INGM), Italy

***Correspondence:**
James J. Hickman
jhickman@ucf.edu;
jhickman@hesperosinc.com

**Specialty section:**
This article was submitted to Stem Cell Research, a section of the journal Frontiers in Cell and Developmental Biology

**Received:** 22 July 2021
**Accepted:** 14 October 2021
**Published:** 22 November 2021

**Citation:**
Smith VM, Nguyen H, Rumsey JW, Long CJ, Shuler ML and Hickman JJ (2021) A Functional Human-on-a-Chip Autoimmune Disease Model of Myasthenia Gravis for Development of Therapeutics. Front. Cell Dev. Biol. 9:745897. doi: 10.3389/fcell.2021.745897

Myasthenia gravis (MG) is a chronic and progressive neuromuscular disease where autoantibodies target essential proteins such as the nicotinic acetylcholine receptor (nAChR) at the neuromuscular junction (NMJ) causing muscle fatigue and weakness. Autoantibodies directed against nAChRs are proposed to work by three main pathological mechanisms of receptor disruption: blocking, receptor internalization, and downregulation. Current *in vivo* models using experimental autoimmune animal models fail to recapitulate the disease pathology and are limited in clinical translatability due to disproportionate disease severity and high animal death rates. The development of a highly sensitive antibody assay that mimics human disease pathology is desirable for clinical advancement and therapeutic development. To address this lack of relevant models, an NMJ platform derived from human iPSC differentiated motoneurons and primary skeletal muscle was used to investigate the ability of an anti-nAChR antibody to induce clinically relevant MG pathology in the serum-free, spatially organized, functionally mature NMJ platform. Treatment of the NMJ model with the anti-nAChR antibody revealed decreasing NMJ stability as measured by the number of NMJs before and after the synchrony stimulation protocol. This decrease in NMJ stability was dose-dependent over a concentration range of 0.01–20 μg/mL. Immunocytochemical (ICC) analysis was used to distinguish between pathological mechanisms of antibody-mediated receptor disruption including blocking, receptor internalization and downregulation. Antibody treatment also activated the complement cascade as indicated by complement protein 3 deposition near the nAChRs. Additionally, complement cascade activation significantly altered other readouts of NMJ function including the NMJ fidelity parameter as measured by the number of muscle contractions missed in response to increasing motoneuron stimulation frequencies. This synchrony readout mimics the clinical phenotype of neurological blocking that results in failure of muscle contractions despite motoneuron stimulations. Taken together, these data indicate the establishment of a relevant disease model of MG that mimics reduction

of functional nAChRs at the NMJ, decreased NMJ stability, complement activation and blocking of neuromuscular transmission. This system is the first functional human *in vitro* model of MG to be used to simulate three potential disease mechanisms as well as to establish a preclinical platform for evaluation of disease modifying treatments (etiology).

**Keywords: acetylcholine receptor, neuromuscular junction (NMJ), myasthenia gravis, autoantibodies, microphysiological systems, human-on-a-chip, induced pluripotent stem cells (iPSCs), disease pathology**

## INTRODUCTION

Myasthenia gravis (MG) is a rare autoimmune disease that affects intra- and extracellular proteins involved in the neuromuscular junction (NMJ), impairing signal transduction (Lindstrom, 2000; Gilhus and Verschuuren, 2015; Gilhus, 2016). The classic clinical feature of MG is muscle weakness which becomes more severe after repetitive muscle contractions over time. Although most patients will initially develop oculobulbar muscle weakness, 85% of the cases will progress to generalized MG (non-ocular muscle) (Kerty et al., 2014) with antibodies directed against the nicotinic acetylcholine receptor (nAChR; Meriggioli and Sanders, 2009, 2012). The nAChR is a pentameric transmembrane protein consisting of two α1 subunits, one β1 subunit, one δ subunit and either one γ subunit (in embryonic AChR) or one ε subunit (in adult AChR). Due to the heterogeneous nature of anti-nAChR antibodies, the epitope location on the AChR surface is crucial in the disease pathogenesis. Generally, anti-nAChR antibodies (Abs) have three pathogenic mechanisms: (I) direct blocking of the AChR, (II) modulation of the receptor through crosslinking of two AChRs leading to internalization and subsequent degradation, or (III) binding to the receptor at a different antigenic site and activating the complement cascade (Kang et al., 2015; **Figure 1**). We describe here a system to simulate these three mechanisms. Currently, one of the most common tests to detect autoantibodies against AChR is by a radioimmunoprecipitation assay (RIA) to quantify the patient antibody titer by the precipitation of the specific binding of radiolabeled α-bungarotoxin ($I^{125}$-BTX) to the α1 subunits of AChR (Leite et al., 2010; Zisimopoulou et al., 2013). For antibodies that directly block the ACh-binding site, there will be a decrease in $I^{125}$-BTX-AChR complexes, resulting in a rare but acute inhibition of function (Whiting et al., 1983; Lang et al., 1988; Burges et al., 1990; Bufler et al., 1996). The subtype of nAChR Ab present in seropositive patients has rarely been related to clinical severity (Howard et al., 1987), although, limited evidence suggests blocking and modulating antibodies have been found to have unfavorable prognosis (Kang et al., 2015). There is a need for a more specific human-based platform that could work synergistically with the current detection assays to understand the pathology of MG as well as to develop therapeutic interventions.

Until recently, autoimmune diseases have been studied using cell-based assays to assess antigen activation, cellular interaction, and migration and in animal models by inducing the disease pathophysiology (Giese and Marx, 2014; van de Stolpe and Kauffmann, 2015). However, both approaches lack clinical disease relevance due to the simplistic nature of the assays and intrinsic differences between clinical and experimental autoimmune MG (EAMG) immune responses. These differences further limits understanding of the underlying disease mechanisms. Specifically, in EAMG models, animals are immunized with foreign AChRs and later develop MG-like symptoms providing a potential method to understand MG and the mechanisms involved (Patrick et al., 1973; Losen et al., 2015). Although animal studies have led to advances in MG disease understanding while mimicking symptomatic parameters (Christadoss et al., 2000) and evaluating new immunotherapies (Baggi et al., 2012), the mouse/rat immune system is fundamentally different than a human. Additionally, some EAMG experimental parameters can lead to severe animal suffering and death resulting in skewed statistical analysis (Mantegazza et al., 2016). There is a need to establish new models to create ethically sound experiments that can translate to human disease.

Recently, human-based *in vitro* platform systems have been used to model disease neuronal pathogenesis, develop novel therapeutics, reduce animal experimentation, and improve disease understanding (Mantegazza et al., 2016). These systems use representative human cell cultures utilizing healthy and diseased subjects from primary cells cultured directly from human biopsies (Bellin et al., 2012; Sato and Clevers, 2013) as well as induced pluripotent stem (iPS) and adult stem cells from patients that can be differentiated into varying cell types (Takahashi et al., 2007; Bellin et al., 2012; Sato and Clevers, 2013). Several advances have been made using human-based *in vitro* systems to study diseases that affect the neuromuscular junction (NMJ; Park et al., 2013; Zahavi et al., 2015; Santhanam et al., 2018; Bakooshli et al., 2019). These *in vitro* systems include serum free, functionally relevant mimics of the human NMJ (Santhanam et al., 2018; Guo et al., 2020a,b) that allow crosstalk of the two different cell types (skeletal muscle and motoneurons), real-time functional analysis of direct and indirect stimulation of skeletal muscle and spatially controlled dosing of compounds to provide improved systems to understand human disease mechanisms as well as to study therapeutic options.

Here we report the use of a human functional NMJ model system treated with a commercially available antibody against nAChR to mimic the MG disease phenotype. The NMJ chambers were used for the co-culture of primary human skeletal muscle (SKM) and wild-type human induced-pluripotent stem cell (hiPSC)-derived motoneurons (MNs; **Figure 2**). Separation of the cultures by microtunnels allowed for axonal progression through the tunnels to innervate the myotubes, creating complete electrical and chemical stimulation isolation and enabled selective dosing of compounds to each chamber. Historically, synaptic

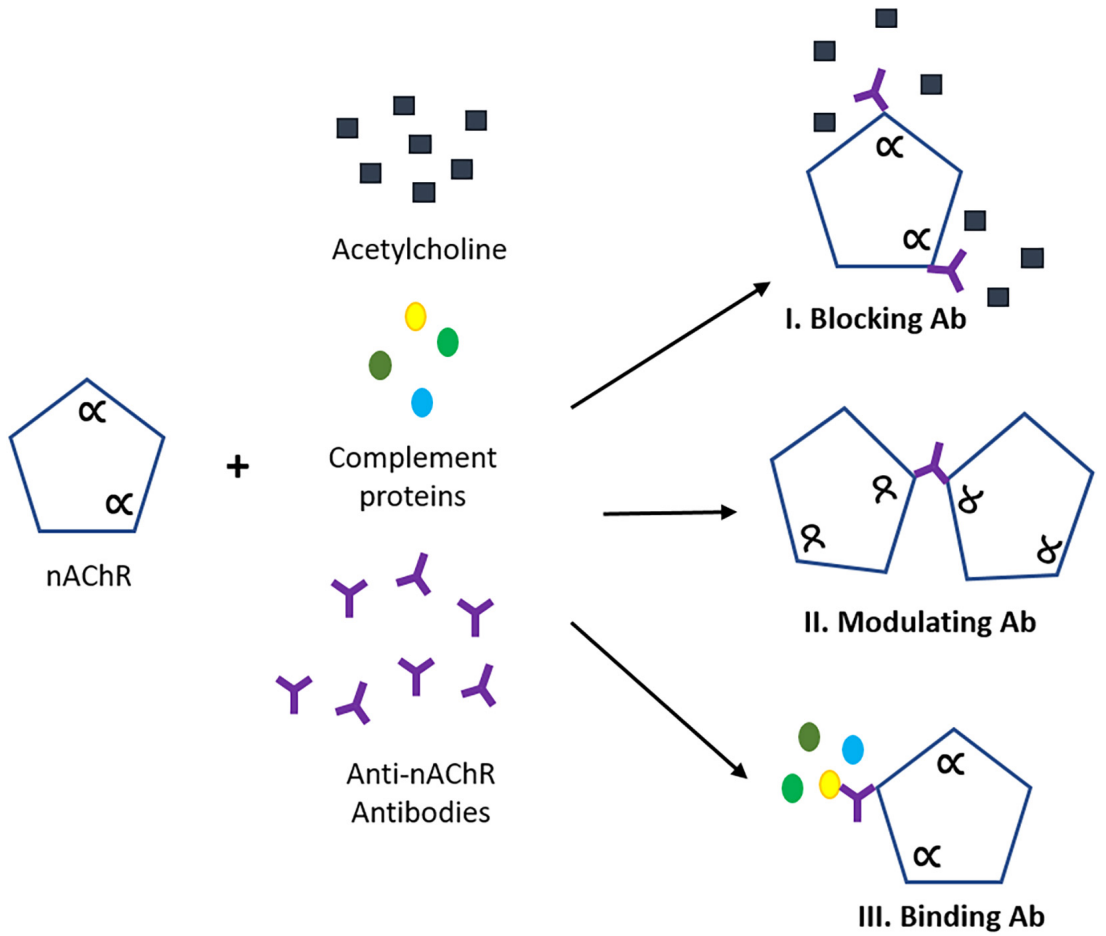


**FIGURE 1 |** Pathogenic mechanisms of anti-nAChR antibody (Ab). (I) Blocking abs interfere with ACh binding site interrupting neuromuscular transmission. (II) Modulating Abs that bind to two nAChRs causing receptor endocytosis leading to AChR degradation and reduction of expression. (III) Binding Abs that complex with a distinct location on the nAChR, triggering the activation of the complement cascade and subsequent formation of the membrane attack complex (MAC). Scheme adopted from Conti-Fine (Conti-Fine et al., 2006). The alpha (α) refers to the alpha subunit(s) on the nAChR.

connections in NMJs have been confirmed through ICC with co-localization of pre- and postsynaptic staining of neurofilament or synaptic protein and bungarotoxin (Arnold et al., 2014; Sleigh et al., 2014; Falk et al., 2015). We have also met this standard in our current NMJ systems based on ICC in our previous publications (Guo et al., 2011; Smith et al., 2013; Santhanam et al., 2018; Guo et al., 2020b). However, our functional NMJ model (indirect stimulation of MNs and real-time contraction of skeletal muscle) is now the best indicator of synaptic connection, validates the co-localization of ICC, and ultimately advances the current standard.

To mimic the disease phenotype and pathology of MG, a commercially available polyclonal antibody against the nAChR was dosed on the muscle side and functional readouts of NMJ stability and fidelity were analyzed. These two parameters were chosen based on the disease mechanisms of MG and reliable clinical measurements used to assess the MG disease pathology, such as muscle weakness after exercise. Since antibody induced effects can result in temporary or permanent reduction of nAChRs, NMJ stability then NMJ number is evaluated to focus on the ability of an NMJ to be maintained after strenuous exercise (indirect stimulation of the SKM at 0.33, 0.5, 1.0, and 2.0 Hz). Since many electromyography (EMG) labs use high frequency stimulation (∼3 Hz) as a standard for NMJ testing, the synchrony of contractions (fidelity) were monitored at 2.0 Hz (the historic frequency used in our systems). A concentration dependent dose response curve was determined using the anti-nAChR IgG antibody to establish the optimal dosing to elicit a functional deficit in NMJ stability. Complement activation in the presence of antibody caused a functional, dose-dependent loss of NMJs. Additionally, complement protein deposition can be initiated, as confirmed by immunocytochemistry, to reduce the number of contracting myotubes utilizing direct and indirect skeletal muscle (SKM) fidelity. Thus, the described MG model provides a diagnostic platform sensitive to the pathogenic mechanisms of MG and more importantly, can be utilized for the development of potential patient-specific treatments. These data indicate that this human-based NMJ system can mimic key

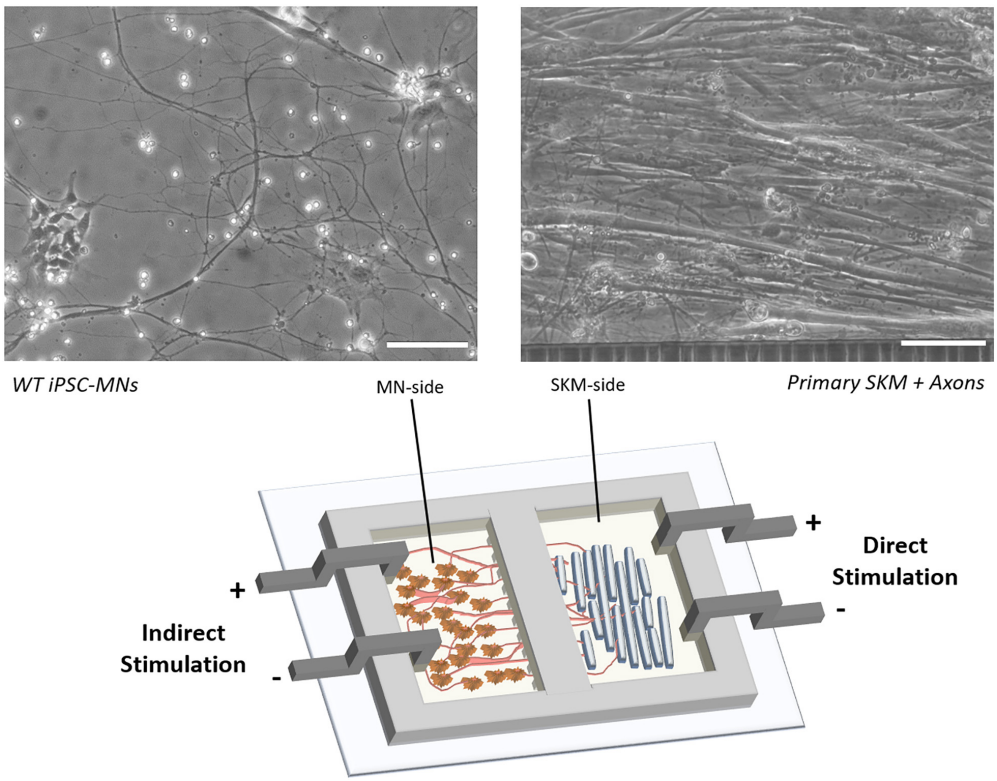


**FIGURE 2 |** Schematic of NMJ chamber with primary SKM innervated by WT iPSC-MNs and electrically stimulated by electrodes for either direct (SKM-side) or indirect (MN-side) stimulation. Phase images indicate the morphology of co-culture on SKM innervated by axons progressing through tunnels (right) and WT iPSC derived MNs (left). Scale bars = 100 microns.

aspects of antibody- and complement-mediated MG pathology and can be used to evaluate disease modifying treatments (DMTs) of MG.

# MATERIALS AND METHODS

## Study Design

To determine the dose-response of the NMJ system to anti-nAChR IgG, dosages were selected across a range of more than 2 orders of magnitude initially to identify the upper and lower plateau values, as well as the approximate range in which the $IC_{50}$ occurred. The range of a single order of magnitude around the $IC_{50}$ was further evaluated in more detail across the range with dosages split approximately equally in the log scale. Regression analysis using least square multiple regression to a sigmoidal equation with upper and lower plateau values, Hill coefficient, and $IC_{50}$ was performed to numerically determine the response shape. Sample sizes for the functional experiments were determined using estimated sample variance from preliminary experiments, such that statistical analysis would detect differences among treatment groups of 50% with 80% power and type I error rate of 0.05 ($\alpha = 0.05$). For the five main conditions (WT, 2 μg/mL anti-nAChR Ab, 2 μg/mL non-specific IgG, 0.05% hCS, and the combination of 2 μg/mL anti-nAChR Ab + 0.05% hCS), a minimum of eight replicates were assessed from at least two separate experiments ($N = 2$). Following data collection, treatment groups were statistically compared using one-way ANOVA followed by Fisher's LSD with $\alpha = 0.05$.

## Fabrication and Assembly of the Neuromuscular Junction Chamber Co-culture System

Neuromuscular junction chambers were cast using polydimethylsiloxane (PDMS) (Sylgard-184, Dow Silicones Corp., Cat. No. 2065622) at a 10:1 (base: curing agent) ratio. Once the base and curing agent were properly mixed, the PDMS was poured onto the SU-8 wafer mold. The fabrication of the SU-8 wafers used for the casting of the NMJ chambers were prepared using previously described methods (Santhanam et al., 2018). The wafer was then placed in the oven at 80°C overnight. After curing, the PDMS NMJ chambers were cut from the mold and soaked in 70% isopropyl alcohol (IPA) overnight to sterilize and remove any uncured monomers. The chambers were rinsed with additional 70% IPA and dried overnight in a biosafety cabinet in preparation for assembly.

Glass coverslips (VWR, Cat. No. 48366067) were plasma treated using a Harrick Plasma cleaner (model PDC-32G) with high-purity oxygen gas for 2 min at 750 mTorr. The coverslips were then sterilized using 70% ethanol and allowed to air dry.

Sterilized NMJ chambers were sealed onto the glass coverslips by gently pressing the PDMS chambers on top of the plasma treated glass coverslips.

## Surface Coating

Once sealed, the skeletal muscle (SKM) side of the NMJ chamber system (Santhanam et al., 2018) was coated with 60 μg/mL of rat tail collagen I (Gibco, Cat. No. A10483-01) in 1X phosphate buffer solution (PBS). The motoneuron (MN) side was coated with 3 μg/ml of laminin solution (Invitrogen, Cat. No. 23017-015) in 1X PBS. The chambers were left to incubate at room temperature for 2 h. The collagen coating solution was then removed and rinsed with sterile 1X PBS. Serum-free adult growth medium (AGM) was added to the muscle side and the systems were placed in a 4°C refrigerator overnight. The laminin coating solution was removed after overnight refrigeration and human motoneuron (hMN) medium was added to the MN-side. The chambers were incubated at 37°C, 5% $CO_2$ for 1 h prior to skeletal muscle plating.

## Culture of Human Skeletal Muscle Myoblasts

Primary human skeletal muscle myoblasts (Lonza, Cat. No. CC2580; lot 483427) were expanded once and used for all experiments. Myoblasts were seeded at a density of 300 cells/$mm^2$ in the NMJ chambers. At 70–80% confluency, the cultures were switched to differentiation medium (NbActiv4, BrainBits LLC, Cat. No. Nb4-500) to induce myogenesis. A one-third medium change with NbActiv4 was conducted every 2 days until day 12 of testing.

## Culture of Human Induced Pluripotent Stem Cell-Derived Motoneurons

Human motoneurons were derived by differentiation of human iPSCs isolated from a healthy subject (Coriell Institute, Cat. No. ND41865). Wild-type human motoneurons used in this study were differentiated from iPSCs (cell passaging number 6–10) using previously established protocols (Santhanam et al., 2018) and plated on the MN-side of the NMJ chamber system 4 days after myoblast differentiation. Motoneurons were seeded at a density of 1,500 cells/$mm^2$. A one-third medium change in the NMJ chambers was conducted every 2 days until day 12 of testing.

## Anti-nicotinic Acetylcholine Receptor Antibody and Human Complement Serum Dosing

After 12 days post-differentiation of SKM, systems were dosed with either an antibody against the nAChR α1 (Abcam, Cat. No. ab221868), or a non-specific IgG1 antibody (Calbiochem, Cat. No. NE1023), and human complement sera (Sigma-Aldrich, Cat. No. S1764-1ML). Systems were dosed on the SKM side with anti-nAChR antibody only (0.01–20 μg/mL), non-specific IgG1 (2.0 and 10 μg/mL), human complement sera only (0.05%), or both anti-nAChR antibody and human complement sera at 2 μg/mL and 0.05%, respectively. After dosing, systems were incubated at 37°C, 5% $CO_2$ for 3 h prior to testing.

## Electrophysiological Testing

Prior to evaluation of NMJ physiology (i.e., SKM contraction in response to MN stimulation), electrical isolation of the MN-side and SKM-side was determined to ensure no electrical leakage between compartments. Briefly, chlorinated silver electrodes connected to an epithelial voltohmmeter (EVOM) were submerged into the NMJ chambers. The current between the 2 compartments was recorded. Cultures with a resistance value <5000 Ω were excluded from further electrical testing due to risk of electrical leakage that could interfere with isolated skeletal muscle contraction. Systems that met the criteria for electrophysiological testing were transferred onto a temperature controlled heated stage set at 37°C for testing. Cultures were imaged using an upright Zeiss Hal 100 microscope and videos were recorded using a Hamamatsu digital camera (Model C8484-056) with LabVIEW software. Throughout the stimulations, myotube contractions were monitored by live video recordings of pixel differentials.

Single pulses of 4 V were manually delivered to either the SKM-side (direct stimulation) or the MN-side (indirect stimulation) and the pixel subtraction generated (pixel differentials) was used to visually quantify the total number of contracting myotubes in six different frames. The number of contracting SKMs under indirect stimulation (number of NMJs pre-stimulation) was collected within 2 min. One myotube is selected (Region of interest – ROI) from each chamber system and undergoes electrical stimulation (see stimulation protocol in **Table 1**) with pulses of increasing frequency (0.33, 0.5, 1.0, and 2.0 Hz) under indirect and direct stimulation. Skipping during the duration of each stimulation frequency was recorded. The number of synchronized contractions ($N_s$) at a given pulse was divided by the number of stimulation pulses within a set duration ($N_\tau$) to give NMJ fidelity:

$$\frac{N_s}{N_\tau} = \text{NMJ Fidelity} \quad (1)$$

After the completion of the stimulation protocol, the total number of contracting SKM under indirect stimulation (NMJs) were recorded again using manual stimulation and visual assessment of the pixel differentials. To measure the stability of NMJs per system, the total number of NMJs counted post-stimulation divided by the total number of NMJs pre-stimulation was recorded as a percentage. Each condition was subjected to this stimulation process once in at least four different systems.

**TABLE 1 |** Stimulation protocol for direct and indirect stimulation of SKM.

| Stimulation protocol | |
|---|---|
| **Frequency (Hz)** | **Duration (s)** |
| 0.33 | 60 |
| 0.5 | 40 |
| 1.0 | 20 |
| 2.0 | 10 |

## Immunocytochemistry

### General Immunocytochemistry

Monocultures of SKM at day 12 of differentiation were fixed using 4% paraformaldehyde for 10 min and washed twice with 1X PBS (Life Technologies). Cells were blocked using donkey blocking buffer (5% donkey serum, 5% bovine serum albumin, 1X PBS) for 1 h at room temperature. The cells were then incubated with primary antibodies overnight at 4°C. After overnight incubation, the primary antibody was removed, and the cells were washed with 1X PBS for 5 min per wash. The secondary antibodies were incubated for 2 h in the dark at room temperature. The secondary antibodies were removed, and the cells were washed three times with 1X PBS for 5 min each wash. The cells were then incubated with 4′,6-Diamidino-2-Phenylindole (DAPI) (Thermo Fisher Scientific, Cat. No. 62248) for 5 min. The DAPI solution was removed, and the cells were washed three times with 1X PBS for 3 min each wash. The coverslips were then mounted using a ProLong® Gold Antifade Mountant (Thermo Fisher Scientific, Cat. No. P36930). Fluorescence imaging was performed using UltraView$^{TM}$ spinning disk confocal microscope (PerkinElmer) with an Axio Observer Z1 (Carl Zeiss) stand utilizing 20x/0.75 air and 40x/0.75 air objectives. Volocity software was used to process Z-stack projections of scanned images.

### Complement Deposition Studies

The ICC protocol was followed with the following modifications: Before fixing the SKM monocultures, cells were either incubated at 37°C, 5% $CO_2$ for 3 h with a combinatory dosing of anti-nAChR Ab (Abcam, Cat. No. ab221868, 2 μg/mL) and human complement sera (Sigma-Aldrich, Cat. No. S1764-1ML, 0.05%) or single dosing of human complement sera at varying dilutions (0, 0.1, 1.0, and 10%). Cultures were rinsed with 1X PBS prior to fixing and blocking. The primary antibody used to detect complement deposition was mouse anti-C3/C3b (Abcam, Cat. No. ab11871, 1:500 dilution in blocking buffer). The corresponding secondary antibody (Life Technologies, Cat. No. A10037, anti-mouse-568, 1:250 dilution in blocking buffer) and Alexa Fluor 488 conjugated α-bungarotoxin (Life Technologies, Cat. No. B13422, 1:100 dilution in blocking buffer) were then incubated for 2 h in the dark at room temperature.

### Endogenous and Diseased Receptor Internalization Studies

The ICC protocol was followed with the following modifications: prior to SKM fixing, monocultures were either incubated at 37°C, 5% $CO_2$ for 3 h with anti-nAChR Ab (Abcam, Cat. No. ab221868, 2 μg/mL or 10 μg/mL) for diseased receptor internalization studies or with SKM medium for the endogenous internalization control. For each condition, the monocultures were either permeabilized with 0.1% Triton X-100 or not for 15 min before blocking for 1 h. The endogenous internalization control cultures (pre-incubation with medium) were fixed and then incubated for 3 h with anti-nAChR Ab (Abcam, Cat. No. ab221868, 2 μg/mL). The corresponding secondary antibodies were then added to all cultures.

Using ImageJ, myotubes were selected from at least ten fluorescence images using a freeform tool and measured against non-fluorescent backgrounds to obtain values for integrated density, area of selected cell, and mean fluorescence of background readings to calculate the corrected total cell fluorescence (CTCF) of cells +/− triton.

$$CTCF = Integrated\ density - (Area\ of\ selected\ cell\ x \\ Mean\ fluorescence\ of\ background\ readings) \quad (2)$$

To determine the nAChR internalization, the change in *CTCF* of SKM +/− triton was determined by Eq. 3 below (Howard and Sanders, 1980).

$$nAchR\ Internalization\ =\ CTCF_{+triton} - CTCF_{-triton}/ \\ CTCF_{+triton} * 100 \quad (3)$$

# RESULTS

## Anti-nicotinic Acetylcholine Receptor Antibodies Affect Neuromuscular Junction Stability and the SKM Excitation-Contraction Coupling Mechanism in a Dose-Dependent Manner

Anti-nAChR antibodies reduce NMJ stability and the SKM excitation-contraction coupling mechanism in a dose-dependent manner. Most MG autoantibodies are directed against the nAChR with more than 50% against the α subunit, specifically the main immunogenic region (MIR) in both innate and experimental autoimmune MG (EAMG; Tzartos et al., 1998; Luo et al., 2009). These nAChR autoantibodies are mainly of the IgG1 and IgG3 subclasses (Lefvert et al., 1981; Rodgaard et al., 1987) and can initiate varying disease pathogenicity depending on the epitope location (Tzartos et al., 1998). To establish the effect of the anti-nAChR IgG antibody on the NMJ *in vitro* system, a concentration curve against NMJ function was generated to evaluate NMJ stability based on criteria described in our previous publications (Santhanam et al., 2018; Guo et al., 2020b) and in the materials. In brief, after a 3 h incubation period a single field electrical stimulation was applied to the MN side of the chamber and the total number of NMJs before and after the stimulation protocol was applied, were visually assessed. This was represented as a percentage of NMJ stability. Since anti-AChR Abs can induce both direct blocking and internalization of receptors, potentially causing variable NMJ numbers at any given time, the stability of an established NMJ was evaluated instead.

The muscle-side of the NMJ systems was dosed with a commercially available antibody against nAChR for 3 h and an $IC_{50}$ of 3.4 μg/mL was generated as a function of change in NMJ stability (**Figure 3A**). A non-specific IgG1 antibody was also dosed for 3 h as a negative control and revealed no functional deficits at concentrations below and above the

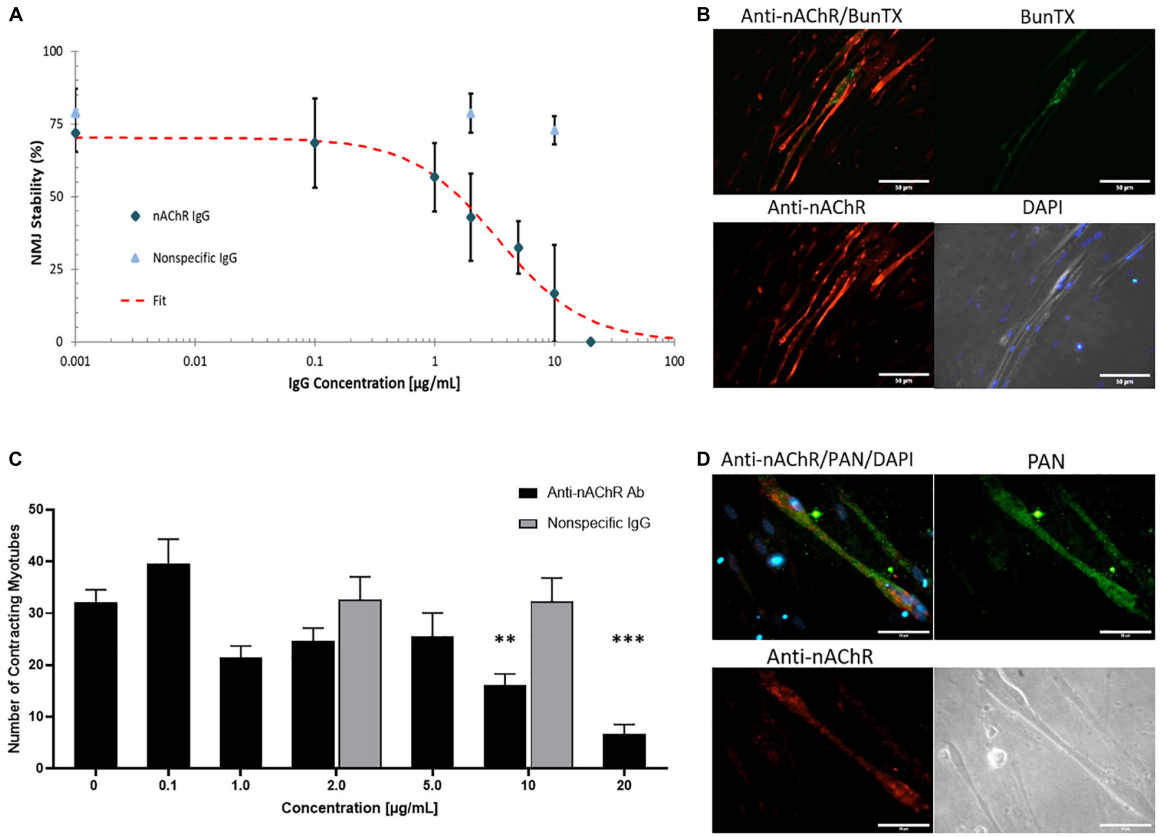


**FIGURE 3 |** Anti-nAChR IgG effects on the NMJ. **(A)** A dose response curve established from NMJ stability of SKM dosed with the anti-nAChR Ab (diamond) from 0 to 20 µg/mL resulting in an IC50 of 3.4 µg/mL (*N* = 2, 3–10 replicates). A non-specific IgG antibody (triangle) did not significantly alter NMJ stability at 2 and 10 µg/mL (*N* = 2, 7–8 replicates). **(B)** ICC images of SKM revealing the antibody-antigen complex with the binding of anti-nAChR Ab (red channel) to the cell surface near the endplate marked by BunTX (green channel), overlay of red and green channels (upper left) and phase image with DAPI (lower right). Scale bars = 50 microns. **(C)** The number of contracting SKM under direct stimulation at dosing concentrations from 0 to 20 µg/mL (*N* = 2, 3–10 replicates). Statistics: One-way ANOVA followed by Dunnett's test (alpha = 0.05) $^{**}p < 0.020$, $^{***}p < 0.002$. **(D)** ICC images of SKM with anti-nAChR Ab staining (red channel), sodium channel (Pan, green channel), overlay of red and green channels (upper left) and phase image on lower right. Scale bars = 50 microns.

established $IC_{50}$ of the antagonistic antibody (**Figure 3A**). Dose-dependent reduction in NMJ stability with anti-nAChR IgG compared to no effect from the negative control, substantiated the specificity of the anti-nAChR antibody in the *in vitro* NMJ system. The formation of the antibody-antigen complex on the SKM was confirmed by ICC with dual BunTX and anti-nAChR Ab staining (**Figure 3B**). The specific IgG anti-nAChR Ab binds near the cell surface endplate marked by BunTX. Since distinguishing the mechanism of antibody binding as direct blocking, antigenic modulation, or complement activation is difficult, the direct effects of anti-nAChR Abs on muscle contraction was investigated (**Figure 3C**). Prior to NMJ testing, direct stimulation of the skeletal muscle (SKM) was initiated and the number of contracting myotubes were measured to establish baseline function. Upon dosing with the antagonist antibody into the muscle chamber, no significant change in the number of contracting myotubes was observed at concentrations equal to or less than 5 µg/mL. However, a significant decrease ($p = 0.0145$ and $p = 0.0018$) in the number of contracting myotubes under direct stimulation at 10 and 20 µg/mL dose of anti-nAChR Ab compared to no dose (0 µg/mL) was observed (**Figure 3C**). There was no significant change at low or high concentrations (2 and 10 µg/mL, respectively) of non-specific IgG compared to no dose. This functional effect had not previously been described in EAMG or clinical studies, however, due to the compartmentalized nature of the NMJ system, motoneuron independent stimulation or direct stimulation of the muscle can be tested. We speculate that this decrease in functional myotubes was due to a reduction of the number of plasma membrane-bound ion channels involved in the excitation-contraction coupling mechanism. Since the human *in vitro* cultures do not exhibit the structures of the NMJ found *in vivo* where postsynaptic machinery form indentions isolating nAChRs, but instead cluster near diffuse receptors responsible for excitation-contraction machinery, it is possible that endocytosis is not limited to nAChRs. Antigenic modulation would not only cause internalization of surface nAChRs but also decrease the number of neighboring receptors, particularly sodium and calcium channel receptors. To further evaluate this possibility, immunocytochemical analysis of sodium channels ($Na_v$-PAN)

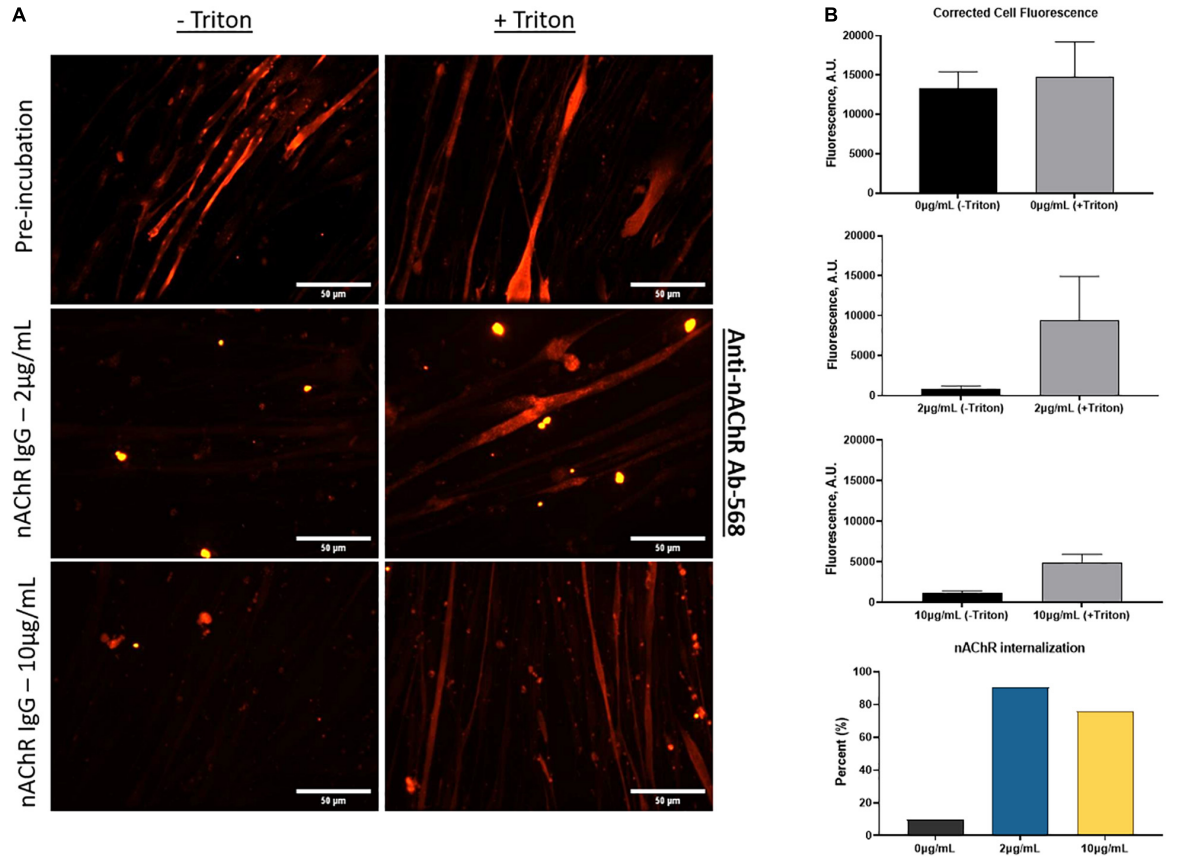


**FIGURE 4 |** Anti-nAChR Abs induce receptor internalization. **(A)** ICC images of SKM stained for anti-nAChR Ab with and without triton (top panel), incubated with 2 μg/mL or 10 μg/mL anti-nAChR Ab, middle and bottom panels, respectively, and later fixed and blocked with and without triton. Scale bars = 50 microns. **(B)** The corrected total cell fluorescence between the surface receptors (black bars) and internalized receptors (gray bars) for each condition. The percent change in fluorescence is represented as a bar graph for nAChR internalization.

revealed a proximity and abundance of PAN channels near nAChRs on the skeletal muscle (**Figure 3D**). A loss of sodium channels, and the resultant reduction in sodium current, in MG patients, increasing the threshold for triggering an endplate potential (EPP; Ruff and Lennon, 1998, 2008). Therefore, the reduction of contracting myotubes at higher concentrations of antibody in **Figure 3C** maybe due, in part, to an increase in internalization and a decrease in neighboring ion receptors critical for eliciting a contractile response.

## Addition of Anti-nicotinic Acetylcholine Receptor Antibodies Increases Receptor Internalization

Cells continuously internalize surface receptors by receptor mediated endocytosis. The internalized receptors can undergo a multifaceted array of recycling or degradative pathways. MG patient autoantibodies can induce increased recycling and degradation of AChRs and although significant progress has been made, the mechanism of endocytosis and receptor trafficking is still not well understood (Heinemann et al., 1977; Kao and Drachman, 1977; Drachman et al., 1978; Merlie et al., 1979; Lee et al., 2014). To evaluate whether the anti-nAChR Abs act as modulating antibodies, inducing receptor internalization, the endogenous internalization of nAChRs was first assessed. This evaluation was achieved by fluorescently tagging nAChRs on SKM that were treated with and without a permeabilizing detergent (i.e., Triton X-100). The location of the nAChRs was monitored by labeling the receptors and quantifying the degree of fluorescently tagged receptors that were internalized (with triton) to those on the cell membrane (no triton) using Eq. 2. This steady state of receptor recycling was then compared to internalization due to antigenic modulation by incubation with the anti-nAChR Ab at either 2 or 10 μg/mL. Immunofluorescence analysis of the nAChRs on the SKM surface (no triton) vs. internalized (with triton) is shown in **Figure 4A** with the corresponding corrected cell fluorescence in **Figure 4B** (top three panels). The endogenous internalization of the nAChRs was shown to be continuously recycled as the overall fluorescence for both conditions was similar (**Figure 4B**, top panel). When the anti-nAChR Ab was incubated in the SKM compartment at 2 and 10 μg/mL, there was a near 9-fold and 7-fold increase, respectively, of internalized receptors compared to the pre-incubated SKM (**Figure 4B**, fourth panel). Surprisingly, incubation with 10 μg/mL anti-nAChR Ab

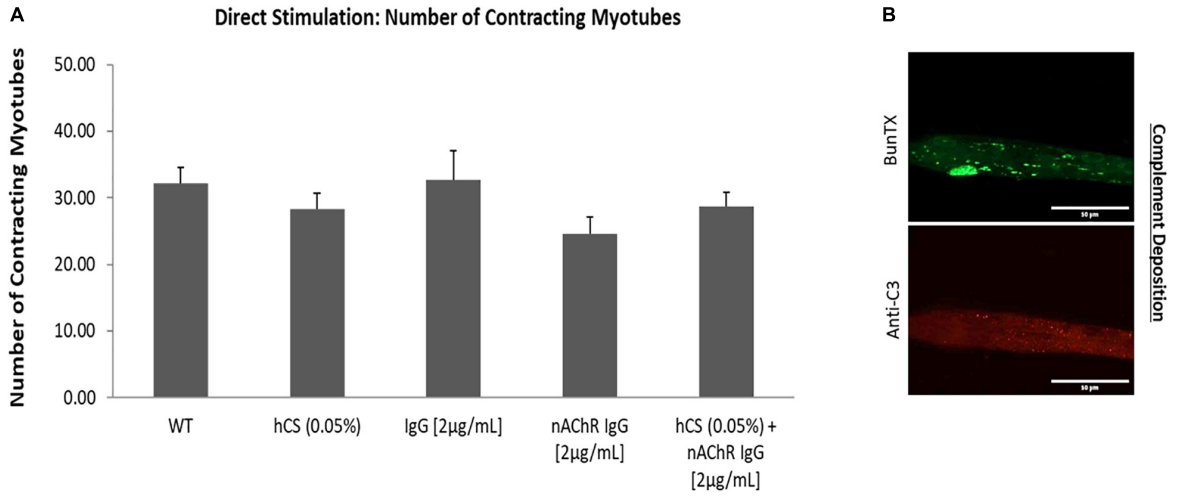


**FIGURE 5 |** Direct effects of hCS and anti-nAChR on SKM. **(A)** Demonstrates the number of contracting myotubes under direct stimulation after dosing with 0.05% hCS (*N* = 2, 8 replicates), non-specific IgG (2 μg/mL, *N* = 3, 8 replicates), anti-nAChR-Ab (2 μg/mL, *N* = 2, 10 replicates) and a combination of 0.05% hCS and 2 μg/mL anti-nAChR-Ab (*N* = 2, 9 replicates). **(B)** ICC images of SKM incubated with 2 μg/mL of anti-nAChR with 0.05% hCS for 3 h and stained with anti-C3 (red channel) and BunTX (green channel). Scale bars = 50 microns.

resulted in a lower increase in receptor internalization compared to 2 μg/mL. We propose this observation was due to an increased rate of internalization and degradation, as well as downregulation of the receptor expression. However, further experiments will be necessary to confirm this hypothesis. Increased internalization and degradation would support the decrease in the number of contracting myotubes observed under direct stimulation of SKM at 10 μg/mL (**Figure 3C**).

## Complement Deposition at the Neuromuscular Junction Significantly Reduces Neuromuscular Junction and SKM Fidelity

The previous experiments determined that the addition of the anti-nAChR Ab can disrupt NMJ stability in a dose-dependent manner. Increased internalization was also confirmed with addition of antibody compared to pre-incubated SKM resulting in a decrease in the number of functional myotubes at higher concentrations of the antibody (>10 μg/mL). To further understand deficits observed in MG, the antibody-induced complement cascade was activated with the addition of anti-nAChR Ab (2 μg/mL) and human complement serum (hCS, 0.05%). To avoid non-specific deposition of complement (Ab-free induced activation), the optimal dosing of complement proteins on the SKM, based on maximal dosing without complement deposition, was confirmed. By quantifying the fluorescence intensity from complement protein 3 (C3) deposition after incubation of hCS on SKM, the optimal dosing of hCS was confirmed to be <0.1% (**Supplementary Figure 1**). To include functional deficits due to antibody-mediated deposition of complement proteins, a pre-dose of SKM with either 0.05% hCS only or non-specific IgG1 Ab (2 μg/mL) were tested to establish negative controls. To assess functional deficits, the SKM-side of the system was dosed with either 2 μg/mL of anti-nAChR Ab only or the combination of 0.05% hCS and anti-nAChR Ab (2 μg/mL). After direct stimulation of the SKM-side of the chambers, there were no significant effects on the number of contracting myotubes compared to negative controls (**Figure 5A**). Immunofluorescent analysis of complement activation revealed deposition of complement protein C3 on the SKM after incubation with 2 μg/mL of anti-nAChR Ab and 0.05% hCS (**Figure 5B**). Deposition confirmed that the antibody can induce activation of the complement cascade, but not reduce the number of contracting myotubes at that combinatory dosage.

Neurological tests for MG patients include repetitive stimulation of the nerve at 3 Hz to reveal a decline in the compound muscle action potential (CMAP; Liik and Punga, 2016; Gilhus et al., 2019) and single fiber electromyography (SFEMG) to measure neurological jitters or synchrony between the time of nerve stimulation and muscle contraction (Thornton and Michell, 2012). To mimic the clinical phenotype of neurological jitters (we describe here as fidelity), the muscle was electrically stimulated at 2 Hz and the number of resulting synchronized contractions over the number of stimulation pulses was evaluated (Eq. 1). Representative images of the five conditions under direct and indirect stimulation at 2 Hz is shown in **Figure 6A**. Once analyzed, the synchrony readouts from each chamber under direct stimulation at 2 Hz demonstrated a ∼60% reduction in fidelity after complement activation with no change observed with the anti-nAChR Ab alone (**Figure 6B**). Subsequent indirect stimulation of SKM revealed a nearly 57% and 45% reduction in NMJ fidelity in the presence of anti-nAChR Ab and complement activation (hCS + anti-nAChR Ab), respectively, compared to negative controls (**Figure 6C**). The combinatory deficits found under both direct and indirect stimulation of systems dosed with compliment sera and antibody

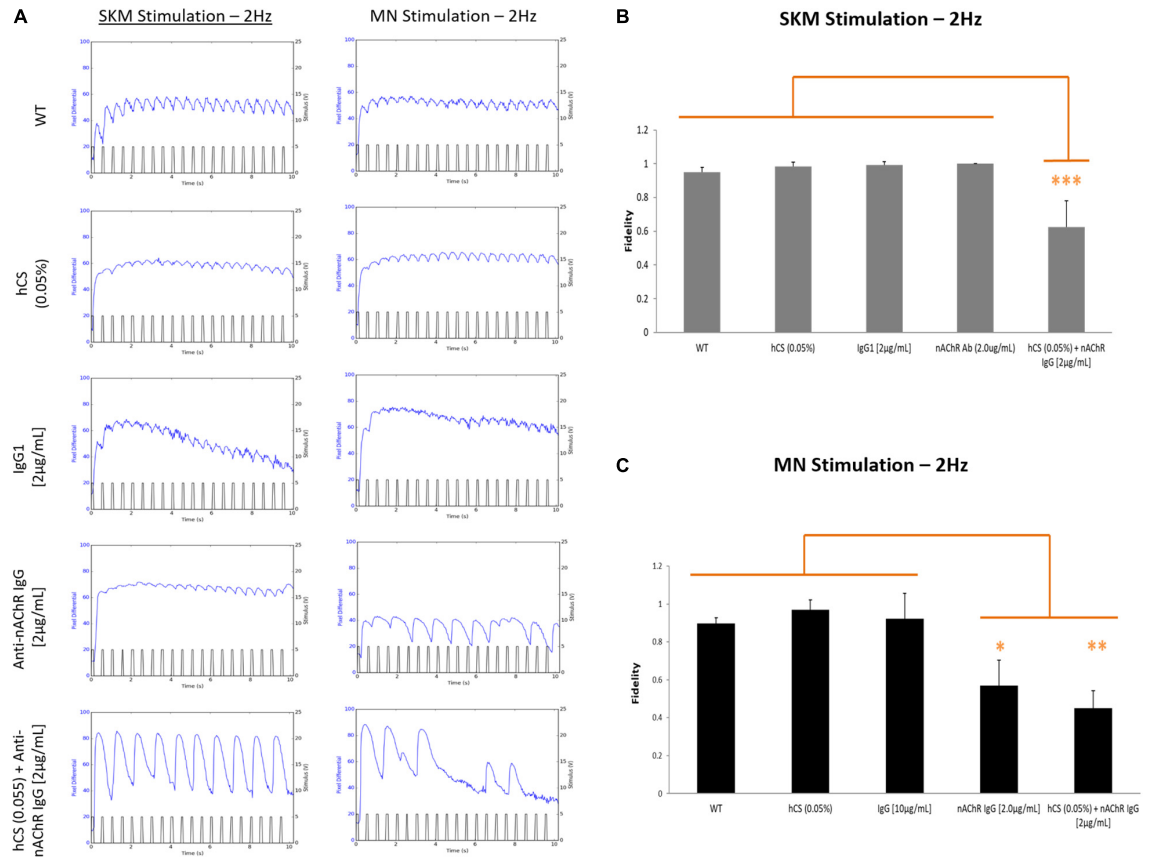


**FIGURE 6 |** Complement activation reduces SKM and NMJ fidelity. SKM fidelity at 2 Hz under direct and indirect stimulation after incubation with 0.05% hCS ($N$ = 2, 6 replicates), non-specific IgG1 ($N$ = 3, 7 replicates), anti-nAChR Ab and a combination of 0.05% hCS ($N$ = 2, 4 replicates) and 2 μg/mL of anti-nAChR Ab ($N$ = 2, 4 replicates). **(A)** Representative stimulation traces generated at 2 Hz from both direct (SKM stimulation) and indirect (MN stimulation) of a myotube under the five conditions. Mean fidelity of peaks under direct **(B)** and indirect **(C)** stimulation. Significant reduction of fidelity with antibody and complement under direct and indirect stimulation and antibody only under indirect stimulation. Statistics: Fisher LSD Method *$p < 0.050$; **$p < 0.020$; ***$p < 0.010$.

suggests that we can mimic a more severe pathology when complement is activated.

## DISCUSSION

Here we report the use of our established human *in vitro* NMJ BioMEMs system (Santhanam et al., 2018; Guo et al., 2020b) to dose SKM with a commercially available antibody against nAChR to simulate the three proposed pathogenic mechanisms of MG – blocking, modulation, and binding (**Figure 1**). Our work was complementary to the clinical phenotype produced from MG patients. In MG, anti-nAChR antibodies reduce the number of AChRs at the endplate resulting in decrease sensitivity to acetylcholine (ACh), impairment of sodium ($Na^+$) channels and increased threshold depolarization needed to trigger an action potential (AP), ultimately decreasing the safety factor (SF) for neuromuscular transmission (Ruff and Lennon, 2008). We have shown in our functional NMJ system and subsequent ICC, reduction in NMJ stability and excitation-contraction coupling capability of SKM in the presence of anti-nAChR Abs in a dose-dependent manner. An increase in receptor internalization due to modulation of Abs was also observed compared to pre-dosed SKM. This effect appears to be sensitive to antibody concentration as higher concentrations of antibody had a reduction in recycling and possibly an increase in degradation. Further evaluation of AChR degradation through reduction of AChR clusters will be needed to confirm this speculation. We have also noted that the proximity of sodium ($Na^+$) channels to AChR clusters could result in reduction of $Na^+$ channels during antibody mediated internalization of AChRs. A reduction of $Na^+$ channels and AChRs has been linked to a reduced safety factor (neuromuscular transmission) in MG patients (Ruff and Lennon, 2008) and therefore is a reasonable explanation of the reduction of functional NMJs found in our model system. Complement deposition was also confirmed in the presence of anti-nAChR Ab to the antigen on the cell surface through ICC from complement protein C3 staining near the endplate. Complement activation significantly altered the excitation-coupling capabilities of SKM and NMJ SKM fidelity at 2 Hz. In electromyography (EMG) laboratories, a frequency of 3 Hz is standard for RNS to assess neurological diseases (Zivković and Shipe, 2005; Selvan, 2011;

Stålberg et al., 2017). In our fidelity studies, we were able to detect deficits at lower frequency with no significant change below 2 Hz (data not shown). This similarity in frequencies suggests that our *in vitro* systems are translatable to the physical tests measured in clinical studies (Stålberg et al., 2017; Patel and Pobre, 2020). Altogether, this combinatory fidelity readout mimics the clinical phenotype of neurological blocking or "jitters" and suggests binding antibodies with complement activation may have a more persistent disease pathology. Based on these data, we believe the synchronous firing metric is important for mimicking the clinical hallmarks of MG – neurological jitters and reduction of AChRs.

Myasthenia gravis is a disorder caused by specific autoantibodies at the neuromuscular junction. The current methods for MG diagnosis include serological tests for specific antibodies (Sanders et al., 2014; Li et al., 2019) and electrodiagnostic test for repetitive nerve stimulation (RNS) to monitor deficits in neuromuscular transmission (Tim and Sanders, 1994). However, there are varying antibodies that contribute to MG and the identification of the most common Ab, anti-AChR Ab, has not been linked to disease severity (Sanders et al., 2014). Additionally, electrodiagnostic tests are invasive and painful and the results can be misinterpreted with other neuromuscular diseases. Once diagnosed, MG patients are subject to broad-based immunosuppressive treatments (IST) that are relatively effective in regulating symptoms, however, long-term side-effects and susceptibility to life threatening infections are often intolerable for patients (Sanders et al., 2016). The development of more directed therapeutics has helped reduce toxicity and create more fast acting and effective treatments. For example, eculizumab, the first FDA approved treatment for MG, is a monoclonal antibody that prevents the cleavage of C5 and essentially inhibits complement-mediated membrane lysis (Wijnsma et al., 2019). For patients that suffer from binding antibodies that activate the complement cascade, this drug reduces the severity of their symptoms, however, additional IST treatments are required as eculizumab only inhibits terminal complement activation but does control circulating antibodies that can lead to muscle fatigue. Animal models of MG (EAMG) are currently used to analyze MG pathology and study new interventions including induction of peripheral tolerance in the thymus, immunomodulating dendritic cells to induce tolerance and protect from autoimmune diseases, inhibitors of complement activation and RNA interference (Mantegazza et al., 2016). Despite EAMG models reproducing some aspects of the disease pathology, several differences are apparent including the inability to recapitulate the spontaneous disease progression, alterations, and general involvement of the thymus in EAMG. In addition, there are inherent differences between animal and human innate and adaptive immunity including immune system development, activation, and response (Mestas and Hughes, 2004). Therefore, any response in EAMG may not occur in the same way as in humans and therefore should be considered with these differences in mind.

Although our system is the first human MG model system to mimic the three pathogenic mechanisms in a concentration-dependent manner, we understand that our functional model needs further complexity to begin to deduce mechanistic insights. In future studies, we will dose our NMJ systems with MG patient sera and extrapolate the anti-AChR Ab concentration to the NMJ functional readout using our concentration curve. Dosing of MG sera within an NMJ system is not a new concept as rudimentary neuromuscular function has been assessed through optogenetics (MN-side only) and chemical stimulation (Bakooshli et al., 2019; Vila et al., 2019). However, the novelty of our system allows not only for a graded response due to Ab concentration but also the ability to assess complement-induced responses under direct and indirect electrical stimulation. In addition, we will be able to use this MG model system to test current therapeutics for MG and its ability to reverse the patient specific disease phenotype. Furthermore, we understand the limitations of our system and like EAMG models, we will not be able to mimic the contributions of the thymus in MG unless we develop a multi-organ model. We are confident that our human MG system has the potential to be a sensitive mimic of MG pathology and provide a quick and cost-effective platform to evaluate patient-specific treatment and DMTs.

## DATA AVAILABILITY STATEMENT

The raw data supporting the conclusions of this article will be made available by the authors, without undue reservation.

## AUTHOR CONTRIBUTIONS

VS, JR, and JH designed the experiments. VS and HN conducted the experiments. VS, JR, CL, and JH contributed to data analysis and interpretation. CL contributed to statistics. VS, HN, and JH drafted the original manuscript. VS, CL, JR, MS, and JH edited the manuscript. MS and JH provided funding acquisition and project administration. All authors contributed to the article and approved the submitted version.

## FUNDING

Funding for this research was provided by the National Institutes of Health grant number R01NS050452 and National Center for Advancing Translational Sciences of the National Institutes of Health under Award Number R44TR001326.

## ACKNOWLEDGMENTS

We thank Jeffrey Guptill (Duke University School of Medicine) and Christopher McAleer for their comments and edits to the manuscript.

## SUPPLEMENTARY MATERIAL

The Supplementary Material for this article can be found online at: https://www.frontiersin.org/articles/10.3389/fcell.2021.745897/full#supplementary-material

## REFERENCES


Arnold, A. S., Gill, J., Christe, M., Ruiz, R., McGuirk, S., St-Pierre, J., et al. (2014). Morphological and functional remodelling of the neuromuscular junction by skeletal muscle PGC-1α. *Nat. Commun.* 5:3569. doi: 10.1038/ncomms4569

Baggi, F., Antozzi, C., Toscani, C., and Cordiglieri, C. (2012). Acetylcholine receptor-induced experimental myasthenia gravis: what have we learned from animal models after three decades? *Arch. Immunol. Ther. Exp.* 60, 19–30. doi: 10.1007/s00005-011-0158-6

Bakooshli, M. A., Lippmann, E. S., Mulcahy, B., Iyer, N., Nguyen, C. T., Tung, K., et al. (2019). A 3D culture model of innervated human skeletal muscle enables studies of the adult neuromuscular junction. *Elife* 8:e44530. doi: 10.7554/eLife.44530

Bellin, M., Marchetto, M. C., Gage, F. H., and Mummery, C. L. (2012). Induced pluripotent stem cells: the new patient? *Nat. Rev. Mol. Cell Biol.* 13, 713–726.

Bufler, J., Kahlert, S., Tzartos, S., Toyka, K. V., Maelicke, A., and Franke, C. (1996). Activation and blockade of mouse muscle nicotinic channels by antibodies directed against thebinding site of the acetylcholine receptor. *J. Physiol.* 492, 107–114. doi: 10.1113/jphysiol.1996.sp021293

Burges, J., Wray, W. D., Pizzighella, S., Hall, Z., and Vincent, A. (1990). A myasthenia gravis plasma immunoglobin reduces miniature endplate potentials at human endplates in vitro. *Muscle Nerve* 13, 407–413. doi: 10.1002/mus.880130507

Christadoss, P., Poussin, M., and Deng, C. (2000). Animal models of myasthenia gravis. *Clin. Immunol.* 94, 75–87. doi: 10.1006/clim.1999.4807

Conti-Fine, B. M., Milani, M., and Kaminski, H. J. (2006). Myasthenia gravis: past, present, and future. *J. Clin. Invest.* 116, 2843–2854. doi: 10.1172/jci29894

Drachman, D. B., Angus, C. W., Adams, R. N., Michelson, J. D., and Hoffman, G. J. (1978). Myasthenic antibodies cross-link acetylcholine receptors to accelerate degradation. *N. Engl. J. Med.* 298, 1116–1122. doi: 10.1056/nejm197805182982004

Falk, D. J., Todd, A. G., Lee, S., Soustek, M. S., ElMallah, M. K., Fuller, D. D., et al. (2015). Peripheral nerve and neuromuscular junction pathology in Pompe disease. *Hum. Mol. Genet.* 24, 625–636. doi: 10.1093/hmg/ddu476

Giese, C., and Marx, U. (2014). Human immunity in vitro - solving immunogenicity and more. *Adv. Drug Deliv. Rev.* 69-70, 103–122. doi: 10.1016/j.addr.2013.12.011

Gilhus, N. E. (2016). Myasthenia gravis. *N. Engl. J. Med.* 375, 2570–2581.

Gilhus, N. E., and Verschuuren, J. J. (2015). Myasthenia gravis: subgroup classification and therapeutic strategies. *Lancet Neurol.* 14, 1023–1036. doi: 10.1016/S1474-4422(15)00145-3

Gilhus, N. E., Tzartos, S., Evoli, A., Palace, J., Burns, T. M., and Verschuuren, J. J. G. M. (2019). Myasthenia gravis. *Nat. Rev. Dis. Primers* 5:30.

Guo, X., Badu-Mensah, A., Thomas, M. C., McAleer, C. W., and Hickman, J. J. (2020a). Characterization of functional human skeletal myotubes and neuromuscular junction derived-from the same induced pluripotent stem cell source. *Bioengineering* 7:133. doi: 10.3390/bioengineering7040133

Guo, X., Gonzalez, M., Stancescu, M., Vandenburgh, H., and Hickman, J. J. (2011). Neuromuscular junction formation between human stem cell-derived motoneurons and human skeletal muscle in a defined system. *Biomaterials* 32, 9602–9611. doi: 10.1016/j.biomaterials.2011.09.014

Guo, X., Smith, V., Jackson, M., Tran, M., Thomas, M., Patel, A., et al. (2020b). A human-based functional NMJ system for personalized ALS modeling and drug testing. *Adv. Ther.* 3:2000133. doi: 10.1002/adtp.202000133

Heinemann, S., Bevan, S., Kullberg, R., Lindstrom, J., and Rice, J. (1977). Modulation of acetylcholine receptor by antibody against the receptor. *Proc. Natl. Acad. Sci. U.S.A.* 74, 3090–3094. doi: 10.1073/pnas.74.7.3090

Howard, F. M. J., Lennon, V. A., Finley, J., Matsumoto, J., and Elveback, L. R. (1987). Clinical correlations of antibodies that bind, block, or modulate human acetylcholine receptors in myasthenia gravis. *Ann. N.Y. Acad. Sci.* 505, 526–538. doi: 10.1111/j.1749-6632.1987.tb51321.x

Howard, J. F. J., and Sanders, D. B. (1980). Passive transfer of human myasthenia gravis to rats: 1. electrophysiology of the developing neuromuscular block. *Neurology* 30, 760–764. doi: 10.1212/wnl.30.7.760

Kang, S. Y., Oh, J. H., Song, S. K., Lee, J. S., Choi, J. C., and Kang, J. H. (2015). Both binding and blocking antibodies correlate with disease severity in myasthenia gravis. *Neurol. Sci.* 36, 1167–1171. doi: 10.1007/s10072-015-2236-8

Kao, I., and Drachman, D. B. (1977). Myasthenic immunoglobulin accelerates acetylcholine receptor degradation. *Science* 196, 527–529.

Kerty, E., Elsais, A., Argov, Z., Evoli, A., and Gilhus, N. E. (2014). EFNS/ENS guidelines for the treatment of ocular myasthenia. *Eur. J. Neurol.* 21, 687–693.

Lang, B., Richardson, G., Rees, J., Vincent, A., and Newsom-Davis, J. (1988). Plasma from myasthenia gravis patients reduces acetylcholine receptor agonist-induced Naþflux intoTE671 cell line. *J. Neuroimmunol.* 19, 141–148. doi: 10.1016/0165-5728(88)90043-4

Lee, C. W., Zhang, H., Geng, L., and Peng, H. B. (2014). Crosslinking-induced endocytosis of acetylcholine receptors by quantum dots. *PLoS One* 9:e90187. doi: 10.1371/journal.pone.0090187

Lefvert, A. K., Cuenoud, S., and Fulpius, B. W. (1981). Binding properties and subclass distribution of anti-acetylcholine receptor antibodies in myasthenia gravis. *J. Neuroimmunol.* 1, 125–135. doi: 10.1016/0165-5728(81)90015-1

Leite, M. I., Waters, P., and Vincent, A. (2010). Diagnostic use of autoantibodies in myasthenia gravis. *Autoimmunity* 43, 371–379. doi: 10.3109/08916930903541208

Li, Y., Peng, Y., and Yang, H. (2019). Serological diagnosis of myasthenia gravis and its clinical significance. *Ann. Transl. Med.* doi: 10.21037/atm.2019.07.86

Liik, M., and Punga, A. R. (2016). Repetitive nerve stimulation often fails to detect abnormal decrement in acute severe generalized myasthenia gravis. *Clin. Neurophysiol.* 127, 3480–3484. doi: 10.1016/j.clinph.2016.09.012

Lindstrom, J. (2000). Acetylcholine receptors and myasthenia. *Muscle Nerve* 23, 453–477.

Losen, M., Martinez-Martinez, P., Molenaar, P. C., Lazaridis, K., Tzartos, S., Brenner, T., et al. (2015). Standardization of the experimental autoimmune myasthenia gravis (EAMG) model by immunization of rats with Torpedo californica acetylcholine receptors–Recommendations for methods and experimental designs. *Exp. Neurol.* 270, 18–28. doi: 10.1016/j.expneurol.2015.03.010

Luo, J., Taylor, P., Losen, M., de Baets, M. H., Shelton, G. D., and Lindstrom, J. (2009). Main immunogenic region structure promotes binding of conformation-dependent myasthenia gravis autoantibodies, nicotinic acetylcholine receptor conformation maturation, and agonist sensitivity. *J. Neurosci.* 29, 13898–13908. doi: 10.1523/JNEUROSCI.2833-09.2009

Mantegazza, R., Cordiglieri, C., Consonni, A., and Baggi, F. (2016). Animal models of myasthenia gravis: utility and limitations. *Int. J. Gen. Med.* 9, 53–64. doi: 10.2147/ijgm.s88552

Meriggioli, M. N., and Sanders, D. B. (2009). Autoimmune myasthenia gravis: emerging clinical and biological heterogeneity. *Lancet Neurol.* 8, 475–490. doi: 10.1016/s1474-4422(09)70063-8

Meriggioli, M. N., and Sanders, D. B. (2012). Muscle autoantibodies in myasthenia gravis: beyond diagnosis. *Expert Rev. Clin. Immunol.* 8, 427–438.

Merlie, J. P., Heinemann, S., and Lindstrom, J. M. (1979). Acetylcholine receptor degradation in adult rat diaphragms in organ culture and the effect of anti-acetylcholine receptor antibodies. *J. Biol. Chem.* 254, 6320–6327.

Mestas, J., and Hughes, C. C. W. (2004). Of mice and not men: differences between mouse and human immunology. *J. Immunol.* 172, 2731–2738. doi: 10.4049/jimmunol.172.5.2731

Park, H. S., Liu, S., McDonald, J., Thakor, N., and Yang, I. H. (2013). Neuromuscular junction in a microfluidic device. *Annu. Int. Conf. IEEE Eng. Med. Biol. Soc.* 2013, 2833–2835. doi: 10.1109/EMBC.2013.6610130

Patel, P., and Pobre, T. (2020). *Electrodiagnostic Evaluation Of Neuromuscular Junction Disorder*. Treasure Island, FL: StatPearls.

Patrick, J., Lindstrom, J., Culp, B., and Mcmillan, J. (1973). Studies on purified eel acetylcholine receptor and anti-acetlycholine receptor antibody. *Proc. Natl. Acad. Sci. U.S.A.* 70, 3334–3338. doi: 10.1073/pnas.70.12.3334

Rodgaard, A., Nielsen, F. C., Djurup, R., Somnier, F., and Gammeltoft, S. (1987). Acetylcholine receptor antibody in myasthenia gravis: predominance of IgG subclasses 1 and 3. *Clin. Exp. Immunol.* 67, 82–88.

Ruff, R. L., and Lennon, V. A. (1998). Endplate voltage-gated sodium channels are lost in clinical and experimental myasthenia gravis. *Ann. Neurol.* 43, 370–379. doi: 10.1002/ana.410430315

Ruff, R. L., and Lennon, V. A. (2008). How myasthenia gravis alters the safety factor for neuromuscular transmission. *J. Neuroimmunol.* 201–202, 13–20. doi: 10.1016/j.jneuroim.2008.04.038

Sanders, D. B., Burns, T. M., Cutter, G. R., Massey, J. M., Juel, V. C., Hobson-Webb, L., et al. (2014). Does change in acetylcholine receptor antibody level correlate with clinical change in myasthenia gravis. *Muscle Nerve* 49, 483–486. doi: 10.1002/mus.23944

Sanders, D. B., Wolfe, G. I., Benatar, M., Evoli, A., Gilhus, N., Illa, I., et al. (2016). International consensus guidance for management of myasthenia gravis. *Neurology* 87, 419–425.

Santhanam, N., Kumanchik, L., Guo, X., Sommerhage, F., Cai, Y., Jackson, M., et al. (2018). Stem cell derived phenotypic human neuromuscular junction model for dose response evaluation of therapeutics. *Biomaterials* 166, 64–78. doi: 10.1016/j.biomaterials.2018.02.047

Sato, T., and Clevers, H. (2013). Growing self-organizing mini-guts from a single intestinal stem cell: mechanism and applications. *Science* 340, 1190–1194. doi: 10.1126/science.1234852

Selvan, V. A. (2011). Single-fiber EMG: a review. *Ann. Indian Acad. Neurol.* 14, 64–67. doi: 10.4103/0972-2327.78058

Sleigh, J. N., Burgess, R. W., Gillingwater, T. H., and Cader, M. Z. (2014). Morphological analysis of neuromuscular junction development and degeneration in rodent lumbrical muscles. *J. Neurosci. Methods* 227, 159–165. doi: 10.1016/j.jneumeth.2014.02.005

Smith, A. S. T., Long, C. J., Pirozzi, K., and Hickman, J. J. (2013). A functional system for high-content screening of neuromuscular junctions in vitro. *Technology* 1, 37–48. doi: 10.1142/S2339547813500015

Stålberg, E., Sanders, D. B., and Kouyoumdjian, J. A. (2017). Pitfalls and errors in measuring jitter. *Clin. Neurophysiol.* 128, 2233–2241. doi: 10.1016/j.clinph.2017.09.001

Takahashi, K., Tanabe, K., Ohnuki, M., Narita, M., Ichisaka, T., Tomoda, K., et al. (2007). Induction of pluripotent stem cells from adult human fibroblasts by defined factors. *Cell* 131, 861–872. doi: 10.1016/j.cell.2007.11.019

Thornton, R. C., and Michell, A. W. (2012). Techniques, and applications of EMG: measuring motor units from structure to function. *J. Neurol.* 259, 585–594. doi: 10.1007/s00415-011-6350-0

Tim, R. W., and Sanders, D. B. (1994). Repetitive nerve stimulation studies in the Lambert-Eaton myasthenic syndrome. *Muscle Nerve* 17, 995–1001. doi: 10.1002/mus.880170906

Tzartos, S. J., Barkas, T., Cung, M. T., Mamalaki, A., Marraud, M., Orlewski, P., et al. (1998). Anatomy of the antigenic structure of a large membrane autoantigen, the muscle type nicotinic acetylcholine receptor. *Immunol. Rev.* 163, 89–120. doi: 10.1111/j.1600-065x.1998.tb01190.x

van de Stolpe, A., and Kauffmann, R. H. (2015). Innovative human-specific investigational approaches to autoimmune disease. *RSC Adv.* 5, 18451–18463. doi: 10.1039/c4ra15794j

Vila, O. F., Uzel, S. G. M., Ma, S. P., Williams, D., Pak, J., Kamm, R. D., et al. (2019). Quantification of human neuromuscular function through optogenetics. *Theranostics* 9, 1232–1246. doi: 10.7150/thno.25735

Whiting, P. J., Vincent, A., and Newsom-Davis, J. (1983). Acetylcholine receptor antibody characteristic in myasthenia gravis. *J. Neuroimmunol.* 5, 1–9.

Wijnsma, K. L., Heine, R. T., Moes, D. J. A. R., Langemeijer, S., Schols, S. E. M., Volokhina, E. B., et al. (2019). Pharmacology, pharmacokinetics and pharmacodynamics of eculizumab, and possibilities for an individualized approach to eculizumab. *Clin. Pharmacokinet.* 58, 859–874. doi: 10.1007/s40262-019-00742-8

Zahavi, E. E., Ionescu, A., Gluska, S., Gradus, T., Ben-Yaakov, K., and Perlson, E. (2015). A compartmentalized microfluidic neuromuscular co-culture system reveals spatial aspects of GDNF functions. *J. Cell Sci.* 128, 1241–1252. doi: 10.1242/jcs.167544

Zisimopoulou, P., Brenner, T., Trakas, N., and Tzartos, S. J. (2013). Serological diagnostics in myasthenia gravis based on novel assays and recently identified antigens. *Autoimmun. Rev.* 12, 924–930. doi: 10.1016/j.autrev.2013.03.002

Zivković, S. A., and Shipe, C. (2005). Use of repetitive nerve stimulation in the evaluation of neuromuscular junction disorders. *Am. J. Electroneurodiagnostic Technol.* 45, 248–261. doi: 10.1080/1086508x.2005.11079542

**Conflict of Interest:** JH has ownership interest and is Chief Scientist and member of the Board of Directors in Hesperos, Inc., which may benefit financially as a result of the outcomes of the research or work reported in this publication.

The remaining authors declare that the research was conducted in the absence of any commercial or financial relationships that could be construed as a potential conflict of interest.

**Publisher's Note:** All claims expressed in this article are solely those of the authors and do not necessarily represent those of their affiliated organizations, or those of the publisher, the editors and the reviewers. Any product that may be evaluated in this article, or claim that may be made by its manufacturer, is not guaranteed or endorsed by the publisher.

frontiers in Cell and Developmental Biology

REVIEW
published: 03 January 2022
doi: 10.3389/fcell.2021.801819

# An Integrated Approach to Studying Rare Neuromuscular Diseases Using Animal and Human Cell-Based Models

*Timothy J. Hines, Cathleen Lutz, Stephen A. Murray and Robert W. Burgess**

*The Jackson Laboratory, Bar Harbor, ME, United States*

As sequencing technology improves, the identification of new disease-associated genes and new alleles of known genes is rapidly increasing our understanding of the genetic underpinnings of rare diseases, including neuromuscular diseases. However, precisely because these disorders are rare and often heterogeneous, they are difficult to study in patient populations. In parallel, our ability to engineer the genomes of model organisms, such as mice or rats, has gotten increasingly efficient through techniques such as CRISPR/Cas9 genome editing, allowing the creation of precision human disease models. Such *in vivo* model systems provide an efficient means for exploring disease mechanisms and identifying therapeutic strategies. Furthermore, animal models provide a platform for preclinical studies to test the efficacy of those strategies. Determining whether the same mechanisms are involved in the human disease and confirming relevant parameters for treatment ideally involves a human experimental system. One system currently being used is induced pluripotent stem cells (iPSCs), which can then be differentiated into the relevant cell type(s) for *in vitro* confirmation of disease mechanisms and variables such as target engagement. Here we provide a demonstration of these approaches using the example of tRNA-synthetase-associated inherited peripheral neuropathies, rare forms of Charcot-Marie-Tooth disease (CMT). Mouse models have led to a better understanding of both the genetic and cellular mechanisms underlying the disease. To determine if the mechanisms are similar in human cells, we will use genetically engineered iPSC-based models. This will allow comparisons of different CMT-associated *GARS* alleles in the same genetic background, reducing the variability found between patient samples and simplifying the availability of cell-based models for a rare disease. The necessity of integrating mouse and human models, strategies for accomplishing this integration, and the challenges of doing it at scale are discussed using recently published work detailing the cellular mechanisms underlying *GARS*-associated CMT as a framework.

**Keywords: rare disease, charcot-marie-tooth disease, motor and sensory neuropathy, mouse model, iPSC model**

OPEN ACCESS

***Edited by:***
*Alec S. T. Smith,*
*University of Washington,*
*United States*

***Reviewed by:***
*Henna Tyynismaa,*
*University of Helsinki, Finland*
*Joseph W. Lewcock,*
*Genentech, Inc., United States*

****Correspondence:***
*Robert W. Burgess*
*Robert.burgess@jax.org*

***Specialty section:***
*This article was submitted to Stem Cell Research, a section of the journal Frontiers in Cell and Developmental Biology*

***Received:*** *25 October 2021*
***Accepted:*** *30 November 2021*
***Published:*** *03 January 2022*

***Citation:***
*Hines TJ, Lutz C, Murray SA and Burgess RW (2022) An Integrated Approach to Studying Rare Neuromuscular Diseases Using Animal and Human Cell-Based Models. Front. Cell Dev. Biol. 9:801819. doi: 10.3389/fcell.2021.801819*

## INTRODUCTION

The number of disease-associated genes and pathogenic variants in those genes is rapidly increasing through the efforts of large-scale discovery programs such as the Centers for Mendelian Genomics (Posey et al., 2019). According to numbers from the World Health Organization, there are now as many as 8,000 rare diseases, many of which are genetic, and in aggregate, these disorders affect ~1 in 15 people. However, there is no treatment for ~90% of these disorders. With this increased rate of discovery and ongoing unmet clinical need comes the challenge of understanding how a given mutation leads to a given disease or phenotype. In some cases, this may be clear from the known function of the mutated gene, but more frequently, it requires a detailed exploration of the underlying genetic, cellular, and molecular mechanisms. Accomplishing such studies in patient populations is challenging for both ethical and practical reasons. It is even more challenging in the case of rare diseases, where access to patients is difficult and research materials such as surgical discards or postmortem samples are not available or are too rare to provide an experimentally feasible approach. In such cases, animal models can be powerful tools for *in vivo* experimentation. Animals can be used in sufficient numbers to provide well-powered studies and are more amenable to experiments that cannot be performed in humans. Furthermore, these animal models can be used to identify possible therapeutic strategies based on the identified disease mechanism, and to test these strategies in preclinical studies.

However, translation from animal models to patients is not always successful. Notable examples of this in neuroscience and neurology are failures to translate findings in animal models of amyotrophic lateral sclerosis (ALS) or Alzheimer's Disease into successful clinical trials (Drummond and Wisniewski, 2017; Perrin, 2014; Philips and Rothstein, 2015). Sometimes this may reflect limitations of the model, such as when it does not fully recapitulate the human pathophysiology; for instance, a mouse model of CMT type 2D (CMT2D; *Gars*$^{C201R}$) develops a neuropathy with smaller axons, decreased nerve conduction velocity, grip strength, and body weight, but does not have frank axon loss. Due to the lack of axon degeneration, this would not be a good mouse model for testing therapies aimed at preventing axon loss, such as SARM1 inhibitors (Moss and Hoke, 2020). Fortunately, more severe CMT2D mouse models that do show axon degeneration exist (**Table 1**), and we will generate cell lines carrying multiple pathogenic *GARS* alleles. Alternatively, even if the mechanisms and targets are shared, the therapeutic tested in animals may not be equally effective in humans due to differences between mouse and human genetics, metabolism, or development. To address these issues and thus improve the translational potential of animal studies, it becomes necessary to also have a human experimental system. Induced pluripotent stem cells [iPSCs, (Takahashi et al., 2007)] potentially provide such a system, particularly as they can be derived directly from patients, or alternatively, specific patient mutations can be engineered into existing "healthy control" cell lines. In addition, iPSCs can be differentiated into many cell types of interest, such as motor neurons or cortical neurons, so that one is not restricted to studying neurodegeneration in skin fibroblasts or lymphocytes, for example. However, cell-based models also have inherent limitations, including the relative immaturity of their post-differentiation states, the comparatively isolated nature of the cell compared to their *in vivo* milieu, and the inevitable abstraction of the disease to a cellular phenotype (Santoso and Mccain, 2020). For example, patients do not see a neurologist because of reduced axonal transport, they go because of weakness or sensory deficits in their feet or hands, and whether improving axonal transport is truly tantamount to improving sensory/motor function *in vivo* is often a hopeful assumption.

We propose a solution to address the limitations of both animal models and cell-based models in which the findings in each are integrated to provide the best chance for successful translation of experimental approaches into clinical application. Here we will use the example of forms of Charcot-Marie-Tooth disease (CMT) to demonstrate how animal models have led to a better understanding of these diseases and have identified therapeutic targets and strategies that have been validated *in vivo*. We will also describe our strategy for using engineered human cell-based models to test whether the same pathogenic mechanisms and therapeutic strategies translate to a human system.

## TRNA SYNTHETASE-ASSOCIATED FORMS OF CHARCOT-MARIE-TOOTH DISEASE

The clinical hallmarks of CMT include degeneration and dysfunction in motor and sensory axons in the peripheral nervous system, leading to a length-dependent loss of

**TABLE 1** | Current mouse models of *Gars*/CMT2D.

| Mutation | Method of mutagenesis | Severity | Original publication |
|---|---|---|---|
| C201R | ENU-induced | Mild | Achilli et al., Dis Model Mech., 2009 |
| ΔETAQ | CRISPR knock-in | Severe | Morelli et al., J Clin Invest., 2018 |
| P278KY | Spontaneous | Severe | Seburn et al., Neuron, 2006 |
| G240R | Adenovirus overexpression | Moderate | Seo et al., J Mol Histol., 2014 |
| L129P | Adenovirus overexpression | Pain | Seo et al., J Korean Med Soc., 2014 |

***Table 1*** *The C201R allele is not found in patients. While it causes marked weakness and reduced nerve conduction velocity, it has very little axon loss in motor or sensory nerves. The ΔETAQ allele is a mouse model recreating a* de novo *human mutation. It has a severe phenotype and pronounced axon loss in motor and sensory axons beginning at a few weeks of age. The P278KY allele is also not found in patients. It has a phenotype slightly more severe than ΔETAQ and can lead to premature mortality in an inbred genetic background. All three mutations are dominant and lead to a similar activation of the integrated stress response. The G240R and L129P mouse models were generated by viral overexpression of the mutant proteins. This has the advantage of efficiently testing pathogenicity for potential gain-of-function or dominant-negative alleles, but axonopathy was not characterized in these models.*

sensation and muscle strength that is most pronounced in the feet and hands (Saporta and Shy, 2013). Mutations in close to 100 genes are now associated with CMT, suggesting a diverse array of mechanisms that can lead to a similar condition clinically (Timmerman et al., 2014; Laura et al., 2019). The largest gene family associated with CMT is the amino-acyl tRNA synthetase (aaRS) family, with dominant mutations in as many as six aaRS genes leading to forms of CMT (Wei et al., 2019). The first to be identified was Glycyl-tRNA synthetase (*GARS*), as the cause of CMT2D (Antonellis et al., 2003). Since that discovery in 2003, dominant mutations in Tyrosyl- (*YARS*), Alanyl- (*AARS*), Histidyl- (*HARS*), Tryptophanyl- (*WARS*), and possibly methionyl- (*MARS*) tRNA synthetases have been associated with forms of CMT (Jordanova et al., 2006; Latour et al., 2010; Gonzalez et al., 2013; Vester et al., 2013; Tsai et al., 2017). Most of these mutations lead to axonal forms of CMT, in which the motor and sensory axons themselves degenerate, without obvious involvement of the peripheral myelinating Schwann cells. However, mutations in *YARS* lead to an "intermediate" form of CMT (dominant intermediate CMT type C/diCMTC), with moderately reduced nerve conduction velocities, suggesting demyelination. Like many forms of CMT, the age of onset and severity vary both with gene and with the allele. For example, mutations in *GARS*/CMT2D patients may be incompletely penetrant, or lead to exclusively motor neuropathy, even in patients carrying the same allele (L129P) (Sivakumar et al., 2005). In contrast, at least one *GARS* patient was ascertained at 13 months of age with severe motor neuropathy resembling spinal muscular atrophy (Morelli et al., 2019). *GARS*/CMT2D patients are also distinctive in that they often have more severe symptoms in their hands than in their feet, whereas most forms of CMT are more severe in the lower extremities (Antonellis et al., 2003). Despite these idiosyncrasies, the neuropathies resulting from dominant tRNA synthetase mutations generally fit the clinical criteria for CMT.

How mutations in these genes lead to neuropathy was initially unclear. A primary question is whether the mutations cause a gain- or loss-of-function in the mutant protein? A second question is why the disease is specific to motor and sensory neurons, since the genes are expressed ubiquitously and involved in the "housekeeping" function of charging amino acids onto their cognate tRNAs as the first step in translation? We will summarize progress on the first point, as the genetic, cellular and molecular underpinnings of these disorders are becoming clearer, even if the second point of cellular specificity remains puzzling.

## GENETIC MECHANISMS INFORM GENE THERAPY STRATEGIES

Many of the dominant mutations in tRNA synthetase genes that cause peripheral neuropathy also cause a reduction or loss of the mutant enzyme's tRNA charging activity (Griffin et al., 2014). Furthermore, these enzymes form homodimers, and this is necessary for activity, leading to the possibility that there could be dominant negative effects in which the mutant subunit poisons the activity of the dimer. There are notable exceptions, such as *GARS*$^{E71G}$ and *YARS*$^{E196K}$, which retain most of their enzymatic activity in *in vitro* assays; however, loss of function *in vivo* could also result from mechanisms such as protein instability or mislocalization (Jordanova et al., 2006; Nangle et al., 2007).

However, data also argue against a simple loss of function and instead suggest a toxic gain-of-function (neomorphic) mechanism, in which the mutant gene product takes on a new, toxic function that cannot be corrected or out competed by the wild type gene product. First, in both humans and mice, a heterozygous null allele of *GARS* does not have a phenotype, indicating the neuropathy is not the result of a simple haploinsufficiency (Seburn et al., 2006; Oprescu et al., 2017). Furthermore, patients with recessive partial-loss-of-function mutations have severe, multisystem syndromic disorders in which peripheral neuropathy is not a prominent feature. If the dominant mutations led to peripheral neuropathy through a loss-of-function mechanism and thus served as a bellwether of dysfunction, then presumably these more severe recessive syndromes would also include peripheral neuropathy as an early and severe outcome. However, perhaps the most convincing data supporting a neomorphic activity comes from animal models. In *Drosophila*, the transgenic overexpression of mutant *GARS* or *YARS* leads to axon degeneration and CMT-relevant phenotypes, whereas overexpression of the wild-type genes has no effect, and the endogenous fly *Gars* and *Yars* are still functional (Storkebaum et al., 2009; Grice et al., 2015; Niehues et al., 2015). Indeed, levels of tRNA charging activity in tissue homogenates were never reduced below wild-type levels, arguing against a dominant negative effect leading to loss of function (Niehues et al., 2015). In a reciprocal experiment in mice, transgenic overexpression of wild-type *GARS* did not rescue the neuropathy phenotype of dominant *Gars* mutations (Motley et al., 2011). The failure of robust overexpression of the wild-type protein to rescue is most consistent with a neomorphic activity, whereas a loss of function or even dominant negative should be at least partially corrected by excess wild-type expression.

Confirming the genetic mechanism is critical for designing gene therapies, such as gene replacement or gene knockdown. As an example in neuromuscular diseases, spinal muscular atrophy can be treated by delivery of the wild-type *SMN1* gene by AAV9-mediated delivery to motor neurons (Mendell et al., 2017). This is now an approved therapeutic approach for SMA. A similar gene replacement strategy was shown to be effective in a mouse model of CMT type 4J, caused by recessive mutations in *Fig4* (Presa et al., 2021). However, the *Gars* transgenic mouse result showing that transgenic overexpression of the wild-type gene does not correct the phenotype argues against a gene replacement approach for *GARS*/CMT2D. Instead, the fact that heterozygous null mice and human carriers are healthy suggests that allele-specific knockdown of the mutant gene product while preserving the expression of the wild type allele should be an effective strategy. If done with complete efficiency and specificity, this strategy would effectively reproduce the heterozygous null situation and eliminate any neomorphic effect of the mutant protein.

This was indeed shown to be an effective strategy in mouse models (Morelli et al., 2019). Two alleles of *Gars*, including one carrying an engineered human disease-associated allele, were treated with allele-specific RNAis that precisely matched the mutant allele but mismatched with the wild-type mRNA. The RNAi was generated from an engineered mir30 microRNA shuttle that was expressed behind an RNA PolIII U6 promoter. This was delivered to the nervous system *in vivo* using self-complementary AAV9. When delivered at birth, 2–3 weeks before the onset of a neuropathy phenotype, the disease was almost completely prevented, and consistent with the perdurance of expression from AAVs, beneficial effects lasted at least 1 year. Benefit was still obtained with delivery after the onset of neuropathy, but decreased the later treatment was started. Whether the declining efficacy is because the phenotype is irreversible or whether it is because AAV9 spread and transduction efficiency decreases with age is unclear.

The preclinical gene therapy studies described above provide the *in vivo* proof-of-concept confirmation that eliminating the mutant gene product produces clinical benefit. It is likely that similar effects could be produced with other approaches, such as allele-specific antisense oligonucleotides. However, target sequence-specific strategies require extensive research and development and regulatory efforts for each new sequence entity. An alternative approach that may provide a "generic" strategy for any *GARS* mutation (or any dominant neomorphic mutation) is to knockdown all transcripts, mutant and wild type, and to replace them with a knockdown-resistant wild-type cDNA, ideally delivered in the same vector as the knockdown RNAi so that any cell getting the knockdown also gets the replacement. Such a strategy has been successfully executed in mice for alpha-1 antitrypsin (Li et al., 2011), and is being explored for *GARS*/CMT2D.

## CELLULAR AND BIOCHEMICAL MECHANISMS SUGGEST THERAPEUTIC STRATEGIES

Axonal peripheral neuropathies are generally considered to be problems of axon degeneration and clearly axon degeneration disconnects neurons from their targets, whether these are sensory endings in the periphery, or muscles in the case of motor neurons. However, in *Gars*/CMT2D mouse models, it was also shown that while axons maintained neuromuscular junctions (NMJ), but had perturbed synaptic morphology and function at the NMJ (Spaulding et al., 2016). In fact, this was true even in proximal muscles that had little frank denervation. Therefore, part of the neuromuscular phenotype of these mice could be considered a myasthenia and not just an axonal neuropathy. This raises the possibility that therapeutics designed to enhance synaptic transmission at the NMJ may be beneficial in CMT2D. Whether defects in NMJ transmission are commonplace in other axonal neuropathies remains to be tested, but it stands to reason that the axons that remain intact in these diseases may not be functioning perfectly, and that this would manifest itself at the NMJ. This possibility is now being explored in a clinical trial in CMT patients (NCT04980807). Improving synaptic transmission at the NMJ is unlikely to address the core pathophysiology of these disorders and would therefore not necessarily be expected to slow progression or promote regeneration. However, it may improve function for patients who already have the disease, and a further exploration of NMJ involvement in different forms of CMT is warranted in both mouse models and patients.

Investigations of the neomorphic activities of mutant tRNA synthetases have focused on novel interactions mediated by the mutant protein that are not found in the wild-type protein. Mutations in both *GARS* and *YARS* (also known as GlyRS and TyrRS for proteins) result in conformational changes that potentially expose new protein surfaces, enabling novel interactions (Nangle et al., 2007; Xie et al., 2007; Blocquel et al., 2017). One intriguing interaction identified is the binding of Neuropilin-1 (NRP1) to mutant GlyRS (He et al., 2015). NRP1 is a developmental receptor that has both semaphorins and vascular endothelial growth factors (VEGFs) as ligands. Both semaphorin and VEGF signaling have neurodevelopmental roles, but the binding of mutant GlyRS specifically competes with VEGF. VEGF overexpression mitigates some aspects of the neuropathy seen in Gars mutant mice. The necessity of GlyRS binding NRP1 for the disease mechanism leading to neuropathy is called into question by the failure of NRP1 to bind ΔETAQ, a four amino acid internal deletion in GlyRS that causes a severe, early onset neuropathy in both mice and humans (Morelli et al., 2019). Nonetheless, several other neuropathy-associated mutant GlyRS proteins bind NRP1, as do CMT2N-associated alleles of *AARS*, suggesting that it may in some way be contributing to the disease severity and pathogenesis (He et al., 2015; Sun et al., 2021). This also suggests that small molecules to block this interaction or antibodies to clear mutant GlyRS proteins could be therapeutic strategies.

Recent results suggest an alternative biochemical mechanism that may extend more logically across the tRNA synthetase-associated neuropathies (**Figure 1**). The mutant forms of GlyRS and TyrRS bind their cognate tRNAs, but have a much slower off-rate, effectively resulting in the sequestration of the tRNAs and precluding their transfer to the ribosome to participate in translation. Consistent with tRNA sequestration being considered a toxic, gain-of-function activity, overexpression of mutant forms of *GARS* in HEK293 cells resulted in ribosome stalling at Glycine codons, as expected if the mutant enzymes were expressed at high enough levels to sequester tRNAs in cell types where the tRNAs are not typically limiting (Mendonsa et al., 2021). In addition to these biochemical findings, this mechanism is also supported genetically for *GARS*. The overexpression of $tRNA^{Gly}$ rescues neuropathy and axon degeneration phenotypes in both mouse and fly models of *GARS*/CMT2D (Zuko et al., 2021). This is in contrast to overexpression of the wild-type synthetase in mice (Motley et al., 2011), which despite being active does not rescue, and would have a paucity of tRNA substrate to charge under this mechanistic model.

The result of tRNA sequestration is stalling of elongating ribosomes at Glycine codons. Stalled ribosomes are potent

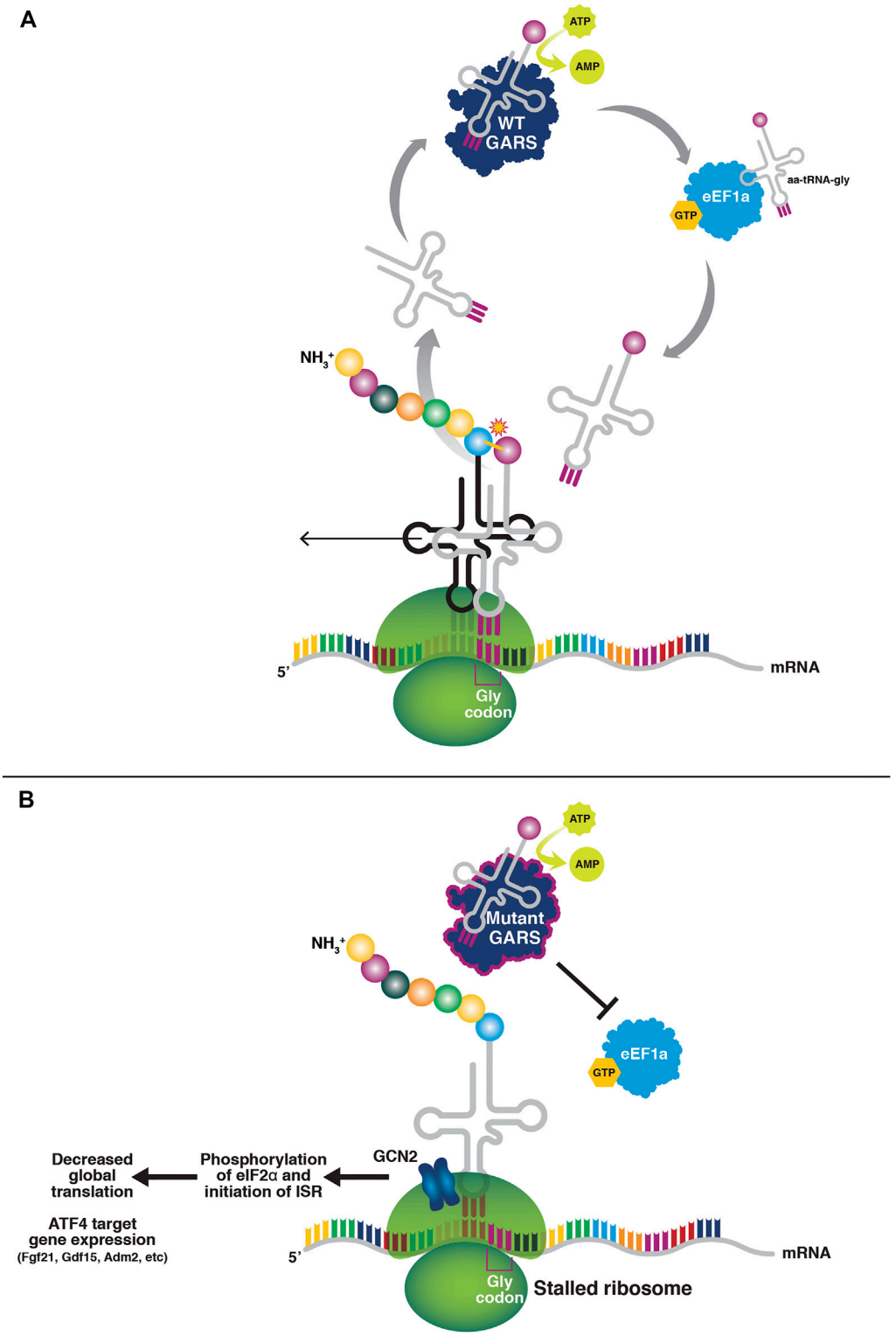


**FIGURE 1 |** tRNA sequestration by mutant tRNA synthetases. **(A)** In normal tRNA charging, the amino acid binds the tRNA synthetase and is coupled with ATP to form an aminoadenylate intermediate. The amino acid is then charged onto the 3′ end of the cognate tRNA. The amino acid-charged tRNA is shuttled to the ribosome by eEF1A to participate in translation. **(B)** Mutant tRNA synthetases do not release the tRNAs to eEF1A, thus resulting in a paucity of charged tRNAs for translation elongation and subsequently ribosome stalling at Glycine codons (in the case of mutant glycyl tRNA-synthetase). The stalled ribosomes activate GCN2 and the integrated stress response, resulting in a suppression of global cap-dependent translation through eIF2α phosphorylation, and activation of ATF4 target gene expression.

activators of the kinase GCN2 and subsequently, the integrated stress response (ISR) (Inglis et al., 2019). Interestingly, mitochondrial dysfunction is also an ISR activator, and GlyRS is a bifunctional enzyme that also encodes the mitochondrial glycyl-tRNA synthetase (Turner et al., 2000). In fact, patients with recessive loss-of-function *GARS* mutations experience a multisystem developmental syndrome with mitochondrial abnormalities (Mcmillan et al., 2014; Oprescu et al., 2017). While mitochondrial dysfunction has not been explicitly ruled out as an activator of the ISR in mouse models of CMT2D, the fact that TyrRS (and all of the other known CMT-associated synthetases, AlaRS, HisRS, MetRS, and TrpRS) is cytosolic and not mitochondrial, yet CMT-associated *YARS* mutations in mice and humans cause a similar phenotype, argues against mitochondrial involvement as the primary disease mechanism.

The ISR is beneficial under many forms of cellular stress (Pakos-Zebrucka et al., 2016). For example, amino acid starvation also causes uncharged tRNA and stalled ribosomes, both of which activate GCN2. The result is the phosphorylation of elongation initiation factor 2-alpha (eIF2α). This globally suppresses cap-dependent translation. In addition, the translation of the stress-response transcription factor, ATF4, is increased through an upstream open reading frame mechanism that regulates its synthesis (Vattem and Wek, 2004). ATF4 promotes the expression of cell-type-specific stress response genes. Thus, by suppressing cap-dependent translation and enhancing expression of stress response genes, the ISR can be beneficial in the face of a transient stress such as amino acid starvation.

Importantly, in tRNA synthetase-associated CMTs, the ISR is not being activated by a transient stress, but instead by the chronic sequestration of tRNAs. In an analogous case of neurodegeneration caused by ribosome stalling during translation elongation due to a combination of a $tRNA^{Ala}$ mutation and loss of GTPBP2, which rescues stalled ribosomes from mRNAs, the inhibition of GCN2 and the ISR is detrimental, exacerbating the associated neurodegeneration (Ishimura et al., 2014; Ishimura et al., 2016). However, in the case of *Gars*/CMT2D mouse models, genetically deleting or pharmacologically inhibiting GCN2 not only eliminates ISR activation, but also greatly mitigates the severity of the neuropathy phenotype (Spaulding et al., 2021). That an experimental drug was also effective in mitigating neuropathy in the Gars mice speaks to the translational potential of inhibiting GCN2 to treat dominant tRNA synthetase-associated peripheral neuropathies.

Although these studies provide a biochemical mechanism through which tRNA synthetase mutations may act and identify GCN2 as a therapeutic target, they do not directly resolve whether the neuropathy results from the further decrease in protein synthesis that results from phosphorylation of eIF2α, from a toxic effect of ATF4 target-gene expression, or from a combination of these ISR actions. Nor does this biochemical mechanism explain the cell-type specificity of the disease and why only alpha motor neurons and a subset of sensory neurons are affected. The finding that the ISR is similarly activated in both *Gars* and *Yars* mutant mice suggests that this mechanism may be in play across the tRNA synthetase-associated neuropathies, though this remains to be tested for mutations in *HARS*, *WARS* and *AARS*. Furthermore, though the *Gars*/CMT2D mouse models accurately recapitulate the human disease, it also remains to be determined whether the same ISR mechanism is active in human motor and sensory neurons. Circulating levels of one prominently upregulated, secreted ATF4 target gene, GDF15, were elevated in patients with tRNA synthetase mutations; however, GDF15 was also elevated in *PMP22*/CMT1A patients (Spaulding et al., 2021). This is interesting and may suggest GDF15 is a general biomarker for multiple forms of CMT, but it makes the direct relevance to ISR activation in the tRNA synthetase mutations less definitive. Confirming activation of the ISR and further exploring the biochemical mechanisms and cellular specificity of the disease are all questions that can be efficiently addressed using human cell-based models.

## HUMAN CELL-BASED MODELS OF TRNA SYNTHETASE-ASSOCIATED NEUROPATHY

Rare diseases present a challenge for iPSC derivation and experimentation. Namely, patients are challenging to find and generating an experimentally robust battery of patient-derived cell lines accounting for multiple genes and multiple alleles of each gene, as well as other biological variables such as sex, age, and ethnicity may simply not be feasible. Other technical variables, such as the cell type from which the iPSCs were derived, the protocol for reprogramming those cells, and the culture conditions may all create additional complications, particularly if cell lines are being sourced globally and are not being generated through a centralized facility or research program. While there are large research programs attempting to overcome these challenges by increasing the number of control and mutant cell lines being compared, such as AnswerALS (https://www.answerals.org/), for most laboratories, it would quickly lead to even the simplest experiments becoming unwieldy.

One possible solution to these practical and technical challenges is to use engineered cell-based models. Efficient genome editing in human cell lines makes the introduction of most human disease-associated mutations in a "healthy control" iPSC line relatively straightforward (**Figure 2**). For rigor, these mutations can be introduced into multiple cell lines to begin to capture human genetic diversity. Cell-based models can also be engineered so that they can be reverted, such that both the parental cell line and the revertant can serve as controls for the mutated cell line. The use of revertant cells is most important when the pathogenicity of the allele is uncertain, or if only a single pathogenic variant is known or available, as is sometimes the case for rare diseases. For patient-derived cells, revertant cells would control for genetic background by fixing the causative mutation. In the engineered cells, revertant lines serve as a stringent control for the targeting and gene editing process required to introduce the mutation. The use of revertant strains may be unnecessary if a large number of independent disease-associated and healthy

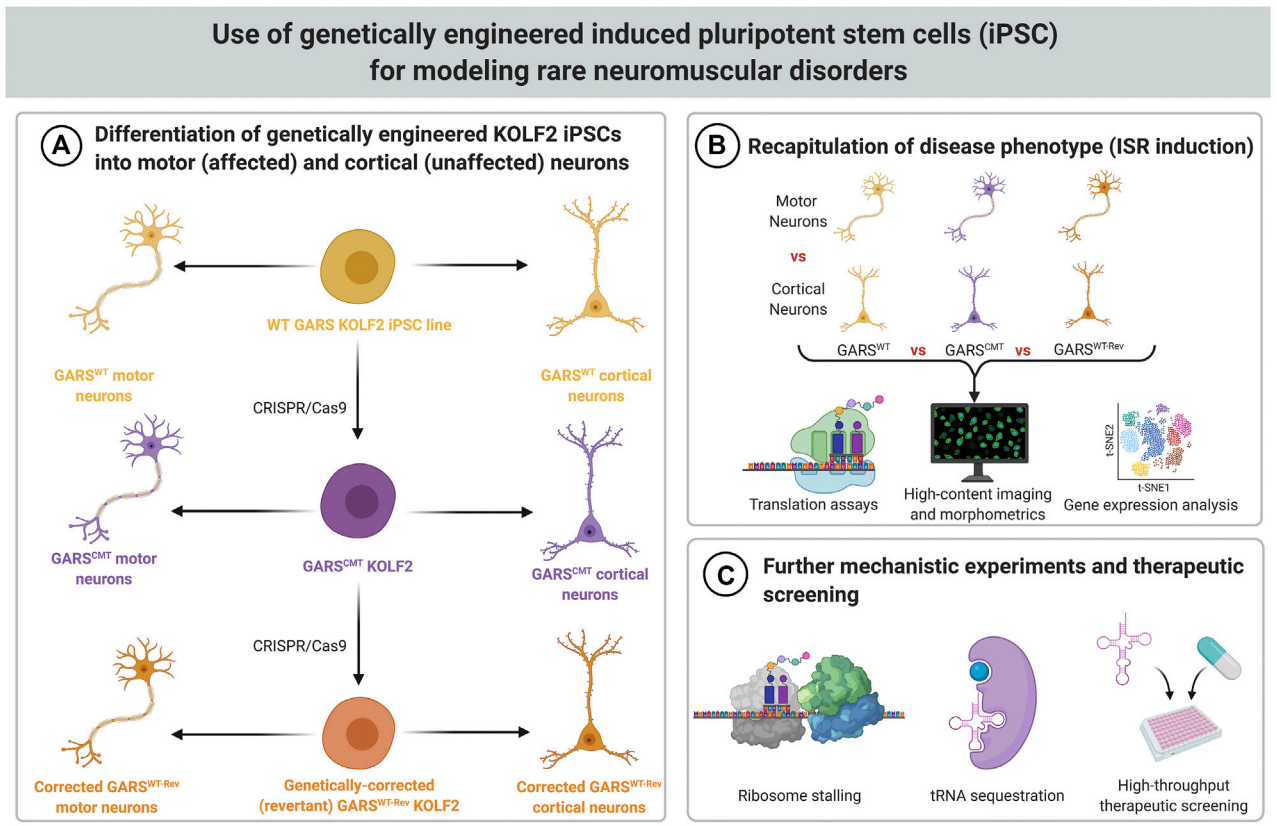


**FIGURE 2 |** Schematic for modeling rare neuromuscular disorders using genetically engineered iPSCs. **(A)** KOLF2 iPSCs genetically engineered to carry CMT-associated *GARS* mutations can be differentiated into motor neurons, which are affected by CMT, and cortical neurons, which are not affected by CMT. The wild-type parental cells and revertant cells (which have had the introduced *GARS* mutation corrected back to WT) can be used as controls. **(B)** Translation assays, high content imaging and morphometrics, and gene expression analysis can be used to determine if the ISR is activated in *GARS* mutant motor neurons. **(C)** If motor neurons have the expected phenotype (ISR induction), then they can be used for further mechanistic experiments, such as ribosome stalling assays and analysis of biochemical properties of tRNA sequestration. These cells can also be used for high-throughput screens of therapeutics.

control cell lines are available. In such a case, rigor is provided by consistency across independent cell lines and the use of revertant cell lines could again make the approach unwieldy.

Another advantage of the engineered cell lines is that multiple, related mutations can be introduced independently into the same cell line. Thus, cell-based models, each carrying a disease-associated allele of *GARS*, for example, can be generated and compared to otherwise isogenic lines carrying mutations in other tRNA synthetase genes such as *YARS*, *AARS*, *WARS* or *HARS*. Much like engineering disease models in a single inbred mouse strain allows for consistency and an "apples-to-apples" comparison of phenotypes and mechanisms, these cell-based models should vary only in their disease-associated mutation or allele that they carry. This approach of introducing disease-associated variants into a well-defined cell line is being used to study genes and variants associated with Alzheimer's and related dementias, through the iPSC Neurodegenerative Disease Initiative (iNDI) program, for example (Ramos et al., 2021).

In addition to the obvious advantage of demonstrating the same pathophysiological mechanisms are engaged in a human disease model, iPSC-based models also have advantages for exploring disease mechanisms (**Figure 2**). In the case of *GARS*/CMT2D, the human disease is a predominantly motor neuropathy, and there are no reproducible pleiotropic effects. In mouse models, the activation of the integrated stress response is specific to alpha motor neurons and a subset of sensory neurons, and presumably this indicates that ribosome stalling is restricted to these cell types. Consistent with this, when the ribosome rescue factor *Gtpbp2* was genetically deleted, the neuropathy phenotype of *Gars* mice become more severe, providing indirect genetic evidence for ribosome stalling; however, the ISR did not appear in other cell types even after the ribosome rescue factor was deleted (Zuko et al., 2021).

This specificity of ribosome stalling presents a challenge for detailed studies of this mechanism *in vivo*. Motor neurons represent a small fraction of the total cells in the spinal cord, and ribosomes isolated from bulk tissue complicate interpretation of assays such as ribosome footprinting, in which RNase digestion removes mRNA except those regions protected by a stalled ribosome. Such assays could identify particular mRNAs or particular Glycine codons that are particularly sensitive to ribosome stalling in motor neurons. The latter may identify

specific anticodon tRNAs that are most limiting after sequestration by the mutant synthetase. Since iPSCs can be differentiated to motor neurons with high efficiency, resulting in a relatively homogeneous population of cells, experiments such as ribosome footprinting will be much more straightforward in cell-based models, where ribosomes can be rapidly isolated from the bulk culture. It is even possible to generate specific sub-populations of motor neurons, such as cranial motor neurons, or limb-innervating lateral motor column motor neurons (Amoroso et al., 2013; An et al., 2019). This is additional degree of differentiation is potentially useful given that CMT2D primarily affects spinal alpha motor neurons.

The homogeneity and scalability of culture systems will also be an advantage for probing the cell-type specificity of ISR activation. The same iPSCs can be differentiated into motor neurons, where we expect to see ISR activation, or into a closely related cell type, such as cortical neurons, or even an unrelated cell type such as cardiac myocytes, where we do not expect to see ISR activation. Thus, detailed characterization of gene expression, codon usage, tRNA expression, and other parameters can be performed to see if they may explain why motor neurons exhibit ribosome stalling and ISR activation and other cell types do not.

## ENHANCING CELL MATURITY AND EXPLORING CELL BIOLOGICAL MECHANISMS

While the homogeneity of an iPSC-based system can be a great advantage for the types of studies detailed above, it may also be beneficial for us to use a co-culture system with motor neurons and other relevant cell types. For example, human iPSC-derived co-cultures of astrocytes and motor neurons were recently used in a study showing that astrocytes exhibit non-cell autonomous effects on motor neurons in an *in vitro* ALS model (Zhao et al., 2020). For studies on neuromuscular disease, co-cultures of iPSC-derived motor neurons with skeletal muscle cells (such as those derived from C2C12 mouse myoblasts, primary human-derived myoblasts, or differentiated from hiPSCs, with varying degrees of difficulty and availability) to simulate a simplified version of the neuromuscular system present *in vivo*, and allowing for assays of NMJ function (Demestre et al., 2015; Picchiarelli et al., 2019; Lin et al., 2020; Yoshioka et al., 2020; Stoklund Dittlau et al., 2021). Furthermore, organoid culture systems allow for the differentiation of multiple cell types to form a miniature version and experimentally approachable model of the tissue of interest (Vieira de Sa et al., 2021). Recently, iPSC-derived human sensorimotor organoids, which contain motor and sensory neurons, skeletal muscle, astrocytes, microglia, and vasculature, have been used to assess how familial ALS mutations affect NMJ and muscle function *in vitro* (Pereira et al., 2021).

In addition to single-well co-cultures, a variety of multiple compartmentalized culture platforms are also available. These house the motor neurons and muscle cells in separate chambers with microgrooves between them, which allows the motor axons to extend through the grooves to form a spatially and chemically isolated synapse on the muscle cells (Santhanam et al., 2018; Altman et al., 2019; Ionescu and Perlson, 2019). An added benefit of this system is that treatments can be restricted to either the cell body compartment or the axon terminal/muscle compartment if using microfluidic chambers. A recently published protocol describes the creation of an "NMJ chip"—a 3D culture system with neurons and myocytes in separate compartments which form functional NMJs and allows imaging and functional assessment of the motor unit. The myocyte compartment contains two pillars made of flexible polydimethylsiloxane (PDMS) to which the myocytes attach to form a skeletal muscle bundle. Muscle contractile force is measured based on the flexion of the PDMS pillars (Osaki et al., 2018; Osaki et al., 2020). One advantage of the single-well co-culture systems is that they do not require specialized culture dishes; however, the compartmentalized system allows for localized treatment of axon terminals or neuronal cell bodies.

An intriguing hypothesis regarding the motor and sensory neuron sensitivity to tRNA synthetase mutations and ribosome stalling relates to translation in distal axons. In both mice and humans, it is the longest and largest axons that are most affected (Antonellis et al., 2003; Sleigh et al., 2014). Unfortunately, this invokes many possible mechanisms. Presumably these cells are more metabolically active to maintain their resting potential with the large cell volume and are more dependent on efficient axonal transport to maintain their distal processes, to name just two logical possibilities. However, they may also be more dependent upon local protein synthesis in the distal axon to maintain processes such as mitochondrial function that may not be sufficiently supported by transport of components from the cell body. The evidence supporting the importance of local protein synthesis in axons is increasingly convincing (Baleriola and Hengst, 2015; Spaulding and Burgess, 2017; Fernandopulle et al., 2021). Axonal translation could intersect with the tRNA sequestration mechanism described above for tRNA-synthetase-associated neuropathies if the tRNAs become limiting, and therefore most susceptible to sequestration, in the distal axon. This is very challenging to test *in vivo*, but is straightforward to test *in vitro* using compartmentalized culturing systems, which would allow levels of both mRNAs and tRNAs in axons to be compared to levels in cell bodies. In addition, manipulations such as GCN2 inhibitors could be applied specifically to axons or cell bodies to see if one compartment or the other was the primary site of ISR activation. It is unclear how such experiments could be done *in vivo*.

Thus, while caveats remain such as the maturity of the cells in culture and whether the ISR will in fact be activated *in vitro*, the iPSC cell-based models have the potential to greatly expand the level of mechanistic studies regarding translation and ribosome stalling. The cells also offer a rapid system for testing GCN2 and ISR inhibitors, with cellular level readouts of ISR such as levels of phospho-eIF2α, phospho-GCN2, or ATF4, even if frank axon degeneration is not evident in the culture system. Importantly though, even though the iPSC model may have also led to the discovery of ISR activation, the *in vivo* animal models were necessary to show that GCN2/ISR inhibition was an effective

treatment for neuropathy given that in other neurodegenerative conditions it has been found that activation of the ISR is actually neuroprotective (Ishimura et al., 2016; Sidoli et al., 2016). With this knowledge, the studies in the cell-based models can be interpreted with the sound assumption that inhibiting the ISR *in vitro* should be beneficial for treating neuropathy *in vivo*.

## SCALABILITY

The findings and proposed research above present a template for studies of rare neuromuscular diseases using a combination of animal and human cell-based models. Animal models reveal genetic mechanisms, leading to gene therapy strategies that can then be tested for *in vivo* efficacy in those same models. Similarly, animal models can reveal mechanistic insights that may again suggest therapeutic strategies, such as the identification of ISR activation as a contributor to the pathophysiology and GCN2 as a drug target for *GARS*/CMT2D. Human cell-based models can be used to confirm those same mechanisms. They also provide a higher throughput platform of compound testing and a more homogeneous system for biochemistry and -omics studies, at least compared to a cell type such as motor neurons, where the cells of interest represent a small proportion of cells resident in the tissue. However, this example is still incomplete, as the cell-based models are in their early stages of analysis, and it already represents 18 years of work if the identification of *GARS* as the causative gene for CMT2D is considered the start date. In light of this, what are the prospects for streamlining such studies and doing them at scale?

With current technologies and infrastructure, it is feasible to generate hundreds of genetically modified mouse strains every year. This is exemplified by large programs such as the Knockout Mouse Phenotyping Program (KOMP2), and even small-scale programs such as the Resource for Research on Peripheral Neuropathy (RRPN, NINDS R24 NS098523), which was able to generate multiple mouse models of human disease in any given year at the scale of a single lab and modest funding. The KOMP2 phenotyping pipeline was established to capture data for gene knockouts for the entire mammalian genome, and is (intentionally) broad and not deep for any specific physiological system (Brown et al., 2018). A given phenotype domain, such as neuromuscular performance, may be covered by only one or two tests, and is not supported by detailed physiology, histology, or biomarker analysis. Therefore, high-throughput pipelines such as KOMP2 are best suited for establishing baseline data to describe gene function, and as discovery tools to identify and prioritize disease-relevant mutant phenotypes for more extensive analysis. The output from the program has been significant. For example, data from the International Mouse Phenotyping Consortium (IMPC), to which KOMP2 contributes, has revealed that ~40% of all lines generated have phenotypic overlap with human disease and that for a significant majority, the IMPC model was the first mutant mouse line reported for the gene-disease (Meehan et al., 2017). IMPC data has been mined to identify novel disease-relevant phenotype associations for deafness, metabolic disease, and skeletal abnormalities, among others (Bowl et al., 2017; Rozman et al., 2018; Swan et al., 2020). Although the KOMP2 program has focused on generating null alleles, repurposing this capacity for more precise and/or disease-relevant alleles is quite feasible, and would take full advantage of the engineering and production platforms investments made to support these programs.

Despite the potential benefits of high-throughput phenotyping for target discovery and disease gene prioritization, a significant phenotyping gap remains to not only make them convincing human disease models, but also to provide the necessary information for future mechanistic and preclinical studies. Mechanistically, parameters such as the cell-autonomy and tissue-specificity of the pathophysiology, or whether the disease is developmental or degenerative need to be determined, to name just two important considerations. For preclinical studies, the age of onset, potential for sex-specific differences, the most informative outcome measures, and the rate of progression all need to be determined before any therapeutic testing can begin. While these analyses can be pipelined to some extent by running a standard battery of tests, each mouse model, like each human disease, inevitably has specific characteristics that need to be addressed, requiring a deviation from the script. All of this requires a certain amount of bespoke analysis and represents a somewhat slow and somewhat trial-and-error process that reduces throughput.

Generating *in vivo* animal models through other technologies such as viral delivery of mutant genes is also an option to increase throughput. This requires the generation of many different allele sequences and packaging these into viruses for *in vivo* delivery, but these technologies are well established. Constraints on this system are the size of constructs that can be packaged into viral vectors, and that such overexpression systems, at least in a wild-type background, will only model gain-of-function or dominant-negative alleles. Nonetheless, this approach has been used effectively in *C9ORF72* ALS, and has been attempted for *GARS*/CMT2D (**Table 1**), although axonopathy was not described (Lee et al., 2014; Seo et al., 2014; Chew et al., 2015; Herranz-Martin et al., 2017). While such viral approaches allow a large number of alleles to be generated, phenotyping is still required.

Cell-based models may offer greater opportunity to increase scale. For diseases with relatively large patient populations, generating a large and diverse patient-derived iPSC collection may be feasible. This strategy is currently being used for sporadic forms of ALS (SALS) by the Answer ALS Research Project, who hope to gather and characterize iPSCs from 1000 SALS patients to find biomarkers of the disease, determine why motor neurons are the primary affected cell type, and what role genetic background plays in these sporadic cases (https://www.answerals.org/). For rarer mutations, engineering disease-associated mutations into control iPSC lines is feasible at reasonable scale. The iNDI program is an example, where over 100 alleles of Alzheimer's and related dementia genes will be engineered into a "healthy control" iPSC line and then phenotyped in an automated platform (Ramos et al., 2021). The approach of engineering mutations into an otherwise isogenic background has other potential benefits, as described above.

Provided the cell types of interest have established differentiation protocols, experiments can largely be done using high-content imaging platforms and automated morphometry and related assays. Similarly-omics studies are highly feasible in such models. Additional assays, such as mitochondrial function, organelle trafficking, etc. can also be done with reasonable throughput. Cell lines do not necessarily have to recapitulate the disease to be useful. For example, if iPSCs engineered to carry *GARS*/CMT2D mutations show ISR activation when differentiated to motor neurons, this will be a useful model even if they do not show axon degeneration. However, this requires sufficient understanding of the disease mechanism to accurately interpret these secondary phenotypes. Ultimately, gaining that level of understanding may require an *in vivo* model, which may again limit the scale of these studies. Nonetheless, the cell-based models may identify mechanisms to be tested *in vivo*, improving efficiency, and once such mechanisms are identified, the cell-based systems provide an efficient platform for testing interventions. Approaches such as transcriptomics or biomarker analysis may also provide ways to readily bridge cell-based models with *in vivo* results and predictions.

An example of the successful use of an iPSC-based platform to interrogate disease mechanism with the goal of bringing a therapeutic to the clinic was done using cell-based models of amyotrophic lateral sclerosis (ALS). Patient iPSC-derived motor neurons with a disease-causing mutation in superoxide dismutase 1 (*SOD1*) were found to exhibit hyperexcitability. This was similar to findings from clinical neurophysiological studies (Wainger et al., 2014). This phenotype was abolished when the *SOD1* mutation was reversed in the cells using CRISPR genome editing (Kiskinis et al., 2014). In addition, it was found that the hyperexcitability was conserved across multiple forms of ALS using iPSC-derived motor neurons from patients with mutations in *C9ORF72*, *FUS*, and different *SOD1* alleles (Wainger et al., 2014). The hyperexcitability was successfully corrected and motor neuron survival increased when treated with the drug ezogabine (also known as retigabine), a Kv7.2/3 potassium channel agonist used to treat epilepsy (Wainger et al., 2014). Data from these studies led to a recently published double-blind, placebo-controlled phase 2 clinical trial using ezogabine to reduce motor neuron hyperexcitability in both familial and sporadic ALS patients. Notably, this drug was not tested in the canonical *SOD1* transgenic mouse model of ALS before moving to clinical trials, as the human cell-based data was deemed sufficient (Mcneish et al., 2015; Wainger et al., 2021).

## ADDRESSING SCALABILITY

While the challenges of creating, validating and using disease models at scale are significant, they are at least somewhat addressable. CRISPR/Cas9 technology allows for the rapid creation of patient-based mutations in mice. Mutations in any one disease gene can be strategically prioritized based on criteria, such as common mutations based on founder affects or mutations that may be more amenable to genomic based therapeutic strategies, such as ASOs, read through drugs, or gene therapy. By creating an allelic series for a particular disease-causing gene, potential therapeutics can be properly aligned with specific mutations. Phenotyping of these mouse models can also be strategically prioritized by matching prominent clinical features of the patients with a battery of tests in mice that would zero in on these deficiencies. The creation of these mini-pipelines allows for a first pass, direct interrogation of translationally relevant preclinical phenotypes that can be rapidly evaluated with specific therapeutics. Keeping in mind that ultimately, not every clinical feature in a patient may be addressable. The goal of many therapeutics is not curative but is to alleviate some of the features with the goal of improving the quality of life for patients.

Approaches for achieving this are being piloted by programs such as the JAX Center for Precision Genetics. This NIH-funded program seeks to better integrate current efforts in human genetics, disease modeling both in mice and in other systems, and preclinical studies to lessen the time from gene discovery to clinical trial. An important part of this effort is bioinformatics, to evaluate the feasibility/necessity for making a model and for optimizing the probability that such a model will be successful. For example, if a disease mechanism or relevant biological pathway is known, are some strains of inbred mice more or less likely to be good genetic backgrounds for producing valid disease models based on known differences in those pathways across mouse strains? As described above, the genome engineering capacity, although ultimately finite, is unlikely to be limiting. Instead, the phenotyping capacity for validation of disease models, as well as evaluating preclinical studies are still the most labor intensive and time-consuming phase. It is not making the model that is the challenge in 2021, it is proving it is a valid model and using it productively that takes time and effort.

## SUMMARY

We have provided an example of a rare neuromuscular disease, inherited peripheral neuropathy caused by dominant tRNA synthetase mutations, as a demonstration of how mouse and human cell-based models can be integrated to understand disease mechanisms, test therapeutic approaches, and improve the likelihood of successful translation to clinical practice. Both *in vivo* models such as mice and human cell-based models have advantages and limitations. Relying on either alone has risks, so the clear solution is to incorporate both approaches and thus hopefully minimize those risks. For each, the challenge currently is not genetically engineering the model, it is the effort of validating the model as disease-relevant and using it in well-designed preclinical studies. This is being successfully done for many diseases besides inherited peripheral neuropathies, but it remains a challenge to do it at a scale that will rapidly deliver results for the ~7,000 rare diseases now identified.

## AUTHOR CONTRIBUTIONS

All authors listed have made a substantial, direct, and intellectual contribution to the work and approved it for publication.

## FUNDING

The authors are supported by grants from the National Institutes of Health (NS054154, NS098523 and NS105116 to RB, and OD030187 to SM and CL), and the Young Investigator Draft from Uplifting Athletes and the CMTA to TH.

## ACKNOWLEDGMENTS

The authors would like to thank Jane Cha in the JAX Creative service and Emily Spaulding for assistance with **Figure 1**. **Figure 2** was adapted from "iPSC-Based Disease Modeling of Childhood Neurogenetic Disorders", by BioRender.com (2021). Retrieved from https://app.biorender.com/biorender-templates.

## REFERENCES

Altman, T., Geller, D., Kleeblatt, E., Gradus-Perry, T., and Perlson, E. (2019). An *In Vitro* Compartmental System Underlines the Contribution of Mitochondrial Immobility to the ATP Supply in the NMJ. *J. Cel Sci* 132, jcs234492. doi:10.1242/jcs.234492

Amoroso, M. W., Croft, G. F., Williams, D. J., O'Keeffe, S., Carrasco, M. A., Davis, A. R., et al. (2013). Accelerated High-Yield Generation of Limb-Innervating Motor Neurons from Human Stem Cells. *J. Neurosci.* 33, 574–586. doi:10.1523/jneurosci.0906-12.2013

An, D., Fujiki, R., Iannitelli, D. E., Smerdon, J. W., Maity, S., Rose, M. F., et al. (2019). Stem Cell-Derived Cranial and Spinal Motor Neurons Reveal Proteostatic Differences between ALS Resistant and Sensitive Motor Neurons. *Elife* 8, e44423. doi:10.7554/eLife.44423

Antonellis, A., Ellsworth, R. E., Sambuughin, N., Puls, I., Abel, A., Lee-Lin, S.-Q., et al. (2003). Glycyl tRNA Synthetase Mutations in Charcot-Marie-Tooth Disease Type 2D and Distal Spinal Muscular Atrophy Type V. *Am. J. Hum. Genet.* 72, 1293–1299. doi:10.1086/375039

Baleriola, J., and Hengst, U. (2015). Targeting Axonal Protein Synthesis in Neuroregeneration and Degeneration. *Neurotherapeutics* 12, 57–65. doi:10.1007/s13311-014-0308-8

Blocquel, D., Li, S., Wei, N., Daub, H., Sajish, M., Erfurth, M.-L., et al. (2017). Alternative Stable Conformation Capable of Protein Misinteraction Links tRNA Synthetase to Peripheral Neuropathy. *Nucleic Acids Res.* 45, 8091–8104. doi:10.1093/nar/gkx455

Bowl, M. R., Simon, M. M., Simon, M. M., Ingham, N. J., Greenaway, S., Santos, L., et al. (2017). A Large Scale Hearing Loss Screen Reveals an Extensive Unexplored Genetic Landscape for Auditory Dysfunction. *Nat. Commun.* 8, 886. doi:10.1038/s41467-017-00595-4

Brown, S. D. M., Holmes, C. C., Mallon, A.-M., Meehan, T. F., Smedley, D., and Wells, S. (2018). High-throughput Mouse Phenomics for Characterizing Mammalian Gene Function. *Nat. Rev. Genet.* 19, 357–370. doi:10.1038/s41576-018-0005-2

Chew, J., Gendron, T. F., Prudencio, M., Sasaguri, H., Zhang, Y.-J., Castanedes-Casey, M., et al. (2015). C9ORF72 Repeat Expansions in Mice Cause TDP-43 Pathology, Neuronal Loss, and Behavioral Deficits. *Science* 348, 1151–1154. doi:10.1126/science.aaa9344

Demestre, M., Orth, M., Föhr, K. J., Achberger, K., Ludolph, A. C., Liebau, S., et al. (2015). Formation and Characterisation of Neuromuscular Junctions between hiPSC Derived Motoneurons and Myotubes. *Stem Cel Res.* 15, 328–336. doi:10.1016/j.scr.2015.07.005

Drummond, E., and Wisniewski, T. (2017). Alzheimer's Disease: Experimental Models and Reality. *Acta Neuropathol.* 133, 155–175. doi:10.1007/s00401-016-1662-x

Fernandopulle, M. S., Lippincott-Schwartz, J., and Ward, M. E. (2021). RNA Transport and Local Translation in Neurodevelopmental and Neurodegenerative Disease. *Nat. Neurosci.* 24, 622–632. doi:10.1038/s41593-020-00785-2

Gonzalez, M., Mclaughlin, H., Houlden, H., Guo, M., Yo-Tsen, L., Hadjivassilious, M., et al. (2013). Exome Sequencing Identifies a Significant Variant in Methionyl-tRNA Synthetase (MARS) in a Family with Late-Onset CMT2. *J. Neurol. Neurosurg. Psychiatry* 84, 1247–1249. doi:10.1136/jnnp-2013-305049

Grice, S. J., Sleigh, J. N., Motley, W. W., Liu, J. L., Burgess, R. W., Talbot, K., et al. (2015). Dominant, Toxic Gain-Of-Function Mutations in Gars lead to Non-cell Autonomous Neuropathology. *Hum. Mol. Genet.* 24, 4397–4406. doi:10.1093/hmg/ddv176

Griffin, L. B., Sakaguchi, R., Mcguigan, D., Gonzalez, M. A., Searby, C., Zuchner, S., et al. (2014). Impaired Function Is a Common Feature of Neuropathy-Associated Glycyl-tRNA Synthetase Mutations. *Hum. Mutat.* 35, 1363–1371. doi:10.1002/humu.22681

He, W., Bai, G., Zhou, H., Wei, N., White, N. M., Lauer, J., et al. (2015). CMT2D Neuropathy Is Linked to the Neomorphic Binding Activity of Glycyl-tRNA Synthetase. *Nature* 526, 710–714. doi:10.1038/nature15510

Herranz-Martin, S., Chandran, J., Lewis, K., Mulcahy, P., Higginbottom, A., Walker, C., et al. (2017). Viral Delivery of C9orf72 Hexanucleotide Repeat Expansions in Mice Leads to Repeat-length-dependent Neuropathology and Behavioural Deficits. *Dis. Model. Mech.* 10, 859–868. doi:10.1242/dmm.029892

Inglis, A. J., Masson, G. R., Shao, S., Perisic, O., Mclaughlin, S. H., Hegde, R. S., et al. (2019). Activation of GCN2 by the Ribosomal P-Stalk. *Proc. Natl. Acad. Sci. USA* 116, 4946–4954. doi:10.1073/pnas.1813352116

Ionescu, A., and Perlson, E. (2019). Patient-derived Co-cultures for Studying ALS. *Nat. Biomed. Eng.* 3, 13–14. doi:10.1038/s41551-018-0333-8

Ishimura, R., Nagy, G., Dotu, I., Chuang, J. H., and Ackerman, S. L. (2016). Activation of GCN2 Kinase by Ribosome Stalling Links Translation Elongation with Translation Initiation. *Elife* 5, e14295. doi:10.7554/eLife.14295

Ishimura, R., Nagy, G., Dotu, I., Zhou, H., Yang, X.-L., Schimmel, P., et al. (2014). Ribosome Stalling Induced by Mutation of a CNS-specific tRNA Causes Neurodegeneration. *Science* 345, 455–459. doi:10.1126/science.1249749

Jordanova, A., Irobi, J., Thomas, F. P., Van Dijck, P., Meerschaert, K., Dewil, M., et al. (2006). Disrupted Function and Axonal Distribution of Mutant Tyrosyl-tRNA Synthetase in Dominant Intermediate Charcot-Marie-Tooth Neuropathy. *Nat. Genet.* 38, 197–202. doi:10.1038/ng1727

Kiskinis, E., Sandoe, J., Williams, L. A., Boulting, G. L., Moccia, R., Wainger, B. J., et al. (2014). Pathways Disrupted in Human ALS Motor Neurons Identified through Genetic Correction of Mutant SOD1. *Cell Stem Cell* 14, 781–795. doi:10.1016/j.stem.2014.03.004

Latour, P., Thauvin-Robinet, C., Baudelet-Méry, C., Soichot, P., Cusin, V., Faivre, L., et al. (2010). A Major Determinant for Binding and Aminoacylation of tRNAAla in Cytoplasmic Alanyl-tRNA Synthetase Is Mutated in Dominant Axonal Charcot-Marie-Tooth Disease. *Am. J. Hum. Genet.* 86, 77–82. doi:10.1016/j.ajhg.2009.12.005

Laurá, M., Pipis, M., Rossor, A. M., and Reilly, M. M. (2019). Charcot-Marie-Tooth Disease and Related Disorders: an Evolving Landscape. *Curr. Opin. Neurol.* 32, 641–650. doi:10.1097/wco.0000000000000735

Lee, S. J., Seo, A. J., Park, B. S., Jo, H. W., and Huh, Y. (2014). Neuropathic Pain Model of Peripheral Neuropathies Mediated by Mutations of Glycyl-tRNA Synthetase. *J. Korean Med. Sci.* 29, 1138–1144. doi:10.3346/jkms.2014.29.8.1138

Li, C., Xiao, P., Gray, S. J., Weinberg, M. S., and Samulski, R. J. (2011). Combination Therapy Utilizing shRNA Knockdown and an Optimized Resistant Transgene for rescue of Diseases Caused by Misfolded Proteins. *Proc. Natl. Acad. Sci.* 108, 14258–14263. doi:10.1073/pnas.1109522108

Lin, C. Y., Yoshida, M., Li, L. T., and Saito, M. K. (2020). *In Vitro* Neuromuscular Junction Induced from Human Induced Pluripotent Stem Cells. *J. Vis. Exp.* 166. doi:10.3791/61396

Mcmillan, H. J., Schwartzentruber, J., Smith, A., Lee, S., Chakraborty, P., Bulman, D. E., et al. (2014). Compound Heterozygous Mutations in Glycyl-tRNA Synthetase Are a Proposed Cause of Systemic Mitochondrial Disease. *BMC Med. Genet.* 15, 36. doi:10.1186/1471-2350-15-36

Mcneish, J., Gardner, J. P., Wainger, B. J., Woolf, C. J., and Eggan, K. (2015). From Dish to Bedside: Lessons Learned while Translating Findings from a Stem Cell Model of Disease to a Clinical Trial. *Cell Stem Cell* 17, 8–10. doi:10.1016/j.stem.2015.06.013

Meehan, T. F., Conte, N., Conte, N., West, D. B., Jacobsen, J. O., Mason, J., et al. (2017). Disease Model Discovery from 3,328 Gene Knockouts by the

International Mouse Phenotyping Consortium. *Nat. Genet.* 49, 1231–1238. doi:10.1038/ng.3901

Mendell, J. R., Al-Zaidy, S., Shell, R., Arnold, W. D., Rodino-Klapac, L. R., Prior, T. W., et al. (2017). Single-Dose Gene-Replacement Therapy for Spinal Muscular Atrophy. *N. Engl. J. Med.* 377, 1713–1722. doi:10.1056/nejmoa1706198

Mendonsa, S., Von Kuegelgen, N., Bujanic, L., and Chekulaeva, M. (2021). Charcot-Marie-Tooth Mutation in Glycyl-tRNA Synthetase Stalls Ribosomes in a Pre-accommodation State and Activates Integrated Stress Response. *Nucleic Acids Res.* 49, 10007–10017. doi:10.1093/nar/gkab730

Morelli, K. H., Griffin, L. B., Pyne, N. K., Wallace, L. M., Fowler, A. M., Oprescu, S. N., et al. (2019). Allele-specific RNA Interference Prevents Neuropathy in Charcot-Marie-Tooth Disease Type 2D Mouse Models. *J. Clin. Invest.* 129, 5568–5583. doi:10.1172/jci130600

Moss, K. R., and Höke, A. (2020). Targeting the Programmed Axon Degeneration Pathway as a Potential Therapeutic for Charcot-Marie-Tooth Disease. *Brain Res.* 1727, 146539. doi:10.1016/j.brainres.2019.146539

Motley, W. W., Seburn, K. L., Nawaz, M. H., Miers, K. E., Cheng, J., Antonellis, A., et al. (2011). Charcot-Marie-Tooth-Linked Mutant GARS Is Toxic to Peripheral Neurons Independent of Wild-type GARS Levels. *Plos Genet.* 7, e1002399. doi:10.1371/journal.pgen.1002399

Nangle, L. A., Zhang, W., Xie, W., Yang, X.-L., and Schimmel, P. (2007). Charcot Marie Tooth Disease-Associated Mutant tRNA Synthetases Linked to Altered Dimer Interface and Neurite Distribution Defect. *Proc. Natl. Acad. Sci.* 104, 11239–11244. doi:10.1073/pnas.0705055104

Niehues, S., Bussmann, J., Steffes, G., Erdmann, I., Köhrer, C., Sun, L., et al. (2015). Impaired Protein Translation in Drosophila Models for Charcot-Marie-Tooth Neuropathy Caused by Mutant tRNA Synthetases. *Nat. Commun.* 6, 7520. doi:10.1038/ncomms8520

Oprescu, S. N., Chepa-Lotrea, X., Takase, R., Golas, G., Markello, T. C., Adams, D. R., et al. (2017). Compound Heterozygosity for Loss-Of-functionGARSvariants Results in a Multisystem Developmental Syndrome that Includes Severe Growth Retardation. *Hum. Mutat.* 38, 1412–1420. doi:10.1002/humu.23287

Osaki, T., Uzel, S. G. M., and Kamm, R. D. (2018). Microphysiological 3D Model of Amyotrophic Lateral Sclerosis (ALS) from Human iPS-Derived Muscle Cells and Optogenetic Motor Neurons. *Sci. Adv.* 4, eaat5847. doi:10.1126/sciadv.aat5847

Osaki, T., Uzel, S. G. M., and Kamm, R. D. (2020). On-chip 3D Neuromuscular Model for Drug Screening and Precision Medicine in Neuromuscular Disease. *Nat. Protoc.* 15, 421–449. doi:10.1038/s41596-019-0248-1

Pakos-Zebrucka, K., Koryga, I., Mnich, K., Ljujic, M., Samali, A., and Gorman, A. M. (2016). The Integrated Stress Response. *EMBO Rep.* 17, 1374–1395. doi:10.15252/embr.201642195

Pereira, J. D., Dubreuil, D. M., Devlin, A.-C., Held, A., Sapir, Y., Berezovski, E., et al. (2021). Human Sensorimotor Organoids Derived from Healthy and Amyotrophic Lateral Sclerosis Stem Cells Form Neuromuscular Junctions. *Nat. Commun.* 12, 4744. doi:10.1038/s41467-021-24776-4

Perrin, S. (2014). Preclinical Research: Make Mouse Studies Work. *Nature* 507, 423–425. doi:10.1038/507423a

Philips, T., and Rothstein, J. D. (2015). Rodent Models of Amyotrophic Lateral Sclerosis. *Curr. Protoc. Pharmacol.* 69, 5–21. doi:10.1002/0471141755.ph0567s69

Picchiarelli, G., Demestre, M., Zuko, A., Been, M., Higelin, J., Dieterlé, S., et al. (2019). FUS-mediated Regulation of Acetylcholine Receptor Transcription at Neuromuscular Junctions Is Compromised in Amyotrophic Lateral Sclerosis. *Nat. Neurosci.* 22, 1793–1805. doi:10.1038/s41593-019-0498-9

Posey, J. E., O'Donnell-Luria, A. H., Chong, J. X., Harel, T., Jhangiani, S. N., Coban Akdemir, Z. H., et al. (2019). Insights into Genetics, Human Biology and Disease Gleaned from Family Based Genomic Studies. *Genet. Med.* 21, 798–812. doi:10.1038/s41436-018-0408-7

Presa, M., Bailey, R. M., Davis, C., Murphy, T., Cook, J., Walls, R., et al. (2021). AAV9-mediated FIG4 Delivery Prolongs Life Span in Charcot Marie Tooth Disease Type 4J Mouse Model. *J. Clin. Invest.* 131, e137159. doi:10.1172/jci137159

Ramos, D. M., Skarnes, W. C., Singleton, A. B., Cookson, M. R., and Ward, M. E. (2021). Tackling Neurodegenerative Diseases with Genomic Engineering: A New Stem Cell Initiative from the NIH. *Neuron* 109, 1080–1083. doi:10.1016/j.neuron.2021.03.022

Rozman, J., Rathkolb, B., Rathkolb, B., Oestereicher, M. A., Schütt, C., Ravindranath, A. C., et al. (2018). Identification of Genetic Elements in Metabolism by High-Throughput Mouse Phenotyping. *Nat. Commun.* 9, 288. doi:10.1038/s41467-017-01995-2

Santhanam, N., Kumanchik, L., Guo, X., Sommerhage, F., Cai, Y., Jackson, M., et al. (2018). Stem Cell Derived Phenotypic Human Neuromuscular junction Model for Dose Response Evaluation of Therapeutics. *Biomaterials* 166, 64–78. doi:10.1016/j.biomaterials.2018.02.047

Santoso, J. W., and Mccain, M. L. (2020). Neuromuscular Disease Modeling on a Chip. *Dis. Model. Mech.* 13, dmm044867. doi:10.1242/dmm.044867

Saporta, M. A., and Shy, M. E. (2013). Inherited Peripheral Neuropathies. *Neurol. Clin.* 31, 597–619. doi:10.1016/j.ncl.2013.01.009

Seburn, K. L., Nangle, L. A., Cox, G. A., Schimmel, P., and Burgess, R. W. (2006). An Active Dominant Mutation of Glycyl-tRNA Synthetase Causes Neuropathy in a Charcot-Marie-Tooth 2D Mouse Model. *Neuron* 51, 715–726. doi:10.1016/j.neuron.2006.08.027

Seo, A. J., Shin, Y. H., Lee, S. J., Kim, D., Park, B. S., Kim, S., et al. (2014). A Novel Adenoviral Vector-Mediated Mouse Model of Charcot-Marie-Tooth Type 2D (CMT2D). *J. Mol. Hist.* 45, 121–128. doi:10.1007/s10735-013-9537-0

Sidoli, M., Musner, N., Silvestri, N., Ungaro, D., D'Antonio, M., Cavener, D. R., et al. (2016). Ablation of Perk in Schwann Cells Improves Myelination in the S63del Charcot-Marie-Tooth 1B Mouse. *J. Neurosci.* 36, 11350–11361. doi:10.1523/jneurosci.1637-16.2016

Sivakumar, K., Kyriakides, T., Puls, I., Nicholson, G. A., Funalot, B., Antonellis, A., et al. (2005). Phenotypic Spectrum of Disorders Associated with Glycyl-tRNA Synthetase Mutations. *Brain* 128, 2304–2314. doi:10.1093/brain/awh590

Sleigh, J. N., Grice, S. J., Burgess, R. W., Talbot, K., and Cader, M. Z. (2014). Neuromuscular junction Maturation Defects Precede Impaired Lower Motor Neuron Connectivity in Charcot-Marie-Tooth Type 2D Mice. *Hum. Mol. Genet.* 23, 2639–2650. doi:10.1093/hmg/ddt659

Spaulding, E. L., and Burgess, R. W. (2017). Accumulating Evidence for Axonal Translation in Neuronal Homeostasis. *Front. Neurosci.* 11, 312. doi:10.3389/fnins.2017.00312

Spaulding, E. L., Hines, T. J., Bais, P., Tadenev, A. L. D., Schneider, R., Jewett, D., et al. (2021). The Integrated Stress Response Contributes to tRNA Synthetase-Associated Peripheral Neuropathy. *Science* 373, 1156–1161. doi:10.1126/science.abb3414

Spaulding, E. L., Sleigh, J. N., Morelli, K. H., Pinter, M. J., Burgess, R. W., and Seburn, K. L. (2016). Synaptic Deficits at Neuromuscular Junctions in Two Mouse Models of Charcot-Marie-Tooth Type 2d. *J. Neurosci.* 36, 3254–3267. doi:10.1523/jneurosci.1762-15.2016

Stoklund Dittlau, K., Krasnow, E. N., Fumagalli, L., Vandoorne, T., Baatsen, P., Kerstens, A., et al. (2021). Human Motor Units in Microfluidic Devices Are Impaired by FUS Mutations and Improved by HDAC6 Inhibition. *Stem Cel Rep.* 16, 2213–2227. doi:10.1016/j.stemcr.2021.03.029

Storkebaum, E., Leitão-Gonçalves, R., Godenschwege, T., Nangle, L., Mejia, M., Bosmans, I., et al. (2009). Dominant Mutations in the Tyrosyl-tRNA Synthetase Gene Recapitulate inDrosophilafeatures of Human Charcot-Marie-Tooth Neuropathy. *Pnas* 106, 11782–11787. doi:10.1073/pnas.0905339106

Sun, L., Wei, N., Kuhle, B., Blocquel, D., Novick, S., Matuszek, Z., et al. (2021). CMT2N-causing Aminoacylation Domain Mutants Enable Nrp1 Interaction with AlaRS. *Proc. Natl. Acad. Sci. U S A.* 118, e2012898118. doi:10.1073/pnas.2012898118

Swan, A. L., Schütt, C., Rozman, J., del Mar Muñiz Moreno, M., Brandmaier, S., Simon, M., et al. (2020). Mouse Mutant Phenotyping at Scale Reveals Novel Genes Controlling Bone mineral Density. *Plos Genet.* 16, e1009190. doi:10.1371/journal.pgen.1009190

Takahashi, K., Tanabe, K., Ohnuki, M., Narita, M., Ichisaka, T., Tomoda, K., et al. (2007). Induction of Pluripotent Stem Cells from Adult Human Fibroblasts by Defined Factors. *Cell* 131, 861–872. doi:10.1016/j.cell.2007.11.019

Timmerman, V., Strickland, A., and Züchner, S. (2014). Genetics of Charcot-Marie-Tooth (CMT) Disease within the Frame of the Human Genome Project Success. *Genes* 5, 13–32. doi:10.3390/genes5010013

Tsai, P.-C., Soong, B.-W., Mademan, I., Huang, Y.-H., Liu, C.-R., Hsiao, C.-T., et al. (2017). A Recurrent WARS Mutation Is a Novel Cause of Autosomal Dominant Distal Hereditary Motor Neuropathy. *Brain* 140, 1252–1266. doi:10.1093/brain/awx058

Turner, R. J., Lovato, M., and Schimmel, P. (2000). One of Two Genes Encoding Glycyl-tRNA Synthetase inSaccharomyces Cerevisiae Provides Mitochondrial and Cytoplasmic Functions. *J. Biol. Chem.* 275, 27681–27688. doi:10.1074/jbc.m003416200

Vattem, K. M., and Wek, R. C. (2004). Reinitiation Involving Upstream ORFs Regulates ATF4 mRNA Translation in Mammalian Cells. *Proc. Natl. Acad. Sci.* 101, 11269–11274. doi:10.1073/pnas.0400541101

Vester, A., Velez-Ruiz, G., Mclaughlin, H. M., Nisc Comparative Sequencing Program, J. R., Lupski, J. R., Talbot, K., et al. (2013). A Loss-Of-Function Variant in the Human Histidyl-tRNA Synthetase (HARS) Gene Is Neurotoxic *In Vivo*. *Hum. Mutat.* 34, 191–199. doi:10.1002/humu.22210

Vieira de Sá, R., Cañizares Luna, M., and Pasterkamp, R. J. (2021). Advances in Central Nervous System Organoids: A Focus on Organoid-Based Models for Motor Neuron Disease. *Tissue Eng. C: Methods* 27, 213–224. doi:10.1089/ten.tec.2020.0337

Wainger, B. J., Kiskinis, E., Mellin, C., Wiskow, O., Han, S. S. W., Sandoe, J., et al. (2014). Intrinsic Membrane Hyperexcitability of Amyotrophic Lateral Sclerosis Patient-Derived Motor Neurons. *Cel Rep.* 7, 1–11. doi:10.1016/j.celrep.2014.03.019

Wainger, B. J., Macklin, E. A., Vucic, S., Mcilduff, C. E., Paganoni, S., Maragakis, N. J., et al. (2021). Effect of Ezogabine on Cortical and Spinal Motor Neuron Excitability in Amyotrophic Lateral Sclerosis. *JAMA Neurol.* 78, 186–196. doi:10.1001/jamaneurol.2020.4300

Wei, N., Zhang, Q., and Yang, X.-L. (2019). Neurodegenerative Charcot-Marie-Tooth Disease as a Case Study to Decipher Novel Functions of Aminoacyl-tRNA Synthetases. *J. Biol. Chem.* 294, 5321–5339. doi:10.1074/jbc.rev118.002955

Xie, W., Nangle, L. A., Zhang, W., Schimmel, P., and Yang, X.-L. (2007). Long-range Structural Effects of a Charcot Marie Tooth Disease-Causing Mutation in Human Glycyl-tRNA Synthetase. *Proc. Natl. Acad. Sci.* 104, 9976–9981. doi:10.1073/pnas.0703908104

Yoshioka, K., Ito, A., Kawabe, Y., and Kamihira, M. (2020). Novel Neuromuscular junction Model in 2D and 3D Myotubes Co-cultured with Induced Pluripotent Stem Cell-Derived Motor Neurons. *J. Biosci. Bioeng.* 129, 486–493. doi:10.1016/j.jbiosc.2019.10.004

Zhao, C., Devlin, A. C., Chouhan, A. K., Selvaraj, B. T., Stavrou, M., Burr, K., et al. (2020). Mutant C9orf72 Human iPSC-derived Astrocytes Cause Non-cell Autonomous Motor Neuron Pathophysiology. *Glia* 68, 1046–1064. doi:10.1002/glia.23761

Zuko, A., Mallik, M., Thompson, R., Spaulding, E. L., Wienand, A. R., Been, M., et al. (2021). tRNA Overexpression Rescues Peripheral Neuropathy Caused by Mutations in tRNA Synthetase. *Science* 373, 1161–1166. doi:10.1126/science.abb3356

**Conflict of Interest:** The authors declare that the research was conducted in the absence of any commercial or financial relationships that could be construed as a potential conflict of interest.

**Publisher's Note:** All claims expressed in this article are solely those of the authors and do not necessarily represent those of their affiliated organizations, or those of the publisher, the editors and the reviewers. Any product that may be evaluated in this article, or claim that may be made by its manufacturer, is not guaranteed or endorsed by the publisher.

frontiers in Cell and Developmental Biology

ORIGINAL RESEARCH
published: 11 January 2022
doi: 10.3389/fcell.2021.760260

# Neuregulin 1 Drives Morphological and Phenotypical Changes in C2C12 Myotubes: Towards *De Novo* Formation of Intrafusal Fibres *In Vitro*

*Philip Barrett*[1], *Tom J. Quick*[2,3], *Vivek Mudera*[1] *and Darren J. Player*[1]*

[1]Centre for 3D Models of Health and Disease, Division of Surgery and Interventional Science, Faculty of Medical Sciences, University College London, London, United Kingdom, [2]Peripheral Nerve Injury Research Unit, Royal National Orthopaedic Hospital, London, United Kingdom, [3]UCL Centre for Nerve Engineering, University College London, London, United Kingdom

Muscle spindles are sensory organs that detect and mediate both static and dynamic muscle stretch and monitor muscle position, through a specialised cell population, termed intrafusal fibres. It is these fibres that provide a key contribution to proprioception and muscle spindle dysfunction is associated with multiple neuromuscular diseases, aging and nerve injuries. To date, there are few publications focussed on *de novo* generation and characterisation of intrafusal muscle fibres *in vitro.* To this end, current models of skeletal muscle focus on extrafusal fibres and lack an appreciation for the afferent functions of the muscle spindle. The goal of this study was to produce and define intrafusal bag and chain myotubes from differentiated C2C12 myoblasts, utilising the addition of the developmentally associated protein, Neuregulin 1 (Nrg-1). Intrafusal bag myotubes have a fusiform shape and were assigned using statistical morphological parameters. The model was further validated using immunofluorescent microscopy and western blot analysis, directed against an extensive list of putative intrafusal specific markers, as identified *in vivo*. The addition of Nrg-1 treatment resulted in a 5-fold increase in intrafusal bag myotubes (as assessed by morphology) and increased protein and gene expression of the intrafusal specific transcription factor, Egr3. Surprisingly, Nrg-1 treated myotubes had significantly reduced gene and protein expression of many intrafusal specific markers and showed no specificity towards intrafusal bag morphology. Another novel finding highlights a proliferative effect for Nrg-1 during the serum starvation-initiated differentiation phase, leading to increased nuclei counts, paired with less myotube area per myonuclei. Therefore, despite no clear collective evidence for specific intrafusal development, Nrg-1 treated myotubes share two inherent characteristics of intrafusal fibres, which contain increased satellite cell numbers and smaller myonuclear domains compared with their extrafusal neighbours. This research represents a minimalistic, monocellular C2C12 model for progression towards *de novo* intrafusal skeletal muscle generation, with the most extensive characterisation to date. Integration of intrafusal myotubes, characteristic of native, *in vivo* intrafusal skeletal muscle into future biomimetic tissue engineered models could provide platforms for developmental or disease state studies, pre-clinical screening, or clinical applications.

OPEN ACCESS

**Edited by:**
*Megan Laura McCain, University of Southern California, United States*

**Reviewed by:**
*Christopher McAleer, Hesperos Inc., United States*
*Qianru Jin, Harvard University, United States*

***Correspondence:**
*Darren J. Player*
*d.player@ucl.ac.uk*

**Specialty section:**
*This article was submitted to Stem Cell Research, a section of the journal Frontiers in Cell and Developmental Biology*

**Received:** *17 August 2021*
**Accepted:** *09 December 2021*
**Published:** *11 January 2022*

**Citation:**
*Barrett P, Quick TJ, Mudera V and Player DJ (2022) Neuregulin 1 Drives Morphological and Phenotypical Changes in C2C12 Myotubes: Towards* De Novo *Formation of Intrafusal Fibres* In Vitro. *Front. Cell Dev. Biol. 9:760260. doi: 10.3389/fcell.2021.760260*

**Keywords: muscle spindle, intrafusal, proprioception, neuromuscular, mechanoreceptor, afferents, skeletal muscle, myotubes**

## INTRODUCTION

Muscle spindles (MS) are mechanosensory organs that detect and mediate static and dynamic information about skeletal muscle fibre length, as well as rate and extent of strain (Thornell et al., 2015). There are three sub-types of intrafusal fibre; nuclear $bag_1$, $bag_2$ and chain, each have a unique morphology, innervation pattern and protein expression profiles, which contribute to a distinctive functional response to static and dynamic muscle stretch. Nuclear bag fibres have a distinctive fusiform shape with a clustering of nuclei at the equatorial region, nuclear chain fibres have a linear morphology and nuclear alignment (Macefield and Knellwolf, 2018). MS provide a significant contribution to proprioceptive function, which can be described as the sense of position and movement of parts of the body relative to one another (Macefield and Knellwolf, 2018). Impairment of proprioception and dysfunction of the MS is linked with many neuromuscular diseases including; multiple sclerosis (Feys et al., 2011; Prather et al., 2011; Fling et al., 2014) Parkinson's disease (Conte et al., 2013; Teasdale et al., 2017), muscular dystrophy (Ovalle and Dow, 1986), and peripheral nerve injuries (Cope et al., 1994; Haftel, 2005; Ruijs et al., 2005; Maas et al., 2007; Bullinger et al., 2011; Prather et al., 2011). Proprioceptive function also deteriorates in diabetic patients (van Deursen et al., 1998; Muller et al., 2008; Muramatsu et al., 2017) and during aging (Miwa et al., 1995; Shaffer and Harrison, 2007). Proprioceptive dysfunction can cause a considerable alteration in the regulation of the speed and precision of limb movement. These effects cause significant physical limitations, including; disruption to balance, locomotion and postural stability (van Deursen et al., 1998; van Deursen and Simoneau, 1999; D'Silva et al., 2016; Ettinger et al., 2018; Ferlinc et al., 2019), which can significantly negatively impact upon the individual's quality of life (Teasdale et al., 2017).

The muscle spindle proprioceptive system have been extensively studied *in vivo*, whereby studies conducted in mice, rats and cats have formed the basis of much of our current understanding (Banks, 1994, 2015; Macefield and Knellwolf, 2018). Intrafusal fibres develop from primary myotubes, whereby the onset of intrafusal specification coincides with Ia afferent innervation and initiates spindle morphogenesis (Chal and Pourquié, 2017). Approaching Ia afferents release neuregulin-1 (Nrg-1), which binds primary muscle tyrosine kinase receptors ErbB (2-4) (erythroblastic leukemia viral oncogene homologue), resulting in downstream expression of the early growth response protein-3 (Egr3) (Tourtellotte and Milbrandt, 1998; Tourtellotte et al., 2001; Albert et al., 2005; Oliveira Fernandes and Tourtellotte, 2015). Disrupting any of these key mechanisms *in vivo* results in aberrant MS development and function (Tourtellotte and Milbrandt, 1998; Andrechek et al., 2002; Hippenmeyer et al., 2002; Leu et al., 2003; Jacobson et al., 2004; Albert et al., 2005; Herndon et al., 2014; Oliveira Fernandes and Tourtellotte, 2015). To date most skeletal muscle models often neglect the integrated nature of the neuromuscular system by not accounting for afferent functions mediated via the muscle spindle. Such experiments are expensive, time consuming and extremely difficult *in vivo* considering the an adult human contains only about 50,000 muscle spindles (Kröger and Watkins, 2021).

Therefore, *in vitro* models of the MS offer the possibility to study the cellular and molecular mechanisms regulating development, function and the effect of injury and disease, in a highly controlled environment. To develop a representative model *in vitro*, it is necessary to identify and recapitulate native tissue characteristics. *In vivo*, postnatal intrafusal fibres contain a higher number of paired-domain transcription factor 7 (PAX7) positive satellite cells and retain the expression of embryonic satellite cell marker, paired-domain transcription factor 3 (PAX3) (Horst et al., 2006; Kirkpatrick et al., 2008, 2010). Their myonuclei maintain the expression of an early myogenic regulatory factor (MRF), Myf5 (Zammit et al., 2004), they remain comparatively small and have reduced myonuclear domains (volume of sarcoplasm per myonucleus) compared to extrafusal fibres (Kozeka and Ontell, 1981). They also have preferential expression of embryonic (MyHC3), neonatal (MyHC8) and specialised (MyHC6, MyHC7b) myosin heavy chains (MyHC) (Walro and Kucera, 1999; Liu et al., 2002), concomitant with the retained expression of developmental protein, Egr3 (Tourtellotte and Milbrandt, 1998; Oliveira Fernandes and Tourtellotte, 2015). To this end, when developing an *in vitro* model, it would be prudent to measure the characteristics outlined above.

Despite this, characterisation *in vitro* has largely relied on morphological identification of what have been termed "bag myotubes" (intrafusal nuclear bag fibres), alongside expression of developmental proteins or putative phenotypical proteins of intrafusal fibres as characterised *in vivo* (Jacobson et al., 2004; Rumsey et al., 2008; Colón et al., 2017, 2020; Guo et al., 2017; Qiao et al., 2018). Previous *in vitro* studies for the purpose of developing *de novo* intrafusal muscle fibres have indicated that Nrg-1 treatment (100–160 ng/ml, 12.5–20 nM) causes an increase in bag-like myotubes with an expanded equatorial region and centrally clustered nuclei in primary human and rat cells (Rumsey et al., 2008; Colón et al., 2017; Guo et al., 2017; Qiao et al., 2018), paired with high magnification images of bag myotube specific MyHC6 and Egr3 staining. (Rumsey et al., 2008; Colón et al., 2017). To date, the only quantitative protein (western blot) analysis of myogenic cells following Nrg-1 (8 ng/ml, 1 nM) treatment indicated a sharp increase of approximately 6-fold in both MyHC8 and a slow developmental isoform (Jacobson et al., 2004) (in other papers this refers to the s46 antibody (Tourtellotte et al., 2001; Albert et al., 2005), which recognises MyHC6) (Jacobson et al., 2004). However, unlike the Hickman papers, MyHC6 immunoreactivity is not exclusive to the Nrg-1 treated myotubes and there is no mention of gross morphological changes following Nrg-1 treatment and therefore no mention of bag myotube specificity associated to MyHC6.

Current models have now progressed rapidly to incorporate afferent and efferent innervation with induced pluripotent stem cell (iPSC)-derived intrafusal myotubes, while overlooking some basic structural and molecular characterisation (Colón et al., 2017; Guo et al., 2017). The extent of *de novo*, *in vitro* intrafusal fibres structural and physiological similarity to native intrafusal fibres is not yet fully elucidated. Therefore, there is a need to further characterise cell engineered, Nrg-1 induced intrafusal myotubes before they can become platforms to integrate muscle spindle associated proprioceptive physiology, disease state modelling or clinical applications. Furthermore, despite the advances in iPSC and primary cell technologies, there are significant challenges with using these cells. Myogenic cell lines (e.g., the C2C12 cell line) provide established, fusion-competent cells, are affordable, sustainable and are easy to maintain. However, the capacity for intrafusal myotube differentiation following Nrg-1 supplementation in myogenic cell lines is currently unknown.

Current literature relies a subjective determination of intrafusal morphology by the investigator (Rumsey et al., 2008, 2010; Colón et al., 2017, 2020; Guo et al., 2017). To improve objectivity, statistical morphological parameters for assigning intrafusal bag myotubes from a heterogeneous population need to be defined. Secondly, MyHC isoform protein sequences are very similar, which has suggested limitations caused by cross-reactivity of antibodies (Thornell et al., 2015). Since MyHC expression is controlled at the transcriptional level (Schiaffino et al., 2015), MyHC gene expression could be a suitable alternative to detect intrafusal specific patterns (Brown et al., 2012).

In addition, there are muscle spindle specific targets, which have not yet been applied for *in vitro* characterisation. These are; Ets variant 4 (Etv4) (Arber et al., 2000; Hippenmeyer et al., 2002), Glial cell derived neurotrophic factor (Gdnf) (Shneider et al., 2009; Schiaffino and Reggiani, 2011), neurotrophin-3 (NT3) (Chen et al., 2002; Kröger and Watkins, 2021), low- affinity neurotrophin receptor p75 (Ngfr), somatostatin receptor type 2 (Sstr2) and the type III inter- mediate filament peripherin 1 (Prph1) (Albert et al., 2005).

*In vitro* skeletal muscle research has gained momentum over the past 10 years, however there are still relatively few publications tackling cell and tissue engineering approaches to generating *de novo* intrafusal muscle fibres *in vitro* (Barrett et al., 2020) and they are not without some inconsistencies, described previously. This study presents an objective, novel method for assignment of intrafusal bag morphology and the most in-depth characterisation of myotubes following Nrg-1 treatment to-date. The aim was to determine the degree to which Nrg-1 induces an intrafusal fibre-like morphology and the extent the myotubes recapitulate features of native intrafusal fibres. Developing a well characterised *in vitro* model of intrafusal fibres using C2C12 myoblasts, will provide an investigative tool for developmental physiology, the framework for multi-cell, innervated, integrated models of the muscle spindle and relevant disease models in a defined, controlled and highly reproducible manner.

# METHODS

## Cell Culture

C2C12 cells were seeded at a density of 10,000 cells/cm$^2$ in growth medium (GM), consisting of high glucose Dulbecco's modified eagle's medium (DMEM; Sigma-Aldrich, United Kingdom), 10% foetal bovine serum (FBS; Gibco, United Kingdom), 1% antibiotic/antimycotic solution (AS; HyClone$^{TM}$ from Thermo Fisher, United Kingdom) until confluent (3 days) at 37°C and 5% $CO_2$. At day 0, cells were encouraged to differentiate by replacing the medium to low serum differentiation medium (DM) consisting of DMEM, 2% Horse serum (HyClone$^{TM}$ from Thermo Fisher, United Kingdom) and 1% AS and cultured for 8 days at 37°C and 5% $CO_2$ (**Figure 1**). Half DM was replaced every 48 h. To induce Intrafusal fibre differentiation, DM was supplemented with 100 ng/ml recombinant Nrg-1 (R&D systems, United States).

## Immunofluorescent Microscopy

Adherent cells in 24 well plates were fixed with 4% paraformaldehyde diluted in molecular grade water for 15 min at room temperature. Cells were permeabilized with 0.25% Triton X-100 in (Sigma-Aldrich, United Kingdom) PBS and blocked with 5% Horse serum (HyClone$^{TM}$ from Thermo Fisher, United Kingdom) for 30 min. Fixed and permeabilized cells were incubated with primary antibodies Egr3 (Santa Cruz Biotechnology, United States, c-390967), MyHC3 (Santa Cruz Biotechnology, sc-53091), MyHC6 (Novus Biologicals, United States, NB300-284) or MyHC8 (Invitrogen™, PA5-72846 through Thermo Fisher Scientific, United Kingdom) at 1:200 at 1:100, 1:100, 1:300 and 1:200, respectively, then incubated at 37°C for 2 h. Secondary antibodies Goat Anti-Mouse 488 (Abcam, United Kingdom, ab150113) or Goat Anti-Rabbit (Abcam, United Kingdom, ab150077) were incubated at 1:1,000 concurrently with NucBlue$^{TM}$ DAPI (Thermo Fisher, United Kingdom) and Phalloidin (Alexa Fluor, A12380) for 1 h at room temperature. Prior to imaging, PBS was removed from the wells and cells were imaged using a ZEISS Axio Observer or ZEISS LSM 880 fluorescent microscope.

## Egr3 Staining Intensity Calculations

All images were taken using the same camera and settings on Zeiss Axio Observer. In Fiji (Schindelin et al., 2012), background fluorescence was removed from images prior to experimental intensity measurements. The background fluorescence was determined by a threshold that removes 99% of positive pixel coverage (grey scale intensity above 0) from a primary negative image. Egr3 image coverage was determined as the total pixels expressing above background fluorescence divided by the total image pixels. Egr3 intensity per nuclei was calculated by dividing total image pixel intensity above background by total image nuclei number. Considering the majority of Egr3 expression occurs in the nucleus, and nuclei numbers are different between groups, making Egr3 expression relative to nuclei number negates the effect of nuclei number on Egr3 expression. Egr3 positive nuclei were visualised following background subtraction by comparing overlap with the DAPI channel.

## Quantification of Myotube Morphogenic Parameters

Using fluorescent micrographs from the control cultures at 8 days differentiation, 10 myotubes were manually identified from the

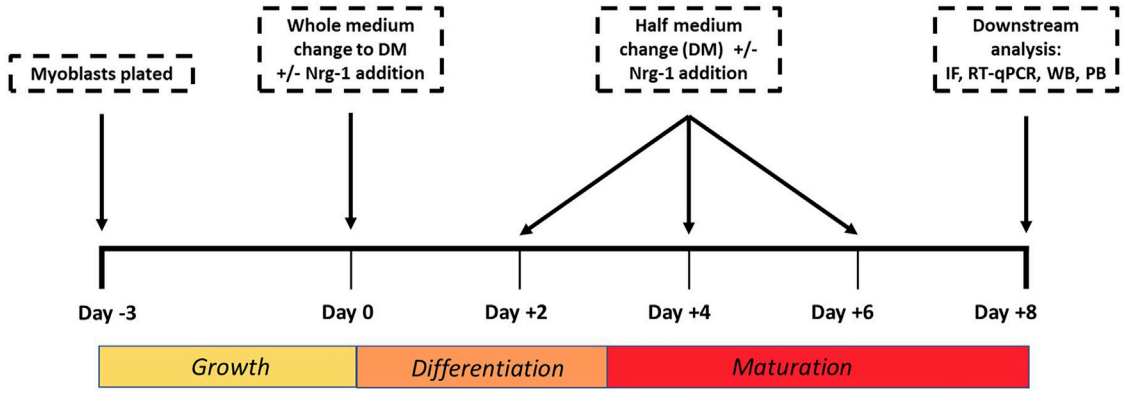


**FIGURE 1 |** Cell culture experimental timeline used to tissue engineer intrafusal skeletal muscle fibres for downstream analysis. IF (Immunofluorescence microscopy), RT- qPCR (Reverse Transcription Quantitative Polymerase Chain Reaction), WB (Western Blot), PB (PrestoBlue).

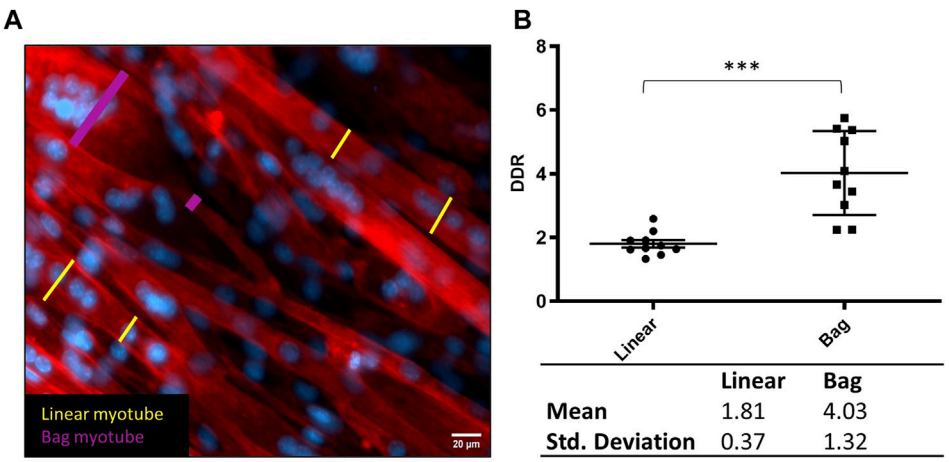


| | Linear | Bag |
|---|---|---|
| Mean | 1.81 | 4.03 |
| Std. Deviation | 0.37 | 1.32 |

**FIGURE 2 |** Defining bag and linear myotubes using Diameter Difference Ratio (DDR). **(A)** Representative fluorescent image with diameter measurements from linear myotubes in yellow and bag myotubes in pink. Phalloidin (red) DAPI (blue) (scale bar, 20 µm). **(B)** Scatter dot plot comparing DDR in Linear and Bag myotubes. Table below displays the mean and standard deviation from the graph which were used to determine the range for myotube populations. Mean ± SEM, $n = 10$, $^{***}p < 0.001$.

mix of images from three biological repeats, each with three technical repeats. They were assigned as either having a typical linear (uniform shape and linear nuclei arrangement), assigned as linear myotube or bag-like morphology (bulging equatorial region with clustered nuclei (Banks, 2015), assigned as bag myotube. A myotube is defined by a single fibre, as defined by actin stain (phalloidin) and containing three or more nuclei (DAPI). The largest and smallest diameter, clearly visible and not interfered by an overlapping myotube were measured in Fiji and used to calculate a diameter difference ratio (DDR) between those measures. Plotting DDR defines two distinct, statistically significantly populations for linear and bag myotubes (**Figure 2**). The Mean DDR ratio of linear and bag fibres was 1.81 ± 0.37 and 4.03 ± 1.32, respectively ($p < 0.001$). The standard deviation sets the range of the two distinct myotube populations: Linear myotube ≤ 2.18, Bag myotube ≥ 2.71, 2.18 < Unassigned myotube < 2.71. This novel method of identifying intrafusal bag fibre morphologies from a heterogeneous myotube population eliminates a significant degree of investigator subjectivity and bias. Fusion efficiency was calculated as the total number of nuclei within myotubes divided by the total image nuclei.

## RNA Extraction, cDNA Synthesis and RT-qPCR

RNA was extracted using the phase separation TRI Reagent® and chloroform method (Rio et al., 2010) (reagents from Sigma-Aldrich, United Kingdom). The total RNA obtained was quantified and tested for integrity using the NanoDrop™. The RNA was then transcribed into cDNA using the High-Capacity cDNA Reverse Transcription Kit (Applied Biosystems through

**TABLE 1 |** Sequence, accession code and efficiency of primers used for mRNA analysis.

| Gene | Primer sequence 5′–3′ | | Efficiency (%) | Accession code |
|---|---|---|---|---|
| | Forward | Reverse | | |
| *Myh1* | GGCCTACAAGAGACAAGCTGA | ACTTTCCTGCACTTGGATCA | 102.3 | NM_030679.2 |
| *Myh2* | TCTAAGGCCAAGGGAAACCTC | TACCAGCGCTTCCTTCTCATC | 107.3 | NM_001039545.2 |
| *Myh3* | TCGCTACAACAGATGCGGAC | CCTGGGGTCTTGGTTTCGTT | 92.4 | NM_001099635.1 |
| *Myh4* | CACCTGGACGATGCTCTCAGA | GCTCTTGCTCGGCCACTCT | 102.4 | NM_010855.3 |
| *Myh6* | CCAACACCAACCTGTCCAAGT | AGAGGTTATTCCTCGTCGTGCAT | 101.3 | NM_001164171.1 |
| *Myh7* | TACTTGCTACCCTCAGGTGGCT | TGTCATCGGGCACAAAAACATC | 90.2 | NM_080728.3 |
| *Myh8* | ACGCTAGTGCTGAAGCAGATGG | ACCGTACGAAGTGAGGGTGT | 103.7 | NM_177369.3 |
| *Myh13* | CGGCAAGAAGCAGATCCAGA | TCCTCGGCCTGGTAAGTCA | 97.4 | NM_001081250.2 |
| *Myh7b/14* | AGACCAGAAGGTGCTGACAGT | CCGGGAGCCATTTGTATGGG | 106.6 | NM_001085378.2 |
| *Csnk2a2* | CACCAACAATGAGAGGGTGG | GGTGTCTTTGACACAGGGTCC | 97.9 | NM_009974.3 |
| *Myf5* | TGACGGCATGCCTGAATGTA | GCTCGGATGGCTCTGTAGAC | 96.0 | NM_008656.5 |
| *Myod1* | TGCTCTGATGGCATGATGGATT | AGATGCGCTCCACTATGCTG | 98.1 | NM_010266.2 |
| *Myog* | ATCCAGTACATTGAGCGCCT | CAAATGATCTCCTGGGTTGGG | 100.2 | NM_031189.2 |
| *Egr3* | CCGGTGACCATGAGCAGTTT | TTGGGCTTCTCGTTGGTCAG | 106.5 | NM_018781.4 |
| *Gdnf* | TGACCAGTGACTCCAATATG | GTTTATCTGGTGACCTTTTCAG | 111.7 | NM_010275.3 |
| *Prph* | AGCTACTGGAAGGGGAGGAG | TCCAGGTCACTGTGCTGTTC | 92.0 | NM_013639.2 |
| *Sstr2* | GAGAACACAGGGAAGCGAGT | GCTGCTTTCCACTCCGTCTA | 110.5 | NM_001042606.3 |
| *Etv4* | CGAGTGCCCTACACCTTCTG | GGGGACTTGATGGCGATTTG | 92.9 | NM_001316365.1 |

Fisher Scientific, United Kingdom) on the T100™ Thermal Cycler (Bio-Rad, United Kingdom). Primers were designed using Primer-BLAST (Ye et al., 2012) for an annealing temperature (Ta) of 60°C, with exception of Myh4 (Zhou et al., 2010), Myh6 (Zhou et al., 2010), Csnk2a2 (Hildyard and Wells, 2014) and Myf5 (Brown et al., 2012). Primer sequences are shown in **Table 1** and were ordered from Sigma-Aldrich (United Kingdom). To be included in the study, primers needed an efficiency of 90–115%, an $r^2$ over 0.95 and contain a single melting peak (Bustin et al., 2009). Myh15 is missing due to very low CT expression at the experimental cDNA concentration ranges. Gene target amplification utilised the iTaq™ Universal SYBR® Green Supermix on the CFX96™ Touch System (Bio-Rad, United Kingdom). Reactions wells were 10 µl, containing 20 ng of sample cDNA, alongside a primer concentration of 0.2 µM. Reactions were carried out in triplicate on 96 well plates. Samples were pre-incubated at 95°C for 5 min followed by 40 PCR amplification cycles (denaturation: 95°C for 10°s; annealing & extension: 60°C 30°s), followed by a melt curve analysis. MIQE guidelines were followed to ensure experimental transparency and repeatability (Bustin et al., 2009). Relative gene expression was calculated using the ΔCt and 2-ΔΔCt method (Schmittgen and Livak, 2008), normalising to the reference gene casein kinase 2, alpha prime polypeptide (Csnk2a2) and expression made relative to the experimental control mean for each plate. To compare the percentage composition of Myh (**Figure 4B**), Target Myh expression was made relative to total Myh delta CT expression for that individual sample. When repeated for all detectable Myh genes, data can be used to display the proportional representation of Myh gene expression.

## Western Blotting

To lyse cells, RIPA buffer containing protease inhibitor at 1:100 dilution (both Sigma-Aldrich, United Kingdom) was used. Lysed cell suspensions underwent protein concentration quantification using the Pierce™ BCA Protein Assay Kit (Thermo Fisher, United Kingdom), as per the manufacturer's instructions. Working solutions were made up to 0.8 µg/µl with RIPA and 2x Concentrate Laemmli Sample Buffer (Sigma-Aldrich, United Kingdom) and 20 µg per sample were loaded onto 4–15% Mini-PROTEAN® TGX™ Precast 10-well protein gels and run at 200 V for approximately 40 min using the Mini-PROTEAN® Tetra Cell and PowerPac™ 300 using tris-glycine SDS running buffer (all Bio-Rad, United Kingdom). Protein ladder SeeBlue™ Plus 2 Pre-stained Protein Standard (Invitrogen™ through Thermo Fisher, United Kingdom) was used. Proteins on the gels were then dry transferred onto nitrocellulose membranes using Trans-Blot® Mini Nitrocellulose Transfer Packs and the Trans-Blot® Turbo™ Transfer System (Bio-Rad, United Kingdom). Membranes were blocked for 1 h with 5% skimmed milk (Sigma-Aldrich, United Kingdom) in tris-buffered saline and 1% Tween 20 (TBST) (both Bio-Rad, United Kingdom), then incubated with 1° antibodies for Egr3, MyHC3, MyHC6 or MyHC8 (Same as immunofluorescent microscopy antibodies) at 1: 250, 1:500, 1:500 and 1:500, respectively. Simultaneously incubating with loading control GAPDH at 1:10,000 (Abcam, United Kingdom, ab8245) in 5% skimmed milk overnight at 4°C followed by TBST washes. 2° antibodies IgG-HRP anti-mouse (Novus Biologicals, HAF018) and IgG-HRP anti-rabbit (Abcam, United Kingdom, ab6721) at 1:1,000 dilutions were incubated for 1 h in 3% skimmed milk, followed by three 15 min washes with TBST. Blots were then developed using Pierce™ ECL Western Blotting Substrate (Thermo Fisher, United Kingdom) and imaged using the ChemiDoc™ XRS imaging system and Image Lab™ software (Bio-Rad, United Kingdom). Quantification was performed in FIJI (Schindelin et al., 2012) and Microsoft Excel using an adjusted relative density method (Taylor et al., 2013).

## Cell Proliferation and Metabolic Assay

After the cell culture protocol explained above, DM plus 10% PrestoBlue® (Thermo Fisher, United Kingdom) viability reagent was added to each well and incubated at 37°C for 2 h. Media was transferred in triplicates into 96 well plates and fluorescence read at 600–640 nm. Relative fluorescent unit (Rfu) readings were corrected to media only controls and then fold change from Nrg-1 treated cells was calculated relative to untreated controls. Cell counts were performed at Day 0 and Day +8 using NucBlue™ Hoechst 33342 (Thermo Fisher, United Kingdom).

## Statistics

All statistical tests were performed in SPSS and GraphPad prism 9.0. *t*- test and ANOVA (with post-hoc Tukey test) analysis were completed in Graph pad 9.0. Firstly, the data was checked for normal distribution using Shapiro-Wilk test. If normally distributed, a student's *t*-test or parametric ANOVA was used to ascertain significance. If not normally distributed, a Mann-Whitney *t* test was used. Egr3 intensity data was square root transformed prior to ANOVA analysis, providing a normally distributed data set (Bland and Altman, 1996). Nuclei Count data per myotube were analysed (treatment and fibre type effect) using negative binominal regression analysis, which accounted for data overdispersion and best fit the distribution of data (Hardin and Hilbe, 2014). All experiments, apart from western blot, were completed with an n of 9, consisting of three experimental (separate vial or plate) with three technical (well) repeats and one image from each repeat was analysed. Western Blot analysis had an *n* of 3, consisting of three experimental repeats ran (1 per lane) on three seperate blots. All raw data stated in the text is followed by ±Standard error of mean (SEM) when applicable.

# RESULTS

## Nrg-1 Treated C2C12 Myotubes Contain Increased Intrafusal Bag Myotubes and Nuclei Number

To assess how Nrg-1 effects C2C12 myotube morphology, fluorescent microscopy targeting cell cytoskeleton (Phalloidin) and nuclei (DAPI) was used. Nrg-1 treatment leads a substantial change in myotube morphology (**Figure 3A**), in which there are visually more equatorially clustered nuclei with expanded myotube diameters. When analysed using DDR, this translates to an increase in bag myotubes from 8.52 ± 5.56% to 41.61 ± 6.77% ($p < 0.01$). Nuclei per field of view increased from 104.80 ± 3.56 in control to 136.30 ± 6.77 ($p < 0.001$) following Nrg-1 treatment (**Figure 3B**). There are no significant changes to other myogenic morphological criteria such as fusion efficiency (Control: 46.88 ± 2.68% v Nrg-1: 47.41 ± 2.82%) or myotubes per FOV (Control: 8.33 ± 0.82 v Nrg-1: 9.22 ± 0.88). In both control and treated populations, bag myotubes contain significantly more nuclei than linear fibres (8.09 ± 1.06 vs 5.48 ± 0.27 and 8.33 ± 0.76 vs 6.10 ± 0.43 respectively, both $p < 0.01$). The source of variation from myotube type was significant ($p < 0.001$) and insignificant for treatment ($p > 0.05$), meaning Nrg-1 treatment does not affect the average nuclei counts in each myotube type (**Figure 3C**). Relative Egr3 gene expression was quantified to confirm downstream Nrg-1 initiated Egr3 upregulation. Nrg-1 treated myotubes display a 3.5 ± 0.21-fold in Egr-3 gene expression (**Figure 3D**, $p < 0.001$), confirming sufficient downstream response. MRFs mediate myoblast proliferation and differentiation into myofibers (Zanou and Gailly, 2013) and provide an early indicator of myotube maturity. To this extent, MRF gene expression was quantified. The only significant difference was a 1.49 ± 0.08-fold increase in Myod1 (**Figure 3F**, $p < 0.001$). Together, the data from **Figure 3** suggests that Nrg-1 upregulates Egr3, which correlates with a robust change of myotube morphology towards an intrafusal bag structure, without interfering with fusion efficiency or myotube numbers. In addition, bag myotubes contain significantly more nuclei than linear myotubes, contributing to increased nuclei counts following Nrg-1 treatment.

## Myosin Heavy Chain Gene Expression Significantly Altered in Nrg-1 Treated C2C12 Myotubes

It is possible to identify intrafusal fibres *in vivo* based on the retained expression of immature (MyHC3 and MyHC8) and specialised (MyHC6 and MyHC7b/14) isoforms (Walro and Kucera, 1999; Liu et al., 2002). MyHC expression is regulated at a gene expression level (Schiaffino et al., 2015), therefore, MyHC gene (Myh) RT-qPCR analysis was completed to determine how Nrg-1 regulates Myh expression. All Myh isoforms, apart from Myh13 and Myh7b/14 displayed a significantly altered expression following Nrg-1 treatment (**Figure 4A**). Fold changes relative to control were as follows: Myh1, 0.49 ± 0.07 ($p < 0.01$), Myh2, 0.51 ± 0.05 ($p < 0.01$), Myh4, 2.17 ± 0.21 ($p < 0.001$), Myh3 0.76 ± 0.05 ($p < 0.01$), Myh8 0.16 ± 0.02 ($p < 0.001$), Myh6 0.44 ± 0.09 ($p < 0.001$) and Myh7, 0.58 ± 0.06 ($p < 0.001$).

**Figure 4B** uses the same data set as **Figure 4A**, however it is analysed and displayed as a relative proportional representation. This highlights the most biologically significant isoforms being represented. The majority of expression in both conditions comes from four genes: Myh1, Myh4, Myh3 and Myh7. Myh1 changes from 7.09 ± 0.87% to 2.68 ± 0.14%, Myh4 from 33.24 ± 0.85% to 60.13 ± 0.82%, Myh3 from 54.70 ± 1.72% to 35.28 ± 0.90% and Myh7 from 3.47 ± 0.22% to 1.63 ± 0.07%. This indicates the probable biological significance of Myh4 and Myh3 fold changes seen in **Figure 4A**, as they represent the greatest proportional expression in both control and Nrg-1 treated myotubes. This MyHC RT-qPCR data demonstrates a unique contractile phenotype in the treated population, however we see decreased expression in Myh isoforms associated with intrafusal fibres *in vivo* and *in vitro* (Barrett et al., 2020).

## Myosin Heavy Chain Protein Expression Significantly Altered in Nrg-1 Treated C2C12 Myotubes

Despite MyHC expression being controlled at a transcriptional level (Schiaffino et al., 2015), analysis was conducted to establish whether gene expression changes resulted in consequential

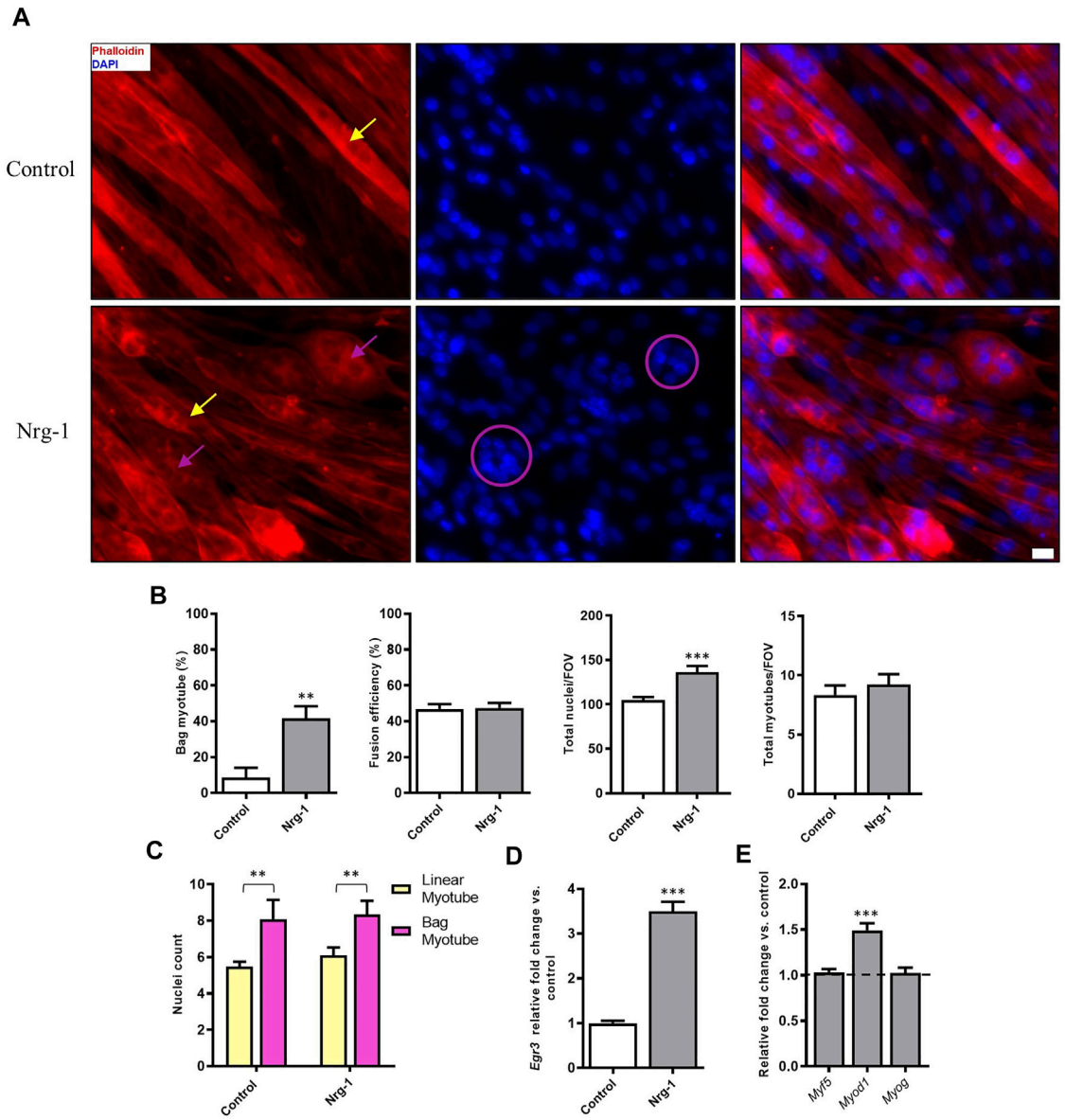


**FIGURE 3 |** Nrg-1 treatment causes a significant increase in bag myotube formation and nuclei number in C2C12 myotubes. **(A)** High magnification representative fluorescent micrographs of cells ± Nrg-1 used for quantification. Phalloidin (red) and DAPI (blue), yellow arrows point toward myotubes with linear morphology and purple arrows toward bag morphology (Scale bar, 20 μm). **(B)** Comparison of key morphological criteria between myotubes ± Nrg-1. **(C)** Nuclei counts within bag and linear myotubes and ± Nrg-1. Control-Linear -60 myotubes, Control-Bag - 11 myotubes, Nrg-1-Linear - 40 myotubes, Nrg-1-Bag -33 myotubes. **(D)** qRT-PCR analysis of Egr3 expression. **(E)** qRT-PCR analysis of MRFs following Nrg-1 treatment vs. control. Control values are not shown and are represented by the dotted line at 1.0. Mean ± SEM, $n = 9$, $^{**}p < 0.01$, $^{***}p < 0.001$.

MyHC protein expression. To this extent, Immunofluorescence microscopy and western blot quantification was completed for MyHC3, MyHC8 and MyHC6. Immunofluorescence microscopy provides an opportunity to identify preferential expression (increased intensity) in myotubes with an intrafusal bag morphology compared to linear, providing a method to identify potential intrafusal bag myotube specific markers. Contradictory to previous literature, Nrg-1 treated myotubes did not display increased staining intensity for the aforementioned MyHCs, with MyHC6 actually appearing to have a lower staining intensity. Additionally, there was no obvious bag myotube specific staining (**Figures 5A–C**). Western blot analysis reveals a reduced expression across all tested MyHCs relative to control (**Figures 5A–C**): MyHC3 fold change relative to control was 0.27 ± 0.03, MyHC8 was 0.43 ± 0.07 and MyHC6 was 0.54 ± 0.06 (all $p < 0.001$). Gene expression changes from **Figure 4** correlate with MyHC protein expression from **Figure 5**, highlighting reduced expression of putative intrafusal specific proteins and no bag myotube specific markers.

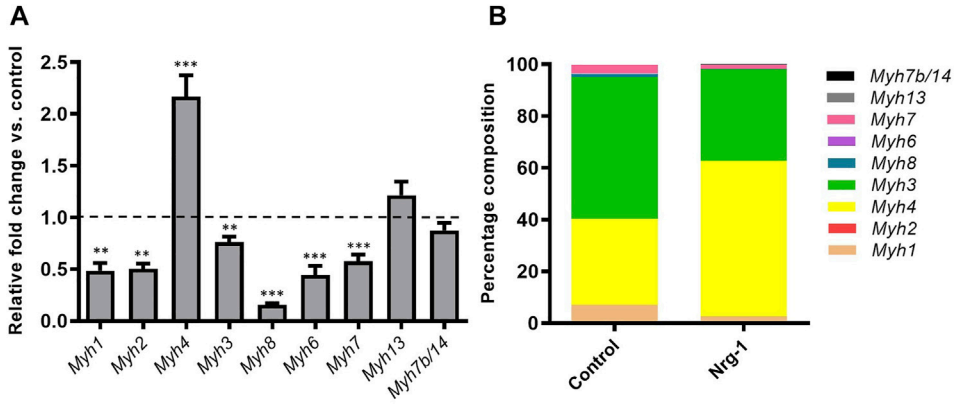


**FIGURE 4 |** Nrg-1 treatment led to significant changes in Myh expression in all but two isoforms. **(A)** RT-qPCR analysis of all detectable Myh isoforms following Nrg-1 treatment vs control. Control values are not shown and are represented by the dotted line at 1.0. **(B)** Proportional representation for Myh expression. Mean ± SEM, $n$ = 9, $^{**}p < 0.01$, $^{***}p < 0.001$.

## Intrafusal Bag Myotubes Have an Increased Expression of Egr3 Protein Following Nrg-1 Treatment

At this point, results have presented a clear morphological change and an altered MyHC phenotype in C2C12 myotubes, following Nrg-1 treatment. However, there is no conclusive markers to define intrafusal fibres from extrafusal in this setup. Egr3 is a transcription factor essential for intrafusal myogenesis *in vivo* (Tourtellotte and Milbrandt, 1998; Tourtellotte et al., 2001; Andrechek et al., 2002; Hippenmeyer et al., 2002; Leu et al., 2003; Albert et al., 2005; Oliveira Fernandes and Tourtellotte, 2015) and has previously been associated with bag myotube morphology *in-vitro* (Rumsey et al., 2008, 2010; Colón et al., 2017, 2020; Guo et al., 2017). Therefore, Egr3 was visualised by immunofluorescence to ascertain whether its expression is dependent on treatment and/or morphology. Following this, western blots were performed for quantitative purposes. Finally, several gene candidates (identified from Albert, 2005) were quantified following Nrg-1 treatment to further characterise the extent of putative intrafusal-specific expression in this model.

Egr3 image coverage (Control: 12.60 ± 2.66% vs Nrg-1: 28.37 ± 4.22%, $p < 0.01$) and staining intensity per nuclei (Control: 1.00 ± 0.12 vs Nrg-1: 3.51 ± 0.61, $p < 0.001$) increased following Nrg-1 treatment (**Figure 6B**). ANOVA analysis determined that myotube mean intensity of Egr3 was affected significantly by both treatment and myotube type (both $p < 0.001$) and yielded no interaction effect ($p = 0.27$). Tukey's multiple comparisons post hoc test indicated significant differences between linear myotubes from control cells (control-linear, 0.88 ± 0.13) to linear myotubes from Nrg-1treated cells (Nrg-1-linear, 2.50 ± 0.42, $p < 0.001$) and bag myotubes from Nrg-1 treated cells (Nrg-1-bag, 6.13 ± 1.08, $p < 0.001$). There was a significant difference between Nrg-1-bag myotubes to bag myotubes from control cells (control-bag, 1.85 ± 0.54, $p < 0.01$) and Nrg-1-linear $p < 0.001$). Therefore, Egr3 staining intensity is increased in bag myotubes, and Nrg-1 treated myotubes (linear and bag), providing a possible marker for C2C12 derived intrafusal myotubes (**Figure 6C**).

The only significant source of variation in Egr3 positive nuclei percentage, was myotube type ($p < 0.01$), with a significant difference between control-linear (48.60 ± 4.60%) compared to Nrg-1-bag (72.12 ± 4.78%, $p < 0.01$). Indicating Nrg-1 treatment does not increase the percentage of nuclei expressing Egr3 (**Figure 6C**). In addition, in whole culture lysed population western blot data, Egr3 was increased 2.24 ± 0.08-fold ($p < 0.001$) following Nrg-1 treatment, corroborating with the increased expression visualised through immunofluorescence (**Figure 6D**). Finally, ETV4 mRNA expression was increased 2.88 ± −0.17-fold ($p < 0.001$) and Gdnf, Prph1 and Sstr2 mRNAs displayed no significant change ($p > 0.05$) (**Figure 6E**). Taken together, data from **Figure 6** signifies that Nrg-1 treatment is upregulating Egr3 expression, particularly in myotubes with an intrafusal bag morphology (**Figure 6C**).

## Nrg-1 Treatment Causes Increased Cell Proliferation and Decreased Myotube Area per Myonuclei

**Figure 3C** highlighted a significant increase in total nuclei/FOV, following Nrg-1 treatment after 8 days. To elucidate whether Nrg-1 was contributing to increased proliferation or reducing cell detachment and death, Hoechst nuclei stating was performed for both conditions at day 0 and day 8, followed by a Two-way ANOVA analysis. There was a significant source of variation from both treatment and time ($p < 0.01$), with no interaction effect. Tukey post-hoc comparisons identified the only significant increases between Day 8 Nrg-1 (1.52 ± 0.12) and all other conditions (Day 0 control: 1.00 ± 0.08, $p < 0.001$, Day 0 Nrg-1: 1.11 ± 0.06 and Day 8 Control: 1.112 ± 0.06, both $p < 0.01$), suggesting increased proliferation from day 0 to day 8 following Nrg-1 treatment (**Figure 7A**). To further clarify, Prestoblue™ cell viability assay was performed, Nrg-1 treated myotubes displayed a relative fold increase of 1.15 ± 0.03 ($p < 0.01$), further suggesting Nrg-1 initiated proliferation (**Figure 7B**). Using the data set from **Figure 6**, the area of each myotube was divided by nuclei number to give a 2D *in vitro* version of

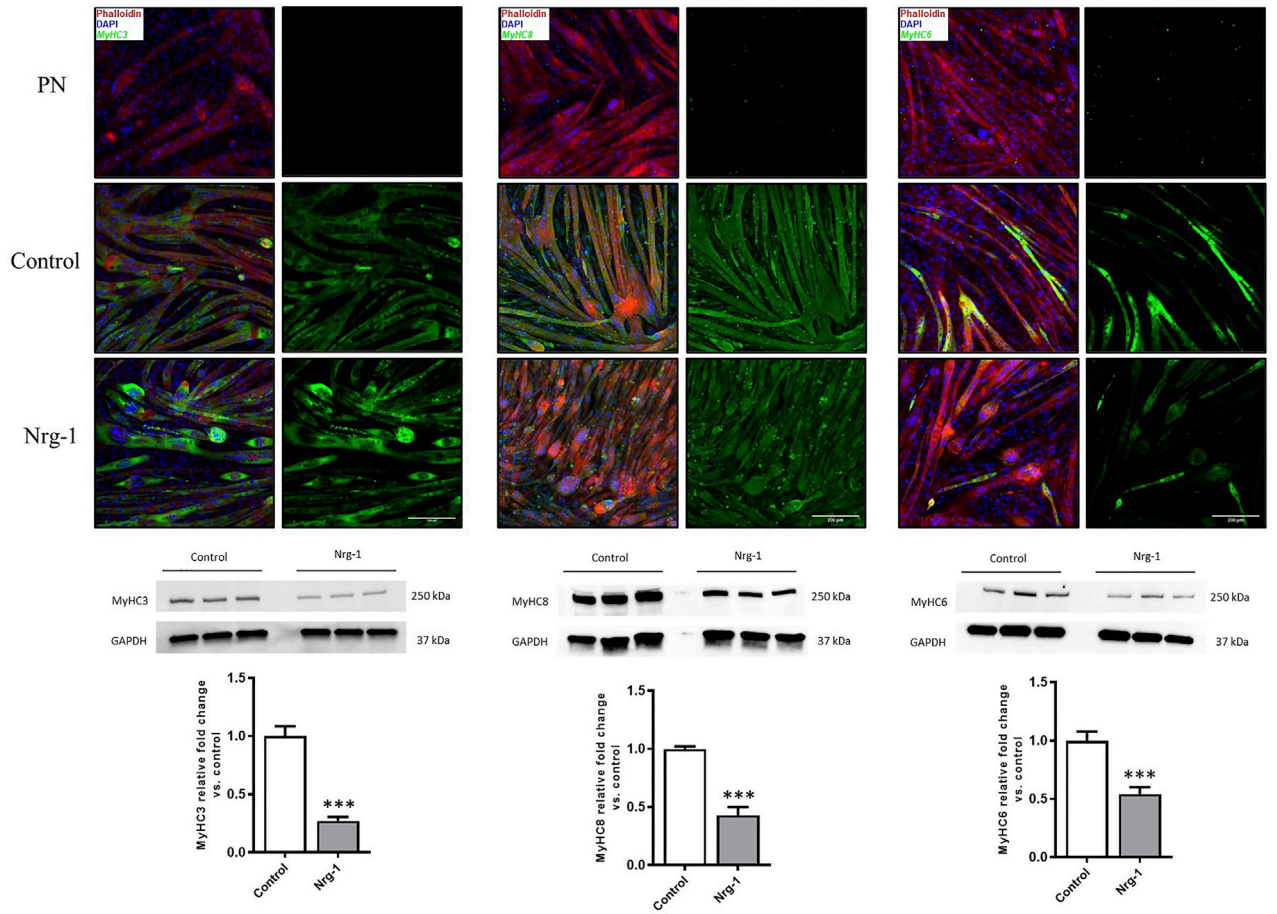


**FIGURE 5 |** Decreased expression of putative intrafusal specific proteins following Nrg-1 treatment in C2C12 myotubes. Immunofluorescent imaging suggested no clear intrafusal bag myotube preferential expression MyHC3, 8 or 6. Phalloidin (red), DAPI (blue) and MyHC (green). Top to bottom: PN (primary negative), control and Nrg-1 treated representative fluorescent micrographs (scale bar, 200 μm), western blot representative gels and finally MyHC fold change relative to control based on western blots. **(A)** MyHC3. **(B)** MyHC8. **(C)** MyHC6. Western blot lanes represent three biological repeats, *n* of 3 achieved by repeating on three separate blots, Mean ± SEM, ***, $n = 3$, $p < 0.001$.

myonuclear domain counts, which is the theoretical amount of sarcoplasm within a muscle fibre controlled by a single myonucleus (Teixeira and Duarte, 2011). Following Nrg-1 treatment, the average myotube area per nuclei reduced from 645.3 ± 30.08 μm to 537.9.0 ± 18.25 μm ($p < 0.01$) (**Figure 7C**). Nrg-1 is having a proliferative effect on C2C12s during the differentiation phase, resulting in increased nuclei counts and correlates with decreased myotube area per myonuclei.

## DISCUSSION

There is an important clinical need to develop robust *in vitro* models of skeletal muscle that account for the sensory function of the muscle spindle through integration of intrafusal skeletal muscle fibres. This will help to investigate the basic molecular and cellular mechanisms regulating their phenotype in health and disease, in a controlled, defined, and ethical environment. In this study, a reductionist, monocellular C2C12 model, for *de novo* intrafusal skeletal muscle generation is presented. The addition of a recombinant, developmentally associated protein, Nrg-1, is used to replicate an innervating Ia afferent neuron. C2C12 myoblasts offer an accessible, fusion competent, reproducible cell line that are widely used in a number of skeletal muscle research applications. C2C12s facilitate rapid model progression, assay development and also an opportunity to investigate intrafusal fibre development in a reductionist pure myoblast population. Progress in such a cell line will facilitate translation to a primary human, multi-cell, integrated, biomimetic model of the muscle spindle.

To firstly investigate the utility of C2C12s as a model of intrafusal fibre development, Nrg-1 was added to developing C2C12 myotubes, which resulted in an over 4-fold increase of bag myotube formation (**Figure 3C**). This supports previous *in vivo* and *in vitro* experiments (Tourtellotte and Milbrandt, 1998; Tourtellotte et al., 2001; Jacobson et al., 2004; Albert et al.,

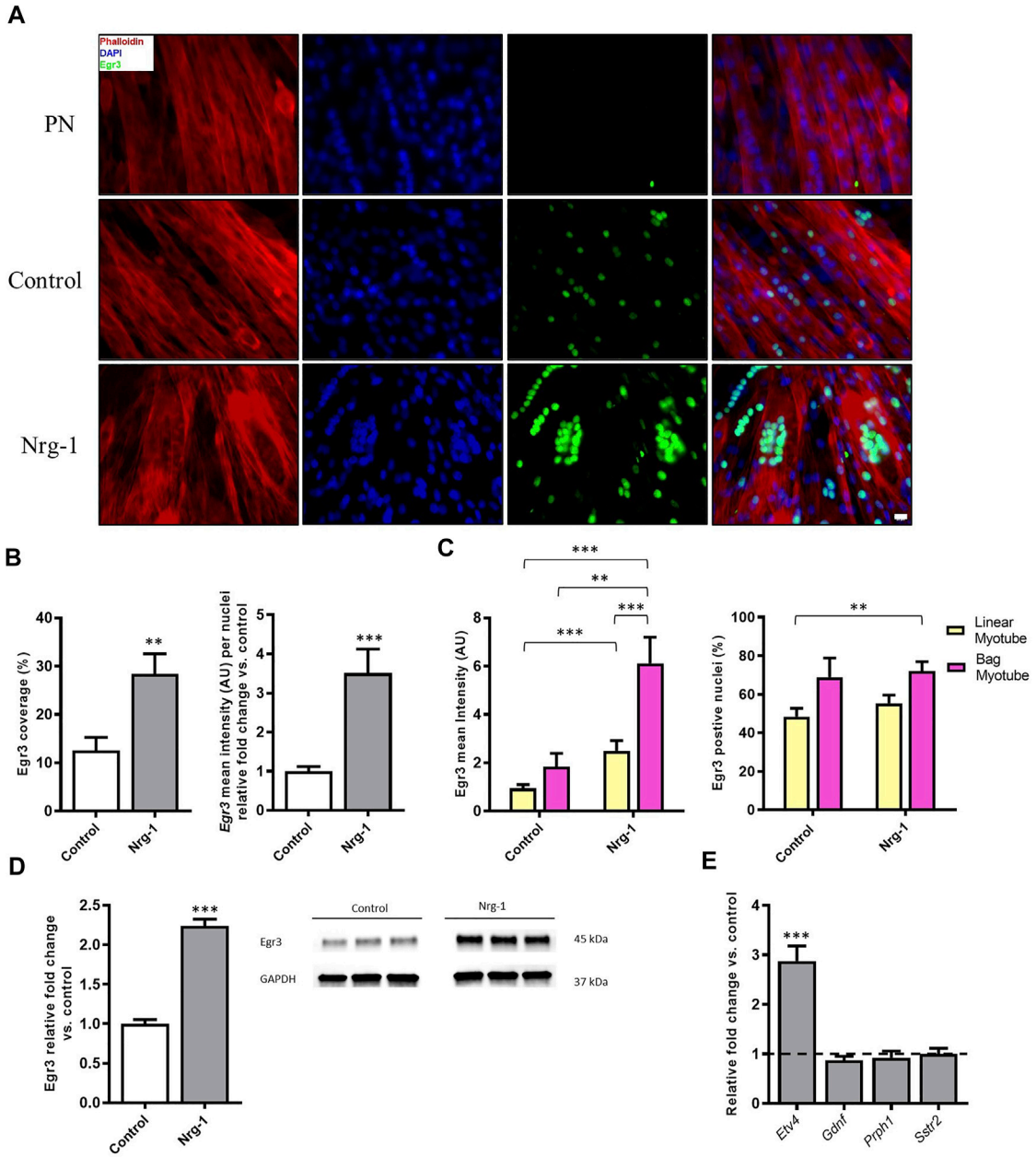


**FIGURE 6 |** Increased expression of Egr3 protein in Nrg-1 treated C2C12 myotubes and intrafusal bag myotubes. **(A)** representative fluorescent micrographs following Nrg-1 treatment, (scale bar, 20 μm) Phalloidin (red), DAPI (blue) and Egr3 (green). **(B)** Percentage of Image covered by positive Egr3 expression (above threshold) and Egr3 intensity fold change per nuclei relative to control. **(C)** Two-way ANOVA analysis of treatment and myotube type, Left- Myotube Egr3 intensity Right- Egr3 positive nuclei %. Control Linear -52 myotubes, Control-Bag - 9 myotubes, Nrg-1-Linear - 47 myotubes, Nrg-1-Bag – 26 myotubes. **(D)** Western blot representative image and relative fold change for Egr3, each lane is a biological repeat ($n$ = 3, from three blots). **(E)** Gene expression of additional putative intrafusal specific proteins relative to control. Mean ± SEM, $n$ = 3, $^{**}p < 0.01$, $^{***}p < 0.001$.

2005; Rumsey et al., 2008; Akay et al., 2014; Herndon et al., 2014; Oliveira Fernandes and Tourtellotte, 2015; Colón et al., 2017, 2020; Guo et al., 2017) that indicate Nrg-1 is essential for the development of intrafusal skeletal muscle fibres. The fold increase in bag myotubes is comparable to Hickman and others, who reported 4-5-fold increases in both primary rat and human cells (Rumsey et al., 2008; Guo et al., 2017). However, the percentage of bag myotubes to the total myotube population is much higher in our C2C12 model compared to human myoblasts as previously published (41.61 ± 6.77% vs 15.80 ± 6.62%). Nevertheless, we must consider in this study, a novel statistical DDR method was used to more objectively define intrafusal bag myotubes, which may be a contributing factor, rather than suggesting C2C12s are more responsive to Nrg-1.

Myoblast fusion is a required event for skeletal muscle development and regeneration, therefore measuring fusion efficiency *in vitro* is a good indicator for overall myogenesis (Sampath et al., 2018). Fusion efficiency was not significantly changed upon Nrg-1 addition in this investigation (**Figure 3C**), which would suggest that the morphological changes observed are independent of other myogenic fusion parameters. There was however, a 1.4-fold increase in total nuclei number per FOV, which did not affect fusion efficiency (**Figure 3B**). This change can be accounted to the increase of bag myotubes, which contain on average over two more myonuclei than linear fibres (**Figure 3C**).

Nrg-1 downstream activation of Egr3 is a key signalling event in muscle spindle and intrafusal skeletal muscle fibre development (Tourtellotte and Milbrandt, 1998; Jacobson et al., 2004; Albert et al., 2005; Herndon et al., 2014; Oliveira Fernandes and Tourtellotte, 2015). Ablation of Erg-3 is accompanied by abnormal muscle spindles, reduced running performance and degradation of locomotor pattern in mice (Tourtellotte et al., 2001; Akay et al., 2014; Oliveira Fernandes and Tourtellotte, 2015). To further validate the role of Nrg-1 on C2C12 intrafusal bag myotube formation, Egr3 expression was quantified. Treated cells displayed a significant increase in gene (**Figure 3D**) and protein expression (**Figure 6D**) of Egr3, similar to that previously evidenced in primary human (Jacobson et al., 2004) and C2C12s (Williams and Jacobson, 2010; Herndon et al., 2014). Fluorescent micrographs demonstrated increased Egr3 protein staining intensity in Nrg-1 treated and intrafusal bag C2C12 myotubes, suggesting an important role for Egr3 toward C2C12 intrafusal bag myotube development. In contrast to the Hickman papers (Rumsey et al., 2008, 2010; Colón et al., 2017, 2020; Guo et al., 2017), control myotubes had visible expression of Egr3 (**Figure 6A**), meaning it was not a binary determinant of the intrafusal phenotype as defined by DDR. In previous studies, Egr3 displayed strong immunoreactivity in untreated myogenic cells (Herndon et al., 2014), is involved in *in vitro* myoblast proliferation (Kurosaka et al., 2017) and upregulated during differentiation (Muñoz et al., 2018; Choi et al., 2020). Therefore, non-binary staining results were expected. Egr3 in **Figure 6**, paired with the increase in intrafusal bag morphology (**Figure 3B**) suggests that Nrg-1 elicits endogenous production of Egr3, suggesting activation of the Nrg1/ErbB2/Egr3 signalling pathway, resulting in intrafusal specific differentiation.

To validate an intrafusal phenotype, the most in depth MyHC characterisation of Nrg-1 treated myotubes was completed. MyHCs are key contractile proteins and are major determinants of force velocity properties of muscle, which are differentially distributed across fibres and transiently expressed during development, regeneration and various stimulus such as injury or exercise (Schiaffino et al., 2015). Therefore, MyHCs are often used to provide an indication of the developing, regenerative or mature phenotype of skeletal muscle (Liu et al., 2005). *In vivo* studies have highlighted MyHC3, MyHC6, MyHC8 and MyHC7b/14 as having preferential or retained expression in mature intrafusal muscle fibres (Kucera et al., 1992; Liu et al., 2002; Österlund et al., 2011; Schiaffino and Reggiani, 2011; Thornell et al., 2015) and therefore are suitable candidates for characterisation *in vitro*. MyHC6 and MyHC8 have been formerly shown to display increased protein expression in human cells *in vitro* following Nrg-1 treatment (Jacobson et al., 2004), even in the absence of bag myotube morphology. *In vitro* bag myotubes have displayed MyHC6 specific staining compared to their morphologically linear neighbours in primary rat (Rumsey et al., 2008), primary human (Guo et al., 2017) and iPSCs (Colón et al., 2020). In contrast, this current paper presents that MyHC3,6 and 8 are all downregulated transcriptionally when analysed by RT-qPCR (**Figures 4A,B**), translationally when analysed by western blots (**Figures 5A–C**), and exhibit no clear preferential immunofluorescent staining in C2C12 myotubes with a bag morphology (**Figures 5A–C**). MyHC6 presented sparse staining in Nrg-1 vs control, as compared to the immature isoforms. Although MyHC6 is a predominately cardiac isoform, it is expressed in slow-twitch skeletal muscle tissue and its reduced expression in Nrg-1 treated cells could be related to a faster MyHC profile, as indicated by the increased Myh4 gene expression (Stuart et al., 2016) Furthermore, s46 (DSHB, United States), an antibody for avian slow developmental isoform, is repeatedly stated as being the best intrafusal specific marker *in vivo* and *in vitro* (Schiaffino and Reggiani, 2011; Schiaffino et al., 2015) gave no immunoreactivity in the present model (data not shown). The only Myh increase was a 2-fold increase in Myh4 following Nrg-1 treatment (**Figure 4A**), representing a rise from 33.24 ± 0.85% to 60.13 ± 0.82% of total Myh expression (**Figure 4B**). Myh4 codes for MyHC-IIb, the most prominent isoform (Pellegrino et al., 2003) expressed in adult mice, associated with high forces of contraction combined with rapid contractile characteristics (Harrison et al., 2011). MyHC4/IIb Immunofluorescence and western blotting were attempted using both BF-F3 (DSHB, United States) and 20140-1-AP (Proteintech, United Kingdom) antibodies. Unfortunately, they proved unsuccessful in achieving a clean and strong signal which would be sufficient for use. Intrafusal bag fibres, especially of the type 1 subset, are associated with a slow phenotype, however intrafusal chain and $bag_2$ fibres express a fast phenotype in both human and rats (Kucera et al., 1992; Soukup et al., 1995; Liu et al., 2005; Österlund et al., 2013). Therefore, an increase in Myh4 is not indicative of poor intrafusal myotube generation in this model, but rather an indication of a more mature, glycolytic and faster contractile phenotype following Nrg-1 supplementation (Kucera et al., 1992; Soukup et al., 1995; Liu et al., 2005; Österlund et al., 2013). Furthermore, previous studies have demonstrated the increased expression of Myh4 mRNA in C2C12 myotubes in similar time course of experimentation (Brown et al., 2012). In addition, rat intrafusal fibres are believed to originate from three sequential generations of myotubes, the MyHC expression displays regional variability across the fibre length, differs throughout development and is dependent on interactions with external factors such as innervation and intracapsular niche (Kucera and Walro, 1990, 1995). This highlights the complexity of using MyHC expression to define an intrafusal myotube *in vitro* in the absence of sensory innervation and functional outputs (Kucera et al., 1992; Liu et al., 2002).

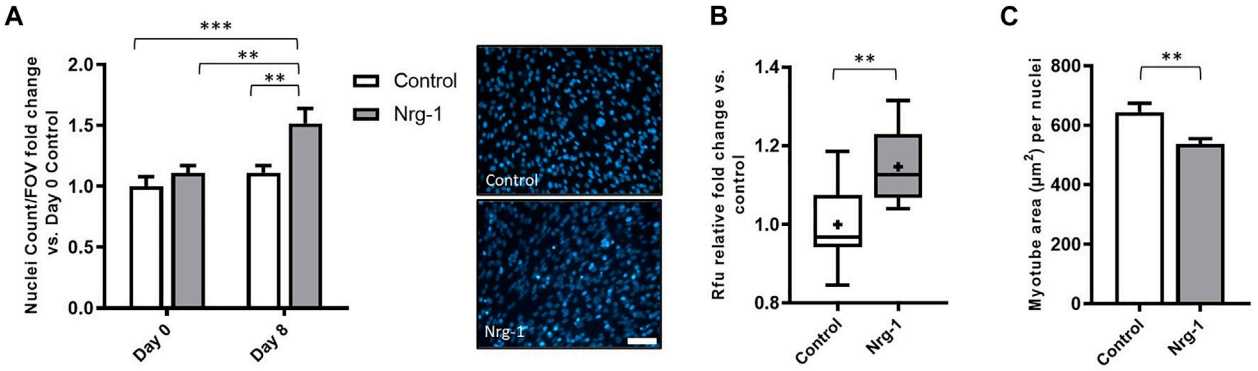


**FIGURE 7 |** Nrg-1 treatment leads to cell proliferation during the differentiation phase in C2C12 cells. **(A)** Nuclei cells counts from day 0 and day 8 in both control and Nrg-1 treated myotubes relative to Day 0 control. To the right, representative fluorescent micrographs with Hoechst stain in blue (scale bar, 200 μm). **(B)** Rfu fold change relative to control from Prestoblue™ cell viability assay. **(C)** Average myotube area (μm²) per myonuclei (using myotube data set from **Figure 6**). Mean ± SEM, $n$ = 9, $^{**}p < 0.01$, $^{***}p < 0.001$.

To characterise this further, supplementary intrafusal markers were employed. Myf5, an early myogenic regulatory factor, retains expression into adult intrafusal muscle fibres *in-vivo* (Zammit et al., 2004). Etv4 transcription factor, is another early stage intrafusal muscle fibre development marker, which similar to Egr3 is induced by afferent innervation (Arber et al., 2000; Hippenmeyer et al., 2002). However, Etv4 is largely involved in patterning motor innervation rather than in spindle morphogenesis *per se* (Albert et al., 2005). Gdnf is another established intrafusal fibre marker that has an essential role in fusimotor survival (Shneider et al., 2009; Schiaffino and Reggiani, 2011). Additionally, a murine knockdown model identified Sstr2 and Prph1 as novel intrafusal specific markers (Albert et al., 2005), which are yet to be utilised for *in vitro* characterisation. Despite this, gene expression changes for the aforementioned targets, aside from a significant 2-fold increase in Etv4 (**Figure 6E**), were insignificant following Nrg-1 treatment (**Figures 3F**, **6E**). Activation of Etv4 expression further clarifies Nrg-1 is replicating afferent signalling pathways in this model. Although Myf5 gene expression was not modified, Myod1 was significantly upregulated. As an intermediate MRF, Myod1 is required for myogenic cells to exit the cell cycle and to enter the differentiation process (Zanou and Gailly, 2013). With the evidence for increased cell proliferation during the differentiation phase in Nrg-1 treated culture (**Figure 7A**), the increase in Myod1 compared to control could be accounted to a greater availability of myoblasts for fusion at the given time point. Myod1 also has a causative relationship with increased Myh4 expression in mice, which may also be a contributing factor to the upregulation of Myh4 discussed above (Wheeler et al., 1999; Seward et al., 2001; Ekmark et al., 2007; Zammit, 2017).

Intrafusal fibres have an increased expression of PAX 7 satellite cells and decreased myonuclear domain compared to their extrafusal neighbours (Kirkpatrick et al., 2008). This highlights the importance of satellite cell and myonuclei distribution to muscle spindle and intrafusal fibre function (Kirkpatrick et al., 2008). In corroboration to this hypothesis, adult mice ablated of satellite cells exhibit no detectable changes in extrafusal muscle fibre morphology, fibre-type composition, aerobic capacity or force generation. However, they display gross motor coordination defects, increased muscle spindle extracellular matrix deposition and decreased intrafusal fibre cross-sectional area (Jackson et al., 2015). A similar phenotype is seen with skeletal muscle specific Egr3 knockout mice, whom are deficient of a functional muscle spindle (Tourtellotte and Milbrandt, 1998; Akay et al., 2014; Oliveira Fernandes and Tourtellotte, 2015). Increased satellite cell number and smaller myonuclear domains are indicative of greater capacities for growth, regeneration, and repair (Rosser et al., 2002; Allouh et al., 2008; Shenkman et al., 2010). In general, higher satellite cells numbers corresponds with greater contractile activity (Gibson and Schultz, 1982, 1983; Yin et al., 2013) and myonuclear domains are smaller in slower, frequently activated fibres (Roy et al., 2005; Aravamudan et al., 2006). Therefore, intrafusal fibres, which are continuously sending and receiving information to the central nervous system, even at rest (Macefield and Knellwolf, 2018), fit these criteria. In this model, C2C12s express a significant upregulation in cell number (**Figure 7A**) and cell viability (**Figure 7B**) alongside reduced myotube area per myonuclei, following Nrg-1 treatment (**Figure 7C**). Therefore, recapitulating several *in vivo* phenotypes discussed above. Nrg-1/ErbB2 signalling activates many genes associated with specific cellular processes including proliferation, differentiation, survival, apoptosis, and migration (Geissler et al., 2020). To this extent, it has previously been associated with and not limited to, upregulating proliferation in myoblasts (Ford et al., 2003), fibroblasts (Kirabo et al., 2017), cardiomyocytes (Geissler et al., 2020), Schwann cells (Fallon et al., 2004) and epithelial cells (Liu and Kern, 2002). Additionally, Egr3 expression has been linked C2C12 myoblast proliferation (Kurosaka et al., 2017), therefore it is hard to speculate on the downstream signalling responsible for increased proliferation following Nrg-1 treatment, without further cell type specific investigations.

We must also consider the maturity of the model, during skeletal muscle development and regeneration, MyHCs and MRFs are transiently expressed, and results *in vitro* will vary depending on the culture environment and time spent differentiating before terminal analysis (Brown et al., 2012; Stuart et al., 2016; Rao et al., 2018). C2C12 myotubes after 8 days differentiation in both control and Nrg-1

treated conditions are still exhibiting an immature phenotype, as determined by high proportions of Myh3 gene expression (**Figure 4B**) and strong staining for MyHC3 and MyHC8 (**Figures 5A,B**). *In vivo* work used to identify intrafusal specific markers are mostly based from adult, or new-born immunohistochemistry samples (Kucera et al., 1992, 1993; Kucera and Walro, 1992, 1995; Tourtellotte and Milbrandt, 1998; Walro and Kucera, 1999; Liu et al., 2002; Zammit et al., 2004; Horst et al., 2006; Kirkpatrick et al., 2008, 2010; Oliveira Fernandes and Tourtellotte, 2015). To overcome this, future model iterations should look to increase the differentiation time span. 2D monolayer cultures will not facilitate this, as spontaneous contractions in C2C12 myotubes detach them from the surface when cultured much past 8 days. Therefore researchers should look to adopt a 3D tissue engineering approach, not only will this facilitate longer culture times (Vandenburgh et al., 1988; Juhas et al., 2014; Rao et al., 2018), but it will better replicate the *in vivo* environment, allowing cell to ECM and cell to cell interactions in three directions and give the user control over orientation, porosity and stiffness (Torii et al., 2018). In turn, 3D skeletal muscle cultures permit more mature molecular, structural and functional differentiation, better representing native adult muscle (Rao et al., 2018; Capel et al., 2019; Wang et al., 2019; Zhuang et al., 2020) and may facilitate identification of retained immature or specialised intrafusal specific phenotypes using C2C12 cells. Other novel future approaches are discussed in detail in a recent review paper by our group (Barrett et al., 2020).

Without a definitive intrafusal phenotype *in vitro*, we cannot speculate on the origins of intrafusal fibres. If a single bipotential population of myocytes can develop into both fibre type (i.e., intrafusal and extrafusal), then theoretically we should be able to achieve a pure, intrafusal-only C2C12 cell culture population. To achieve this, a reliable intrafusal linear and bag fibre marker is required. If a distinct lineage of myoblast intrinsically committed to differentiation into intrafusal fibres exists, then C2C12s may be an incompatible source for an intrafusal fibre model. The data attained in this study highlights several hallmarks of intrafusal fibres within Nrg-1 treated C2C12 myotubes. These warrant future endeavours using more sophisticated, biomimetic cell cultures to tissue engineer functional intrafusal muscle for the applications of both basic science and clinical studies, towards improving complete neuromuscular function in disease and injury.

## CONCLUSION

In conclusion, this study presents a novel minimalistic, monocellular C2C12 model for progression towards *de novo* intrafusal skeletal muscle generation. Recombinant addition of intrafusal muscle developmentally associated protein Nrg-1 was employed to replicate an innervating Ia afferent neuron. The exogenous addition of Nrg-1 elicits elevated endogenous production of Egr3, resulting in intrafusal-like specific differentiation, as determined by the novel morphological characterisation of intrafusal bag myotubes. Concurrently, Nrg-1 increased cell proliferation during the differentiation phase of the protocol, resulting in increased nuclei per FOV and paired with less myotube area per nuclei. Extensive mRNA and Protein analysis of MyHCs is strongly suggestive of a unique phenotype following Nrg-1 addition, however both control and treated myotubes remain in an immature state. All putative intrafusal specific targets apart from developmental proteins Egr3 and Etv4 are not preferentially expressed in Nrg-1 treated myotubes. Egr3 staining, although significantly increased, was not a binary determinant for intrafusal bag myotubes. The suitability for C2C12s to generate intrafusal muscle fibres is still unclear. There is enough promise from the results presented here to encourage future research toward biomimetic tissue engineering approaches, in the hope of producing mature, Nrg-1 treated myotubes, characteristic of native, *in vivo* intrafusal skeletal muscle. These future models could provide platforms for developmental or disease state studies, pre-clinical screening, or clinical applications, including regeneration or replacement of diseased or dysfunctional tissue (Barrett et al., 2020; Kröger and Watkins, 2021).

## DATA AVAILABILITY STATEMENT

The original contributions presented in the study are included in the, further inquiries can be directed to the corresponding author.

## AUTHOR CONTRIBUTIONS

PB, VM and DP conceptualised the article and designed the experimental approach. PB acquired, analyzed, and interpreted the data, and drafted the manuscript as primary author. PB, TQ, VM and DP revised the manuscript, provided intellectual input and approved the final version of the manuscript.

## FUNDING

The author(s) disclosed receipt of the following financial support for the research, authorship, and/or publication of this article: PB is in receipt of the John Scales studentship, UCL.

## REFERENCES

Akay, T., Tourtellotte, W. G., Arber, S., and Jessell, T. M. (2014). Degradation of Mouse Locomotor Pattern in the Absence of Proprioceptive Sensory Feedback. *Proc. Natl. Acad. Sci. USA* 111, 16877–16882. doi:10.1073/pnas.1419045111

Albert, Y. v., Whitehead, J., Eldredge, L., Carter, J., Gao, X., and Tourtellotte, W. G. (2005). Transcriptional Regulation of Myotube Fate Specification and Intrafusal Muscle Fiber Morphogenesis. *J. Cel Biol.* 169, 257–268. doi:10.1083/jcb.200501156

Allouh, M. Z., Yablonka-Reuveni, Z., and Rosser, B. W. C. (2008). Pax7 Reveals a Greater Frequency and Concentration of Satellite Cells at the Ends of Growing Skeletal Muscle Fibers. *J. Histochem. Cytochem.* 56, 77–87. doi:10.1369/jhc.7A7301.2007

Andrechek, E. R., Hardy, W. R., Girgis-Gabardo, A. A., Perry, R. L. S., Butler, R., Graham, F. L., et al. (2002). ErbB2 Is Required for Muscle Spindle and Myoblast

Cell Survival. *Mol. Cel. Biol.* 22, 4714–4722. doi:10.1128/MCB.22.13.4714-4722.2002

Aravamudan, B., Mantilla, C. B., Zhan, W.-Z., and Sieck, G. C. (2006). Denervation Effects on Myonuclear Domain Size of Rat Diaphragm Fibers. *J. Appl. Physiol.* 100, 1617–1622. doi:10.1152/japplphysiol.01277.2005

Arber, S., Ladle, D. R., Lin, J. H., Frank, E., and Jessell, T. M. (2000). ETS Gene Er81 Controls the Formation of Functional Connections between Group Ia Sensory Afferents and Motor Neurons. *Cell* 101, 485–498. doi:10.1016/S0092-8674(00)80859-4

Banks, R. W. (2015). The Innervation of the Muscle Spindle: a Personal History. *J. Anat.* 227, 115–135. doi:10.1111/joa.12297

Banks, R. W. (1994). The Motor Innervation of Mammalian Muscle Spindles. *Prog. Neurobiol.* 43, 323–362. doi:10.1016/0301-0082(94)90059-0

Barrett, P., Quick, T. J., Mudera, V., and Player, D. J. (2020). Generating Intrafusal Skeletal Muscle Fibres *In Vitro*: Current State of the Art and Future Challenges. *J. Tissue Eng.* 11, 204173142098520. doi:10.1177/2041731420985205

Bland, J. M., and Altman, D. G. (1996). Statistics Notes: Transforming Data. *BMJ* 312, 770. doi:10.1136/bmj.312.7033.770

Brown, D. M., Parr, T., and Brameld, J. M. (2012). Myosin Heavy Chain mRNA Isoforms Are Expressed in Two Distinct Cohorts during C2C12 Myogenesis. *J. Muscle Res. Cel Motil.* 32, 383–390. doi:10.1007/s10974-011-9267-4

Bullinger, K. L., Nardelli, P., Pinter, M. J., Alvarez, F. J., and Cope, T. C. (2011). Permanent central Synaptic Disconnection of Proprioceptors after Nerve Injury and Regeneration. II. Loss of Functional Connectivity with Motoneurons. *J. Neurophysiol.* 106, 2471–2485. doi:10.1152/jn.01097.2010

Bustin, S. A., Benes, V., Garson, J. A., Hellemans, J., Huggett, J., Kubista, M., et al. (2009). The MIQE Guidelines: Minimum Information for Publication of Quantitative Real-Time PCR Experiments. *Clin. Chem.* 55, 611–622. doi:10.1373/clinchem.2008.112797

Capel, A. J., Rimington, R. P., Fleming, J. W., Player, D. J., Baker, L. A., Turner, M. C., et al. (2019). Scalable 3D Printed Molds for Human Tissue Engineered Skeletal Muscle. *Front. Bioeng. Biotechnol.* 7, 20. doi:10.3389/fbioe.2019.00020

Chal, J., and Pourquié, O. (2017). Making Muscle: Skeletal Myogenesis *In Vivo* and *In Vitro*. *Development* 144, 2104–2122. doi:10.1242/DEV.151035

Chen, H.-H., Tourtellotte, W. G., and Frank, E. (2002). Muscle Spindle-Derived Neurotrophin 3 Regulates Synaptic Connectivity between Muscle Sensory and Motor Neurons. *J. Neurosci.* 22, 3512–3519. doi:10.1523/JNEUROSCI.22-09-03512.2002

Choi, I. Y., Lim, H., Cho, H. J., Oh, Y., Chou, B.-K., Bai, H., et al. (2020). Transcriptional Landscape of Myogenesis from Human Pluripotent Stem Cells Reveals a Key Role of TWIST1 in Maintenance of Skeletal Muscle Progenitors. *Elife* 9. doi:10.7554/eLife.46981

Colón, A., Badu-Mensah, A., Guo, X., Goswami, A., and Hickman, J. J. (2020). Differentiation of Intrafusal Fibers from Human Induced Pluripotent Stem Cells. *ACS Chem. Neurosci.* 11, 1085–1092. doi:10.1021/acschemneuro.0c00055

Colón, A., Guo, X., Akanda, N., Cai, Y., and Hickman, J. J. (2017). Functional Analysis of Human Intrafusal Fiber Innervation by Human γ-motoneurons. *Sci. Rep.* 7, 17202. doi:10.1038/s41598-017-17382-2

Conte, A., Khan, N., Defazio, G., Rothwell, J. C., and Berardelli, A. (2013). Pathophysiology of Somatosensory Abnormalities in Parkinson Disease. *Nat. Rev. Neurol.* 9, 687–697. doi:10.1038/nrneurol.2013.224

Cope, T. C., Bonasera, S. J., and Nichols, T. R. (1994). Reinnervated Muscles Fail to Produce Stretch Reflexes. *J. Neurophysiol.* 71, 817–820. doi:10.1152/jn.1994.71.2.817

D'Silva, L. J., Lin, J., Staecker, H., Whitney, S. L., and Kluding, P. M. (2016). Impact of Diabetic Complications on Balance and Falls: Contribution of the Vestibular System. *Phys. Ther.* 96, 400–409. doi:10.2522/ptj.20140604

Ekmark, M., Rana, Z. A., Stewart, G., Hardie, D. G., and Gundersen, K. (2007). De-phosphorylation of MyoD Is Linking Nerve-Evoked Activity to Fast Myosin Heavy Chain Expression in Rodent Adult Skeletal Muscle. *J. Physiol.* 584, 637–650. doi:10.1113/jphysiol.2007.141457

Ettinger, L. R., Boucher, A., and Simonovich, E. (2018). Patients with Type 2 Diabetes Demonstrate Proprioceptive Deficit in the Knee. *Wjd* 9, 59–65. doi:10.4239/wjd.v9.i3.59

Fallon, K. B., Havlioglu, N., Hamilton, L. H., Cheng, T. P. H., and Carroll, S. L. (2004). Constitutive Activation of the neuregulin-1/erbB Signaling Pathway Promotes the Proliferation of a Human Peripheral Neuroepithelioma Cell Line. *J. Neurooncol.* 66, 273–284. doi:10.1023/b:neon.0000014521.28294.84

Ferlinc, A., Fabiani, E., Velnar, T., and Gradisnik, L. (2019). The Importance and Role of Proprioception in the Elderly: a Short Review. *Mater. Sociomed* 31, 219. doi:10.5455/msm.2019.31.219-221

Feys, P., Helsen, W., Ilsbroukx, S., and Meurrens, T. (2011). Is MS Intention Tremor Amplitude Related to Changed Peripheral Reflexes? *ISRN Neurol.* 2011, 1–7. doi:10.5402/2011/192414

Fling, B. W., Dutta, G. G., Schlueter, H., Cameron, M. H., and Horak, F. B. (2014). Associations between Proprioceptive Neural Pathway Structural Connectivity and Balance in People with Multiple Sclerosis. *Front. Hum. Neurosci.* 8, 1–11. doi:10.3389/fnhum.2014.00814

Ford, B. D., Han, B., and Fischbach, G. D. (2003). Differentiation-dependent Regulation of Skeletal Myogenesis by Neuregulin-1. *Biochem. Biophysical Res. Commun.* 306, 276–281. doi:10.1016/S0006-291X(03)00964-1

Geissler, A., Ryzhov, S., and Sawyer, D. B. (2020). Neuregulins: Protective and Reparative Growth Factors in Multiple Forms of Cardiovascular Disease. *Clin. Sci.* 134, 2623–2643. doi:10.1042/CS20200230

Gibson, M. C., and Schultz, E. (1983). Age-related Differences in Absolute Numbers of Skeletal Muscle Satellite Cells. *Muscle Nerve* 6, 574–580. doi:10.1002/mus.880060807

Gibson, M. C., and Schultz, E. (1982). The Distribution of Satellite Cells and Their Relationship to Specific Fiber Types in Soleus and Extensor Digitorum Longus Muscles. *Anat. Rec.* 202, 329–337. doi:10.1002/ar.1092020305

Guo, X., Colon, A., Akanda, N., Spradling, S., Stancescu, M., Martin, C., et al. (2017). Tissue Engineering the Mechanosensory Circuit of the Stretch Reflex Arc with Human Stem Cells: Sensory Neuron Innervation of Intrafusal Muscle Fibers. *Biomaterials* 122, 179–187. doi:10.1016/j.biomaterials.2017.01.005

Haftel, V. K. (2005). Central Suppression of Regenerated Proprioceptive Afferents. *J. Neurosci.* 25, 4733–4742. doi:10.1523/JNEUROSCI.4895-04.2005

Hardin, J. W., and Hilbe, J. M. (2014). Regression Models for Count Data Based on the Negative Binomial(p) Distribution. *Stata J.* 14, 280–291. doi:10.1177/1536867X1401400203

Harrison, B. C., Allen, D. L., and Leinwand, L. A. (2011). IIb or Not IIb? Regulation of Myosin Heavy Chain Gene Expression in Mice and Men. *Skelet. Muscle* 1, 5–9. doi:10.1186/2044-5040-1-5/FIGURES/3

Herndon, C. A., Ankenbruck, N., and Fromm, L. (2014). The Erk MAP Kinase Pathway Is Activated at Muscle Spindles and Is Required for Induction of the Muscle Spindle-specific Gene Egr3 by Neuregulin1. *J. Neurosci. Res.* 92, 174–184. doi:10.1002/jnr.23293

Hildyard, J. C., and Wells, D. J. (2014). Identification and Validation of Quantitative PCR Reference Genes Suitable for Normalizing Expression in normal and Dystrophic Cell Culture Models of Myogenesis. *Plos Curr.* 6, faafdde4bea8df4aa7d06cd5553119a6. doi:10.1371/currents.md.faafdde4bea8df4aa7d06cd5553119a6

Hippenmeyer, S., Shneider, N. A., Birchmeier, C., Burden, S. J., Jessell, T. M., and Arber, S. (2002). A Role for Neuregulin1 Signaling in Muscle Spindle Differentiation. *Neuron* 36, 1035–1049. doi:10.1016/S0896-6273(02)01101-7

Horst, D., Ustanina, S., Sergi, C., Mikuz, G., Juergens, H., Braun, T., et al. (2006). Comparative Expression Analysis of Pax3 and Pax7 during Mouse Myogenesis. *Int. J. Dev. Biol.* 50, 47–54. doi:10.1387/ijdb.052111dh

Jackson, J. R., Kirby, T. J., Fry, C. S., Cooper, R. L., McCarthy, J. J., Peterson, C. A., et al. (2015). Reduced Voluntary Running Performance Is Associated with Impaired Coordination as a Result of Muscle Satellite Cell Depletion in Adult Mice. *Skeletal Muscle* 5, 41. doi:10.1186/s13395-015-0065-3

Jacobson, C., Duggan, D., and Fischbach, G. (2004). Neuregulin Induces the Expression of Transcription Factors and Myosin Heavy Chains Typical of Muscle Spindles in Cultured Human Muscle. *Proc. Natl. Acad. Sci.* 101, 12218–12223. doi:10.1073/pnas.0404240101

Juhas, M., Engelmayr, G. C., Fontanella, A. N., Palmer, G. M., and Bursac, N. (2014). Biomimetic Engineered Muscle with Capacity for Vascular Integration and Functional Maturation *In Vivo*. *Proc. Natl. Acad. Sci.* 111, 5508–5513. doi:10.1073/pnas.1402723111

Kirabo, A., Ryzhov, S., Gupte, M., Sengsayadeth, S., Gumina, R. J., Sawyer, D. B., et al. (2017). Neuregulin-1β Induces Proliferation, Survival and Paracrine Signaling in normal Human Cardiac Ventricular Fibroblasts. *J. Mol. Cell Cardiol.* 105, 59–69. doi:10.1016/J.YJMCC.2017.03.001

Kirkpatrick, L. J., Allouh, M. Z., Nightingale, C. N., Devon, H. G., Yablonka-Reuveni, Z., and Rosser, B. W. C. (2008). Pax7 Shows Higher Satellite Cell

Frequencies and Concentrations within Intrafusal Fibers of Muscle Spindles. *J. Histochem. Cytochem.* 56, 831–840. doi:10.1369/jhc.2008.951608

Kirkpatrick, L. J., Yablonka-Reuveni, Z., and Rosser, B. W. C. (2010). Retention of Pax3 Expression in Satellite Cells of Muscle Spindles. *J. Histochem. Cytochem.* 58, 317–327. doi:10.1369/jhc.2009.954792

Kozeka, K., and Ontell, M. (1981). The Three-Dimensional Cytoarchitecture of Developing Murine Muscle Spindles. *Developmental Biol.* 87, 133–147. doi:10.1016/0012-1606(81)90067-1

Kröger, S., and Watkins, B. (2021). Muscle Spindle Function in Healthy and Diseased Muscle. *Skeletal Muscle* 11, 3. doi:10.1186/s13395-020-00258-x

Kucera, J., and Walro, J. M. (1992). Formation of Muscle Spindles in the Absence of Motor Innervation. *Neurosci. Lett.* 145, 47–50. doi:10.1016/0304-3940(92)90200-Q

Kucera, J., Walro, J. M., and Gorza, L. (1992). Expression of Type-specific MHC Isoforms in Rat Intrafusal Muscle Fibers. *J. Histochem. Cytochem.* 40, 293–307. doi:10.1177/40.2.1552171

Kucera, J., and Walro, J. M. (1990). Origin of Intrafusal Muscle Fibers in the Rat. *Histochemistry* 93, 567–580. doi:10.1007/BF00272199

Kucera, J., and Walro, J. (1995). Origin of Intrafusal Fibers from a Subset of Primary Myotubes in the Rat. *Anat. Embryol.* 192, 149–158. doi:10.1007/BF00186003

Kucera, J., Walro, J., and Reichler, J. (1993). Differential Effects of Neonatal Denervation on Intrafusal Muscle Fibers in the Rat. *Anat. Embryol.* 187, 397–408. doi:10.1007/BF00185898

Kurosaka, M., Ogura, Y., Funabashi, T., and Akema, T. (2017). Early Growth Response 3 (Egr3) Contributes a Maintenance of C2C12 Myoblast Proliferation. *J. Cel. Physiol.* 232, 1114–1122. doi:10.1002/jcp.25574

Leu, M., Bellmunt, E., Schwander, M., Fariñas, I., Brenner, H. R., and Müller, U. (2003). Erbb2 Regulates Neuromuscular Synapse Formation and Is Essential for Muscle Spindle Development. *Development* 130, 2291–2301. doi:10.1242/dev.00447

Liu, J.-X., Eriksson, P.-O., Thornell, L.-E., and Pedrosa-Domellöf, F. (2005). Fiber Content and Myosin Heavy Chain Composition of Muscle Spindles in Aged Human Biceps Brachii. *J. Histochem. Cytochem.* 53, 445–454. doi:10.1369/jhc.4A6257.2005

Liu, J.-X., Eriksson, P.-O., Thornell, L.-E., and Pedrosa-Domellöf, F. (2002). Myosin Heavy Chain Composition of Muscle Spindles in Human Biceps Brachii. *J. Histochem. Cytochem.* 50, 171–183. doi:10.1177/002215540205000205

Liu, J., and Kern, J. A. (2002). Neuregulin-1 Activates the JAK-STAT Pathway and Regulates Lung Epithelial Cell Proliferation. *Am. J. Respir. Cel Mol. Biol.* 27, 306–313. doi:10.1165/rcmb.4850

Maas, H., Prilutsky, B. I., Nichols, T. R., and Gregor, R. J. (2007). The Effects of Self-Reinnervation of Cat Medial and Lateral Gastrocnemius Muscles on Hindlimb Kinematics in Slope Walking. *Exp. Brain Res.* 181, 377–393. doi:10.1007/s00221-007-0938-8

Macefield, V. G., and Knellwolf, T. P. (2018). Functional Properties of Human Muscle Spindles. *J. Neurophysiol.* 120, 452–467. doi:10.1152/jn.00071.2018.-Muscle

Miwa, T., Miwa, Y., and Kanda, K. (1995). Dynamic and Static Sensitivities of Muscle Spindle Primary Endings in Aged Rats to Ramp Stretch. *Neurosci. Lett.* 201, 179–182. doi:10.1016/0304-3940(95)12165-X

Muller, K. A., Ryals, J. M., Feldman, E. L., and Wright, D. E. (2008). Abnormal Muscle Spindle Innervation and Large-Fiber Neuropathy in Diabetic Mice. *Diabetes* 57, 1693–1701. doi:10.2337/db08-0022

Muñoz, M., García-Casco, J. M., Caraballo, C., Fernández-Barroso, M. Á., Sánchez-Esquiliche, F., Gómez, F., et al. (2018). Identification of Candidate Genes and Regulatory Factors Underlying Intramuscular Fat Content through Longissimus Dorsi Transcriptome Analyses in Heavy Iberian Pigs. *Front. Genet.* 9, 608. doi:10.3389/fgene.2018.00608

Muramatsu, K., Niwa, M., Tamaki, T., Ikutomo, M., Masu, Y., Hasegawa, T., et al. (2017). Effect of Streptozotocin-Induced Diabetes on Motoneurons and Muscle Spindles in Rats. *Neurosci. Res.* 115, 21–28. doi:10.1016/j.neures.2016.10.004

Oliveira Fernandes, M., and Tourtellotte, W. G. (2015). Egr3-dependent Muscle Spindle Stretch Receptor Intrafusal Muscle Fiber Differentiation and Fusimotor Innervation Homeostasis. *J. Neurosci.* 35, 5566–5578. doi:10.1523/JNEUROSCI.0241-15.2015

Österlund, C., Liu, J.-X., Thornell, L.-E., and Eriksson, P.-O. (2013). Intrafusal Myosin Heavy Chain Expression of Human Masseter and Biceps Muscles at Young Age Shows Fundamental Similarities but Also Marked Differences. *Histochem. Cel Biol.* 139, 895–907. doi:10.1007/s00418-012-1072-7

Österlund, C., Liu, J.-X., Thornell, L.-E., and Eriksson, P.-O. (2011). Muscle Spindle Composition and Distribution in Human Young Masseter and Biceps Brachii Muscles Reveal Early Growth and Maturation. *Anat. Rec.* 294, 683–693. doi:10.1002/ar.21347

Ovalle, W. K., and Dow, P. R. (1986). Alterations in Muscle Spindle Morphology in Advanced Stages of Murine Muscular Dystrophy. *Anat. Rec.* 216, 111–126. doi:10.1002/ar.1092160202

Pellegrino, M. A., Canepari, M., Rossi, R., D'Antona, G., Reggiani, C., and Bottinelli, R. (2003). Orthologous Myosin Isoforms and Scaling of Shortening Velocity with Body Size in Mouse, Rat, Rabbit and Human Muscles. *J. Physiol.* 546, 677–689. doi:10.1113/jphysiol.2002.027375

Prather, J. F., Nardelli, P., Nakanishi, S. T., Ross, K. T., Nichols, T. R., Pinter, M. J., et al. (2011). Recovery of Proprioceptive Feedback from Nerve Crush. *J. Physiol.* 589, 4935–4947. doi:10.1113/jphysiol.2011.210518

Qiao, Y., Cong, M., Li, J., Li, H., and Li, Z. (2018). The Effects of Neuregulin-1β on Intrafusal Muscle Fiber Formation in Neuromuscular Coculture of Dorsal Root Ganglion Explants and Skeletal Muscle Cells. *Skeletal Muscle* 8, 29. doi:10.1186/s13395-018-0175-9

Rao, L., Qian, Y., Khodabukus, A., Ribar, T., and Bursac, N. (2018). Engineering Human Pluripotent Stem Cells into a Functional Skeletal Muscle Tissue. *Nat. Commun.* 9, 1–12. doi:10.1038/s41467-017-02636-4

Rio, D. C., Ares, M., Hannon, G. J., and Nilsen, T. W. (2010). Purification of RNA Using TRIzol (TRI Reagent). *Cold Spring Harb. Protoc.* 2010, pdb.prot5439. doi:10.1101/pdb.prot5439

Rosser, B. W., Dean, M. S., and Bandman, E. (2002). Myonuclear Domain Size Varies along the Lengths of Maturing Skeletal Muscle Fibers. *Int. J. Dev. Biol.* 46, 747–754. doi:10.1387/IJDB.12216987

Roy, R. R., Zhong, H., Siengthai, B., and Edgerton, V. R. (2005). Activity-dependent Influences Are Greater for Fibers in Rat Medial Gastrocnemius Than Tibialis Anterior Muscle. *Muscle Nerve* 32, 473–482. doi:10.1002/mus.20369

Ruijs, A. C. J., Jaquet, J.-B., Kalmijn, S., Giele, H., and Hovius, S. E. R. (2005). Median and Ulnar Nerve Injuries: A Meta-Analysis of Predictors of Motor and Sensory Recovery after Modern Microsurgical Nerve Repair. *Plast. Reconstr. Surg.* 116, 484–494. doi:10.1097/01.prs.0000172896.86594.07

Rumsey, J. W., Das, M., Bhalkikar, A., Stancescu, M., and Hickman, J. J. (2010). Tissue Engineering the Mechanosensory Circuit of the Stretch Reflex Arc: Sensory Neuron Innervation of Intrafusal Muscle Fibers. *Biomaterials* 31, 8218–8227. doi:10.1016/j.biomaterials.2010.07.027

Rumsey, J. W., Das, M., Kang, J.-F., Wagner, R., Molnar, P., and Hickman, J. J. (2008). Tissue Engineering Intrafusal Fibers: Dose- and Time-dependent Differentiation of Nuclear Bag Fibers in a Defined *In Vitro* System Using Neuregulin 1-β-1. *Biomaterials* 29, 994–1004. doi:10.1016/j.biomaterials.2007.10.042

Sampath, S. C., Sampath, S. C., and Millay, D. P. (2018). Myoblast Fusion Confusion: The Resolution Begins. *Skeletal Muscle* 8, 3. doi:10.1186/s13395-017-0149-3

Schiaffino, S., and Reggiani, C. (2011). Fiber Types in Mammalian Skeletal Muscles. *Physiol. Rev.* 91, 1447–1531. doi:10.1152/physrev.00031.2010

Schiaffino, S., Rossi, A. C., Smerdu, V., Leinwand, L. A., and Reggiani, C. (2015). Developmental Myosins: Expression Patterns and Functional Significance. *Skeletal Muscle* 5, 22. doi:10.1186/s13395-015-0046-6

Schindelin, J., Arganda-Carreras, I., Frise, E., Kaynig, V., Longair, M., Pietzsch, T., et al. (2012). Fiji: An Open-Source Platform for Biological-Image Analysis. *Nat. Methods* 9, 676–682. doi:10.1038/nmeth.2019

Schmittgen, T. D., and Livak, K. J. (2008). Analyzing Real-Time PCR Data by the Comparative CT Method. *Nat. Protoc.* 3, 1101–1108. doi:10.1038/nprot.2008.73

Seward, D. J., Haney, J. C., Rudnicki, M. A., and Swoap, S. J. (2001). bHLH Transcription Factor MyoD Affects Myosin Heavy Chain Expression Pattern in a Muscle-specific Fashion. *Am. J. Physiology-Cell Physiol.* 280, C408–C413. doi:10.1152/ajpcell.2001.280.2.c408

Shaffer, S. W., and Harrison, A. L. (2007). Aging of the Somatosensory System: A Translational Perspective. *Phys. Ther.* 87, 193–207. doi:10.2522/ptj.20060083

Shenkman, B. S., Turtikova, O. V., Nemirovskaya, T. L., and Grigoriev, A. I. (2010). Skeletal Muscle Activity and the Fate of Myonuclei. *Acta Naturae* 2, 59–65. doi:10.32607/20758251-2010-2-2-59-65

Shneider, N. A., Brown, M. N., Smith, C. A., Pickel, J., and Alvarez, F. J. (2009). Gamma Motor Neurons Express Distinct Genetic Markers at Birth and Require Muscle Spindle-Derived GDNF for Postnatal Survival. *Neural Dev.* 4, 42. doi:10.1186/1749-8104-4-42

Soukup, T., Pedrosa-Domellöf, F., and Thornell, L.-E. (1995). Expression of Myosin Heavy Chain Isoforms and Myogenesis of Intrafusal Fibres in Rat Muscle Spindles. *Microsc. Res. Tech.* 30, 390–407. doi:10.1002/jemt.1070300506

Stuart, C. A., Stone, W. L., Howell, M. E. A., Brannon, M. F., Hall, H. K., Gibson, A. L., et al. (2016). Myosin Content of Individual Human Muscle Fibers Isolated by Laser Capture Microdissection. *Am. J. Physiology-Cell Physiol.* 310, C381–C389. doi:10.1152/ajpcell.00317.2015

Taylor, S. C., Berkelman, T., Yadav, G., and Hammond, M. (2013). A Defined Methodology for Reliable Quantification of Western Blot Data. *Mol. Biotechnol.* 55, 217–226. doi:10.1007/s12033-013-9672-6

Teasdale, H., Preston, E., and Waddington, G. (2017). Proprioception of the Ankle Is Impaired in People with Parkinson's Disease. *Mov. Disord. Clin. Pract.* 4, 524–528. doi:10.1002/mdc3.12464

Teixeira, C. E., and Duarte, J. A. (2011). Myonuclear Domain in Skeletal Muscle Fibers. A Critical Review. *Aehd* 2, 92–101. doi:10.5628/aehd.v2i2.24

Thornell, L. E., Carlsson, L., Eriksson, P. O., Liu, J. X., Österlund, C., Stål, P., et al. (2015). Fibre Typing of Intrafusal Fibres. *J. Anat.* 227, 136–156. doi:10.1111/joa.12338

Torii, R., Velliou, R.-I., Hodgson, D., and Mudera, V. (2018). Modelling Multi-Scale Cell-Tissue Interaction of Tissue-Engineered Muscle Constructs. *J. Tissue Eng.* 9, 204173141878714. doi:10.1177/2041731418787141

Tourtellotte, W. G., Keller-Peck, C., Milbrandt, J., and Kucera, J. (2001). The Transcription Factor Egr3 Modulates Sensory Axon-Myotube Interactions during Muscle Spindle Morphogenesis. *Developmental Biol.* 232, 388–399. doi:10.1006/dbio.2001.0202

Tourtellotte, W. G., and Milbrandt, J. (1998). Sensory Ataxia and Muscle Spindle Agenesis in Mice Lacking the Transcription Factor Egr3. *Nat. Genet.* 20, 87–91. doi:10.1038/1757

van Deursen, R. W. M., Sanchez, M. M., Ulbrecht, J. S., and Cavanagh, P. R. (1998). The Role of Muscle Spindles in Ankle Movement Perception in Human Subjects with Diabetic Neuropathy. *Exp. Brain Res.* 120, 1–8. doi:10.1007/s002210050371

van Deursen, R. W. M., and Simoneau, G. G. (1999). Foot and Ankle Sensory Neuropathy, Proprioception, and Postural Stability. *J. Orthop. Sports Phys. Ther.* 29, 718–726. doi:10.2519/jospt.1999.29.12.718

Vandenburgh, H. H., Karlisch, P., and Farr, L. (1988). Maintenance of Highly Contractile Tissue-Cultured Avian Skeletal Myotubes in Collagen Gel. In Vitro *Cel Dev Biol* 24, 166–174. doi:10.1007/BF02623542

Walro, J. M., and Kucera, J. (1999). Why Adult Mammalian Intrafusal and Extrafusal Fibers Contain Different Myosin Heavy-Chain Isoforms. *Trends Neurosciences* 22, 180–184. doi:10.1016/s0166-2236(98)01339-3

Wang, J., Khodabukus, A., Rao, L., Vandusen, K., Abutaleb, N., and Bursac, N. (2019). Engineered Skeletal Muscles for Disease Modeling and Drug Discovery. *Biomaterials* 221, 119416. doi:10.1016/j.biomaterials.2019.119416

Wheeler, M. T., Snyder, E. C., Patterson, M. N., and Swoap, S. J. (1999). An E-Box within the MHC IIB Gene Is Bound by MyoD and Is Required for Gene Expression in Fast Muscle. *Am. J. Physiology-Cell Physiol.* 276, C1069–C1078. doi:10.1152/ajpcell.1999.276.5.c1069

Williams, S., and Jacobson, C. (2010). α-Dystroglycan Is Essential for the Induction of Egr3, a Transcription Factor Important in Muscle Spindle Formation. *Devel Neurobio* 70, NA. doi:10.1002/dneu.20793

Ye, J., Coulouris, G., Zaretskaya, I., Cutcutache, I., Rozen, S., and Madden, T. L. (2012). Primer-BLAST: a Tool to Design Target-specific Primers for Polymerase Chain Reaction. *BMC Bioinformatics* 13, 134. doi:10.1186/1471-2105-13-134

Yin, H., Price, F., and Rudnicki, M. A. (2013). Satellite Cells and the Muscle Stem Cell Niche. *Physiol. Rev.* 93, 23–67. doi:10.1152/physrev.00043.2011

Zammit, P. S., Carvajal, J. J., Golding, J. P., Morgan, J. E., Summerbell, D., Zolnerciks, J., et al. (2004). Myf5 Expression in Satellite Cells and Spindles in Adult Muscle Is Controlled by Separate Genetic Elements. *Developmental Biol.* 273, 454–465. doi:10.1016/j.ydbio.2004.05.038

Zammit, P. S. (2017). Function of the Myogenic Regulatory Factors Myf5, MyoD, Myogenin and MRF4 in Skeletal Muscle, Satellite Cells and Regenerative Myogenesis. *Semin. Cel Developmental Biol.* 72, 19–32. doi:10.1016/j.semcdb.2017.11.011

Zanou, N., and Gailly, P. (2013). Skeletal Muscle Hypertrophy and Regeneration: Interplay between the Myogenic Regulatory Factors (MRFs) and Insulin-like Growth Factors (IGFs) Pathways. *Cell. Mol. Life Sci.* 70, 4117–4130. doi:10.1007/s00018-013-1330-4

Zhou, Y., Liu, D., and Kaminski, H. J. (2010). Myosin Heavy Chain Expression in Mouse Extraocular Muscle: More Complex Than Expected. *Invest. Ophthalmol. Vis. Sci.* 51, 6355–6363. doi:10.1167/iovs.10-5937

Zhuang, P., An, J., Chua, C. K., and Tan, L. P. (2020). Bioprinting of 3D *In Vitro* Skeletal Muscle Models: A Review. *Mater. Des.* 193, 108794. doi:10.1016/j.matdes.2020.108794

**Conflict of Interest:** The authors declare that the research was conducted in the absence of any commercial or financial relationships that could be construed as a potential conflict of interest.

**Publisher's Note:** All claims expressed in this article are solely those of the authors and do not necessarily represent those of their affiliated organizations, or those of the publisher, the editors and the reviewers. Any product that may be evaluated in this article, or claim that may be made by its manufacturer, is not guaranteed or endorsed by the publisher.

frontiers | Frontiers in Cell and Developmental Biology

ORIGINAL RESEARCH
published: 06 April 2022
doi: 10.3389/fcell.2022.830415

# Modeling Patient-Specific Muscular Dystrophy Phenotypes and Therapeutic Responses in Reprogrammed Myotubes Engineered on Micromolded Gelatin Hydrogels

*Florian Barthélémy[1,2†], Jeffrey W. Santoso[3†], Laura Rabichow[1,2], Rongcheng Jin[3], Isaiah Little[1,2], Stanley F. Nelson[2,4,5], Megan L. McCain[3,6]* and M. Carrie Miceli[1,2]**

[1]Department of Microbiology Immunology and Molecular Genetics, University of California, Los Angeles, Los Angeles, CA, United States, [2]Center for Duchenne Muscular Dystrophy, University of California, Los Angeles, Los Angeles, CA, United States, [3]Laboratory for Living Systems Engineering, Department of Biomedical Engineering, USC Viterbi School of Engineering, University of Southern California, Los Angeles, CA, United States, [4]Department of Neurology, David Geffen School of Medicine, University of California, Los Angeles, Los Angeles, CA, United States, [5]Department of Pathology and Laboratory Medicine, David Geffen School of Medicine, University of California, Los Angeles, Los Angeles, CA, United States, [6]Department of Stem Cell Biology and Regenerative Medicine, Keck School of Medicine of USC, University of Southern California, Los Angeles, CA, United States

*In vitro* models of patient-derived muscle allow for more efficient development of genetic medicines for the muscular dystrophies, which often present mutation-specific pathologies. One popular strategy to generate patient-specific myotubes involves reprogramming dermal fibroblasts to a muscle lineage through MyoD induction. However, creating physiologically relevant, reproducible tissues exhibiting multinucleated, aligned myotubes with organized striations is dependent on the introduction of physicochemical cues that mimic the native muscle microenvironment. Here, we engineered patient-specific control and dystrophic muscle tissues *in vitro* by culturing and differentiating MyoD–directly reprogrammed fibroblasts isolated from one healthy control subject, three patients with Duchenne muscular dystrophy (DMD), and two Limb Girdle 2A/R1 (LGMD2A/R1) patients on micromolded gelatin hydrogels. Engineered DMD and LGMD2A/R1 tissues demonstrated varying levels of defects in α-actinin expression and organization relative to control, depending on the mutation. In genetically relevant DMD tissues amenable to mRNA reframing by targeting exon 44 or 45 exclusion, exposure to exon skipping antisense oligonucleotides modestly increased myotube coverage and alignment and rescued dystrophin protein expression. These findings highlight the value of engineered culture substrates in guiding the organization of reprogrammed patient fibroblasts into aligned muscle tissues, thereby extending their value as tools for exploration and dissection of the cellular and molecular basis of genetic muscle defects, rescue, and repair.

**Keywords: DMD, LGMD, exon skipping, hydrogels, calpain 3, dystrophin**

OPEN ACCESS

***Edited by:***
*Maurilio Sampaolesi, KU Leuven, Belgium*

***Reviewed by:***
*So-ichiro Fukada, Osaka University, Japan*
*Cesare Gargioli, University of Rome Tor Vergata, Italy*
*Gillian Sandra Butler-Browne, Centre for Research in Myology, France*

****Correspondence:***
*M. Carrie Miceli*
*cmiceli@ucla.edu*
*Megan L. McCain*
*mlmccain@usc.edu*

*†These authors have contributed equally to this work and share first authorship*

***Specialty section:***
*This article was submitted to Stem Cell Research, a section of the journal Frontiers in Cell and Developmental Biology*

***Received:*** *07 December 2021*
***Accepted:*** *22 February 2022*
***Published:*** *06 April 2022*

***Citation:***
*Barthélémy F, Santoso JW, Rabichow L, Jin R, Little I, Nelson SF, McCain ML and Miceli MC (2022) Modeling Patient-Specific Muscular Dystrophy Phenotypes and Therapeutic Responses in Reprogrammed Myotubes Engineered on Micromolded Gelatin Hydrogels. Front. Cell Dev. Biol. 10:830415. doi: 10.3389/fcell.2022.830415*

## INTRODUCTION

Muscular dystrophies are a heterogenous group of genetic disorders characterized by progressive muscle weakness. Duchenne (DMD-OMIM310200) and Limb Girdle 2A/R1 (LGMD2A/R1-OMIM 253600) muscular dystrophies are caused by mutations in the *DMD* and *CAPN3* genes, respectively. *DMD* generally presents early in childhood and results in loss of ambulation in early teenage years and fatal cardiac or respiratory insufficiencies in their twenties (Flanigan, 2014). LMGD2A/R1 has a more variable presentation, with onset of muscle weakness ranging between 0 and 40 years of age and different rates of progression (Kramerova et al., 2007). *DMD*-encoded dystrophin and *CAPN3*-encoded calpain proteins have both been implicated in contributing to the structural integrity and maintenance of the sarcomere and muscle health (Blau et al., 1983; Muntoni, 2001; Kramerova et al., 2007; van der Wal et al., 2018; Pakula et al., 2019; Verhaart et al., 2019; Caputo et al., 2020; Ortiz-Cordero et al., 2021). Therefore, culture platforms that enable sarcomere maturation may help in elucidating the molecular basis of dystrophin and calpain 3 contributions to the organization and maturation of striated skeletal muscle. Whereas molecular characterization of these dystrophies has led to the development of mutation specific genetic medicines, few human mutationally defined pre-clinical cell models suitable for testing of drugs with target mutation subsets have been developed.

A major challenge in developing culture models for muscular dystrophies and other rare muscle diseases is cell source. Primary myoblasts require access to fresh muscle tissue, have limited capacity to divide, and often require purification (Blau et al., 1983; Pakula et al., 2019). Because most diagnoses are now made through genetic testing, biopsies of muscular dystrophy patients are rarely performed, and fresh muscle biopsy tissue is largely unavailable (Muntoni, 2001; Verhaart et al., 2019). Alternatively, dermal fibroblasts derived from patient skin punches can be reprogrammed to induced pluripotent stem cells (iPSCs) and subsequently differentiated to myoblasts (van der Wal et al., 2018). Although iPSC technology has led to useful models for DMD and other muscle disorders (Caputo et al., 2020; Ortiz-Cordero et al., 2021), iPSCs can be difficult and costly to derive and expand (Speciale et al., 2020). A simpler approach is to reprogram dermal fibroblasts directly to myoblasts by expression of MyoD, a master regulator of muscle cell development. We and others have stably expressed an inducible MyoD construct in dermal fibroblasts partially immortalized through expression of human telomerase reverse transcriptase (hTERT), termed iDRMs (induced directly reprogrammed myotubes), which can be expanded as fibroblasts and then reprogrammed to myoblasts and multi-nucleated myotube-like cells upon MyoD induction (Chaouch et al., 2009; Kendall et al., 2012; Kim et al., 2016; Wein et al., 2017; Barthélémy et al., 2019). We previously used iDRM from patients with DMD on standard culture dishes to evaluate exon skipping strategies aimed at dystrophin rescue by reframing the RNA through exclusion of an additional exon (Wein et al., 2014; Barthélémy et al., 2018; Barthélémy et al., 2019; Gibbs et al., 2019). Although we were able to detect low levels of rescued dystrophin protein for certain DMD patient lines (Barthélémy et al., 2019), iDRMs were randomly organized and rarely survived longer than 1 week due to cell death and delamination, which may not be sufficient to detect dystrophin rescue in all patient lines.

To overcome some limitations of conventional *in vitro* techniques, several approaches to engineer DMD muscle tissue have been developed (Santoso and McCain, 2020). Fibronectin has been microcontact-printed as line patterns onto elastomeric polydimethylsiloxane (PDMS) substrates that were then laser-engraved into cantilevers to measure force generation. Primary control and DMD myoblasts seeded on these surfaces fused into aligned myotubes, with DMD myotubes exhibiting less actin and nuclear alignment and therefore lower contractile stress (Nesmith et al., 2016). However, PDMS is far stiffer than native muscle tissues, which is thought to contribute to delamination of cell line-derived myotubes after approximately 1 week in culture (Bettadapur et al., 2016a). Three-dimensional (3-D) muscle tissues have also been engineered by mixing myoblasts in matrix-derived hydrogels and allowing the tissue to compact and align across two anchor points, providing a closer match to the compliance of native tissue and a more relevant microenvironment. 3-D tissues engineered with DMD iPSC-derived myoblasts have demonstrated nuclear, cytoskeletal, and contractile abnormalities (Maffioletti et al., 2018; Ebrahimi et al., 2021). However, 3-D tissues models require high numbers of cells and generally entail complex fabrication procedures, limiting their overall throughput.

Micromolded gelatin hydrogels have been developed by us and others as substrates for lengthening the culture lifetime and improving the alignment and maturation of myotubes differentiated from C2C12 (Bettadapur et al., 2016a; Denes et al., 2019a), primary chick (Santoso et al., 2021a; Gupta et al., 2021), and human control and DMD iPSC-derived myoblasts (Al Tanoury et al., 2021). These gelatin substrates are relatively inexpensive and easy to fabricate while also matching the compliance of native muscle tissue. Here, we cultured iDRM control and DMD patient-derived myotubes on micromolded gelatin hydrogels to promote their alignment and stability. We demonstrate that iDRM on the hydrogels align and form myofiber-like structures with different degrees of maturity, evaluated with α-actinin immunostaining and confocal microscopy. Moreover, we treated tissues with Antisense oligonucleotid-directed exon skipping molecules and evaluated dystrophin gene and protein expression. We also engineered tissues from two newly derived LGMD2A/R1 iDRM, demonstrating the application of these approaches to other rare muscle diseases. Together, these findings

highlight the value of combining patient-derived reprogrammed cell models with engineered substrates to evaluate and screen personalized therapies for rare muscle diseases.

# MATERIAL AND METHODS

## iDRM Derivation and Dermal Fibroblast Donor Characteristics

MyoD-reprogrammed skin punch fibroblasts (iDRM) were derived from three DMD subjects (Wang et al., 2018; Gibbs et al., 2019). As reported, iDRM derived from DMD subject 1003, who lost ambulation at 13.5 years, has an out-of-frame deletion of *DMD* exons 46–51 and is predicted not to express the dystrophin protein (Wang et al., 2018). DMD subject 1023 has an in-frame deletion of *DMD* exons 3 to 23 with sub-typical, albeit significant, sarcolemmal dystrophin protein expression (Gibbs et al., 2019) and remains ambulatory at age 20. Subject 1015 lost ambulation at age 15 and harbors a deletion of *DMD* exon 45, low levels of self-corrected exon 44 "skipped" mRNA in derived iDRM (Wang et al., 2018), and an increased frequency of clusters of dystrophin-positive revertant fibers. Muscle biopsies were only available from subjects 1015 and 1023 and a healthy 20-year-old female volunteer who served as a positive control for normal dystrophin expression and localization.

MyoD-reprogrammed skin fibroblasts (iDRM) from two LGMD2A/R1 were established for this study. Subject 1077 is a 52-year-old male who lost ambulation at 44 years old with compound heterozygous mutations: c.550delA (p.T184Rfs*36) and c.1342C > G (p448R > G) in *CAPN3*. Both mutations are predicted to be pathogenic (https://databases.lovd.nl/shared/genes/CAPN3). Subject 1081 is a 37-year-old female presenting a homozygous deletion of *CAPN3* exons 17 to 24 [ c.(1914 + 1_1915–1)_(*544_?) del]. Deletion of these exons leads to a short truncated non-functional *CAPN3* protein (BhattBHATT1 et al., 2019). All these variants leading to LGMD2A/R1 have been previously described in other patients (BhattBHATT1 et al., 2019; Krahn et al., 2006; Nallamilli et al., 2018).

Skin punches and muscle biopsies were obtained with informed consent from patients of the Center for Duchenne Muscular Dystrophy (CDMD) at UCLA under University of California Los Angeles Institutional Review Board (IRB)–approved protocols #11–001087 and #18–001547. Open or needle skeletal muscle biopsies were performed and processed as previously described (Barthelemy et al., 2020; Lee et al., 2020). Muscle samples were sectioned at 10 μm thickness and stained with hematoxylin and eosin for global histology assessment or dystrophin/laminin using standard immunohistochemistry (Barthelemy et al., 2020), where dystrophin NCL-2 (Leica, Buffalo Grove, IL, United States) at a dilution of 1:50 and laminin L9393 (Sigma, St. Louis, MO, United States) at a dilution of 1:25 were used. Digital histological images were acquired using standard light and fluorescence using an Axioplan 2 microscope (Carl Zeiss Inc., United States). Pictures were then processed with AxioVision software (Zeiss) and/or ImageJ software.

## Inducible Directly Reprogrammable Myotube (iDRM) Lines

iDRMs were generated from dermal fibroblasts cultured from skin punches of 3 mm diameter obtained from each participant. After the establishment of a fibroblast culture, cells were immortalized using a lentivirus encoding hTERT and subsequently infected with a lentivirus encoding a tamoxifen-inducible MyoD to allow commitment to skeletal muscle lineage, as we have previously reported for derivation of DMD 1023 and DMD 1015 iDRM (Barthélémy et al., 2019; Gibbs et al., 2019) (**Figure 1A**).

iDRMs were cultured as previously described, modified by plating on coverslips with micromolded gelatin hydrogels (described below) at the time of fibroblast plating, before MyoD induction (**Figure 1B**) (Barthelemy et al., 2018). Briefly, cells were kept in fibroblast growth media [DMEM (+ phenol red, high glucose) (Thermo Fisher Scientific, Grand Island, NY, United States) + 15% fetal bovine serum (Omega Scientific, Tarzana, CA, United States) + 1% nonessential amino acids (Thermo Fisher Scientific, Grand Island, NY, United States) + 1% penicillin/streptomycin (Thermo Fisher Scientific, Grand Island, NY, United States)]. To induce differentiation to myotubes, cells were first incubated in fibroblast growth media containing 5 μM of 4-OH tamoxifen (Sigma, St. Louis, MO, United States; dissolved in ethanol) for 48 h. On day 3, cells were washed in PBS (Thermo Fisher Scientific), and fusion media containing 1 μM 4-OH-tamoxifen was added [1:1 Ham's F-10: DMEM (phenol red free, high glucose), 2% horse serum (Thermo Fisher Scientific, Grand Island, NY, United States), and 2% insulin-transferrin-selenium (Thermo Fisher Scientific, Grand Island, NY, United States)]. During the first week of differentiation, SB431542 (a TGF-β inhibitor) was added at a final concentration of 5 μM. All lines were kept for up to 2 weeks in fusion conditions before analysis, and the medium was changed every other day (**Figure 1B**).

## Gelatin Hydrogel

The fabrication of micromolded gelatin hydrogels cross-linked with transglutaminase was performed as previously described (Santoso et al., 2021a; Gupta et al., 2021) and illustrated in **Figure 1A**. Briefly, 260-mm$^2$ hexagons were cut from 150-mm polystyrene dishes and masked with tape. Inside each hexagonal coverslip, circles were laser-cut into the tape with a 30W Epilog Mini 24 Laser Engraver. Regions of the tape were removed such that only the outer border of substrates was covered. Coverslips were then treated with plasma (Harrick Plasma, Ithaca, NY, United States) for 10 min in ambient conditions to increase adherence of polystyrene.

PDMS stamps with 10-μm-wide grooves separated by 10 μm and 2 μm in height were manufactured using photolithography

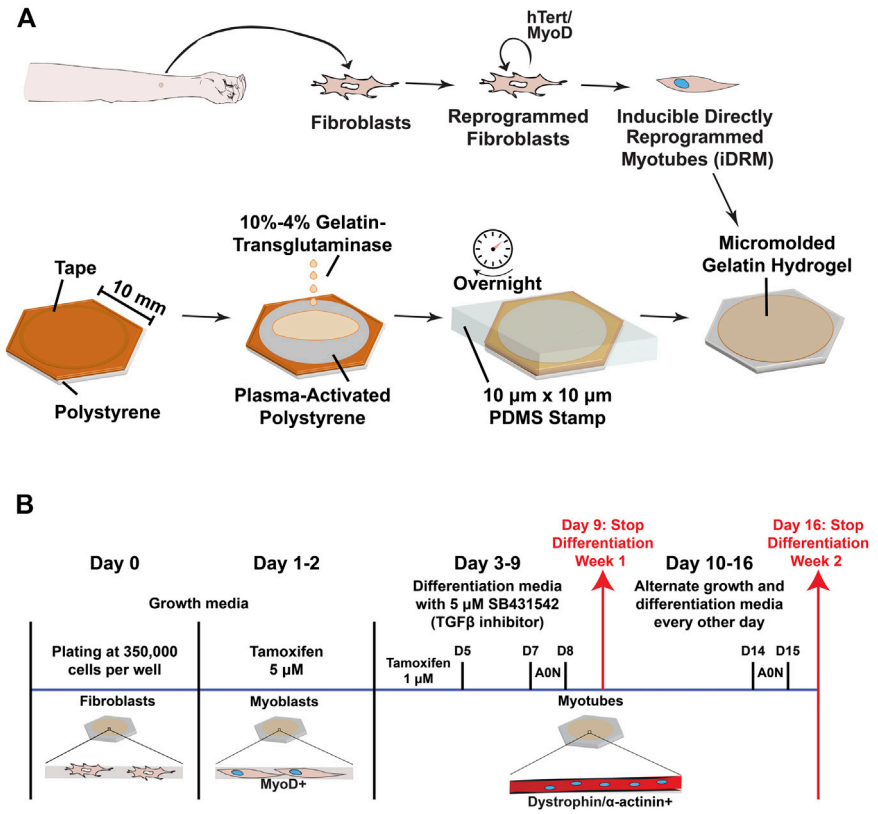


**FIGURE 1 |** Overview of the experimental design and culture timeline. **(A)** A skin punch of 3 mm diameter is performed on the forearm and the tissue dissociated to obtain fibroblasts. Following infection with lentiviruses encoding hTERT and MyoD, cells (renamed induced directly reprogramed myotubes–iDRM) can form myotubes upon induction of MyoD- and fusion-inducing media. Polystyrene coverslips are plasma-treated to enhance gelatin hydrogel adhesion before molding of the surface using soft lithography adhesion before molding of the surface using soft lithography. Hydrogels are rehydrated and stored in PBS before cell seeding. **(B)** A typical timeframe for the generation of myotubes from iDRM with or without AO treatment. Analysis for experiments was performed after 1 (day 9) and 2 (day 16) weeks of differentiation.

and soft lithography (Suh et al., 2017). Then, 20% porcine gelatin solution (Sigma, St. Louis, MO, United States) and 8% transglutaminase (Ajinomoto, Ontario, CA, United States) solutions in ultrapure water were mixed 1:1 with a centrifugal mixer (Thinky United States, Laguna Hills, CA, United States). The mixed solution (200 µl) was added to each coverslip, and stamps were slowly applied. Hydrogels were incubated at room temperature overnight to solidify. The next day, hydrogels were rehydrated. Stamps and remaining tape were carefully removed (**Figure 1A**). Substrates were washed and stored in PBS at 4°C until cell seeding.

## AO Transfection

On day 7 (week 1) or 14 (week 2) of differentiation, iDRM cells (1015 or 1003) were transfected with 25 or 250 nM 2-O-methyl AO targeting exon 44 (using H44A-TGTTCAGCTTCT GTTAGCCACTGA and 45 (using H45A -CCAATGCCATCC TGGAGTTCCTGTAA) (Wilton et al., 2007), respectively, using oligofectamine (Thermo Fisher Scientific) transfection reagent according to our previously published protocol (Barthélémy et al., 2019).

## RNA Isolation and PCR

On the day of analysis, duplicate or triplicate coverslips from each condition were removed from the well, and the remnant cells growing on the side of the coverslips were scraped directly and combined in TRIzol (Thermo Fisher Scientific). Total RNA was isolated using the Purelink RNA mini kit (Thermo Fisher Scientific). Exon skipping analysis was performed accordingly to our previously published protocol, and skipping efficiency is indicated by the ratio of skipped mRNA transcript over the total mRNA transcripts (skipped plus unskipped) (Barthélémy et al., 2019). For both cell lines, a nested PCR was performed to amplify the targeted DMD region: between exons 43 and 52 using the previously described primers for cell line CDMD1003 (Ex42-o, 5′-GTCCGTGAAGAAACGATGATG-3′ + Ex53-0, 5′-CTCCGG TTCTGAAGGTGTTC-3′ and Ex43-i, 5′- TCTCTCCCAGCT TGATTTCC-3′ and Ex52-i, 5′- TCTAGCCTCTTGATTGCT GG-3′) or between exons 42 and 46 (Ex42-o, 5′-CAATGC TCCTGACCTCTGTGC-3′ + Ex46-o, 5′-GCTCTTTTCCAG GTTCAAGTGG-3′ and Ex43-i, 5′-GTCTACAACAAAGCT CAGGTCG-3′ + Ex46-i, 5′-GCAATGTTATCTGCTTCCTCC AACC-3′) for cell line CDMD1015.

## Immunofluorescence Staining and Microscopy

iDRMs were seeded at 350,000 cells onto micromolded gelatin hydrogel coverslips in 12-well plates and MyoD was induced with tamoxifen as described above. During all procedures, cells were kept at room temperature unless specified otherwise. After myotube formation, cells were fixed with acetone for dystrophin staining or ice-cold methanol for α-actinin staining. Primary antibodies were incubated overnight at 4°C: dystrophin NCL-2 (Leica, Buffalo Grove, IL, United States) at a dilution of 1:20 and α-actinin (Sigma, St. Louis, MO, United States) at a dilution of 1:200. Secondary antibodies were used at a dilution of 1:500: goat anti-mouse IgG (SA5-10173) and goat anti-rabbit (35553) from Thermo Fisher Scientific for 1 h. Coverslips were mounted in ProLong Gold Antifade with DAPI (Thermo Fisher Scientific). Confocal fluorescence microscopy was performed using a Confocal Module Nikon C2 with 20× air or 60× oil objectives. Z-stacks were acquired (step size: 1 μm), and average intensity projections were used for data analysis on ImageJ (NIH).

To quantify myogenic index, CellProfiler was first used to mask α-actinin signal. Then, the proportion of total nuclei in masked areas that contained at least three nuclei was taken as the myogenic index; we chose to count areas with at least three nuclei as a stringent filter of multi-nucleated myotubes. The myotube coverage was defined as the area percentage of positive α-actinin signal after autothresholding using ImageJ. As a proxy for myotube width, we used an automated CellProfiler calculation to define a minor axis length based on the ellipse encompassing a mask of α-actinin that defined a single myotube. To quantify the degree of myotube alignment based on α-actinin staining, the ImageJ plugin OrientationJ was used with a Gaussian filter window of $\sigma$ = 10 pixels to calculate the coherency and orientation angles at each pixel. Then, a global orientation order parameter was calculated from the orientation angles of at least three images per sample, as previously described (McCain et al., 2013; Petersen et al., 2020).

## Statistics

Student's t-test was performed between week 1 and week 2 groups for each patient iDRM lines or between them, or between AO and non-treated patient iDRM lines. Comparisons with *p*-values less than 0.05 were considered statistically significant.

# RESULTS

## Engineering Aligned DMD and LGMD2A/R1 iDRMs on Micromolded Gelatin Hydrogels

To engineer mutation-specific DMD muscle tissues *in vitro*, we isolated dermal fibroblasts from DMD 1015, DMD 1023, DMD 1003, and one control subject (1001). All fibroblasts were engineered to iDRM by expressing a tamoxifen-inducible MyoD and hTERT (**Figure 1A**), as described previously (Barthelemy et al., 2018; Wang et al., 2018). iDRMs were seeded on gelatin hydrogels micromolded with 10-μm-wide alternating grooves affixed to coverslips (**Figure 1A**). iDRMs were then triggered to become myoblasts with induction of MyoD 1–2 days after seeding and maintained in differentiation media for 1 to 2 weeks to induce fusion into myotubes (**Figure 1B**).

To characterize the morphological events characteristic of muscle development, we co-visualized nuclei and sarcomeric α-actinin in engineered iDRM tissues after 1 and 2 weeks in culture. We chose sarcomeric α-actinin because it is expressed relatively late in myogenesis, especially compared to other markers, such as desmin, myogenin, or myosin heavy chain (White et al., 2014; Bettadapur et al., 2016b; Nguyen et al., 2016; Denes et al., 2019b; Santoso et al., 2021b). Sarcomeric α-actinin is also present in the z-lines in sarcomeres and thus clearly demarcates mature myofibrils. All cell lines formed multi-nucleated, aligned myotubes at both time points (**Figure 2**), although to different degrees. To compare this, we quantified myotube coverage (α-actinin positive proportion), myogenic index (proportion of nuclei in α-actinin positive myotubes with more than three nuclei), myotube width (minor axis length), and myotube alignment (**Figures 3A–D** and **Supplementary Figure S1**). We report both myotube coverage and myogenic index to collectively indicate myotube fusion, myotube adhesion, and tissue cellularity. Healthy 1001 iDRM formed myotubes with stable sarcomeric α-actinin coverage and myogenic index throughout the 2-week culture period. Organized striations were detectable at week 1 and remained constant through week 2. Myotube width peaked in the first week and declined slightly by week 2, likely due to detachment of some of the most mature myotubes. The distribution of myotube width, shown as histograms in **Supplementary Figure S1**, also illustrates this trend. Myotube alignment for healthy iDRM was also high and indicated successful tissue patterning by the micromolded gelatin hydrogels.

DMD 1015 iDRM performed relatively similar to the healthy 1001 iDRM, in terms of sarcomeric α-actinin coverage (**Figure 3A**), myogenic index (**Figure 3B**), and myotube width (**Figure 3C** and **Supplementary Figure S1**), with a potential modest delay in the time to peak myotube width relative to healthy control. Similar to the healthy control, striations in DMD 1015 myotubes were also detectable (**Figure 2**). We attempted to quantify α-actinin striations, but the heterogeneity of the cells precluded a systematic and meaningful analysis. DMD 1023 and DMD 1003 iDRM also differentiated into multi-nucleated myotubes with near-typical myogenic index and myotube width. These results are similar to previous studies that have shown relatively unimpaired fusion in human iPSC–derived myoblasts from DMD (Caputo et al., 2020) or LGMDR9 (Ortiz-Cordero et al., 2021) patients. However, striations in DMD 1023 and DMD 1003 myotubes were qualitatively impaired relative to healthy 1001 myotubes. Likewise, myotube coverage was lower in DMD 1023 and DMD 1003 compared to healthy 1001. Myotube alignment was also high for the healthy and DMD myotubes (**Figure 3D**), indicating that all cell lines were instructed by the micromolded features. Myotube alignment trended lower for DMD 1003 compared to

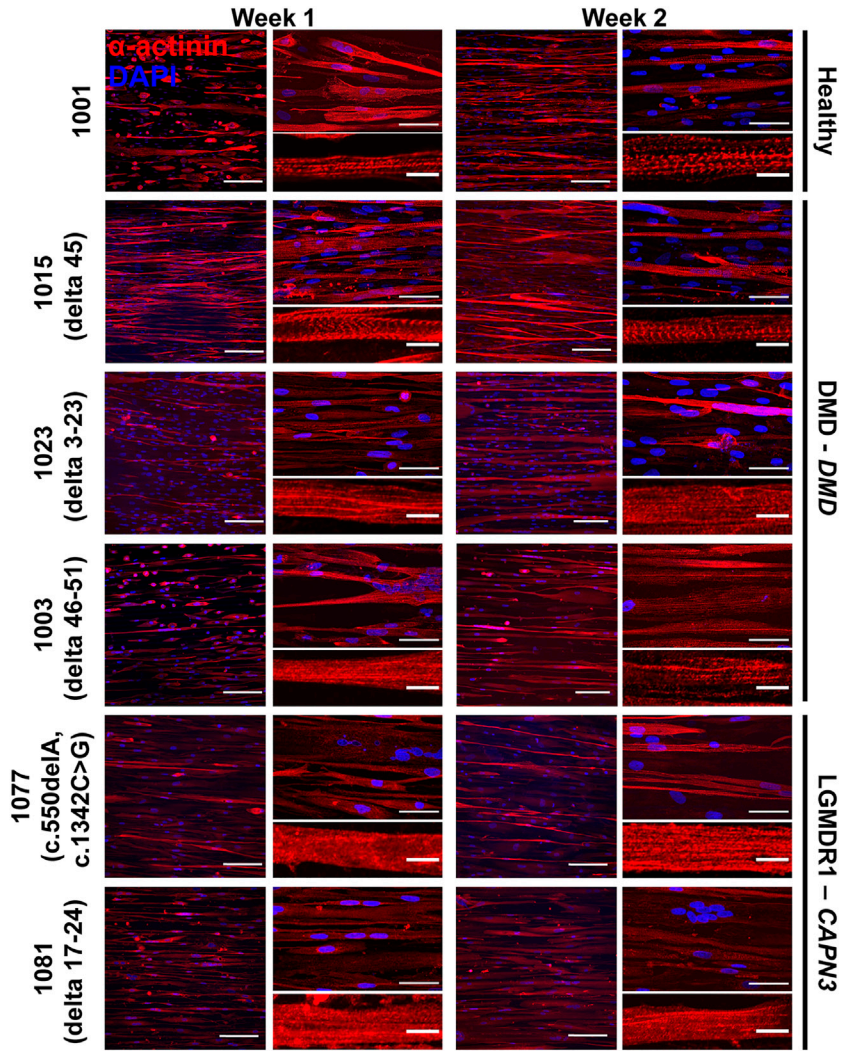


**FIGURE 2 |** iDRMs derived from LGMD2A/R1 or DMD dermal fibroblasts on micromolded gelatin hydrogel coverslips. α-actinin staining was performed to analyze the maturation of myotubes from a healthy donor (1001) or patients presenting with LGMD2A/R1 (1077 - c.550delA, c.1342C > G and 1081 delta 17–24) or DMD (1015 – delta 45; 1023 – delta 3–23; and 1003 - delta 46–51). For each cell line, cells were differentiated for 1 or 2 weeks. Images are shown at 20× magnification on the left panel, where the scale bar represents 100 μm, and at 60× magnification in the upper right panel, where the scale bar represents 50 μm. Representative myotubes shown in the lower right panel enable visualization of sarcomeres where the scale bar represents 10 μm.

DMD 1015 and DMD 1023, possibly due to the greater severity of the mutation in this line. The healthy 1001 myotubes also had relatively low alignment, likely because myotubes tended to bridge across the micromolded features in the control line compared to the DMD lines.

To determine whether our approach was suitable for other genetic muscle diseases, we similarly isolated fibroblasts from two LGMD2A/R1 subjects, engineered them to iDRM, and differentiated them to myotubes on micromolded gelatin hydrogels (**Figure 1A**). LGMD2A/R1 line 1077 exhibits compound heterozygous mutations c.550delA (p.T184Rfs*36) and c.1342C > G (p448R > G) in *CAPN3*. LGMD2A/R1 line 1081 exhibits homozygous deletion of *CAPN3* exons 17 to 24 [c.(1914 + 1_1915–1)_(*544_?)del]. Whereas LGMD2A/R1 1077 showed lower α-actinin coverage (**Figure 3A**) and normal or lower myogenic index (**Figure 3B**) compared to the healthy control, LGMD2A/R1 1081 had similar sarcomere α-actinin coverage and a much higher myogenic index. For certain time points, LGMD2A/R1 1077 had lower myotube width, whereas LGMD2A/R1 1081 had higher myotube width, compared to control (**Figure 3C** and **Supplementary Figure S1**). However, neither LGMD2A/R1 1077 or LGMD2A/R1 1081 developed well-organized, discrete striations (**Figure 2**). Both LGMD2A/R1 1077 and LGMD2A/R1 1081 exhibited high degrees of myotube alignment (**Figure 3D**). Thus, our engineered tissues revealed distinct differences in disease- and mutation-specific muscle morphology, which is an advantage of using patient-derived cells. Importantly, the variability within each cell line is relatively modest.

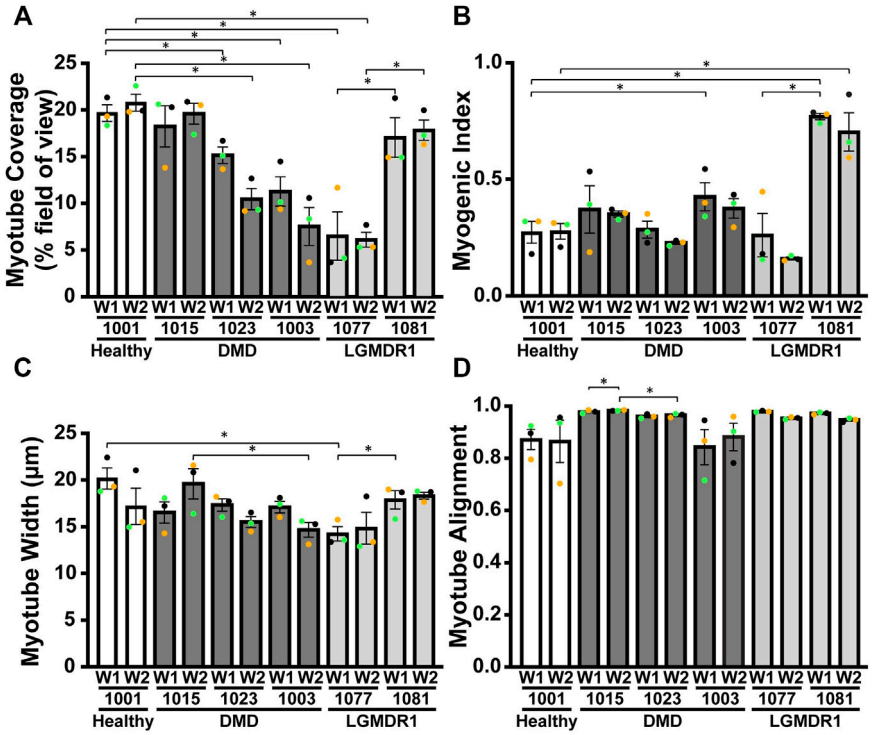


**FIGURE 3 |** Morphological quantification of DMD or LGMD2A/R1 iDRM reveal distinct changes in mutation-specific muscle morphology. Different parameters were measured for each cell line using α-actinin staining: **(A)** α-actinin area coverage per field of view; **(B)** myogenic index representing the proportion of nuclei in myotubes (containing at least three nuclei); **(C)** minor axis length as a proxy for myotube width; **(D)** myotube alignment. Bars represent SEM. *$p < 0.05$; $p$-values reflect a Student's t-test. Each experiment ($n = 3$) is represented by different color dots.

## Morphology of Muscle Fibers in Healthy and DMD Patients

As a baseline comparison for our culture models, we evaluated morphological differences in muscle biopsy tissue sections from a healthy subject and the two DMD subjects for which we had access to muscle tissue sections, DMD 1015 and DMD 1023. Both patients were biopsied before loss of ambulation and had substantial preservation of skeletal myofibers. DMD 1015 exhibits an out-of-frame deletion of *DMD* exon 45 predicted to lead to total loss of dystrophin expression. DMD 1023 exhibits an in-frame deletion of *DMD* exons 3 to 23 predicted to express a partially functional dystrophin protein lacking the actin binding site. As expected, muscle fibers in the healthy subject robustly expressed sarcomeric α-actinin throughout their cross-sectional area, were encircled by dystrophin, and were relatively consistent in size (**Figure 4**). Both DMD biopsies demonstrated weaker sarcomeric α-actinin staining, variations in muscle fiber size, and fibro-fatty infiltrates, concordant with a DMD phenotype (**Figure 5**). Sarcomeric α-actinin expression (**Figure 5**) and fiber size were lowest in DMD 1023 tissues despite significant expression of internally truncated sarcolemmal dystrophin protein in every myofiber (**Figures 4** and **5**). Whereas most 1015 fibers do not express dystrophin, we observe some patches of dystrophin expressing revertant fibers and higher α-actinin expression relative to 1023, in keeping with findings regarding α-actinin coverage in the iDRM culture models (**Figures 2** and **3**). However, it is important to consider that the degeneration process *in vivo* is vastly more complex and on a much longer timescale than what can be observed *in vitro*. Thus, comparing patient muscle biopsies to *in vitro* engineered muscle tissues should be done with much caution and conservativeness (Forbes et al., 2020).

## Evaluation of Dystrophin Rescue in DMD iDRMs Treated With Exon Skipping AOs

Development of precision medicines requires human mutation specific platforms for assessing mechanisms of action and efficacy. AO DMD exon skipping drugs function to reframe mutant *DMD* mRNA through removal of an "extra" exon, enabling rescue of an internally deleted but partially functional dystrophin protein. "Exon skipping" drugs are mutation-specific, in so far as only some *DMD* mutations adjacent to the targeted region can be reframed. 1015 mutation can be rendered in frame by exclusion of exon 44, whereas 1003 mutation is amenable to reframing by targeting exon 45.

To determine whether AO treatment rescued dystrophin expression in iDRM, DMD 1015 and DMD 1003 iDRMs were exposed to exon skipping drug targeting exon 44 or exon 45, respectively, after 1 or 2 weeks of differentiation on micromolded hydrogels. We performed immunostaining on healthy and DMD

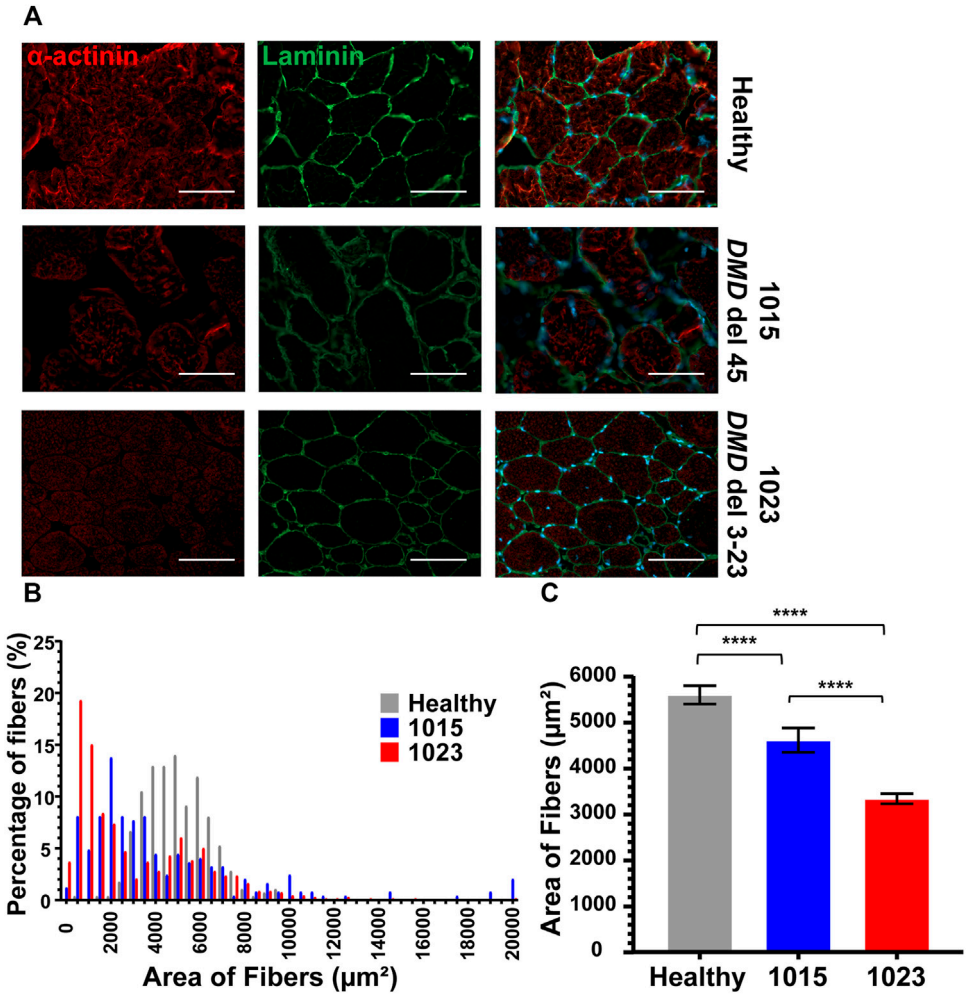


**FIGURE 4 |** Biopsies of patients with DMD show abnormal α-actinin (1023 - delta 3–23; 1015 – delta 45). **(A)** Co-staining for α-actinin and laminin are shown. **(B)** Histogram of fiber area of muscle biopsies from healthy donor and patients presenting Duchenne muscular dystrophy sorted by 500 μm range. Number of fibers analyzed per condition was between 250 and 658. **(C)** The mean average of the fibers is also represented. Bars represent SEM. ****$p < 0.0005$; $p$-values reflect a Student's t-test. Immunostains were taken at 20× magnification, where the scale bar represents 100 μm.

iDRM engineered tissues treated with or without AO to determine whether we could observe rescue of dystrophin (**Figure 6A**). Myotubes generated from the healthy iDRM demonstrated dystrophin staining at both time points (**Figure 6A**). In DMD 1015 iDRMs, low levels of dystrophin protein were detected without AO treatment after 2 week of culture on the micromolded platform, consistent with detection of low levels of skipped DMD message in the absence of AO. Exposure to AO increased the rescued exon 44 deleted DMD mRNA and dystrophin proteins expression and after both 1 and 2 weeks of culture, consistent with levels of exon 45 skipped mRNA induced (**Figure 6B**). In DMD 1003 iDRMs, dystrophin was not detectable in 1003 in the absence of skipping drug. Exposure to exon 45 skipping AO rescued low levels of dystrophin protein when AO was added after 1 week and to a greater extent when AO was added after 2 weeks of differentiation (**Figures 6A,B**). Thus, both DMD 1015 and DMD 1003 demonstrated brighter dystrophin staining with the addition of skipping AO.

We next measured the effects of dystrophin rescue induced by exon skipping on myotube morphology for DMD 1015 and DMD1003 at week 1 or 2 of differentiation (**Figure 7**). We performed staining for α-actinin and nuclei (**Figure 7**) and calculated myotube coverage (**Figure 8A**), myogenic index, (**Figure 8B**), myotube width (**Figure 8C** and **Supplementary Figure S2**), and myotube alignment (**Figure 8D**). DMD 1015 iDRMs developed striations at weeks 1 and 2, regardless of exon skipping and dystrophin rescue. There were also no noticeable changes in myogenic index, myotube coverage, myotube width, or myotube alignment in 1015 due to AO treatment, except for slight but non-significant increases in the first three metrics after 2 weeks of AO treatment. The distribution of myotube width from iDRM DMD 1015 and 1003 samples with and without AO treatment is shown as histograms in **Supplementary Figure S2**

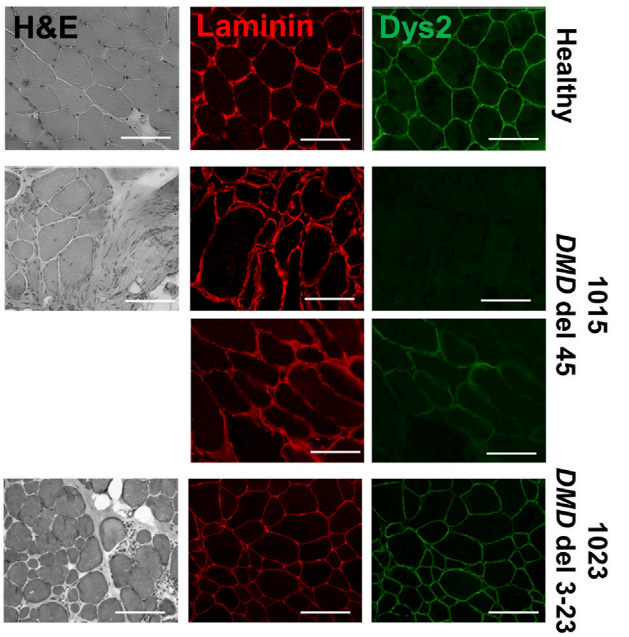


**FIGURE 5 |** Biopsies of patients with DMD show dystrophic features. Muscle biopsy sections from patients presenting DMD (1023 - delta 3–23; 1015 – delta 45) assessed for dystrophin protein using dys2 antibody targeting the C-terminus and laminin using L9393 antibody. Hematoxylin/eosin staining for each biopsy is shown to visualize their morphological features and proceed to morphological assessment. Scale bars represent 100 μM.

and shows a particular shift toward a higher proportion of wider myotubes after AO treatment at week 2. The effects on dystrophin rescue in DMD 1003 were more noticeable, with exon skipping AO inducing greater myotube coverage, myogenic index, and myotube alignment at both time points. However, these increases did not reach statistical significance. Nonetheless, taken together, these findings highlight a potential role for rescued dystrophin protein in maturation or stability of myotubes and sarcomeres.

## DISCUSSION

Development of genetic medicines aimed at repairing or replacing DMD and LGMDDR1/LGMD2A mutations is an active area of research, and several drugs have been already approved or are in human pre-clinical or clinical trials (Sheikh and Yokota, 2021). However, there is a paucity of DMD and LGMD mutation specific human culture models for assessing mechanisms of action or improving efficacy of therapeutic strategies. Here, we report that culturing one heathy subject, three DMD, and two LGMD-derived iDRM on micromolded gelatin hydrogel coverslips induces tissue alignment, prolongs culture lifetime, and promotes myotube development in culture over 2 weeks. This relatively long culture period enabled us to characterize myotube development and dystrophin rescue in DMD myotubes in response to AO skipping drugs. We also show that our approach is compatible with iDRM from LGMD2A/R1 patients, demonstrating its modularity for modeling other forms of muscular dystrophy.

Although all healthy and DMD iDRM demonstrated myogenic potential and a high degree of alignment, DMD 1003 showed the most severe defects in α-actinin expression, followed by DMD 1023. We were largely unable to distinguish DMD 1015 from healthy control using these measures. The *in vitro* results for DMD 1015 and DMD 1023 mirror the trends of the patient muscle biopsies, for which defects were more substantial for DMD 1023 compared to DMD 1015. Thus, our combination of patient-derived iDRM with micromolded gelatin hydrogels replicated select histological phenotypes of native muscle and further demonstrates that muscle development *in vitro* is regulated by distinct *DMD* mutations.

iDRM DMD 1003 harbors a deletion of exons 46–51 of *DMD*, which encodes an out-of-frame mRNA, produces no dystrophin protein, and demonstrates defects in α-actinin coverage and the development of striations. These data support a role for dystrophin in the development or stabilization of myotubes and sarcomeres. Such a suggestion is consistent with reports that the dystrophin-glycoprotein complex slows depolymerization of actin filaments *in vitro* (Rybakova et al., 1996; Rybakova and Ervasti, 1997). Alternatively, low α-actinin coverage and myotube width may be secondary to impaired cell survival or earlier developmental defects dependent on dystrophin. *DMD* reframing and dystrophin rescue induced within DMD 1003 by exposure to exon 45 skipping AO modestly improved measures of myotube coverage, fusion, and alignment, further supporting a role for dystrophin in these processes and highlighting the value of this model as a screening tool for drug development and optimization of precision medicines.

iDRM DMD 1023 has an in-frame mutation *DMD* 3–23, which creates substantial amounts of dystrophin properly localized at the sarcolemma but lacking the primary actin binding site (Gibbs et al., 2019). We identified defects in myotube maturation and organization, potentially highlighting requirements for dystrophin actin binding in myogenesis and myotube sarcomere maturation, consistent with a previous report (Banks et al., 2007). Additional experiments will be needed to support this hypothesis.

iDRM DMD 1015 has an exon 45 deletion of *DMD* amenable to reframing by exon 44 AO skipping. We have previously demonstrated that iDRM DMD 1015 constitutively expresses low levels of exon 45 skipped and reframed *DMD* mRNA, even in the absence of AO, as we have reported for several DMD iDRM with exon 45 deletions (Wang et al., 2018). Likewise, immunostaining frozen muscle biopsy sections from the DMD 1015 fibroblast donor showed some clusters expressing low levels of dystrophin rescue *in vivo*. The predisposition of exon 45 deletion *DMD* mutants to self-correct by skipping exon 44 to produce low levels of dystrophin has been suggested as the molecular basis of mild disease progression relative to typical *DMD* frameshifting mutations and highlights that even low levels of dystrophin can have functional consequences. We also detected low levels of exon 45 skipped *DMD* mRNA in the absence of any treatment and increased exon 44 exclusion and robust induction of dystrophin protein expression in cells exposed to

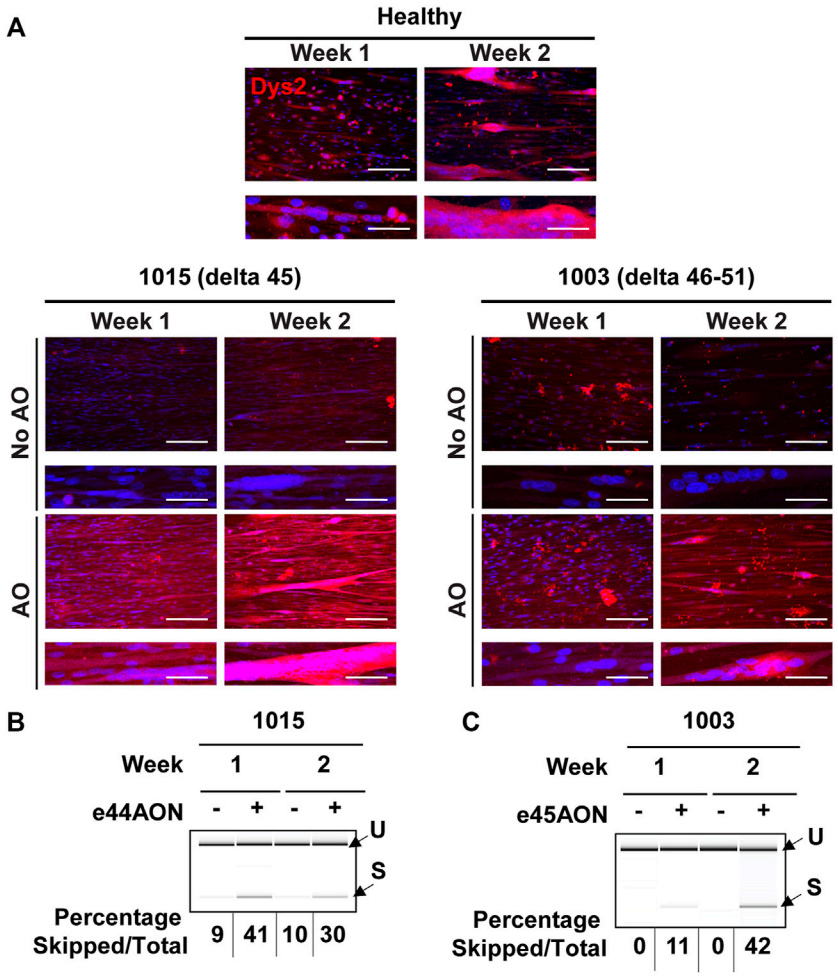


**FIGURE 6 |** Dystrophin rescue by *DMD* exon skipping in DMD 1015 and DMD 1003 iDRMs. DMD 1015 (delta 45) and DMD 1003 (delta 46–51) iDRMs were cultured for 1 or 2 weeks before the addition of antisense oligonucleotides and, 2 days later, immunostaining or RNA extraction (on pooled triplicate) were performed. **(A)** Dystrophin expression in healthy and DMD iDRM tissues was visualized using Dys2 antibody (c-ter). Images are shown at 20x magnification in the top panel, where the scale bar represents 100 µm, and at 60x magnification in the lower panel to enable visualization of sarcomeres, where the scale bar represents 30 µm. After RT-PCR, samples were run on chips to analyze exon skipping. The percentage of skipped mRNA over the total (skipped plus unskipped mRNA) is indicated for **(B)** DMD 1015 and **(C)** DMD 1003.

skipping AO. Unlike the other two DMD patient-derived iDRM, DMD 1015 behaved much closer to wild type, with no defect in α-actinin coverage or striation. It is possible that the low levels of rescued dystrophin constitutively expressed in DMD 1015 are sufficient to partially overcome the developmental defects in myotube development or sarcomere stability observed in dystrophin null DMD 1003. Exon 44 skipping AO increased dystrophin expression and induced modest improvements in myogenic index, myotube coverage, and myotube width, further supporting a role for rescued dystrophin in facilitation of myotube maturation in DMD 1015. Moreover, multiple α-actinin isoforms have been linked to dystrophin and DMD. α-Actinin 3 has been identified as a known modifier of DMD, α-actinin 2 has been identified as an extended member of the DGC, and a progressive depletion of α-actinin proteins has been observed in DMD (Minetti et al., 1991; Hance et al., 1999; Hogarth et al., 2017), making this protein family an underestimated marker of pathophysiological changes in this disease.

Although differentiation on micromolded gelatin hydrogels enabled visualization of rescued dystrophin expression, we did not observe the expected patterning of dystrophin. In native muscle, dystrophin is enriched in costamere protein assemblies, which circumferentially align with the α-actinin enriched Z disk and couple force-generating sarcomeres with the sarcolemma. Similarly, although we did detect some punctate sarcomere-like structures in myotubes derived from select iDRM lines, the overall maturity of the myofibrils and sarcomeres was limited, especially compared to myotubes derived from primary myoblasts. Similar issues related to myofibril immaturity have routinely been observed in myotubes derived from a variety of reprogrammed (Boularaoui et al., 2018) and iPSC-derived myoblasts (Lainé et al., 2018; Rao et al., 2018) and likely reduce the baseline and drug-induced differences

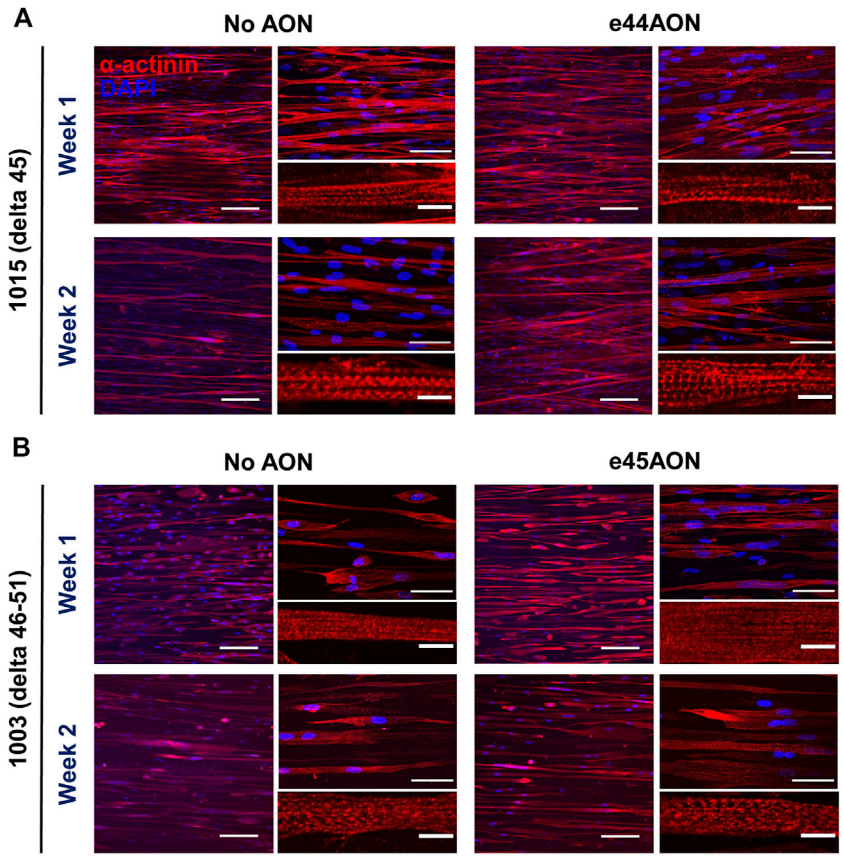


**FIGURE 7 |** Effects of dystrophin rescue by exon skipping on α-actinin expression and organization in. DMD 1015 (delta 45) or DMD 1003 (delta 46–51). **(A)** DMD 1015 or **(B)** DMD 1003 iDRMs were cultured for 1 or 2 weeks before the addition of antisense oligonucleotides. α-actinin staining were performed to analyze the maturation of myotubes. Images are shown at 20× magnification in the left panel, where the scale bar represents 100 μm, and at 60× magnification in the upper right panel, where the scale bar represents 50 μm. Representative myotubes shown in the lower right panel enable visualization of sarcomeres, where the scale bar represents 10 μm.

in the phenotypes of healthy and diseased cells. Overall, the maturity of iDRM-derived myotubes observed in this study was similar or weaker than iPSC-derived myotubes (Caputo et al., 2020; Ortiz-Cordero et al., 2021). Of note, however, iDRMs require less time, cost, and expertise to generate compared to iPSC-derived myoblasts, which may be especially beneficial for generating patient-specific muscle tissues in time-sensitive or resource-limited settings. Extending culture time (Santoso and McCain, 2021), integrating supporting cell types (Juhas et al., 2018; Santosa et al., 2018; Santoso and McCain, 2021), providing electrical (Nedachi et al., 2008; Chen et al., 2021) or mechanical stimulation (Heher et al., 2015; Chang et al., 2016), or engineering 3-D tissues (Madden et al., 2015; Uzel et al., 2016; Costantini et al., 2017; Davis et al., 2019; Ariyasinghe et al., 2020; Ebrahimi et al., 2021) or earlier exposure to AO could also help induce muscle maturation and proper localization of dystrophin and α-actinin.

LGMD2A/R1 1077 express mutations [c.550delA (p.T184Rfs*36) and c.1342C > G (p448R > G] within the catalytic PC1 and the calcium-binding and phospholipid-binding C2 domains, respectively, and these iDRMs show defects in formation of myotube maturation and structure. Patient cells derived from patient LGMD2A/R1 1081, present with a homozygous deletion of the entire c-terminal region of the protein, were able to form myotubes and showed no quantitative defects in α-actinin coverage or axis length but did not develop proper maturation of the clearly defined α-actinin marked sarcomeres upon visual inspection. It is unclear why LGMD 1077 iDRM demonstrates significant defects in myotube maturation, whereas 1081 has an exceptionally high MI and is otherwise near normal.

One advantage of differentiating myotubes in culture is that it allows assessment of sequential myoblast activation, fusion, and the development of mature myofibers with organized sarcomeres, responsible for striated muscle patterning and required for force generation. Thus, iDRM differentiated on micromolded hydrogels may aid in dissecting requirements for each of these developmental

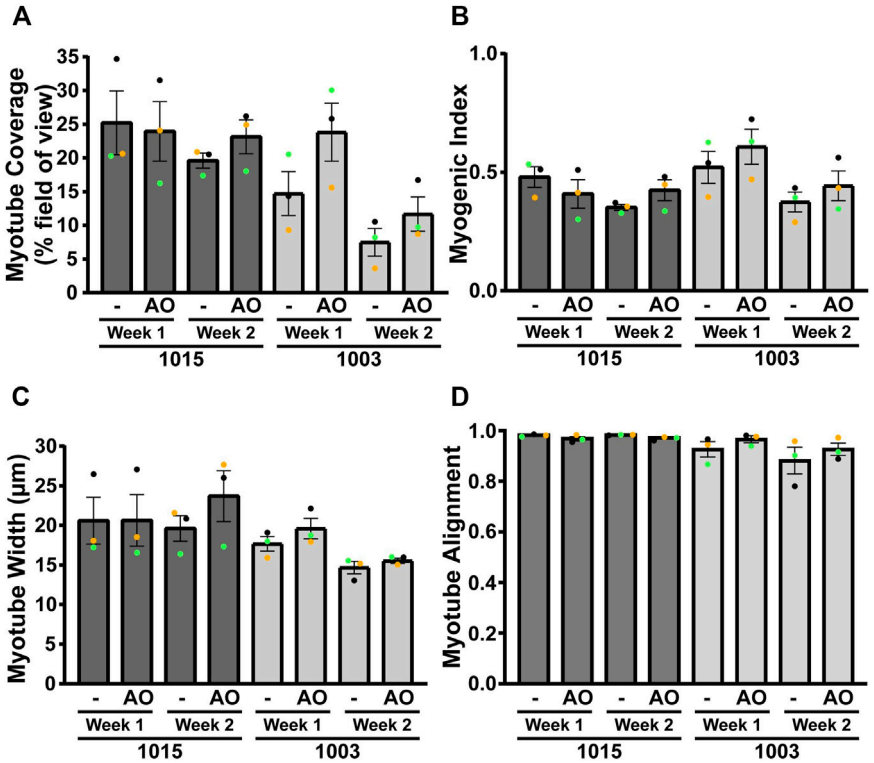


**FIGURE 8 |** Morphological quantification of AO-treated DMD 1015 and DMD 1003 iDRMs. Different parameters were measured for each cell line using α-actinin staining: **(A)** α-actinin area coverage per field of view; **(B)** myogenic index representing the proportion of nuclei in myotubes (containing at least three nuclei); **(C)** minor axis length as a proxy for myotube width; and **(D)** myotube alignment. Bars represent SEM. Each experiment ($n$ = 3) is represented by different color dots.

events (White et al., 2014). However, factors other than DMD or LGMD mutation that might influence iDRM performance include the presence/absence of DMD or LGMD2A/R1 disease modifier genes or artifacts of culture selection. Therefore, comparisons between individually derived iDRM to determine relative myogenic activity of particular mutations should be made with caution. Rather, creation of isogenic iDRM expressing defined DMD or LGMD mutations and full-length dystrophin or a panel of distinct patient iDRM with similar mutations may be necessary to confirm preliminary observations made regarding effects of DMD or LGMD mutation based on comparison between two lines. Alternatively, experiments where iDRM DMD 1003 and 1015 activity is measured before and after exposure to a potential therapeutic or disease modifying entity, such as exon skipping AO, do not suffer from this criticism and thus are likely to prove valuable for precision drug optimization and screening.

In summary, our results establish that patient-derived iDRM differentiate into aligned myotubes on micromolded gelatin hydrogels and enable evaluation of myotube formation as a function of patient-specific mutations. This is a promising approach for screening and testing personalized therapies for muscular dystrophies and other genetic muscle diseases *in vitro*. Together, our findings highlight the benefit of human cell models combined with engineered scaffolds that more closely mimic the *in vivo* microenvironment and encourage the development of new strategies to promote further maturation for proper characterization of morphological differences and evaluation of the efficacy of new therapies.

## DATA AVAILABILITY STATEMENT

The raw data supporting the conclusion of this article will be made available by the authors, without undue reservation.

## ETHICS STATEMENT

The studies involving human participants were reviewed and approved by the UCLA OHRPP (IRB). Written informed consent to participate in this study was provided by the participants' legal guardian/next of kin.

## AUTHOR CONTRIBUTIONS

FB, JS, LR, RJ, and IL performed all experiments. SN collected human specimens. FB, JS, MMi, and MMc drafted the manuscript with contributions from all co-authors. FB, MMi, and MMc conceived the project and designed the experiments.

## FUNDING

NSF GRFP grant DGE1418060 (JS); USC Provost's Fellowship (JS). NSF CAREER Award No. 1944734 (MMc); Rose Hills Foundation Innovator grant (MMc). This work is partially supported by the Center for Duchenne Muscular Dystrophy at UCLA and the California Center for Rare Diseases within the Institute of Precision Health at UCLA.

## SUPPLEMENTARY MATERIAL

The Supplementary Material for this article can be found online at: https://www.frontiersin.org/articles/10.3389/fcell.2022.830415/full#supplementary-material

**Supplementary Figure S1 |** Dystrophic myotubes showed a delayed myotubes enlargement at week 1 that fades away at week 2. α-Actinin staining were performed to analyze the maturation of myotubes from a healthy donor (1001) or patients presenting with LGMD2A/R1 (1077 - c.550delA, c.1342C > G and 1081 - delta 17–24) or DMD (1015 - delta 45; 1023 - delta 3–23; and 1003 - delta 46–51). For each cell line, cells were differentiated for 1 or 2 weeks and all the myotubes showing more than three nuclei from two independent experiments run in duplicates were analyzed and compiled on these graphs representing the width ranges (in μm) observed in our cell culture models.

**Supplementary Figure S2 |** AO treatment promotes enlargement of myotubes from DMD patients' cell lines. DMD 1015 (delta 45) or DMD 1003 (delta 46–51) cells were cultured for 1 or 2 weeks before the addition of antisense oligonucleotides and α-actinin staining were performed to analyze the maturation of myotubes. All the myotubes showing more than three nuclei from three independent experiments run in duplicates were analyzed and compiled on these graphs representing the width ranges (in μm) observed in our cell culture models.

## REFERENCES

Al Tanoury, Z., Zimmerman, J. F., Rao, J., Sieiro, D., McNamara, H. M., Cherrier, T., et al. (2021). Prednisolone Rescues Duchenne Muscular Dystrophy Phenotypes in Human Pluripotent Stem Cell-Derived Skeletal Muscle *In Vitro*. *Proc. Natl. Acad. Sci. USA* 118 (28), e2022960118. doi:10.1073/pnas.2022960118

Ariyasinghe, N. R., Santoso, J. W., Gupta, D., Pincus, M. J., August, P. R., and McCain, M. L. (2020). Optical Clearing of Skeletal Muscle Bundles Engineered in 3-D Printed Templates. *Ann. Biomed. Eng.* 49, 523–535. doi:10.1007/s10439-020-02583-0

Banks, G. B., Gregorevic, P., Allen, J. M., Finn, E. E., and Chamberlain, J. S. (2007). Functional Capacity of Dystrophins Carrying Deletions in the N-Terminal Actin-Binding Domain. *Hum. Mol. Genet.* 16 (17), 2105–2113. doi:10.1093/hmg/ddm158

Barthélémy, F., Courrier, S., Lévy, N., Krahn, M., and Bartoli, M. (2018). Dysferlin Exon 32 Skipping in Patient Cells. *Methods Mol. Biol.* 1828, 489–496. doi:10.1007/978-1-4939-8651-4_31

Barthelemy, F., Wang, D., Nelson, S. F., and Miceli, M. C. (2018). Validation and Detection of Exon Skipping Boosters in DMD Patient Cell Models and Mdx Mouse. *Methods Mol. Biol.* 1828, 309–326. doi:10.1007/978-1-4939-8651-4_19

Barthélémy, F., Wang, R. T., Hsu, C., Douine, E. D., Marcantonio, E. E., Nelson, S. F., et al. (2019). Targeting RyR Activity Boosts Antisense Exon 44 and 45 Skipping in Human DMD Skeletal or Cardiac Muscle Culture Models. *Mol. Ther. - Nucleic Acids* 18, 580–589. doi:10.1016/j.omtn.2019.09.020

Barthelemy, F., Woods, J. D., Nieves-Rodriguez, S., Douine, E. D., Wang, R., Wanagat, J., et al. (2020). A Well-tolerated Core Needle Muscle Biopsy Process Suitable for Children and Adults. *Muscle & Nerve* 62 (6), 688–698. doi:10.1002/mus.27041

Bettadapur, A., Suh, G. C., Geisse, N. A., Wang, E. R., Hua, C., Huber, H. A., et al. (2016). Prolonged Culture of Aligned Skeletal Myotubes on Micromolded Gelatin Hydrogels. *Sci. Rep.* 6, 28855. doi:10.1038/srep28855

Bettadapur, A., Suh, G. C., Geisse, N. A., Wang, E. R., Hua, C., Huber, H. A., et al. (2016). Prolonged Culture of Aligned Skeletal Myotubes on Micromolded Gelatin Hydrogels. *Sci. Rep.* 6, 28855. doi:10.1038/srep28855

BhattBHATT1, A. D. K. S., Shah, K., Puvar, A., Joshi, C. G., and Joshi, M. (2019). A Case of Limb Girdle Muscular Dystrophy Type 2A from India: Copy Number Variation Analysis Using Targeted Amplicon Sequencing. *Jcdr* 13 12812. doi:10.7860/JCDR/2019/40923.12812

Blau, H. M., Webster, C., and Pavlath, G. K. (1983). Defective Myoblasts Identified in Duchenne Muscular Dystrophy. *Proc. Natl. Acad. Sci.* 80 (15), 4856–4860. doi:10.1073/pnas.80.15.4856

Boularaoui, S. M., Abdel-Raouf, K. M. A., Alwahab, N. S. A., Kondash, M. E., Truskey, G. A., Teo, J. C. M., et al. (2018). Efficient Transdifferentiation of Human Dermal Fibroblasts into Skeletal Muscle. *J. Tissue Eng. Regen. Med.* 12 (2), e918–e36. doi:10.1002/term.2415

Caputo, L., Granados, A., Lenzi, J., Rosa, A., Ait-Si-Ali, S., Puri, P. L., et al. (2020). Acute Conversion of Patient-Derived Duchenne Muscular Dystrophy iPSC into Myotubes Reveals Constitutive and Inducible Over-activation of TGFβ-dependent Pro-fibrotic Signaling. *Skeletal Muscle* 10 (1), 13. doi:10.1186/s13395-020-00224-7

Chang, Y.-J., Chen, Y.-J., Huang, C.-W., Fan, S.-C., Huang, B.-M., Chang, W.-T., et al. (2016). Cyclic Stretch Facilitates Myogenesis in C2C12 Myoblasts and Rescues Thiazolidinedione-Inhibited Myotube Formation. *Front. Bioeng. Biotechnol.* 4, 27. doi:10.3389/fbioe.2016.00027

Chaouch, S., Mouly, V., Goyenvalle, A., Vulin, A., Mamchaoui, K., Negroni, E., et al. (2009). Immortalized Skin Fibroblasts Expressing Conditional MyoD as a Renewable and Reliable Source of Converted Human Muscle Cells to Assess Therapeutic Strategies for Muscular Dystrophies: Validation of an Exon-Skipping Approach to Restore Dystrophin in Duchenne Muscular Dystrophy Cells. *Hum. Gene Ther.* 20 (7), 784–790. doi:10.1089/hum.2008.163

Chen, Z., Li, B., Zhan, R.-Z., Rao, L., and Bursac, N. (2021). Exercise Mimetics and JAK Inhibition Attenuate IFN-γ-Induced Wasting in Engineered Human Skeletal Muscle. *Sci. Adv.* 7 9502. doi:10.1126/sciadv.abd9502

Costantini, M., Testa, S., Fornetti, E., Barbetta, A., Trombetta, M., Cannata, S. M., et al. (2017). Engineering Muscle Networks in 3D Gelatin Methacryloyl Hydrogels: Influence of Mechanical Stiffness and Geometrical Confinement. *Front. Bioeng. Biotechnol.* 5, 22. doi:10.3389/fbioe.2017.00022

Davis, B. N. J., Santoso, J. W., Walker, M. J., Oliver, C. E., Cunningham, M. M., Boehm, C. A., et al. (2019). Modeling the Effect of TNF-α upon Drug-Induced Toxicity in Human, Tissue-Engineered Myobundles. *Ann. Biomed. Eng.* 47, 1596–1610. doi:10.1007/s10439-019-02263-8

Denes, L. T., Riley, L. A., Mijares, J. R., Arboleda, J. D., McKee, K., Esser, K. A., et al. (2019). Culturing C2C12 Myotubes on Micromolded Gelatin Hydrogels Accelerates Myotube Maturation. *Skeletal Muscle* 9 (1), 17. doi:10.1186/s13395-019-0203-4

Denes, L. T., Riley, L. A., Mijares, J. R., Arboleda, J. D., McKee, K., Esser, K. A., et al. (2019). Culturing C2C12 Myotubes on Micromolded Gelatin Hydrogels Accelerates Myotube Maturation. *Skeletal Muscle* 9 (1), 17. doi:10.1186/s13395-019-0203-4

Flanigan, K. M. (2014). Duchenne and Becker Muscular Dystrophies. *Neurol. Clin.* 32 (3), 671–688. doi:10.1016/j.ncl.2014.05.002

Forbes, S. C., Arora, H., Willcocks, R. J., Triplett, W. T., Rooney, W. D., Barnard, A. M., et al. (2020). Upper and Lower Extremities in Duchenne Muscular Dystrophy Evaluated with Quantitative MRI and Proton MR Spectroscopy in a Multicenter Cohort. *Radiology* 295 (3), 616–625. doi:10.1148/radiol.2020192210

Gibbs, E. M., Barthélémy, F., Douine, E. D., Hardiman, N. C., Shieh, P. B., Khanlou, N., et al. (2019). Large In-Frame 5′ Deletions in DMD Associated with Mild Duchenne Muscular Dystrophy: Two Case Reports and a Review of the Literature. *Neuromuscul. Disord.* 29 (11), 863–873. doi:10.1016/j.nmd.2019.09.009

Gupta, D., Santoso, J. W., and McCain, M. L. (2021). Characterization of Gelatin Hydrogels Cross-Linked with Microbial Transglutaminase as Engineered

Skeletal Muscle Substrates. *Bioengineering* 8 (1), 6. doi:10.3390/bioengineering8010006

Hance, J. E., Fu, S. Y., Watkins, S. C., Beggs, A. H., and Michalak, M. (1999). α-Actinin-2 Is a New Component of the Dystrophin-Glycoprotein Complex. *Arch. Biochem. Biophys.* 365 (2), 216–222. doi:10.1006/abbi.1999.1172

Heher, P., Maleiner, B., Prüller, J., Teuschl, A. H., Kollmitzer, J., Monforte, X., et al. (2015). A Novel Bioreactor for the Generation of Highly Aligned 3D Skeletal Muscle-like Constructs through Orientation of Fibrin via Application of Static Strain. *Acta Biomater.* 24, 251–265. doi:10.1016/j.actbio.2015.06.033

Hogarth, M. W., Houweling, P. J., Houweling, P. J., Thomas, K. C., Gordish-Dressman, H., Bello, L., et al. (2017). Evidence for ACTN3 as a Genetic Modifier of Duchenne Muscular Dystrophy. *Nat. Commun.*, 8, 14143. doi:10.1038/ncomms14143

Juhas, M., Abutaleb, N., Wang, J. T., Ye, J., Shaikh, Z., Sriworarat, C., et al. (2018). Incorporation of Macrophages into Engineered Skeletal Muscle Enables Enhanced Muscle Regeneration. *Nat. Biomed. Eng.* 2, 942–954. doi:10.1038/s41551-018-0290-2

Kendall, G. C., Mokhonova, E. I., Moran, M., Sejbuk, N. E., Wang, D. W., Silva, O., et al. (2012). Dantrolene Enhances Antisense-Mediated Exon Skipping in Human and Mouse Models of Duchenne Muscular Dystrophy. *Sci. Transl. Med.* 4 (164), 164ra0. doi:10.1126/scitranslmed.3005054

Kim, E. Y., Page, P., Dellefave-Castillo, L. M., McNally, E. M., and Wyatt, E. J. (2016). Direct Reprogramming of Urine-Derived Cells with Inducible MyoD for Modeling Human Muscle Disease. *Skeletal Muscle* 6, 32. doi:10.1186/s13395-016-0103-9

Krahn, M., Bernard, R., Pécheux, C., Hammouda, E. H., Eymard, B., Munain, A. L. d., et al. (2006). Screening of the CAPN3 Gene in Patients with Possible LGMD2A. *Clin. Genet.* 69 (5), 444–449. doi:10.1111/j.1399-0004.2006.00603.x

Kramerova, I., Beckmann, J. S., and Spencer, M. J. (2007). Molecular and Cellular Basis of Calpainopathy (Limb Girdle Muscular Dystrophy Type 2A). *Biochim. Biophys. Acta (Bba) - Mol. Basis Dis.* 1772 (2), 128–144. doi:10.1016/j.bbadis.2006.07.002

Lainé, J., Skoglund, G., Fournier, E., and Tabti, N. (2018). Development of the Excitation-Contraction Coupling Machinery and its Relation to Myofibrillogenesis in Human iPSC-Derived Skeletal Myocytes. *Skeletal Muscle* 8 (1), 1. doi:10.1186/s13395-017-0147-5

Lee, C. C., Hoang, A., Segovia, D., Herbst, A., Barthelemy, F., Gibbs, E., et al. (2020). Enhanced Methods for Needle Biopsy and Cryopreservation of Skeletal Muscle in Older Adults. *jch* 11 553. doi:10.37421/jch.2020.11.553

Madden, L., Juhas, M., Kraus, W. E., Truskey, G. A., and Bursac, N. (2015). Bioengineered Human Myobundles Mimic Clinical Responses of Skeletal Muscle to Drugs. *eLife* 4 4885. doi:10.7554/eLife.04885

Maffioletti, S. M., Sarcar, S., Henderson, A. B. H., Mannhardt, I., Pinton, L., Moyle, L. A., et al. (2018). Three-Dimensional Human iPSC-Derived Artificial Skeletal Muscles Model Muscular Dystrophies and Enable Multilineage Tissue Engineering. *Cel Rep.* 23 (3), 899–908. doi:10.1016/j.celrep.2018.03.091

McCain, M. L., Sheehy, S. P., Grosberg, A., Goss, J. A., and Parker, K. K. (2013). Recapitulating Maladaptive, Multiscale Remodeling of Failing Myocardium on a Chip. *Proc. Natl. Acad. Sci.* 110 (24), 9770–9775. doi:10.1073/pnas.1304913110

Ebrahimi, M., Fusto, H., Tiper, A., Datye, Y., Christine, A., Nguyen, C. T., et al. (2021). De Novo revertant Fiber Formation and Therapy Testing in a 3D Culture Model of Duchenne Muscular Dystrophy Skeletal Muscle. *Acta Biomater.* 132, 227–244. doi:10.1016/j.actbio.2021.05.020

Minetti, C., Ricci, E., and Bonilla, E. (1991). Progressive Depletion of Fast Alpha-Actinin-Positive Muscle Fibers in Duchenne Muscular Dystrophy. *Neurology* 41 (12), 1977. doi:10.1212/wnl.41.12.1977

Muntoni, F. (2001). Is a Muscle Biopsy in Duchenne Dystrophy Really Necessary? *Neurology* 57 (4), 574–575. doi:10.1212/wnl.57.4.574

Nallamilli, B. R. R., Chakravorty, S., Kesari, A., Tanner, A., Ankala, A., Schneider, T., et al. (2018). Genetic Landscape and Novel Disease Mechanisms from a largeLGMDcohort of 4656 Patients. *Ann. Clin. Transl Neurol.* 5 (12), 1574–1587. doi:10.1002/acn3.649

Nedachi, T., Fujita, H., and Kanzaki, M. (2008). Contractile C2C12myotube Model for Studying Exercise-Inducible Responses in Skeletal Muscle. *Am. J. Physiology-Endocrinology Metab.* 295 (5), E1191–E1204. doi:10.1152/ajpendo.90280.2008

Nesmith, A. P., Wagner, M. A., Pasqualini, F. S., O'Connor, B. B., Pincus, M. J., August, P. R., et al. (2016). A Human *In Vitro* Model of Duchenne Muscular Dystrophy Muscle Formation and Contractility. *J. Cel. Biol.* 215 (1), 47–56. doi:10.1083/jcb.201603111

Nguyen, N.-U. -N., Liu, T.-Y., and Wang, H.-V. (2016). Timing Appearance and Integration of Actin-Organizing Palladin Protein in Dynamic Myofibril Assembly. *bioRxiv*, 047183. doi:10.1101/047183

Ortiz-Cordero, C., Bincoletto, C., Dhoke, N. R., Selvaraj, S., Magli, A., Zhou, H., et al. (2021). Defective Autophagy and Increased Apoptosis Contribute toward the Pathogenesis of FKRP-Associated Muscular Dystrophies. *Stem Cel Rep.* 16 (11), 2752–2767. doi:10.1016/j.stemcr.2021.09.009

Pakula, A., Spinazzola, J. M., and Gussoni, E. (2019). Purification of Myogenic Progenitors from Human Muscle Using Fluorescence-Activated Cell Sorting (FACS). *Methods Mol. Biol.* 1889, 1–15. doi:10.1007/978-1-4939-8897-6_1

Petersen, A. P., Cho, N., Lyra-Leite, D. M., Santoso, J. W., Gupta, D., Ariyasinghe, N. R., et al. (2020). Regulation of Calcium Dynamics and Propagation Velocity by Tissue Microstructure in Engineered Strands of Cardiac Tissue. *Integr. Biol.* 12 (2), 34–46. doi:10.1093/intbio/zyaa003

Rao, L., Qian, Y., Khodabukus, A., Ribar, T., and Bursac, N. (2018). Engineering Human Pluripotent Stem Cells into a Functional Skeletal Muscle Tissue. *Nat. Commun.* 9 (1), 126. doi:10.1038/s41467-017-02636-4

Rybakova, I. N., Amann, K. J., and Ervasti, J. M. (1996). A New Model for the Interaction of Dystrophin with F-Actin. *J. Cel Biol* 135 (3), 661–672. doi:10.1083/jcb.135.3.661

Rybakova, I. N., and Ervasti, J. M. (1997). Dystrophin-glycoprotein Complex Is Monomeric and Stabilizes Actin Filaments *In Vitro* through a Lateral Association. *J. Biol. Chem.* 272 (45), 28771–28778. doi:10.1074/jbc.272.45.28771

Santosa, K. B., Keane, A. M., Jablonka-Shariff, A., Vannucci, B., and Snyder-Warwick, A. K. (2018). Clinical Relevance of Terminal Schwann Cells: An Overlooked Component of the Neuromuscular junction. *J. Neuro Res.* 96 (7), 1125–1135. doi:10.1002/jnr.24231

Santoso, J. W., and McCain, M. L. (2021). Engineering Skeletal Muscle Tissues with Advanced Maturity Improves Synapse Formation with Human Induced Pluripotent Stem Cell-Derived Motor Neurons. *NCBI Gene Expr. Omnibus (Geo)*. doi:10.1063/5.0054984

Santoso, J. W., Li, X., Gupta, D., Suh, G. C., Hendricks, E., Lin, S., et al. (2021). Engineering Skeletal Muscle Tissues with Advanced Maturity Improves Synapse Formation with Human Induced Pluripotent Stem Cell-Derived Motor Neurons. *APL Bioeng.* 5 (3), 036101. doi:10.1063/5.0054984

Santoso, J. W., Li, X., Gupta, D., Suh, G. C., Hendricks, E., Lin, S., et al. (2021). Engineering Skeletal Muscle Tissues with Advanced Maturity Improves Synapse Formation with Human Induced Pluripotent Stem Cell-Derived Motor Neurons. *APL Bioeng.* 5 (3), 036101. doi:10.1063/5.0054984

Santoso, J. W., and McCain, M. L. (2020). Neuromuscular Disease Modeling on a Chip. *Dis. Models Mech.* 13 (7), dmm044867. doi:10.1242/dmm.044867

Sheikh, O., and Yokota, T. (2021). Developing DMD Therapeutics: a Review of the Effectiveness of Small Molecules, Stop-Codon Readthrough, Dystrophin Gene Replacement, and Exon-Skipping Therapies. *Expert Opin. Investig. Drugs* 30 (2), 167–176. doi:10.1080/13543784.2021.1868434

Speciale, A. A., Ellerington, R., Goedert, T., and Rinaldi, C. (2020). Modelling Neuromuscular Diseases in the Age of Precision Medicine. *Jpm* 10 (4), 178. doi:10.3390/jpm10040178

Suh, G. C., Bettadapur, A., Santoso, J. W., and McCain, M. L. (2017). Fabrication of Micromolded Gelatin Hydrogels for Long-Term Culture of Aligned Skeletal Myotubes. *Methods Mol. Biol.* 1668, 147–163. doi:10.1007/978-1-4939-7283-8_11

Uzel, S. G. M., Platt, R. J., Subramanian, V., Pearl, T. M., Rowlands, C. J., Chan, V., et al. (2016). Microfluidic Device for the Formation of Optically Excitable, Three-Dimensional, Compartmentalized Motor Units. *Sci. Adv.* 2 (8), e1501429. doi:10.1126/sciadv.1501429

van der Wal, E., Herrero-Hernandez, P., Wan, R., Broeders, M., in 't Groen, S. L. M., van Gestel, T. J. M., et al. (2018). Large-Scale Expansion of Human iPSC-Derived Skeletal Muscle Cells for Disease Modeling and Cell-Based Therapeutic Strategies. *Stem Cel. Rep.* 10 (6), 1975–1990. doi:10.1016/j.stemcr.2018.04.002

Verhaart, I. E. C., Johnson, A., Thakrar, S., Vroom, E., De Angelis, F., Muntoni, F., et al. (2019). Muscle Biopsies in Clinical Trials for Duchenne Muscular

Dystrophy - Patients' and Caregivers' Perspective. *Neuromuscul. Disord.* 29 (8), 576–584. doi:10.1016/j.nmd.2019.06.004

Wang, R. T., Barthelemy, F., Martin, A. S., Douine, E. D., Eskin, A., Lucas, A., et al. (2018). DMD Genotype Correlations from the Duchenne Registry: Endogenous Exon Skipping Is a Factor in Prolonged Ambulation for Individuals with a Defined Mutation Subtype. *Hum. Mutat.* 39, 1193–1202. doi:10.1002/humu.23561

Wein, N., Vulin, A., Falzarano, M. S., Szigyarto, C. A.-K., Maiti, B., Findlay, A., et al. (2014). Translation from a DMD Exon 5 IRES Results in a Functional Dystrophin Isoform that Attenuates Dystrophinopathy in Humans and Mice. *Nat. Med.* 20 (9), 992–1000. doi:10.1038/nm.3628

Wein, N., Vulin, A., Findlay, A. R., Gumienny, F., Huang, N., Wilton, S. D., et al. (2017). Efficient Skipping of Single Exon Duplications in DMD Patient-Derived Cell Lines Using an Antisense Oligonucleotide Approach. *Jnd* 4 (3), 199–207. doi:10.3233/JND-170233

White, J., Barro, M. V., Makarenkova, H. P., Sanger, J. W., and Sanger, J. M. (2014). Localization of Sarcomeric Proteins during Myofibril Assembly in Cultured Mouse Primary Skeletal Myotubes. *Anat. Rec.* 297 (9), 1571–1584. doi:10.1002/ar.22981

Wilton, S. D., Fall, A. M., Harding, P. L., McClorey, G., Coleman, C., and Fletcher, S. (2007). Antisense Oligonucleotide-Induced Exon Skipping across the Human Dystrophin Gene Transcript. *Mol. Ther.* 15 (7), 1288–1296. doi:10.1038/sj.mt.6300095

**Conflict of Interest:** MLM is an inventor on US Patent No. US9857356B2 by Harvard University, which includes the design and use of micrmolded gelatin hydrogels.

The authors declare that the research was conducted in the absence of any commercial or financial relationships that could be construed as a potential conflict of interest.

**Publisher's Note:** All claims expressed in this article are solely those of the authors and do not necessarily represent those of their affiliated organizations or those of the publisher, the editors, and the reviewers. Any product that may be evaluated in this article, or claim that may be made by its manufacturer, is not guaranteed or endorsed by the publisher.

frontiers | Frontiers in Cell and Developmental Biology

TYPE Review
PUBLISHED 24 August 2022
DOI 10.3389/fcell.2022.902225



OPEN ACCESS

EDITED BY
David Lee Mack,
University of Washington, United States

REVIEWED BY
D. Cornelison,
University of Missouri, United States
Irina Conboy,
University of California, Berkeley,
United States

*CORRESPONDENCE
Michael A. Rudnicki,
mrudnicki@ohri.ca

SPECIALTY SECTION
This article was submitted to Stem Cell Research,
a section of the journal
Frontiers in Cell and Developmental Biology

RECEIVED 22 March 2022
ACCEPTED 26 July 2022
PUBLISHED 24 August 2022

CITATION
Hekmatnejad B and Rudnicki MA (2022), Transplantation to study satellite cell heterogeneity in skeletal muscle. *Front. Cell Dev. Biol.* 10:902225. doi: 10.3389/fcell.2022.902225



# Transplantation to study satellite cell heterogeneity in skeletal muscle

Bahareh Hekmatnejad[1,2] and Michael A. Rudnicki[1,2]*

[1]The Sprott Centre for Stem Cell Research, Regenerative Medicine Program, Ottawa Hospital Research Institute, Ottawa, ON, Canada, [2]Department of Cellular and Molecular Medicine, Faculty of Medicine, University of Ottawa, Ottawa, ON, Canada

Skeletal muscle has a remarkable capacity to regenerate throughout life, which is mediated by its resident muscle stem cells, also called satellite cells. Satellite cells, located periphery to the muscle fibers and underneath the basal lamina, are an indispensable cellular source for muscle regeneration. Satellite cell transplantation into regenerating muscle contributes robustly to muscle repair, thereby indicating that satellite cells indeed function as adult muscle stem cells. Moreover, satellite cells are a heterogenous population in adult tissue, with subpopulations that can be distinguished based on gene expression, cell-cycle progression, ability to self-renew, and bi-potential ability. Transplantation assays provide a powerful tool to better understand satellite cell function *in vivo* enabling the separation of functionally distinct satellite cell subpopulations. In this review, we focus on transplantation strategies to explore satellite cells' functional heterogeneity, approaches targeting the recipient tissue to improve transplantation efficiency, and common strategies to monitor the behaviour of the transplanted cells. Lastly, we discuss some recent approaches to overcome challenges to enhance the transplantation potential of muscle stem cells.

KEYWORDS

**satellite cells, muscle stem cell, self-renewal, differentiation, engraftment, transplantation, heterogeneity**

## Introduction

Skeletal muscle exhibits a strong capability for tissue expansion and repair. It is a striated muscle tissue, which accounts for a large portion of adult human body weight. Skeletal muscle consists of highly specialized post-mitotic, large multinucleated cells referred to as myofibers, which can contain thousands of nuclei, that form following fusion from myogenic progenitors. During postnatal growth, the number of myofibers does not increase in number, but each myofiber grows in size by fusion of muscle stem cells (MuSCs), also known as satellite cells, readily adapting to changing functional needs.

Satellite cells were described in 1961 by Alexander Mauro as mononucleated cells "wedged" during the characterization of frog myofibers by electron microscopy (Mauro, 1961). Satellite cells are located between the basal lamina and sarcolemma of the muscle fiber. Under normal physiological conditions, they are actively maintained in a quiescent

state in adult muscle and are identified through the expression of the transcription factor Pax7 (Seale et al., 2000). In response to physiological insults, such as an injury or exercise, they quickly become activated, enter the cell cycle, and give rise to proliferating myoblasts that eventually differentiate and fuse to repair damaged myofibers (Bentzinger et al., 2012). A subset of activated MuSCs, are also able to undergo self-renewal to maintain the muscle stem cell reservoir for future regeneration. Therefore, the interplay between extrinsic and intrinsic mechanisms tightly controls the balance between the satellite cells committed to forming new myofibers and those to self-renew (Kuang et al., 2007; Rocheteau et al., 2012a).

Transplantation studies involving satellite cells derived from adult muscles allow researchers to explore satellite cell functional heterogeneity (including self-renewal, differentiation, and multipotential specification). Transplantation of skeletal muscle came into play in the late 1980s by the work of Partridge's group (Partridge et al., 1989) who demonstrated that injecting myoblasts into the hind limb of the *mdx* mouse model for DMD (Duchenne muscular dystrophy) resulted in a significant reconstitution of dystrophin positive muscle fibers. These initial studies on myoblast transplantation resulted in low survival rates post-injection with a minimal number of donor cells exhibiting stem cell properties that behave as long-term repopulating cells and contribute to muscle homeostasis (Beauchamp et al., 1999). Typically, transplantation experiments involve the isolation of cells from dissected muscle by mechanical and enzymatic digestion. Muscle stem cells are then enriched by FACS (fluorescent activated cell sorting), using MuSC-specific cell surface markers (α7-integrin, Vcam1, and CD34) and negative markers (CD31, CD45, CD11b, and Sca1) (Pasut et al., 2012; Maesner et al., 2016). Lastly, the isolated muscle stem cells are injected into a recipient muscle tissue.

Lineage tracing together with engraftment studies in mice have identified a putative long-term self-renewing stem cell within the satellite cell population (Kuang et al., 2007; Wang et al., 2019). Muscle stem cells undergo planar-symmetric divisions to give rise to two stem cells. Alternatively, they undergo an apical-basal asymmetric division to give rise to a stem cell and a committed cell (Kuang et al., 2007; Wang et al., 2019; Feige and Rudnicki, 2020). Thus, the majority of satellite cells represent a short-term repopulating cell (Kuang et al., 2007; Feige et al., 2018), while a subset we term muscle stem cells can self-renew over a long period of time and can rise to committed progenitors via asymmetric cell divisions (Kuang et al., 2007; Rocheteau et al., 2012b; Gurevich et al., 2016; Wang et al., 2019; Evano et al., 2020).

In this review, we first summarize studies utilizing transplantation experiments to measure satellite cell functional capabilities. We then discuss evidence indicating that satellite cells are indeed the repopulating cell. Moreover, we review different preconditioning strategies of host tissue to enhance engraftment efficiency in animal models, and common methods to monitor the engraftment of host cells. We note that poor engraftment is one of the greatest challenges limiting the success of cell transplantation experiments, which depends on several parameters such as survival, host immune response, migration to the degenerating tissue, and differentiation of the transplanted cells. Therefore, we provide discussion with possible approaches to overcome the biological challenges associated with engraftment that could be applied to help improve the outcome.

## Satellite cells represent the ideal source for muscle transplantation

Satellite cells are widely recognized as the most crucial stem cell type for muscle repair with tremendous *in vivo* regenerative potential. Transplantation of a single fiber or even a single satellite cell contributes considerably to the regeneration of the damaged skeletal muscles by participating in the reconstitution of both the fiber and the muscle stem cell niche (Collins et al., 2005; Sacco et al., 2008).

Over the past decade, studies using single-cell technologies together with engraftment experiments demonstrated that satellite cells are functionally and molecularly heterogenous. Our group and other researchers have characterized subpopulations of Pax7-expressing satellite cells with varying functional potential (Kuang et al., 2007; Sacco et al., 2008; Rocheteau et al., 2012a; Chakkalakal et al., 2014; Scaramozza et al., 2019). We identified a small subset of the satellite cells that have increased levels of Pax7 and lack Myf5 ($Pax7^+/Myf5^-$), demonstrating a greater ability for self-renewal compared with their more committed progenitors ($Pax7^+/Myf5^+$) (Kuang et al., 2007). Chakkalakal and colleagues (Chakkalakal et al., 2012; Chakkalakal et al., 2014) used a doxycycline (DOX)-inducible TetO-H2B-GFP reporter system to examine the satellite cell heterogeneity with regard to their cell cycle dynamics. Mice containing the Histone2B (H2B)-Green Fluorescent Protein (GFP) fusion protein were transiently subjected to doxycycline to achieve widespread incorporation of the fusion protein into chromatin. Following doxycycline withdrawal, mice were chased for the retention of H2B-GFP label at defined intervals. The GFP label is retained in quiescent non-dividing cells, while it is diluted by half with each cell division in dividing cells (Foudi et al., 2009). The authors demonstrated that the adult satellite cell pool is composed of ~30% label-retaining satellite cells (LRCs), while the vast majority lost it (non-LRCs). They showed that both these cell populations are present at birth and persist throughout postnatal development and adult life. Furthermore, transplantation studies showed that LRCs function similar to stem cells, generating self-renewing cells capable of differentiation. Meanwhile, non-LRCs are restricted to differentiation, thereby functioning as committed progenitors (Chakkalakal et al., 2012; Chakkalakal et al., 2014). More recently, employing *Mx1-Cre* transgenic

reporter mice, which allows monitoring of resident stem cells in the majority of adult tissues, Scaramozza et al. (2019) identified a rare subset of Pax7$^+$ satellite cells that are enriched for both the *Mx1-Cre* and *Pax3* expression. After irradiation, the Mx1$^+$ SCs undergo clonal expansion and contribute extensively to muscle repair and niche repopulation. Therefore, the radiotolerant Pax7$^+$ Mx1$^+$ subpopulation functions as a reserve muscle stem cell population. Of note, examination of the lineage commitment using markers of self-renewal and differentiation, suggested that Mx1$^+$ satellite cells and LRCs display cellular and functional overlap, and thus they have similar fate biases.

Notably, apart from satellite cells, lineage tracing has identified a variety of stem cell populations in skeletal muscle and the satellite cell compartment including side population cells (Challen et al., 2006), mesenchymal stromal cells (Boppart et al., 2013), pericytes (Dellavalle et al., 2007), interstitial stem cells (Cottle et al., 2017), and fibro/adipogenic progenitors (FAPs) (Joe et al., 2010). These cell populations proliferate following muscle injury and have many features in common, namely cell-surface marker expression and multipotency. *In vivo* transplantation assays and *in vitro* co-culture experiments demonstrated that these endogenous stem cell types play an important role in promoting self-renewal, proliferation, and commitment to myogenic differentiation of satellite cells (Peault et al., 2007; Dunn et al., 2019).

Satellite cells are best described by the expression of their canonical marker, Pax7. Several studies have demonstrated that Pax7 expression is necessary for the normal function of satellite cells during both neonatal and adult skeletal muscle myogenesis. By utilizing genetic models of the conditional deletion of Pax7$^+$ cells using tamoxifen-inducible diphtheria toxin from the *Rosa* locus, studies showed that skeletal muscle regeneration was impeded following muscle injury (Lepper et al., 2011; Murphy et al., 2011; Sambasivan et al., 2011). Interestingly, skeletal muscle without satellite cells was incapable of regeneration even after transplantation of the Pax7-deficient muscle into a healthy host muscle (Lepper et al., 2011; Sambasivan et al., 2011). Furthermore, observations by our group also indicated that deletion of Pax7 in adult satellite cells, by using floxed alleles and tamoxifen-induced inactivation, resulted in a significant reduction in regeneration as evidenced by reduced formation of myofibers (von Maltzahn et al., 2013). Notably, other stem cell populations within the skeletal muscle did not compensate for the loss of Pax7$^+$ satellite cells, and the satellite cell depletion and regeneration defect could only be rescued upon transplantation of Pax7$^+$ cells. Together, these findings provide compelling evidence that these stem cell populations can only contribute to muscle repair in the satellite cell rich environment during injury-induced muscle regeneration, and these observations emphasize the important implication of satellite cells for cell-based transplantation assays.

## Transplantation-based approach to assess satellite cell functions

Numerous studies have employed transplantation strategies to assess the self-renewal and differentiation potential of satellite cells. In an early study, satellite cells-expressing GFP were directly isolated from adult muscle tissues and engrafted into the dystrophin-deficient *mdx* nude muscle and were found to contribute to both myofiber repair and to the muscle satellite cell reservoir (Montarras et al., 2005). Recently, in a two-armed transplantation assay, Kyba and colleagues (Arpke et al., 2021), transplanted simultaneously donor-derived Pax7-ZsGreen satellite cells into both *tibialis anterior* (TA) muscles of young and old NSG-*mdx* mice. One limb was used for flow cytometry to quantify the number of undifferentiated (ZsGreen$^+$) satellite cells 1 month after transplantation, i.e., measuring self-renewal capability. The other limb was used in histological analysis to determine the number of dystophin$^+$ fibers, quantifying the contribution of the donor cells to form new myofiber. They found that the ability of satellite cells to self-renew and to properly differentiate was comparable between the old and young mice. In another study, Pax7-YFP knock in satellite cells were isolated by FACS and transplanted into injury-induced regenerating limb muscle of *mdx* mice. It was found that YFP$^+$ donor-derived satellite cells were able to repopulate the satellite cell compartment, suggesting that this population is capable of self-renewal. They, also observed that could also differentiate and restore dystrophin in *mdx* myofibers (Kitajima and Ono, 2018).

Most importantly, transplantation experiments from our group using the *Myf5-Cre/ROSA-YFP* lineage tracing technique, demonstrated satellite cell heterogeneity through their stemness and indicated that about 10% of satellite cells are true stem cells (Kuang et al., 2007). Furthermore, we observed that only the transplanted YFP$^-$ satellite cells could produce both self-renewed Pax7$^+$/YFP$^-$ satellite stem cells and Pax7$^+$/YFP$^+$ satellite committed progenitor cells through apical-basal asymmetric division. By contrast, isolation and transplantation of YFP$^+$ satellite cells resulted in poor survival and migration, lower engraftment capacity, and precociously differentiated. Similarly, using transgenic *Pax7-nGFP* reporter mice, Rocheteau et al. 2012a) revealed that a *Pax7*$^{high}$ cell population is less primed to commitment and maintain stemness in quiescent satellite cells. They showed that proliferating satellite cells with high Pax7 expression asymmetrically segregate their DNA during cell division, while the Pax7$^{low}$ cell population distributes their DNA randomly. Moreover, by serial transplantation they demonstrated that the Pax7 high population has a higher engraftment potential, can self-renew, and give rise to committed progenitors, while the Pax7 low population has a higher propensity for differentiation.

A study by Blau's group used cytometry by time-of-flight (CyTOF) to identify novel populations of MuSCs based on their

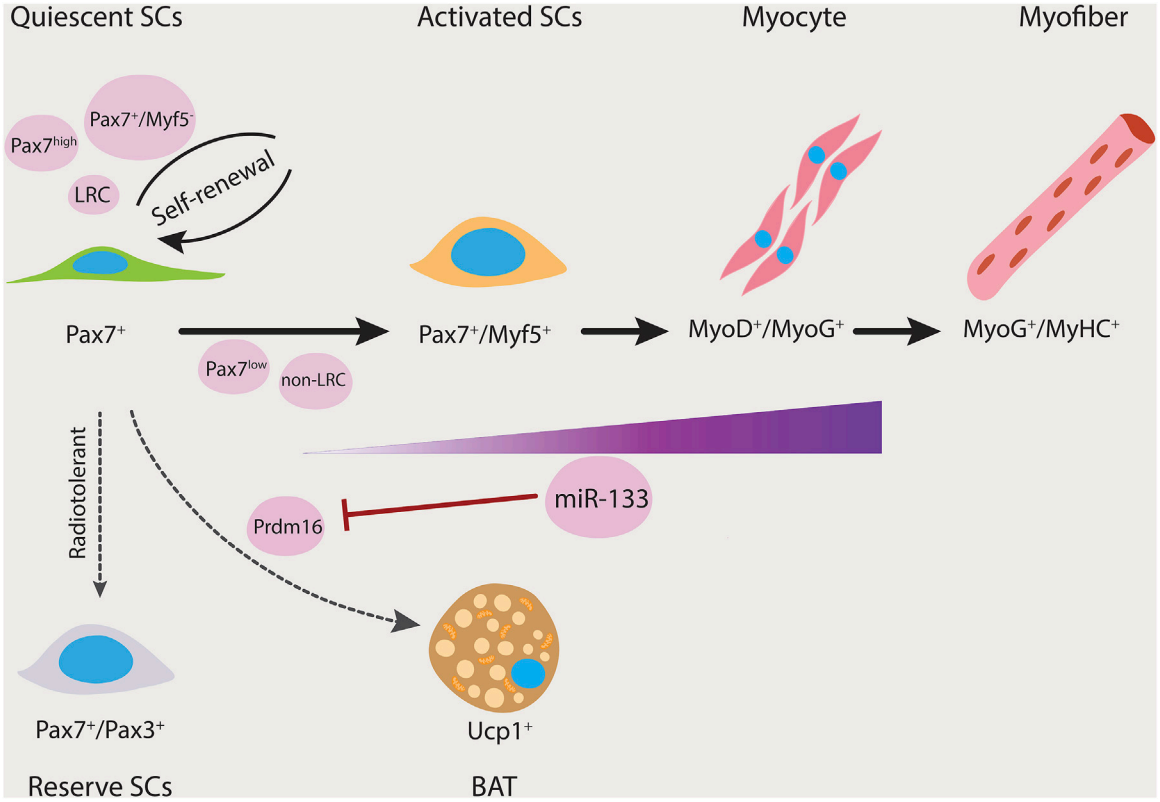


FIGURE 1
Satellite cell heterogeneity. Satellite cells can give rise to both myogenic and brown adipogenic lineages. miR-133 expression is upregulated as the myogenic program progresses. Prdm16 regulates satellite cell differentiation into brown adipocytes and its expression is inhibited by miR-133. Thereby, miR-133 controls brown adipose determination (dashed arrow). Subsets of satellite cells have differing functional potential (black arrows). $Pax7^{+}/Myf5^{-}$, $Pax7^{high}$, and long-term label-retaining populations have the ability to repopulate the stem cell pool. Furthermore, $Pax7^{+}/Pax3^{+}$ is a rare subpopulation that is resistant to radiation and contains reserve stem cell properties. LRC, label-retaining cells; non-LRC, non-label-retaining cells; SCs, satellite cells.

surface markers. They discovered two progenitor cell populations, P1 and P2, expressing either CD9 alone or both CD9 and CD104, respectively. Notably, the $CD9^{+}/CD104^{-}$ subpopulation demonstrated higher regenerative capacity upon transplantation into irradiated muscle, suggesting that they possess a greater self-renewal potential to replenish the satellite cell compartment (Porpiglia et al., 2017).

Accumulating evidence demonstrates that primary cilia are critical for satellite cell maintenance in a quiescent state. During quiescence, primary cilia are shown on MuSCc surfaces but rapidly disassembles upon activation and reassembles preferentially in self-renewing MuSCs (Jaafar Marican et al., 2016). Adult MuSCs devoid of primary cilia exhibit a defect in muscle regeneration, poor engraftment, and an increased cell cycle transcriptome signature. The histone deacetylase 6 (Hdac6) has been shown to promote the disassembly of the primary cilium (Palla et al., 2020). *In vitro* culture experiments demonstrated that tubastatin A (TubA), an agonist of Hdac6, inhibits primary cilium resorption, thereby maintaining satellite cells in their quiescent state and increasing their survival rate. Moreover, treatment of MuSCs with TubA improved engraftment potential upon transplantation (Arjona et al., 2022). In addition, data from our group demonstrated that primary cilia-mediated regulation of GLI3 transcription factor plays an important role in keeping the satellite cells in their dormant G0 state and inhibiting their activation (Brun et al., 2022).

Interestingly, our group has identified that satellite cells also represent heterogeneity with regard to their cell fate capacity (Yin et al., 2013). By clonal analysis, we identified that a subset of satellite cells is bi-potential, thereby being capable of generating myogenic progenitors, or alternatively, brown adipocytes. The switch from myogenic to brown adipogenic fates is regulated by microRNA-133 (miR-133). Downregulation of miR-133 results in upregulation of Prdm16, a brown adipose determination factor. Both muscle and brown adipose tissue (BAT) increase metabolic rates by regulating thermogenesis. Brown adipose is relatively rare in adult humans, and thus transplantation of BAT

or promoting endogenous production of BAT from satellite stem cells in muscle could provide a novel approach to stimulate BAT volume, regulate energy expenditure, and impair the development of obesity.

Altogether, multiple lines of evidence utilized transplantation experiments to demonstrate the heterogeneity of satellite cells and that satellite cells vary in their stemness and lineage commitment (Figure 1). However, the stemness properties between satellite stem cell subpopulations (e.g., $Pax7^{high}$, $Pax7^{+}/YFP^{-}$, and non-LRCs) or the differentiation potential between satellite myogenic cell subpopulations (e.g., $Pax7^{low}$, $Pax7^{+}/YFP^{+}$, and non-LRCs) are currently not known. With the emergence of single-cell technologies, one can delineate the differences between these subpopulations based on their gene expression and protein signatures, lineage commitment, and potentially reveal novel cell populations. It will also be interesting to explore the role of the subpopulations of satellite cells in fiber types specification. The lineage tracing mouse models would allow for flow cytometric purification of the satellite cell subtypes from any muscles. Transplanting these cell subtypes into a regenerating host muscle, then harvesting in 1 month, and immunostaining for terminally differentiated Myosin Heavy Chains (MyHC) would allow for the visualization of different muscle fiber types. This experiment would then determine the satellite cell subpopulations contribution to specific fiber types.

## Irradiation and injury-preconditioning the host environment for efficient transplantation

A number of studies have focused on approaches to generate a supportive environment within the skeletal muscle to enhance the engraftment efficiency of the transplanted cells. High dose irradiation of the host mouse muscle has been shown to be an effective preconditioning procedure for satellite stem cell transplantation (Morgan et al., 2002; Boldrin et al., 2012). Previous work has suggested that irradiation results in a substantial proliferation of the transplanted cells and their progeny (Beauchamp et al., 1999). It also promotes the transplanted cells to form high numbers of myofibers, and migration to neighbouring muscles is enhanced.

Subjecting *mdx* nude mice muscles to an 18 Gy dose of irradiation dramatically depletes the satellite cell pool while keeping the basal lamina intact and promoting cell engraftment. However, when the mice were subjected to a 25 Gy dose of irradiation, complete ablation of the host satellite cells resulted, thus impeding donor cell engraftment (Boldrin et al., 2012). This suggests in order to keep the host environment functional, it requires some viable host satellite cells to allow robust donor-derived engraftment to occur. While high dose irradiation is not feasible in a clinical setting, characterizing the pertaining molecular mechanisms could provide more clinically-appropriate strategies to alter the host muscle environment and ameliorate donor cell engraftment. Recent work from Morgan's group demonstrated that the innate immune response genes were upregulated 3 days after irradiation compared to non-irradiated muscles. Mice with defective innate immune response showed significantly less donor-derived cell engraftment compared to the control. Therefore, this study suggests that irradiation-mediated innate immune system activation plays an important role in increasing donor satellite cell engraftment. It would be of interest to elucidate what cell types are involved within the irradiated host muscle and the mechanism(s) by which they promote donor cell engraftment (Doreste et al., 2020).

In addition to irradiation, muscle pre-treatment regimes to induce injury such as mechanical injury (cryoinjury) (Le et al., 2016), injection of myotoxins (cardiotoxin and notexin) (Heslop et al., 2000; Garry et al., 2016), or chemical agent ($BaCl_2$) (Tierney and Sacco, 2016) are commonly used to augment engraftment. Myotoxins and $BaCl_2$ injure skeletal muscle by compound mechanisms that result in selective breakdown of endogenous myofiber membranes without affecting the blood vessels, nerves, or muscle fiber basal lamina (Couteaux et al., 1988; Harris, 2003). Notably, cryoinjury is the most damaging model resulting in depletion of satellite cells up to 96% and in the destruction of their environment, forming a "dead zone" lacking viable cells (Hardy et al., 2016).

A study published by Hardy and colleagues compared these different commonly used injury models in immune-competent mice (Hardy et al., 2016). It was found that all these injury models display similar necrosis at onset, and that a full regeneration was achieved 1 month after injury. They, however, demonstrated significant variation in parameters such as satellite cell survival and expansion, re-vascularization of the tissue, and immune profile during regeneration. Thereby each model represents a distinct regeneration profile. Interestingly, the production of the inflammatory cytokines in the cardiotoxin injury model was restored to normal levels once histological analysis of the muscle tissue revealed a complete regeneration. However, in the other models, despite a normal histological appearance, the expression level of cytokines was never returned to normal, suggesting prolonged inflammation. In another report (Silva-Barbosa et al., 2005), however, the level of inflammatory cell infiltration was higher in the host TA muscles of the cardiotoxin-treated immunocompromised mice when compared to that induced by cryoinjury. This study also found more transplanted donor cells after cryoinjury when compared to the cardiotoxin group. The authors thus claimed that the difference observed between the two injury models, can be at least partially, explained by the higher number of inflammatory cells following cardiotoxin-induced injury.

It has been demonstrated that the interaction of the satellite cell with inflammatory cells (mostly the macrophages) is crucial for efficient regeneration (Chazaud et al., 2003; Yang and Hu, 2018). In addition, most studies focusing on muscle injury models have been utilizing immune-competent mice, who display varying responses. Thus, it would be interesting to investigate the effect of these injury methods in immunodeficient mice, where inflammation may be suppressed. Taken together, while the muscle tissue is able to fully regenerate in all these injury models, one should consider that the alterations in the satellite cells microenvironment (niche) and the trajectories of the regenerative process vary considerably among these injury models. Thus, the preferred type of injury model depends on the study design and desired outcome.

Additionally, Olwin and his group (Hall et al., 2010) demonstrated that transplantation combined with an injury (Cardiotoxin or $BaCl_2$) modifies the host environment and results in a greater regenerative capacity in the engrafted satellite cells, thus eliciting an increase in muscle mass and muscle function. Similar observations have been made by our group (Price et al., 2014; Wang et al., 2019; Feige and Rudnicki, 2020) whereby the skeletal muscle transplantation experiments incorporated cardiotoxin injection of the host muscle prior to the transplantation, resulted in efficient engraftment into immunocompromised *mdx* recipient mice.

To further investigate the effect of the modulation of the host muscle environment on skeletal muscle stem cell regenerative potential, Morgan and colleagues (Meng et al., 2015) used human skeletal muscle-derived stem cell types in two immunodeficient mouse strains (*mdx* nude and $C5^-$/γ $chain^-$/$Rag2^-$) that had been subjected to either irradiation, or cryoinjury, or both. Cryoinjury or a combination of cryoinjury and irradiation resulted in higher muscle fibers of donor origin in both mouse strains, than by irradiation alone. An interesting finding was that when the two mouse strains were challenged with similar conditions, the $C5^-$/γ $chain^-$/$Rag2^-$ mice was shown to be a superior recipient mouse strain than *mdx* nude mice for transplantation of human muscle stem cells, mostly due to the fact that the $C5^-$/γ $chain^-$/Rag2 mice have a more profound immunodeficiency. This study revealed that the ability of the exogenous stem cells to contribute to muscle regeneration is affected by the different environments present in the recipient mouse strains and also is dependent on the types of modulations of the host muscle prior to cell transplantation (Meng et al., 2015).

Subsequently, the benefit of irradiation coupled with injury was further confirmed in transplantation assays of low numbers of hindlimb satellite cells (as few as 300 cells) with and without irradiation and showed that the contribution of satellite cells to repopulate the niche and form new myofibers were substantially reduced in the absence of irradiation (Arpke et al., 2021). Data from the irradiation-tolerant immunodeficient NOD-Rag (NRG) mice (Pearson et al., 2008) undergoing a high level of irradiation at 25 Gy in combination with cardiotoxin injection showed that this preconditioning of the host environment not only eliminated almost all of the host tissue of the mouse origin but also the development of hybrid human donor-murine host fibers (Sakellariou et al., 2016). Taken together, these observations support the notion that acute muscle injury in combination with irradiation as a strategy to induce changes in the cellular composition of the host environment prior to transplantation results in an extensive self-renewal to replenish the satellite cell pool and contribution to muscle repair (Figure 2).

## Assessing the success of engraftment

Optimizing stem cell-based transplantation assays requires a good understanding of their cellular kinetics, differentiation potential, and fate following engraftment. Therefore, reliable imaging assays play a critical role in the assessment of engraftment. The classical approach for evaluating engraftment in animals is the analysis of muscle histopathology. Donor-derived cells are typically genetically labeled with reporter genes encoding for the *GFP* gene, β-galactosidase gene (Asakura and Rudnicki, 2002; Asakura et al., 2007), or the alkaline phosphatase gene (Gerard et al., 2009). These reporter genes are typically introduced into cells using transfection or viral infection assays. Alternatively, the cells are derived from transgenic reporter mice carrying a transgene.

For example, primary myoblasts expressing tdTomato derived from transgenic *Pax7-CreER;R26R-tdTomato* mice after treatment with tamoxifen were transplanted into an immunocompromised host. Scoring for tdTomato + myofibers that represents fusion of the transplanted cells was performed 1 week following transplantation to provide insights into the behavior of the transplanted tdTomato + myoblasts (Bentzinger et al., 2014). In another example from our group, the TA muscle of immunocompromised *mdx* mice was pre-injured with cardiotoxin and transplanted with Pax7-ZsGreen expressing satellite cells freshly sorted from reporter mice (Price et al., 2014). The benefit of using *mdx* mouse model is that the restoration of dystrophin by transplanted donor stem cells can be assessed. To evaluate the efficacy of satellite cell transplantations in mice, Chakkalakal et al. (2014) used a novel lineage tracing system, the Tet-on-H2B-GFP transgenic reporter mice. H2B is a histone protein that plays a role in the DNA packaging of eukaryotic cells, thereby any H2B-GFP signal will be restricted to nucleus. This is crucial as the GFP signal will not diffuse through the muscle fibers once the H2B-$GFP^+$ cells have fused into the fibers. In addition, recent studies using endogenous reporter *Myf5-Cre/R26R-nTnG* mouse model allowed for discrimination between the committed satellite myogenic cells ($nGFP^{Pos}$) from satellite stem cells ($nTdT^{Pos}$) (Wang et al., 2019; Feige and Rudnicki, 2020).

The conventional histological analysis is, however, extremely challenging to quantify, time-consuming, and

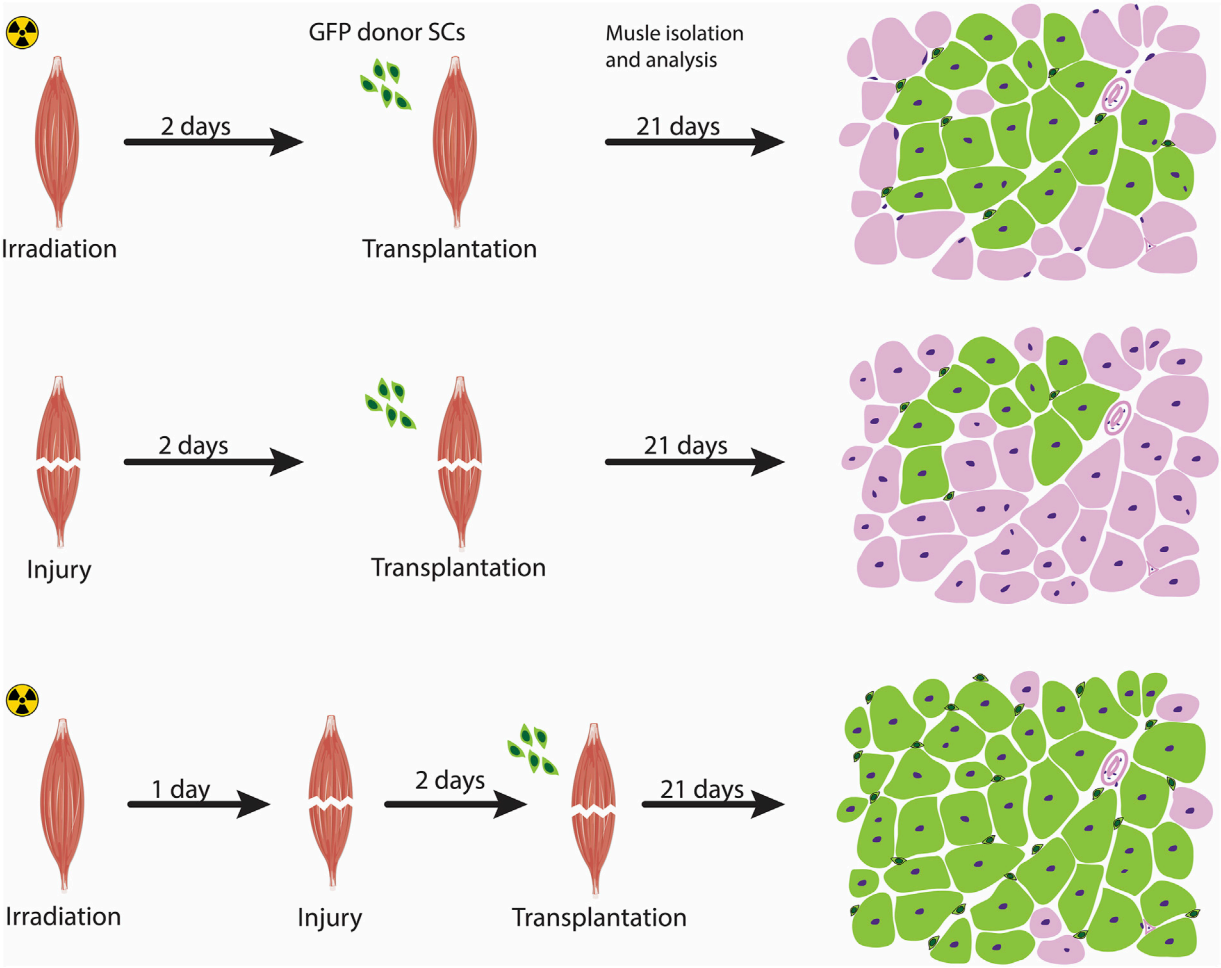


FIGURE 2
Preconditioning the host muscle environment prior to transplantation. Pre-treatment strategies to modulate the host muscle environment includes irradiation (top panel), injury-induced (middle panel), or a combination of irradiation and acute injury (bottom panel). Acute muscle injury combined with irradiation exhibit a high level of engraftment, as schematized by a transverse section of a transplanted muscle showing an increased contribution of fibers by transplanted cells (marked as green fibers) compared with the other two approaches. The Green cells surrounding the fibers represent satellite cells donor-derived cells that have undergone self-renewal.

dependent on sacrificing the experimental animals at different time points. Thus, over the past years, investigators sought non-invasive or minimally invasive methods. The Blau laboratory (Sacco et al., 2008) discovered a non-invasive *in vivo* bioluminescence imaging (BLI) technique to monitor muscle stem cells behaviour by crossing *Myf5-nLacZHet* mice with firefly luciferase (FLuc) transgenic mice. The BLI assay allows the dynamics of stem cell behavior to be evaluated in ways not feasible when using conventional histological approaches. For example, viability, proliferation, and engraftment of the donor-derived muscle stem cells can be monitored following transplantation until muscle homeostasis is reached. Additionally, the response of the stem cells to injury and their contribution to regeneration can be tracked over time without the need to sacrifice animals at different time point. Of note, the bioluminescence signal penetration depth is maximal (upto 2 cm) in the skin and muscle tissues and thus reduction in signal is not a limiting factor (Massoud and Gambhir, 2003). Interestingly, reports from Rando's group (Maguire et al., 2013; Filareto et al., 2018) described "regeneration and degeneration reporter" mice strains by conditionally expressing luciferase in satellite cells or in the myofiber of the skeletal muscle, respectively. Mating these mice with dystrophic mouse models, such as *mdx*, allowed for the assessment of disease progression directly in living animals overtime. These results collectively highlight the usefulness of luciferase reporter animals as quantitative and robust tools for the non-invasive long-term assessment of experimental therapeutic interventions for animal models of muscular dystrophy. We

note that although the histological analysis is technically challenging and time-consuming, it still offers certain advantages over BLI, in that it allows for tracing of multi-lineage commitment of satellite cell subtypes and exploring satellite cell heterogeneity.

## Approaches to overcome transplantation challenges

While satellite cells represent the ideal cell type to be utilized in transplantation assays not only because of their remarkable regenerative capacity but also their contribution to the satellite cell pool, a number of caveats limit their engraftment potential. Satellite cells' remarkable regenerative capacity is rapidly lost once they are isolated and expanded in culture. For instance, the engraftment ability of the mouse myoblasts grown *ex vivo* after 3 days in culture was significantly reduced (Montarras et al., 2005; Sacco et al., 2008). Similarly, growing canine primary myoblasts *in vitro* cultures demonstrated lower engraftment capacity compared with freshly isolated canine muscle stem cells (Parker et al., 2012). Expansion of human myoblasts *in vitro* prior to transplantation into DMD patients also resulted in a considerable reduction in engraftment efficiency and failure to contribute to the muscle stem cell reservoir (Gussoni et al., 1992; Bouchentouf et al., 2007). Therefore, a number of recent studies have been focusing in developing approaches to alleviate this problem to a certain extent. Remarkably, manipulation of biophysical properties, in terms of tissue stiffness, geometry, and extracellular matrix composition, helped researchers to develop culture systems to mimic the natural microenvironment of the satellite stem cell niche. In contrast to rigid plastic cell culture dishes, growing the satellite stem cells on soft hydrogels, which mimic the plastic module of muscle tissue, supports *in vitro* self-renewal and thus can help maintain engraftment and niche repopulation capacity (Gilbert et al., 2010). Moreover, bioengineering strategies have also been employed to enhance the delivery, survival, and maturation of transplanted cells following expansion. Generation of injectable, encapsulating 3D biomaterials, such as synthetic macromers (Han et al., 2018) and bioactive hydrogels (Quarta et al., 2017), that mimic the hierarchical structural organization of muscle and can be used to deliver growth factors has been shown to boost transplantation potential in *mdx* muscles.

Alternative approaches rely on supplementation of culture media with small molecules to modulate signaling pathways that aim to retain stemness properties while inhibiting terminal myogenic commitment. Work from our own lab has identified the Wnt7a/Fzd7/Vangl2 and EGFR/Aurka pathways as key modulators of the symmetric and asymmetric satellite stem cell divisions, respectively (Le Grand et al., 2009; Wang et al., 2019). Wnt7a and EGFR control satellite stem cell division in the myofiber niche by regulating centrosome recruitment. Wnt7a was shown to increase the pool of self-renewing stem cells by favoring symmetric division, while EGFR promotes asymmetric division and thus increases the pool of committed progenitors. EGF treatment *in vivo* rescued asymmetric divisions in dystrophin-deficient satellite stem cells, thereby stimulating the productive generation of myogenic progenitors and enhancing regeneration and muscle strength (Wang et al., 2019).

The ability of satellite cells to regenerate declines with age largely due to the decrease in their number and molecular changes in their niche. In aged animals, the Notch-p53 axis is downregulated, resulting in mitotic cell death and thus impaired muscle repair (Liu et al., 2018). In contrast, some key morphogenic signaling pathways, such as Wnt (Brack et al., 2007), JAK-STAT (Price et al., 2014), and TGFβ/pSmad3 (Carlson et al., 2008) are prematurely activated in aged muscle, causing inflammation and a defect in satellite cell proliferation. The application of heterochronic parabiosis strategies restored a more "youthful" calibration of these pathways in the aged satellite cells, and consequently promoted rejuvenation of the aged tissue and significant muscle regeneration (Conboy and Rando, 2012; Conboy et al., 2013). In addition, pharmacological targeting of the aged satellite cells to enhance or attenuate these signaling pathways in defined culture conditions, prior to their transplantation into old animals, contributed to new myofiber formation with enhanced efficiency than the control untreated satellite cells (Price et al., 2014; Liu et al., 2018; Mehdipour et al., 2019).

The limited migratory capacity of transplanted cells is another substantial issue associated with poor cell engraftment. Several strategies have been explored to enhance satellite cell migration upon intramuscular transplantation in mice, most of which involve the activation of specific signaling pathways. We showed that Wnt7a regulated the motility of the satellite cells through activation of noncanonical Wnt signaling, thereby improving donor cell engraftment ability and increasing muscle strength upon transplantation into dystrophic muscles (Bentzinger et al., 2014). Coinjection of mouse pro-inflammatory macrophages along with satellite cells or myoblasts showed improved donor-derived regeneration, which was attributed to improved donor cell proliferation, migration, and delayed differentiation (Lesault et al., 2012; Rybalko et al., 2015). miR-708 is a quiescence-specific mirtron that acts as a downstream target of Notch signaling to repress Tensin3 and thus maintain satellite cells within their quiescent niche. Tensin3 is a major component of focal adhesion (FA)-associated proteins that play a critical role in regulating cell adhesion and migration. Therefore, Notch signaling maintains satellite cell quiescence by antagonizing the migratory machinery. It thus remains interesting to further investigate whether downregulation of

Notch signaling and hence miR-708 would result in increased migration capacity of the satellite cells and thereby enhanced engraftment efficiency (Baghdadi et al., 2018).

## Concluding remarks and perspectives

Satellite cells are the critical cellular source for muscle regeneration, and hence they are the most promising means in cell engraftment assays. As discussed in this review, they possess self-renewal and myogenic differentiation potential, and can be easily identified based on their location and molecular signature. Moreover, growing evidence indicates that the satellite cell population is not homogenous and that the transplantation approaches involving them provide an important tool to understand their fate decisions and heterogeneity *in vivo*. Additionally, studies using single-cell technologies in combination with transplantation approaches can represent promising avenues to further investigate the heterogeneity of the satellite cell compartment. This can help identify novel subpopulations and delineate a myogenic trajectory from quiescent stem cells to committed progenitors *in vivo* in skeletal muscle. Therefore, such studies will be valuable to characterize satellite cell regulation to gain a deeper understanding of the components of homeostasis and the regeneration capabilities of skeletal muscle.

Significant progress has been made in recent years in the isolation of satellite cells, leading to the extensive characterization of human satellite cells and their transplantation (Garcia et al., 2017). The transplantation of human satellite cells into mice demonstrated that these cells can successfully integrate with irradiated host muscles to produce muscle fibers and self-renew (Marg et al., 2014). The ability to grow human muscle fibers in a host animal can be helpful for many research applications, including the study of their cellular heterogeneity and the potential development and testing of therapeutics in preclinical models.

## Author contributions

BH conceptualized and wrote the review article. MR edited the review article.

## Funding

The studies from the Rudnicki lab were carried out with the support of grants from the Canadian Institutes of Health Research [FDN-148387], the US National Institutes for Health [R01AR044031], E-Rare-3 (Canadian Institutes of Health Research/Muscular Dystrophy Canada), the Foundation for Gene & Cell Therapy, and the Stem Cell Network.

## Acknowledgments

We thank David Datzkiw for assistance with the illustrations, John Saber for critical reading of the manuscript.

## Conflict of interest

The authors declare that the research was conducted in the absence of any commercial or financial relationships that could be construed as a potential conflict of interest.

## Publisher's note



## References

Arjona, M., Goshayeshi, A., Rodriguez-Mateo, C., Brett, J. O., Both, P., Ishak, H., et al. (2022). Tubastatin A maintains adult skeletal muscle stem cells in a quiescent state *ex vivo* and improves their engraftment ability *in vivo*. *Stem Cell Rep.* 17 (1), 82–95. doi:10.1016/j.stemcr.2021.11.012

Arpke, R. W., Shams, A. S., Collins, B. C., Larson, A. A., Lu, N., Lowe, D. A., et al. (2021). Preservation of satellite cell number and regenerative potential with age reveals locomotory muscle bias. *Skelet. Muscle* 11 (1), 22. doi:10.1186/s13395-021-00277-2

Asakura, A., Hirai, H., Kablar, B., Morita, S., Ishibashi, J., Piras, B. A., et al. (2007). Increased survival of muscle stem cells lacking the MyoD gene after transplantation into regenerating skeletal muscle. *Proc. Natl. Acad. Sci. U. S. A.* 104 (42), 16552–16557. doi:10.1073/pnas.0708145104

Asakura, A., and Rudnicki, M. A. (2002). Side population cells from diverse adult tissues are capable of *in vitro* hematopoietic differentiation. *Exp. Hematol.* 30 (11), 1339–1345. doi:10.1016/s0301-472x(02)00954-2

Baghdadi, M. B., Firmino, J., Soni, K., Evano, B., Di Girolamo, D., Mourikis, P., et al. (2018). Notch-induced miR-708 antagonizes satellite cell migration and maintains quiescence. *Cell Stem Cell* 23 (6), 859–868. doi:10.1016/j.stem.2018.09.017

Beauchamp, J. R., Morgan, J. E., Pagel, C. N., and Partridge, T. A. (1999). Dynamics of myoblast transplantation reveal a discrete minority of precursors with stem cell-like properties as the myogenic source. *J. Cell Biol.* 144 (6), 1113–1122. doi:10.1083/jcb.144.6.1113

Bentzinger, C. F., Wang, Y. X., and Rudnicki, M. A. (2012). Building muscle: Molecular regulation of myogenesis. *Cold Spring Harb. Perspect. Biol.* 4 (2), a008342. doi:10.1101/cshperspect.a008342

Bentzinger, C. F., von Maltzahn, J., Dumont, N. A., Stark, D. A., Wang, Y. X., Nhan, K., et al. (2014). Wnt7a stimulates myogenic stem cell motility and engraftment resulting in improved muscle strength. *J. Cell Biol.* 205 (1), 97–111. doi:10.1083/jcb.201310035

Boldrin, L., Neal, A., Zammit, P. S., Muntoni, F., and Morgan, J. E. (2012). Donor satellite cell engraftment is significantly augmented when the host niche is preserved and endogenous satellite cells are incapacitated. *Stem Cells* 30 (9), 1971–1984. doi:10.1002/stem.1158

Boppart, M. D., De Lisio, M., Zou, K., and Huntsman, H. D. (2013). Defining a role for non-satellite stem cells in the regulation of muscle repair following exercise. *Front. Physiol.* 4, 310. doi:10.3389/fphys.2013.00310

Bouchentouf, M., Skuk, D., and Tremblay, J. P. (2007). Early and massive death of myoblasts transplanted into skeletal muscle: Responsible factors and potential solutions. *Curr. Opin. Organ Transpl.* 12, 664–667. doi:10.1097/MOT.0b013e3282f19f20

Brack, A. S., Conboy, M. J., Roy, S., Lee, M., Kuo, C. J., Keller, C., et al. (2007). Increased Wnt signaling during aging alters muscle stem cell fate and increases fibrosis. *Science* 317 (5839), 807–810. doi:10.1126/science.1144090

Brun, C. E., Sincennes, M. C., Lin, A. Y. T., Hall, D., Jarassier, W., Feige, P., et al. (2022). GLI3 regulates muscle stem cell entry into GAlert and self-renewal. *Nat. Commun.* 13 (1), 3961. doi:10.1038/s41467-022-31695-5

Carlson, M. E., Hsu, M., and Conboy, I. M. (2008). Imbalance between pSmad3 and Notch induces CDK inhibitors in old muscle stem cells. *Nature* 454 (7203), 528–532. doi:10.1038/nature07034

Chakkalakal, J. V., Jones, K. M., Basson, M. A., and Brack, A. S. (2012). The aged niche disrupts muscle stem cell quiescence. *Nature* 490 (7420), 355–360. doi:10.1038/nature11438

Chakkalakal, J. V., Christensen, J., Xiang, W., Tierney, M. T., Boscolo, F. S., Sacco, A., et al. (2014). Early forming label-retaining muscle stem cells require p27kip1 for maintenance of the primitive state. *Development* 141 (8), 1649–1659. doi:10.1242/dev.100842

Challen, G. A., Bertoncello, I., Deane, J. A., Ricardo, S. D., and Little, M. H. (2006). Kidney side population reveals multilineage potential and renal functional capacity but also cellular heterogeneity. *J. Am. Soc. Nephrol.* 17 (7), 1896–1912. doi:10.1681/ASN.2005111228

Chazaud, B., Sonnet, C., Lafuste, P., Bassez, G., Rimaniol, A. C., Poron, F., et al. (2003). Satellite cells attract monocytes and use macrophages as a support to escape apoptosis and enhance muscle growth. *J. Cell Biol.* 163 (5), 1133–1143. doi:10.1083/jcb.200212046

Collins, C. A., Olsen, I., Zammit, P. S., Heslop, L., Petrie, A., Partridge, T. A., et al. (2005). Stem cell function, self-renewal, and behavioral heterogeneity of cells from the adult muscle satellite cell niche. *Cell* 122 (2), 289–301. doi:10.1016/j.cell.2005.05.010

Conboy, I. M., and Rando, T. A. (2012). Heterochronic parabiosis for the study of the effects of aging on stem cells and their niches. *Cell Cycle* 11 (12), 2260–2267. doi:10.4161/cc.20437

Conboy, M. J., Conboy, I. M., and Rando, T. A. (2013). Heterochronic parabiosis: Historical perspective and methodological considerations for studies of aging and longevity. *Aging Cell* 12 (3), 525–530. doi:10.1111/acel.12065

Cottle, B. J., Lewis, F. C., Shone, V., and Ellison-Hughes, G. M. (2017). Skeletal muscle-derived interstitial progenitor cells (PICs) display stem cell properties, being clonogenic, self-renewing, and multi-potent *in vitro* and *in vivo*. *Stem Cell Res. Ther.* 8 (1), 158. doi:10.1186/s13287-017-0612-4

Couteaux, R., Mira, J. C., and d'Albis, A. (1988). Regeneration of muscles after cardiotoxin injury. I. Cytological aspects. *Biol. Cell* 62 (2), 171–182. doi:10.1111/j.1768-322x.1988.tb00719.x

Dellavalle, A., Sampaolesi, M., Tonlorenzi, R., Tagliafico, E., Sacchetti, B., Perani, L., et al. (2007). Pericytes of human skeletal muscle are myogenic precursors distinct from satellite cells. *Nat. Cell Biol.* 9 (3), 255–267. doi:10.1038/ncb1542

Doreste, B., Torelli, S., and Morgan, J. (2020). Irradiation dependent inflammatory response may enhance satellite cell engraftment. *Sci. Rep.* 10 (1), 11119. doi:10.1038/s41598-020-68098-9

Dunn, A., Talovic, M., Patel, K., Patel, A., Marcinczyk, M., and Garg, K. (2019). Biomaterial and stem cell-based strategies for skeletal muscle regeneration. *J. Orthop. Res.* 37 (6), 1246–1262. doi:10.1002/jor.24212

Evano, B., Khalilian, S., Le Carrou, G., Almouzni, G., and Tajbakhsh, S. (2020). Dynamics of asymmetric and symmetric divisions of muscle stem cells *in vivo* and on artificial niches. *Cell Rep.* 30 (10), 3195–3206. doi:10.1016/j.celrep.2020.01.097

Feige, P., Brun, C. E., Ritso, M., and Rudnicki, M. A. (2018). Orienting muscle stem cells for regeneration in homeostasis, aging, and disease. *Cell Stem Cell* 23 (5), 653–664. doi:10.1016/j.stem.2018.10.006

Feige, P., and Rudnicki, M. A. (2020). Isolation of satellite cells and transplantation into mice for lineage tracing in muscle. *Nat. Protoc.* 15 (3), 1082–1097. doi:10.1038/s41596-019-0278-8

Filareto, A., Maguire-Nguyen, K., Gan, Q., Aldanondo, G., Machado, L., Chamberlain, J. S., et al. (2018). Monitoring disease activity noninvasively in the mdx model of Duchenne muscular dystrophy. *Proc. Natl. Acad. Sci. U. S. A.* 115 (30), 7741–7746. doi:10.1073/pnas.1802425115

Foudi, A., Hochedlinger, K., Van Buren, D., Schindler, J. W., Jaenisch, R., Carey, V., et al. (2009). Analysis of histone 2B-GFP retention reveals slowly cycling hematopoietic stem cells. *Nat. Biotechnol.* 27 (1), 84–90. doi:10.1038/nbt.1517

Garcia, S. M., Tamaki, S., Xu, X., and Pomerantz, J. H. (2017). Human satellite cell isolation and xenotransplantation. *Methods Mol. Biol.* 1668, 105–123. doi:10.1007/978-1-4939-7283-8_8

Garry, G. A., Antony, M. L., and Garry, D. J. (2016). Cardiotoxin induced injury and skeletal muscle regeneration. *Methods Mol. Biol.* 1460, 61–71. doi:10.1007/978-1-4939-3810-0_6

Gerard, X., Vignaud, L., Charles, S., Pinset, C., Scherman, D., Kichler, A., et al. (2009). Real-time monitoring of cell transplantation in mouse dystrophic muscles by a secreted alkaline phosphatase reporter gene. *Gene Ther.* 16 (6), 815–819. doi:10.1038/gt.2009.28

Gilbert, P. M., Havenstrite, K. L., Magnusson, K. E., Sacco, A., Leonardi, N. A., Kraft, P., et al. (2010). Substrate elasticity regulates skeletal muscle stem cell self-renewal in culture. *Science* 329 (5995), 1078–1081. doi:10.1126/science.1191035

Gurevich, D. B., Nguyen, P. D., Siegel, A. L., Ehrlich, O. V., Sonntag, C., Phan, J. M., et al. (2016). Asymmetric division of clonal muscle stem cells coordinates muscle regeneration *in vivo*. *Science* 353 (6295), aad9969. doi:10.1126/science.aad9969

Gussoni, E., Pavlath, G. K., Lanctot, A. M., Sharma, K. R., Miller, R. G., Steinman, L., et al. (1992). Normal dystrophin transcripts detected in Duchenne muscular dystrophy patients after myoblast transplantation. *Nature* 356 (6368), 435–438. doi:10.1038/356435a0

Hall, J. K., Banks, G. B., Chamberlain, J. S., and Olwin, B. B. (2010). Prevention of muscle aging by myofiber-associated satellite cell transplantation. *Sci. Transl. Med.* 2 (57), 57ra83. doi:10.1126/scitranslmed.3001081

Han, W. M., Anderson, S. E., Mohiuddin, M., Barros, D., Nakhai, S. A., Shin, E., et al. (2018). Synthetic matrix enhances transplanted satellite cell engraftment in dystrophic and aged skeletal muscle with comorbid trauma. *Sci. Adv.* 4 (8), eaar4008. doi:10.1126/sciadv.aar4008

Hardy, D., Besnard, A., Latil, M., Jouvion, G., Briand, D., Thepenier, C., et al. (2016). Comparative study of injury models for studying muscle regeneration in mice. *PLoS One* 11 (1), e0147198. doi:10.1371/journal.pone.0147198

Harris, J. B. (2003). Myotoxic phospholipases A2 and the regeneration of skeletal muscles. *Toxicon* 42 (8), 933–945. doi:10.1016/j.toxicon.2003.11.011

Heslop, L., Morgan, J. E., and Partridge, T. A. (2000). Evidence for a myogenic stem cell that is exhausted in dystrophic muscle. *J. Cell Sci.* 113 (12), 2299–2308. doi:10.1242/jcs.113.12.2299

Jaafar Marican, N. H., Cruz-Migoni, S. B., and Borycki, A. G. (2016). Asymmetric distribution of primary cilia allocates satellite cells for self-renewal. *Stem Cell Rep.* 6 (6), 798–805. doi:10.1016/j.stemcr.2016.04.004

Joe, A. W., Yi, L., Natarajan, A., Le Grand, F., So, L., Wang, J., et al. (2010). Muscle injury activates resident fibro/adipogenic progenitors that facilitate myogenesis. *Nat. Cell Biol.* 12 (2), 153–163. doi:10.1038/ncb2015

Kitajima, Y., and Ono, Y. (2018). Visualization of PAX7 protein dynamics in muscle satellite cells in a YFP knock-in-mouse line. *Skelet. Muscle* 8 (1), 26. doi:10.1186/s13395-018-0174-x

Kuang, S., Kuroda, K., Le Grand, F., and Rudnicki, M. A. (2007). Asymmetric self-renewal and commitment of satellite stem cells in muscle. *Cell* 129 (5), 999–1010. doi:10.1016/j.cell.2007.03.044

Le, G., Lowe, D. A., and Kyba, M. (2016). Freeze injury of the tibialis anterior muscle. *Methods Mol. Biol.* 1460, 33–41. doi:10.1007/978-1-4939-3810-0_3

Le Grand, F., Jones, A. E., Seale, V., Scime, A., and Rudnicki, M. A. (2009). Wnt7a activates the planar cell polarity pathway to drive the symmetric expansion of satellite stem cells. *Cell Stem Cell* 4 (6), 535–547. doi:10.1016/j.stem.2009.03.013

Lepper, C., Partridge, T. A., and Fan, C. M. (2011). An absolute requirement for Pax7-positive satellite cells in acute injury-induced skeletal muscle regeneration. *Development* 138 (17), 3639–3646. doi:10.1242/dev.067595

Lesault, P. F., Theret, M., Magnan, M., Cuvellier, S., Niu, Y., Gherardi, R. K., et al. (2012). Macrophages improve survival, proliferation and migration of engrafted myogenic precursor cells into MDX skeletal muscle. *PLoS One* 7 (10), e46698. doi:10.1371/journal.pone.0046698

Liu, L., Charville, G. W., Cheung, T. H., Yoo, B., Santos, P. J., Schroeder, M., et al. (2018). Impaired Notch signaling leads to a decrease in p53 activity and mitotic catastrophe in aged muscle stem cells. *Cell Stem Cell* 23 (4), 544–556. doi:10.1016/j.stem.2018.08.019

Maesner, C. C., Almada, A. E., and Wagers, A. J. (2016). Established cell surface markers efficiently isolate highly overlapping populations of skeletal muscle satellite

cells by fluorescence-activated cell sorting. *Skelet. Muscle* 6, 35. doi:10.1186/s13395-016-0106-6

Maguire, K. K., Lim, L., Speedy, S., and Rando, T. A. (2013). Assessment of disease activity in muscular dystrophies by noninvasive imaging. *J. Clin. Invest.* 123 (5), 2298–2305. doi:10.1172/JCI68458

Marg, A., Escobar, H., Gloy, S., Kufeld, M., Zacher, J., Spuler, A., et al. (2014). Human satellite cells have regenerative capacity and are genetically manipulable. *J. Clin. Invest.* 124 (10), 4257–4265. doi:10.1172/JCI63992

Massoud, T. F., and Gambhir, S. S. (2003). Molecular imaging in living subjects: Seeing fundamental biological processes in a new light. *Genes Dev.* 17 (5), 545–580. doi:10.1101/gad.1047403

Mauro, A. (1961). Satellite cell of skeletal muscle fibers. *J. Biophys. Biochem. Cytol.* 9, 493–495. doi:10.1083/jcb.9.2.493

Mehdipour, M., Etienne, J., Chen, C. C., Gathwala, R., Rehman, M., Kato, C., et al. (2019). Rejuvenation of brain, liver and muscle by simultaneous pharmacological modulation of two signaling determinants, that change in opposite directions with age. *Aging (Albany NY)* 11 (15), 5628–5645. doi:10.18632/aging.102148

Meng, J., Bencze, M., Asfahani, R., Muntoni, F., and Morgan, J. E. (2015). The effect of the muscle environment on the regenerative capacity of human skeletal muscle stem cells. *Skelet. Muscle* 5, 11. doi:10.1186/s13395-015-0036-8

Montarras, D., Morgan, J., Collins, C., Relaix, F., Zaffran, S., Cumano, A., et al. (2005). Direct isolation of satellite cells for skeletal muscle regeneration. *Science* 309 (5743), 2064–2067. doi:10.1126/science.1114758

Morgan, J. E., Gross, J. G., Pagel, C. N., Beauchamp, J. R., Fassati, A., Thrasher, A. J., et al. (2002). Myogenic cell proliferation and generation of a reversible tumorigenic phenotype are triggered by preirradiation of the recipient site. *J. Cell Biol.* 157 (4), 693–702. doi:10.1083/jcb.200108047

Murphy, M. M., Lawson, J. A., Mathew, S. J., Hutcheson, D. A., and Kardon, G. (2011). Satellite cells, connective tissue fibroblasts and their interactions are crucial for muscle regeneration. *Development* 138 (17), 3625–3637. doi:10.1242/dev.064162

Palla, A. R., Hilgendorf, K. I., Yang, A. V., Kerr, J. P., Hinken, A. C., Demeter, J., et al. (2020). *Ciliation of muscle stem cells is critical to maintain regenerative capacity and is lost during aging*. bioRxiv 2020.03.20.000943. doi:10.1101/2020.03.20.000943

Parker, M. H., Loretz, C., Tyler, A. E., Duddy, W. J., Hall, J. K., Olwin, B. B., et al. (2012). Activation of Notch signaling during *ex vivo* expansion maintains donor muscle cell engraftment. *Stem Cells* 30 (10), 2212–2220. doi:10.1002/stem.1181

Partridge, T. A., Morgan, J. E., Coulton, G. R., Hoffman, E. P., and Kunkel, L. M. (1989). Conversion of mdx myofibres from dystrophin-negative to -positive by injection of normal myoblasts. *Nature* 337 (6203), 176–179. doi:10.1038/337176a0

Pasut, A., Oleynik, P., and Rudnicki, M. A. (2012). Isolation of muscle stem cells by fluorescence activated cell sorting cytometry. *Methods Mol. Biol.* 798, 53–64. doi:10.1007/978-1-61779-343-1_3

Pearson, T., Shultz, L. D., Miller, D., King, M., Laning, J., Fodor, W., et al. (2008). Non-obese diabetic-recombination activating gene-1 (NOD-Rag1 null) interleukin (IL)-2 receptor common gamma chain (IL2r gamma null) null mice: A radioresistant model for human lymphohaematopoietic engraftment. *Clin. Exp. Immunol.* 154 (2), 270–284. doi:10.1111/j.1365-2249.2008.03753.x

Peault, B., Rudnicki, M., Torrente, Y., Cossu, G., Tremblay, J. P., Partridge, T., et al. (2007). Stem and progenitor cells in skeletal muscle development, maintenance, and therapy. *Mol. Ther.* 15 (5), 867–877. doi:10.1038/mt.sj.6300145

Porpiglia, E., Samusik, N., Ho, A. T. V., Cosgrove, B. D., Mai, T., Davis, K. L., et al. (2017). High-resolution myogenic lineage mapping by single-cell mass cytometry. *Nat. Cell Biol.* 19 (5), 558–567. doi:10.1038/ncb3507

Price, F. D., von Maltzahn, J., Bentzinger, C. F., Dumont, N. A., Yin, H., Chang, N. C., et al. (2014). Inhibition of JAK-STAT signaling stimulates adult satellite cell function. *Nat. Med.* 20 (10), 1174–1181. doi:10.1038/nm.3655

Quarta, M., Cromie, M., Chacon, R., Blonigan, J., Garcia, V., Akimenko, I., et al. (2017). Bioengineered constructs combined with exercise enhance stem cell-mediated treatment of volumetric muscle loss. *Nat. Commun.* 8, 15613. doi:10.1038/ncomms15613

Rocheteau, P., Gayraud-Morel, B., Siegl-Cachedenier, I., Blasco, M. A., and Tajbakhsh, S. (2012). A subpopulation of adult skeletal muscle stem cells retains all template DNA strands after cell division. *Cell* 148 (1-2), 112–125. doi:10.1016/j.cell.2011.11.049

Rocheteau, P., Gayraud-Morel, B., Siegl-Cachedenier, I., Blasco Maria, A., and Tajbakhsh, S. (2012). A subpopulation of adult skeletal muscle stem cells retains all template DNA strands after cell division. *Cell* 148 (1-2), 112–125. doi:10.1016/j.cell.2011.11.049

Rybalko, V., Hsieh, P. L., Merscham-Banda, M., Suggs, L. J., and Farrar, R. P. (2015). The development of macrophage-mediated cell therapy to improve skeletal muscle function after injury. *PLoS One* 10 (12), e0145550. doi:10.1371/journal.pone.0145550

Sacco, A., Doyonnas, R., Kraft, P., Vitorovic, S., and Blau, H. M. (2008). Self-renewal and expansion of single transplanted muscle stem cells. *Nature* 456 (7221), 502–506. doi:10.1038/nature07384

Sakellariou, P., O'Neill, A., Mueller, A. L., Stadler, G., Wright, W. E., Roche, J. A., et al. (2016). Neuromuscular electrical stimulation promotes development in mice of mature human muscle from immortalized human myoblasts. *Skelet. Muscle* 6, 4. doi:10.1186/s13395-016-0078-6

Sambasivan, R., Yao, R., Kissenpfennig, A., Van Wittenberghe, L., Paldi, A., Gayraud-Morel, B., et al. (2011). Pax7-expressing satellite cells are indispensable for adult skeletal muscle regeneration. *Development* 138 (17), 3647–3656. doi:10.1242/dev.067587

Scaramozza, A., Park, D., Kollu, S., Beerman, I., Sun, X., Rossi, D. J., et al. (2019). Lineage tracing reveals a subset of reserve muscle stem cells capable of clonal expansion under stress. *Cell Stem Cell* 24 (6), 944–957. doi:10.1016/j.stem.2019.03.020

Seale, P., Sabourin, L. A., Girgis-Gabardo, A., Mansouri, A., Gruss, P., and Rudnicki, M. A. (2000). Pax7 is required for the specification of myogenic satellite cells. *Cell* 102 (6), 777–786. doi:10.1016/s0092-8674(00)00066-0

Silva-Barbosa, S. D., Butler-Browne, G. S., Di Santo, J. P., and Mouly, V. (2005). Comparative analysis of genetically engineered immunodeficient mouse strains as recipients for human myoblast transplantation. *Cell Transpl.* 14 (7), 457–467. doi:10.3727/000000005783982837

Tierney, M. T., and Sacco, A. (2016). Inducing and evaluating skeletal muscle injury by notexin and barium chloride. *Methods Mol. Biol.* 1460, 53–60. doi:10.1007/978-1-4939-3810-0_5

von Maltzahn, J., Jones, A. E., Parks, R. J., and Rudnicki, M. A. (2013). Pax7 is critical for the normal function of satellite cells in adult skeletal muscle. *Proc. Natl. Acad. Sci. U. S. A.* 110 (41), 16474–16479. doi:10.1073/pnas.1307680110

Wang, Y. X., Feige, P., Brun, C. E., Hekmatnejad, B., Dumont, N. A., Renaud, J. M., et al. (2019). EGFR-aurka signaling rescues polarity and regeneration defects in dystrophin-deficient muscle stem cells by increasing asymmetric divisions. *Cell Stem Cell* 24 (3), 419–432. doi:10.1016/j.stem.2019.01.002

Yang, W., and Hu, P. (2018). Skeletal muscle regeneration is modulated by inflammation. *J. Orthop. Transl.* 13, 25–32. doi:10.1016/j.jot.2018.01.002

Yin, H., Pasut, A., Soleimani, V. D., Bentzinger, C. F., Antoun, G., Thorn, S., et al. (2013). MicroRNA-133 controls Brown adipose determination in skeletal muscle satellite cells by targeting Prdm16. *Cell Metab.* 17 (2), 210–224. doi:10.1016/j.cmet.2013.01.004

# Advantages of publishing in Frontiers

**OPEN ACCESS**
Articles are free to read for greatest visibility and readership

**FAST PUBLICATION**
Around 90 days from submission to decision

**HIGH QUALITY PEER-REVIEW**
Rigorous, collaborative, and constructive peer-review

**TRANSPARENT PEER-REVIEW**
Editors and reviewers acknowledged by name on published articles

**Frontiers**
Avenue du Tribunal-Fédéral 34
1005 Lausanne | Switzerland

**Visit us:** www.frontiersin.org
**Contact us:** frontiersin.org/about/contact

**REPRODUCIBILITY OF RESEARCH**
Support open data and methods to enhance research reproducibility

**DIGITAL PUBLISHING**
Articles designed for optimal readership across devices

**FOLLOW US**
@frontiersin

**IMPACT METRICS**
Advanced article metrics track visibility across digital media

**EXTENSIVE PROMOTION**
Marketing and promotion of impactful research

**LOOP RESEARCH NETWORK**
Our network increases your article's readership